



minerals

Special Issue Reprint

Genesis and Evolution of Pb-Zn-Ag Polymetallic Deposits

Edited by
Yitian Wang and Changqing Zhang

mdpi.com/journal/minerals



Genesis and Evolution of Pb-Zn-Ag Polymetallic Deposits

Genesis and Evolution of Pb-Zn-Ag Polymetallic Deposits

Editors

Yitian Wang

Changqing Zhang



Basel • Beijing • Wuhan • Barcelona • Belgrade • Novi Sad • Cluj • Manchester

Editors

Yitian Wang
Chinese Academy of
Geological Sciences
Beijing
China

Changqing Zhang
Chinese Academy of
Geological Sciences
Beijing
China

Editorial Office

MDPI AG
Grosspeteranlage 5
4052 Basel, Switzerland

This is a reprint of articles from the Special Issue published online in the open access journal *Minerals* (ISSN 2075-163X) (available at: https://www.mdpi.com/journal/minerals/special_issues/III1YVZ6CM9).

For citation purposes, cite each article independently as indicated on the article page online and as indicated below:

Lastname, A.A.; Lastname, B.B. Article Title. <i>Journal Name</i> Year , Volume Number, Page Range.
--

ISBN 978-3-7258-2271-3 (Hbk)

ISBN 978-3-7258-2272-0 (PDF)

doi.org/10.3390/books978-3-7258-2272-0

© 2024 by the authors. Articles in this book are Open Access and distributed under the Creative Commons Attribution (CC BY) license. The book as a whole is distributed by MDPI under the terms and conditions of the Creative Commons Attribution-NonCommercial-NoDerivs (CC BY-NC-ND) license.

Contents

Yitian Wang and Changqing Zhang

Editorial for Special Issue “Genesis and Evolution of Pb-Zn-Ag Polymetallic Deposits”

Reprinted from: *Minerals* **2024**, *14*, 494, doi:10.3390/min14050494 1

Jiangpeng Shi, Guang Wu, Gongzheng Chen, Fei Yang, Tong Zhang, Biao Jiang and Wen Yuan Liu

Genesis of the Supergiant Shuangjianzishan Ag–Pb–Zn Deposit in the Southern Great Xing’an Range, NE China: Constraints from Geochronology, Isotope Geochemistry, and Fluid Inclusion

Reprinted from: *Minerals* **2024**, *14*, 60, doi:10.3390/min14010060 3

Shihui Li, Zhenxiang Li, Gongzheng Chen, Huineng Yi, Fei Yang, Xin Lü, et al.

Age, Fluid Inclusion, and H–O–S–Pb Isotope Geochemistry of the Superlarge Huaaobaote Ag–Pb–Zn Deposit in the Southern Great Xing’an Range, NE China

Reprinted from: *Minerals* **2023**, *13*, 939, doi:10.3390/min13070939 34

Dengfei Duan, Haobo Jia and Yue Wu

Origin of the Yinshan Pb-Zn-Ag Deposit in the Edong District Section of the Middle–Lower Yangtze River Metallogenic Belt: Insights from In-Situ Sulfur Isotopes

Reprinted from: *Minerals* **2023**, *13*, 810, doi:10.3390/min13060810 64

Qiaoqing Hu, Yitian Wang, Shaocong Chen, Ran Wei, Xielu Liu, Junchen Liu, et al.

Genesis of the Dongtangzi Zn-Pb Deposit of the Fengxian–Taibai Ore Cluster in West Qinling, China: Constraints from Rb-Sr and Sm-Nd Geochronology, and In Situ S-Pb Isotopes

Reprinted from: *Minerals* **2024**, *14*, 297, doi:10.3390/min14030297 80

Ruiting Wang, Zhenjia Pang, Qingfeng Li, Geli Zhang, Jiafeng Zhang, Huan Cheng, et al.

Metallogenic Model and Prospecting Progress of the Qiangongshan–Dongtangzi Large Pb-Zn Deposit, Fengtai Orefield, West Qinling Orogeny

Reprinted from: *Minerals* **2023**, *13*, 1163, doi:10.3390/min13091163 109

Lei Wang, Runsheng Han, Yan Zhang and Xiaodong Li

Mixing in Two Types of Fluids Responsible for Some Carbonate-Hosted Pb–Zn Deposits, SW China: Insights from the Maoping Deposit

Reprinted from: *Minerals* **2023**, *13*, 600, doi:10.3390/min13050600 137

Yongsheng Yao, Hongsheng Gong, Runsheng Han, Changqing Zhang, Peng Wu and Gang Chen

Metallogenesis and Formation of the Maliping Pb-Zn Deposit in Northeastern Yunnan: Constraints from H-O Isotopes, Fluid Inclusions, and Trace Elements

Reprinted from: *Minerals* **2023**, *13*, 780, doi:10.3390/min13060780 158

Ye Qian, Lixiang Zhao and Jinlei Sun

Geology, Fluid Inclusions, and C–H–O–S–Pb Isotope Geochemistry of Pb–Zn Deposits within the Tuotuohe Region of the Tibetan Plateau: Implications for Ore Genesis

Reprinted from: *Minerals* **2023**, *13*, 762, doi:10.3390/min13060762 179

Xinyu Wang, Shulai Wang, Huiqiong Zhang, Yuwang Wang, Xinyou Zhu and Xing Yang

Geochemical Characteristics of the Mineral Assemblages from the Niukutou Pb-Zn Skarn Deposit, East Kunlun Mountains, and Their Metallogenic Implications

Reprinted from: *Minerals* **2023**, *13*, 18, doi:10.3390/min13010018 209

Jana Ulmanová, Zdeněk Dolníček, Pavel Škácha and Jiří Sejkora

Origin of Zn-Pb Mineralization of the Vein Bt23C, Bytíz Deposit, Příbram Uranium and Base-Metal Ore District, Czech Republic: Constraints from Occurrence of Immiscible Aqueous–Carbonic Fluids

Reprinted from: *Minerals* **2024**, *14*, 87, doi:10.3390/min14010087 **234**

Editorial

Editorial for Special Issue “Genesis and Evolution of Pb-Zn-Ag Polymetallic Deposits”

Yitian Wang * and Changqing Zhang

MNR Key Laboratory of Metallogeny and Mineral Assessment, Institute of Mineral Resources, Chinese Academy of Geological Sciences, Beijing 100037, China; zcchangqing@163.com

* Correspondence: wyt69@263.net

Pb-Zn-Ag polymetallic deposits are complex and diverse. In the last dozen years or so, applications of high resolution in situ analytical techniques have contributed to a better understanding of the genesis and evolution of Pb-Zn-Ag polymetallic deposits. The contributions of this Special Issue report new data using state-of-the-art analytical techniques for Pb-Zn-Ag deposits, mainly from China, and with one from the Czech Republic.

The studied deposits from China include the main metallogenic belts from the southern Great Xing’an Range in NE China, the middle-lower reaches of Yangtze River in east China, the West Qinling orogen in central China, the Sichuan-Yunnan-Guizhou region and the Tibetan Plateau in SW China, and the East Kunlun Mountains in west China. The Shuangjianshan Ag-Pb-Zn deposit, located in the Great Xing’an Range metallogenic belt, is the largest Ag deposit in China. New geochronologic, isotope geochemical, and fluid inclusion data from Shuangjianshan’s Xinglongshan ore block [1] indicate that the ore-forming fluids were predominantly a mixture of Cretaceous magmatic and meteoric water, with fluid mixing as the dominant mechanism for mineral precipitation. The Huaobaote Ag-Pb-Zn deposit was also formed during the Early Cretaceous Epoch (136.3–134.3 Ma). The ore-forming fluid was dominantly a mixture of magmatic and meteoric water, with fluid mixing, cooling, and immiscibility as the primary mechanisms for mineral precipitation [2]. The Yinshan Pb-Zn-Ag deposit is located in the Middle-Lower Reaches of Yangtze River metallogenic belt. In situ sulfur isotopes imply that the mineralization was related to a granite of ~130 Ma [3].

The Fengxian-Taibai (abbr. Fengtai) ore field in the West Qinling orogen is an important Pb-Zn producer in China. Most previous studies suggested that the Pb-Zn mineralization resulted from Devonian sedimentary-exhalative processes. New geochronologic, stable and radiogenic isotopic, and trace element data indicate that the representative Qiangtang-Dongtangzi Pb-Zn deposit is not the product of sedimentary-exhalative processes, but is rather the product of epigenetic magmatic hydrothermal fluid processes, driven by regional tectono-magmatic activities in the Late Triassic Epoch [4,5].

The Sichuan-Yunnan-Guizhou metallogenic belt, located on the western margin of the Yangtze Block, includes over 400 carbonate-hosted Pb-Zn-Ag deposits. The fluid inclusion and H-O-He-Ar isotopic data suggests that ore-forming fluids in the Maoping deposit are the result of mixing of metamorphic fluids from the Precambrian basement and basinal brines from the Youjiang Basin [6]. Similarly, the new data from the Maliping deposit suggest that the ore-forming fluids are derived from the mixing of deep sourced fluids flowing through the basement and organic-bearing basinal brines [7].

Studies of Pb-Zn deposits in the Tuotuohe region located on the northern Qiangtang Block of the Tibetan Plateau demonstrate that the ore-forming fluids are of medium-low temperature, medium-low salinity, and low density. They are the result of mixing of Cenozoic magmatic and meteoric water modified by wall-rock interactions. The ore-forming metals were transported in solution as chloride complexes and precipitated as a consequence of cooling, fluid mixing/dilution, and fluid-rock reactions [8].

Citation: Wang, Y.; Zhang, C. .

Editorial for Special Issue “Genesis and Evolution of Pb-Zn-Ag Polymetallic Deposits”. *Minerals* **2024**, *14*, 494.

<https://doi.org/10.3390/min14050494>

Received: 18 April 2024

Revised: 3 May 2024

Accepted: 6 May 2024

Published: 7 May 2024



Copyright: © 2024 by the authors. Licensee MDPI, Basel, Switzerland. This article is an open access article distributed under the terms and conditions of the Creative Commons Attribution (CC BY) license (<https://creativecommons.org/licenses/by/4.0/>).

To the north of the Tibetan Plateau stand the Kunlun Mountains, and the Niukutou Pb-Zn skarn deposit is located in the East Kunlun. This deposit resulted from early hydrothermal fluids that migrated from deep plutons to the shallow marble, during which time these fluids evolved from high f_{O_2} and high temperatures to low f_{O_2} and low temperatures, as well as increasing pH and Mn contents [9].

The Příbram ore district within the Bohemian massif in the west-central Czech Republic is renowned for its uranium deposits, but Pb-Zn-Ag polymetallic deposits are also important. The study on the Bt23C Zn-Pb vein of the Bytíz deposit reveals three complex types/sources of aqueous fluids: early high temperature and high salinity fluids from an unspecified deep source, followed by low salinity and low temperature waters, likely infiltrating from overlying evaporated freshwater piedmont basins; and late high-salinity chloridic solutions that may be either externally derived marine brines, or local shield brines [10].

The genesis and evolution of Pb-Zn-Ag polymetallic deposits are unlikely to be elucidated completely in the near future, so more precise and systematic studies are needed to further advance our understanding of Pb-Zn-Ag polymetallic mineralization.

Conflicts of Interest: The authors declare no conflict of interest.

References

1. Shi, J.P.; Wu, G.; Chen, G.Z.; Yang, F.; Zhang, T.; Jiang, B.; Liu, W.Y. Genesis of the Supergiant Shuangjianzishan Ag–Pb–Zn Deposit in the Southern Great Xing’an Range, NE China: Constraints from Geochronology, Isotope Geochemistry, and Fluid Inclusion. *Minerals* **2024**, *14*, 60. [CrossRef]
2. Li, S.H.; Li, Z.X.; Chen, G.Z.; Yi, H.N.; Yang, F.; Lü, X.; Shi, J.P.; Dou, H.B.; Wu, G. Age, Fluid Inclusion, and H–O–S–Pb Isotope Geochemistry of the Superlarge Huaaobaote Ag–Pb–Zn Deposit in the Southern Great Xing’an Range, NE China. *Minerals* **2023**, *13*, 939. [CrossRef]
3. Duan, D.F.; Jia, H.B.; Wu, Y. Origin of the Yinshan Pb-Zn-Ag Deposit in the Edong District Section of the Middle–Lower Yangtze River Metallogenic Belt: Insights from In-Situ Sulfur Isotopes. *Minerals* **2023**, *13*, 810. [CrossRef]
4. Hu, Q.Q.; Wang, Y.T.; Chen, S.C.; Wei, R.; Liu, X.L.; Liu, J.C.; Wang, R.T.; Gao, W.H.; Wang, C.A.; Tang, M.J.; et al. Genesis of the Dongtangzi Zn-Pb Deposit of the Fengxian–Taibai Ore Cluster in West Qinling, China: Constraints from Rb-Sr and Sm-Nd Geochronology, and In Situ S-Pb Isotopes. *Minerals* **2024**, *14*, 297. [CrossRef]
5. Wang, R.T.; Pang, J.G.; Li, Q.F.; Zhang, G.L.; Zhang, J.F.; Cheng, H.; Wu, W.T.; Yang, H.B. Metallogenic Model and Prospecting Progress of the Qiandongshan–Dongtangzi Large Pb-Zn Deposit, Fengtai Orefield, West Qinling Orogeny. *Minerals* **2023**, *13*, 1163. [CrossRef]
6. Wang, L.; Han, R.S.; Zhang, Y.; Li, X.D. Mixing in Two Types of Fluids Responsible for Some Carbonate-Hosted Pb–Zn Deposits, SW China: Insights from the Maoping Deposit. *Minerals* **2023**, *13*, 600. [CrossRef]
7. Yao, Y.S.; Gong, H.S.; Han, R.S.; Zhang, C.Q.; Wu, P.; Chen, G. Metallogenesis and Formation of the Maliping Pb-Zn Deposit in Northeastern Yunnan: Constraints from H-O Isotopes, Fluid Inclusions, and Trace Elements. *Minerals* **2023**, *13*, 780. [CrossRef]
8. Qian, Y.; Zhao, L.X.; Sun, J.L. Geology, Fluid Inclusions, and C–H–O–S–Pb Isotope Geochemistry of Pb–Zn Deposits within the Tuotuohe Region of the Tibetan Plateau: Implications for Ore Genesis. *Minerals* **2023**, *13*, 762. [CrossRef]
9. Wang, X.Y.; Wang, S.L.; Zhang, H.Q.; Wang, Y.W.; Zhu, X.Y.; Yang, X. Geochemical Characteristics of the Mineral Assemblages from the Niukutou Pb-Zn Skarn Deposit, East Kunlun Mountains, and Their Metallogenic Implications. *Minerals* **2023**, *13*, 18. [CrossRef]
10. Ulmanová, J.; Dolníček, Z.; Škácha, P.; Sejkora, J. Origin of Zn-Pb Mineralization of the Vein Bt23C, Bytíz Deposit, Příbram Uranium and Base-Metal Ore District, Czech Republic: Constraints from Occurrence of Immiscible Aqueous–Carbonic Fluids. *Minerals* **2024**, *14*, 87. [CrossRef]

Disclaimer/Publisher’s Note: The statements, opinions and data contained in all publications are solely those of the individual author(s) and contributor(s) and not of MDPI and/or the editor(s). MDPI and/or the editor(s) disclaim responsibility for any injury to people or property resulting from any ideas, methods, instructions or products referred to in the content.

Article

Genesis of the Supergiant Shuangjanzishan Ag–Pb–Zn Deposit in the Southern Great Xing’an Range, NE China: Constraints from Geochronology, Isotope Geochemistry, and Fluid Inclusion

Jiangpeng Shi ^{1,2}, Guang Wu ^{1,2,3,*}, Gongzheng Chen ³, Fei Yang ^{1,2}, Tong Zhang ⁴, Biao Jiang ¹ and Wenyuan Liu ⁵

- ¹ MNR Key Laboratory of Metallogeny and Mineral Assessment, Institute of Mineral Resources, Chinese Academy of Geological Sciences, Beijing 100037, China; shijiangpeng@stu.pku.edu.cn (J.S.); yangfeixt@126.com (F.Y.); jiangbiao334223@163.com (B.J.)
- ² School of Earth and Space Sciences, Peking University, Beijing 100871, China
- ³ College of Earth Sciences, Hebei GEO University, Shijiazhuang 050031, China; a86793604@163.com
- ⁴ Inner Mongolia Institute of Geological Survey, Hohhot 010020, China; zhangtnm@126.com
- ⁵ The Provincial Key Laboratory of Mineral Resources, College of Zijin Mining, Fuzhou University, Fuzhou 350108, China; 15146@163.com
- * Correspondence: wuguang65@163.com

Abstract: The supergiant Shuangjanzishan (SJS) Ag–Pb–Zn deposit, located in the southern Great Xing’an Range (SGXR), is the largest Ag deposit in China. The SJS deposit can be divided into two ore blocks: the Shuangjanzishan ore block and the Xinglongshan ore block. Given the importance of the Xinglongshan ore block in the SJS deposit, our work is focused on the Xinglongshan ore block. The vein orebodies in the Xinglongshan ore block mainly occur in the NW-, NNW-, and NNE-trending fault zones, and its mineralization is mainly related to a deep concealed syenogranite. Here, we present new geochronology, isotope geochemistry, and fluid inclusion data for the Xinglongshan ore block and provide additional insights into the metallogenic mechanism of the deposit. The dating results show that the syenogranite related to the mineralization formed at approximately 137 Ma, which is coherent with some previous age determinations in sulfides from the ore deposit. The mineralization of the Xinglongshan ore block can be divided into four stages: sphalerite–arsenopyrite–pyrite–chalcopyrite–quartz stage (stage I), sphalerite–galena–pyrite–silver-bearing mineral–quartz stage (stage II), sphalerite–galena–silver-bearing mineral–quartz–calcite stage (stage III), and weakly mineralized quartz–calcite stage (stage IV). Four types of fluid inclusions (FIs) have been identified within quartz and calcite veins: liquid-rich, gas-rich, pure-liquid, and pure-gas FIs. The homogenization temperatures in the four stages exhibit a gradual decrease, with stage I ranging from 253 to 302 °C, stage II from 203 to 268 °C, stage III from 184 to 222 °C, and stage IV from 153 to 198 °C, respectively. The salinity for stages I, II, III, and IV falls within the ranges of 3.4–6.6 wt% NaCl eqv., 2.6–7.2 wt% NaCl eqv., 2.9–7.0 wt% NaCl eqv., and 1.2–4.8 wt% NaCl eqv., respectively, indicative of a low-salinity ore-forming fluid. The $\delta^{18}\text{O}_{\text{water}}$ and δD values of the ore-forming fluid span from -13.9‰ to 7.4‰ and -145‰ to -65‰ , with $\delta^{13}\text{C}_{\text{V-PDB}}$ values between -11.0‰ and -7.9‰ . These values suggest that the ore-forming fluid predominantly originated from a mixture of magmatic and meteoric water. The $^{206}\text{Pb}/^{204}\text{Pb}$, $^{207}\text{Pb}/^{204}\text{Pb}$, and $^{208}\text{Pb}/^{204}\text{Pb}$ ratios of sulfides range from 18.278 to 18.361, 15.530 to 15.634, and 38.107 to 38.448, respectively. These ratios imply that the ore-forming material was primarily derived from the Early Cretaceous granitic magma, which resulted from the mixing of depleted mantle- and crustal-derived magmas. The fluid mixing was the dominant mechanism for mineral precipitation. The Xinglongshan ore block belongs to a magmatic-hydrothermal vein-type deposit related to the Early Cretaceous syenogranite, and the Shuangjanzishan ore block belongs to an intermediate sulfidation epithermal deposit related to coeval subvolcanic rocks. The Ag–Pb–Zn mineralization at Shuangjanzishan is genetically related to the Early Cretaceous volcanic–intrusive complex.

Citation: Shi, J.; Wu, G.; Chen, G.; Yang, F.; Zhang, T.; Jiang, B.; Liu, W. Genesis of the Supergiant Shuangjanzishan Ag–Pb–Zn Deposit in the Southern Great Xing’an Range, NE China: Constraints from Geochronology, Isotope Geochemistry, and Fluid Inclusion. *Minerals* **2024**, *14*, 60. <https://doi.org/10.3390/min14010060>

Academic Editor: Giorgio Garuti

Received: 21 October 2023

Revised: 28 December 2023

Accepted: 28 December 2023

Published: 3 January 2024



Copyright: © 2024 by the authors. Licensee MDPI, Basel, Switzerland. This article is an open access article distributed under the terms and conditions of the Creative Commons Attribution (CC BY) license (<https://creativecommons.org/licenses/by/4.0/>).

Keywords: zircon U–Pb age; fluid inclusion; H–O–C–Pb isotopes; volcanic–intrusive complex; Shuangjianzishan Ag–Pb–Zn deposit; southern Great Xing’an Range

1. Introduction

Silver (Ag), lead (Pb), and zinc (Zn) are widely developed in different genetic types of deposits [1–3]. The Ag–Pb–Zn deposits in the world can be divided into the following genetic types: (1) volcanic-hosted massive sulfide (VHMS or VMS) deposit [4–6]; (2) sedimentary exhalative (SEDEX) deposit [7–9]; (3) carbonate-hosted Mississippi Valley type (MVT) deposit [10]; (4) skarn-type deposit [11–13]; (5) magmatic-hydrothermal vein-type deposit [14,15]; and (6) epithermal deposit [16–18]. In addition, a few researchers have identified porphyry-type Ag–Pb–Zn deposits [19]. The vein-type Ag–Pb–Zn deposits occupy an important position in the global supply of Ag and base metals of Pb–Zn [18] and have become the hotspot of deposit research in the world. The southern Great Xing’an Range (SGXR), located in the eastern section of the Central Asian Orogenic Belt, spanning approximately 600 km in the northeast direction with a width of around 200 km [20–23], represents the preeminent Ag–Pb–Zn–Sn metallogenic belt in northern China. To date, forty-two Pb–Zn–Ag deposits have been discovered in the SGXR (Figure 1a,b), boasting proven reserves totaling 8,130,000 tons of Pb + Zn and 57,000 tons of Ag [21,24–26]. This area is distinguished by three types of Pb–Zn–Ag deposits: skarn type, subvolcanic-related vein type, and intrusion-related vein type (as depicted in Figure 1b). Some of these deposits also exhibit the presence of Cu and Sn, such as the Hua’aobaote deposit [26]. The ore-forming element assemblages of these deposits are mainly Ag–Pb–Zn, Ag–Pb–Zn–Cu, and Ag–Pb–Zn–Sn–Cu [21,27]. Recently, many studies have shown that the mineralization age of these deposits and the formation age of magmatic rocks related to mineralization are concentrated in the Late Jurassic to Early Cretaceous, suggesting that the mineralization is closely related to the late Yanshanian magmatic activity in the SGXR [22,28–32]. Among these Ag–Pb–Zn deposits in the SGXR, the Shuangjianzishan (SJS) deposit is the largest one, and it contains proven reserves of 15,214 tons Ag, 392,200 tons Pb, and 1,523,000 tons Zn, with average grades of 139.3 g/t Ag, 1.03% Pb, and 1.46% Zn, respectively, making this deposit the largest Ag deposit in China [18,33]. According to the classification criteria for the size of Zn–Pb–Ag deposits proposed by Large et al. [8,34], the SJS deposit belongs to a supergiant deposit.

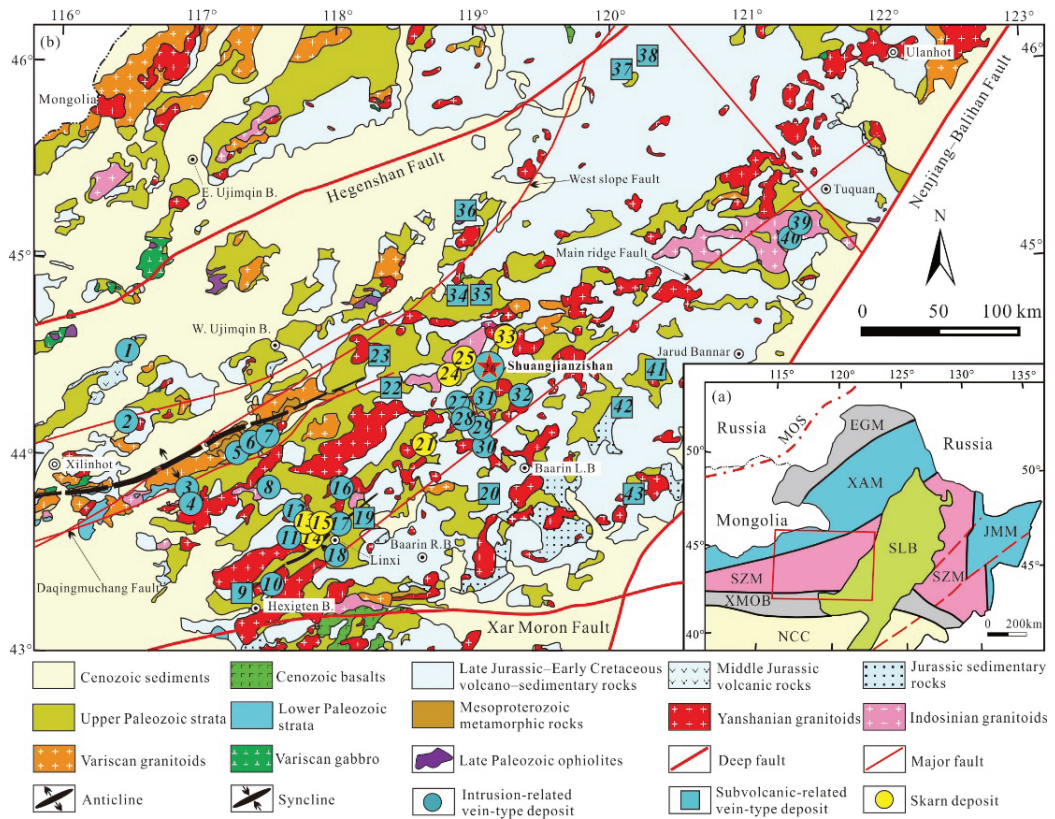


Figure 1. (a) Simplified geotectonic division of NE China (after [35]); (b) geological map of the southern Great Xing’an Range, highlighting the key Pb–Zn–Ag polymetallic deposit locations (modified after [27,36]). Notes: MOS = Mongol–Okhotsk suture zone; EGM = Ergun massif; SLB = Songliao basin; JMM = Jiamusi massif; SZM = Songnen–Zhangguangcai Range massif; NCC = North China craton; XMOB = Xar Moron orogenic belt; XAM = Xing’an massif. Detailed names of Pb–Zn–Ag–polymetallic deposits marked with numbers: 1 = Baiyinchagandongshan; 2 = Maodeng–Xiaogushan; 3 = Aobaoshan; 4 = Harchulutu; 5 = Bayanwula; 6 = Weilasituo; 7 = Bairendaba; 8 = Anle; 9 = Shidi; 10 = Dadi; 11 = Yonglong; 12 = Huangtuliang; 13 = Hadatu; 14 = Nasitai; 15 = Shalonggou; 16 = Xishi-jiangshan; 17 = Erbadi; 18 = Bianjiadayuan; 19 = Dajing; 20 = Hongguangmchang; 21 = Daihuanggou; 22 = Chaowula; 23 = Wulanbaiqi; 24 = Baiyinnuoer; 25 = Nailinba; 26 = Shuangjianzishan; 27 = Agui-hundelun; 28 = Baiyinwula; 29 = Biliutaibe; 30 = Taipingdi; 31 = Erdaoyingzi; 32 = Dongshan; 33 = Haobugao; 34 = Bujinhei; 35 = Shabulengshan; 36 = Huaaobaote; 37 = Zhamuqin; 38 = Fuxingtun; 39 = Meng’entaolegai; 40 = Maohuduger; 41 = Shuiquan; 42 = Aobaotui; 43 = Panjiaduan.

Previous researchers have extensively investigated the SJS deposit, covering a range of aspects such as the geological characteristics of the deposit [33], geochronology and petrogeochemistry of ore-forming rocks [18,37,38], mineralogical assemblages [39], and the origins of ore-forming fluids and materials [18,40]. Nonetheless, the mineralization age and the ore genesis of the SJS deposit still remain controversial. The mineralization age of the SJS deposit, as investigated by previous researchers, falls within a wide range of 160–130 Ma [18,24,27,33,37,39,40]. Furthermore, there is an ongoing debate regarding the types of mineralization in the SJS deposit, which primarily revolves around two main types: the epithermal type [18,37] and the magmatic-hydrothermal vein type [27,33]. Further study is needed on the origin and evolution of ore-forming fluids, source of ore-forming

materials, mechanisms of metal precipitation, and genetic types of the SJS deposit. In this study, we present new data concerning the zircon U–Pb age, fluid inclusions, and H–O–C–Pb isotopes associated with the SJS deposit. These various data are used to decipher the source, feature, and evolution of the ore-forming fluid and to explore the metallogenic mechanism. As a result, we are able to constrain the genesis of the SJS Ag–Pb–Zn deposit.

2. Regional Geology

The SGXR is located in the central section of the Songnen–Zhangguangcai Range block (SZM, Figure 1a), and four boundaries of the east, west, north, and south are the Nenjiang–Balihan fault, East Ujimqin Banner–Xilinhot belt, Hegenshan fault, and Xar Moron fault, respectively. The SGXR underwent sequential tectonic control from the Paleo-Asian Ocean in the Paleozoic, followed by the Mongol–Okhotsk Ocean and Paleo-Pacific tectonic domains in the Mesozoic [27,41,42]. These tectonic transitions are documented as intricate geodynamic processes marked by multiple tectonic events. The geological formations visible in the SGXR comprise the Mesoproterozoic metamorphic rock series, Paleozoic marine volcanic–clastic rocks, Paleozoic continental clastic rocks, Mesozoic continental volcanic–clastic rocks, as well as Cenozoic basalt, and Quaternary loose sediment (Figure 1b). Prominent geological structures within the SGXR encompass the Ganzhuermiao anticline, Linxi syncline, Hegenshan fault, and Xar Moron fault, which originated during the Late Paleozoic [43,44], and the Nenjiang–Balihan fault formed during the Mesozoic [45,46], which constitute the basic tectonic framework of the SGXR. This region underwent widespread Variscan, Indosinian, and Yashanian volcanic and intrusive activity, and different types of granitoids emplaced at different stages are widely distributed. Most importantly, the Mesozoic I- and A-type granitoids comprise > 20% of the surface area in the SGXR [14], which was triggered by the subduction of the Paleo-Pacific plate, making the eastern Asian Mesozoic continental margin the most important metallogenic area [18]. Numerous studies showed that the Jurassic subduction of the Paleo-Pacific plate led to the extension of the back-arc area and the lithospheric delamination and that the subsequent rollback of the subduction plate triggered the large-scale emplacement of the Early Cretaceous volcanic–intrusive complex [47,48].

The SGXR hosts a number of intrusion-related vein types, subvolcanic-related vein types, and skarn-type polymetallic (Ag–Pb–Zn–Cu–Sn) deposits [18,22,27]. Regional mineralization is spatially and temporally closely related to the Jurassic to Cretaceous volcanic–intrusive complex [40]. These deposits are predominantly distributed along an approximately 600-km-long and 200-km-wide zone of NE-trending and are mainly hosted by the Permian strata and Mesozoic granites. With the discoveries of a large number of new Ag–Pb–Zn deposits recently [28,49], the Ag–Pb–Zn–Sn–Cu metallogenic belt of the SGXR has become more important.

3. Ore District and Deposit Geology

3.1. Ore District Geology

The supergiant SJS Ag–Pb–Zn deposit (44°29′30″–44°31′30″ N, 119°03′30″–119°10′00″ E) is located in the north of Baarin Left Banner, Chifeng City, Inner Mongolia Autonomous Region, which is tectonically located in the central part of the Songnen–Zhangguangcai Range massif (Figure 1a). The exposed lithological units in the SJS ore district can be seen in Figure 2.

The Permian strata, including the Shoushangou, Dashizhai, Zhesi, and Linxi formations, are mainly composed of marine clastic rocks and intermediate–felsic volcanic rocks, with a small amount of continental calstic rocks. The ore bodies of the SJS deposit are mainly hosted in the Dashizhai Formation, which is predominantly characterized by marine thick sandstone layers, along with andesite, silty slate, altered andesite, basalt, and andesitic tuff, with a total thickness exceeding 900 m. The Mesozoic strata, including the Xinmin, Manketouebo, Manitu, and Baiyin’gaolao formations, are mainly composed of continental intermediate–felsic volcanic rocks and pyroclastic rocks with a small amount of calstic rocks. The Yanshanian granites are exposed 2 km northwest of the SJS deposit and

lie concealed in the central part of the ore district. The concealed granite bodies revealed by deep drilling include biotite granite, syenogranite, and granite. In addition, granite porphyry, diorite porphyry, and rhyolite porphyry occur as NW- or NE-trending veins, dipping SW at ~60° and typically measuring up to 300 m long and 8 m wide, some of which are crosscut by Ag–Pb–Zn mineralized veins. The main structures in the ore district include the NE-trending Yaoerya–Pangjiawan anticline, NW-trending fracture zone, and NNE- and NW-trending faults.

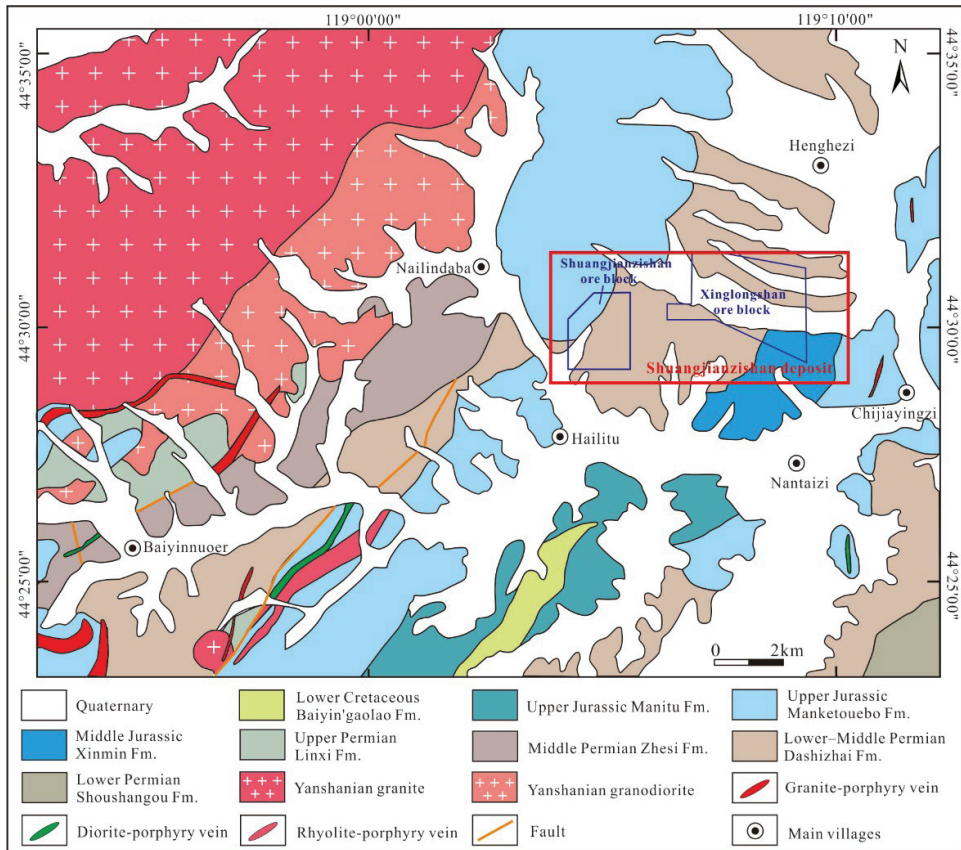


Figure 2. Simplified regional geological map of the Shuangjianzishan area (modified after [25,33]).

3.2. Ore Deposit Geology

The SJS Ag–Pb–Zn deposit was discovered in 2013 and was divided into two ore blocks, namely the western ore block (Shuangjianzishan ore block) and the eastern ore block (Xinglongshan ore block) [18] (Figure 2). The Xinglongshan ore block accounts for the vast majority of the total reserves of the SJS deposit [18,33]. A total of 276 industrial orebodies have been delineated in the block, including 39 large-sized, 32 medium-sized, and 205 small-sized orebodies [18,33]. However, only 4 industrial orebodies, including 1 medium-sized and 3 small-sized orebodies, have been delineated in the Shuangjianzishan ore block [18,33].

3.2.1. Xinglongshan Ore Block

The exposed strata in the Xinglongshan ore block include the Lower–Middle Permian Dashizhai Formation, Middle Jurassic Xinmin Formation, and Upper Jurassic Manketouebo

Formation (Figure 3a). Except for a small amount of rhyolite porphyry veins exposed on the surface, other granitic intrusions, including granite, biotite granite, and syenogranite, are all concealed below 500 m of the ore block surface (Figure 3a,c). The fault structures, including NE-, NW-, and NNE-trending faults, are well-developed (Figure 3a). According to the direction of orebodies, the orebodies in the Xinglongshan ore block are mainly divided into (1) NW-trending Ag–Pb–Zn (Cu) ore vein group, (2) NNW-trending Ag–Pb–Zn orebodies, and (3) NNE-trending Ag–Pb–Zn orebodies. In addition, small amounts of near E–W-trending Au-bearing Ag–Pb–Zn orebodies are also developed in this ore block.

- (1) The NW-trending Ag–Pb–Zn (Cu) ore vein group: The orebodies in the ore vein group distributed in the central and eastern parts of the ore block are controlled by a NW-trending thick and large fractured zone. The ore-hosting rocks are slate and silty slate of the Lower–Middle Permian Dashizhai Formation (Figure 3b). The overall strike of the ore-vein group is 300° – 310° , inclined towards the southwest, with dip angles of 50° – 65° and a length > 2000 m and a width > 1200 m. The ore-vein group is mainly composed of Ag–Pb–Zn orebodies and Ag–Zn orebodies, with a small amount of Zn orebodies and Ag–Cu–Pb–Zn orebodies (Figure 3b). The individual orebodies occur as veins, usually having a length of 100–800 m and a thickness of 1–10 m, with a maximum thickness exceeding 100 m (Figure 3b). The ore structure is mainly of fine-vein, stockwork, disseminated, and dense disseminated (Figure 4a–d). The major wall-rock alteration includes silicification and chloritization, with minor sericitization (Figure 4a–d). These altered minerals mainly occur in the form of fine veins and stockworks within a thick NW-trending alteration zone, with minor veins and crumbs of quartz. The grade of the Ag–Pb–Zn orebodies is relatively low, with average grades of 98 g/t Ag, 1.6% Zn, and 0.6% Pb, respectively [23]. The Ag–Cu–Pb–Zn orebodies usually occur at the top of the ore-vein group, with a controlled length greater than 300 m and a thickness of 0.6–2.8 m. The Ag–Cu–Pb–Zn orebodies have average grades of 263 g/t Ag, 0.7% Cu, 2.2% Zn, and 0.9% Pb, respectively [23].
- (2) The NNW-trending Ag–Pb–Zn orebodies: These orebodies, mainly distributed in the central and eastern parts of the ore block, are controlled by NNW-trending faults. The overall trend of these orebodies is approximately 310° , with a thickness of 3–15 m and a length of > 400 m. The ore structure is mainly of massive and vein (Figure 4e,f). The wall-rock alteration is characterized by silicification and carbonation, with minor chloritization, and quartz and calcite mainly occur as fine veins within the orebodies and within a range of no more than two meters nearby (Figure 4e,f). The NW-trending Ag–Pb–Zn orebodies have average grades of 400 g/t Ag (some up to 10,000 g/t), 2.8% Zn, and 4.3% Pb, respectively [23].
- (3) The NNE-trending Ag–Pb–Zn orebodies: These orebodies, distributed in the eastern part of the ore block, are composed of five parallel orebodies. They are controlled by NNE-trending faults, which dip to NWW at $> 65^{\circ}$. The ore structure is mainly of massive and vein (Figure 4g,h). The types and distribution characteristics of wall-rock alteration are similar to those of the NNW-trending orebodies. These orebodies have a thickness of 2–6 m and a control length > 600 m, with average grades of 400 g/t Ag, 2.5% Zn, and 3.2% Pb, respectively [23].

The near E–W-trending Au-bearing Ag–Pb–Zn orebodies occur as veins and are interspersed within the aforementioned NW-, NNW-, and NNE-trending Ag–Pb–Zn orebodies. The ore structure is mainly of fine veins and disseminated (Figure 4i). The wall-rock alteration is characterized by silicification and carbonation, which develop in the form of clumps and veins within the orebodies and nearby wall-rocks (Figure 4i).

3.2.2. Shuangjianzishan Ore Block

The exposed strata in the Shuangjianzishan ore block include the Lower–Middle Permian Dashizhai Formation and Upper Jurassic Manketouebo Formation (Figure 2). The ore block is located within a Yanshanian volcanic edifice, and no intrusives are exposed. The orebodies are controlled by two sets of NW- and NE-trending faults, which belong

to the derived structures of the volcanic edifice. The NW-trending faults dip to NE at approximately 50° , and NE-trending faults dip to SE at 57° – 61° . The NW-trending #501 orebody is the largest in the Shuangjianzishan ore block. Its ore-hosting rocks consist of andesitic tuff, breccia tuff, altered andesite, and argillaceous slate. The orebody is 332 m long, with an inclined depth of 240 m and a thickness of 4.88 m. Its average grades are 99 g/t Ag, 1.0% Pb, and 0.8% Zn, respectively.

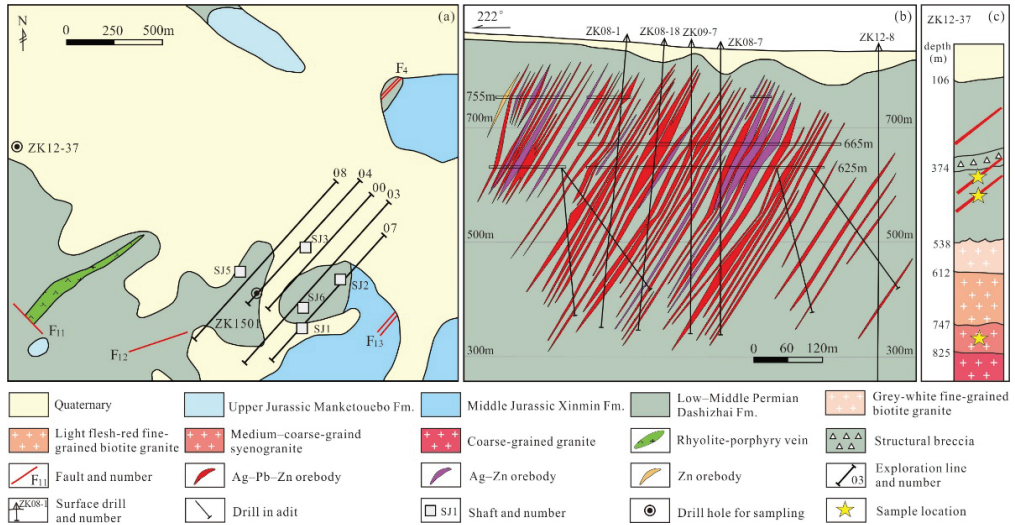


Figure 3. (a) Geologic map of the Xinglongshan ore block (modified after [39]); (b) simplified geological section along the 00-exploration line, showing the occurrence of the NW-trending Ag–Pb–Zn (Cu) ore vein group (modified after [39]); (c) log of drill no. ZK12-37, showing the distribution of granites (modified after [18]).

3.2.3. Ore Mineralogy and Textures of the Xinglongshan Ore Block

The ore minerals in the NW-trending ore vein group are mainly sphalerite, arsenopyrite, and pyrite, followed by galena, chalcopyrite, and pyrrhotite, with minor canfieldite and cassiterite (Figure 5a–d). The major gangue minerals are quartz, followed by chlorite, with minor sericite (Figure 5m,p). The ore texture includes anhedral granular, subhedral granular, euhedral granular, metasomatic dissolution, poikilitic, and exsolution textures (Figure 5a–d). Sphalerite is chiefly of anhedral granular texture (Figure 5a–c) and occasionally involves cassiterite particles, developing a poikilitic texture (Figure 5d); arsenopyrite is mainly of subhedral–euhedral granular texture (Figure 5c), with minor anhedral granular texture (Figure 5a); pyrite is mainly of anhedral granular texture, followed by subhedral–euhedral granular texture (Figure 5b); galena, pyrrhotite, canfieldite, and cassiterite are chiefly of anhedral granular texture (Figure 5a,c,d); chalcopyrite occurs as emulsion droplet within sphalerite, developing an exsolution texture (Figure 5a,b), and chalcopyrite is generally replaced by galena and canfieldite, developing a metasomatic dissolution texture (Figure 5c).

The ore minerals in the NNW-trending orebodies are mainly sphalerite and galena, followed by freibergite, polybasite, pyrrargyrite, and aguilarite, with minor canfieldite, chalcopyrite, and argentite (Figure 5e–h). The major gangue minerals are mainly quartz and chlorite (Figure 5n,p). The ore texture includes anhedral granular, metasomatic dissolution, and exsolution textures (Figure 5e–h). Chalcopyrite occurs as an emulsion droplet within sphalerite, developing an exsolution texture (Figure 5e,f); galena is often replaced by freibergite and polybasite (Figure 5e), chalcopyrite and pyrrargyrite (Figure 5f), and canfieldite and aguilarite (Figure 5g), developing a metasomatic dissolution texture.



Figure 4. Representative photos of orebodies in the Xinglongshan ore block. (a) fine-vein Ag–Pb–Zn orebody of the NW-trending ore vein group; (b) stockwork Pb–Zn orebody of the NW-trending ore vein group orebody; (c) disseminated Pb–Zn ore of the NW-trending ore vein group, with silification; (d) dense disseminated Cu–polymetallic ore of the NW-trending ore vein group, with silification; (e) high-grade Ag–Pb–Zn orebody of the NNW-trending orebodies, with silification; (f) Ag–Pb–Zn orebody of the NNW-trending orebodies, with silification and carbonation; (g) high-grade Ag–Pb–Zn orebody of the NNE-trending orebodies; (h) high-grade Ag–Pb–Zn orebody of the NNE-trending orebodies, with silification and carbonation; (i) Au-bearing Ag–Pb–Zn orebody with silification and carbonation, occurring in the near E–W-trending faults. Abbreviations: Cal = calcite; Ccp = chalcopryite; Gn = galena; Kut = kustelite; Qtz = quartz; Sp = sphalerite.

The ore minerals in the NNE-trending orebodies are mainly sphalerite and galena, followed by pyrite, freibergite, polybasite, pyrargyrite, canfieldite, and argentite (Figure 5i–k). The gangue minerals are mainly quartz and calcite (Figure 5o,p), with minor chlorite. The ore texture includes anhedral granular, metasomatic dissolution, poikilitic, and exsolution textures (Figure 5i–k). Canfieldite replaces galena along the edge of galena, developing a metasomatic dissolution texture (Figure 5i); chalcopryite occurs as an emulsion droplet within sphalerite, developing an exsolution texture (Figure 5j); sphalerite involves cassiterite and galena, developing a poikilitic texture, and canfieldite replaces galena and sphalerite, developing a metasomatic dissolution texture (Figure 5k).

The ore minerals in the near E–W-trending Au-bearing Ag–Pb–Zn orebodies are mainly sphalerite, galena, pyrite, pyrargyrite, freibergite, argentite, and polybasite, with minor native silver and kustelite (Figure 5l). The gangue minerals are mainly quartz and calcite (Figure 5p). The ore texture includes anhedral granular and metasomatic dissolution textures (Figure 5l).

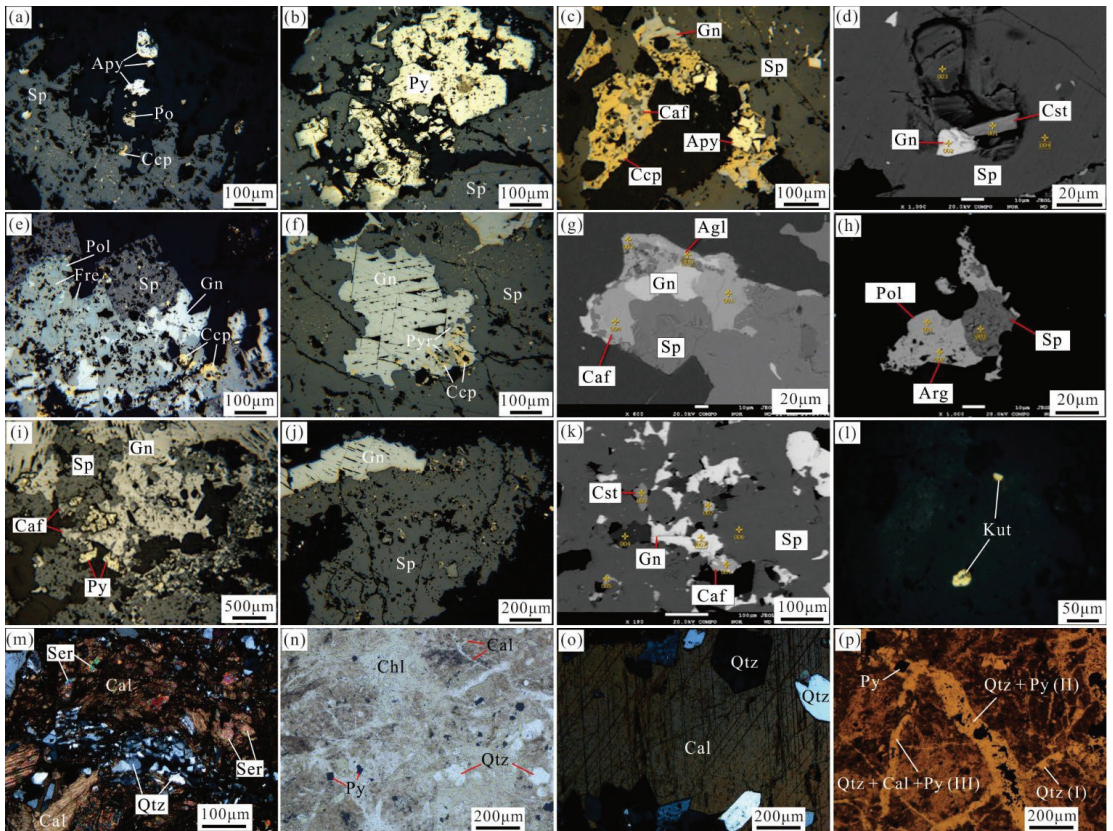


Figure 5. Representative photos of ores and major wall-rock alteration types in the Xinglongshan ore block. (a–d) Mineral assemblages of the NW-trending ore vein group, including sphalerite, arsenopyrite, pyrite, chalcopyrite, galena, pyrrhotite, canfieldite, and cassiterite; (e–h) mineral assemblages of the NNW-trending orebodies, including sphalerite, galena, freibergite, polybasite, pyrrargyrite, agularite, canfieldite, chalcopyrite, and argentite; (i–k) mineral assemblages of the NNE-trending orebodies, including sphalerite, galena, pyrite, freibergite, polybasite, pyrrargyrite, canfieldite, and argentite; (l) kustelite occurring within quartz and/or freibergite in the near E–W-trending Au-bearing Ag–Pb–Zn orebodies; (m) sericitization and silicification in stage I, superimposed by later carbonation; (n) silicification and chloritization developing in stages II and III, superimposed by later carbonation; (o) silicification and carbonation developing in stage III; (p) vein bodies cutting relationship, displaying quartz vein of stage I, quartz–pyrite vein of stage II, and quartz–calcite–pyrite vein of stage III. (a–c,e,f,i,j,l): plainlight under reflected light; (d,g,h,k): back-scatter electron (BSE) images; (m) and (o): cross-polarized light under transmitted light; (n) and (p): plainlight under transmitted light. Abbreviations: Agl = agularite; Apy = arsenopyrite; Arg = argentite; Caf = canfieldite; Cal = calcite; Ccp = chalcopyrite; Chl = chlorite; Cst = cassiterite; Fre = freibergite; Gn = galena; Kut = kustelite; Po = pyrrhotite; Pol = polybasite; Py = pyrite; Pyr = pyrrargyrite; Qtz = quartz; Ser = sericite; Sp = sphalerite.

3.2.4. Mineralization Stages

Based on mineral assemblages, ore fabrics, and crosscutting relationships between the veins, the ore-forming process in the Xinglongshan ore block can be divided into four stages (Figure 6): (1) sphalerite–arsenopyrite–pyrite–chalcopyrite–quartz stage (stage I); (2) sphalerite–galena–pyrite–silver-bearing minerals–quartz stage (stage II); (3) sphalerite–

galena–silver-bearing minerals–quartz–calcite stage (stage III); and (4) weakly mineralized quartz–calcite stage (stage IV). The ore minerals of stage I are mainly iron sphalerite, arsenopyrite, and pyrite, followed by chalcopyrite, galena, pyrrhotite, and aguilarite, with minor canfieldite, freibergite, polybasite, and cassiterite. The ore minerals of stage II are mainly sphalerite and galena, followed by pyrite, aguilarite, canfieldite, freibergite, polybasite, and pyrargyrite, with minor pyrrhotite, arsenopyrite, and chalcopyrite. The ore minerals of stage III are mainly sphalerite and galena, followed by pyrite, canfieldite, freibergite, polybasite, pyrargyrite, and argentite. In addition, kustelite and native silver can be observed within Au-bearing Ag–Pb–Zn ores of stage III. The ore minerals of stage IV are dominated by pyrite, with minor sphalerite, galena, argentite, and native silver.

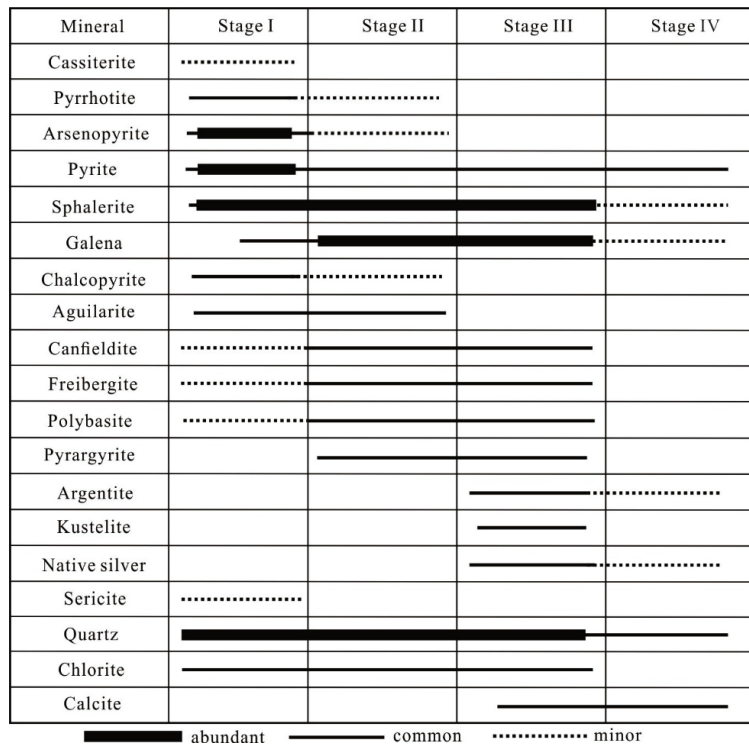


Figure 6. The paragenetic sequence of minerals in the Xinglongshan ore block.

4. Sampling and Analytical Methods

4.1. Sampling

In this research, we carefully handpicked 37 samples sourced from diverse mining levels and drill holes in the Xinglongshan ore block. These samples were chosen to undergo a range of analytical processes, including U-Pb dating, fluid inclusion analysis, and H–O–C–Pb isotope investigations.

These samples, mainly medium-coarse-grained syenogranite specimens, characterized by their predominant composition of K-feldspar (50%), quartz (35%), plagioclase (10%), and biotite (5%), were carefully selected for laser ablation inductively coupled plasma mass spectrometry (LA-ICP-MS) zircon U-Pb dating, as indicated in Table 1 (refer to Figures 3c and 7). For fluid inclusion (FI) analysis, we collected six quartz samples and two calcite samples, each sourced from four distinct mineralization stages, as outlined in Table 1. In addition, thirteen quartz samples obtained from these mineralization stages underwent H–O isotope analysis, while seven calcite samples, specifically from stages III and IV, were

subjected to H–O–C isotope analysis. Detailed information about these samples can be found in Table 1. Furthermore, our investigation extended to the analysis of twenty sulfide samples derived from seven different samples across the four mineralization stages. This set of samples encompassed seven galena, seven sphalerite, and six pyrite specimens. A comprehensive overview of these samples can be found in Table 1, alluding to the extensive and thorough nature of our analytical approach.

Table 1. List of analytical samples for the Xinglongshan ore block.

Sample	Orebody No./Lithology	Position	Stage	Mineral	Analysis
SJ49-1	Syenogranite	Drill No. ZK12-37 at 780 m deep		Zrn	U–Pb dating
SJ49-10	Syenogranite	Drill No. ZK12-37 at 1071 m deep		Zrn	U–Pb dating
SJ14	No. 2 Pb–Zn–Cu orebody	625-m level	I	Qtz	Fls study
SJ6	Disseminated Pb–Zn–Ag orebody	625-m level	II	Qtz	Fls study
SJ31	No. 2 Pb–Zn–Ag orebody	Drill No. ZK1501 at 1207 m deep	II	Qtz	Fls study
SJ11	No. 1-3 Pb–Zn–Ag orebody		III	Qtz	Fls study
SJ12	No. 2 Pb–Zn–Ag orebody	625-m level	III	Qtz	Fls study
SJ13-1	Pb–Zn–Ag–Au orebody	625-m level	III	Cal	Fls study
SJ8	No. 2 Pb–Zn–Ag mineralized orebody	625-m level	IV	Qtz	Fls study
SJ45	No. 2-16 Pb–Zn–Ag mineralized body	665-m level	IV	Cal	Fls study
2-3m-3	No. 2-3 Pb–Zn–Cu orebody	625-m level	I	Qtz	H–O isotopes
8-16m-1	No. 8-16 Pb–Zn–Cu orebody	665-m level	I	Qtz	H–O isotopes
1m-3	No. 1 Pb–Zn–Cu orebody	625-m level	I	Qtz	H–O isotopes
8-16m-3	No. 8-16 Pb–Zn–Cu orebody	665-m level	I	Qtz	H–O isotopes
8-16m-4	No. 8-16 Pb–Zn–Cu orebody	665-m level	I	Qtz	H–O isotopes
2-3m-7	No. 2-3 Pb–Zn–Cu orebody	625-m level	I	Qtz	H–O isotopes
2-3m-6	No. 2-3 Pb–Zn–Ag orebody	625-m level	II	Qtz	H–O isotopes
1-5-1m-2	No. 1-5-1 Pb–Zn–Ag–Au orebody	625-m level	II	Qtz	H–O isotopes
5#KD-2-1	No. 2 Pb–Zn–Ag orebody	625-m level	II	Qtz	H–O isotopes
5#KD-2-2	No. 2 Pb–Zn–Ag orebody	625-m level	II	Qtz	H–O isotopes
ZD4-1-1m-1	No. 1-1 Pb–Zn–Ag orebody	665-m level	III	Cal	H–O–C isotopes
ZD4-1-1m-2	No. 1-1 Pb–Zn–Ag orebody	665-m level	III	Cal	H–O–C isotopes
ZD4-1-1m-3	No. 1-1 Pb–Zn–Ag orebody	665-m level	III	Cal	H–O–C isotopes
ZD4-1-1m-4	No. 1-1 Pb–Zn–Ag orebody	665-m level	III	Qtz	H–O isotopes
ZD4-1-1m-4	No. 1-1 Pb–Zn–Ag orebody	665-m level	III	Cal	H–O–C isotopes
5#KD-1	No. 1-1 Pb–Zn–Ag mineralized body	665-m level	IV	Qtz	H–O isotopes
8-12m-1	No. 8-12 Pb–Zn–Ag mineralized body	665-m level	IV	Cal	H–O–C isotopes
8-12m-2	No. 8-12 Pb–Zn–Ag mineralized body	665-m level	IV	Qtz	H–O isotopes
8-12m-2	No. 8-12 Pb–Zn–Ag mineralized body	665-m level	IV	Cal	H–O–C isotopes
8-12m-3	No. 8-12 Pb–Zn–Ag mineralized body	665-m level	IV	Cal	H–O–C isotopes
2-3m-1	No. 2-3 Pb–Zn–Cu orebody	625-m level	I	Gn, Sp, Py	Pb isotope
2m-3	No. 2-3 Pb–Zn–Cu orebody	625-m level	I	Gn, Sp, Py	Pb isotope
1m-1	No. 1 Pb–Zn–Cu orebody	625-m level	I	Gn, Sp, Py	Pb isotope
ZD5-1-1m-1	No. 1-1 Pb–Zn–Ag orebody	625-m level	II	Gn, Sp	Pb isotope
ZD4-1-1m-1	No. 1-1 Pb–Zn–Ag orebody	665-m level	III	Gn, Sp, Py	Pb isotope
8-16m-2	No. 8-16 Pb–Zn–Ag mineralized body	665-m level	IV	Gn, Sp, Py	Pb isotope
8-12m-1	No. 8-12 Pb–Zn–Ag mineralized body	665-m level	IV	Gn, Sp, Py	Pb isotope

Abbreviations: Cal = calcite; Gn = Galena; Py = pyrite; Qtz = quartz; Sp = sphalerite; Zrn = zircon.

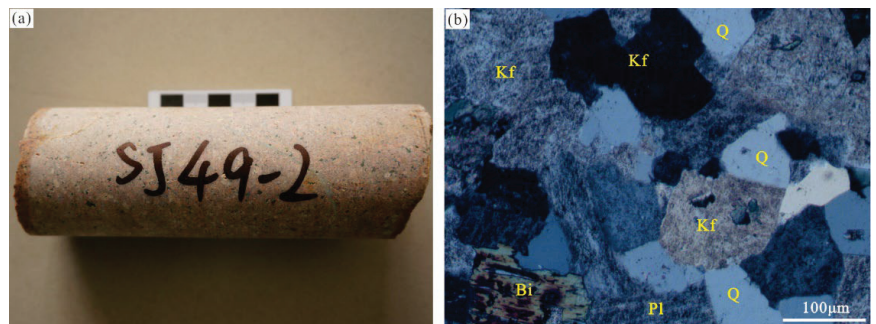


Figure 7. Field (a) and microscopic (b) photos of concealed syenogranite in the Xinglongshan ore block.

4.2. Syenogranite Zircon U–Pb Dating

Zircon grains were separated through traditional heavy liquid and magnetic separation techniques. Following this, they underwent meticulous purification through handpicking under a binocular microscope, a process carried out at the Langfang Chengxin Geological Service Co., Ltd. in Hebei Province, China. The handpicked zircon grains were mounted in epoxy and polished to expose the cores of the grains for subsequent cathodoluminescence (CL) imaging and zircon U–Pb analyses. The CL images were obtained at the Zircon Navigation Technology Co., Ltd., Beijing, China. The LA-ICP-MS zircon U–Pb dating was undertaken at the Yandu Zhongshi Testing Technology Co., Ltd., Beijing, China, using a Finnigan Neptune MC-ICP-MS attached to a New Wave UP 213 laser ablation system with an in-house sample cell. The detailed analytical procedures were similar to those described by Griffin et al. [50] and Hou et al. [51]. U–Pb fractionation was corrected using zircon standard GEMOC GJ-1 ($^{207}\text{Pb}/^{206}\text{Pb}$ age of 608.5 ± 1.5 Ma, [52]), and accuracy was controlled using zircon standard Mud Tank (intercept age of 732 ± 5 Ma, [53]). U–Pb ages were calculated from raw signal data using ISOPLOT 3.0 [54]. Because ^{204}Pb could not be measured due to a low signal and interference from ^{204}Hg in the gas supply, a common lead correction was carried out using the EXCEL program CompPbCorr#3.15G [55]. Errors on individual analyses by LA-ICP-MS were quoted at the 1σ level, while errors on pooled ages were quoted at the 95% (2σ) confidence level.

4.3. Fluid Inclusion Microthermometry and Laser Raman Spectroscopy

Microthermometric measurements of fluid inclusions (FIs) were conducted at the Institute of Mineral Resources, Chinese Academy of Geological Sciences, located in Beijing, China. This process utilized a LINKAM THMSG 600 programmable heating-freezing stage paired with a high-quality German Zeiss microscope. The homogenization temperature spanned from -190 °C to 600 °C, with estimated accuracies of ± 0.1 °C between -100 °C and 25 °C, ± 1 °C from 25 °C to 400 °C, and ± 2 °C above 400 °C, respectively. The heating rate during testing typically ranged from 0.2 °C to 5 °C per minute, with a reduction to 0.2 °C per minute near phase transitions. To determine the salinity of the gas–liquid two-phase aqueous solution inclusions, ice-melting temperatures were employed [56], and the density of the fluid inclusions was calculated using Flicor software (version 1.4) [57]. Additionally, the volatile compositions of individual fluid inclusions were identified using a Renishaw RM-2000 Raman probe located at the Institute of Mineral Resources, Chinese Academy of Geological Sciences in Beijing, China. The excitation wavelength utilized was 514.53 nm from an argon laser, with a measurement spectrum time of 20 s. The counting rate remained consistent at one per centimeter, maintaining precision throughout. The laser beam was consistently set at a 1 μm size, offering a spectral resolution within the range of 1 – 2 cm^{-1} . Spectral data were acquired over the extensive wavenumber span of 1000 – 4000 cm^{-1} , ensuring comprehensive coverage.

4.4. H–O–C–Pb Isotope Analyses

4.4.1. H–O–C Isotope Analyses

All the samples were smashed at the Langfang Chengxin Geological Service Co., Ltd., Hebei Province, China. The mineral separates were extracted and handpicked under a binocular microscope to achieve a purity of 99%. Isotope analyses for H–O–C were conducted utilizing a MAT 251EM mass spectrometer located at the Beijing Research Institute of Uranium Geology in China. The analytical precision was outstanding, with results surpassing the following margins: $\pm 2\text{‰}$ for δD , $\pm 0.2\text{‰}$ for $\delta^{18}\text{O}$, and $\pm 0.1\text{‰}$ for $\delta^{13}\text{C}$. In the case of quartz, O isotope analysis was performed using the BrF_5 method to extract CO_2 [58]. The calcite samples reacted with phosphoric acid at 25 °C to produce CO_2 for the C–O isotope analyses of calcite. The H isotope of water in fluid inclusions of quartz and calcite was measured for vapors released from FIs in quartz and calcite grains with the thermal crack method. Hydrogen, produced by the reaction of the released water and zinc at 400 °C [59], was used for H isotope analysis. The $\delta^{18}\text{O}$ of water for quartz was calculated

from the O isotopes of quartz by using the fractionation equation $1000\ln a_{\text{quartz-water}} = (3.38 \times 10^6) T^{-2} - 3.40$, and the $\delta^{18}\text{O}$ of water for calcite was calculated from the O isotopes of calcite by using the fractionation equation $1000\ln a_{\text{calcite-water}} = (4.01 \times 10^6) T^{-2} - (4.66 \times 10^6) T^{-1} + 1.71$ [60], where the T (in Kelvin) represents the average fluid inclusion homogeneous temperature associated with the mineralization stage.

4.4.2. Pb Isotope Analyses

The procedure for isolating individual sulfides followed the methodology outlined in Section 4.4.1. Subsequently, the Pb isotope composition of the sulfides was determined at the Analytical Laboratory of the Beijing Research Institute of Uranium Geology, China, using a GV IsoProbe-T multi-collector thermal ionization mass spectrometer. Remarkably, the measurement precision for both $^{208}\text{Pb}/^{206}\text{Pb}$ and $^{207}\text{Pb}/^{206}\text{Pb}$ ratios exceeded 0.005‰ (2σ). The isotopic ratios were reported relative to the Pb standard reference NBS-981 values, as follows: $^{206}\text{Pb}/^{204}\text{Pb} = 16.934 \pm 0.007$, $^{207}\text{Pb}/^{204}\text{Pb} = 15.486 \pm 0.012$, and $^{208}\text{Pb}/^{204}\text{Pb} = 36.673 \pm 0.033$, respectively [61].

5. Results

5.1. Syenogranite Zircon U–Pb Dating

Fifteen zircon grains and twenty zircon grains from the syenogranite samples SJ49-1 and SJ49-10, respectively, were selected for LA-ICP-MS U–Pb dating. Zircon U–Pb compositions were analyzed based on the texture shown on CL images (Figure 8a,b). The analytical data are presented in Table 2 and are plotted on Concordia diagrams (Figure 8c,d).

Table 2. LA-ICP-MS zircon U–Pb dating data for the syenogranite in the Shuangjianzishan area.

Spot No.	Isotopic Ratios						Age (Ma)			
	$^{207}\text{Pb}/^{206}\text{Pb}$	1σ	$^{207}\text{Pb}/^{235}\text{U}$	1σ	$^{206}\text{Pb}/^{238}\text{U}$	1σ	$^{238}\text{U}/^{206}\text{Pb}$	1σ	$^{206}\text{Pb}/^{238}\text{U}$	1σ
Sample SJ49-1										
SJ49-1-5	0.05207	0.00419	0.15345	0.00467	0.02148	0.00034	145	11	137	3
SJ49-1-6	0.05151	0.00219	0.15133	0.00427	0.02143	0.00029	143	6	137	2
SJ49-1-7	0.05404	0.00366	0.15977	0.00201	0.02136	0.00036	151	11	136	2
SJ49-1-8	0.05460	0.00363	0.16211	0.00490	0.02168	0.00035	153	9	138	3
SJ49-1-9	0.04866	0.00210	0.14663	0.00447	0.02204	0.00039	139	6	141	2
SJ49-1-10	0.05433	0.00359	0.16148	0.00411	0.02166	0.00032	152	10	138	3
SJ49-1-11	0.05142	0.00149	0.15133	0.00442	0.02139	0.00030	143	4	136	2
SJ49-1-12	0.05311	0.00273	0.15878	0.00418	0.02162	0.00034	150	7	138	2
SJ49-1-13	0.05426	0.00331	0.16184	0.00580	0.02173	0.00033	152	9	139	5
SJ49-1-14	0.05297	0.00267	0.15271	0.00588	0.02122	0.00037	144	6	135	2
SJ49-1-15	0.05326	0.00183	0.16031	0.00529	0.02201	0.00032	151	5	140	2
Sample SJ49-10										
SJ49-10-1	0.05360	0.00234	0.15744	0.00366	0.02150	0.00036	354	98	149	6
SJ49-10-2	0.05298	0.00273	0.15447	0.00351	0.02152	0.00036	328	117	146	7
SJ49-10-3	0.05103	0.00178	0.15186	0.00530	0.02159	0.00033	243	77	144	5
SJ49-10-4	0.05306	0.00211	0.16012	0.00674	0.02171	0.00027	332	91	151	6
SJ49-10-5	0.05211	0.00203	0.15586	0.00647	0.02165	0.00035	300	89	147	6
SJ49-10-6	0.05381	0.00304	0.16331	0.00512	0.02198	0.00037	365	128	154	8
SJ49-10-7	0.05146	0.00127	0.15120	0.00409	0.02123	0.00030	261	53	143	4
SJ49-10-8	0.05294	0.00370	0.15308	0.00681	0.02095	0.00047	328	155	145	9
SJ49-10-9	0.05087	0.00207	0.15079	0.00669	0.02135	0.00032	235	94	143	6
SJ49-10-10	0.05095	0.00659	0.15175	0.00241	0.02123	0.00048	239	283	144	21
SJ49-10-11	0.05309	0.00244	0.16196	0.00318	0.02201	0.00039	332	101	152	7
SJ49-10-12	0.05295	0.00226	0.15167	0.00605	0.02077	0.00046	328	94	143	5
SJ49-10-13	0.05161	0.00190	0.14800	0.00525	0.02093	0.00029	333	81	140	5
SJ49-10-14	0.05390	0.00150	0.16319	0.00505	0.02185	0.00034	369	63	154	4
SJ49-10-15	0.05386	0.00215	0.15455	0.00616	0.02084	0.00027	365	91	146	5
SJ49-10-16	0.05468	0.00306	0.16463	0.00531	0.02207	0.00042	398	94	155	7
SJ49-10-17	0.05391	0.00209	0.16044	0.00622	0.02162	0.00038	369	89	151	5
SJ49-10-18	0.05461	0.00307	0.15926	0.00573	0.02129	0.00036	395	126	150	8
SJ49-10-19	0.05024	0.00245	0.14607	0.00689	0.02130	0.00033	206	118	138	6
SJ49-10-20	0.05368	0.00154	0.16087	0.00483	0.02167	0.00028	367	60	152	4

Zircon grains retrieved from the syenogranite exhibit euhedral–subhedral shapes and demonstrate distinctive oscillatory zoning in CL images (Figure 8a,b), which, combined with their relatively high Th/U ratios (0.25–0.58), indicates their magmatic origin. Fifteen analyses from sample SJ49-1 form a tight cluster on a concordial diagram and yield a weighted mean $^{206}\text{Pb}/^{238}\text{U}$ age of 137 ± 1.4 Ma (MSWD = 1.5; Figure 8c), and twenty analyses from sample SJ49-10 form a tight cluster on a concordial diagram and yield a weighted mean $^{206}\text{Pb}/^{238}\text{U}$ age of 137 ± 1.2 Ma (MSWD = 1.6; Figure 8d), suggesting that the syenogranite formed during the Early Cretaceous.

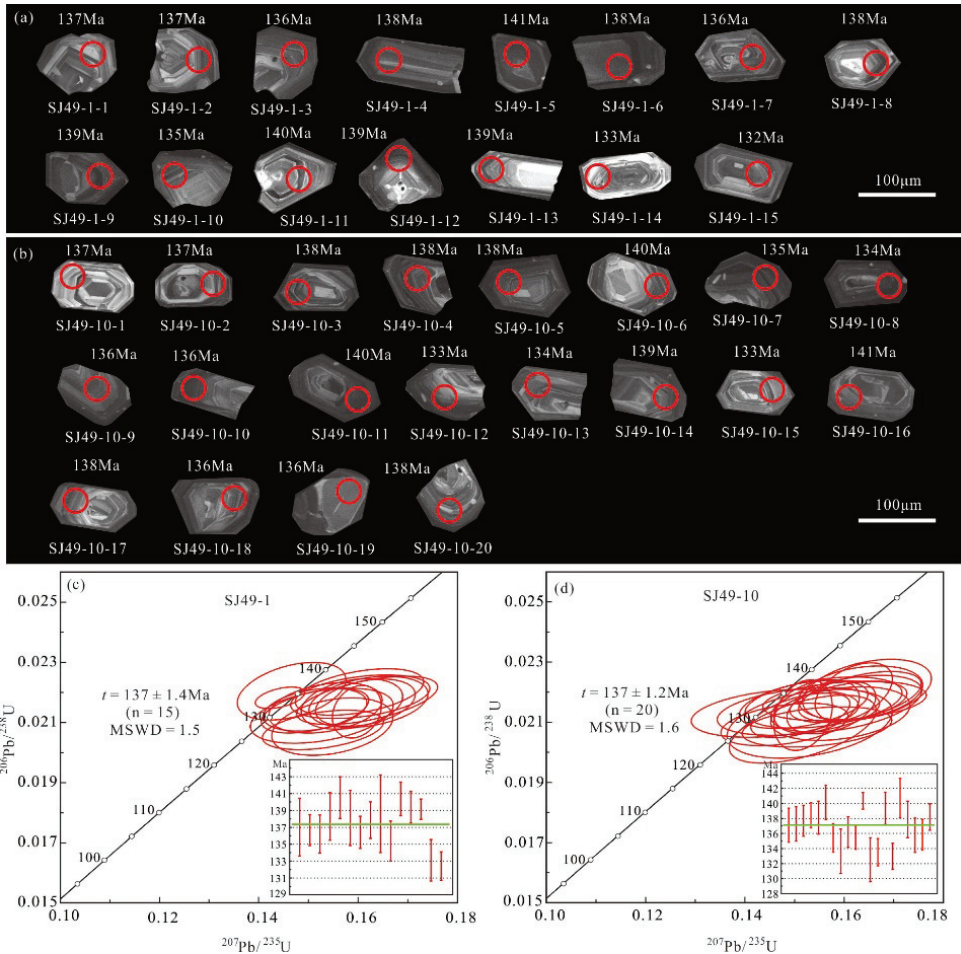


Figure 8. Representative cathodoluminescence (CL) images of zircon grains for samples sj49-1 (a) and sj49-10 (b) from the Shuangjanzishan syenogranite, showing U–Pb analytical spots and corresponding $^{206}\text{Pb}/^{238}\text{U}$ ages, and zircon U–Pb concordia diagrams of samples sj49-1 (c) and sj49-10 (d).

5.2. Fluid Inclusion Data

5.2.1. Petrography

A fluid inclusion assemblage (FIA) is defined as a collection of fluid inclusions that were contemporaneously trapped, enabling us to obtain more reliable and precise data through fluid inclusion microthermometry using the FIA approach [62]. In this research, the

criteria put forth by Goldstein and Reynolds [62] were applied to designate fluid inclusions that occur in close proximity or isolated positions as having a primary origin, thereby classifying them as FIA. Here, we focus on the primary inclusions (Figure 9), of which there are four types in the Xinglongshan ore block, using criteria such as phase ratios at room temperature (21 °C), phase transitions observed during heating and cooling, and findings from laser Raman spectroscopy.

- (1) Liquid-rich inclusions (WL-type): Within the examined quartz and calcite samples from all stages, these fluid inclusions are prevalent, constituting approximately 85% of the total number of inclusions. They exhibit elliptical, elongated columnar, and irregular shapes, with long axes ranging from 5 to 35 μm . Notably, the bubbles within them occupy 5%–45% of the total volume at room temperature (Figure 9a–f). When subjected to heating, these fluid inclusions underwent homogenization, transitioning into a liquid phase.
- (2) Gas-rich inclusions (WG-type): Exclusively found in quartz from stage I, these inclusions make up approximately 5% of the total number of fluid inclusions, with long axes ranging from 45 to 60 μm . WG-type inclusions are typically oval or circular in shape, with bubbles occupying 55%–70% of their total volume (Figure 9b). Upon heating, these inclusions homogenized into a vapor phase.
- (3) Pure gas inclusions (G-type): Predominantly present in quartz from stage I, these inclusions measure 5–10 μm in size and display irregular or round shapes (Figure 9a). They account for 3% of the total number of fluid inclusions and remain in a gaseous phase at room temperature, undergoing no phase change when heated.
- (4) Pure liquid inclusions (L-type): Primarily hosted within quartz and calcite from stages III and IV, these inclusions exhibit irregular and negative crystal shapes and have a size of 5–10 μm (Figure 9f). They constitute approximately 7% of the total number of fluid inclusions and remain in a liquid phase at room temperature. Upon heating, the L-type inclusions do not undergo any phase change.

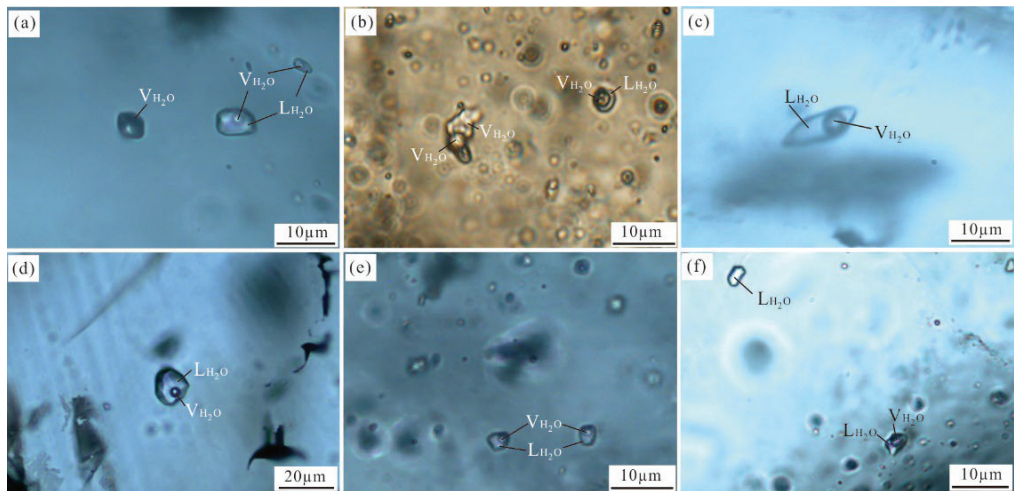


Figure 9. Illustrative microphotographs of fluid inclusions within quartz and calcite crystals sourced from the Xinglongshan ore block. (a) G- and WL-type FIs in quartz of stage I; (b) WG- and WL-type FIs in quartz of stage I; (c) WL-type FIs in quartz of stage II; (d) WL-type FIs in quartz of stage II; (e) WL-type FIs in quartz of stage III; (f) WL- and L-type FIs in calcite of stage IV. LH_2O = liquid phase H_2O ; VH_2O = vapor phase H_2O .

5.2.2. Microthermometry

The microthermometric results, along with the parameters of the FIA, are presented in Table 3 and depicted in Figure 10.

- (1) FIs in quartz of stage I (sample SJ14): Three FIAs have been recognized. The homogenization temperature of two WL-type FIAs varies from 253 °C to 302 °C (Figure 10a), and the final ice melting temperature is −3.2 °C to −1.9 °C, corresponding to salinities of 3.4–5.3 wt% NaCl eqv. (Figure 10b), and the density of the fluid is 0.74–0.83 g/cm³. The homogenization temperature of one WG-type FIA varies from 279 °C to 289 °C, and the final ice melting temperature is −4.1 °C to −2.4 °C, corresponding to salinities of 4.0–6.6 wt% NaCl eqv., and the density of the fluid is 0.79–0.80 g/cm³.
- (2) FIs in quartz of stage II (samples SJ6 and SJ31): Three FIAs have been recognized. The homogenization temperature of these FIAs varies from 203 °C to 268 °C (Figure 10c), and the final ice melting temperature ranges from −4.5 °C to −1.6 °C, corresponding to salinities of 2.6–7.2 wt% NaCl eqv. (Figure 10d), and the fluid density is 0.80–0.88 g/cm³.
- (3) FIs in quartz and calcite of stage III (samples SJ11, SJ12, and SJ13-1): Three FIAs have been recognized. The homogenization temperature of two WL-type FIAs in quartz varies from 200 °C to 222 °C (Figure 10e), and the final ice melting temperature ranges from −3.5 °C to −1.8 °C, corresponding to salinities of 3.1–5.7 wt% NaCl eqv. (Figure 10f), and the fluid density is 0.86–0.91 g/cm³. The homogenization temperature of one WL-type FIA in calcite varies from 184 °C to 199 °C, and the final ice melting temperature ranges from −4.4 °C to −1.7 °C, corresponding to salinities of 2.9–7.0 wt% NaCl eqv., and the fluid density is 0.89–0.92 g/cm³.
- (4) FIs in quartz and calcite of stage IV (samples SJ8 and SJ45): Two FIAs have been recognized. The homogenization temperature of one WL-type FIA in quartz varies from 185 °C to 198 °C (Figure 10g), and the final ice melting temperature ranges from −2.2 °C to −1.5 °C, corresponding to salinities of 2.6–3.7 wt% NaCl eqv. (Figure 10h), and the fluid density is 0.89–0.91 g/cm³. The homogenization temperature of one WL-type FIA in calcite varies from 153 °C to 187 °C, and the final ice melting temperature ranges from −2.9 °C to −0.7 °C, corresponding to salinities of 1.2–4.8 wt% NaCl eqv., and the fluid density is 0.90–0.93 g/cm³.

Table 3. Microthermometric data and relevant parameters of the fluid inclusion assemblage (FIA) in quartz and calcite from the Xinglongshan ore block.

Type	Host Mineral	FIA No.	No.	Size (µm)	V (vol.%)	$T_{m(ice)}$ (°C)		T_h (°C)		Salinity (wt% NaCl Eqv.)	Density (g/cm ³)
						Range	Range	Mean	Range		
Stage I: sphalerite–arsenopyrite–pyrite–chalcopyrite–quartz stage (sample SJ14)											
WL	Quartz	1	6	5–30	5–40	−3.2 to −1.9	278–302	288		3.4–5.3	0.74–0.79
WL	Quartz	2	5	10–30	10–35	−3.2 to −2.2	253–274	263		3.7–5.3	0.80–0.83
WG	Quartz	3	3	45–60	55–70	−4.1 to −2.4	279–289	284		4.0–6.6	0.79–0.80
Stage II: sphalerite–galena–pyrite–silver-bearing minerals–quartz stage (samples SJ6 and SJ31)											
WL	Quartz	4	11	5–30	10–25	−4.5 to −2.5	224–248	238		3.9–7.2	0.84–0.88
WL	Quartz	5	16	10–35	5–45	−4.2 to −1.6	229–268	238		3.2–6.7	0.83–0.87
WL	Quartz	6	6	10–30	5–20	−2.3 to −1.8	203–221	220		2.6–3.9	0.80–0.88
Stage III: sphalerite–galena–silver-bearing minerals–quartz–calcite stage (samples SJ11, SJ12, and SJ13-1)											
WL	Quartz	7	20	10–35	5–20	−3.5 to −1.8	200–222	212		3.1–5.7	0.86–0.91
WL	Quartz	8	12	10–30	10–20	−2.8 to −1.9	200–216	208		3.2–4.6	0.87–0.90
WL	Calcite	9	12	10–30	10–20	−4.4 to −1.7	184–199	192		2.9–7.0	0.89–0.92
Stage IV: weakly mineralized quartz–calcite stage (samples SJ8 and SJ45)											
WL	Quartz	10	4	15–20	5–20	−2.2 to −1.5	185–198	191		2.6–3.7	0.89–0.91
WL	Calcite	11	9	10–35	10–20	−2.9 to −0.7	153–187	176		1.2–4.8	0.90–0.93

Abbreviations: $T_{m(ice)}$ = final melting temperature of ice; T_h = total homogenization temperature; V = volume fraction of gas phase in the total volume of inclusion.

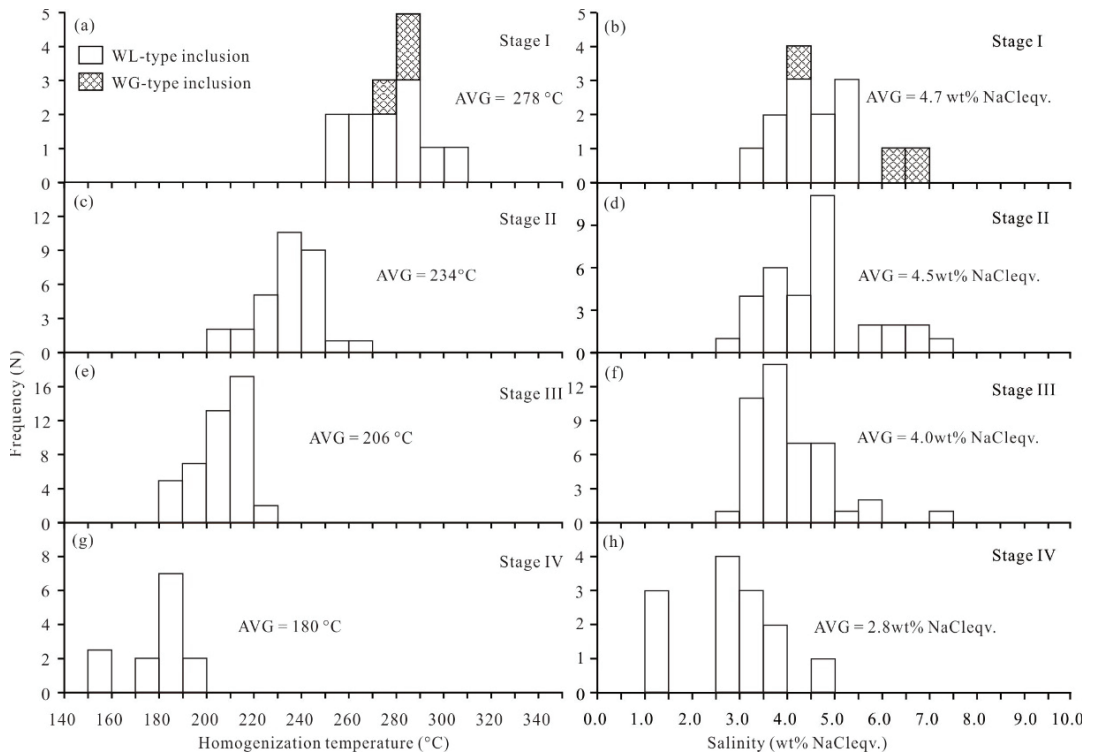


Figure 10. Histograms illustrating the homogenization temperatures and salinity of fluid inclusions within quartz and calcite from the Xinglongshan ore block. (a) Homogenization temperature of stage I; (b) salinity of stage I; (c) homogenization temperature of stage II; (d) salinity of stage II; (e) homogenization temperature of stage III; (f) salinity of stage III; (g) homogenization temperature of stage IV; (h) salinity of stage IV.

5.2.3. Laser Raman Spectra

The results of comprehensive laser Raman spectroscopic examinations on individual fluid inclusions within quartz and calcite from various stages are visually represented in Figure 11. In stage I, the gas-phase composition of FIs primarily consists of H_2O , although an inconspicuous CH_4 peak is also displayed. For stages II and III, the gas-phase composition is predominantly H_2O . In stage IV, the gas-phase of FIs is mainly composed of H_2O with a minor presence of C_6H_6 . Overall, the ore-forming fluid is characterized as belonging to an $\text{H}_2\text{O}\text{--NaCl} \pm \text{C}_6\text{H}_6$ system. Raman spectroscopy analysis shows that the ore-forming fluid of stages I, II, and III belongs to an $\text{H}_2\text{O}\text{--NaCl}$ system and that the fluid of stage IV belongs to an $\text{H}_2\text{O}\text{--NaCl}\text{--}(\text{C}_6\text{H}_6)$ system. The presence of a small amount of C_6H_6 in stage IV indicates that the late meteoric water carries organic matter components from the strata into the ore-forming fluid.

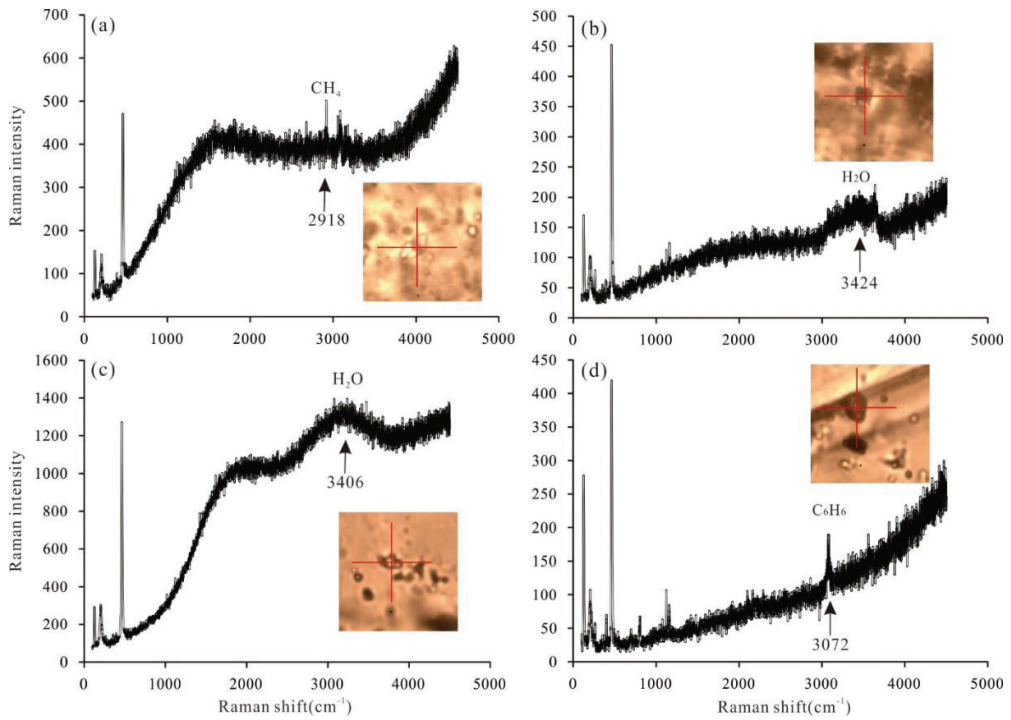


Figure 11. Laser Raman spectra for fluid inclusions in quartz and calcite from the Xinglongshan ore block. (a) Gas-phase composition of WL-type inclusions in quartz of stage I; (b) gas-phase composition of WL-type inclusions in quartz of stage II; (c) gas-phase composition of WL-type inclusions in quartz of stage III; (d) gas-phase composition of WL-type inclusions in calcite of stage IV.

5.3. Isotope Data

5.3.1. Hydrogen and Oxygen Isotopes

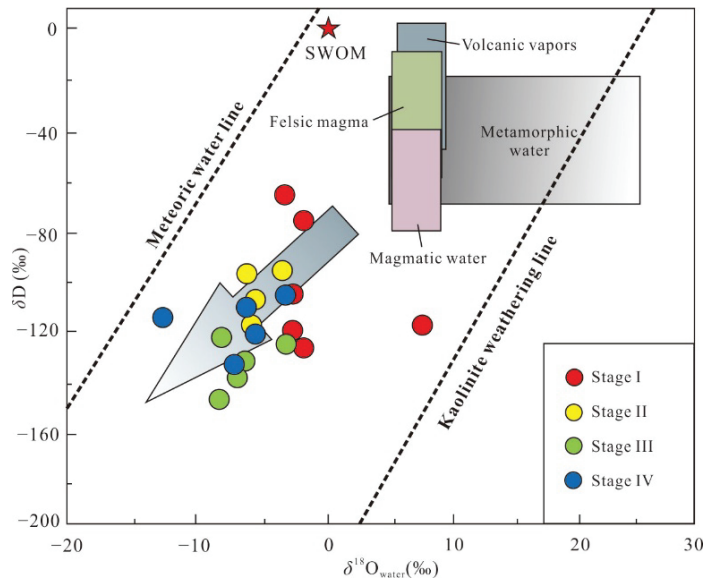
Isotope data for hydrogen and oxygen are presented in Table 4 and depicted in Figure 12. Within stage I, six quartz samples exhibit δD values ranging from -126‰ to -65‰ , $\delta^{18}O_{\text{quartz}}$ values spanning 4.1‰ to 15.1‰ , and $\delta^{18}O_{\text{water}}$ values ranging from -3.6‰ to 7.4‰ . For stage II, four quartz samples display δD values between -118‰ and -94‰ , $\delta^{18}O_{\text{quartz}}$ values in the range of 4.1‰ to 4.6‰ , and $\delta^{18}O_{\text{water}}$ values from -5.6‰ to -3.6‰ . In stage III, one quartz and four calcite samples yield δD values between -145‰ and -121‰ , $\delta^{18}O_{\text{mineral}}$ values within the range of 1.0‰ to 7.4‰ , and $\delta^{18}O_{\text{water}}$ values spanning -8.5‰ to -3.9‰ . Similarly, within stage IV, two quartz and three calcite samples exhibit δD values ranging from -134‰ to -106‰ , $\delta^{18}O_{\text{quartz}}$ values spanning from -0.8‰ to 7.9‰ , and $\delta^{18}O_{\text{water}}$ values between -13.9‰ and -5.2‰ . Notably, the $\delta^{18}O_{\text{mineral}}$ values of quartz samples (ranging from -0.8‰ to 15.1‰ , mostly $>4\text{‰}$) in stages I to IV are generally higher than those of calcite samples (ranging from 1.0‰ to 4.5‰ , mostly $<3\text{‰}$) from stages III to IV.

Table 4. Oxygen isotopic composition (‰) of quartz and calcite, hydrogen and oxygen isotopic compositions (‰) of fluid inclusions, and carbon isotopic composition (‰) of calcite from the Xinglongshan ore block.

Sample No.	Mineral	Stage	T_h (°C)	$\delta^{18}O_{\text{quartz}}$ (V-SMOW)	$\delta^{18}O_{\text{water}}$ (V-SMOW)	$\delta D_{\text{V-SMOW}}$	$\delta^{13}C_{\text{V-PDB}}$
2-3m-3	Quartz	I	278	4.1	-3.6	-65	
8-16m-1	Quartz	I	278	5.8	-1.9	-75	

Table 4. Cont.

Sample No.	Mineral	Stage	T_h (°C)	$\delta^{18}O_{\text{quartz}}$ (V-SMOW)	$\delta^{18}O_{\text{water}}$ (V-SMOW)	$\delta D_{\text{V-SMOW}}$	$\delta^{13}C_{\text{V-PDB}}$
1m-3	Quartz	I	278	5.8	-1.9	-126	
8-16m-3	Quartz	I	278	5.1	-2.6	-106	
8-16m-4	Quartz	I	278	5.1	-2.6	-120	
2-3m-7	Quartz	I	278	15.1	7.4	-117	
2-3m-6	Quartz	II	234	4.1	-5.6	-97	
5#KD-2-1	Quartz	II	234	4.4	-5.3	-118	
5#KD-2-2	Quartz	II	234	4.5	-5.2	-103	
1-5-1m-2	Quartz	II	234	6.1	-3.6	-94	
ZD4-1-1m-1	Calcite	III	206	2.5	-7.0	-133	-11.0
ZD4-1-1m-2	Calcite	III	206	1.9	-7.6	-138	-10.7
ZD4-1-1m-3	Calcite	III	206	1.0	-8.5	-145	-10.5
ZD4-1-1m-4	Quartz	III	206	7.4	-3.9	-123	
ZD4-1-1m-4	Calcite	III	206	1.3	-8.2	-121	-10.9
5#KD-1	Quartz	IV	180	7.9	-5.2	-106	
8-12m-1	Calcite	IV	180	4.5	-6.5	-123	-9.9
8-12m-2	Quartz	IV	180	-0.8	-13.9	-116	
8-12m-2	Calcite	IV	180	3.6	-7.4	-112	-7.9
8-12m-3	Calcite	IV	180	2.5	-8.5	-134	-9.4

Figure 12. $\delta^{18}O_{\text{water}}$ versus δD diagram of the Xinglongshan ore block (base map from [63]).

5.3.2. Carbon Isotope

Carbon isotope data are given in Table 4. Four calcite samples from stage III have $\delta^{13}C$ values of -11.0‰ to -10.5‰ , and three calcite samples from stage IV have $\delta^{13}C$ values of -9.9‰ to -7.9‰ .

5.3.3. Lead Isotope

The lead isotopic data for 21 sulfide samples are listed in Table 5. The $^{206}\text{Pb}/^{204}\text{Pb}$, $^{207}\text{Pb}/^{204}\text{Pb}$, and $^{208}\text{Pb}/^{204}\text{Pb}$ ratios for 3 galena, 3 sphalerite, and 3 pyrite samples from stage I are 18.285–18.361, 15.536–15.634, and 38.130–38.448, respectively. The $^{206}\text{Pb}/^{204}\text{Pb}$, $^{207}\text{Pb}/^{204}\text{Pb}$, and $^{208}\text{Pb}/^{204}\text{Pb}$ ratios for 1 galena and 1 sphalerite samples from stage II are 18.311–18.358, 15.567–15.630, and 38.234–38.438, respectively. The $^{206}\text{Pb}/^{204}\text{Pb}$, $^{207}\text{Pb}/^{204}\text{Pb}$,

and $^{208}\text{Pb}/^{204}\text{Pb}$ ratios for 1 galena, 1 sphalerite, and 1 pyrite samples from stage III are 18.278–18.310, 15.530–15.570, and 38.107–38.234, respectively. The $^{206}\text{Pb}/^{204}\text{Pb}$, $^{207}\text{Pb}/^{204}\text{Pb}$, and $^{208}\text{Pb}/^{204}\text{Pb}$ ratios for 2 galena, 2 sphalerite, and 2 pyrite samples from stage IV are 18.293–18.346, 15.564–15.616, and 38.229–38.389, respectively.

Table 5. Lead isotopic composition of sulfide samples from the Xinglongshan ore block.

Sample No.	Mineral	Stage	$^{206}\text{Pb}/^{204}\text{Pb}$	$^{207}\text{Pb}/^{204}\text{Pb}$	$^{208}\text{Pb}/^{204}\text{Pb}$	t (Ma)	μ	ω	κ	$\Delta\alpha$	$\Delta\beta$	$\Delta\gamma$
2-3m-1	I	Galena	18.308	15.569	38.229	137	9.31	35.5	3.69	65.2	15.9	26.1
2-3m-1	I	Sphalerite	18.285	15.536	38.130	137	9.29	35.1	3.65	63.9	13.7	23.5
2-3m-1	I	Pyrite	18.303	15.564	38.205	137	9.31	35.4	3.67	64.9	15.6	25.5
2m-3	I	Galena	18.361	15.634	38.448	137	9.37	36.3	3.75	68.3	20.1	32.0
2m-3	I	Sphalerite	18.290	15.545	38.179	137	9.29	35.3	3.67	64.2	14.3	24.8
2m-3	I	Pyrite	18.308	15.566	38.240	137	9.31	35.5	3.69	65.2	15.7	26.4
1m-1	I	Galena	18.355	15.626	38.419	137	9.36	36.2	3.75	67.9	19.6	31.2
1m-1	I	Sphalerite	18.323	15.585	38.261	137	9.33	35.6	3.69	66.1	16.9	27.0
1m-1	I	Pyrite	18.302	15.561	38.211	137	9.31	35.4	3.68	64.8	15.4	25.6
ZD5-1-1m-1	II	Galena	18.358	15.630	38.438	137	9.36	36.3	3.75	68.1	19.9	31.7
ZD5-1-1m-1	II	Sphalerite	18.311	15.567	38.234	137	9.31	35.5	3.69	65.4	15.8	26.2
ZD4-1-1m-1	III	Galena	18.278	15.530	38.107	137	9.28	35.0	3.65	63.5	13.3	22.8
ZD4-1-1m-1	III	Sphalerite	18.310	15.570	38.234	137	9.31	35.5	3.69	65.3	16.0	26.2
ZD4-1-1m-1	III	Pyrite	18.299	15.555	38.199	137	9.30	35.3	3.68	64.7	15.0	25.3
8-16m-2	IV	Galena	18.311	15.569	38.239	137	9.31	35.5	3.69	65.4	15.9	26.4
8-16m-2	IV	Sphalerite	18.293	15.571	38.234	137	9.30	35.5	3.69	64.3	16.0	26.2
8-16m-2	IV	Pyrite	18.332	15.597	38.319	137	9.34	35.8	3.71	66.6	17.7	28.5
8-12m-1	IV	Galena	18.346	15.616	38.389	137	9.35	36.1	3.74	67.4	19.0	30.4
8-12m-1	IV	Sphalerite	18.329	15.598	38.331	137	9.33	35.9	3.72	66.4	17.8	28.9
8-12m-1	IV	Pyrite	18.307	15.564	38.229	137	9.31	35.5	3.69	65.1	15.6	26.1

Abbreviations: $\mu = ^{238}\text{U}/^{204}\text{Pb}$; $\omega = ^{232}\text{Th}/^{204}\text{Pb}$; $\kappa = \text{Th}/\text{U}$; $\Delta\alpha = [(^{206}\text{Pb}/^{204}\text{Pb})_{\text{d(t)}} / (^{206}\text{Pb}/^{204}\text{Pb})_{\text{m(t)}} - 1] \times 1000$; $\Delta\beta = [(^{207}\text{Pb}/^{204}\text{Pb})_{\text{d(t)}} / (^{207}\text{Pb}/^{204}\text{Pb})_{\text{m(t)}} - 1] \times 1000$; $\Delta\gamma = [(^{208}\text{Pb}/^{204}\text{Pb})_{\text{d(t)}} / (^{208}\text{Pb}/^{204}\text{Pb})_{\text{m(t)}} - 1] \times 1000$; d is the Pb of ore mineral; and m is mantle Pb calculated by Chen et al. [64].

6. Discussion

6.1. Timing of the Syenogranite and Mineralization

Different attempts to date mineralization have been made in the last years, either by dating igneous rocks considered to be genetically related to mineralization or by dating hydrothermal alteration and ore minerals themselves. Cui [65] proposed that the age of Ag–Pb–Zn mineralization is 249 ± 2 Ma based on a zircon U–Pb age from one of the diorite dikes. Based on a zircon U–Pb date for granite porphyry that was believed to be related to the mineralization, Ouyang et al. [66] proposed an age of 159.3 ± 2.3 Ma. Wang [67] reported a U–Pb age of 148 ± 1 Ma for hydrothermal zircons. Wang et al. [37] indirectly dated the mineralization by determining the age of sericite using the Ar–Ar method and obtained an age of 147 ± 2 Ma. Zhai et al. [18] reported Re–Os ages of 135 ± 3.4 Ma for molybdenite and 135 ± 0.6 Ma for pyrite. Wu et al. [39] obtained an age of 133 ± 4 Ma from a sphalerite Rb–Sr isochron. Wang [67] used the Re–Os method on arsenopyrite and pyrite to obtain an age of 159 ± 6 Ma for the Ag–Pb–Zn mineralization. However, the wide range of the dating results shows that the age of the mineralization is still controversial.

The discovery of the concealed syenogranite by geophysical methods and drilling and evidence provided by the geophysical and geochemical models [68] suggest that the syenogranite intrusive is closely related to the mineralization and provide new insights into the timing of the mineralization processes. It can be seen from field observations that the syenogranite intrusion has undergone strong potassium and silicide alteration and contains many fine ore veins, as well as a large amount of potassium feldspar–quartz veinlets/stockworks and magmatic-hydrothermal breccias. Strong sericitization and sili-cification are seen in the contact between the intrusion and wall-rocks, and there are molybdenite–quartz \pm albite fine veins and hydrothermal breccia zones in the local area [18]. The contact relationship between the syenogranite and mineralization suggests that the crystallization age of the syenogranite can be considered to be a pre-ore mineralization age close to the mineralization age. As described earlier, the concealed syenogranite yields a

zircon-weighted mean $^{206}\text{Pb}/^{238}\text{U}$ age of 137 Ma, which is basically consistent with the peak ages of the Early Cretaceous granites in the SGXR obtained from previous studies and suggests that the dioritic dike and the granite porphyry dated in earlier studies [65,66] are unlikely linked to the mineralization. Furthermore, this age is earlier than the average Re–Os model ages of molybdenite (135 ± 3.4 Ma) and pyrite (135 ± 0.6 Ma) reported by Zhai et al. [18] and the Rb–Sr isochron age of sphalerite (133 ± 4 Ma) reported by Wu et al. [68], thus, discarding ages determined from sericite [69], hydrothermal zircon, pyrite, and arsenopyrite [67]. Therefore, we infer that the mineralization age of the SJS deposit is not earlier than 137 Ma, and taking into account the above sphalerite, pyrite, and molybdenite dating results [18,37], an average 135 Ma age for the SJS deposit is likely to be a good estimation. This age is comparable to that of numerous other magmatic-hydrothermal ore deposits located in the SGXR, such as the Baiyinnuoer skarn Pb–Zn deposit (135 ± 1 Ma, [22]), the Bairendaba Ag–Pb–Zn deposit (135 ± 11 Ma, [70]), and the Weilasituo Sn–Li–Zn–Pb–Cu–Mo deposit (135 ± 7 Ma, [71]). Considering the U–Pb age of the syenogranite obtained by us in this study and previous dating results together, we conclude that the Early Cretaceous was an important mineralization period in the SJS ore district and that the vein-type Pb–Zn–Ag mineralization was closely related to granitic magma activity.

6.2. Source and Evolution of Ore-Forming Fluids

The $\delta^{18}\text{O}_{\text{water}}$ and δD values of the ore-forming fluids in the Xinglongshan ore block vary from -3.6‰ to 7.4‰ and -126‰ to -65‰ for stage I, -5.6‰ to -3.6‰ and -118‰ to -94‰ for stage II, -8.5‰ to -3.9‰ and -145‰ to -121‰ for stage III, and -13.9‰ to -5.2‰ and -134‰ to -106‰ for stage IV, respectively (Table 4). As shown in Figure 12, all samples, with a single exception, are plotted between the magmatic water box and the meteoric water evolution line. This feature indicates that the ore-forming fluid has a mixture source between magmatic and meteoric water and that the initial fluid may have derived from magmatic water. The $\delta^{18}\text{O}_{\text{water}}$ and δD values of the Xinglongshan ore block are consistent with those of high-latitude meteoric water [71,72]. In addition, there is a gradually decreasing trend in H–O isotope composition from the early to late stage, indicating a continuous influx of meteoric water with the evolution of ore-forming fluids. This is also supported by C isotopic compositions. The $\delta^{13}\text{C}$ values of stages III and IV vary from -11.0‰ to -7.9‰ (mean -10.0‰). In general, there are three major carbon reservoirs on Earth: marine carbonate with a $\delta^{13}\text{C}$ mean of 0‰ [73]; carbonatite with $\delta^{13}\text{C}$ values varying from -7‰ to -3‰ , averaging -5‰ [73,74]; and organic matter having a $\delta^{13}\text{C}$ mean of -25‰ [75]. The carbon isotope composition of the ore block is significantly different from that of marine carbonate and organic matter but slightly lower than that of carbonatite or granite. Given the geological context, we suggest that the carbon mainly came from granitic magma rather than carbonatites. In the $\delta^{18}\text{O}_{\text{calcite}}-\delta^{13}\text{C}_{\text{V-PDB}}$ diagram (Figure 13), all samples are projected on the left side of the C–O isotope composition region of igneous rocks, which is similar to the C–O isotope compositions reported by Zhang et al. [40] and Wang et al. [37] (Figure 13). The $\delta^{13}\text{C}$ value of atmospheric CO_2 ranges from -11‰ to -7‰ proposed by Hoefs [76]. In addition, compared to magmatic water, meteoric water has lower $\delta^{13}\text{C}$ values. Therefore, the involvement of meteoric water will cause the C–O isotope composition of the ore-forming fluid to migrate toward the lower left. Therefore, the C–O isotope composition of the ore-forming fluid in the Xinglongshan ore block shows a mixing of magmatic and meteoric water, indicating that the initial ore-forming fluid came from magma and mixed with meteoric water with the evolution of ore-forming fluid.

The laser Raman spectroscopy results indicate that the ore-forming fluid of the Xinglongshan ore block overall belongs to an $\text{H}_2\text{O}-\text{NaCl}-(\text{C}_6\text{H}_6)$ system. The FIs in stage I, mainly consisting of WL-type with minor WG-type, are characterized by medium–high temperature (mean 278 °C) and low salinity (mean $4.7\text{ wt\% NaCl eqv.}$). The FIs in stages II and III, predominantly composed of WL-type, are featured by medium–low temperature

(mean 234 °C for stage II and mean 206 °C for stage III) and low salinity (mean 4.5 wt% NaCl eqv. for stage II and mean 4.0 wt% NaCl eqv. for stage III). The FIs in stage IV, mainly consisting of WL-type, have low temperature (mean 180 °C) and low salinity (mean 2.8 wt% NaCl eqv.). It should be noticed that the coexisting WL- and WG-type FIs were developed in stage I, while only WL-type FIs occurred in stages II, III, and IV. The homogenization temperature and salinity of the ore-forming fluid in the main mineralization stage (stages II and III) of the Xinglongshan ore block are consistent with the previous study [40], in which the homogenization temperature and salinity range from 201 °C to 280 °C and 0.5 wt% NaCl eqv. to 8.4 wt% NaCl eqv., respectively, indicating that this ore block mainly formed in a medium- to low-temperature and low salinity environment. The evolution of the system from early to late stage indicates that the temperature gradually decreases and that the salinity slightly changes but still shows a downward trend (Figures 10 and 14).

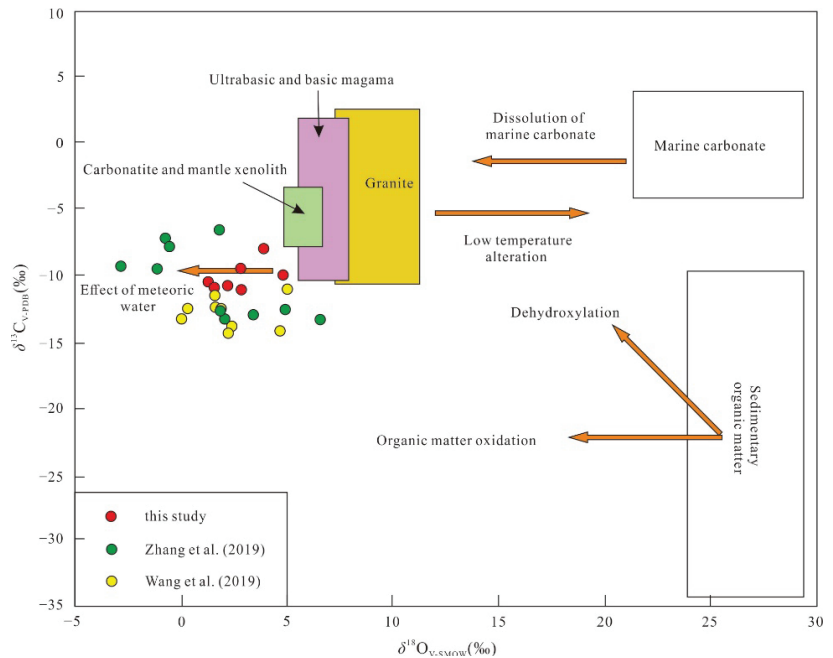


Figure 13. $\delta^{18}\text{O}$ versus $\delta^{13}\text{C}$ diagram of calcite from stages III and IV of the Xinglongshan ore block (base map from [37,40]).

In summary, the initial fluid of the Xinglongshan ore block was derived from magma, the ore-forming fluid is characterized by a mixture of magmatic and meteoric water, and the involvement of meteoric water gradually increased with the evolution of ore-forming fluids. Additionally, the homogenization temperature of the ore-forming fluid gradually decreases from stage I to stage IV, while the salinity is nearly constant, except for a significant decrease in stage IV (Figure 14). Overall, the ore-forming fluid is featured by medium–low temperature and low salinity and roughly belongs to an $\text{H}_2\text{O}\text{--NaCl} \pm \text{C}_6\text{H}_6$ system.

6.3. Sources of Ore-Forming Materials

The Pb isotopic composition is rarely fractionated in the processes of elemental migration and precipitation. Thus, it can be used to trace the source of metallogenic materials [77–81]. The μ , ω , and κ values of the Pb isotope for crust and mantle are 9.60 and 8.92, 36.84 and 31.84, and 5.85 and 3.45, respectively [82]. These values of the Xinglongshan ore block are 9.28–9.37, 35.0–36.3, and 3.65–3.75, with mean values of 9.32, 35.6, and 3.70,

respectively (Table 5), which are between those of crust and mantle. This feature implies that Pb was derived from a mixed source of the crust and mantle. In Figure 15a, all samples are plotted between the upper crust and mantle evolution curves, forming a steep straight line crossing the evolution line of the orogenic belt; in Figure 15b, all samples are projected between the lower crust and orogenic belt evolution lines and near the orogenic belt evolution line. The Pb isotopic composition of the Xinglongshan ore block indicates that Pb was derived from an orogenic belt or a mixed source of mantle and crust.

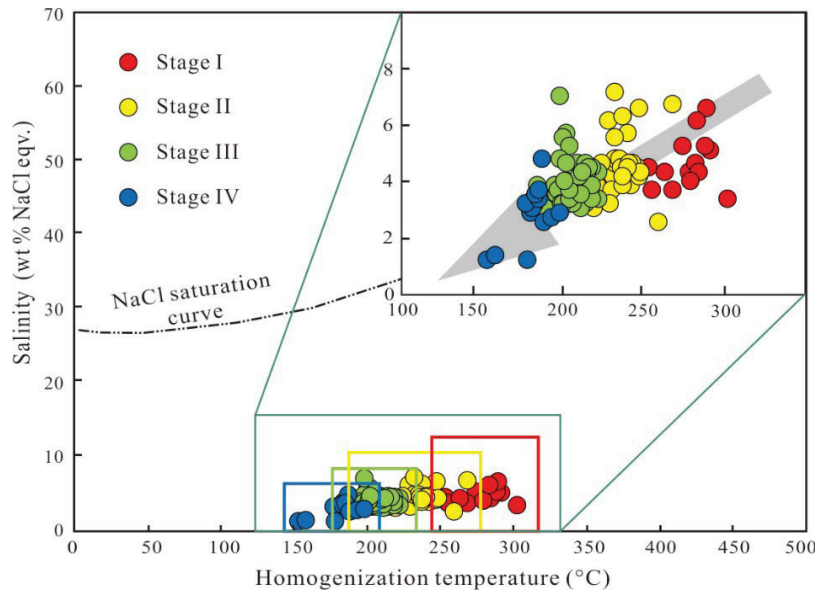


Figure 14. Diagram of homogenization temperature versus salinity of FIs in quartz and calcite from the Xinglongshan ore block. NaCl saturation curve from [56].

Zhu et al. [83] proposed that combining $\Delta\beta$ and $\Delta\gamma$ values can distinguish the tectonic backgrounds from which the ore minerals originated. In Figure 16, these data points of the Xinglongshan ore block are projected into the domain of magmatism, where the lead isotope composition has the characteristics of mixed lead sources from the upper crust and mantle [83]. Given that the SGXR was in an extensional background during the Early Cretaceous [14,27], we suggest that the ore-related magma originated from the mixing of depleted mantle- and crustal-derived magmas. Moreover, this primitive magma underwent the MASH (melting-assimilation-storage-homogenization) process in the lower crust, as proposed by Richards [84]. Wang et al. [28] reported the $\delta^{34}\text{S}$ values of 28 sulfide samples from the Xinglongshan ore block, ranging from -4.70‰ to 1.40‰ . Zhai et al. [18] obtained 77 in situ sulfur isotope data for sulfides and Ag-bearing sulfosalts from the ore block, and their $\delta^{34}\text{S}$ values vary from -4.67‰ to 2.44‰ , with a mean value of -2.11‰ . The sulfur isotope composition of the Xinglongshan ore block is consistent with that of the magmatic and meteorite, indicative of a magmatic sulfur source.

In summary, the lead isotope composition obtained in this study and the sulfur isotope composition obtained by predecessors suggest that the ore-forming material of the Xinglongshan ore block mainly came from granitic magma.

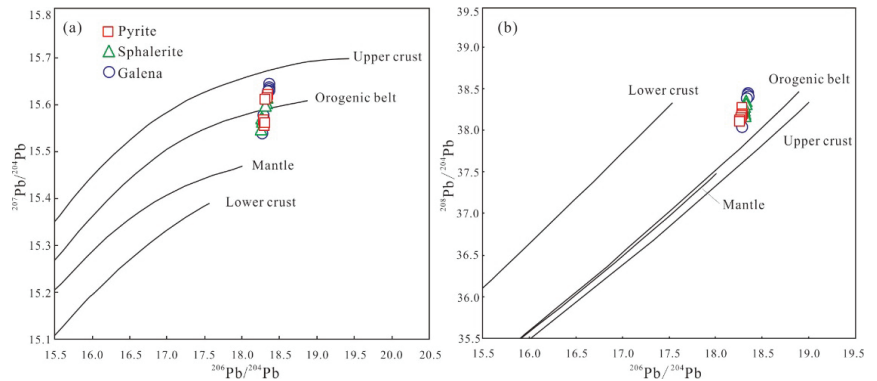


Figure 15. Diagrams of $^{206}\text{Pb}/^{204}\text{Pb}$ versus $^{207}\text{Pb}/^{204}\text{Pb}$ (a) and $^{206}\text{Pb}/^{204}\text{Pb}$ versus $^{208}\text{Pb}/^{204}\text{Pb}$ (b) for sulfides from the Xinglongshan ore block (base map from [82]).

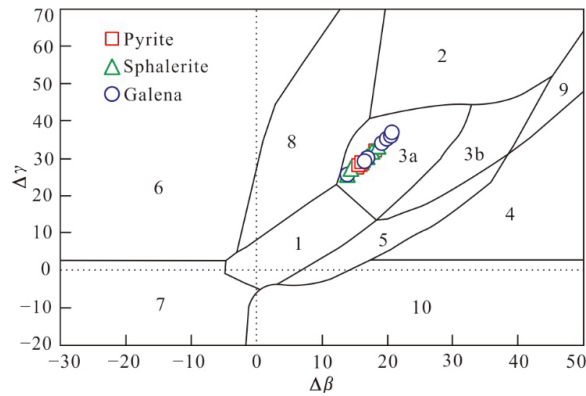


Figure 16. $\Delta\beta$ versus $\Delta\gamma$ genetic classification diagram for lead isotopes of ore minerals from the Xinglongshan ore block (base map after [83]). Names of the number: 1 = mantle-derived lead; 2 = upper crust lead; 3 = subduction zone lead originated from the mixing of the upper crust and mantle lead (3a = lead related to magmatism; 3b = lead related to sedimentation); 4 = chemically deposited lead; 5 = submarine hydrothermal lead; 6 = medium–high grade metamorphism lead; 7 = lower crust lead of high-grade metamorphism; 8 = orogenic belt lead; 9 = upper crust lead in ancient shale; 10 = retrograde metamorphism lead.

6.4. Mechanism of Mineral Deposition

The sulfides of the Xinglongshan ore block are dominated by sphalerite, galena, pyrite, chalcopyrite, and pyrrhotite, and no sulfate minerals were detected, indicating that H_2S dominated the hydrothermal system with a low oxygen fugacity during the mineralization. The mean homogenization temperatures of FIs are 278 °C for stage I, 234 °C for stage II, 206 °C for stage III, and 180 °C for stage IV, respectively, indicating that the ore block formed in a medium–low temperature hydrothermal environment. The ore-forming fluid is characterized by low salinity, with salinities of 4.7 wt% NaCl eqv. for stage I, 4.5 wt% NaCl eqv. for stage II, 4.0 wt% NaCl eqv. for stage III, and 2.8 wt% NaCl eqv. for stage IV, respectively. Silver mainly exists in the form of Ag^+ in hydrothermal fluids and preferentially bonds with HS^- [85], and in S-bearing systems, $\text{Ag}(\text{HS})_2^-$ is the main species up to $T = 300\text{--}400$ °C and $P = 50$ MPa [86]. $\text{Pb}(\text{HS})_2^0$ is the main Pb complex in a reduced hydrothermal fluid system under the conditions of low salinity (3.4 wt% NaCl eqv.), a temperature between 150 °C and 500 °C, and pressure greater than 100 MPa [66]. In a

low salinity and reduced hydrothermal fluids system, Cu^+ is the dominant form of Cu, forming strong complexes with HS^- [87]. As for zinc, considering the low salinity of the ore-forming fluid, we speculate that it mainly exists in the form of $\text{Pb}(\text{HS})_2^0$, although some researchers proposed that ZnCl^+ is the main Zn species in low salinity (3.4 wt% NaCl eqv.) hydrothermal fluid under the conditions of temperature ranging from 200 °C to 400 °C and pressure greater than 100 MPa [87,88]. In summary, the ore-forming elements, such as Ag, Pb, Zn, and Cu in the Xinglongshan ore block migrate in the form of hydrosulfide complexes.

The following mechanisms may cause the decomposition of complex, inducing mineral precipitation from solution [89–92]: (1) temperature decrease, (2) fluid immiscibility or boiling, (3) fluid mixing/dilution, and (4) fluid/rock interaction. The H–O isotopic compositions indicate that the mixture of magmatic and meteoric water took place during the mineralization of the Xinglongshan ore block (Figure 12); thus, fluid mixing is one of the main mechanisms for mineral precipitation. The homogenization temperatures of FIs from stage I to stage IV gradually decrease (Figure 13), implying that fluid cooling is also one of the mineral precipitation mechanisms. The quartz veins from stage I consist of WL- and WG-type FIs. These FIs coexist in the same quartz matrix (Figure 6b) and have similar homogenization temperatures and different salinities (Figure 10a,b). The WL-type FIs were homogenized to liquid, and the WG-type ones were homogenized to vapor when heated. The FIs of stage I exhibit typical features of fluid immiscibility. The Xinglongshan ore block belongs to a medium- to low-temperature hydrothermal deposit, and its $\delta^{13}\text{C}$ values range from -11.0‰ to -7.9‰ , which is slightly lower than that of carbonatite (mean -5.0‰), but much higher than that of organic matter (mean -25‰). Therefore, we infer that the fluid–rock interaction was not the main mechanism of mineral precipitation in the ore block. Given the supergiant size of the SJS deposit, we do not believe that simple cooling is an efficient mechanism of ore precipitation because it does not sharply change the stability conditions of the complexes. In brief, fluid mixing was the main mechanism for mineral precipitation in the Xinglongshan ore block, despite the presence of a small amount of fluid immiscibility in stage I.

6.5. Ore Deposit Type and Metallogenic Model

The genetic type of the SJS deposit has always been controversial, with two main viewpoints: epithermal type [18,28,40] and magmatic-hydrothermal vein type [27,33,68]. The main difference between the two views is whether the igneous rocks related to mineralization are granites, subvolcanic rocks, or porphyry intrusives. Zhai et al. [18] considered that the SJS mineralization is related to a granite porphyry, where shallow Ag–polymetallic vein ores and deep disseminated Mo ores form a porphyry Mo and epithermal Ag–polymetallic mineralization system. Jiang et al. [93] argued that the mineralization of the deposit is related to a highly-fractionated syenogranite and belongs to a magmatic-hydrothermal vein-type deposit. Zhao et al. [94] also deemed that the deposit belongs to a magmatic-hydrothermal vein-type deposit, but they thought that the mineralization is related to a highly-fractionated quartz syenite porphyry. The ore-forming fluid of the Xinglongshan ore block is characterized by medium–low temperature and low salinity, with a mineralogical assemblage including sphalerite, galena, arsenopyrite, pyrite, pyrrhotite, chalcopyrite, and silver-bearing sulfosalt minerals. These are typical characteristics of intermediate sulfidation epithermal (IS) deposits proposed by Chinchilla et al. [95] and Wang et al. [17]. Our study using field and microscopic investigation showed that the concealed granitic intrusive rocks in the Xinglongshan ore block have obvious granitic and porphyritic-like textures but do not show porphyritic structures. From bottom to top, the granitic complex consists of coarse-grained granite, medium to coarse-grained syenite granite, and fine-grained biotite granite (Figures 3c and 7). These indicate that the mineralization of the ore block is genetically related to granitic plutons and that the ore-forming depth is relatively deep. The main types of Ag–Sn–polymetallic deposits in the SGXR are classified into skarn, epithermal, and magmatic-hydrothermal vein types [14,27,30]. Of

them, deposits of magmatic-hydrothermal vein and skarn types are genetically related to granitic intrusions, while epithermal deposits are related to subvolcanic rocks [27]. Except for a small amount of porphyry Cu–Mo deposits, such as the Banlashan Cu–Mo, Aolunhua Mo–Cu, and Laojiagou Mo–polymetallic deposits, occurring on the eastern slope of the SGXR, no significant porphyry deposits occur on the main ridge and western slope of the SGXR, which, by contrast, is a huge Ag–Sn–polymetallic metallogenic belt characterized by magmatic-hydrothermal veins and epithermal deposits [27]. It is worth noting that in the same mining area, magmatic-hydrothermal vein-type and epithermal deposits often occur simultaneously, such as Baiyinchagandongshan, where the Baiyinchagandongshan magmatic-hydrothermal vein-type Ag–Sn–polymetallic and the Budunwula epithermal Ag–Pb–Zn deposits are developed [14]. In fact, the magmatic-hydrothermal vein-, porphyry-, and epithermal-type deposits in a region usually belong to the same magmatic-hydrothermal system [96], and the determination of different types of deposits mainly depends on their respective formation depths. Sillitoe [96] referred to vein ores that occur within noncarbonate rocks on the lateral to porphyry intrusives as subepithermal deposits. Strictly speaking, these vein deposits are not considered epithermal since they form in a deeper environment (lateral to a porphyry intrusive), although in common with IS epithermal veins, they also form from IS-type fluids and, therefore, can share similar mineralogy and alteration patterns [16]. Our study shows that the mineralization of the Xinglongshan ore block is closely related to the syenogranite and that it belongs to a magmatic-hydrothermal vein-type deposit; the mineralization of the Shuangjianzishan ore block is closely related to the Early Cretaceous subvolcanic rocks and that it belongs to an IS epithermal deposit. We therefore conclude that the Ag–Pb–Zn mineralization at Shuangjianzishan is genetically related to granites and subvolcanic rocks and that it belongs to a magmatic-hydrothermal vein–epithermal metallogenic system rather than a porphyry–epithermal metallogenic system.

Based on the above views, we establish a metallogenic model of volcanic–intrusive complex system to explain the Ag–Pb–Zn mineralization at Shuangjianzishan (Figure 17). Details are as follows:

During the Early Cretaceous, the rollback of the subducted Paleo-Pacific plate resulted in an extensional environment in the SGXR, triggering asthenospheric mantle upwelling [14,27,30]. Mantle-derived basaltic magma underplated beneath the lower crust, leading to partial melting of the crust. Crustal-derived magma mixed with mantle-derived magma to form crust–mantle mixed magma, and the mixed magma rose to the shallow part to form magma chambers [27,30]. The magma underwent fractional crystallization in the shallow magma chamber, forming metal-bearing granitic magma. The metal-bearing magma further rose, forming hypabyssal granitic intrusions. Ore-forming fluid exsolved from the ore-bearing granite mixed with meteoric water, leading to the precipitation of ore-forming materials within the preexisting faults, forming magmatic-hydrothermal vein-type Ag–polymetallic orebodies in the Xinglongshan ore block (Figure 17a). The metal-bearing granitic magma further rose, forming volcanic rocks on the surface and subvolcanic cupolas in volcanic edifices. Ore-forming fluid separated from the subvolcanic cupola mixed with meteoric water, resulting in mineral precipitation to form IS epithermal Ag-dominated Ag–Pb–Zn orebodies in the Shuangjianzishan ore block (Figure 17a). The Early Cretaceous volcanic rocks and intrusive rocks, sharing a common magma chamber, constitute coeval volcanic–intrusive complexes, forming a magmatic-hydrothermal vein-type and epithermal Ag–Pb–Zn–Cu–Sn metallogenic system related to granites and subvolcanic rocks at Shuangjianzishan (Figure 17b).

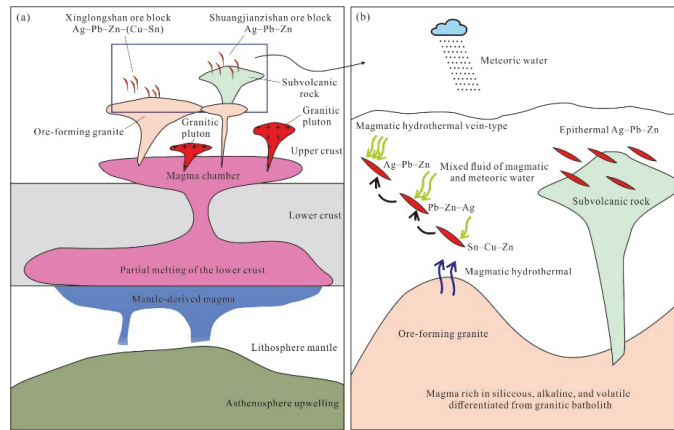


Figure 17. Metallogenic model of the SJS deposit. (a) magmatic-hydrothermal vein-type Ag-polymetallic orebodies in the Xinglongshan ore block. (b) magmatic-hydrothermal vein-type and epithermal Ag-Pb-Zn-Cu-Sn metallogenic system.

7. Conclusions

- (1) The concealed syenogranite genetically related to the mineralization of the Xinglongshan ore block formed at approximately 137 Ma.
- (2) The ore-forming fluid of the Xinglongshan ore block originated from a mixture of magmatic and meteoric water. With the evolution of ore-forming fluid, the amount of meteoric water increased gradually. The ore-forming fluid is characterized by medium-low temperature and low salinity and has an affinity of $\text{H}_2\text{O}-\text{NaCl} \pm \text{CH}_4 \pm \text{C}_6\text{H}_6$ in composition.
- (3) The ore-forming material dominantly came from the Early Cretaceous granitic magma. Fluid mixing was the main mechanism for mineral precipitation.
- (4) The Xinglongshan ore block belongs to a magmatic-hydrothermal vein-type deposit related to the Early Cretaceous syenogranite, and the Shuangjianzishan ore block belongs to an intermediate sulfidation epithermal deposit related to subvolcanic rocks. The Ag-Pb-Zn mineralization at Shuangjianzishan was genetically closely related to the Early Cretaceous volcanic-intrusive complex.

Author Contributions: Conceptualization, J.S. and G.W.; methodology, J.S.; software, J.S. and G.C.; validation, G.W.; formal analysis, J.S., G.C., F.Y. and G.C.; writing—original draft preparation, J.S.; writing—review and editing: G.W.; investigation, J.S., G.C. and B.J.; resources, W.L. and G.W.; data collection, T.Z, J.S. and B.J.; data curation: G.W. and T.Z.; visualization, G.C. and J.S.; supervision, G.W. and W.L.; project administration and funding acquisition, G.W. All authors have read and agreed to the published version of the manuscript.

Funding: This research was financially supported by the National Natural Science Foundation of China (Grant No. 42372111), the Geological Survey Project of Copper and Gold Mineral Resources in Key Metallogenic Zones (Grant No. DD20230287), and the Scientific Research Project of Inner Mongolia Yulong Mining Co., Ltd. (Grant No. 2020110033002072).

Data Availability Statement: Data are contained within the article.

Acknowledgments: We would like to thank Engineers Xuejiao Li, Jing Zhao, Jie Yan, Tingting Zhang, and Yaling Wei from the Inner Mongolia Institute of Geological Survey for their participation during the field geological survey.

Conflicts of Interest: The authors declare no conflicts of interest.

References

1. Gulson, B.L. Differences in lead isotope composition in the stratiform McArthur zinc–lead–silver deposit. *Miner. Deposita* **1975**, *10*, 277–286. [CrossRef]
2. Beaudoin, G.; Sangster, D.F. A descriptive model for silver–lead–zinc veins in clastic metasedimentary terranes. *Econ. Geol.* **1992**, *87*, 1005–1021. [CrossRef]
3. Leach, D.L.; Bradley, D.C.; Huston, D.; Pisarevsky, S.A.; Taylor, R.D.; Gardoll, S.J. Sediment-hosted lead–zinc deposits in Earth history. *Econ. Geol.* **2010**, *105*, 593–625. [CrossRef]
4. Wei, C.; Ye, L.; Huang, Z.L.; Gao, W.; Hu, Y.S.; Li, Z.L.; Zhang, J.W. Ore Genesis and Geodynamic Setting of Laochang Ag–Pb–Zn–Cu Deposit, Southern Sanjiang Tethys Metallogenic Belt, China: Constraints from Whole Rock Geochemistry, Trace Elements in Sphalerite, Zircon U–Pb Dating and Pb Isotopes. *Minerals* **2018**, *8*, 516. [CrossRef]
5. Yu, P.P.; Zheng, Y.; Wang, C.M. Trace elemental and sulfur–lead isotopic variations in metamorphosed volcanogenic massive sulfide (VMS) mineralization systems: An example from the Keketale Pb–Zn (–Ag) deposit, NW China. *Ore Geol. Rev.* **2020**, *125*, 103685. [CrossRef]
6. Sun, C.; Yang, X.Y.; Zhang, H.S.; Ji, W.H.; Chen, B.; Dong, Z.C.; Faisal, M.; Xi, D.H. Tracing the formation and modification of the Keketale VMS-type Pb–Zn deposit, Altai Mountains: Insights from ore deposit geology, geochronology, and magnetite geochemistry. *Ore Geol. Rev.* **2022**, *144*, 104852. [CrossRef]
7. Cooke, D.R.; Bull, S.W.; Large, R.R.; McGoldrick, P.J. The importance of oxidized brines for the formation of Australian Proterozoic stratiform sediment-hosted Pb–Zn (SEDEX) deposits. *Econ. Geol.* **2000**, *95*, 1–18. [CrossRef]
8. Large, R.R.; Bull, S.W.; McGoldrick, P.J.; Walters, S.; Derrick, G.M.; Carr, G.R. Stratiform and strata-bound Zn–Pb–Ag deposits in Proterozoic sedimentary basins, northern Australia. *Econ. Geol.* **2005**, *100*, 931–963.
9. Sangster, D.F. Evidence that Broken Hill-type Pb–Zn deposits are metamorphosed SEDEX deposits. *Miner. Deposita* **2020**, *55*, 1263–1270. [CrossRef]
10. Box, S.E.; Bookstrom, A.A.; Anderson, R.G. Origins of mineral deposits, Belt–Purcell basin, United States and Canada: An introduction. *Econ. Geol.* **2010**, *107*, 1081–1088. [CrossRef]
11. Newberry, R.J.; Einaudi, M.T.; Eastman, H.S. Zoning and genesis of the Darwin Pb–Zn–Ag skarn deposit, California: A reinterpretation based on new data. *Econ. Geol.* **1991**, *86*, 960–982. [CrossRef]
12. Roache, T.J.; Williams, P.J.; Richmond, J.M.; Chapman, L.H. Vein and skarn formation at the Cannington Ag–Pb–Zn deposit, Northeastern Australia. *Can. Mineral.* **2009**, *43*, 241–262. [CrossRef]
13. Megaw, P.K.; Ruiz, J.; Titley, S.R. High-temperature, carbonate-hosted Ag–Pb–Zn (Cu) deposits of northern Mexico. *Econ. Geol.* **1988**, *83*, 1856–1885. [CrossRef]
14. Yang, F.; Wu, G.; Li, R.H.; Zhang, T.; Chen, G.Z.; Xu, Y.M.; Li, Y.L.; Li, T.G.; Liu, R.H.; Chen, Y.J. Age, fluid inclusion, and H–O–S–Pb isotope geochemistry of the Baiyinchagan Sn–Ag–polymetallic deposit in the southern Great Xing’an Range, NE China. *Ore Geol. Rev.* **2022**, *150*, 105194. [CrossRef]
15. Ouyang, H.G.; Mao, J.W.; Santosh, M.; Zhou, J.; Zhou, Z.H.; Wu, Y.; Hou, L. Geodynamic setting of Mesozoic magmatism in NE China and surrounding regions: Perspectives from spatio–temporal distribution patterns of ore deposits. *J. Asian Earth Sci.* **2013**, *78*, 222–236. [CrossRef]
16. Camprubí, A.; Albinson, T. Epithermal deposits in México—Update of current knowledge, and an empirical reclassification. *Geol. Soc. Am. Spec. Pap.* **2007**, *422*, 377–415.
17. Wang, L.; Qin, K.Z.; Song, G.X.; Li, G.M. A review of intermediate sulfidation epithermal deposits and subclassification. *Ore Geol. Rev.* **2019**, *107*, 434–456. [CrossRef]
18. Zhai, D.G.; Williams-Jones, A.E.; Liu, J.J.; Selby, D.; Voudouris, P.C.; Tombros, S.; Li, K.; Li, P.L.; Sun, H.J. The genesis of the giant Shuangjianzishan epithermal Ag–Pb–Zn deposit, Inner Mongolia, northeastern China. *Econ. Geol.* **2020**, *115*, 101–128. [CrossRef]
19. Macario, P.R. Metallogenesis of the Penasquito Polymetallic Deposit: A Contribution to the Understanding of the Magmatic Ore System. Ph.D. Thesis, University of Nevada, Reno, NV, USA, 2016; pp. 1–310.
20. Wang, J.B.; Wang, Y.W.; Wang, L.J.; Uemoto, T. Tin–polymetallic mineralization in the southern part of the Da Hinggan Mountains, China. *Resour. Geol.* **2001**, *51*, 283–291. [CrossRef]
21. Zhou, Z.H.; Mao, J.W.; Lyckberg, P. Geochronology and isotopic geochemistry of the A-type granites from the Huanggang Sn–Fe deposit, southern Great Hinggan Range, NE China: Implication for their origin and tectonic setting. *J. Asian Earth Sci.* **2012**, *49*, 272–286. [CrossRef]
22. Ouyang, H.G.; Mao, J.W.; Zhou, Z.H.; Su, H.M. Late Mesozoic metallogeny and intracontinental magmatism, southern Great Xing’an Range, northeastern China. *Gondwana Res.* **2015**, *27*, 1153–1172. [CrossRef]
23. Liu, H.; Yuan, F.; Zhao, S.J.; Fan, M.J.; Guo, X.G. SHRIMP U–Pb Zircon Ages, Geochemistry and Sr–Nd–Hf Isotope Systematics of the Zalute Intrusive Suite in the Southern Great Xing’an Range, NE China: Petrogenesis and Geodynamical Implications. *Minerals* **2020**, *10*, 927. [CrossRef]
24. Mao, J.W.; Zhou, Z.H.; Wu, G.; Jiang, S.H.; Liu, C.L.; Li, H.M.; Ouyang, H.G.; Liu, J. Metallogenic regularity and minerogenetic series of ore deposits in Inner Mongolia and adjacent areas. *Miner. Depos.* **2013**, *32*, 715–729. (In Chinese with English Abstract).
25. Ouyang, H.G.; Mao, J.W.; Santosh, M.; Wu, Y.; Hou, L.; Wang, X.F. The Early Cretaceous Weilasituo Zn–Cu–Ag vein deposit in the southern Great Xing’an Range, northeast China: Fluid inclusions, H, O, S, Pb isotope geochemistry and genetic implications. *Ore Geol. Rev.* **2014**, *56*, 503–515. [CrossRef]

26. Li, S.H.; Li, Z.X.; Chen, G.Z.; Yi, H.N.; Yang, F.; Lü, X.; Shi, J.P.; Dou, H.B.; Wu, G. Age, Fluid Inclusion, and H–O–S–Pb Isotope Geochemistry of the Superlarge Huaaobaote Ag–Pb–Zn Deposit in the Southern Great Xing’an Range, NE China. *Minerals* **2023**, *13*, 939. [CrossRef]
27. Wu, G.; Liu, R.L.; Chen, G.Z.; Li, T.G.; Li, R.H.; Li, Y.L.; Yang, F.; Zhang, T. Mineralization of the Weilasituo rare metal–tin–polymetallic ore deposit in Inner Mongolia: Insights from fractional crystallization of granitic magmas. *Acta Petrol. Sin.* **2021**, *37*, 637–664. (In Chinese with English Abstract)
28. Wang, F.X.; Bagas, L.; Jiang, S.H.; Liu, Y.F. Geological, geochemical, and geochronological characteristics of Weilasituo Sn–polymetal deposit, Inner Mongolia, China. *Ore Geol. Rev.* **2017**, *80*, 1206–1229. [CrossRef]
29. Chen, G.Z.; Wu, G.; Li, T.G.; Liu, R.L.; Li, R.H.; Li, Y.L.; Yang, F. Mineralization of the Daolundaba Cu–Sn–W–Ag deposit in the southern Great Xing’an Range, China: Constraints from geochronology, geochemistry, and Hf isotope. *Ore Geol. Rev.* **2021**, *133*, 104–117. [CrossRef]
30. Chen, G.Z.; Wu, G.; Yang, F.; Zhang, T.; Li, T.G.; Liu, R.L.; Li, R.H.; Li, Y.L.; Wu, L.W.; Zhang, P.C. Ages, H–O–C–S–Pb isotopes, and fluid inclusion study of the Daolundaba Cu–Sn–W–Ag deposit in Inner Mongolia, NE China. *Ore Geol. Rev.* **2022**, *150*, 105171. [CrossRef]
31. Yang, F.; Wu, G.; Li, R.H.; Zhang, T.; Chen, G.Z.; Chen, Y.J. Petrogenesis of the Alubaogeshan intrusion in the Maodeng–Xiaogushan area, southern Great Xing’an Range, NE China: Implications for magma evolution and tin–polymetallic mineralization. *J. Asian Earth Sci.* **2022**, *238*, 105395. [CrossRef]
32. Yang, F.; Wu, G.; Chen, G.Z.; Li, S.H.; Li, Y.L.; Zhang, T.; Chen, Y.J. Petrogenesis and implications for tin mineralization of the Beidashan granitic pluton, southern Great Xing’an Range, NE China: Constraints from whole-rock and accessory mineral geochemistry. *J. Asian Earth Sci.* **2023**, *259*, 105883. [CrossRef]
33. Kuang, Y.S.; Zheng, G.R.; Lu, M.J.; Liu, Y.L.; Zhang, S.J.; Li, R.Y.; Cheng, W.J. Basic characteristics of Shuangjianzishan silver polymetallic deposit in Chifeng City, Inner Mongolia. *Miner. Depos.* **2014**, *33*, 847–856. (In Chinese with English Abstract)
34. Large, R.R.; Bull, S.W.; Selley, D.; Yang, J.W.; Cooke, D.R.; Garven, G.; McGoldrick, P.J. Controls on the Formation of Giant Stratiform Sediment-Hosted Zn–Pb–Ag Deposits: With Particular Reference to the North Australian Proterozoic. In *Giant Ore Deposits: Characteristics, Genesis and Exploration*; Centre for Special Ore Deposit and Exploration (CODES) Special Publication; Cooke, D.R., Pongratz, J., Eds.; University of Tasmania: Hobart, Australia, 2002; Volume 4, pp. 107–149.
35. Xu, Z.G.; Chen, Y.C.; Wang, D.H.; Chen, Z.H.; Li, H.M. *Scheme of the Classification of the Minerogenetic Units in China*; Geological Publishing House: Beijing, China, 2008; pp. 1–128. (In Chinese)
36. Hedenquist, J.W.; Lowenstern, J.B. The role of magmas in the formation of hydrothermal ore deposits. *Nature* **1994**, *370*, 519–527. [CrossRef]
37. Wang, F.X.; Bagas, L.; Jiang, S.H.; Zhang, F.X.; Liu, Y.F.; Chong, X.X. Geochronology and ore genesis of the Shuangjianzishan Ag–polymetallic deposit, Inner Mongolia, China. *Ore Geol. Rev.* **2019**, *107*, 1020–1045. [CrossRef]
38. Liu, C.H.; Leon, B.; Wang, F.X. Isotopic analysis of the superlarge Shuangjianzishan Pb–Zn–Ag deposit in Inner Mongolia, China: Constraints on magmatism, metallogenesis, and tectonic setting. *Ore Geol. Rev.* **2016**, *75*, 252–267. [CrossRef]
39. Wu, G.B.; Liu, J.M.; Zeng, Q.D.; Sun, H.S.; Liu, M.T. The metallogenic age of Shuangjianzishan Ag–Pb–Zn deposit of Great Hinggan Range, Inner Mongolia. *Acta Miner. Sin.* **2013**, *33*, 619. (In Chinese with English Abstract)
40. Zhang, H.Y.; Zhai, D.G.; Liu, J.J.; Li, P.L.; Li, K.; Sun, H.J. Fluid inclusion and stable (H–O–C) isotope studies of the giant Shuangjianzishan epithermal Ag–Pb–Zn deposit, Inner Mongolia, NE China. *Ore Geol. Rev.* **2019**, *115*, 103–170. [CrossRef]
41. Xue, J.X.; Shi, Y.; Liu, Z.H.; Xue, L.F. Closure of the Eastern Paleo-Asian Ocean: Evidence from Permian–Triassic Volcanic Rocks in the Northern Margin of the North China Craton. *Minerals* **2023**, *13*, 606. [CrossRef]
42. Wang, T.; Guo, L.; Zheng, Y.D.; Donskaya, T.; Gladkochub, D.; Zeng, L.S.; Li, J.B.; Wang, Y.B.; Mazukabzov, A. Timing and processes of late Mesozoic mid–lower-crustal extension in continental NE Asia and implications for the tectonic setting of the destruction of the North China Craton: Mainly constrained by zircon U–Pb ages from metamorphic core complexes. *Lithos* **2012**, *154*, 315–345. [CrossRef]
43. Chen, B.; Jahn, B.M.; Tian, W. Evolution of the Solonker suture zone: Constraints from zircon U–Pb ages, Hf isotopic ratios and whole-rock Sr–Nd isotope compositions of subduction- and collision-related magmas and forearc sediments. *J. Asian Earth Sci.* **2009**, *34*, 245–257. [CrossRef]
44. Lu, L.; Qin, Y.; Zhang, K.J.; Han, C.Y.; Wei, T.; Li, F.Z.; Qu, Z.H. Provenance and tectonic settings of the late Paleozoic sandstones in central Inner Mongolia, NE China: Constraints on the evolution of the southeastern Central Asian Orogenic Belt. *Gondwana Res.* **2019**, *77*, 111–135. [CrossRef]
45. Xu, W.L.; Pei, F.P.; Wang, F.; Meng, E.; Ji, W.Q.; Yang, D.B.; Wang, W. Spatialtemporal relationships of Mesozoic volcanic rocks in NE China: Constraints on tectonic overprinting and transformations between multiple tectonic regimes. *J. Asian Earth Sci.* **2013**, *74*, 167–193. [CrossRef]
46. Zhou, J.B.; Li, L. The Mesozoic accretionary complex in Northeast China: Evidence for the accretion history of Paleo-Pacific subduction. *J. Asian Earth Sci.* **2017**, *145*, 91–100. [CrossRef]
47. Dong, P.P.; Li, Y.J.; Xie, Y.; Wang, J.F.; Li, H.Y. Petrogenesis of the Late Carboniferous Trondhjemite in Central Inner Mongolia in North China and Constraints of Intra-Oceanic Subduction in the Southern Paleo-Asian Ocean. *Minerals* **2022**, *12*, 1212. [CrossRef]

48. Zhang, J.H.; Gao, S.; Ge, W.C.; Wu, F.Y.; Yang, J.H.; Wilde, S.A.; Li, M. Geochronology of the Mesozoic volcanic rocks in the Great Xing'an Range, northeastern China: Implications for subduction-induced delamination. *Chem. Geol.* **2010**, *276*, 144–165. [CrossRef]
49. Zhai, D.G.; Liu, J.J.; Zhang, H.Y.; Tombros, S.; Zhang, A.L. A magmatic-hydrothermal origin for Ag–Pb–Zn vein formation at the Bianjiadayuan deposit, Inner Mongolia, NE China: Evidences from fluid inclusion, stable (C–H–O) and noble gas isotope studies. *Ore Geol. Rev.* **2018**, *101*, 1–16. [CrossRef]
50. Griffin, W.L.; Belousova, E.A.; Shee, S.R.; Pearson, N.J.; O'reilly, S.Y. Archean crustal evolution in the northern Yilgarn Craton: U–Pb and Hf-isotope evidence from detrital zircons. *Precambrian Res.* **2004**, *131*, 231–282. [CrossRef]
51. Frei, D.; Gerdes, A. Precise and accurate in situ U–Pb dating of zircon with high sample throughput by automated LA–SF–ICP–MS. *Chem. Geol.* **2009**, *261*, 261–270. [CrossRef]
52. Jackson, S.E.; Pearson, N.J.; Griffin, W.L.; Belousova, E.A. The application of laser ablation-inductively coupled plasma-mass spectrometry to in situ U–Pb zircon geochronology. *Chem. Geol.* **2004**, *211*, 47–69. [CrossRef]
53. Black, L.P.; Gulson, B.L. The age of the mud tank carbonatite, strangways range, northern territory. *Geol. Geophys.* **1978**, *3*, 227–232.
54. Ludwig, K.R. *User's Manual for Isoplot/Ex, Version 3.0, A Geochronological Toolkit for Microsoft Excel*; Berkeley Geochronology Center: Berkeley, CA, USA, 2003; pp. 1–74.
55. Andersen, T. Correction of common lead in U–Pb analyses that do not report ^{204}Pb . *Chem. Geol.* **2002**, *192*, 59–79. [CrossRef]
56. Bodnar, R.J. Revised equation and table for determining the freezing-point depression of H_2O – NaCl solutions. *Geochim. Cosmochim. Acta* **1993**, *57*, 683–684. [CrossRef]
57. Brown, P.E. FLINCOR: A microcomputer program for the reduction and investigation of fluid-inclusion data. *Am. Mineral.* **1989**, *74*, 1390–1393.
58. Clayton, R.N.; Mayeda, T.K. The use of bromine pentafluoride in the extraction of oxygen from oxides and silicates for isotopic analysis. *Geochim. Cosmochim. Acta* **1963**, *27*, 43–52. [CrossRef]
59. Coleman, M.L.; Shepherd, T.J.; Durham, J.J.; Rouse, J.E.; Moore, G.R. Reduction of water with zinc for hydrogen isotope analysis. *Anal. Chem.* **1982**, *54*, 993–995. [CrossRef]
60. Clayton, R.N.; Mayeda, T.K.; Oneil, J.R. Oxygen isotope: Exchange between quartz and water. *J. Geophys. Res.–Earth* **1972**, *77*, 3057–3067. [CrossRef]
61. Todt, W.; Cliff, R.A.; Hanser, A.; Hofmann, A.W. Re-calibration of NBS lead standards using a ^{202}Pb – ^{205}Pb double spike. *Terra Abstr.* **1993**, *5*, 396.
62. Goldstein, R.H.; Reynolds, T.J. *Systematics of Fluid Inclusions in Diagenetic Minerals*; SEPM Society for Sedimentary Geology: Tulsa, OK, USA, 1994; pp. 1–199.
63. Sheppard, S.M.F. Characterization and isotopic variations in natural-waters. *Rev. Mineral. Geochem.* **1986**, *16*, 165–183.
64. Chen, Y.W.; Mao, C.X.; Zhu, B.Q. Lead isotopic composition and genesis of Phanerozoic metal deposit in China. *Geochemistry* **1982**, *1*, 137–158. [CrossRef]
65. Cui, M. The Geochemical Characteristics and Diagenesis of Ore-Forming Diorite-Porphyrite from Shuangjianzishan Ag Polymetallic Deposit in Inner Mongolia. Master's Thesis, China University of Geosciences (Beijing), Beijing, China, 2015. (In Chinese with English Abstract).
66. Ouyang, H.G.; Li, R.H.; Zhou, Z.H. The Jurassic mineralization of the Shuangjianzishan Ag-polymetallic deposit and its significance in prospecting: Evidence from geochronology. *Acta Geol. Sin.* **2016**, *90*, 1835–1845, (In Chinese with English Abstract).
67. Wang, F.X. Magmatic Activity and Silver Polymetallic Mineralization in the Shuangjianzishan Silver Polymetallic Deposit and Its Surrounding Areas in Inner Mongolia. Ph.D. Thesis, China University of Geosciences, Wuhan, China, 2018; pp. 1–189. (In Chinese with English Abstract)
68. Wu, Y.H.; Han, J.T.; Liu, Y.H.; Ma, G.Q.; Han, F.X.; Yang, Y.C.; Liu, L.J.; Guo, L.; Guan, Y.; Zhang, Y.H.; et al. Metallogenic model of the Shuangjianzishan Ag–Pb–Zn district, Northeast China: Revealed from integrated geophysical investigation. *Geosci. Front.* **2022**, *13*, 101321. [CrossRef]
69. Wang, F.X.; Sun, H.J.; Pei, R.F.; Liu, Y.F.; Liu, C.H.; Jiang, S.H. The geologic features and genesis of Shuangjianzishan silver-polymetallic deposit, Balinzuo Qi, Inner Mongolia. *Geol. Rev.* **2016**, *62*, 1241–1256. (In Chinese with English Abstract)
70. Liu, Y.F.; Jiang, S.H.; Bagas, L. The genesis of metal zonation in the Weilasituo and Bairendaba Ag–Zn–Pb–Cu–(Sn–W) deposits in the shallow part of a porphyry Sn–W–Rb system, Inner Mongolia, China. *Ore Geol. Rev.* **2016**, *75*, 150–173. [CrossRef]
71. Yang, F.; Sun, J.G.; Wang, Y.; Fu, J.Y.; Na, F.C.; Fan, Z.Y.; Hu, Z.Z. Geology, Geochronology and Geochemistry of Weilasituo Sn–Polymetallic Deposit in Inner Mongolia, China. *Minerals* **2019**, *9*, 104. [CrossRef]
72. Rye, R.O.; Ohmoto, H. Sulfur and carbon isotopes and ore genesis: A review. *Econ. Geol.* **1974**, *69*, 826–842. [CrossRef]
73. Wilkinson, J.J.; Jenkin, G.R.T.; Fallick, A.E.; Foster, R.P. Oxygen and hydrogen isotopic evolution of Variscan crustal fluids, south Cornwall, UK. *Chem. Geol.* **1995**, *123*, 239–254. [CrossRef]
74. Ohmoto, H. Formation of volcanogenic massive sulfide deposits: The Kuroko perspective. *Ore Geol. Rev.* **1996**, *10*, 135–177. [CrossRef]
75. Taylor, H.P., Jr.; Frechen, J.; Degens, E.T. Oxygen and carbon isotope studies of carbonatites from the Laacher See District, West Germany and the Alnö District, Sweden. *Geochim. Cosmochim. Acta* **1967**, *31*, 407–430. [CrossRef]
76. Hoefs, J. Isotope Fractionation Processes of Selected Elements. In *Stable Isotope Geochemistry*, 9th ed.; Springer Nature Switzerland AG: Cham, Switzerland, 2021; pp. 1–528.

77. Faure, G. *Origin of Igneous Rocks: The Isotopic Evidence*; Springer Science & Business Media: Cham, Switzerland, 2013; pp. 1–398.
78. Townley, B.K.; Godwin, C.I. Isotope characterization of lead in galena from ore deposits of the Aysen Region, southern Chile. *Miner. Depos.* **2001**, *36*, 45–57. [CrossRef]
79. Kamenov, G.D.; Macfarlane, A.W.; Riciputi, L.R. Sources of lead in the San Cristobal, Pulacayo, and Potosi mining districts, Bolivia, and a reevaluation of regional ore lead isotope provinces. *Econ. Geol.* **2002**, *97*, 573–592.
80. Marcoux, E.; Grancea, I.; Lupulescu, M. Lead isotope signatures of epithermal and porphyry-type ore deposits from the Romanian Carpathian Mountains. *Miner. Depos.* **2002**, *37*, 173–184. [CrossRef]
81. Chiaradia, M.; Fontboté, L.; Paladines, A. Metal sources in mineral deposits and crustal rocks of Ecuador (1 N–4 S): A lead isotope synthesis. *Econo. Geol.* **2004**, *99*, 1085–1106.
82. Zartman, R.E.; Doe, B.R. Plumbotectonics: The model. *Tectonophysics* **1981**, *75*, 135–162. [CrossRef]
83. Zhu, B.Q. Tri-dimension spacial topological diagrams of ore lead isotopes and their application to the division of geochemical provinces and mineralizations. *Geochimica* **1993**, *21*, 209–216. (In Chinese with English Abstract)
84. Richards, J.P. Magmatic to hydrothermal metal fluxes in convergent and collided margins. *Ore Geol. Rev.* **2011**, *40*, 1–26. [CrossRef]
85. Pearson, R.G. Hard and soft acids and their bases. *J. Am. Chem. Soc.* **1963**, *85*, 3533–3539. [CrossRef]
86. Stefansson, A.; Seward, T.M. Experimental determination of the stability and stoichiometry of sulphide complexes of silver (I) in hydrothermal solutions to 400 degrees. *Geochim. Cosmochim. Acta* **2003**, *67*, 1395–1413. [CrossRef]
87. Williams-Jones, A.E.; Migdisov, A.A. Experimental Constraints on the Transport and Deposition of Metals in Ore-Forming Hydrothermal Systems. In *Building Exploration Capability for the 21st Century*; Society of Economic Geologists, Inc.: Littleton, CO, USA, 2014; pp. 77–95.
88. Zhong, R.C.; Brugger, J.; Chen, Y.J.; Li, W.B. Contrasting regimes of Cu, Zn and Pb transport in ore-forming hydrothermal fluids. *Chem. Geol.* **2015**, *395*, 154–164. [CrossRef]
89. Wood, S.A.; Samson, I.M. The hydrothermal geochemistry of tungsten in granitoid environments: I. Relative solubilities of ferberite and scheelite as a function of T, P, pH, and m (NaCl). *Econ. Geol.* **2000**, *95*, 143–182. [CrossRef]
90. Pirajno, F. *Hydrothermal Processes and Mineral Systems*; Springer Science & Business Media B.V.: Perth, Australia, 2009; pp. 1–1250.
91. Seward, T.M.; Williams-Jones, A.E.; Migdisov, A.A. The Chemistry of Metal Transport and Deposition by Ore-Forming Hydrothermal Fluids. In *Treatise on Geochemistry*; Elsevier Ltd.: Amsterdam, The Netherlands, 2014; pp. 29–57.
92. Korges, M.; Weis, P.; Lüders, V.; Laurent, O. Depressurization and boiling of a single magmatic fluid as a mechanism for tin–tungsten deposit formation. *Geology* **2017**, *46*, 75–78. [CrossRef]
93. Jiang, S.H.; Chen, C.L.; Bagas, L.; Liu, Y.; Han, N.; Kang, H.; Wang, Z.H. Two mineralization events in the Baiyinnuoer Zn–Pb deposit in Inner Mongolia, China: Evidence from field observations, S–Pb isotopic compositions and U–Pb zircon ages. *J. Asian Earth Sci.* **2017**, *144*, 339–367. [CrossRef]
94. Zhao, J.Q.; Zhou, Z.H.; Ouyang, H.G.; Chen, B.Q.; Liu, W.J.; Yang, F. Zircon U–Pb age and geochemistry of quartz syenite porphyry in Shuangjianzishan Ag–Pb–Zn (Sn) deposit, Inner Mongolia, and their geological implications. *Miner. Depos.* **2022**, *41*, 324–344. (In Chinese with English Abstract).
95. Chinchilla, D.; Ortega, L.; Piña, R.; Merinero, R.; Moncada, D.; Bodnar, R.J.; Quesada, C.; Valverde, C.; Lunar, R. The Patricia Zn–Pb–Ag epithermal ore deposit: An uncommon type of mineralization in northeastern Chile. *Ore Geol. Rev.* **2016**, *73*, 104–126. [CrossRef]
96. Sillitoe, R.H. Porphyry copper systems. *Econ. Geol.* **2010**, *105*, 3–41. [CrossRef]

Disclaimer/Publisher’s Note: The statements, opinions and data contained in all publications are solely those of the individual author(s) and contributor(s) and not of MDPI and/or the editor(s). MDPI and/or the editor(s) disclaim responsibility for any injury to people or property resulting from any ideas, methods, instructions or products referred to in the content.

Article

Age, Fluid Inclusion, and H–O–S–Pb Isotope Geochemistry of the Superlarge Huaaobaote Ag–Pb–Zn Deposit in the Southern Great Xing’an Range, NE China

Shihui Li^{1,2,3}, Zhenxiang Li³, Gongzheng Chen⁴, Huineng Yi³, Fei Yang^{1,2}, Xin Lü³, Jiangpeng Shi^{1,2}, Haibo Dou³ and Guang Wu^{1,2,4,*}

- ¹ MNR Key Laboratory of Metallogeny and Mineral Assessment, Institute of Mineral Resources, Chinese Academy of Geological Sciences, Beijing 100037, China; leshihui@126.com (S.L.)
² School of Earth and Space Sciences, Peking University, Beijing 100871, China
³ Inner Mongolia Yulong Mining Co., Ltd., Xilinhot 026200, China
⁴ College of Earth Sciences, Hebei GEO University, Shijiazhuang 050031, China
* Correspondence: wuguang65@163.com

Abstract: The superlarge Huaaobaote Ag–Pb–Zn deposit is located on the western slope of the southern Great Xing’an Range (SGXR). The deposit includes four ore blocks, namely, ore blocks I, II, III, and V. Except for the no. I orebody of ore block I, which is hosted in the contact zone between the Carboniferous serpentinized harzburgite and the Permian siltstone, the other orebodies all occur as veins controlled by faults. The mineralization process at the deposit can be divided into four stages: cassiterite–arsenopyrite–pyrite–quartz stage (stage I), cassiterite–chalcopyrite–pyrite–freibergite–arsenopyrite–pyrrhotite–quartz stage (stage II), sphalerite–galena–jamesonite–stibnite–freibergite–silver mineral–quartz–calcite–chlorite stage (stage III), and argentite–pyrrargyrite–pyrite–quartz–calcite (stage IV). Cassiterite U–Pb dating of the Huaaobaote deposit yielded ages of 136.3–134.3 Ma, indicating that the deposit formed in the Early Cretaceous period. Two types of fluid inclusions (FIs), including liquid-rich and gas-rich FIs, have been distinguished in the quartz vein and sphalerite. The homogenization temperature during the four stages gradually decreases, with temperatures of 302–340 °C for stage I, 267–304 °C for stage II, 186–273 °C for stage III, and 166–199 °C for stage IV, respectively. The salinity (wt% NaCl eqv.) at stages I, II, III, and IV is 3.7–6.6, 0.2–4.5, 0.2–5.0, and 0.4–1.6, respectively, indicating that the ore-forming fluid is characterized by low salinity. The $\delta^{18}\text{O}_{\text{water}}$ and δD values of the ore-forming fluid range from -11.9‰ to 7.9‰ and -168‰ to -76‰ , respectively, indicating that the ore-forming fluid was dominantly derived from a mixture of magmatic and meteoric water. The calculated $\delta^{34}\text{S}_{\text{H}_2\text{S}}$ values range from -3.6‰ to 1.2‰ , indicating that the sulfur mainly came from granitic magma. The $^{206}\text{Pb}/^{204}\text{Pb}$, $^{207}\text{Pb}/^{204}\text{Pb}$, and $^{208}\text{Pb}/^{204}\text{Pb}$ ratios of sulfides are in the ranges of 18.195–18.317, 15.509–15.667, and 37.965–38.475, respectively, implying that the ore-forming material was mainly derived from felsic magma that may be formed by the partial melting of orogenic materials. Fluid mixing, cooling, and immiscibility were the three primary mechanisms for mineral precipitation in the Huaaobaote deposit.

Keywords: cassiterite U–Pb age; fluid inclusion; H–O–S–Pb isotopes; Huaaobaote Ag–Pb–Zn deposit; southern Great Xing’an Range

Citation: Li, S.; Li, Z.; Chen, G.; Yi, H.; Yang, F.; Lü, X.; Shi, J.; Dou, H.; Wu, G. Age, Fluid Inclusion, and H–O–S–Pb Isotope Geochemistry of the Superlarge Huaaobaote Ag–Pb–Zn Deposit in the Southern Great Xing’an Range, NE China. *Minerals* **2023**, *13*, 939. <https://doi.org/10.3390/min13070939>

Academic Editors: Yitian Wang, Changqing Zhang, Alfons M. Van den Kerkhof and Jan Marten Huizenga

Received: 29 April 2023

Revised: 6 July 2023

Accepted: 10 July 2023

Published: 13 July 2023



Copyright: © 2023 by the authors. Licensee MDPI, Basel, Switzerland. This article is an open access article distributed under the terms and conditions of the Creative Commons Attribution (CC BY) license (<https://creativecommons.org/licenses/by/4.0/>).

1. Introduction

The southern Great Xing’an Range (SGXR), located in the intersection of the Paleo-Asian and the circum-Pacific metallogenic megaprovinces (Figure 1a,b), is the most important Pb–Zn–Ag–Sn metallogenic belt in northern China [1–5]. To date, the range is known to host six superlarge, seven large, thirty-nine medium, and numerous small-sized Pb–Zn–Ag–polymetallic deposits (Figure 1c), with proven reserves of 8,130,000 tons Pb + Zn, 57,000 tons Ag, 850,000 tons Sn, 580,000 tons Cu, and 600,000 tons Li_2O [2,6–11].

The types of these Pb–Zn–Ag–polymetallic deposits in this area can be classified into an intrusion-related vein type, a subvolcanic-related vein type, and a skarn type. Some examples include the intrusion-related vein-type Baiyinchagandongshan Ag–Sn–Pb–Zn–Cu deposit [12] and Weilasituo Li–Sn–Pb–Zn–Cu deposit [13], the subvolcanic-related vein-type Huaobaote Ag–Pb–Zn–Cu–Sn deposit [14] and Dajing Sn–Cu–Pb–Zn–Ag deposit [15], and the skarn-type Baiyinnuoer Pb–Zn deposit [16] and Haobugao Pb–Zn–Cu–Fe deposit [17]. The ore-forming element assemblage in these deposits is dominated by Ag–Pb–Zn, followed by Ag–Pb–Zn–Cu and Sn–Ag–Pb–Zn–Cu [2,13]. Numerous studies have revealed that the ages of mineralization and ore-related igneous rocks of these deposits are concentrated during the Late Jurassic–Early Cretaceous, especially in the Early Cretaceous [3,18–23].

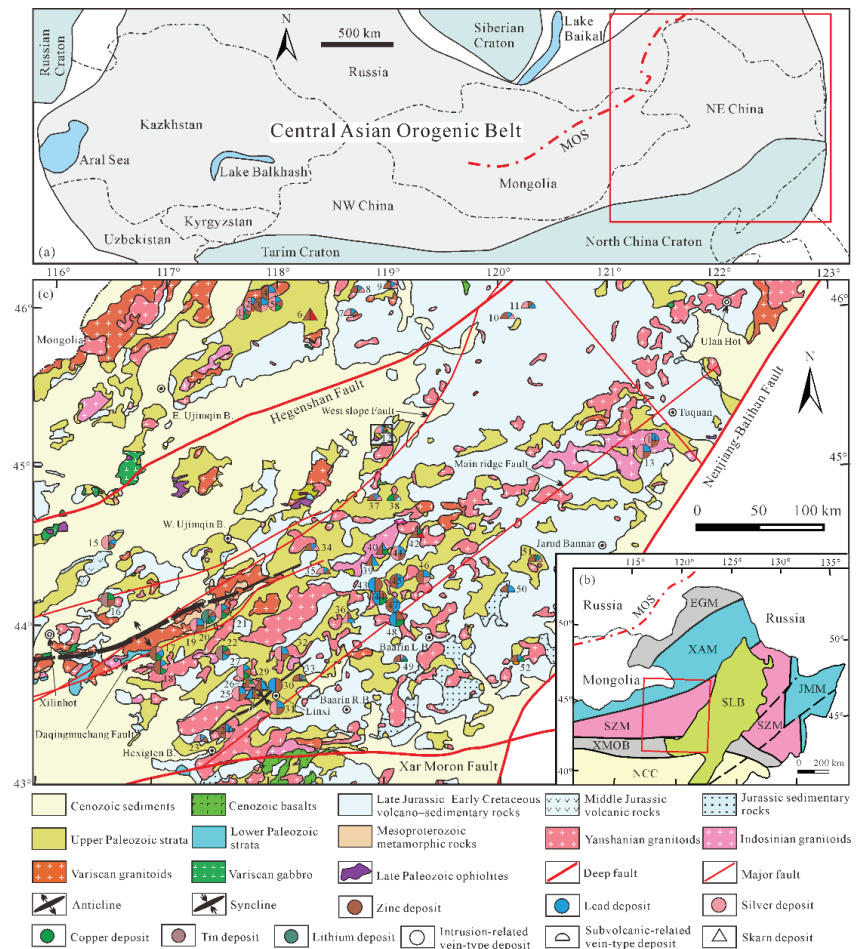


Figure 1. (a) Sketch geological map of the Central Asian Orogenic Belt (modified after [24]), showing the location of NE China; (b) simplified geotectonic division of NE China (after [25]); (c) geological map of the southern Great Xing’an Range and its neighboring areas, showing locations of major Pb–Zn–Ag–polymetallic deposits (geological base map modified after [9]); ore deposits modified after [13]. Notes: EGM = Ergun massif; JMM = Jiamusi massif; MOS = Mongol–Okhotsk suture zone; NCC = North China craton; SLB = Songliao basin; SZM = Songnen–Zhangguangcai Range massif;

XAM = Xing'an massif; XMOB = Xar Moron orogenic belt. Names of numbered Pb–Zn–Ag–polymetallic deposits: 1 = Hua'naote Ag–Pb–Zn–Cu deposit; 2 = Highland 1017 Ag–Pb–Zn deposit; 3 = Buyan'alin Pb–Zn–Ag deposit; 4 = Dugerlin Pb–Zn–Ag deposit; 5 = Jilinbaolige Ag–Pb–Zn–Cu deposit; 6 = Chagan'aobao Zn–Fe deposit; 7 = Wulantaolegaidong Ag–Pb–Zn deposit; 8 = Gunhudugengou Pb–Zn–Ag deposit; 9 = Lemageshan Pb–Zn–Ag deposit; 10 = Zhamuqin Pb–Zn–Ag deposit; 11 = Fuxingtun Ag–Pb–Zn deposit; 12 = Huaaobaote Ag–Pb–Zn–Cu–Sn deposit; 13 = Maohuduger Ag–Pb–Zn deposit; 14 = Meng'entaolegai Ag–Pb–Zn deposit; 15 = Baiyinchagandongshan Ag–Sn–Pb–Zn–Cu deposit; 16 = Maodeng–Xiaogushan Sn–Cu–Zn deposit; 17 = Aobaoshan Pb–Zn–Ag–Cu deposit; 18 = Harchulutu Pb–Zn–Ag–Cu deposit; 19 = Bayanwula Ag–Pb–Zn deposit; 20 = Weilasituo Li–Sn–Pb–Zn–Cu deposit; 21 = Bairendaba Ag–Pb–Zn–Cu deposit; 22 = Anle Sn–Cu–Pb–Zn deposit; 23 = Shidi Ag–Pb–Zn deposit; 24 = Dadi Ag–Pb–Zn deposit; 25 = Yonglong Ag–Pb–Zn deposit; 26 = Hadatu Pb–Zn–Cu–Ag deposit; 27 = Huangtuliang Ag–Pb–Zn–Cu deposit; 28 = Nasitai Pb–Zn deposit; 29 = Shalonggou Pb–Zn deposit; 30 = Erbadi Pb–Zn deposit; 31 = Bianjiadayuan Ag–Pb–Zn deposit; 32 = Xishijiangshan Ag–Pb–Zn deposit; 33 = Dajing Sn–Cu–Pb–Zn–Ag deposit; 34 = Wulanbaiqi Pb–Zn–Ag deposit; 35 = Chaowula Ag–Pb–Zn deposit; 36 = Daihuanggou Ag–Pb–Zn deposit; 37 = Bujinhei Pb–Zn–Ag deposit; 38 = Shabulengshan Cu–Zn–Mo deposit; 39 = Baiyinnuoer Pb–Zn deposit; 40 = Nailinba Pb–Zn–Cu deposit; 41 = Shuangjianzishan Ag–Pb–Zn deposit; 42 = Haobugao Pb–Zn–Cu–Fe deposit; 43 = Aguihundelun Pb–Zn deposit; 44 = Baiyinwula Pb–Zn–Cu deposit; 45 = Erdaoyingzi Pb–Zn deposit; 46 = Dongshan Pb–Zn–Ag deposit; 47 = Biliutaibei Pb–Zn deposit; 48 = Taipingdi Pb–Zn–Cu deposit; 49 = Hongguangmuchang Zn–Ag–Cu deposit; 50 = Aobaotu Pb–Zn deposit; 51 = Shuiquan Pb–Zn–Cu–Ag deposit; 52 = Panjiaduan Pb–Zn–Cu deposit.

The superlarge Huaaobaote Ag–Pb–Zn deposit accompanied by Cu, Sn, and Sb is located on the west slope of the SGXR. Previous studies have mainly focused on the characteristics of the Ag–Pb–Zn orebodies of the deposit [14,26,27] and the age of the igneous rocks in the ore district [28–30]. The mineralization of the Huaaobaote deposit is closely related to the subvolcanic rocks [14] and is distinguished from the Sn–Ag–polymetallic deposits in the SGXR, which are mainly related to Early Cretaceous highly fractionated granite [13]. Nevertheless, the lack of an accurate mineralization age and information on ore-forming fluids considerably constrains the understanding of genesis for the deposit. In this paper, we report cassiterite U–Pb age, fluid inclusions, and H–O–S–Pb isotopes of the Huaaobaote deposit, and discuss its possible ore-forming fluid source, metal source, and metallogenic mechanism. We intend to improve our understanding of the mineralization of Ag–Pb–Zn–polymetallic deposits related to subvolcanic magmatic activity in the SGXR.

2. Regional Geology

The SGXR, located in the central part of the Songnen–Zhangguangcai Range massif (Figure 1b), is bounded by the Hegenshan fault in the north, the Xar Moron fault in the south, the Nenjiang–Balihan fault in the east, and the East Ujimqin Banner–Xilinhot area in the west (Figure 1c). The tectonic evolution of the SGXR is dominated by the Paleo-Asian Ocean tectonic regime during the Paleozoic, and the Mongol–Okhotsk Ocean and Paleo-Pacific tectonic regimes in the Mesozoic [13,31,32].

The exposed strata in the SGXR include Mesoproterozoic, Paleozoic, Mesozoic, and Cenozoic (Figure 1c). The Mesoproterozoic (Xilin Gol complex), the oldest formation in the SGXR, being mainly composed of amphibole–plagioclase gneisses, biotite-bearing granitic gneiss, and mica schist, is mainly distributed in the southern part of Xilinhot and West Ujimqin Banner. The Lower Paleozoic primarily consists of marine volcanic rocks, carbonate rocks, and clastic rocks, which are only scattered in the southeast of Xilinhot and the southwest of Hexigten Banner. The Upper Paleozoic, including a set of marine clastic rocks, volcanic rocks, pyroclastic rocks, carbonates rocks assemblages, and continental clastic rocks, is widely distributed in the SGXR. The Mesozoic strata, including Jurassic–Cretaceous continental intermediate–felsic volcanic rocks and pyroclastic rocks, are widely distributed in a NE-trending belt, but the Triassic strata are absent due to the rapid uplifting

during this period [33]. The Cenozoic strata are composed of unconsolidated sediments and basalts [33]. Fold and fault structures are well-developed in the SGXR. Fold structures mainly formed in the late Variscan and are orientated in a NE or NEE direction, such as the Ganzhuermiao anticline and Linxi syncline (Figure 1c). Compared with the Variscan, the Yanshanian folds are fewer and exhibit broad anticline and syncline. The major faults include the NEE–NE-trending Hegenshan fault, approximate EW-trending Xar Moron fault, NE–NNE-trending Nenjiang–Balihan fault, and Great Xing’an Range main ridge fault (Figure 1c). The Ganzhuermiao anticline, Linxi syncline, Hegenshan fault, and Xar Moron fault formed in the Late Paleozoic due to the subduction, accretion, and closure of the Paleo-Asian Ocean, and established the basic tectonic framework in the SGXR [34,35]. The Great Xing’an Range main ridge and Nenjiang–Balihan faults formed during the Mesozoic, primarily in response to NW-dipping subduction of the Paleo-Pacific plate beneath the Eurasian continent and the subsequent subduction plate rollback [36,37]. The intrusive rocks in the SGXR can be subdivided into the Variscan, Indosinian, and Yanshanian [21,38,39]. The Variscan intrusive rocks, including hornblende gabbro, hornblende diorite, tonalite, granodiorite, and granite, with ages of 354–305 Ma, are scattered in southern Xilinhot and on both sides of the Hegenshan fault [40–45]. The Indosinian intrusive rocks with ages of 248–216 Ma, consisting of two-mica granite, biotite granodiorite, and granodiorite porphyry, are widely and sporadically distributed in the SGXR [16,46,47]. The Yanshanian intrusive rocks, being mainly composed of the Late Jurassic–Early Cretaceous granite and granite porphyry, as stock or batholith, are widely distributed along the NE–NNE-trending main ridge of the SGXR, and their zircon U–Pb ages range from 184 to 120 Ma, concentrated at 140–130 Ma [13,21,47–51]. Among them, the Late Jurassic–Early Cretaceous magmatism has a close genetic connection with the Ag–Pb–Zn–polymetallic mineralization of the SGXR [13].

3. Ore Geology

The superlarge Huaaobaote Ag–Pb–Zn deposit (No. 12 deposit in Figure 1c) is located 138 km northeast of West Ujimqin Banner, Inner Mongolia, with geographic coordinates of 118°56′30″–118°58′00″ longitude (east) and 45°15′00″–45°16′00″ latitude (north).

In the Huaaobaote area, the outcrop rocks are stratigraphically assigned to the Lower Permian Shoushangou Formation, Lower–Middle Permian Dashizhai Formation, Middle Jurassic Wanbao Formation, Upper Jurassic Manketouebo and Manitu formations, Lower Cretaceous Baiyin’gaolao Formation, Upper Neogene Baogedawula and Wuchagou formations, and Quaternary (Figure 2). The Shoushangou Formation consists of marine sandstone. The Dashizhai Formation is composed of marine intermediate–acidic volcanic rocks and pyroclastic rocks. The Wanbao Formation comprises continental clastic rocks. The Manketouebo consists of continental rhyolite, tuff, and pyroclastic rocks. The Manitu Formation is composed of continental intermediate–acidic lavas and pyroclastic rocks. The Baiyin’gaolao Formation comprises continental acidic lava and tuff. The Baogedawula Formation consists of sandy mudstone. The Wuchagou Formation is mainly composed of basalt, and the Quaternary comprises loose sediments. The Shoushangou and Dashizhai formations, the main host rock, are widely distributed in the northeastern part of the Huaaobaote area. The volcanic rocks and volcanoclastic rocks of the Jurassic–Cretaceous unconformably overlie the pre-Mesozoic strata.

The period of magmatism at Huaaobaote can be divided into the Variscan and Yanshanian. The former primarily consists of the Carboniferous serpentinized harzburgite and a small volume of gabbro, as well as the Permian diorite porphyry (Figure 2). The latter is generally composed of the Cretaceous syenogranite and monzogranite, as well as hypabyssal rhyolite. The serpentinized harzburgite and gabbro, with a zircon U–Pb age of 337.3 ± 3.2 Ma [29], are distributed along the Huaaobaote tectonic mélange belt that is part of the Meilaotewula ophiolite belt. The Permian diorite porphyry, with zircon U–Pb ages of 285.9 ± 4.1 Ma [29] and 294.8 ± 3.2 Ma [30], is scattered in the eastern part of the Huaaobaote area. The Early Cretaceous intrusions are mainly distributed in the southwestern part of the

Huaaobaote area, such as the Ganggantewula intrusion. Moreover, there are also quantities of the Early Cretaceous granite porphyry and hypabyssal rhyolite veins, with zircon U–Pb ages of 136–132.6 Ma [27,29,30], which are closely related to the spatial distribution of the orebodies.

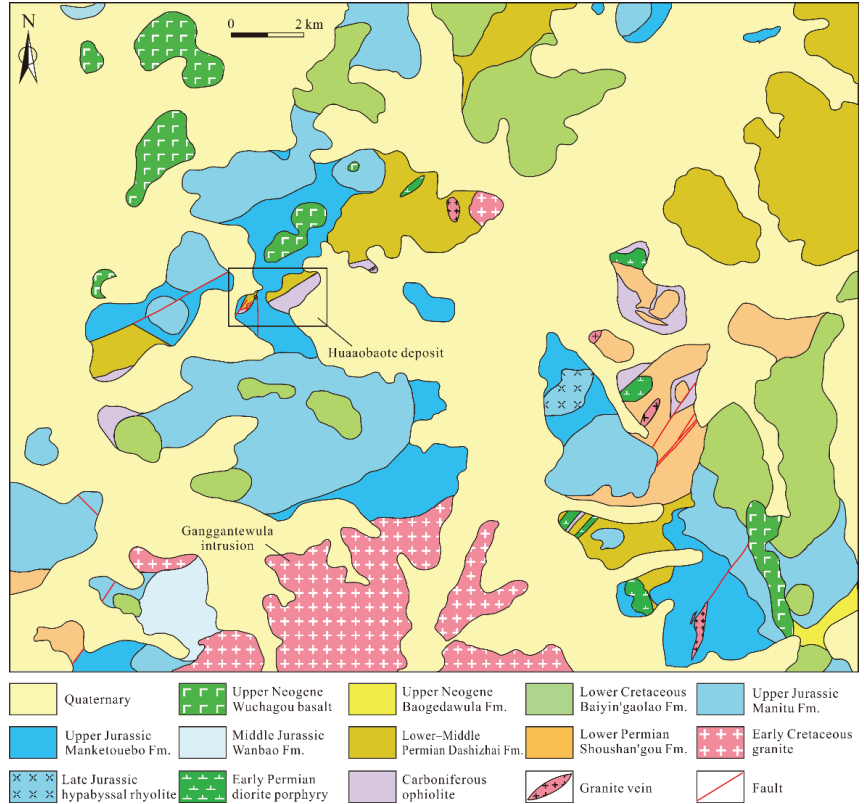


Figure 2. Simplified regional geological map of the Huaaobaote area (modified after [52]).

Structures in the Huaaobaote area are dominated by faults and folds. The NW-, NNE-, near N-trending faults, including the NEE-trending tectonic mélangé belt, are the major ore-controlling structures in the Huaaobaote area, which may have originally formed during the accretion or closure stage of the Paleo-Asian Ocean and reactivated in the Yanshanian [14,33]. The NE-trending faults largely formed during the Yanshanian, with extensional features, which control the placement of the Early Cretaceous magmatic rocks [14,33]. Fold deformation mainly involves the Permian strata, while the Mesozoic strata are weakly deformed [52].

The Huaaobaote deposit, discovered by the Inner Mongolia Autonomous Region No. 10 Institute of Geological and Mineral Exploration and Development in 2001, contains proven reserves of 6369 tons Ag, 710,000 tons Pb, 920,000 tons Zn, 57,000 tons Cu, and 14,000 tons Sn, with average grades of 193 g/t Ag, 1.99% Pb, 2.37% Zn, 1.70% Cu, and 0.42% Sn, respectively, and is associated with 94,000 tons Sb [53].

According to the distribution of the orebodies, the deposit is divided into four ore blocks numbered I to IV (Figure 3). Ore block I, at the southern end of the deposit, is mainly composed of Ag–Pb–Zn–Sb orebodies and pyrite–pyrrhotite orebodies (Figures 3 and 4a). Of them, orebody I₁, with a length of 250 m and an extended depth of 273 m, is one of the typical Ag–Pb–Zn–Sb orebodies in the deposit. The orebody is mainly hosted in the contact

zone between the Carboniferous serpentinized harzburgite and the Permian sandstone, which dips SSE at 45° – 60° . At the intersection of the NW-trending faults and the contact zone, orebody I₁ usually dilates as a cystic column or rhombic column (Figures 3 and 4a). Ore blocks II and III, located in the west and east of the deposit, respectively, consist of Pb–Zn–Ag–Sb orebodies. These orebodies are dominantly hosted in the Permian siltstone and are mainly controlled by the NW-trending faults, with some being controlled by near N- and NNE-trending faults (Figures 3 and 4b,c). Orebody II₂, with a length of 450 m, a thickness of 0.7–60.1 m, and an extended depth of 530 m, is the largest orebody in ore blocks II and III and dips to the NE at 45° – 70° . Ore block V, located in the central region of the deposit, is dominated by Ag–Cu–Sn orebodies, and these orebodies are controlled by NNE- and near N-trending faults with a large dip angle of 80° – 90° (Figures 3 and 4d). The Early Cretaceous hypabyssal rhyolite veins are mainly distributed along nearly N-trending faults with dip angles of 70° – 80° , in which a small amount of low-grade stockwork mineralization develops (Figure 3).

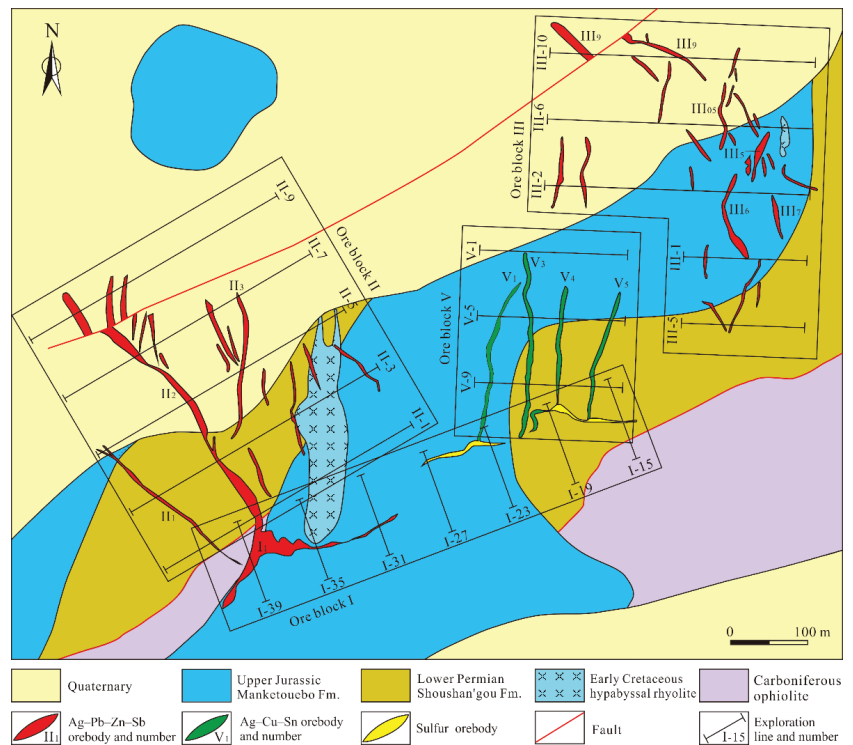


Figure 3. Geological map of the Huaaobaote deposit, showing the surface projection positions of the concealed orebodies at the 855-m level.

The ore minerals of the Sn orebodies in ore block V are mainly cassiterite, pyrite, and arsenopyrite, with gangue mineral of quartz (Figure 5a,i). The ore minerals of the Ag–Cu–Sn orebodies in ore block V are mainly chalcopyrite, cassiterite, arsenopyrite, pyrite, and freibergite, with gangue minerals of quartz, sericite, and chlorite (Figure 5b,c,j,k). The ore minerals of the Ag–Pb–Zn–Sb orebodies in the deposit are mainly galena, sphalerite, jamesonite, and freibergite, with gangue minerals of quartz and calcite (Figure 5d,e,l). The ore minerals of the Ag orebodies in ore block II are mainly argentite and pyrargyrite, with gangue minerals of quartz and calcite (Figure 5f). The ores' texture is anhedral granular, subhedral granular, radial, metasomatic dissolution, and exsolution (Figure 5a–f). The ore structure is mainly vein, massive, and densely disseminated structures, followed by

stockwork and breccia structures (Figure 6a–f). The wall-rock alteration is well-developed in all of these four ore blocks, and mainly includes silicification, sericitization, chloritization, carbonation, and pyritic phyllic alteration, with a small amount of pyrophyllization and kaolinization (Figure 5g–l).

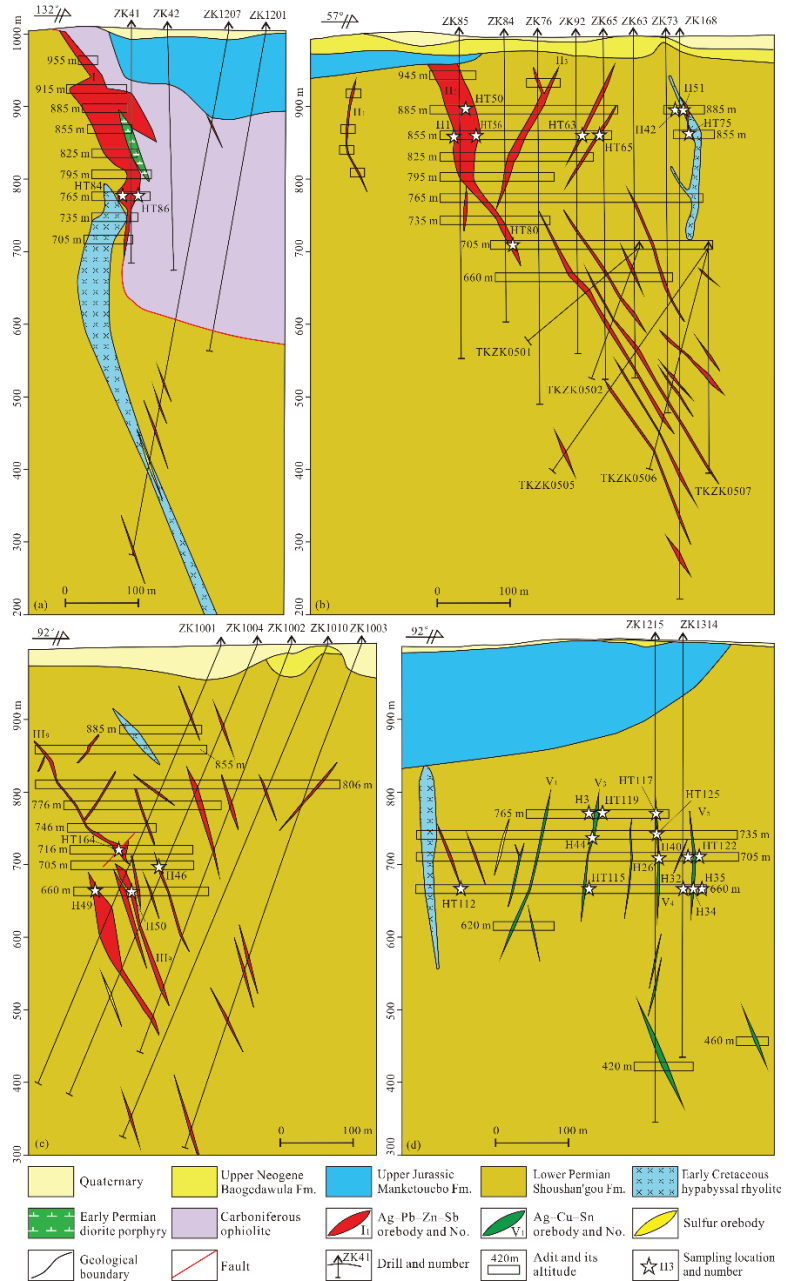


Figure 4. Simplified geological section along the exploration lines of I-39 (a), II-5 (b), III-10 (c), and V-9 (d) of the Huaobaote deposit.

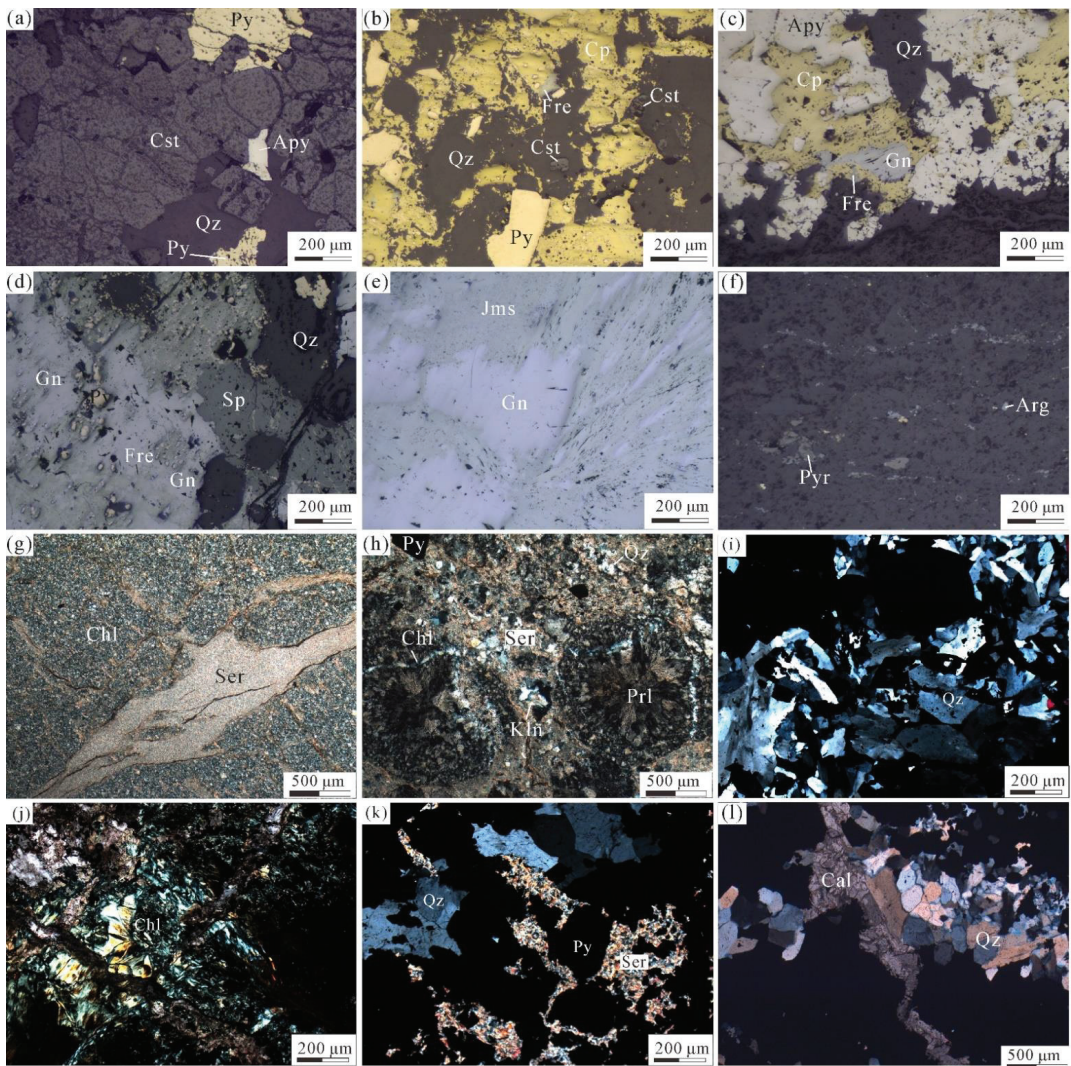


Figure 5. Representative photos of ores and major wall-rock alteration types in the Huaobaote deposit. (a) Coexisting cassiterite, pyrite, and arsenopyrite with silicification in Sn ore of stage I; (b) coexisting cassiterite, pyrite, chalcopyrite, and freibergite with silicification in Ag–Cu–Sn ore of stage II; (c) coexisting arsenopyrite, chalcopyrite, and freibergite with silicification in Ag–Cu ore of stage II, replaced by galena of stage III; (d) coexisting galena, sphalerite, and freibergite with silicification in Ag–Pb–Zn ore of stage III; (e) coexisting galena and jamesonite in Ag–Pb–Zn–Sb ore of stage III; (f) argentite and pyrargyrite in Ag ore of stage IV; (g) strongly altered siltstone represented by chloritization and silicification; (h) sericitization, pyrophyllization, chloritization, kaolinization, silicification, and pyritization developed in the ore-hosting volcanoclastic rocks of the Dashizhai Formation; (i) silicification in stage I; (j) chloritization in stage II; (k) pyritic phyllic alteration in stage II; (l) silicification and carbonation developed in stage III. Abbreviations: Apy = arsenopyrite; Arg = argentite; Cal = calcite; Chl = chlorite; Ccp = chalcopyrite; Cst = cassiterite; Fre = freibergite; Gn = galena; Jms = jamesonite; Kln = kaolinite; Prl = pyrophyllite; Py = pyrite; Pyr = pyrargyrite; Qz = quartz; Ser = sericite; Sp = sphalerite.

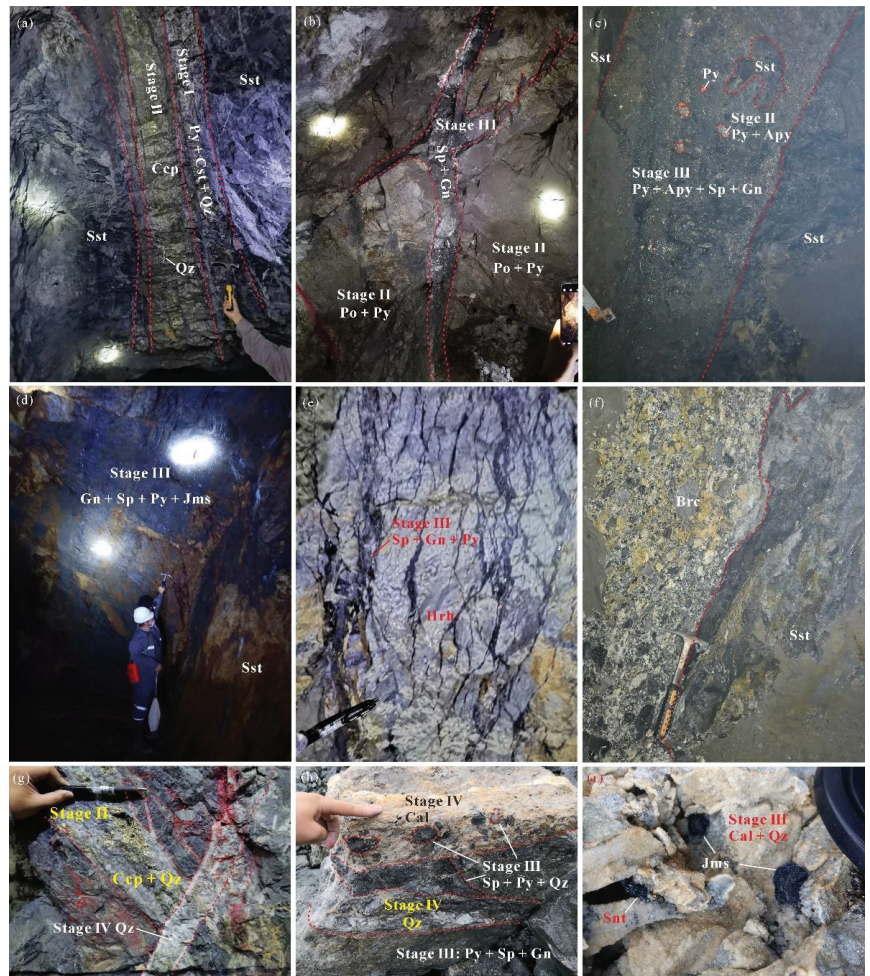


Figure 6. Representative photos of orebodies in the Huaaobaote deposit. (a) No. V₃ Ag–Cu–Sn orebody of stage II and Sn orebody of stage I, both occurring as steep veins; (b) Pb–Zn–Ag orebody of stage III cutting through sulfur orebody of stage II; (c) breccia ore in the Pb–Zn–Ag orebody of stage III, enclosing pyrite and arsenopyrite of stage II; (d) Pb–Zn–Ag–Sb orebody of stage III mainly composed of galena and sphalerite massive ores; (e) Pb–Zn–Ag orebody of stage III occurring in hypabyssal rhyolite, and sphalerite and galena distributing along the stockwork fractures within hypabyssal rhyolite; (f) cryptoexplosive breccia occurring within hypabyssal rhyolite near the contact zone of hypabyssal rhyolite and siltstone; (g) Ag-bearing quartz vein of stage IV cutting through Ag–Cu–Sn orebody of stage II; (h) Ag-bearing quartz and calcite veins of stage IV cutting through Pb–Zn–Ag orebody of stage III and wrapping ore breccia of stage III; (i) stibnite and jamesonite assemblages in quartz and calcite of stage III. Abbreviations: Apy = arsenopyrite; Bre = breccia; Cal = calcite; Ccp = chalcopyrite; Gn = galena; Hrh = hypabyssal rhyolite; Jms = jamesonite; Po = pyrrhotite; Py = pyrite; Qz = quartz; Snt = Stibnite; Sp = sphalerite; Sst = siltstone.

Based on the crosscutting relationships of veins, ore fabrics, and mineral assemblages, four ore-forming stages are recognized (Figure 6): cassiterite–arsenopyrite–pyrite–quartz (stage I), cassiterite–chalcopyrite–pyrite–freibergite–arsenopyrite–pyrrhotite–quartz (stage II), sphalerite–galena–jamesonite–stibnite–freibergite–silver mineral–quartz–calcite–chlorite (stage III), and argentite–pyrargyrite–pyrite–quartz–calcite (stage IV).

4. Sampling and Analytical Methods

4.1. Sampling

In this study, we selected 36 samples from different ore blocks, levels, and ore-forming stages of the Huaaobaote deposit for U–Pb dating, a fluid inclusion study, and H–O–S–Pb isotope analyses, and the details are listed in Table 1. Of these samples, two were selected for laser ablation inductively coupled plasma mass spectrometry (LA-ICP-MS) cassiterite U–Pb dating (Table 1, Figures 4d and 5a–c). Thirteen quartz and one sphalerite from four stages were collected for an FI study (Table 1, Figure 4). Twelve quartz samples from the four mineralization stages were collected for H–O isotope analysis (Table 1, Figure 4b–d). Nine sulfide samples from the first three mineralization stages were collected for S–Pb isotope analysis, including five pyrite, one arsenopyrite, one sphalerite, and two galena (Table 1, Figure 4b–d).

Table 1. List of analytical samples from the Huaaobaote deposit.

Sample	Orebody No.	Level (m)	Metal Assemblage	Stage	Mineral	Analysis
HT122	V ₅	705	Sn	I	Cassiterite	U–Pb dating
HT125	V ₄	735	Ag–Cu–Sn	II	Cassiterite	U–Pb dating
HT117	V ₄	765	Sn	I	Quartz	FIs study
HT119	V ₃	765	Sn	I	Quartz	FIs study
H44	V ₃	735	Ag–Cu–Sn	II	Quartz	FIs study
HT115	V ₃	660	Ag–Cu–Sn	II	Quartz	FIs study
HT50	II ₂	885	Ag–Pb–Zn–Sb	III	Quartz	FIs study
HT56	II ₂	855	Ag–Pb–Zn–Sb	III	Quartz	FIs study
HT80	II ₂	705	Ag–Pb–Zn–Sb	III	Quartz	FIs study
HT84	I ₁	765	Ag–Pb–Zn–Sb	III	Quartz	FIs study
HT86	I ₁	765	Ag–Pb–Zn–Sb	III	Quartz	FIs study
HT112	Ore block V	660	Ag–Pb–Zn–Sb	III	Quartz	FIs study
HT164	III ₉	716	Ag–Pb–Zn–Sb	III	Sphalerite	FIs study
HT63	Ore block II	855	Ag	IV	Quartz	FIs study
HT65	Ore block II	855	Ag	IV	Quartz	FIs study
HT75	Ore block II	855	Ag	IV	Quartz	FIs study
H32	V ₅	660	Sn	I	Quartz	H–O isotope analysis
H34	V ₅	660	Sn	I	Quartz	H–O isotope analysis
H40	V ₅	705	Sn	I	Quartz	H–O isotope analysis
H3-5	V ₃	765	Ag–Cu–Sn	II	Quartz	H–O isotope analysis
H3-7	V ₃	765	Ag–Cu–Sn	II	Quartz	H–O isotope analysis
H3-8	V ₃	765	Ag–Cu–Sn	II	Quartz	H–O isotope analysis
H3-9	V ₃	765	Ag–Cu–Sn	II	Quartz	H–O isotope analysis
H46	III ₉	705	Ag–Pb–Zn–Sb	III	Quartz	H–O isotope analysis
H49	III ₉	660	Ag–Pb–Zn–Sb	III	Quartz	H–O isotope analysis
H50	III ₉	660	Ag–Pb–Zn–Sb	III	Quartz	H–O isotope analysis
H42	Ore block II	885	Ag–Pb–Zn–Sb	IV	Quartz	H–O isotope analysis
H51	Ore block II	885	Ag–Pb–Zn–Sb	IV	Quartz	H–O isotope analysis
H32	V ₅	660	Sn	I	Pyrite	S–Pb isotope analysis
H34	V ₅	660	Sn	I	Pyrite	S–Pb isotope analysis
H35	V ₅	660	Sn	I	Pyrite	S–Pb isotope analysis
H3-1	V ₃	765	Ag–Cu–Sn	II	Arsenopyrite	S–Pb isotope analysis
H26	V ₃	765	Ag–Cu–Sn	II	Pyrite	S–Pb isotope analysis
H1-4	II ₂	855	Ag–Pb–Zn–Sb	III	Galena, Sphalerite	S–Pb isotope analysis
H1-5	II ₂	855	Ag–Pb–Zn–Sb	III	Galena	S–Pb isotope analysis
H46	III ₉	705	Ag–Pb–Zn–Sb	III	Pyrite	S–Pb isotope analysis

4.2. Cassiterite U–Pb Dating

The cassiterite grains were separated by conventional heavy liquid and magnetic techniques and purified by handpicking under a binocular microscope at the Tuoxuan Rock and Mineral Testing Service Co., Ltd., Langfang, Hebei Province, China (TRMTS).

The cassiterite target preparation, cathodoluminescence (CL) image photography, and LA-ICP-MS cassiterite U–Pb analysis were carried out at the Beijing Yandu Zhongshi Test Technology Co., Ltd., Beijing, China. The cassiterite U–Pb analysis was performed using an Analytik Jena Plasma Quant MC-ICP-MS with an NWR 193 nm Ar–F excimer laser system. The ^{118}Sn and SRM610 were used as the internal and external reference materials, respectively, and Yankee cassiterite was utilized for validation of the U–Pb isotope determinations (TIMS U–Pb age of 246.48 ± 0.51 Ma [54]). The test was performed by passing blank gas for 15 s, followed by 40 s of laser exfoliation analysis with a beam diameter of 35 μm , frequency of 8 Hz, and energy density of $4.0 \text{ J}/\text{cm}^2$. The test was performed by selecting particles with better crystal shape and fewer cleavages and inclusions to reduce the effect of common Pb. The raw data were corrected offline using ICPMSDataCal and Zskits, and the common Pb correction was performed using the ^{207}Pb -based correction mentioned in Chew et al. [55]. Isoplot 4.15 was used to calculate the U–Pb age and draw a Tera–Wasserburg diagram, and the lower intercept represents the age of cassiterite in the Tera–Wasserburg diagram [56].

4.3. Fluid Inclusion Microthermometry and Laser Raman Spectroscopy

Eighteen fluid plates of sixteen quartz and two sphalerite samples were double-polished at the TRMITS, with a thickness of 100–300 μm . The microthermometric measurements of the FIs were determined at the Institute of Mineral Resources, Chinese Academy of Geological Sciences, China (IMRCAGS), using a LINKAM THMSG 600 programmable heating-freezing stage equipped with a German Zeiss microscope, which allowed a temperature range from -190 $^{\circ}\text{C}$ to 600 $^{\circ}\text{C}$. Before each batch of microthermometry, the purified water and synthetic fluid inclusion standards, manufactured by Geofluid, Hong Kong, were used to calibrate the heating–freezing stage. The estimated accuracies were ± 0.1 $^{\circ}\text{C}$ from -100 $^{\circ}\text{C}$ to 25 $^{\circ}\text{C}$, ± 1 $^{\circ}\text{C}$ from 25 $^{\circ}\text{C}$ to 400 $^{\circ}\text{C}$, and ± 2 $^{\circ}\text{C}$ above 400 $^{\circ}\text{C}$, respectively. The test heating rate was generally 0.2 to 5 $^{\circ}\text{C}/\text{min}$, and the heating rate was reduced to 0.2 $^{\circ}\text{C}/\text{min}$ near the phase transition. The salinity of the gas–liquid two-phase aqueous solution inclusions was estimated by ice-melting temperatures [57], and the density of the fluid inclusions was calculated using Flicor software [58]. Volatile compositions of single fluid inclusion were identified using a Renishaw RM-2000 Raman probe at the IMRCAGS. The excitation wavelength was 514.53 nm argon laser line, and the measured spectrum time was 20 s. The counting rate was one per centimeter. The laser beam size was fixed at 1 μm with a spectral resolution of 1 – 2 cm^{-1} . The spectrum diagram was taken from the wavenumber of 1000 – 4000 cm^{-1} .

4.4. H–O–S–Pb Isotope Analyses

4.4.1. H–O Isotope Analyses

The samples were smashed, and the quartz grains were purified under binocular microscope to above 99% at the TRMITS. Then, the quartz H–O isotopes were accomplished with a MAT 251EM mass spectrometer at the IMRCAGS, with analytical accuracy better than $\pm 2\text{‰}$ for δD and $\pm 0.2\text{‰}$ for $\delta^{18}\text{O}$. For analysis of the H isotopic compositions, water was first released from the fluid inclusions by a crushing method, then the water was reacted with zinc at 400 $^{\circ}\text{C}$ to produce H_2 [59], which was finally frozen in liquid nitrogen and collected in a sample bottle with activated carbon for testing. For the oxygen isotope, oxygen was liberated from quartz through a reaction with BrF_5 [60] and converted to CO_2 on a platinum-coated carbon rod. The CO_2 was then frozen, collected, and analyzed for the O isotope. The detailed operating conditions and analytical methods are discussed in [61]. The O isotope of the water in the quartz was calculated by the O isotope of the quartz using the fractionation equation: $1000 \ln \alpha_{\text{quartz-water}} = 3.38 \times 10^6/T^2 - 3.40$ [62], where T (in degrees Kelvin) is the mean value of the fluid inclusion homogeneous temperature corresponding to the stage of mineralization. The isotopic ratios were reported in per mil (‰) relative to the Vienna Standard Mean Ocean Water (V-SMOW).

4.4.2. S–Pb Isotope Analyses

The separation of a single sulfide was performed in the same way as described in Section 4.4.1. The S–Pb isotope compositions of the sulfides were measured at the Analytical Laboratory of the Beijing Research Institute of Uranium Geology, Beijing, China. The sulfur isotope analysis was first separated from the sulfides for SO₂ [63], and the test was performed using a Delta V mass spectrometer, and the experimental results were reported relative to the Vienna Canyon Diablo Troilite (V-CDT) with an analytical accuracy better than 0.2‰. The Pb isotope analysis was performed using an IsoProbe-T multi-receiver thermal ionization mass spectrometer. The measurement accuracy of the ²⁰⁸Pb/²⁰⁶Pb and ²⁰⁷Pb/²⁰⁶Pb ratios was better than 0.005‰ (2σ). The isotopic ratios were reported with respect to the Pb standard reference NBS-981 values [64]: ²⁰⁶Pb/²⁰⁴Pb = 16.934 ± 0.007, ²⁰⁷Pb/²⁰⁴Pb = 15.486 ± 0.012, and ²⁰⁸Pb/²⁰⁴Pb = 36.673 ± 0.033, respectively.

5. Results

5.1. Cassiterite U–Pb Age

Most of the cassiterite grains from the Huaaobaote deposit are reddish-brown under an optical microscope, with lengths mostly between 50 and 110 μm. Cassiterite in the CL image presents as a black color with well-developed oscillatory zonation and a relatively homogeneous internal structure, most of which exhibit irregular shapes, most likely due to mechanical fragmentation during mineral selection (Figure 7). The cassiterite U–Pb isotopic data of two samples (HT122 and HT125) are listed in Table 2 and plotted on Tera–Wasserburg diagrams (Figure 8). The projection points of the two samples are both linearly aligned, indicating that their respective cassiterite grains have consistent U–Pb isotopic age, varying only in the content of common Pb.

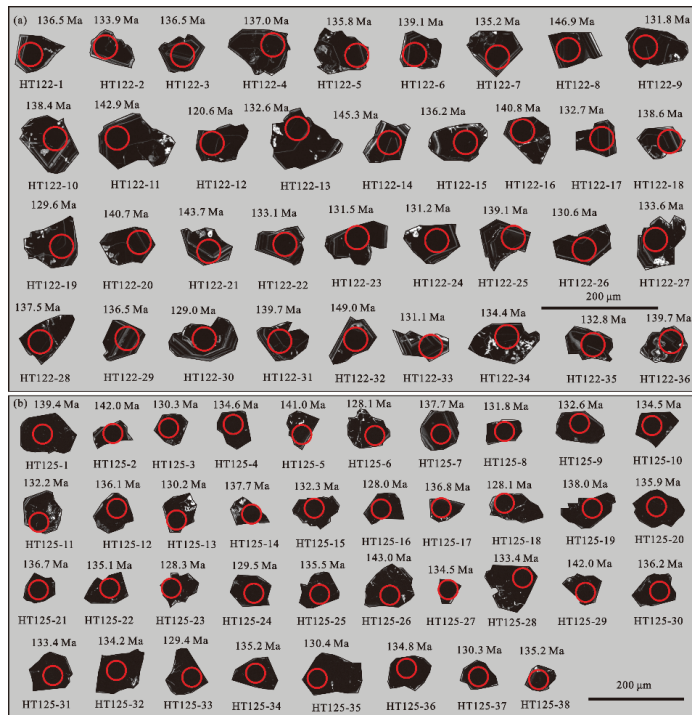


Figure 7. Representative cathodoluminescence (CL) images of cassiterite grains for samples HT122 (a) and HT125 (b) from the Huaaobaote deposit, showing U–Pb analytical spots and corresponding to ²⁰⁷Pb-corrected ²⁰⁶Pb/²³⁸U ages.

Table 2. LA-ICP-MS cassiterite U–Pb dating data for cassiterite samples HT122 and HT125 from of the Huaaobaote deposit.

Spot No.	Isotopic Ratios						Age (Ma)			
	$^{207}\text{Pb}/^{206}\text{Pb}$	1 σ	$^{207}\text{Pb}/^{235}\text{U}$	1 σ	$^{206}\text{Pb}/^{238}\text{U}$	1 σ	$^{238}\text{U}/^{206}\text{Pb}$	1 σ	$^{206}\text{Pb}/^{238}\text{U}$	1 σ
Sample HT122										
HT122-1	0.18218	0.01383	0.60982	0.04370	0.02556	0.00075	39.117	1.14860	136.5	4.8
HT122-2	0.30034	0.01448	1.17095	0.04923	0.03026	0.00069	33.052	0.75895	133.9	4.6
HT122-3	0.37176	0.02786	1.71566	0.11972	0.03528	0.00143	28.342	1.14960	136.5	9.4
HT122-4	0.20013	0.01145	0.70995	0.03903	0.02634	0.00054	37.967	0.77523	137.0	3.7
HT122-5	0.22319	0.01769	0.81919	0.06489	0.02703	0.00088	36.997	1.20590	135.8	5.8
HT122-6	0.27049	0.01844	1.06468	0.06628	0.02987	0.00116	33.482	1.30380	139.1	6.9
HT122-7	0.15183	0.01308	0.48058	0.03878	0.02424	0.00072	41.249	1.22980	135.2	4.7
HT122-8	0.33183	0.01858	1.54452	0.08127	0.03517	0.00090	28.436	0.72889	146.9	6.3
HT122-9	0.25919	0.01373	0.96060	0.04462	0.02778	0.00058	36.004	0.75039	131.8	4.1
HT122-10	0.38154	0.02464	1.98932	0.15360	0.03649	0.00131	27.407	0.98350	138.4	8.6
HT122-11	0.19588	0.01269	0.69459	0.03995	0.02731	0.00073	36.618	0.98444	142.9	4.7
HT122-12	0.40236	0.02763	1.80693	0.12910	0.03317	0.00100	30.148	0.90554	120.6	8.0
HT122-13	0.26315	0.03690	0.84534	0.08896	0.02812	0.00134	35.562	1.69210	132.6	10.2
HT122-14	0.22995	0.01729	0.88285	0.06680	0.02924	0.00092	34.199	1.07760	145.3	6.0
HT122-15	0.35397	0.02345	1.59832	0.10045	0.03399	0.00142	29.421	1.22970	136.2	8.4
HT122-16	0.24847	0.02076	0.95929	0.07770	0.02917	0.00132	34.278	1.55160	140.8	7.9
HT122-17	0.38626	0.02350	1.85798	0.13570	0.03530	0.00139	28.332	1.11580	132.7	8.3
HT122-18	0.25020	0.01460	0.95098	0.04669	0.02880	0.00066	34.727	0.79707	138.6	4.6
HT122-19	0.25124	0.02134	0.81666	0.05903	0.02696	0.00100	37.089	1.36970	129.6	6.5
HT122-20	0.52991	0.02117	3.88042	0.22128	0.05329	0.00200	18.764	0.70451	140.7	10.4
HT122-21	0.17166	0.01381	0.60705	0.04775	0.02651	0.00078	37.726	1.11050	143.7	5.1
HT122-22	0.31733	0.01468	1.32790	0.05656	0.03101	0.00075	32.248	0.78457	133.1	4.8
HT122-23	0.33752	0.01440	1.42328	0.05381	0.03179	0.00075	31.453	0.74608	131.5	4.8
HT122-24	0.32182	0.02448	1.26495	0.07958	0.03080	0.00121	32.470	1.27580	131.2	7.8
HT122-25	0.14340	0.01481	0.44976	0.04233	0.02466	0.00080	40.556	1.32290	139.1	5.3
HT122-26	0.35254	0.02453	1.45846	0.08065	0.03248	0.00111	30.791	1.05120	130.6	7.6
HT122-27	0.47591	0.02731	2.77106	0.16801	0.04363	0.00159	22.919	0.83258	133.6	10.5
HT122-28	0.22748	0.02325	0.81743	0.07506	0.02755	0.00108	36.295	1.42880	137.5	7.3
HT122-29	0.47537	0.01878	2.80595	0.09893	0.04453	0.00110	22.457	0.55362	136.5	7.5
HT122-30	0.36279	0.03071	1.55365	0.12622	0.03274	0.00115	30.541	1.06940	129.0	9.0
HT122-31	0.40657	0.02633	2.15246	0.16348	0.03881	0.00191	25.769	1.26830	139.7	10.5
HT122-32	0.53636	0.02193	4.22953	0.20672	0.05753	0.00189	17.383	0.57147	149.0	11.2
HT122-33	0.31196	0.02183	1.22766	0.07475	0.03023	0.00104	33.076	1.13850	131.1	6.8
HT122-34	0.27147	0.02640	1.05910	0.10508	0.02891	0.00145	34.589	1.73390	134.4	8.9
HT122-35	0.31703	0.03105	1.26983	0.10187	0.03091	0.00125	32.351	1.30510	132.8	9.2
HT122-36	0.46278	0.01903	2.86966	0.16269	0.04417	0.00152	22.641	0.77716	139.7	8.2
Sample HT125										
HT125-1	0.23209	0.01648	0.82036	0.04439	0.02815	0.00088	35.524	1.10990	139.4	5.6
HT125-2	0.12594	0.01146	0.41757	0.03330	0.02458	0.00075	40.681	1.24430	142.0	4.8
HT125-3	0.45501	0.01522	2.45790	0.07407	0.04040	0.00081	24.752	0.49765	130.3	5.4
HT125-4	0.12802	0.01112	0.38123	0.02755	0.02335	0.00064	42.821	1.17780	134.6	4.2
HT125-5	0.35582	0.01448	1.71781	0.06462	0.03531	0.00074	28.324	0.59438	141.0	4.9
HT125-6	0.47452	0.01936	2.59055	0.08873	0.04170	0.00109	23.979	0.62429	128.1	7.1
HT125-7	0.18274	0.01192	0.60364	0.03338	0.02579	0.00074	38.779	1.10750	137.7	4.6
HT125-8	0.42584	0.01803	2.11959	0.07174	0.03819	0.00089	26.188	0.60867	131.8	6.1
HT125-9	0.10556	0.01240	0.31141	0.03164	0.02233	0.00062	44.777	1.25130	132.6	4.2
HT125-10	0.25480	0.01468	0.93686	0.05344	0.02814	0.00088	35.531	1.10590	134.5	5.3
HT125-11	0.34228	0.01540	1.52473	0.07484	0.03224	0.00073	31.013	0.70531	132.2	4.9
HT125-12	0.34589	0.02015	1.51632	0.06840	0.03343	0.00080	29.912	0.71313	136.1	6.1
HT125-13	0.39094	0.01662	1.84290	0.08269	0.03497	0.00086	28.597	0.70575	130.2	5.5
HT125-14	0.35610	0.01571	1.63173	0.06322	0.03450	0.00087	28.986	0.73147	137.7	5.4
HT125-15	0.21478	0.01789	0.72135	0.05500	0.02599	0.00083	38.479	1.22450	132.3	5.5
HT125-16	0.29524	0.01245	1.15921	0.05036	0.02865	0.00064	34.898	0.77847	128.0	4.0
HT125-17	0.12691	0.01183	0.38632	0.03342	0.02371	0.00064	42.181	1.13200	136.8	4.3

Table 2. Cont.

Spot No.	Isotopic Ratios						Age (Ma)			
	$^{207}\text{Pb}/^{206}\text{Pb}$	1σ	$^{207}\text{Pb}/^{235}\text{U}$	1σ	$^{206}\text{Pb}/^{238}\text{U}$	1σ	$^{238}\text{U}/^{206}\text{Pb}$	1σ	$^{206}\text{Pb}/^{238}\text{U}$	1σ
HT125-18	0.51924	0.02029	3.26313	0.11403	0.04700	0.00122	21.275	0.55083	128.1	8.1
HT125-19	0.38652	0.02564	1.91581	0.14534	0.03675	0.00166	27.211	1.22990	138.0	9.5
HT125-20	0.34791	0.01688	1.56082	0.07380	0.03352	0.00080	29.831	0.71228	135.9	5.5
HT125-21	0.06820	0.00984	0.20369	0.03092	0.02195	0.00071	45.566	1.47830	136.7	4.7
HT125-22	0.26047	0.01596	0.96227	0.04704	0.02853	0.00068	35.048	0.82956	135.1	4.8
HT125-23	0.22954	0.01747	0.73737	0.05215	0.02579	0.00075	38.768	1.12700	128.3	5.1
HT125-24	0.19399	0.01821	0.59303	0.04814	0.02466	0.00080	40.551	1.31720	129.5	5.4
HT125-25	0.26297	0.01022	1.03694	0.04228	0.02873	0.00049	34.811	0.59889	135.5	3.3
HT125-26	0.41415	0.02364	2.29300	0.14495	0.04040	0.00132	24.754	0.81013	143.0	8.8
HT125-27	0.11492	0.01005	0.35371	0.02850	0.02294	0.00056	43.600	1.07270	134.5	3.7
HT125-28	0.32207	0.02154	1.31142	0.07402	0.03134	0.00093	31.909	0.94627	133.4	6.6
HT125-29	0.37509	0.01823	1.84603	0.08242	0.03695	0.00096	27.064	0.70453	142.0	6.5
HT125-30	0.34016	0.01459	1.52785	0.07061	0.03310	0.00084	30.212	0.76785	136.2	5.1
HT125-31	0.45724	0.01781	2.55851	0.09571	0.04161	0.00097	24.032	0.55766	133.4	6.7
HT125-32	0.46947	0.01560	2.67440	0.06923	0.04314	0.00096	23.180	0.51849	134.2	6.2
HT125-33	0.31778	0.02045	1.29124	0.08431	0.03015	0.00100	33.163	1.09710	129.4	6.4
HT125-34	0.41380	0.01523	2.11095	0.06994	0.03815	0.00085	26.210	0.58120	135.2	5.5
HT125-35	0.23452	0.01357	0.79918	0.03912	0.02641	0.00060	37.870	0.86509	130.4	4.1
HT125-36	0.24305	0.01643	0.90284	0.06345	0.02768	0.00084	36.131	1.10260	134.8	5.4
HT125-37	0.41542	0.01787	2.07215	0.09657	0.03688	0.00103	27.114	0.76006	130.3	6.4
HT125-38	0.36834	0.02640	1.66470	0.11191	0.03471	0.00106	28.812	0.88334	135.2	8.2

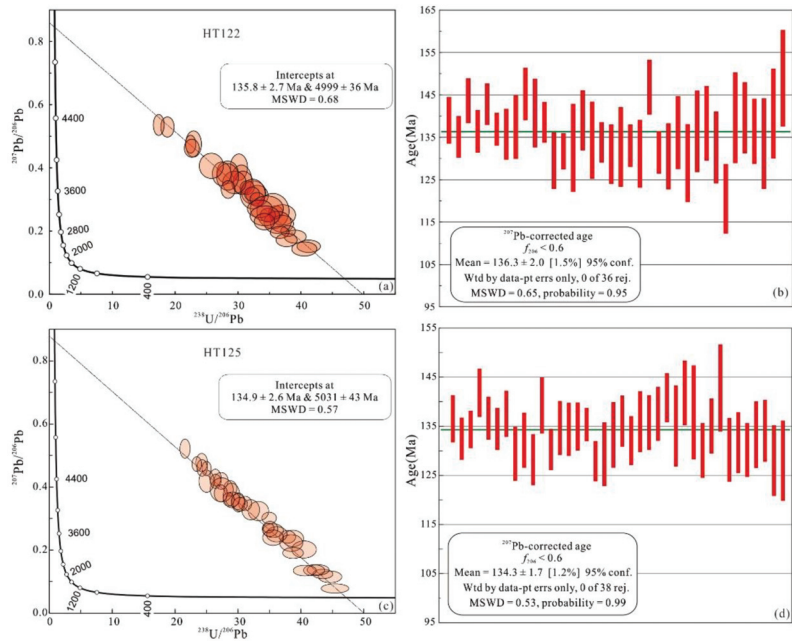


Figure 8. LA-ICP-MS cassiterite U-Pb Tera-Wasserburg concordia diagrams (a,c) and ^{207}Pb -corrected $^{206}\text{Pb}/^{238}\text{U}$ age histograms (b,d) for samples HT122 and HT125 from the Huaobaote deposit.

Thirty-six spots on sample HT122 yielded a Tera-Wasserburg concordia lower intercept age of 135.8 ± 2.7 Ma (MSWD = 0.68; Figure 8a) and a weighted mean age of 136.3 ± 2.0 Ma (MSWD = 0.65; Figure 8b). Thirty-eight spots on sample HT125 yielded a Tera-Wasserburg concordia lower intercept age of 134.9 ± 2.6 Ma (MSWD = 0.57; Figure 8c)

and a weighted mean age of 134.3 ± 1.7 Ma (MSWD = 0.53; Figure 8d). All these age data are consistent within the limits of error; thus, the age of 136.3–134.3 Ma is interpreted to be the mineralization age of the Huaaobaote deposit.

5.2. Fluid Inclusion Study

5.2.1. Petrography

Based on the phase proportions at room temperature, the phase transitions during heating and cooling, and the results of laser Raman spectroscopy, FIs in the Huaaobaote deposit can be divided into the following four types:

- (1) Liquid-rich inclusions (WL type): These FIs are extensively hosted in the tested quartz of all the stages and sphalerite of stage III, accounting for approximately 88% of the total number of FIs. They are polygonal, elliptical, long columnar, and irregular in shape, with diameters of 5–20 μm . The bubbles account for 5%–40% of the total volume at room temperature (Figure 9a,c,d,g–i). These FIs were homogenized to liquid when heated. In addition, in this type of FIs, some FIs contain needle-like opaque minerals that did not dissolve when heated (Figure 9b,c,g), implying that they are not daughter minerals. According to the morphology of opaque minerals, we speculate that they may be stibnite and/or jamesonite.
- (2) Gas-rich inclusions (WG type): These are exclusively developed in the quartz veins of stages II and III, accounting for about 5% of the total number of FIs, with diameters of 5–40 μm . The WG-type FIs are mostly oval and negative crystal shapes, with bubbles accounting for 52%–85% of the total volume (Figure 9e,f). These FIs were homogenized to vapor when heated.
- (3) Pure liquid inclusions (L type): These inclusions are mostly found in stages III and IV, have an irregular or polygonal shape with a size of 4–9 μm , accounting for about 4% of the total number of FIs. They are in a liquid phase at room temperature; when heated, these L-type FIs have no phase change.
- (4) Pure gas inclusions (G type): These inclusions predominantly occur in stages II and III. They are 5–8 μm in size and irregular or round in shape, accounting for 3% of the total number of FIs. They are in a gas phase at room temperature and have no phase change when heated.

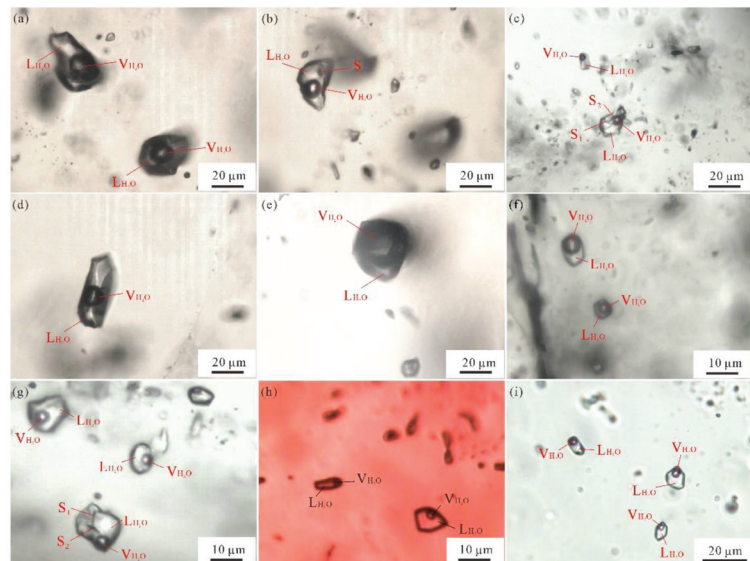


Figure 9. Representative microphotographs of fluid inclusions in quartz and sphalerite from the

Huaaobaote deposit. (a) WL-type Fis in the quartz of stage I; (b) WL-type FIs in the quartz of stage I, some of which contain solid sulfide; (c) WL-type FIs in the quartz of stage II, some of which contain one or more solid sulfide particles; (d) WL-type FIs in the quartz of stage II; (e) WG-type FIs in the quartz of stage II; (f) WL- and WG-type FIs in the quartz of stage III; (g) WL-type FIs in the quartz of stage III, some of which contain several solid sulfide particles; (h) WL-type FIs in the sphalerite of stage III; (i) WL-type FIs in the quartz of stage IV. L_{H2O} = liquid phase H₂O; S = solid sulfide particle; V_{H2O} = vapor phase H₂O.

5.2.2. Microthermometry

The microthermometric results and fluid inclusion assemblage (FIA) parameters are shown in Table 3 and Figure 10.

Table 3. Microthermometry data and relative parameters of fluid inclusion assemblage (FIA) in the Huaaobaote deposit.

Type	Host Mineral	FIA No.	No.	Size (µm)	V (vol.%)	T _m (ice) (°C)		T _h (°C)		Salinity (wt% NaCl eqv.)		Density (g/cm ³)
						Range	Mean	Range	Mean	Range	Mean	
Stage I: cassiterite–arsenopyrite–pyrite–quartz stage (samples HT117 and HT119)												
WL	Quartz	1	7	6–22	20–35	−3.0 to −2.2	−2.7	315–340	327	3.7–5.0	4.5	0.69–0.72
WL	Quartz	2	13	7–28	20–35	−4.1 to −2.8	−3.3	323–339	332	4.6–6.6	5.4	0.70–0.72
WL	Quartz	3	5	8–15	15–20	−3.0 to −2.6	−2.8	302–306	304	4.3–5.0	4.7	0.74–0.76
Stage II: cassiterite–chalcopyrite–pyrite–freibergite–arsenopyrite–pyrrhotite–quartz stage (samples H44 and HT115)												
WL	Quartz	1	8	8–14	15–20	−2.7 to −2.3	−2.5	282–291	286	3.9–4.5	4.2	0.77–0.79
WL	Quartz	2	8	13–60	10–40	−2.4 to −1.9	−2.1	267–304	286	3.2–4.0	3.5	0.74–0.80
WG	Quartz	3	2	15–40	68–85	−2.1 to −1.9	−2.0	288–293	291	3.2–3.5	3.4	0.75–0.77
WL	Quartz	4	8	3–17	10–30	−1.3 to −0.1	−1.0	271–286	277	0.2–2.2	1.7	0.73–0.78
Stage III: sphalerite–galena–jamesonite–stibnite–freibergite–silver mineral–quartz–calcite–chlorite stage (samples HT50, HT56, HT80, HT84, HT86, HT112, and HT164)												
WL	Quartz	1	5	4–11	15–30	−0.4 to −0.1	−0.2	196–210	206	0.2–0.7	0.4	0.85–0.88
WL	Quartz	2	14	4–12	10–25	−3.0 to −0.9	−2.0	189–267	242	1.6–5.0	3.4	0.81–0.91
WL	Quartz	3	10	5–24	8–30	−2.3 to −2.0	−2.2	194–228	209	3.4–3.9	3.6	0.86–0.90
WL	Quartz	4	2	7–18	15–20	−2.1 to −0.1	−1.1	196–225	211	0.2–3.5	1.9	0.86–0.87
WL	Quartz	5	1	16	18	−0.7	−0.7	222	222	1.2	1.2	0.85
WL	Quartz	6	4	8–12	15–35	−0.5 to −0.1	−0.3	235–273	249	0.2–0.9	0.5	0.76–0.83
WG	Quartz	7	2	5–9	52–65	−0.3 to −0.2	−0.3	236–237	237	0.4–0.5	0.5	0.81–0.82
WL	Quartz	8	14	3–20	10–35	−2.7 to −0.4	−1.3	196–263	227	0.7–4.5	2.2	0.78–0.88
WG	Quartz	9	1	8	73	−0.8	−0.8	224	224	1.4	1.4	0.85
WL	Sphalerite	10	16	4–16	5–35	−2.9 to −0.4	−1.3	186–223	207	0.7–4.8	2.3	0.84–0.91
WL	Quartz	11	3	3–13	10–15	−0.9 to −0.8	−0.8	197–198	198	1.4–1.6	1.5	0.88
Stage IV: argentite–pyrrargyrite–pyrite–quartz–calcite stage (samples HT63, HT65, and HT75)												
WL	Quartz	1	5	4–13	5–10	−0.9 to −0.6	−0.8	188–199	193	1.1–1.6	1.4	0.88–0.89
WL	Quartz	2	4	4–9	10–15	−0.9 to −0.6	−0.8	187–194	190	1.1–1.6	1.4	0.88–0.89
WL	Quartz	3	24	5–10	10–20	−0.8 to −0.2	−0.5	166–192	180	0.4–1.4	0.9	0.88–0.91

Abbreviations: T_h = total homogenization temperature; T_m(ice) = final melting temperature of ice; V = volume fraction of gas phase in the total volume of inclusion.

FIs in the quartz of stage I: Three FIAs have been recognized. The homogenization temperature of these FIAs varies from 302 °C to 340 °C; the final ice melting temperature is −4.1 °C to −2.2 °C, corresponding to salinities of 3.7–6.6 wt% NaCl eqv.; and the density of the fluid is 0.69–0.76 g/cm³.

FIs in the quartz of stage II: Four FIAs have been recognized. The homogenization temperature of the WL-type FIAs varies from 267 °C to 304 °C; the final ice melting temperature ranges from −2.7 °C to −0.1 °C, corresponding to salinities of 0.2–4.5 wt% NaCl eqv.; and the fluid density is 0.73–0.80 g/cm³. The homogenization temperature of the WG-type FIAs varies from 288 °C to 293 °C; the final ice melting temperature ranges from −2.1 °C to −1.9 °C, corresponding to salinities of 3.2–3.5 wt% NaCl eqv.; and the density of the fluid is in the range of 0.75–0.77 g/cm³.

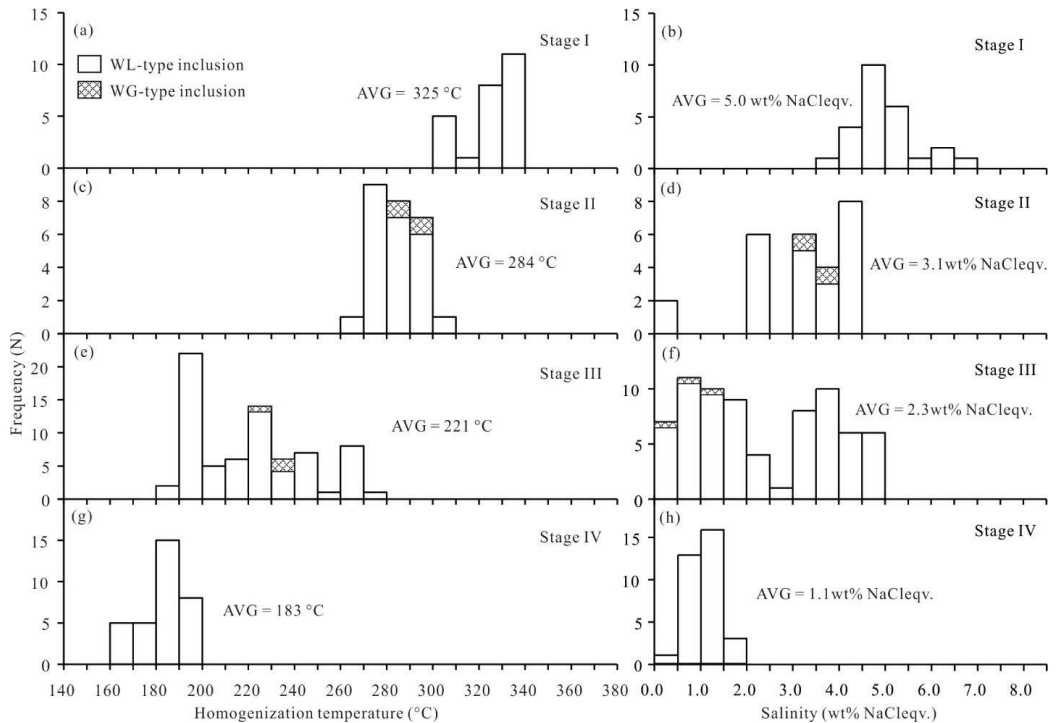


Figure 10. Histograms of homogenization temperature and salinity of fluid inclusions in the Huaaobaote deposit. (a) Homogenization temperature of stage I, (b) salinity of stage I, (c) homogenization temperature of stage II, (d) salinity of stage II, (e) homogenization temperature of stage III, (f) salinity of stage III, (g) homogenization temperature of stage IV, (h) salinity of stage IV.

FIs in the quartz and sphalerite of stage III: Eleven FIAs have been recognized. The homogenization temperature of the WL-type FIAs varies from 186 °C to 273 °C; the final ice melting temperature ranges from -3.0 °C to -0.1 °C, corresponding to salinities of 0.2–5.0 wt% NaCl eqv.; and the fluid density is 0.76–0.91 g/cm³. The homogenization temperature of the WG-type FIAs is 224–237 °C; the final ice melting temperature varies from -0.8 °C to -0.2 °C, corresponding to salinities 0.4–1.4 wt% NaCl eqv.; and the density of the fluid is 0.81–0.85 g/cm³.

FIs in the quartz of stage IV: Three FIAs have been recognized. The homogenization temperature of these FIAs varies from 166 °C to 199 °C; the final ice melting temperature ranges from -0.9 °C to -0.2 °C, corresponding to salinities of 0.4–1.6 wt% NaCl eqv.; and the fluid density is 0.88–0.91 g/cm³.

5.2.3. Laser Raman Spectra

The results of the representative laser Raman spectroscopic analyses of the individual FIAs from different stages are shown in Figure 11. The gas-phase components in stage I are dominated by H₂O and CH₄ (Figure 11a). The gas-phase components of stage II are characterized by H₂O and N₂ (Figure 11b). The gas-phase components for stages III and IV are mainly H₂O (Figure 11c,d). In general, it seems that the metallogenic fluid evolves gradually from the early-stage H₂O–NaCl–CH₄ system, through the middle-stage H₂O–NaCl–N₂ system, to the late-stage H₂O–NaCl system.

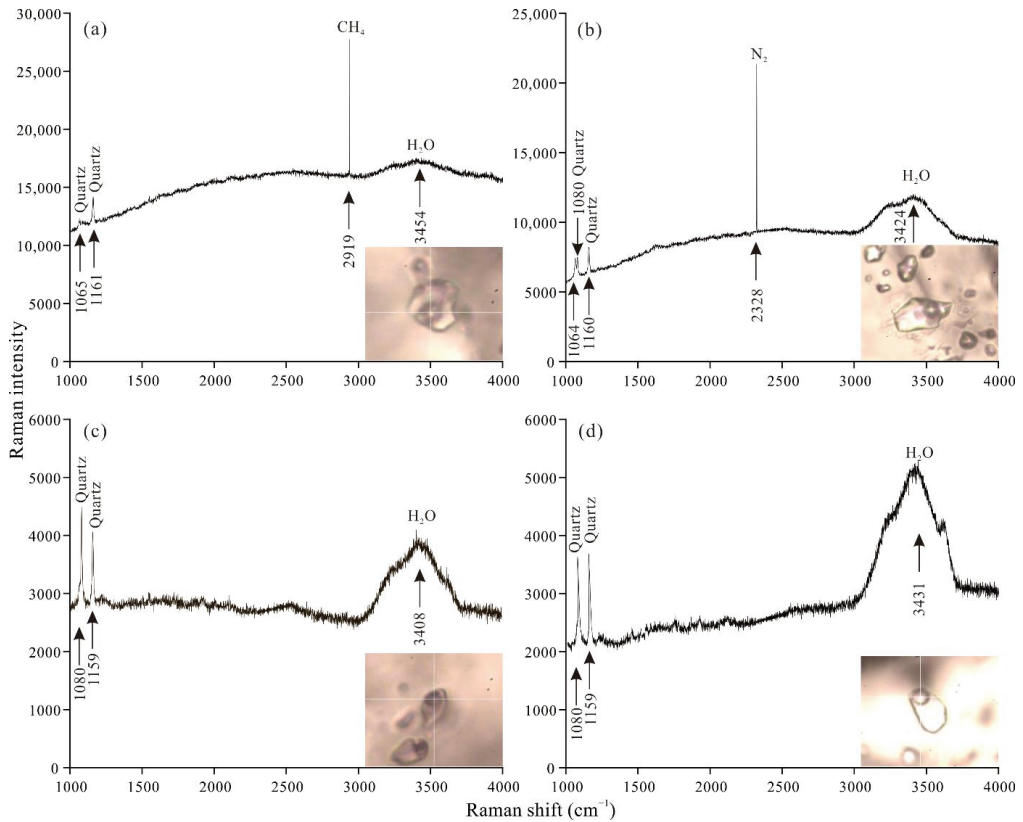


Figure 11. Laser Raman spectra for fluid inclusions in quartz from the Huaaobaote deposit. (a) WL-type FIs of stage I; (b) WL-type FIs of stage II; (c) WL-type FIs of stage III; and (d) WL-type FIs of stage IV.

5.3. Isotope Data

5.3.1. Hydrogen and Oxygen Isotopes

The analytical results for the oxygen isotopes of 12 quartz samples and hydrogen isotopes of fluid inclusions of the Huaaobaote deposit are listed in Table 4 and plotted in Figure 12. Three samples from stage I have δD values of -140‰ to -102‰ , $\delta^{18}O_{\text{quartz}}$ values of $1.4\text{--}13.9\text{‰}$, and $\delta^{18}O_{\text{water}}$ values of -4.6‰ to 7.9‰ , respectively. The δD , $\delta^{18}O_{\text{quartz}}$, and $\delta^{18}O_{\text{water}}$ values of four samples from stage II are -141‰ to -76‰ , -0.9‰ to 8.0‰ , and -8.4‰ to 0.5‰ , respectively. The δD , $\delta^{18}O_{\text{quartz}}$, and $\delta^{18}O_{\text{water}}$ values of three samples from stage III are -165‰ to -161‰ , $1.7\text{--}12.1\text{‰}$, and -8.7‰ to 1.7‰ , respectively. Two samples from stage IV have δD values of -168‰ and -92‰ , $\delta^{18}O_{\text{quartz}}$ values of 0.9‰ and 1.3‰ , and $\delta^{18}O_{\text{water}}$ values of -11.9‰ and -11.5‰ , respectively.

Table 4. Oxygen isotopic composition (‰) for quartz and hydrogen and oxygen compositions (‰) for fluid inclusions in quartz from the Huaaobaote deposit.

Sample No.	Stage	Mineral	T_h (°C)	$\delta^{18}O_{\text{quartz}}$ (V-SMOW)	$\delta^{18}O_{\text{water}}$ (V-SMOW)	δD_{V-SMOW}
H32	I	Quartz	325	1.5	-4.5	-102
H34	I	Quartz	325	1.4	-4.6	-140
H40	I	Quartz	325	13.9	7.9	-137

Table 4. Cont.

Sample No.	Stage	Mineral	T _h (°C)	δ ¹⁸ O _{quartz} (V-SMOW)	δ ¹⁸ O _{water} (V-SMOW)	δD _{V-SMOW}
H3-5	II	Quartz	284	1.4	−6.1	−76
H3-7	II	Quartz	284	8.0	0.5	−141
H3-8	II	Quartz	284	−0.9	−8.4	−83
H3-9	II	Quartz	284	1.1	−6.4	−120
H46	III	Quartz	221	12.1	1.7	−165
H49	III	Quartz	221	1.7	−8.7	−161
H50	III	Quartz	221	6.0	−4.4	−163
H42	IV	Quartz	183	1.3	−11.5	−168
H51	IV	Quartz	183	0.9	−11.9	−92

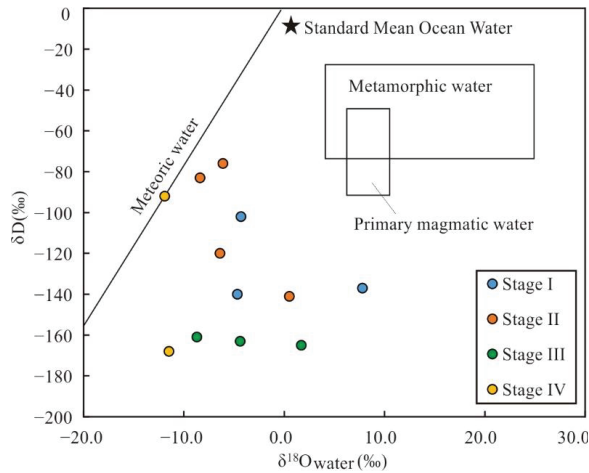


Figure 12. δD versus δ¹⁸O_{H₂O} diagram of the Huaaobaote deposit (base map from [65]).

5.3.2. Sulfur Isotope

The sulfur isotopic compositions of the five pyrite, one sphalerite, one arsenopyrite, and two galena samples are presented in Table 5 and Figure 13. The δ³⁴S (‰) values of three pyrite samples from stage I are between −0.2 and 0.3. The δ³⁴S (‰) values of one arsenopyrite sample and pyrite sample from stage II are 0.6 and 1.1, respectively. The δ³⁴S (‰) values of two galena samples, one pyrite sample, and one sphalerite sample from stage III are −3.4 to −0.9. In brief, the overall variation range of the δ³⁴S values is −3.4‰ to 1.1‰ (mean −0.5‰).

Table 5. Sulfur and lead isotopic compositions of sulfide samples from the Huaaobaote deposit.

Sample No.	Mineral	Stage	δ ³⁴ S _{V-CDT} (‰)	δ ³⁴ S _{H₂S} (‰)	²⁰⁶ Pb/ ²⁰⁴ Pb	²⁰⁷ Pb/ ²⁰⁴ Pb	²⁰⁸ Pb/ ²⁰⁴ Pb	t (Ma)	μ	ω	κ	Δα	Δβ	Δγ
H32	Pyrite	I	−0.2	−1.3	18.219	15.535	38.048	135	9.4	35.4	3.7	59.9	13.7	21.2
H34	Pyrite	I	0.3	−0.8	18.232	15.552	38.100	135	9.4	35.7	3.7	60.6	14.8	22.6
H35	Pyrite	I	0.1	−1.0	18.225	15.545	38.080	135	9.4	35.6	3.7	60.2	14.3	22.0
H3-1	Arsenopyrite	II	0.6	−0.7	18.225	15.546	38.084	135	9.4	35.6	3.7	60.2	14.4	22.1
H26	Pyrite	II	1.1	−0.2	18.237	15.565	38.137	135	9.4	35.9	3.7	60.9	15.6	23.6
H1-4	Galena	III	−3.4	−0.8	18.216	15.531	38.027	135	9.4	35.3	3.7	59.7	13.4	20.6
H1-4	Sphalerite	III	−0.9	−1.3	18.317	15.667	38.475	135	9.6	37.8	3.8	65.6	22.3	32.6
H1-5	Galena	III	−1.4	1.2	18.257	15.586	38.207	135	9.5	36.3	3.7	62.1	17.0	25.4
H46	Pyrite	III	−2.0	−3.6	18.195	15.509	37.965	135	9.3	34.9	3.6	58.5	12.0	18.9

Abbreviations: μ = ²³⁸U/²⁰⁴Pb; ω = ²³²Th/²⁰⁴Pb; κ = Th/U; Δα = [(²⁰⁶Pb/²⁰⁴Pb)_{d(t)} / (²⁰⁶Pb/²⁰⁴Pb)_{m(t)} − 1] × 1000; Δβ = [(²⁰⁷Pb/²⁰⁴Pb)_{d(t)} / (²⁰⁷Pb/²⁰⁴Pb)_{m(t)} − 1] × 1000; Δγ = [(²⁰⁸Pb/²⁰⁴Pb)_{d(t)} / (²⁰⁸Pb/²⁰⁴Pb)_{m(t)} − 1] × 1000; d is the Pb of ore mineral; and m is mantle Pb calculated by the equation of Chen et al. [66].

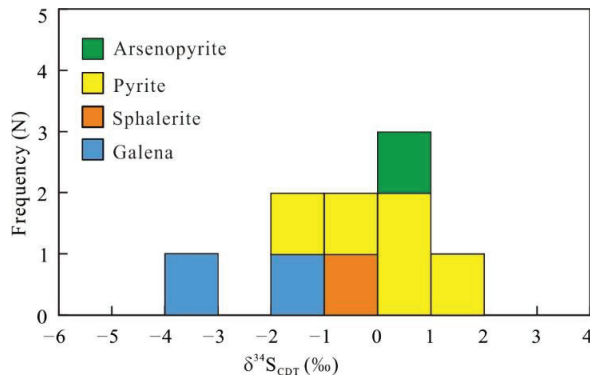


Figure 13. Sulfur isotope histogram of sulfides from the Huaaobaote deposit.

5.3.3. Lead Isotope

The lead isotopic data for nine sulfide samples are presented in Table 5 and Figure 14. The ²⁰⁶Pb/²⁰⁴Pb, ²⁰⁷Pb/²⁰⁴Pb, and ²⁰⁸Pb/²⁰⁴Pb ratios for three pyrite samples from stage I are between 18.219 and 18.232, 15.535 and 15.552, and 38.048 and 38.100, respectively. The ²⁰⁶Pb/²⁰⁴Pb, ²⁰⁷Pb/²⁰⁴Pb, and ²⁰⁸Pb/²⁰⁴Pb ratios for one arsenopyrite sample and one pyrite sample from stage II are 18.225 and 18.237, 15.546 and 15.565, and 38.084 and 38.137, respectively. The ²⁰⁶Pb/²⁰⁴Pb, ²⁰⁷Pb/²⁰⁴Pb, and ²⁰⁸Pb/²⁰⁴Pb ratios for two galena samples, one pyrite sample, and one sphalerite sample from stage III range from 18.195 to 18.317, 15.509 to 15.667, and 37.965 to 38.475, respectively.

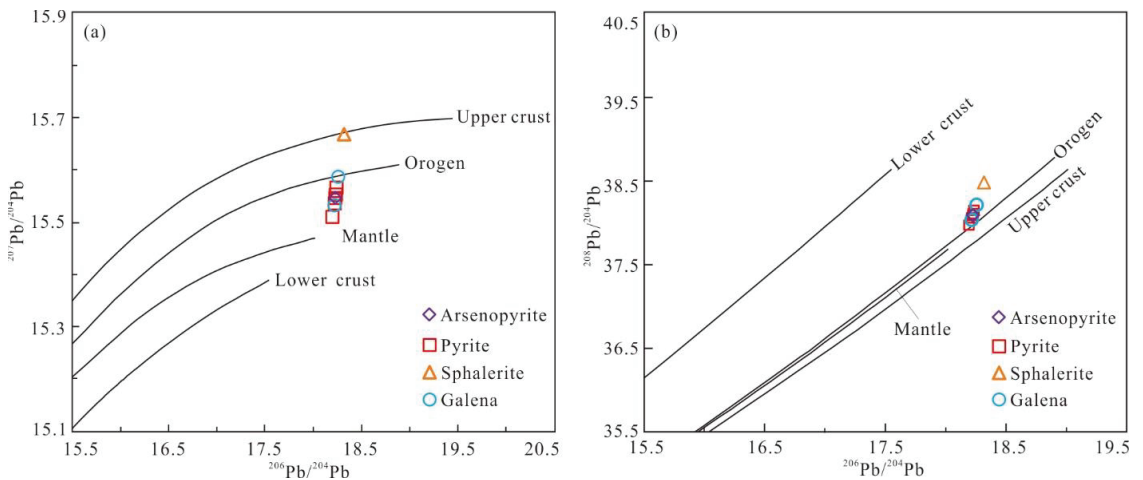


Figure 14. Diagrams of ²⁰⁶Pb/²⁰⁴Pb versus ²⁰⁷Pb/²⁰⁴Pb (a) and ²⁰⁶Pb/²⁰⁴Pb versus ²⁰⁸Pb/²⁰⁴Pb (b) for sulfides from the Huaaobaote deposit (base map from [67]).

6. Discussion

6.1. Mineralization Age

Chen et al. [27] reported a zircon U–Pb age of 136 ± 0.8 Ma for the hypabyssal rhyolite in the Huaaobaote deposit. The Fujian Institute of Geological Survey [52] obtained zircon U–Pb ages of 132.6–127.0 Ma for the granite, monzogranite, and syenogranite of the Ganggantewula intrusion in the southern part of the Huaaobaote area. In addition, Zhou [29] and Shang et al. [30] obtained zircon U–Pb ages of 285.9 ± 4.1 Ma and 294.8 ± 3.2 Ma for the diorite porphyry, respectively, which is mainly distributed along the Huaaobaote

tectonic mélangé belt and spatially accompanies the orebodies. However, a portion of the Ag–Pb–Zn–Sb mineralization in the Huaaobaote deposit crosscuts the hypabyssal rhyolite, suggesting the mineralization postdates the hypabyssal rhyolite crystallization, as well as the diorite porphyry. Some researchers have argued that the Early Cretaceous felsic-magmatism in the Huaaobaote area is related to the Ag–Pb–Zn–Cu–Sn–Sb mineralization [14,27,28,30], and infer that the mineralization is contemporaneous or slightly later than the granite and hypabyssal rhyolite (136–127 Ma) [27,30,52].

Cassiterite is the main ore mineral in the Ag–Cu–Sn orebodies of the Huaaobaote deposit. Petrographic observations revealed that the cassiterite is largely distributed in granular form within the quartz veins and coexisted with chalcopyrite, arsenopyrite, and pyrite. The U–Pb closure temperature of cassiterite ranges from 500 °C to 800 °C [68–70]. Therefore, the cassiterite U–Pb age can accurately define the mineralization time of the Huaaobaote deposit. In this study, we obtained cassiterite U–Pb ages of 136.3–134.3 Ma for the Sn and Ag–Cu–Sn ores, indicating that the mineralization of Sn and Ag–Cu–Sn in the Huaaobaote deposit occurred during the Early Cretaceous period. Our cassiterite U–Pb dating data indicate a clear temporal relationship between the Huaaobaote deposit and the Early Cretaceous hypabyssal rhyolite (136 ± 0.8 Ma), rather than the Permian diorite porphyry (285.9 ± 4.1 Ma and 294.8 ± 3.2 Ma) and the Early Cretaceous granite (132.6–127 Ma).

Previous studies have conducted extensive mineralization dating on representative deposits, including tin–polymetallic deposits, Ag–Pb–Zn deposits, and W–Mo deposits in the SGXR (Table 6). The dating results suggest that all the deposits formed during the Early Cretaceous (145–130 Ma).

Table 6. Mineralization ages of the major Ag–Pb–Zn–Sn–polymetallic deposits in the southern Great Xing’an Range.

Deposit	Metal Assemblage	Analytical Method	Mineralization Age (Ma)	References
Baiyinchagandongshan	Ag–Sn–Pb–Zn–Cu	Cassiterite U–Pb	140–134	[23,51]
Daolundaba	Cu–Sn–W–Ag	Cassiterite U–Pb	136.8–134.7	[38]
Maodeng–Xiaogushan	Sn–Cu–Zn	Cassiterite U–Pb	135–133	[39,51]
Weilasituo	Li–Sn–Pb–Zn–Cu	Muscovite ^{40}Ar – ^{39}Ar	133.4	[71]
		Cassiterite U–Pb	136	[21]
Dajing	Sn–Cu–Pb–Zn–Ag	Cassiterite U–Pb	144	[15]
Huanggang	Fe–Sn–W	Molybdenite Re–Os	135	[48,72]
Bairendaba	Ag–Pb–Zn–Cu	Muscovite ^{40}Ar – ^{39}Ar	135	[73]
Bianjiadayuan	Ag–Pb–Zn	Molybdenite Re–Os	140	[74]
Haobugao	Pb–Zn–Cu–Fe	Molybdenite Re–Os	142	[17,75]
Chamuhan	W–Mo	Molybdenite Re–Os	139	[76,77]
Dongshanwan	Mo–W	Molybdenite Re–Os	140.5	[78]

The Huaaobaote deposit formed during the period of 136.3–134.3 Ma, which is contemporaneous with other deposits in the SGXR, indicating that the Early Cretaceous was the peak season for Ag–Pb–Zn–Sn–polymetallic mineralization in the SGXR.

6.2. Nature and Evolution of Ore-Forming Fluids

The results of the FIs petrography, microthermometry, and laser Raman spectroscopy indicate that ore-forming fluids of the Huaaobaote deposit have a fluid characteristic with multistage evolution from stage I to stage IV. The FIs in stage I are mainly WL-type, are characterized by moderate–high temperature (302–340 °C, mean 325 °C), low salinity (3.7–6.6 wt% NaCl eqv., mean 5.0 wt% NaCl eqv.), and low density (0.69–0.76g/cm³, mean 0.72g/cm³), and contain CH₄, indicating that it belongs to an H₂O–NaCl–CH₄ system. The FIs in stage II are dominantly WL-type, with a small amount of WG-type FIs. The ore-forming fluids are characterized by moderate temperature (267–304 °C, mean

284 °C), low salinity (0.2–4.5 wt% NaCl eqv., mean 3.1 wt% NaCl eqv.), and low density (0.73–0.80 g/cm³, mean 0.77g/cm³), and contain N₂, indicating that it belongs to an H₂O–NaCl–N₂ system. For stage III, the FIs are mainly WL-type, with a small amount of WG-type FIs. The ore-forming fluids are characterized by moderate–low temperature (186–273 °C, mean 221 °C), low salinity (0.2–5.0 wt% NaCl eqv., mean 2.3 wt% NaCl eqv.), and low density (0.76–0.91 g/cm³, mean 0.85g/cm³), and only contain H₂O, indicating that it belongs to an H₂O–NaCl system. This stage is essentially consistent with the data reported by Chen et al. [27] for FIs, i.e., the homogenization temperature ranges from 145 to 274 °C, the salinity is 0.5–8.5 wt% NaCl eqv., and the density is 0.79–0.94 g/cm³. With regard to stage IV, the ore-forming fluids are characterized by relatively low temperature (166–199 °C, mean 183 °C), low salinity (0.4–1.6 wt% NaCl eqv., mean 0.9 wt% NaCl eqv.), and low density (0.88–0.91 g/cm³, mean 0.89g/cm³), and only contain H₂O, the same as stage III, and also belongs to an H₂O–NaCl system.

In general, both the temperature and salinity of the ore-forming fluid gradually decrease from stage I to stage IV (Figure 10), while the FIs' density slightly increases, with a mean density of 0.72 g/cm³ for stage I, 0.77 g/cm³ for stage II, 0.85 g/cm³ for stage III, and 0.89 g/cm³ for stage IV. The coexisting WL- and WG-type FIs were developed in stages II and III, while only WL-type FIs occurred in stages I and IV.

6.3. Sources of Ore-Forming Fluid and Materials

6.3.1. Origin of Ore-Forming Fluids

As shown in Table 4, the H–O isotope compositions of fluids in various stages of the Huaaobaote deposit have a significant range of variation. In the $\delta^{18}\text{O}_{\text{water}}-\delta\text{D}$ diagram (Figure 12), the H–O isotope compositions of the samples from each stage are projected between the primary magmatic water box and the meteoric water evolution line, indicating that the ore-forming fluids are dominantly originated from a mixture of magmatic and meteoric water. Previous studies also suggested that the ore-forming fluids of the deposit are characterized by the mixing of magmatic and meteoric water [27]. Overall, the ore-forming fluid of the Huaaobaote deposit is characterized by low H and O isotope composition, which is consistent with that of high-latitude meteoric water [79,80]. From early to late, the H–O isotope composition of the Huaaobaote deposit shows a gradual decreasing trend, although the projection points are relatively scattered, indicating that with the evolution of ore-forming fluids, the involvement of meteoric water gradually increases.

In summary, the ore-forming fluids of the deposit predominantly originate from a mixture of magmatic and meteoric water, and the involvement of meteoric water gradually increases with the evolution of ore-forming fluids.

6.3.2. Source of Ore-Forming Materials

As shown in Figure 13, the statistical histogram of the $\delta^{34}\text{S}$ values in the Huaaobaote deposit shows a tower-style distribution and varies within a narrow range (−3.4‰ to 1.1‰), which are in the same range as previously reported values (−3.6‰ to 1.2‰ [27]), indicating the sulfur source is isotopically uniform. In a hydrothermal system, the S isotopic composition of the sulfides is a function of the total S isotopic compositions ($\delta^{34}\text{S}_{\Sigma}$), oxygen fugacity ($f\text{O}_2$), pH, ionic strength, and temperature of the ore-forming solution [81]. This suggests that the S isotopic compositions of hydrothermal sulfides depend not only on the $\delta^{34}\text{S}$ value of the source materials, but also on the physical and chemical condition of the ore-forming fluids. However, when the hydrothermal fluids are dominated by H₂S with low oxygen fugacity, the relationship $\delta^{34}\text{S}_{\Sigma} \approx \delta^{34}\text{S}_{\text{H}_2\text{S}} \approx \delta^{34}\text{S}_{\text{fluid}} \approx \delta^{34}\text{S}_{\text{melt}}$ holds in the equilibrium state [82]. The absence of sulfate minerals in all the mineralization stages of the Huaaobaote deposit indicates that the metal minerals precipitated in a relatively reductive environment. The variation law of sulfur isotope composition in the Huaaobaote deposit is $\delta^{34}\text{S}_{\text{Py}} > \delta^{34}\text{S}_{\text{Sph}} > \delta^{34}\text{S}_{\text{Gn}}$ (Figure 13), which is consistent with the $\delta^{34}\text{S}$ enrichment condition of $\delta^{34}\text{S}_{\text{Py}} > \delta^{34}\text{S}_{\text{Sph}} > \delta^{34}\text{S}_{\text{Ccp}} > \delta^{34}\text{S}_{\text{Gn}}$ [82–85]. The mineral species and sulfur isotope characteristics indicate that the metal minerals of the Huaaobaote deposit precipitated in

an equilibrium state with a relatively reductive environment. Therefore, the $\delta^{34}\text{S}_{\text{H2S}}$ value can represent the total S isotopic composition of the ore-forming fluids. The $\delta^{34}\text{S}_{\text{H2S}}$ values were calculated using the equation $\delta^{34}\text{S}_{\text{H2S}} = \delta^{34}\text{S}_i - A_i (10^6 \times T^{-2})$, where i stands for different sulfides; the A_i value is 0.4 for pyrite and arsenopyrite, 0.1 for sphalerite, and -0.63 for galena, respectively; and T is the temperature in Kelvin [86]. The average FIA homogenization temperatures for different mineralization stages were used to calculate the $\delta^{34}\text{S}_{\text{H2S}}$ values of respective stages.

As shown in Table 5, the $\delta^{34}\text{S}_{\text{H2S}}$ values range from -1.3‰ to -0.8‰ for stage I, -0.7‰ to -0.2‰ for stage II, and -3.6‰ to 1.2‰ for stage III. The sulfur isotope composition of the Huaaobaote deposit is consistent with that of the magmatic and meteorite, implying the ore-forming materials of the deposit predominantly originated from magma.

The Pb isotopic composition of the ore is mainly controlled by the initial Pb isotopic composition and formation time and is rarely fractionated in the processes of element migration and precipitation. Therefore, the Pb isotope serves as a useful geological tracer for tracing the source of ore-forming material [87–89]. The μ , ω , and κ values of the Pb isotope of sulfides from the Huaaobaote deposit are 9.3–9.6, 34.9–37.8, and 3.6–3.8, with average values of 9.4, 35.8, and 3.7, respectively (Table 5). Zartman and Doe [67] obtained μ values of 9.60 and 8.92, ω values of 36.84 and 31.84, and κ values of 5.85 and 3.45 for the crust and mantle, respectively. The Pb isotope μ , ω and, κ values of the Huaaobaote deposit are between the crust and mantle, implying that Pb was derived from a mixed source of the crust and mantle. In the $^{206}\text{Pb}/^{204}\text{Pb}$ versus $^{207}\text{Pb}/^{204}\text{Pb}$ diagram (Figure 14a), except for one sample with a high $^{207}\text{Pb}/^{204}\text{Pb}$ ratio, all the remaining samples are plotted in the area between the mantle and orogenic belt evolution curves. In the $^{206}\text{Pb}/^{204}\text{Pb}$ versus $^{208}\text{Pb}/^{204}\text{Pb}$ diagram (Figure 14b), all of the data points are located between the lower crust and orogenic belt evolution lines, and near the orogenic belt evolution line. In the $\Delta\gamma$ versus $\Delta\gamma$ genetic classification diagram (Figure 15), all of the ore lead data of the Huaaobaote deposit are projected within a transition area of the mantle-derived lead and the subduction zone lead related to magmatism, implying that the Pb of the Huaaobaote deposit originated from a mixed source of the upper crust and mantle lead. In addition, all the data are arranged in a straight line with steep slope in Figure 14a, implying that it is not an isochronous line, but a mixed lead line of orogen and mantle. Furthermore, the data points are also close to the range of the orogenic belt lead, although they are projected within the ranges of the mantle-derived lead and subduction zone lead related to magmatism (Figure 15). Chen et al. [27] reported the Pb isotope composition of nine galena samples from the Huaaobaote deposit and believed that the ore Pb mainly originates from the upper mantle and has Pb isotopic characteristics of the subduction zone with crust–mantle mixing. Based on the lead isotopic compositions above, and with the knowledge that the Huaaobaote deposit is located in the eastern section of the Central Asian orogenic belt, meaning that the mineralization of this deposit is closely related to the Mesozoic granitic magmatic activity, we infer that the ore lead of the Huaaobaote deposit mainly originated from the partial melting of orogenic belt materials.

In summary, the ore-forming materials of the Huaaobaote deposit mainly came from the Early Cretaceous magma, which originated from a partial melting of orogenic materials, which were composed of a mixture of the crust and mantle.

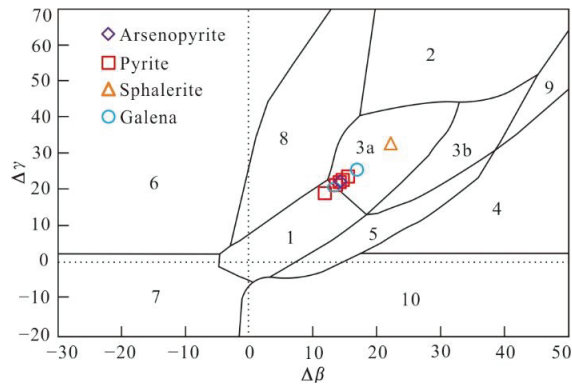


Figure 15. $\Delta\beta$ versus $\Delta\gamma$ genetic classification diagram for lead isotopes of ore minerals from the Huaaoabaote deposit (base map after [90]). Numbered sections: 1 = mantle-derived lead; 2 = upper crust lead; 3 = subduction zone lead originated from the mixing of the upper crust and mantle lead (3a = lead related to magmatism; 3b = lead related to sedimentation); 4 = chemically deposited lead; 5 = submarine hydrothermal lead; 6 = medium–high grade metamorphism lead; 7 = lower crust lead of high-grade metamorphism; 8 = orogenic belt lead; 9 = upper crust lead in ancient shale; 10 = retrograde metamorphism lead.

6.4. Mechanism of Mineral Deposition

The capacity of hydrothermal fluids to transport metals in concentrations sufficient to form ore deposits is due in large part to the polar nature of the water molecule and the ability of metals to form strong aqueous complexes with a number of ligands [91]. Most hydrothermal liquids contain significant concentrations of solutes such as NaCl, CO₂, SO₂, H₂S, NH₃, HF, and H₃PO₄, and even some organic complexes, which interact with liquid water producing ligands that enable metal complexation [91–94]. Among them, the dominant ligands are Cl[−], HS[−], and OH[−] [92,94]. According to Pearson’s hard/soft acid/base (HSAB) principle [95], tin has a valence of 2⁺ or 4⁺ in hydrothermal fluids, and is a hard or borderline acid. In a reduced hydrothermal fluid, tin generally has a valence of 2⁺ [96,97], and Sn²⁺ as a borderline acid preferentially bonds with borderline bases, such as Cl[−] [91,95]. Fls studies indicate that the tin mineralization stages are a relatively reduced environment, which is further supported by the symbiotic pyrrhotite in the same stages. Thus, we assume that tin is mainly composed of Sn²⁺ transported as chloride complexes. A possible reaction for the cassiterite precipitates is SnCl_x^{2−x} + 2H₂O = SnO₂ + 2H⁺ + xCl[−] + H₂ [98]. Copper is a soft acid or intermediate acid, depending on whether it has a valence of 1⁺ or 2⁺, respectively [95]. Similarly, at low salinity and with a reduced hydrothermal fluids system, Cu⁺ is the dominant form of copper, a soft acid, and forms strong complexes with HS[−] [91]. Zinc is transported as chloride complexes in most physicochemical conditions, even Mississippi Valley-type (MVT) deposits, a fact that has been borne out by many solubility, spectroscopic, and thermodynamic studies [91,99]. However, the acidity of Pb²⁺ is softer than Zn²⁺ [95]; therefore, Pb²⁺ may bond with HS[−]. The thermodynamic modeling of Zhong et al. [99] revealed that Pb(HS)₂⁰ is the main Pb complex in a reduced hydrothermal fluid system under the conditions of low salinity (3.4 wt% NaCl eqv.), a temperature between 150 °C and 500 °C, and pressure greater than 1.0 kbar. Silver mainly exists in the form of Ag⁺ in hydrothermal fluids and preferentially bonds with soft ligands, such as HS[−] [95]. Indeed, in sulphide-containing solutions at temperatures between 25 °C and 400 °C, and a chloride concentration up to 0.5 mol kg^{−1}, silver (I) sulphide complexes are most important [91,100]. Sulfide ores, except for stage I, account for the majority of ore resources in the Huaaoabaote deposit, in addition to a considerable amount of pyrite and pyrrhotite vein-bodies in the mine, indicating a high concentration of sulfur in the ore-forming fluid. Thus, we infer that silver was transported as a hydrosulfide complex. In summary, both Sn and Zn migrate in

the form of chloride complexes, while Cu, Pb, and Ag migrate in the form of hydrosulfide complexes in the Huaaobaote deposit.

The precipitation of the dissolved constituents in hydrothermal fluid may be attributed to temperature variations, fluid immiscibility or boiling, reactions between wall rocks and solutions, and fluid mixing [93,94,101,102], which, in essence, affect the availability and stability of complexes of ligands. Figure 12 shows that the ore-forming fluid of the Huaaobaote deposit is characterized by the mixing of magmatic and meteoric water; thus, fluid mixing is one of the main mechanisms for mineral precipitation in the deposit. From early to late periods, the temperature of the ore-forming fluid gradually decreased (Figure 16), indicating that fluid cooling is another one of the main mechanisms for mineral precipitation in the deposit. There are significant differences in the FIs type and fluid salinity at different stages, implying that the mineral precipitation mechanisms at each stage are not identical. For the first stage, the FIs are dominated by WL-type inclusions, with the highest homogenization temperature (302–340 °C) and salinity (3.7–6.6 wt% NaCl eqv.), suggesting that cooling was the main mechanism of cassiterite precipitation in the Huaaobaote deposit. In stages II and III, WL- and WG-type inclusions coexist in the same quartz crystal. These different types of inclusions with different gas–liquid filling degrees have different homogenization patterns and contrasting salinities, but analogous homogenization temperatures (Figures 9 and 16), indicating that the fluids of the Ag–Cu–Sn and Ag–Pb–Zn–Sb mineralization stages are both immiscible. We believe that the phase separation caused by decompression induced fluid immiscibility, which is also demonstrated by the cryptoexplosive breccias developed in stage III. Therefore, fluid immiscibility is the main mechanism for the precipitation of the Ag–Cu–Sn of stage II and the Ag–Pb–Zn–Sb of stage III. Only WL-type FIs were observed in stage IV, and the ore-forming fluid is dominated by meteoric water with the lowest homogenization temperature (166–199 °C) and salinity (0.4–1.6 wt% NaCl eqv.), indicating that fluid cooling was the main mechanism of silver mineral precipitation in stage IV.

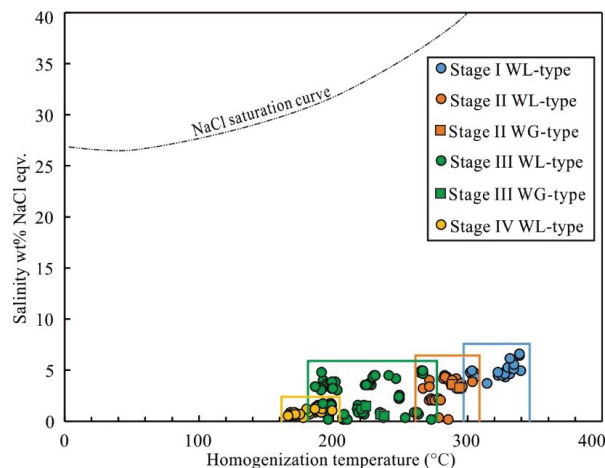


Figure 16. Diagram of homogenization temperature versus salinity of fluid inclusions in quartz and sphalerite from the Huaaobaote deposit. NaCl saturation curve from [57].

In summary, fluid mixing, cooling, and immiscibility are the three main mechanisms for mineral precipitation in the Huaaobaote deposit. Fluid mixing runs through the entire mineralization process. The cooling of the mixed fluid is the main mechanism for the Sn precipitation of stage I; fluid immiscibility is mainly responsible for the precipitation of the Ag–Cu–Sn of stage II and the Ag–Pb–Zn–Sb of stage III; and the Ag mineralization of stage IV is related to fluid cooling dominated by meteoric water.

7. Conclusions

- (1) Cassiterite U–Pb dating indicates that the Huaobaote deposit formed in the Early Cretaceous (136.3–134.3 Ma).
- (2) The ore-forming fluid is characterized by low salinity and has an affinity of $\text{H}_2\text{O}-\text{NaCl} \pm \text{CH}_4 \pm \text{N}_2$ in composition. From early to late periods, the ore-forming fluid underwent an evolution from the high temperature of stage I, through the medium temperature of stages II and III, to the low temperature of stage IV.
- (3) The ore-forming fluid of the Huaobaote deposit originated from a mixture of magmatic and meteoric water. With the evolution of ore-forming fluid, the amount of meteoric water increased gradually. The ore-forming materials were dominantly derived from the Early Cretaceous felsic magma.
- (4) Fluid mixing, cooling, and immiscibility were the three major mechanisms for the deposition of ore-forming materials. Of these, phase separation caused by fluid immiscibility was important for the precipitation of the Ag–Cu–Sn of stage II and the Ag–Pb–Zn–Sb of stage III, while fluid cooling was main mechanism for the Ag mineral precipitation of stage IV.

Author Contributions: Conceptualization, S.L. and G.W.; methodology, S.L.; software, S.L. and F.Y.; validation, G.W. and Z.L.; formal analysis, S.L., G.C., F.Y. and J.S.; writing—original draft preparation, S.L.; writing—review and editing: G.W., and Z.L.; investigation, S.L., G.C., X.L. and H.D.; resources, H.Y. and G.W.; data collection, X.L., J.S. and H.D.; data curation: G.W. and Z.L.; visualization, X.L. and J.S.; supervision, Z.L., G.W. and H.Y.; project administration and funding acquisition, G.W. All authors have read and agreed to the published version of the manuscript.

Funding: This research was funded by the Scientific Research Project of Inner Mongolia Yulong Mining Co., Ltd. (Grant No. 2020110033002072), the Geological Survey Project of Copper and Gold Mineral Resources in Key Metallogenic Zones (Grant No. DD20230287), and the Youth Fund of the National Natural Science Foundation of China (Grant No. 42202080).

Data Availability Statement: Not applicable.

Acknowledgments: We would like to thank the leaders from the Inner Mongolia Yulong Mining Co., Ltd. for their great support during the field investigation. Engineers Xiaoqi Zhang, Xiaobo Xu, Haidong Li, Li Song, Huder, Wenming Yang, Zhuo Zhan, Jianwei Wang, Haipeng Li, and Wei Shi are thanked for their participation during the field geological survey.

Conflicts of Interest: The authors declare no conflict of interest.

References

1. Wang, J.B.; Wang, Y.W.; Wang, L.J.; Uemoto, T. Tin–polymetallic mineralization in the southern part of the Da Hinggan Mountains, China. *Resour. Geol.* **2001**, *51*, 283–291. [CrossRef]
2. Ouyang, H.G.; Mao, J.W.; Zhou, Z.H.; Su, H.M. Late Mesozoic metallogeny and intracontinental magmatism, southern Great Xing’an Range, northeastern China. *Gondwana Res.* **2015**, *27*, 1153–1172. [CrossRef]
3. Zeng, Q.D.; Liu, J.M.; Chu, S.X.; Guo, Y.P.; Gao, S.; Guo, L.X.; Zhai, Y.Y. Poly-metal mineralization and exploration potential in southern segment of Da Hinggan Mountains. *J. Jilin Univ. Earth Sci. Ed.* **2016**, *46*, 1100–1123. (In Chinese)
4. Jiang, S.H.; Zhang, L.L.; Liu, Y.F.; Liu, C.H.; Kang, H.; Wang, F.X. Metallogeny of Xing–Meng Orogenic Belt and some related problems. *Miner. Depos.* **2018**, *37*, 671–711. (In Chinese)
5. Zhou, Z.H.; Mao, J.W. Metallogenic patterns and ore deposit model of the tin–polymetallic deposits in the southern segment of Great Xing’an Range. *Earth Sci. Front.* **2022**, *29*, 176–199. (In Chinese)
6. Zhao, Y.M. *Metallogenic Regularity and Evaluation of Copper Polymetallic Deposits in the Great Xing’an Range and Its Adjacent Areas*; Seismological Press: Beijing, China, 1997; pp. 1–318. (In Chinese)
7. Liu, J.M.; Zhang, R.; Zhang, Q.Z. The regional metallogeny of Da Hinggan Ling, China. *Earth Sci. Front.* **2004**, *11*, 269–277. (In Chinese)
8. Shao, J.D.; Wang, S.G.; Zhao, W.T.; Jia, H.Y.; Wang, X.L.; Zhang, M.; Ren, Y.P. Geological characteristics and prospecting potential in the Daxing’anling region. *Geol. Resour.* **2007**, *16*, 252–262. (In Chinese)
9. Xu, Z.G.; Chen, Y.C.; Wang, D.H.; Chen, Z.H.; Li, H.M. *Scheme of the Classification of the Minerogenetic Units in China*; Geological Publishing House: Beijing, China, 2008; pp. 1–128. (In Chinese)
10. Mao, J.W.; Zhou, Z.H.; Wu, G.; Jiang, S.H.; Liu, C.L.; Li, H.M.; Ouyang, H.G.; Liu, J. Metallogenic regularity and minerogenetic series of ore deposits in Inner Mongolia and adjacent areas. *Miner. Depos.* **2013**, *32*, 715–729. (In Chinese)

11. Wang, C.N.; Wang, Q.M.; Yu, X.F.; Han, Z.Z. Metallogenic characteristics of tin and ore-search prospect in the southern part of Da Hinggan Mountains. *Geol. Explor.* **2016**, *52*, 220–227. (In Chinese)
12. Yao, L.; Lü, Z.C.; Ye, T.Z.; Pang, Z.S.; Jia, H.X.; Zhang, Z.H.; Jia, R.Y.; Wu, Y.F. Geological and Sr–Nd–S–Pb isotopic constraints on the genesis of the Baiyinchagan tin–polymetallic deposit, southern Great Xing’an Range. *Acta Petrol. Sin.* **2021**, *37*, 1731–1748. (In Chinese)
13. Wu, G.; Liu, R.L.; Chen, G.Z.; Li, T.G.; Li, R.H.; Li, Y.L.; Yang, F.; Zhang, T. Mineralization of the Weilasituo rare metal–tin–polymetallic ore deposit in Inner Mongolia: Insights from fractional crystallization of granitic magmas. *Acta Petrol. Sin.* **2021**, *37*, 637–664. (In Chinese)
14. Li, Z.X.; Xie, Z.Y.; Liu, Z.; Li, S.G. Geology and genesis of the Huaaobaote lead–zinc deposit in Inner Mongolia. *Geol. Resour.* **2008**, *17*, 278–281. (In Chinese)
15. Liao, Z.; Wang, Y.W.; Wang, J.B.; Li, H.M.; Long, L.L. LA-MC-ICP-MS cassiterite U–Pb ages of Dajing tin–polymetallic deposit in Inner Mongolia and their geological significance. *Miner. Depos.* **2014**, *33*, 421–422. (In Chinese)
16. Jiang, S.H.; Nie, F.J.; Bai, D.M.; Liu, Y.F.; Liu, Y. Geochronology evidence for Indosinian mineralization in Baiyinnuoer Pb–Zn deposit of Inner Mongolia. *Miner. Depos.* **2011**, *30*, 787–798. (In Chinese)
17. Liu, Y.F.; Jiang, S.H.; Bagas, L.; Han, N.; Chen, C.L.; Kang, H. Isotopic (C–O–S) geochemistry and Re–Os geochronology of the Haobugao Zn–Fe deposit in Inner Mongolia, NE China. *Ore Geol. Rev.* **2017**, *82*, 130–147. [CrossRef]
18. Zhou, Z.H.; Mao, J.W.; Lyckberg, P. Geochronology and isotopic geochemistry of the A-type granites from the Huanggang Sn–Fe deposit, southern Great Hinggan Range, NE China: Implication for their origin and tectonic setting. *J. Asian Earth Sci.* **2012**, *49*, 272–286. [CrossRef]
19. Wang, C.G.; Sun, F.Y.; Sun, G.S.; Sun, J.D.; Li, Y.; Feng, H.D. Geochronology, geochemical and isotopic constraints on petrogenesis of intrusive complex associated with Bianjiadayuan polymetallic deposit on the southern margin of the Greater Khingan, China. *Arab. J. Geosci.* **2016**, *9*, 334–350. [CrossRef]
20. Wang, F.X.; Bagas, L.; Jiang, S.H.; Liu, Y.F. Geological, geochemical, and geochronological characteristics of Weilasituo Sn–polymetal deposit, Inner Mongolia, China. *Ore Geol. Rev.* **2017**, *80*, 1206–1229. [CrossRef]
21. Liu, R.L.; Wu, G.; Li, T.G.; Chen, G.Z.; Wu, L.W.; Zhang, P.C.; Zhang, T.; Jiang, B.; Liu, W.Y. LA-ICP-MS cassiterite and zircon U–Pb ages of the Weilasituo tin–polymetallic deposit in the southern Great Xing’an Range and their geological significance. *Earth Sci. Front.* **2018**, *25*, 183–201. (In Chinese)
22. Chen, G.Z.; Wu, G.; Li, T.G.; Liu, R.L.; Li, R.H.; Li, Y.L.; Yang, F. Mineralization of the Daolundaba Cu–Sn–W–Ag deposit in the southern Great Xing’an Range, China: Constraints from geochronology, geochemistry, and Hf isotope. *Ore Geol. Rev.* **2021**, *133*, 104117. [CrossRef]
23. Yang, F.; Wu, G.; Li, R.H.; Zhang, T.; Chen, G.Z.; Xu, Y.M.; Li, Y.L.; Li, T.G.; Liu, R.L.; Chen, Y.J. Age, fluid inclusion, and H–O–S–Pb isotope geochemistry of the Baiyinchagan Sn–Ag–polymetallic deposit in the southern Great Xing’an Range, NE China. *Ore Geol. Rev.* **2022**, *150*, 105194. [CrossRef]
24. Shen, P.; Shen, Y.C.; Pan, H.D.; Wang, J.B.; Zhang, R.; Zhang, Y.X. Baogutu porphyry Cu–Mo–Au deposit, west Junnggar, northwest China: Petrology, alteration, and mineralization. *Econ. Geol.* **2010**, *105*, 947–970. [CrossRef]
25. Ge, W.C.; Wu, F.Y.; Zhou, C.Y.; Zhang, J.H. Porphyry Cu–Mo deposits in the eastern Xing’an–Mongolian Orogenic Belt: Mineralization ages and their geodynamic implications. *Chin. Sci. Bull.* **2007**, *52*, 3416–3427. [CrossRef]
26. Chen, W.; Li, Y.X.; Wang, S.; Li, Z.; Xue, H.M.; Tong, Y. Geological and mineralizing fluid’s characters of Hua’aobaote silver–polymetallic ore deposit. *Nonferrous Met. (Min. Sect.)* **2008**, *60*, 32–50. (In Chinese)
27. Chen, Y.Q.; Zhou, D.; Guo, L.F. Genetic study on the Huaaobaote Pb–Zn–Ag polymetallic deposit in Inner Mongolia: Evidence from fluid inclusions and S, Pb, H, O isotopes. *J. Jilin Univ. Earth Sci. Ed.* **2014**, *44*, 1478–1491. (In Chinese)
28. Zhao, S.J.; Piao, L.L.; Mi, K.F.; Yi, H.N.; Zhang, X.Q.; Yan, Y.H. Characteristics of the cryptoblastic breccia and subrhyolite at the Huaaobaote silver–lead–zinc deposit. *Mod. Min.* **2015**, *31*, 137–143. (In Chinese)
29. Zhou, G.W. The characteristics and formation mechanism discussion of Huaaobaote ophiolite belt. *Geol. Fujian* **2016**, *35*, 266–276. (In Chinese)
30. Shang, Z.; Chen, Y.Q.; Guo, X.G. Felsic igneous rocks in the Hua’aobaote Pb–Zn–Ag polymetallic orefield, Southern Great Xing’an Range: Genesis, metallogenic and tectonic significance. *Acta Geol. Sin.* **2022**, *96*, 221–239. [CrossRef]
31. Mao, J.W.; Xie, G.Q.; Zhang, Z.H.; Li, X.F.; Wang, Y.T.; Zhang, C.Q.; Li, Y.F. Mesozoic large–scale metallogenic pulses in North China and corresponding geodynamic settings. *Acta Petrol. Sin.* **2005**, *21*, 169–188. (In Chinese)
32. Wang, T.; Guo, L.; Zheng, Y.D.; Donskaya, T.; Gladkochub, D.; Zeng, L.S.; Li, J.B.; Wang, Y.B.; Mazukabzov, A. Timing and processes of late Mesozoic mid–lower–crustal extension in continental NE Asia and implications for the tectonic setting of the destruction of the North China Craton: Mainly constrained by zircon U–Pb ages from metamorphic core complexes. *Lithos* **2012**, *154*, 315–345. [CrossRef]
33. Inner Mongolian Autonomous Region Bureau of Geology and Mineral Resources. *People’s Republic of China Ministry of Geology and Mineral Resources Geological Memoirs*; Geological Publishing House: Beijing, China, 1991; pp. 1–498. (In Chinese)
34. Chen, B.; Jahn, B.M.; Tian, W. Evolution of the Solonker suture zone: Constraints from zircon U–Pb ages, Hf isotopic ratios and whole-rock Sr–Nd isotope compositions of subduction- and collision-related magmas and forearc sediments. *J. Asian Earth Sci.* **2009**, *34*, 245–257. [CrossRef]

35. Lu, L.; Qin, Y.; Zhang, K.J.; Han, C.Y.; Wei, T.; Li, F.Z.; Qu, Z.H. Provenance and tectonic settings of the late Paleozoic sandstones in central Inner Mongolia, NE China: Constraints on the evolution of the southeastern Central Asian Orogenic Belt. *Gondwana Res.* **2019**, *77*, 111–135. [CrossRef]
36. Xu, W.L.; Pei, F.P.; Wang, F.; Meng, E.; Ji, W.Q.; Yang, D.B.; Wang, W. Spatialtemporal relationships of Mesozoic volcanic rocks in NE China: Constraints on tectonic overprinting and transformations between multiple tectonic regimes. *J. Asian Earth Sci.* **2013**, *74*, 167–193. [CrossRef]
37. Zhou, J.B.; Li, L. The Mesozoic accretionary complex in Northeast China: Evidence for the accretion history of Paleo-Pacific subduction. *J. Asian Earth Sci.* **2017**, *145*, 91–100. [CrossRef]
38. Chen, G.Z.; Wu, G.; Yang, F.; Zhang, T.; Li, T.G.; Liu, R.L.; Li, R.H.; Li, Y.L.; Wu, L.W.; Zhang, P.C. Ages, H–O–C–S–Pb isotopes, and fluid inclusion study of the Daolundaba Cu–Sn–W–Ag deposit in Inner Mongolia, NE China. *Ore Geol. Rev.* **2022**, *150*, 105171. [CrossRef]
39. Yang, F.; Wu, G.; Li, R.H.; Zhang, T.; Chen, G.Z.; Chen, Y.J. Petrogenesis of the Alubaogeshan intrusion in the Maodeng–Xiaogushan area, southern Great Xing’an Range, NE China: Implications for magma evolution and tin–polymetallic mineralization. *J. Asian Earth Sci.* **2022**, *238*, 105395. [CrossRef]
40. Liu, J.F.; Chi, X.G.; Zhang, X.Z.; Ma, Z.H.; Zhao, Z.; Wang, T.F.; Hu, Z.C.; Zhao, X.Y. Geochemical characteristic of Carboniferous quartz–diorite in the southern Xiwuqi area, Inner Mongolia and its tectonic significance. *Acta Geol. Sin.* **2009**, *83*, 365–376. (In Chinese)
41. Xue, H.M.; Guo, L.J.; Hou, Z.Q.; Tong, Y.; Pan, X.F.; Zhou, X.W. SHRIMP zircon U–Pb ages of the middle Neopaleozoic unmetamorphosed magmatic rocks in the southwestern slope of the Da Hinggan Mountains, Inner Mongolia. *Acta Petrol. Mineral.* **2010**, *29*, 811–823. (In Chinese)
42. Jian, P.; Kröner, A.; Windley, B.F.; Shi, Y.R.; Zhang, W.; Zhang, L.Q.; Yang, W.R. Carboniferous and Cretaceous mafic–ultramafic massifs in Inner Mongolia (China): A SHRIMP zircon and geochemical study of the previously presumed integral “Hegenshan ophiolite”. *Lithos* **2012**, *142–143*, 48–66. [CrossRef]
43. Dong, J.Y. Characteristics and Geological Significance of Ophiolite on the Area Daqingmuchang in Xiwuqi, Inner Mongolia. Master’s Thesis, China University of Geosciences (Beijing), Beijing, China, 2014. (In Chinese).
44. Song, S.G.; Wang, M.J.; Wang, C.; Niu, Y.L. Magmatism during continental collision, subduction, exhumation and mountain collapse in collisional orogenic belts and continental net growth: A perspective. *Sci. China Earth Sci.* **2015**, *58*, 1284–1304. [CrossRef]
45. Zhang, Z.C.; Li, K.; Li, J.F.; Tang, W.H.; Chen, Y.; Luo, Z.W. Geochronology and geochemistry of the eastern Erenhot ophiolitic complex: Implications for the tectonic evolution of the Inner Mongolia–Daxinganling Orogenic Belt. *J. Asian Earth Sci.* **2015**, *97*, 279–293. [CrossRef]
46. Ge, W.C.; Wu, F.Y.; Zhou, C.Y.; Zhang, J.H. Zircon U–Pb ages and its significance of the Mesozoic granites in the Wulanhaote region, central Da Hinggan Mountain. *Acta Petrol. Sin.* **2005**, *21*, 749–762. (In Chinese)
47. Wu, F.Y.; Sun, D.Y.; Ge, W.C.; Zhang, Y.B.; Grant, M.L.; Wilde, S.A.; Jahn, B.M. Geochronology of the Phanerozoic granitoids in Northeastern China. *J. Asian Earth Sci.* **2011**, *41*, 1–30. [CrossRef]
48. Zhou, Z.H.; Lü, L.S.; Feng, J.R.; Li, C.; Li, T. Molybdenite Re–Os ages of Huanggang skarn Sn–Fe deposit and their geological significance, Inner Mongolia. *Acta Petrol. Sin.* **2010**, *26*, 667–679. (In Chinese)
49. Chen, G.Z.; Wu, G.; Wu, W.H.; Zhang, T.; Li, T.G.; Liu, R.L.; Wu, L.W.; Zhang, P.C.; Jiang, B.; Wang, Z.L. Fluid inclusion study and isotope characteristics of the Daolundaba copper–polymetallic deposit in the southern Great Xing’an Range. *Earth Sci. Front.* **2018**, *25*, 202–221. (In Chinese)
50. Guo, S.; He, P.; Zhang, X.B.; Cui, Y.R.; Zhang, T.F.; Zhang, K.; Lai, L.; Liu, C.B. Geochronology and geochemistry of Maodeng–Xiaogushan tin–polymetallic ore field in Southern Da Hinggan Mountains and their geological significances. *Miner. Depos.* **2019**, *38*, 509–525. (In Chinese)
51. Li, R.H. Metallogenesis of Tin–Copper–Polymetallic Ore Deposits in the Xilinhot Area, the Southern Great Xing’an Range. Ph.D. Thesis, Peking University, Beijing, China, 2019; pp. 1–238. (In Chinese).
52. Fujian Institute of Geological Survey. *1/50,000 Geological Map Specification (Huaaobaote Frame)*; Geological Survey of China Geological Survey: Beijing, China, 2013. (In Chinese)
53. Inner Mongolia Autonomous Region No. 10 Institute of Geological and Mineral Exploration and Development. *Exploration Report of Silver–Lead–Zinc Deposit in Huaaobao Mining Area, West Ujimqin Banner, Inner Mongolia Autonomous Region*; Inner Mongolia Yulong Mining Co., Ltd.: Xilinhot, China, 2009. (In Chinese)
54. Carr, P.A.; Zink, S.; Bennett, V.C.; Norman, M.D.; Amelin, Y.; Blevin, P.L. A new method for U–Pb geochronology of cassiterite by ID-TIMS applied to the Mole Granite polymetallic system, eastern Australia. *Chem. Geol.* **2020**, *539*, 11953. [CrossRef]
55. Chew, D.M.; Petrus, J.A.; Kamber, B.S. U–Pb LA-ICPMS dating using accessory mineral standards with variable common Pb. *Chem. Geol.* **2014**, *363*, 185–199. [CrossRef]
56. Ludwig, K.R. *Isoplot: Isoplot 4.15: A Geochronological Toolkit for Microsoft Excel*; Berkeley Geochronology Center: Berkeley, CA, USA, 2008.
57. Bodnar, R.J. Revised equation and table for determining the freezing-point depression of H₂O–NaCl solutions. *Geochim. Cosmochim. Acta* **1993**, *57*, 683–684. [CrossRef]

58. Brown, P.E. FLINCOR: A microcomputer program for the reduction and investigation of fluid-inclusion data. *Am. Mineral.* **1989**, *74*, 1390–1393.
59. Coleman, B.D.; Mares, M.A.; Willig, M.R.; Hsieh, Y.H. Randomness, area, and species richness. *Ecology* **1982**, *63*, 1121–1133. [CrossRef]
60. Clayton, R.N.; Mayeda, T.K. The use of bromine pentafluoride in the extraction of oxygen from oxides and silicates for isotopic analysis. *Geochim. Cosmochim. Acta* **1963**, *27*, 43–52. [CrossRef]
61. Cao, H.W.; Li, G.M.; Zhang, R.Q.; Zhang, Y.H.; Zhang, L.K.; Dai, Z.W.; Zhang, Z.; Liang, W.; Dong, S.L.; Xia, X.B. Genesis of the Cuonadong tin polymetallic deposit in the Tethyan Himalaya: Evidence from geology, geochronology, fluid inclusions and multiple isotopes. *Gondwana Res.* **2021**, *92*, 72–101. [CrossRef]
62. Clayton, R.N.; Mayeda, T.K.; Oneil, J.R. Oxygen isotope: Exchange between quartz and water. *J. Geophys. Res.* **1972**, *77*, 3057–3067. [CrossRef]
63. Robinson, B.W.; Kusakabe, M. Quantitative preparation of sulfur dioxide, for $^{34}\text{S}/^{32}\text{S}$ analyses, from sulfides by combustion with cuprous oxide. *Anal. Chem.* **1975**, *47*, 1179–1181. [CrossRef]
64. Todt, W.; Cliff, R.A.; Hanser, A.; Hofmann, A.W. Re-calibration of NBS lead standards using a ^{202}Pb – ^{205}Pb double spike. *Terra Abstract* **1993**, *5*, 1–396.
65. Sheppard, S.M.F. Characterization and isotopic variations in natural-waters. *Rev. Mineral. Geochem.* **1986**, *16*, 165–183.
66. Chen, Y.W.; Mao, C.X.; Zhu, B.Q. Lead isotopic composition and genesis of Phanerozoic metal deposit in China. *Geochemistry* **1982**, *1*, 137–158. [CrossRef]
67. Zartman, R.E.; Doe, B.R. Plumbotectonics: The model. *Tectonophysics* **1981**, *75*, 135–162. [CrossRef]
68. Gulson, B.L.; Jones, M.T. Cassiterite: Potential for direct dating of mineral deposits and a precise age for the Bushveld complex granites. *Geology* **1992**, *20*, 355–358. [CrossRef]
69. Yuan, S.D.; Peng, J.T.; Hu, R.Z.; Li, H.M.; Shen, N.P.; Zhang, D.L. A precise U–Pb age on cassiterite from the Xianghualing tin–polymetallic deposit (Hunan, south China). *Miner. Depos.* **2008**, *43*, 375–382. (In Chinese) [CrossRef]
70. Yuan, S.D.; Peng, J.T.; Hao, S.; Li, H.M.; Geng, J.Z.; Zhang, D.L. In situ LA-MC-ICP-MS and ID-TIMS U–Pb geochronology of cassiterite in the giant Furong tin deposit, Hunan Province, South China: New constraints on the timing of tin–polymetallic mineralization. *Ore Geol. Rev.* **2011**, *43*, 235–242. [CrossRef]
71. Pan, X.F.; Guo, L.J.; Wang, S.; Xue, H.M.; Hou, Z.Q.; Tong, Y.; Li, Z.M. Laser microprobe Ar–Ar dating of biotite from the Weilasituo Cu–Zn polymetallic deposit in Inner Mongolia. *Acta Petrol. Mineral.* **2009**, *28*, 473–479. (In Chinese)
72. Zhai, D.G.; Liu, J.J.; Zhang, H.Y.; Yao, M.J.; Wang, J.P.; Yang, Y.Q. S–Pb isotopic geochemistry, U–Pb and Re–Os geochronology of the Huanggangliang Fe–Sn deposit, Inner Mongolia, NE China. *Ore Geol. Rev.* **2014**, *59*, 109–122. [CrossRef]
73. Chang, Y.; Lai, Y. Study on characteristics of ore-forming fluid and chronology in the Yindu Ag–Pb–Zn polymetallic ore deposit, Inner Mongolia. *Acta Sci. Nat. Univ. Pekinensis.* **2010**, *46*, 581–593. (In Chinese)
74. Zhai, D.G.; Liu, J.J.; Zhang, A.L.; Sun, Y.Q. U–Pb, Re–Os, and $^{40}\text{Ar}/^{39}\text{Ar}$ geochronology of porphyry Sn \pm Cu \pm Mo and polymetallic (Ag–Pb–Zn–Cu) vein mineralization at Bianjiadayuan, Inner Mongolia, northeast China: Implications for discrete mineralization events. *Econ. Geol.* **2017**, *112*, 2041–2059. [CrossRef]
75. Wang, C.Y.; Li, J.F.; Wang, K.Y. Fluid inclusions, stable isotopes, and geochronology of the Haobugao lead–zinc deposit, Inner Mongolia, China. *Resour. Geol.* **2019**, *69*, 65–84. [CrossRef]
76. Wang, M.Y.; He, L. Re–Os dating of molybdenites from Chamuhan W–Mo deposit, Inner Mongolia and its geological implications. *Geotecton. Metallog.* **2013**, *37*, 49–56. (In Chinese)
77. Zhang, L.L.; Jiang, S.H.; Bagas, L.; Han, N.; Liu, Y.; Liu, Y.F. Element behavior during interaction of magma and fluid: A case study of Chamuhan granite, and implications on the genesis of W–Mo mineralization. *Lithos* **2019**, *342–343*, 31–44. [CrossRef]
78. Zhang, X.B.; Wang, K.Y.; Wang, C.Y.; Li, W.; Yu, Q.; Wang, Y.; Li, J.F.; Wan, D.; Huang, G.H. Age, genesis, and tectonic setting of the Mo–W mineralized Dongshanwan granite porphyry from the Xilamulun metallogenic belt, NE China. *J. Earth Sci.* **2017**, *28*, 433–446. [CrossRef]
79. Rye, R.O.; Ohmoto, H. Sulfur and carbon isotopes and ore genesis: A review. *Econ. Geol.* **1974**, *69*, 826–842. [CrossRef]
80. Wilkinson, J.J.; Jenkin, G.R.T.; Fallick, A.E.; Foster, R.P. Oxygen and hydrogen isotopic evolution of Variscan crustal fluids, south Cornwall, UK. *Chem. Geol.* **1995**, *123*, 239–254. [CrossRef]
81. Ohmoto, H. Systematics of sulfur and carbon isotopes in hydrothermal ore deposits. *Econ. Geol.* **1972**, *67*, 551–578. [CrossRef]
82. Ohmoto, H.; Rye, R.O. Isotopes of sulphur and carbon. In *Geochemistry of Hydrothermal Ore Deposits*, 2nd ed.; Bames, H.L., Ed.; John Wiley & Sons: New York, NY, USA, 1979; pp. 509–567.
83. Sakai, H. Isotopic properties of sulfur compounds in hydrothermal processes. *Geochem. J.* **1968**, *2*, 29–49. [CrossRef]
84. Bachinski, D.J. Bond strength and sulfur isotope fractionation in coexisting sulfides. *Econ. Geol.* **1969**, *64*, 56–65. [CrossRef]
85. Hoefs, J. Isotope Fractionation Processes of Selected Elements. In *Stable Isotope Geochemistry*, 9th ed.; Springer Nature: Cham, Switzerland, 2021; pp. 1–528.
86. Xu, J.H.; He, Z.L.; Shen, S.L.; Yang, Z.L.; Du, J.F. Stable isotope geology of the Dongchuang and the Wenyu gold deposits and the source of ore-forming fluids and materials. *Contrib. Geol. Miner. Resour. Res.* **1993**, *8*, 87–100. (In Chinese)
87. Townley, B.K.; Godwin, C.I. Isotope characterization of lead in galena from ore deposits of the Aysen Region, southern Chile. *Miner. Depos.* **2001**, *36*, 45–57. [CrossRef]

88. Kamenov, G.; Macfarlane, A.W.; Riciputi, L. Sources of lead in the San Cristobal, Pulacayo, and Potosi mining districts, Bolivia, and a reevaluation of regional ore lead isotope provinces. *Econ. Geol.* **2002**, *97*, 573–592. [CrossRef]
89. Chiaradia, M.; Fontbote, L.; Paladines, A. Metal sources in mineral deposits and crustal rocks of Ecuador (1° N–4° S): A lead isotope synthesis. *Econ. Geol.* **2004**, *99*, 1085–1106.
90. Zhu, B.Q. Tri-dimension spacial topological diagrams of ore lead isotopes and their application to the division of geochemical provinces and mineralizations. *Geochimica* **1993**, *21*, 209–216. (In Chinese)
91. Williams-Jones, A.E.; Migdisov, A.A. Experimental constraints on the transport and deposition of metals in ore-forming hydrothermal Systems. In *Building Exploration Capability for the 21st Century*; Kelley, K.D., Golden, H.C., Eds.; Society of Economic Geologists, Inc.: Littleton, CO, USA, 2014; pp. 77–95.
92. Barnes, H.L. Solubilities of ore minerals. In *Geochemistry of Hydrothermal Ore Deposits*, 2nd ed.; Barnes, H.L., Ed.; J Wiley & Sons: New York, NY, USA, 1979; pp. 404–410.
93. Pirajno, F. *Hydrothermal Processes and Mineral Systems*; Springer Science & Business Media B.V.: Perth, Australia, 2009; pp. 1–1250.
94. Seward, T.M.; Williams-Jones, A.E.; Migdisov, A.A. The chemistry of metal transport and deposition by ore-forming hydrothermal fluids. In *Treatise on Geochemistry*; Heinrich Holland, H., Turekian, K., Eds.; Elsevier Ltd.: Amsterdam, The Netherlands, 2014; pp. 29–57.
95. Pearson, R.G. Hard and soft acids and their bases. *J. Am. Chem. Soc.* **1963**, *85*, 3533–3539. [CrossRef]
96. Yuan, S.D.; Williams-Jones, A.E.; Romer, R.L.; Zhao, P.L.; Mao, J.W. Protolith-related thermal controls on the decoupling of Sn and W in Sn–W metallogenic provinces: Insights from the Nanling region, China. *Econ. Geol.* **2019**, *114*, 1005–1012. [CrossRef]
97. Lehmann, B. Formation of tin ore deposits: A reassessment. *Lithos* **2021**, *402–403*, 105756. [CrossRef]
98. Heinrich, C.A. The chemistry of hydrothermal tin(–tungsten) ore deposition. *Econ. Geol.* **1990**, *85*, 457–481. [CrossRef]
99. Zhong, R.C.; Brugger, J.; Chen, Y.J.; Li, W.B. Contrasting regimes of Cu, Zn and Pb transport in ore-forming hydrothermal fluids. *Chem. Geol.* **2015**, *395*, 154–164. [CrossRef]
100. Stefansson, A.; Seward, T.M. Experimental determination of the stability and stoichiometry of sulphide complexes of silver (I) in hydrothermal solutions to 400 °C at 500 bar. *Geochim. Cosmochim. Acta* **2003**, *67*, 1395–1413. [CrossRef]
101. Wood, S.A.; Samson, I.M. The hydrothermal geochemistry of tungsten in granitoid environments: I. Relative solubilities of ferberite and scheelite as a function of T, P, pH, and m (NaCl). *Econ. Geol.* **2000**, *95*, 143–182. [CrossRef]
102. Korges, M.; Weis, P.; Lüders, V.; Laurent, O. Depressurization and boiling of a single magmatic fluid as a mechanism for tin–tungsten deposit formation. *Geology* **2017**, *46*, 75–78. [CrossRef]

Disclaimer/Publisher’s Note: The statements, opinions and data contained in all publications are solely those of the individual author(s) and contributor(s) and not of MDPI and/or the editor(s). MDPI and/or the editor(s) disclaim responsibility for any injury to people or property resulting from any ideas, methods, instructions or products referred to in the content.

Article

Origin of the Yinshan Pb-Zn-Ag Deposit in the Edong District Section of the Middle–Lower Yangtze River Metallogenic Belt: Insights from In-Situ Sulfur Isotopes

Dengfei Duan, Haobo Jia and Yue Wu *

Hubei Key Laboratory of Petroleum Geochemistry and Environment, Yangtze University, Wuhan 430100, China; cugddef@163.com (D.D.); 13474290126@163.com (H.J.)

* Correspondence: leadzinc@163.com

Abstract: The investigation into the enigmatic origin of Pb-Zn mineralization within the Middle-Lower Yangtze River Metallogenic Belt has long been marred by a paucity of prior studies. Seeking to alleviate this dearth of knowledge, our study meticulously scrutinizes the Yinshan Pb-Zn-Ag deposit nestled within the Edong district of the belt, endeavoring to cast an illuminating spotlight upon its enigmatic genesis. We identify two distinct epochs: (1) the pre-mineralization pyrite epoch (Epoch I) mainly characterized by colloform and massive pyrite, and (2) the hydrothermal mineralization epoch (Epoch II) which can be further divided into three stages: pyrite-arsenopyrite (stage 1), galena-sphalerite (stage 2), and vein pyrite (stage 3). We conduct in-situ sulfur isotope analyses on sulfide minerals from both epochs, revealing $\delta^{34}\text{S}$ values ranging from -0.5 to 4.8‰ for Epoch I and varying from 2.2 – 4.9‰ (stage 1), 1.1 – 3.0‰ , 4.2 – 7.1‰ (stage 2), and 2.1 – 3.8‰ (stage 3) for Epoch II. Integrating our sulfur isotope data with the geological characteristics of the deposit, we infer that Pb-Zn mineralization was related to a granite of ~ 130 Ma age. Additionally, our study suggests the possibility of coexisting Mo mineralization beneath the Pb-Zn mineralization. Our findings contribute to a better understanding of the origin of Pb-Zn mineralization in the Middle-Lower Yangtze River Metallogenic Belt.

Keywords: Yinshan deposit; Edong district; in-situ sulfur isotope; Pb-Zn mineralization

Citation: Duan, D.; Jia, H.; Wu, Y. Origin of the Yinshan Pb-Zn-Ag Deposit in the Edong District Section of the Middle–Lower Yangtze River Metallogenic Belt: Insights from In-Situ Sulfur Isotopes. *Minerals* **2023**, *13*, 810. <https://doi.org/10.3390/min13060810>

Academic Editor: Maria Boni

Received: 17 April 2023

Revised: 4 June 2023

Accepted: 7 June 2023

Published: 14 June 2023



Copyright: © 2023 by the authors. Licensee MDPI, Basel, Switzerland. This article is an open access article distributed under the terms and conditions of the Creative Commons Attribution (CC BY) license (<https://creativecommons.org/licenses/by/4.0/>).

1. Introduction

The Middle–Lower Yangtze River Valley metallogenic belt (MYRB) resides along the northern margin of the Yangtze craton, renowned for its porphyry–skarn–stratabound Cu–Au–Mo–Fe deposits in uplift areas and magnetite–apatite deposits within Cretaceous fault basins [1]. Despite some investigations into Pb-Zn mineralization within the region, it has received comparably less attention than Cu-Fe deposits [2–8]. Typically, Pb-Zn mineralization in skarn systems is observed at a distance from associated igneous rocks, with limited skarn minerals present due to the requisite lower temperatures for Pb-Zn sulfide mineral deposition [9]. Consequently, the occurrence of Pb-Zn mineralization serves as a valuable indicator for identifying deep-seated magmatic fluid mineralization [9]. Thus, comprehending the genesis of Pb-Zn mineralization assumes paramount importance in the pursuit of exploring Cu-Fe-Au-Mo deposits in the MYRB. Nonetheless, the origin of Pb-Zn deposits in the MYRB remains an issue subject to contention, with varying hypotheses proposed, including: (1) magmatic origin [2–5,7,8,10–20]; (2) Hercynian sedimentary sulfide minerals overprinted by Yanshanian magmatic hydrothermal fluid [21–25]; (3) basinal fluid origin [6]; or (4) organic fluid origin [26,27]. This state of uncertainty has hindered the exploration of Pb-Zn and other metals within the MYRB.

This study focuses specifically on the Yinshan Pb-Zn-Ag deposit, located within the westernmost Edong district of the MYRB. Previous investigations have posited diverse models, such as the sedimentary-exhalative (SedEx) model and sedimentary-reworked

model [28], as well as the epithermal model [10]. Through our examination of the Yinshan deposit, our objective is twofold: to enhance our understanding of its origin and to illuminate the genesis of Pb-Zn deposits within the broader MYRB. We do so by leveraging the potency of in-situ sulfur isotope analysis, a formidable tool for revealing the evolution of sulfur isotopes with high spatial resolution. Due to its small analysis size of 33 μm , this technique is capable of avoiding mixing compositions and providing detailed insights into the sulfur isotopic signatures of individual mineral phases [29]. We employ this technique in conjunction with geological evidence. In doing so, we unveil the magmatic origin of the Yinshan deposit, with some contribution from Hercynian sulfide minerals, albeit without exerting control over the system. Furthermore, our study advances the notion of potential Mo mineralization beneath the Pb-Zn mineralization, thereby underscoring the prospects for further exploration in this region.

2. Regional and Deposit Geology

The Yangtze Craton represents a distinct geological entity that exhibits notable distinctions from both the North China Craton and the Cathaysian block. It is spatially separated from these regions by the Dabie Ultrahigh Pressure (UHP) metamorphic belt to the north and a Neoproterozoic suture to the south [30]. Within the eastern part of the Yangtze Craton, three prominent faults traverse the landscape: the Xiangfan-Guangji fault (XGF) to the northwest, the Tangcheng-Lujiang regional strike-slip fault (TLF) to the northeast, and the Yangxin-Changzhou fault (YCF) to the south (Figure 1a). The Middle and Lower Yangtze River metallogenic belt, positioned between the North China Craton and the Yangtze Craton, encompasses various districts, including the Edong, Jiurui, Anqing, Luzong, Tongling, Ningwu, and Ningzhen districts, from west to east (Figure 1a). We specifically focus on the Edong district, which is demarcated by three major fault systems: the Tan-Lu, Xiangfan-Guangji, and Ma-Tuan faults (Figure 1b).

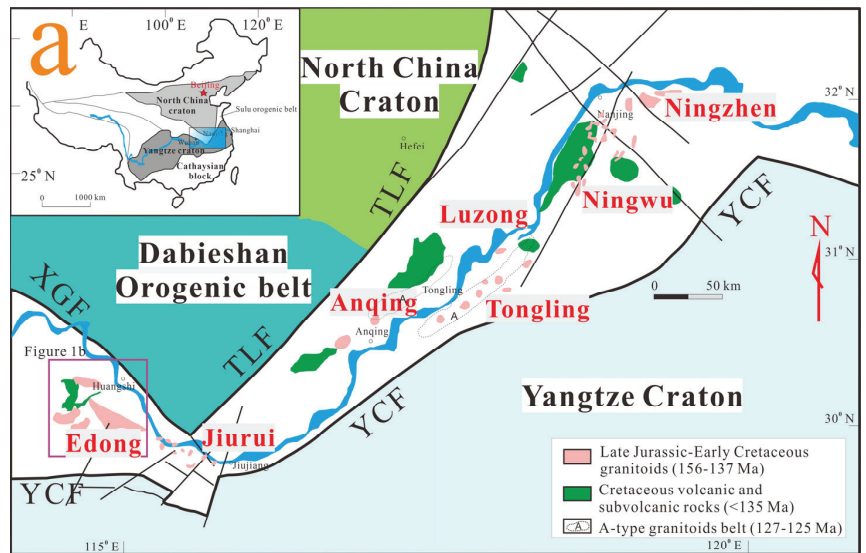


Figure 1. Cont.

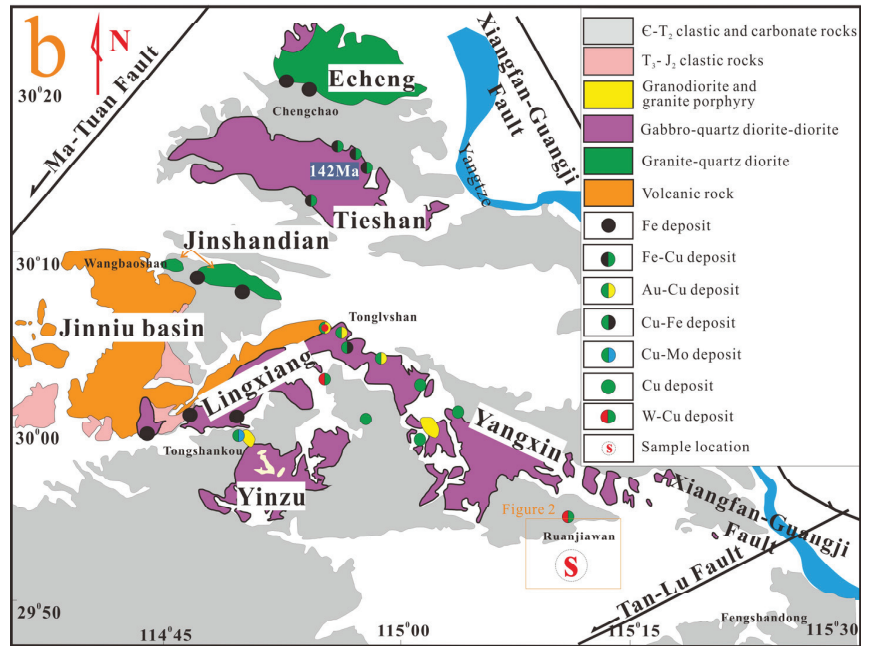


Figure 1. (a) Schematic illustration of the seven magmatic and metallogenic districts of the Middle and Lower Yangtze River metallogenic belt in the northeastern Yangtze Craton; (b) Granitoid batholiths in the Edong district. TLF-Tangcheng-Lujiang fault, XGF-Xiangfan-Guangji fault, YCF-Yangxin-Changzhou fault. Modified from Xie et al. (2011) [31].

Within the Edong district, the stratigraphic sequence primarily comprises a substantial accumulation of marine sedimentary rocks ranging from the Ordovician to the middle Triassic and exhibiting a thickness exceeding 10 km. Subsequently, continental deposits and Cretaceous volcanic assemblages, spanning the late Triassic to the Cenozoic period, follow this sequence (Figure 1b) [30,32]. The collision between the Yangtze and North China cratons during the middle Triassic period resulted in the folding of pre-Triassic strata within the Edong district [33]. Magmatic events within the Edong district can be classified into two distinct stages. The initial plutonic stage, occurring between 157–132 million years ago (Ma), emplaced the Echeng, Tieshan, Jinshandian, Lingxiang, Yinzu and Yangxin batholiths, alongside numerous smaller intrusions (Figure 1b) [34,35]. It is worth noting that the plutonic rocks can be classified into two categories: one exhibiting elevated Sr/Y and La/Yb ratios, devoid of significant Eu anomalies predating 136 Ma, and the other characterized by diminished Sr/Y and La/Yb ratios, accompanied by a conspicuously negative Eu anomaly ranging from 133 to 127 Ma [36]. The former category is thought to be associated with Cu-Fe mineralization, while the latter is related to Fe mineralization with a more substantial contribution of crust materials [37]. During the subsequent volcanic stage, which erupted between 130–125 Ma [31], over 2 km of volcanic and related sedimentary rocks were deposited, including the Majiashan Formation, the Lingxiang Formation, and the Dasi Formation (in order from the base to the top). For a more detailed lithology description, refer to *Regional Geology of the Hubei Province* [33].

The Yinshan Pb-Zn-Ag deposit (115°10'11"–115°11'19", 29°54'29"–29°53'58"), located in the southern region of the Edong district, lies within the MYRB (Figure 1b). The deposit is mainly comprised of Pb and Zn mineralization, in addition to Ag, Au, Cd, Fe and Mn, with 95 kt Pb @ 2.0%; 262 kt Zn @ 5.6%; 501.7 t Ag @ 107 g/t; 2 t Au @ 0.43 g/t; 1.2 kt Cd @ 261 ppm. It is situated on the south side of the east part of the Huanggushan-Xiniushan overturned anticline, and the ore body primarily occurs within the northwest interlayer

fracture zone located within the northern side of the Xiaojiawan-Xingjiawan syncline, as shown in Figure 2. The outcrop rocks in the orefield primarily consist of the lower Permian, middle Carboniferous, and middle Silurian strata, with the Devonian and Ordovician strata absent due to tectonic activity. The Silurian strata is primarily comprised of shale and sandstone (Fentou group, S_1f). The upper part of Carboniferous strata (Huanglong Group, C_2h) consists of limestone that gradually evolves into dolomite, which was subsequently deformed into breccia and is considered an ideal place for mineralization. The Permian strata is composed of the Qixia Group (P_1q) of carbonaceous limestone and quartz sandstone, and the Maokou Group (P_1m) of limestone. The granite porphyry is common but is primarily found in dykes (Figure 3). Chemical analyses show that the granite porphyry dykes have $>0.2\%$ Pb + Zn content near the ore body, but only ~ 150 ppm Pb and 200 ppm Zn far from the ore body (Edong Geological Survey, 1995).

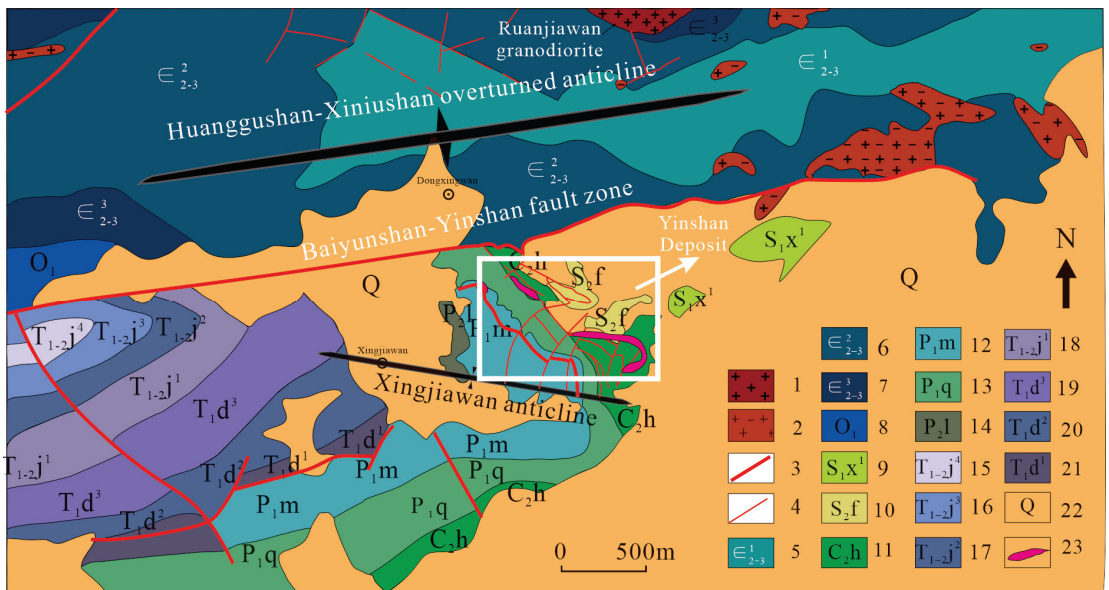


Figure 2. Schematic regional geological map of the Yinshan Pb-Zn-Ag deposit (modified from [10]). 1—Granodiorite; 2—Granodiorite porphyry; 3—main fault; 4—secondary fault; 5—1st member of the middle to upper Cambrian strata; 6—2nd member of the middle to upper Cambrian strata; 7—3rd member of the middle to upper Cambrian strata; 8—lower Ordovician strata; 9—Xintan Group of lower Silurian strata; 10—Fentou Group of middle Silurian strata; 11—Huanglong Group of middle Carboniferous strata; 12—Maokou Group of the lower Permian strata; 13—Qixia Group of the lower Permian strata; 14—Longtan Group of the middle Permian strata; 15—4th member of the Jialingjiang Group in the lower Triassic strata; 16—3rd member of the Jialingjiang Group in the lower Triassic strata; 17—2nd member of the Jialingjiang Group in the lower Triassic strata; 18—1st member of the Jialingjiang Group in the lower Triassic strata; 19—3rd member of the Daye Group in the lower Triassic strata; 20—2nd member of the Daye Group in the lower Triassic strata; 21—1st member of the Daye Group in the lower Triassic strata; 22—Quaternary strata; 23—Pb-Zn-Ag ore body.

The Yinshan deposit is comprised of five ore bodies, with the first ore body being the largest. The first ore body is located within the interlayer fracture zone between the Huanglong Group (C_2h) and the Fentou Group (S_1f), bound by F_1 and F_2 (Figure 4). As a result of post-mineralization tectonic activity, the ore body was uplifted and oxidized. This study specifically focuses on the sulfide minerals.

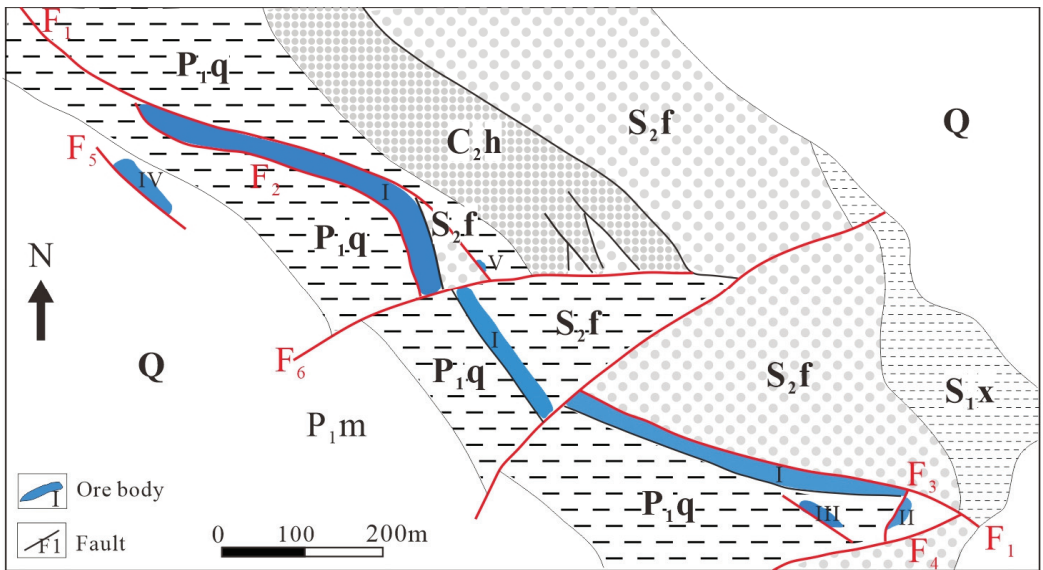


Figure 3. Geological map of the Yinshan Pb-Zn-Ag deposit (modified from Yan (2013) [10]). The abbreviation of the strata is the same as in Figure 2.

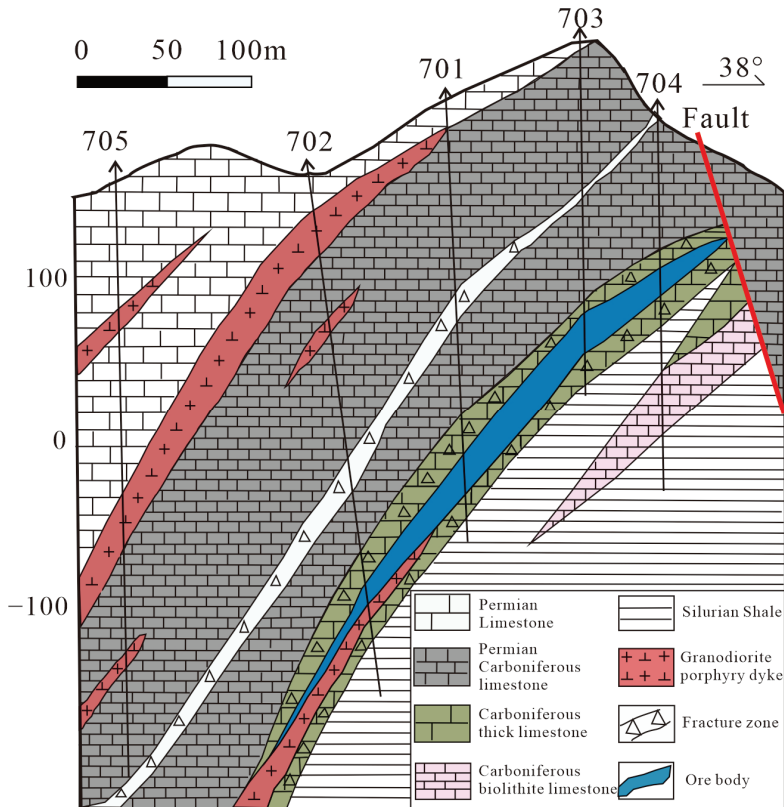


Figure 4. Geological map of Yinshan Pb-Zn-Ag deposit (modified from Yan (2013) [10]).

The sulfide mineralization at the Yinshan Pb-Zn-Ag deposit can be divided into two epochs: the pre-mineralization pyrite epoch and the hydrothermal mineralization epoch. The former primarily consists of colloform and massive pyrite, accompanied by minor marcasite (Figure 5a). Colloform pyrite exhibits varying amounts of non-sulfide minerals, displaying either a dirty or clean surface in polished thin sections (Figure 5b,c). These non-sulfide minerals may comprise detrital and authigenic minerals, including quartz, illite, dolomite and organic matter. Colloform pyrite has undergone replacement by massive pyrite, and both have been subsequently replaced by marcasite (Figure 5d,f). The sulfide minerals from the pre-mineralization epoch have undergone deformation, forming breccia and being cemented by sulfide minerals and gangue minerals from the hydrothermal epoch (Figure 5c,e,f). The hydrothermal mineralization epoch can be further divided into three stages: (1) The pyrite-arsenopyrite stage, characterized by the replacement of colloform and massive pyrite by euhedral pyrite and arsenopyrite along fractures; (2) The galena-sphalerite stage, in which galena and sphalerite formed in relatively open spaces compared to the pyrite-arsenopyrite stage, serving primarily as cement within the breccia. Polished sections reveal the progression of euhedral pyrite and arsenopyrite being replaced by galena, followed by subsequent replacement of galena by sphalerite (Figure 5g); (3) The vein pyrite stage, where straight pyrite veins cut across all preceding minerals (Figure 5h), exhibiting distinct and straight boundaries (Figure 5i).

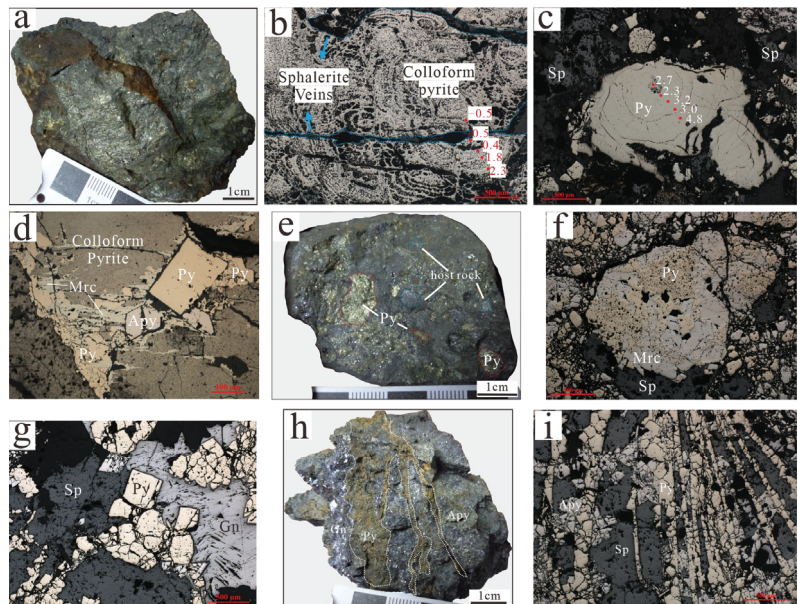


Figure 5. (a) Colloform and massive pyrite ores; Reflected light photomicrographs shown that (b) Colloform pyrite containing non-sulfide minerals was cut by sphalerite veins; (c) Colloform pyrite with little non-sulfide minerals was replaced by sphalerite; (d) Colloform pyrite was replaced by massive pyrite, and they were both replaced by marcasite. Euhedral pyrite and arsenopyrite veins cut all the above minerals; (e) Hand specimen of breccia ores, with massive pyrite and host rock as breccia, and cemented by hydrothermal minerals, such as sphalerite, galena, and so on; Reflected light photomicrographs show that (f) the massive pyrite breccia were replaced by marcasite, and cemented by sphalerite; (g) The euhedral pyrite was replaced by galena and then sphalerite; (h) The hand specimen of the pyrite vein cut the early sulfide minerals, such as galena and arsenopyrite; (i) The pyrite vein cut through arsenopyrite and sphalerite in reflected light photomicrographs. The read scale bars represent 500 μm in (b,c,f,g,i) and 100 μm in (d). *Apy*—Arsenopyrite, *Gn*—Galena, *Mrc*—Marcasite, *Py*—Pyrite, *Sp*—Sphalerite.

Figure 6 provides a summary of the metallogenic epochs and stage, incorporating findings from previous studies. The mineralogy of the supergene epochs were referenced from Yan (2013) [10].

Stages Mineral	Pre-mineralization epoch		Hydrothermal mineralization epoch			Supergene epoch
	Stage 1	Stage 2	Stage 1	Stage 2	Stage 3	
			Pyrite + Arsenopyrite	Galena + Sphalerite	Vein Pyrite	
Colloform pyrite	█					
Massive pyrite	█					
Marcasite		█				
Pyrite			█			
Arsenopyrite			█			
Galena				█		
Sphalerite				█		
Psilomelane						█
Pyrolusite						█
Hematite						█
Goethite						█
limonite						█
Cerussite						█
Native silver						█
Mimetite						█
Malachite						█

Figure 6. Mineral paragenesis for the Yinshan Pb-Zn-Ag deposit.

3. Samples and Analytical Methods

To conduct the in-situ sulfur isotope study, we collected samples from different epochs and selected sulfide minerals from various stages for analysis. The selected samples with the least oxidation were divided into polished sections (~200 μm). Through detailed microscopic examination, sulfide minerals representing different stages were chosen for in-situ sulfur isotope analysis.

The sulfur isotope analysis was performed using in-situ methods at the State Key Laboratory of Geological Processes and Mineral Resources (GPMR, China University of Geosciences, Wuhan, China). The Nu Plasma II MC-ICP-MS was employed, equipped with a Resonetics-S155 excimer ArF laser ablation system. The laser beam had a diameter of 33 μm and operated at a repetition rate of 10 Hz, with each ablation process lasting 40 s. To determine the δ³⁴S values, we employed the standard-sample bracketing (SSB) technique throughout the MC-ICP-MS analytical sessions [38]. Instrumental mass bias correction was carried out by linearly interpolating the biases calculated from two adjacent standard analyses, enabling accurate calculation of the true sulfur isotope values. The isotope data are reported in delta notation (‰) relative to Vienna Cañon Diablo Troilite (V-CDT):

$$\delta^{34}\text{S}_{\text{V-CDT}} = [((^{34}\text{S}/^{32}\text{S})_{\text{sample}} / (^{34}\text{S}/^{32}\text{S})_{\text{V-CDT}}) - 1] \times 10^3$$

where (³⁴S/³²S)_{sample} is the measured ³⁴S/³²S ratio in the sample and (³⁴S/³²S)_{V-CDT} is defined as 0.044163 [39]. The analytical precision (2σ) was estimated to be ±0.2 per mil.

The laboratory’s internal standards were calibrated using international standards, including a sphalerite standard (NBS-123) and two pyrite standards (WS-1 and WS-2). NBS-123 served as the reference standard for sphalerite and yielded a δ³⁴S value of +17.1 ± 0.1 ‰. WS-1 and WS-2 were natural pyrite samples collected from the Wenshan polymetallic skarn deposit in Yunnan Province, China. WS-1 was utilized as the reference standard for pyrite, galena, marcasite and arsenopyrite, while WS-2 served as the monitor standard. The δ³⁴S values for WS-1 and WS-2 were determined at GPMR, China University of Geosciences, and were found to be +0.9‰ and +2.0‰, respectively.

4. Results

The detailed sulfur isotope data are shown in Table 1 and Figure 7.

Table 1. The in-situ sulfur isotope data of sulfide minerals in Yinshan Pb-Zn-Ag deposit.

Epoch	Stage	Sulfide Mineral	$\delta^{34}\text{S}$ Value (‰)	Comment
The pre-mineralization pyrite	Colloform pyrite	Pyrite	−0.5	Grain 1, spot 1
		Pyrite	0.5	Grain 1, spot 2
		Pyrite	−0.4	Grain 1, spot 3
		Pyrite	1.8	Grain 1, spot 4
		Pyrite	2.3	Grain 1, spot 5
		Pyrite	2.7	Grain 2, spot 1
		Pyrite	2.3	Grain 2, spot 2
		Pyrite	3.2	Grain 2, spot 3
		Pyrite	3.0	Grain 2, spot 4
		Pyrite	4.8	Grain 2, spot 5
	Massive pyrite	Pyrite	1.0	
		Pyrite	1.8	
		Pyrite	2.2	
		Pyrite	2.2	
		Pyrite	2.5	
		Pyrite	2.5	
		Pyrite	2.6	
		Pyrite	2.7	
		Pyrite	2.9	
		Pyrite	3.0	
Marcasite	Pyrite	3.0		
	Pyrite	3.0		
	Pyrite	3.0		
	Pyrite	3.1		
	Pyrite	3.1		
	Pyrite	3.3		
	Pyrite	3.4		
	Pyrite	3.6		
	Pyrite	3.7		
	Pyrite	3.7		
The hydrothermal mineralization	The euhedral pyrite and arsenopyrite	Marcasite	1.9	
		Marcasite	2.5	
		Marcasite	3.1	
		Marcasite	3.6	
		Arsenopyrite	2.2	
		Arsenopyrite	2.4	
		Arsenopyrite	2.6	
		Arsenopyrite	4.8	
		Arsenopyrite	6.3	
		Arsenopyrite	3.1	
		Arsenopyrite	3.5	
		Arsenopyrite	2.7	
		Arsenopyrite	3.4	
		Arsenopyrite	4.3	
		Arsenopyrite	3.7	
	Arsenopyrite	4.2		
	Arsenopyrite	3.5		
	Arsenopyrite	4.5		
	Arsenopyrite	4.5		
	Arsenopyrite	4.9		
	Arsenopyrite	4.2		
	Arsenopyrite	4.2		
	Pyrite	3.7		
	Pyrite	3.3		
	Pyrite	2.7		
Pyrite	3.1			
Pyrite	2.6			

Table 1. Cont.

Epoch	Stage	Sulfide Mineral	$\delta^{34}\text{S}$ Value (‰)	Comment
		Sphalerite	4.5	
		Sphalerite	4.4	
		Sphalerite	5.2	
		Sphalerite	4.7	
		Sphalerite	4.2	
		Sphalerite	4.8	
		Sphalerite	6.5	
		Sphalerite	6.5	
		Sphalerite	6.2	
		Sphalerite	4.4	
		Sphalerite	4.6	
		Sphalerite	4.3	
		Sphalerite	2.9	
	The Galena-Sphalerite	Sphalerite	4.5	
		Sphalerite	4.4	
		Galena	3.0	
		Galena	4.6	
		Galena	7.1	
		Galena	5.7	
		Galena	5.9	
		Galena	5.0	
		Galena	5.4	
		Galena	2.6	
		Galena	2.0	
		Galena	2.5	
		Galena	2.6	
		Galena	2.0	
	Galena	1.1		
	The vein pyrite	Pyrite	2.1	
		Pyrite	2.1	
		Pyrite	2.4	
		Pyrite	3.2	
		Pyrite	3.4	
		Pyrite	3.8	

Regarding the pre-mineralization sulfide minerals, it is noteworthy that the colloform pyrite exhibits a gradual increase in $\delta^{34}\text{S}$ values towards the edge of the grain, with values ranging from -0.5 to 2.3 ‰ and 2.7 to 4.8 ‰, respectively. Similarly, the massive pyrite shows a narrow range of $\delta^{34}\text{S}$ values, ranging from 1.0 to 3.7 ‰, with the majority falling between 2.5 and 3.7 ‰. The marcasite also displays similar $\delta^{34}\text{S}$ values, ranging from 1.9 to 3.6 ‰ (Figure 7a). In contrast, the hydrothermal sulfide minerals exhibit larger variations in $\delta^{34}\text{S}$ values compared to the pre-mineralization sulfide minerals (Figure 7). The $\delta^{34}\text{S}$ values of the euhedral pyrite-arsenopyrite stage range from 2.2 to 4.9 ‰, with one exception of 6.3 ‰ (Figure 7b). The $\delta^{34}\text{S}$ values of the galena-sphalerite stage exhibit a bimodal distribution, with a range of 1.1 – 3.0 ‰ and 4.2 – 7.1 ‰, respectively (Figure 7c). Finally, the vein pyrite stage displays the lowest $\delta^{34}\text{S}$ values, ranging from 2.1 to 3.8 ‰ (Figure 7d).

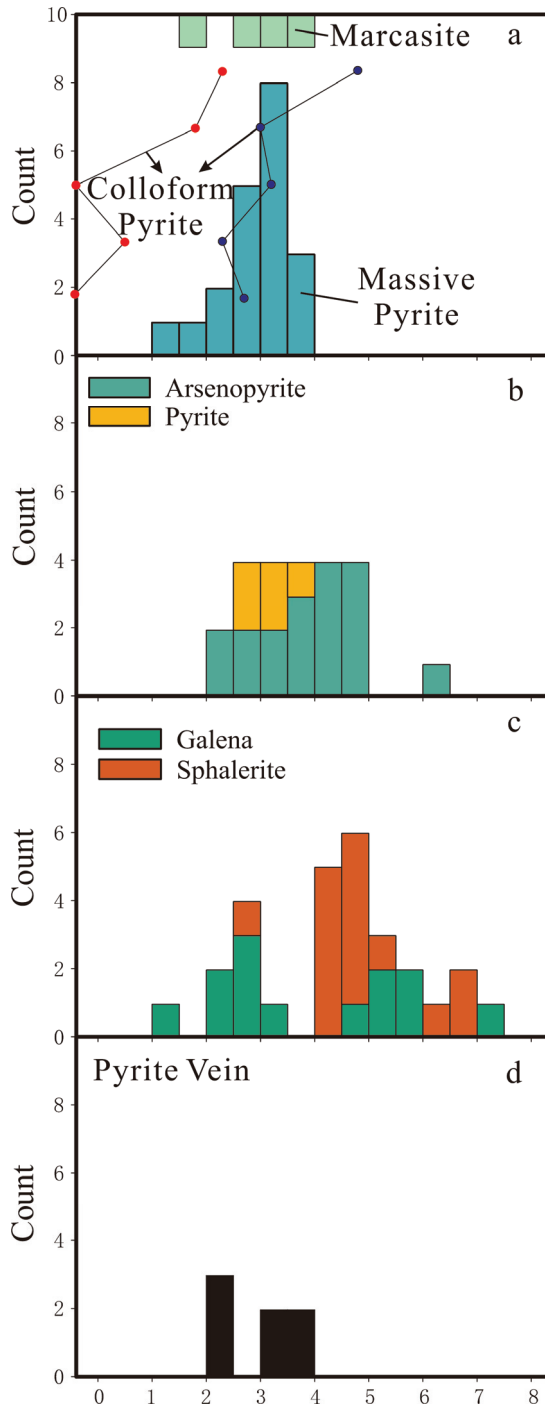


Figure 7. Histograms of sulfur isotopes for sulfide minerals from different epochs and stages. (a) The pre-mineralization pyrite epoch, followed by (b) the pyrite-arsenopyrite stage, (c) the galena-sphalerite stage, and (d) the vein pyrite stage during the hydrothermal mineralization epoch.

5. Discussion

5.1. Source of Sulfur

The $\delta^{34}\text{S}$ values of both colloform and massive pyrite in this study range from -0.5 to 4.8‰ (Figure 7a), which is similar to the observations in the Qixiashan Pb-Zn-Ag polymetallic deposit [24]. The presence of detrital and authigenic minerals, such as quartz, illite, dolomite and organic matter in colloform pyrite ores suggests their formation under euxinic marine sedimentary conditions during the Hercynian period [40].

During the hydrothermal epoch, the narrow range of sulfur isotope values at all stages suggests an equilibrium between sulfide minerals and the hydrothermal fluid. The absence of sulfate minerals indicates that the sulfur in the hydrothermal fluid was mainly in the form H_nS^{n-2} [41–43]. The sulfur isotope composition of sulfide minerals can represent the composition of the hydrothermal fluid [44,45]. Within the same stage, paired sulfide minerals were analyzed, but the equilibrium composition was not determined. Euhedral pyrite and arsenopyrite represent the initial sulfide mineral precipitation during mineralization, followed by the formation of breccia during the transition to the galena-sphalerite stage, which coincided with fluid boiling. The alternating characteristics of Hercynian sulfide minerals are limited in extent and distribution, and there is no significant deposition of sulfide minerals after the pyrite-arsenopyrite stage. This suggests the Hercynian sulfide minerals contribute minor amounts of sulfur, insufficient to precipitate significant sulfur minerals. Although organic matter may also provide some reduced sulfur during alternation [44], the significantly lower abundance compared to sulfide minerals diminishes its importance in the process of mineral precipitation. Despite significant overlap, the sulfur isotope values of pyrite and arsenopyrite (stage 1) are relatively higher than those of Hercynian sulfide minerals (Figure 7a,b). The decrease in sulfur isotope values (Figure 7b) could be attributed to both the assimilation of Hercynian sulfur and Rayleigh fractionation of pyrite and arsenopyrite, but properly evaluating the relative importance of these factors is challenging.

During the galena and sphalerite stage, the boiling of hydrothermal fluids resulted in the degassing of H_2 and H_2S , thereby increasing the $f\text{O}_2$ and decreasing the $f\text{S}_2$ in the residual liquid [46]. This process efficiently fractionated elements due to the segregation of vapor and liquid phases. The $\delta^{34}\text{H}_2\text{S}$ composition of the fluid (and coexisting vapor) likely decreased due to the preferential oxidation of H_2^{34}S during boiling [46,47]. As a result, some sphalerite and galena exhibit lower sulfur isotope values [48,49] compared to the euhedral pyrite-arsenopyrite stage (Figure 7b,c). During the crystallization of sphalerite and galena, the $\delta^{34}\text{S}$ values increased, likely due to Rayleigh fractionation of galena, which preferentially incorporates lighter ^{32}S [43], or due to the assimilation of sulfur from massive pyrite. Galena formed relatively earlier than sphalerite, consistent with Rayleigh fractionation. Both pyrite and sphalerite prefer heavier ^{34}S than H_2S , but pyrite has a higher preference [43]. The decrease in $\delta^{34}\text{S}$ values from the galena-sphalerite stage to the vein pyrite stage may be attributed to the Rayleigh fractionation of sphalerite, which removes the heavier ^{34}S .

The $\delta^{34}\text{S}$ values exhibit variation among different geological reservoirs: (1) meteorites typically show values near 0‰ , (2) igneous rocks range from -2‰ to 8‰ , (3) modern and ancient biogenic pyrite display values between -20‰ and $+20\text{‰}$ [43], and (4) anhydrite in MYRB demonstrates values from $+21.1\text{‰}$ to $+34.4\text{‰}$ [50–52]. The $\delta^{34}\text{S}$ value of the ore-forming fluid is estimated to be around $0\text{--}5\text{‰}$, indicating a likely origin from magma, as magmatic sulfur shares similar $\delta^{34}\text{S}$ values. This finding aligns with the conclusions drawn from trace element data of sulfide minerals [10]. However, it is plausible that sulfide minerals formed during the Hercynian period also made some contribution.

5.2. Contribution of Colloform and Massive Pyrite to Mineralization

In the Yangtze River Metallogenic belt, it is expected that Pb-Zn-Ag deposits in the other districts share similar metallogenic processes with the Yinshan deposit [2,3,5,6,11–19,21–25]. Comparisons to other deposits can provide insights into the controlling factors influencing Pb-Zn mineralization. Overprinting of Hercynian

stratabound sulfides is only reported in the Baiyangfan Pb-Zn-Ag deposit in the Jiurui district [21,22] and the Qixiashan Pb-Zn-Ag deposit in Ningzhen district [23–25]. However, in most other deposits, Pb-Zn ore bodies typically develop in weak zones of the host rock, such as the interlayer fracture zone between clastic and carbonate rocks, as observed in the Huangshanling Pb-Zn-Ag-Mo deposit in Anqing-Guichi district [11–13], the Qixiashan Pb-Zn deposit in the Ningzhen district [23–25], or in volcanic sedimentary rock, as seen in the Yueshan Ag-Pb-Zn deposit [14,16,17]. Another example of this development can be found in fault zones, as seen in the Hehuashan Pb-Zn deposit [6]. The absence of a preference for a specific stratum indicates that the alternation of Hercynian stratabound sulfide, i.e., colloform and massive pyrite, may contribute in part to the ore-forming element and promote the precipitation of sulfide minerals, but these sulfide materials are not the decisive factor. In fact, the ore bodies of the Yinshan Pb-Zn-Ag deposit are also located at the interface of Carbonaceous clastic rock and Carbonaceous-Permian carbonate rock, where the interlayer fracture zone is an ideal site for Pb-Zn mineralization due to the discrepancy in lithology. Sphalerite and galena crystallize following fluid boiling, rather than during the initial alternation of colloform and massive pyrite. This suggests that the alternation of colloform and massive pyrite does not play a prominent role in controlling mineralization.

5.3. Possible Parental Magma of Pb-Zn Mineralization in Yinshan Deposit

The previous understanding of the Yinshan Pb-Zn deposit suggested it was a distal skarn Pb-Zn associated with the Ruanjiawan Cu-W skarn deposit [10]. However, recent in-situ sulfur studies conducted for the Ruanjiawan Cu-W skarn deposit have revealed an increase in sulfur isotopes from ~0‰ to ~15‰ towards the host rock, suggesting the assimilation of evaporite [53]. If the Ruanjiawan intrusion were the parent rock of the Yinshan deposit, its sulfur isotope signature would be significantly higher than what was observed in this study. Additionally, the granodiorite porphyry in the orefield has undergone alteration by Pb-Zn hydrothermal fluids, as evidenced by the higher Pb and Zn content (>0.2% Pb + Zn) in dykes closer to the ore body, eliminating the possibility of it being the parental magma source. Therefore, it is reasonable to assume the presence of a hidden magma body beneath the Yinshan deposit.

Although no absolute radiogenic age was determined in this study, the relative rock- and ore-forming age can be inferred based on geological evidence. The inference relies on the understanding that the rocks and minerals with different origins or closure temperatures can record geological processes of different ages. The Ruanjiawan granodiorite and Xiniushan granodiorite porphyry, located north of the Yinshan deposit (Figure 3), have zircon U-Pb ages of 143 ± 1 Ma and 147 ± 1 Ma, respectively [54]. Since the granodiorite porphyry dykes in the Yinshan orefield resemble the Ruanjiawan and Xiniushan magmatic rocks, it is likely that the mineralization age of the Yinshan deposit is later than 147 Ma. Notably, the titanite in the Ruanjiawan granodiorite measures a U-Pb age of 132 ± 1 Ma, which is more than 10 Ma later than the zircon U-Pb age and titanite U-Pb age in the skarn (142 ± 2 Ma). This age difference suggests a thermal overprinting event associated with diabase dyke emplacement (Zircon U-Pb age of 133 ± 1 Ma) [55]. Therefore, magmatic activity around ~133 Ma is present in the Ruanjiawan-Yinshan area. However, since there is no exposed felsic magma body in the Yinshan deposit at ~133 Ma, the parental magma characteristics can only be evaluated by comparing them with the Pb-Zn deposit in the MYRB, assuming that all of these Pb-Zn deposits share a similar origin.

Isotopic and trace element studies conducted on sulfide minerals in other Pb-Zn deposits within the MYRB consistently indicate a significant contribution from magmatic fluid [2,3,5–8,11–17,19,21–25]. The Huangshanling and Yaojialing deposits, with well-exposed ore bodies and magmatic rocks, serve as ideal examples for examining the parental magma of Pb-Zn mineralization. The Huangshanling Pb-Zn-Ag-Mo deposit in the Anqing-Guichi district shares geological characteristics with the Yinshan deposit. Quartz diorite porphyry dykes were found at shallow depths replacing skarn minerals [12], while deeper granite porphyries with A-type granite characters were also discovered. The diorite por-

phyry dykes exhibit zircon U-Pb ages of 144 ± 1.4 Ma [12] or 137 ± 1.5 Ma [13], whereas the granite porphyry has a zircon U-Pb age over 10 million years younger, at 125 ± 1.2 Ma. The molybdenite Re-Os age of 127.5 Ma suggests a relationship between mineralization and the deep granite porphyry [11]. Pb-Zn-Ag mineralization develops in the shallow interlay fracture zone between clastic and carbonate rocks [12,13], while Mo mineralization takes place at greater depths near the granite porphyry.

In the Yaojialing deposit, the Pb-Zn ore body is closely situated to granodiorite porphyry, similar to the formation of Cu-Au mineralization [2,3,5,7,8]. Previous studies have proposed a connection between Pb-Zn mineralization and granodiorite porphyry based on the similarity of granite zircon U-Pb ages (~ 141 Ma [2,7,8]) and molybdenite Re-Os ages (~ 142 Ma [2,5]) in the Yaojialing Pb-Zn deposit. However, this conclusion assumes that Pb-Zn and Cu-Au mineralization occurred simultaneously. The proximity of the Pb-Zn ore body to the parental magmatic rock only occurs when the granite exhibits a high concentration of F, which lowers the solidus temperature of magma, resulting in the formation of low-temperature hydrothermal fluid. These fluids need to have a sufficiently low temperature for Pb-Zn to exhibit low solubility and precipitate, as observed in the Empire Cu-Zn Mine in Idaho [56,57]. However, the granodiorite porphyry in Yaojialing does not display elevated F levels, and it is evident that numerous Pb-Zn veins cut through the granodiorite rock [3]. Therefore, it is likely that the Pb-Zn mineralization in Yaojialing is associated with a later magmatic-hydrothermal event. Furthermore, in addition to the ~ 141 Ma granodiorite, late-stage granodiorite porphyry dykes with an age of 130.3 ± 1.5 Ma have also been reported [4], resembling the situation in the Huangshanling Pb-Zn-Ag-Mo deposit. The Pb-Zn mineralization in Yaojialing may be related to the ~ 130 Ma magmatism.

Based on the aforementioned findings, it can be inferred that the Pb-Zn (Ag) deposit in the Yangtze River Metallogenic belt is associated with a magmatic event that took place approximately 133 Ma ago.

5.4. Ore Genesis and Its Implications for Exploration Strategies

Based on the preceding discussion, we propose a revised model for the ore genesis of the Yinshan Pb-Zn-Ag deposit. Our model suggests that the mineralization can be divided into two distinct stages: the sedimentary stage and the hydrothermal stage, each characterized by different processes. During the Hercynian period, colloform and massive pyrite formed in the sedimentary stage [40]. In the early Cretaceous period, a granite intrusion was emplaced at a deep level, around 130 Ma. This intrusion released ore-forming fluid, leading to the formation of Mo mineralization in close proximity to the magma rock. These hydrothermal fluids, originating from the deep magma, were likely enriched in oxidized sulfur species, primarily composed of SO_2 . However, during retrograde alteration, magnetite formation occurred, reducing the fluid's oxygen fugacity ($f\text{O}_2$) and transforming SO_2 into H_2S . This process provided the necessary reduced level of sulfur for Mo mineralization. As Mo has a higher depositional temperature compared to Pb-Zn, the fluid still retained significant concentrations of Pb-Zn after Mo mineralization. As the remaining hydrothermal fluid ascended and reached the interface between carbonate and shale rocks, boiling of the fluid occurred, resulting in its cooling. This decrease in temperature led to a significant drop in the solubility of Pb-Zn, causing the precipitation of galena and sphalerite. It is important to note that the alternation of colloform and massive pyrite may contribute to the content of reduced sulfur in the fluid and promote the crystallization of sphalerite and galena.

The genetic relationship between distal epithermal Pb-Zn mineralization and proximal Mo or other mineralization is widely recognized in other deposits [58–62]. Pb-Zn mineralization can serve as a useful indicator for the presence of proximal mineralization. In the case of the Yinshan deposit, the occurrence of shallow Pb-Zn-Ag mineralization suggests the potential presence of deeper Mo mineralization. However, the exploration target for deep Mo mineralization has been narrowed down by the surface occurrence of

Pb-Zn mineralization. Geophysical prospecting techniques, therefore, play a crucial role in identifying hidden magmatic rocks and expanding exploration targets.

6. Conclusions

After a thorough analysis of the Yinshan Pb-Zn-Ag deposit, we have concluded that the sulfide isotope composition of the deposit indicates a magmatic origin. Furthermore, the geological features suggest that the mineralization is associated with a ~130 Ma granite. Although the colloform and massive pyrite formed during the Hercynian period, they may still have contributed to the mineralization and are not the primary controlling factors. Our findings suggest that there is likely Mo mineralization at a deeper level, which is consistent with the presence of Pb-Zn mineralization in the Yangtze River Metallogenic belt. Overall, our research provides valuable insights into the mineralization process of the Yinshan Pb-Zn-Ag deposit and sheds light on the potential for further exploration of Mo mineralization in the area.

Author Contributions: Writing—original draft preparation, D.D., H.J. and Y.W.; writing—review and editing, D.D., H.J. and Y.W. All authors have read and agreed to the published version of the manuscript.

Funding: This research was funded by the National Natural Science Foundation of China, grant number 42172088 and 42203065 and Natural Science Foundation of Hubei Province, grant number 2019CFB586.

Data Availability Statement: The data presented in this study are available within the article.

Acknowledgments: We thank the editor and reviewers for their constructive comments which helped in improving our paper.

Conflicts of Interest: The authors declare no conflict of interest.

References

- Mao, J.; Xie, G.; Duan, C.; Pirajno, F.; Ishiyama, D.; Chen, Y. A Tectono-Genetic Model for Porphyry–Skarn–Stratabound Cu–Au–Mo–Fe and Magnetite–Apatite Deposits along the Middle–Lower Yangtze River Valley, Eastern China. *Ore Geol. Rev.* **2011**, *43*, 294–314. [CrossRef]
- Zhong, G.X.; Zhou, T.F.; Yuan, F.; Jiang, Q.S.; Fan, Y.; Zhang, D.Y.; Huang, J.M. LA-ICPMS U–Pb Zircon Age and Molybdenite Re–Os Dating of Yaojialing Large Zinc–Gold Polymetallic Deposits, Tongling, Anhui Province, China. *Acta Petrol. Sin.* **2014**, *30*, 1075–1086. (In Chinese)
- Liu, S.F. The Metallogenesis Research of Yaojialing Zn–Au Polymetallic Deposit in Tongling, Anhui Province. Ph.D. Thesis, China University of Geosciences (Beijing), Beijing, China, 2012. (In Chinese).
- Liu, Z. The Petrogenesis and Metallogenesis of the Yaojialing Polymetallic Zn–Au Deposit in Tongling City, Anhui Province. Master’s Thesis, Hefei University of Technology, Hefei, China, 2016. (In Chinese).
- Yin, Y.D.; Hong, T.Q.; Jia, Z.H.; Zhao, H.; Li, C.; Luo, L.; Huang, J.M. The Re–Os Age of Molybdenite and Ore-Forming Material Source from the Yaojialing Zn–Au Polymetallic Deposit, Tongling. *Geol. Rev.* **2016**, *62*, 248–256. (In Chinese)
- Liu, G.X.; Yuan, F.; Deng, Y.F. The sphalerite trace element and ore forming fluid character of Hehuashan Pb–Zn deposit, Tongling district, Anhui province. In Proceedings of the ninth National Symposium on Metallogenic Theory and Prospecting Methods, Nanjing, China, 13–16 December 2019; pp. 27–28. (In Chinese).
- Liu, S.F.; Du, Y.S.; Fu, S.X.; Zhong, H.; Cao, Y. U–Pb Age and Hf Isotopic Characteristics of Zircons from Granodiorite Porphyry in the Yaojialing Zn–Au Polymetallic Mine, Anhui Province and Their Geological Significance. *Earth Sci.–J. China Univ. Geosci.* **2013**, *38*, 91–102. (In Chinese)
- Liu, J.M.; Yan, J.; Li, Q.Z.; Song, C.Z.; Liu, X.Q.; Xie, J.C. Zircon Dating and Petrogenesis of the Yaojialing Intrusion in Tongling Area. *Chin. J. Geol.* **2014**, *49*, 494–512. (In Chinese)
- Meinert, L.D.; Dipple, G.M.; Nicolescu, S. World Skarn Deposits. In *One Hundredth Anniversary Volume*; Hedenquist, J.W., Thompson, J.F.H., Goldfarb, R.J., Richards, J.P., Eds.; Society of Economic Geologists: Littleton, CO, USA, 2005; pp. 299–336. ISBN 978-1-887483-01-8.
- Yan, D.R. Geological Characteristics and Genesis of the Ruanjiawan Cu–Mo–W and Yinshan Pb–Zn–Ag Deposits. Ph.D. Thesis, China University of Geosciences, Wuhan, China, 2013. (In Chinese).
- Chen, X.F. Ore-Forming System of Guilinzheng–Huangshanling Deposit in Jiangnan Transitional Zone. Master’s Thesis, Hefei University of Technology, Hefei, China, 2016. (In Chinese).

12. Tian, K. The origin of Huangshanling Pb-Zn-Mo deposit, Guichi district, Anhui province: Evidence from zircon U-Pb and Pb isotope study. In Proceedings of the Topic 1: Meso-Cenozoic Large Scale Mineralization and Prospecting in Eastern China, Changsha, China, 11–14 December 2015; Volume S1, p. 59. (In Chinese).
13. Zuo, N. Study on Geological Characteristics and Genesis of the Huangshanling Pb-Zn-Mo Deposit in Chizhou, Anhui Province. Master's Thesis, China University of Mining & Technology, Xuzhou, China, 2018. (In Chinese).
14. Ge, N.J.; Li, P.; Huang, X.A.; Zhang, S.B.; Han, Z.Y. Research on physical chemistry condition and materials source of mineralization of Ag-Pb-Zn ore deposit in Yueshan. *J. China Univ. Sci. Technol.* **1989**, *19*, 365–374. (In Chinese)
15. Lan, B.Y.; Yuan, F.; Deng, Y.F.; Cheng, P.S.; Li, X.H.; Zhang, J.M.; Li, Z. In situ trace element composition of sphalerite and ore-forming fluid characteristics of Xiwan Pb-Zn deposit, Anhui Province. *Miner. Depos.* **2023**, *42*, 192–210. (In Chinese)
16. Qian, B.; Yuan, F.; Zhou, T.F.; Fan, Y.; Zhang, L.J.; Ma, L. The geological character and sulfur isotope geochemical study on Yueshan Ag-Pb-Zn deposit, Luzong basin. In *Proceedings of the Topic 9: Geochemical Tracers of Mineralization and Metallogenic Chronology*; Mineral Deposits: Changchun, China, 2010; Volume S1. (In Chinese)
17. Zha, S.X.; Han, Z.Y. Geochemical characteristics and genetic study of Yueshan Ag-Pb-Zn deposit, Anhui. *Resour. Surv. Environ.* **2002**, *23*, 272–280. (In Chinese)
18. Zhang, H.Q.; Han, S.C.; Zhang, Y.; Pan, J.Y.; Zhang, Y.Q.; Zhao, B.B.; Ding, Y.; Jiang, Y.; Hu, S.P. Trace element characteristics and geological significance of sphalerite in Xiwan lead-zinc deposit, Luzong Basin, Anhui Province. *Geol. J. China Univ.* **2022**. (In Chinese) [CrossRef]
19. Zhang, Y.Q. Research on the geochemical characteristic and genesis of the Xiwan lead-zinc deposit in Anhui Province. Master's Thesis, East China University of Technology, Nanchang, China, 2019. (In Chinese).
20. Liu, G.; Deng, Y.; Yuan, F.; Chen, X.; Yang, B. Rb–Sr Dating and S–Sr–Nd Isotopic Constraints on the Genesis of the Hehuashan Pb–Zn Deposit in the Middle–Lower Yangtze River Metallogenic Belt, China. *Solid Earth Sci.* **2021**, *6*, 57–69. [CrossRef]
21. Jia, L.; Yang, D.; Wang, L.; Long, N. Discussion on characteristics and mineralization of Yanshanian medium-low temperature thermal fluid system in Jiujiang–Ruichang ore concentration area, Jiangxi province. *China Min. Mag.* **2018**, *27* (Suppl. S1), 191–196+210. (In Chinese)
22. Zhong, H.; Xu, Y.M.; Gao, R.; Dong, Y.Y.; Zhang, L. *On Characteristics of Sulfides and Sulfur Lead Isotopic and Trace Elements of the Baiyangfan Lead-Zinc-Silver Deposit in the Jiurui Ore Concentration Area of Jiangxi Province*, 2016th ed.; Jiangxi Science and Technology Press: Nanchang, China, 2016. (In Chinese)
23. Sun, X.J.; Ni, P.; Yang, Y.L.; Qin, H.; Chen, H.; Gui, C.J.; Jing, S. Formation of the Qixiashan Pb–Zn Deposit in Middle-Lower Yangtze River Valley, Eastern China: Insights from Fluid Inclusions and in Situ LA-ICP-MS Sulfur Isotope Data. *J. Geochem. Explor.* **2018**, *192*, 45–59. [CrossRef]
24. Zhang, W.D.; Li, B.; Lu, A.H.; Zhao, K.D.; Elatikpo, S.M.; Chen, X.D.; Zhu, L.; Yu, M. In-Situ Pyrite Trace Element and Sulfur Isotope Characteristics and Metallogenic Implications of the Qixiashan Pb-Zn-Ag Polymetallic Deposit, Eastern China. *Ore Geol. Rev.* **2022**, *144*, 104849. [CrossRef]
25. Zhang, W.D.; You, H.T.; Li, B.; Zhao, K.D.; Chen, X.D.; Zhu, L. Ore-Forming Processes of the Qixiashan Carbonate-Hosted Pb-Zn Deposit, South China: Constraints from Sulfide Trace Elements and Sulfur Isotopes. *Ore Geol. Rev.* **2022**, *143*, 104786. [CrossRef]
26. Xie, S.C.; Yin, H.F. Biometallogenesis of Pb-Zn-Ag Polymetallic Deposit of Qixiashan in Nanjing. *Geol. J. China Univ.* **1997**, *16*, 65–74. (In Chinese)
27. Xie, S.C.; Yin, H.F.; Wang, H.M.; Zhou, X.G.; Zhang, W.H. Characteristics of Ore-Forming Fluids in Pb-Zn-Ag Polymetallic Deposit, Qixiashan, Nanjing. *Geol. Sci. Technol. Inf.* **1998**, *42* (Suppl. S1), 78–81. (In Chinese)
28. Junquan, L.; Qiuming, T.; Jiangzhou, L. *Metallogenic Series of Deposits in Hubei Province*; Hubei Science & Technology Press: Wuhan, China, 2005. (In Chinese)
29. Bendall, C.; Lahaye, Y.; Fiebig, J.; Weyer, S.; Brey, G.P. In Situ Sulfur Isotope Analysis by Laser Ablation MC-ICPMS. *Appl. Geochem.* **2006**, *21*, 782–787. [CrossRef]
30. Chang, Y.F.; Liu, X.P.; Wu, Y.C. *The cOpper-Iron Belt of the Lower and Middle Reaches of the Changjiang River*; Geology Publication House: Beijing, China, 1991. (In Chinese)
31. Xie, G.; Mao, J.; Xiongwei, L.; Duan, C.; Yao, L. Late Mesozoic Bimodal Volcanic Rocks in the Jinni Basin, Middle–Lower Yangtze River Belt (YRB), East China: Age, Petrogenesis and Tectonic Implications. *Lithos* **2011**, *127*, 144–164. [CrossRef]
32. Shu, Q.A.; Chen, P.L.; Cheng, J.R. *Geology of Iron-Copper Deposits in Eastern Hubei Province*; Press of Metallurgical Industry: Beijing, China, 1992. (In Chinese)
33. Hubei Bureau of Geology. *Mineral Resources Regional Geology of Hubei Province*; Geological Publishing House: Beijing, China, 1990. (In Chinese)
34. Li, J.W.; Zhao, X.F.; Zhou, M.F.; Ma, C.Q.; de Souza, Z.S.; Vasconcelos, P. Late Mesozoic Magmatism from the Daye Region, Eastern China: U–Pb Ages, Petrogenesis, and Geodynamic Implications. *Contrib. Mineral. Petrol.* **2009**, *157*, 383–409. [CrossRef]
35. Li, J.W.; Vasconcelos, P.M.; Zhou, M.F.; Deng, X.D.; Cohen, B.; Bi, S.J.; Zhao, X.F.; Selby, D. Longevity of Magmatic–Hydrothermal Systems in the Daye Cu–Fe–Au District, Eastern China with Implications for Mineral Exploration. *Ore Geol. Rev.* **2014**, *57*, 375–392. [CrossRef]
36. Xie, G.; Mao, J.; Zhao, H. Zircon U–Pb Geochronological and Hf Isotopic Constraints on Petrogenesis of Late Mesozoic Intrusions in the Southeast Hubei Province, Middle–Lower Yangtze River Belt (MLYRB), East China. *Lithos* **2011**, *125*, 693–710. [CrossRef]

37. Xie, G.; Mao, J.; Zhu, Q.; Yao, L.; Li, Y.; Li, W.; Zhao, H. Geochemical Constraints on Cu–Fe and Fe Skarn Deposits in the Edong District, Middle–Lower Yangtze River Metallogenic Belt, China. *Ore Geol. Rev.* **2015**, *64*, 425–444. [CrossRef]
38. Craddock, P.R.; Rouxel, O.J.; Ball, L.A.; Bach, W. Sulfur Isotope Measurement of Sulfate and Sulfide by High-Resolution MC-ICP-MS. *Chem. Geol.* **2008**, *253*, 102–113. [CrossRef]
39. Ding, T.; Valkiers, S.; Kipphardt, H.; De Bièvre, P.; Taylor, P.D.P.; Gonfiantini, R.; Krouse, R. Calibrated Sulfur Isotope Abundance Ratios of Three IAEA Sulfur Isotope Reference Materials and V-CDT with a Reassessment of the Atomic Weight of Sulfur. *Geochim. Cosmochim. Acta* **2001**, *65*, 2433–2437. [CrossRef]
40. Xu, L.; Xie, Q.; Zhou, Y.; Wang, J.; Chen, T.; Xu, X.; Xie, J. Recognizing the Evolution of the Stratabound Polymetallic Massive Sulfide Deposits in Tongling Mineralization Cluster, East China through Colloform Pyrite. *Ore Geol. Rev.* **2022**, *146*, 104915. [CrossRef]
41. Ohmoto, H. Sulfur and Carbon Isotopes. In *Geochemistry of Hydrothermal Ore Deposits*; Wiley: Hoboken, NJ, USA, 1997; pp. 517–611.
42. Ohmoto, H. Systematics of Sulfur and Carbon Isotopes in Hydrothermal Ore Deposits. *Econ. Geol.* **1972**, *67*, 551–578. [CrossRef]
43. Seal, R.R. Sulfur Isotope Geochemistry of Sulfide Minerals. *Rev. Mineral. Geochem.* **2006**, *61*, 633–677. [CrossRef]
44. Anderson, G.M. Kerogen as a Source of Sulfur in MVT Deposits. *Econ. Geol.* **2015**, *110*, 837–840. [CrossRef]
45. Kesler, S.E.; Jones, H.D.; Furman, F.C.; Sassen, R.; Anderson, W.H.; Kyle, J.R. Role of Crude Oil in the Genesis of Mississippi Valley-Type Deposits: Evidence from the Cincinnati Arch. *Geology* **1994**, *22*, 609–612. [CrossRef]
46. Drummond, S.E.; Ohmoto, H. Chemical Evolution and Mineral Deposition in Boiling Hydrothermal Systems. *Econ. Geol.* **1985**, *80*, 126–147. [CrossRef]
47. Giggenbach, W.F. Geothermal Gas Equilibria. *Geochim. Cosmochim. Acta* **1980**, *44*, 2021–2032. [CrossRef]
48. Schaarschmidt, A.; Haase, K.M.; Klemm, R.; Keith, M.; Voudouris, P.C.; Alfieris, D.; Strauss, H.; Wiedenbeck, M. Boiling Effects on Trace Element and Sulfur Isotope Compositions of Sulfides in Shallow-Marine Hydrothermal Systems: Evidence from Milos Island, Greece. *Chem. Geol.* **2021**, *583*, 120457. [CrossRef]
49. Stefánsson, A.; Keller, N.S.; Robin, J.G.; Ono, S. Multiple Sulfur Isotope Systematics of Icelandic Geothermal Fluids and the Source and Reactions of Sulfur in Volcanic Geothermal Systems at Divergent Plate Boundaries. *Geochim. Cosmochim. Acta* **2015**, *165*, 307–323. [CrossRef]
50. Pan, Y.; Dong, P. The Lower Changjiang (Yangzi/Yangtze River) Metallogenic Belt, East Central China: Intrusion- and Wall Rock-Hosted Cu–Fe–Au, Mo, Zn, Pb, Ag Deposits. *Ore Geol. Rev.* **1999**, *15*, 177–242. [CrossRef]
51. Xu, X.C.; Yin, T.; Lou, J.W.; Lu, S.M.; Xie, Q.Q.; Chu, P.L. Origin of Dongguashan Stratabound Cu–Au Skarn Deposit in Tongling: Restraints of Sulfur Isotope. *Acta Petrol. Sin.* **2010**, *26*, 2739–2750. (In Chinese)
52. Zhou, T. Isotope Geochemistry of Copper Mineralization in Yueshan, Anhui. *Miner. Depos.* **1996**, *15*, 341–350.
53. Hu, D.L.; Jiang, S.Y.; Duan, D.F.; Xiong, S.F. Fluid Origin and Evolution of the Ruanjiawan W–Cu–(Mo) Deposit from the Edong District in the Middle-Lower Yangtze River Metallogenic Belt of China: Constraints from Fluid Inclusions and H–O–C–S Isotopes. *Ore Geol. Rev.* **2021**, *139*, 104428. [CrossRef]
54. Yan, D.R.; Deng, X.D.; Hu, H.; Li, J.W. U–Pb Age and Petrogenesis of the Ruanjiawan Granodiorite Pluton and Xiniushan Granodiorite Porphyry, Southeast Hubei Province: Implications for Cu–Mo Mineralization. *Acta Petrol. Sin.* **2012**, *28*, 3373–3388.
55. Deng, X.D.; Li, J.W.; Zhou, M.F.; Zhao, X.F.; Yan, D.R. In-Situ LA-ICPMS Trace Elements and U–Pb Analysis of Titanite from the Mesozoic Ruanjiawan W–Cu–Mo Skarn Deposit, Daye District, China. *Ore Geol. Rev.* **2015**, *65*, 990–1004. [CrossRef]
56. Chang, Z.; Meinert, L.D. The Empire Cu–Zn Mine, Idaho: Exploration Implications of Unusual Skarn Features Related to High Fluorine Activity. *Econ. Geol.* **2008**, *103*, 909–938. [CrossRef]
57. Chang, Z.; Meinert, L.D. The Magmatic–Hydrothermal Transition—Evidence from Quartz Phenocryst Textures and Endoskarn Abundance in Cu–Zn Skarns at the Empire Mine, Idaho, USA. *Chem. Geol.* **2004**, *210*, 149–171. [CrossRef]
58. Guilbert, J.M.; Park, C.F. *The Geology of Ore Deposits*, 4th ed.; WH Freeman: New York, NY, USA, 1986; p. 59.
59. Einaudi, M.T.; Hedenquist, J.W.; Inan, E.E. Sulfidation state of fluids in active and extinct hydrothermal systems: Transitions from porphyry to epithermal environments. In *Volcanic, Geothermal, and Ore-Forming Fluids: Rulers and Witnesses of Processes within the Earth*; Society of Economic Geologists, Special Publication: Littleton, CO, USA, 2003; pp. 285–314.
60. Sillitoe, R.H. Porphyry copper systems. *Econ. Geol.* **2010**, *105*, 3–41. [CrossRef]
61. Catchpole, H.; Kouzmanov, K.; Putlitz, B.; Seo, J.H.; Fontboté, L. Zoned base metal mineralization in a porphyry system: Origin and evolution of mineralizing fluids in the Morococha district, Peru. *Econ. Geol.* **2015**, *110*, 39–71. [CrossRef]
62. Zhai, D.G.; Williams-Jones, A.E.; Liu, J.J.; Selby, D.; Voudouris, P.C.; Tombros, S.; Li, K.; Li, P.L.; Sun, H.J. The genesis of the giant Shuangjanzhishan epithermal Ag–Pb–Zn deposit, Inner Mongolia, Northeastern China. *Econ. Geol.* **2020**, *114*, 101–128. [CrossRef]

Disclaimer/Publisher’s Note: The statements, opinions and data contained in all publications are solely those of the individual author(s) and contributor(s) and not of MDPI and/or the editor(s). MDPI and/or the editor(s) disclaim responsibility for any injury to people or property resulting from any ideas, methods, instructions or products referred to in the content.

Article

Genesis of the Dongtangzi Zn-Pb Deposit of the Fengxian–Taibai Ore Cluster in West Qinling, China: Constraints from Rb-Sr and Sm-Nd Geochronology, and In Situ S-Pb Isotopes

Qiaoping Hu ¹, Yitian Wang ^{1,*}, Shaocong Chen ², Ran Wei ¹, Xielu Liu ³, Junchen Liu ⁴, Ruiting Wang ⁵, Weihong Gao ⁵, Changan Wang ⁶, Minjie Tang ⁶ and Wentang Wu ⁶

- ¹ MNR Key Laboratory of Metallogeny and Mineral Assessment, Institute of Mineral Resources, Chinese Academy of Geological Sciences, Beijing 100037, China; huqiaoping@cags.ac.cn (Q.H.); weiranyspa@126.com (R.W.)
 - ² MNR Key Laboratory for Polar Science, Polar Research Institute of China, Ministry of Natural Resources, Shanghai 200136, China; shaocong0211@163.com
 - ³ Beijing Institute of Exploration Engineering, Beijing 100083, China; liuxielu@mail.cgs.gov.cn
 - ⁴ Collaborative Innovation Center for Exploration of Nonferrous Metal Deposits and Efficient Utilization of Resources by the Province and Ministry, Guilin University of Technology, Guilin 541004, China; ljccugb@163.com
 - ⁵ Northwest Nonferrous Geological and Mining Group Co., Ltd., Xi'an 710054, China; wrtyf@163.com (R.W.); 717gwh@163.com (W.G.)
 - ⁶ Baoji No.717 Corps Limited of Northwest Nonferrous Geological and Mining Group, Baoji 721015, China; wangchangan1463@163.com (C.W.)
- * Correspondence: wyt69@263.net

Citation: Hu, Q.; Wang, Y.; Chen, S.; Wei, R.; Liu, X.; Liu, J.; Wang, R.; Gao, W.; Wang, C.; Tang, M.; et al. Genesis of the Dongtangzi Zn-Pb Deposit of the Fengxian–Taibai Ore Cluster in West Qinling, China: Constraints from Rb-Sr and Sm-Nd Geochronology, and In Situ S-Pb Isotopes. *Minerals* **2024**, *14*, 297. <https://doi.org/10.3390/min14030297>

Academic Editor: George M. Gibson

Received: 27 December 2023

Revised: 11 February 2024

Accepted: 6 March 2024

Published: 12 March 2024



Copyright: © 2024 by the authors. Licensee MDPI, Basel, Switzerland. This article is an open access article distributed under the terms and conditions of the Creative Commons Attribution (CC BY) license (<https://creativecommons.org/licenses/by/4.0/>).

Abstract: The large Dongtangzi Zn-Pb deposit is located in the southwest of the Fengxian–Taibai (abbreviated as Fengtai) ore cluster in the west Qinling orogen. The origin of the deposit is controversial, positing diverse genesis mechanisms such as sedimentary-exhalative (SEDEX), sedimentary-reformed, and epigenetic-hydrothermal types. This study combines systematic ore geology observations with high-precision Rb-Sr and Sm-Nd ages of 211 Ma and in situ S-Pb isotopes to constrain the timing and origin of mineralization. In situ S-Pb isotopic studies show that the sulfide ores display a narrow range of $\delta^{34}\text{S}$ values from 1.1‰ to 10.2‰, with $^{206}\text{Pb}/^{204}\text{Pb}$, $^{207}\text{Pb}/^{204}\text{Pb}$, and $^{208}\text{Pb}/^{204}\text{Pb}$ ratios of 18.07 to 18.27, 15.64 to 15.66, and 38.22 to 38.76, respectively. On the other hand, pyrites of the sedimentary period and the granite porphyry dike have $\delta^{34}\text{S}$ values ranging from 15.8 to 21.4‰ and from 2.1 to 4.3‰ (with $^{206}\text{Pb}/^{204}\text{Pb}$ ratios of 18.09 to 18.10, $^{207}\text{Pb}/^{204}\text{Pb}$ ratios of 15.59 to 15.61, and $^{208}\text{Pb}/^{204}\text{Pb}$ ratios of 38.17 to 38.24), respectively. The above-mentioned S-Pb isotopic compositions indicate that the metallic materials involved in ore formation originated from a mixture of Triassic magmatic hydrothermal fluid and metamorphic basement. By integrating the regional geology, mineralization ages, and S-Pb isotopic studies, we propose that the Dongtangzi Zn-Pb deposit is the product of epigenetic hydrothermal fluid processes, driven by Late Triassic regional tectono-magmatic processes.

Keywords: Rb-Sr and Sm-Nd isotopic dating; in situ S-Pb isotopes; ore genesis; Zn-Pb deposit; Dongtangzi; west Qinling orogen

1. Introduction

The Fengxian–Taibai (abbreviated as “Fengtai”) ore cluster, located in the west Qinling orogen, forms part of the giant Qinling Pb-Zn-Au metallogenic belt, which is itself a subsidiary component of the Qinling orogenic belt. Several large and medium-sized Zn-Pb deposits are present, including, from west to east, the Fengya, Yindongliang, Qiandongshan–Dongtangzi, Bafangshan–Erlihe, and Yinmusi deposits, along with many other small-sized

deposits and occurrences. Moreover, there are two large Au deposits, known as Baguamiao and Shuangwang, along with many small-sized Au deposits, and several small Cu deposits. The total reserve contains over 5 Mt of Pb + Zn and there is more than 200 t of gold in the ore cluster [1,2]. The large Dongtangzi Zn-Pb deposit, located in the southwest of the Fengtai ore cluster (Figure 1), contains over 1.5 Mt of Pb + Zn, with an average grade of 7.7 wt% Zn and 1.7 wt% Pb [3]. The Dongtangzi Zn-Pb deposit was discovered in the late 1950s and was formerly known as the Qiandongshan deposit. Around 2002, the newly discovered, concealed west area of the Qiandongshan main ore body was called the Dongtangzi mine section. After the year 2004, the two mine sections were merged under one name and collectively called the Dongtangzi Zn-Pb deposit. Previous research work has mainly focused on the Qiandongshan mine section, while less work has been carried out on the Dongtangzi mine section. Since the 1980s, extensive investigations have been conducted into the Dongtangzi Zn-Pb deposit to understand its geological characteristics and ore-controlling structures [3–6], stable isotope and trace element geochemistry [7–11], and ore genesis [5,11–17]. Despite decades of research, the origin of the ore remains contentious.

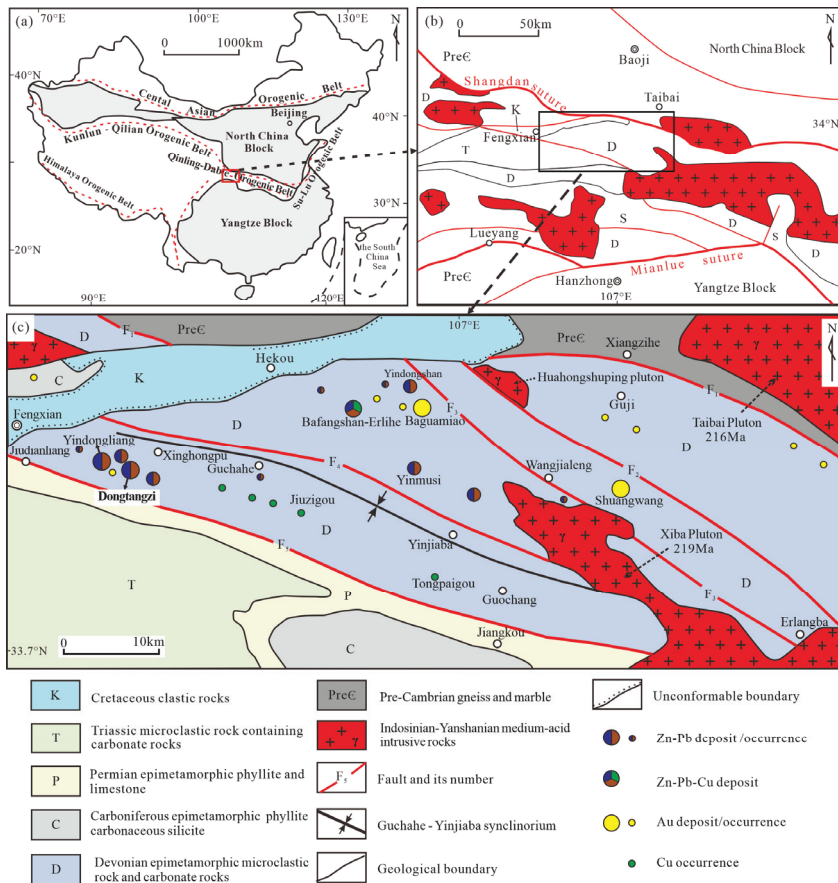


Figure 1. Sketch maps of (a) tectonic units of China and (b) west Qinling orogenic belt, along with a geological map of (c) the Fengxian-Taibai (abbreviated as “Fengtai”) ore cluster (modified from Wang X. et al., 1996; Hu Q.Q. et al., 2020 [18,19]). Notes: F₁: Xiangzihe–Huangbaiyuan Fault (Shang-Dan suture zone); F₂: Xiushiyān–Guanyinxia Fault; F₃: Wangjialeng–Erlangba Fault; F₄: Daohuigou–Zheliyuan Fault; F₅: Jiudianliang–Jiangkou Fault.

Many researchers [5,15,20] believe that it is a sedimentary exhalative (SEDEX) deposit developed in the Devonian period. Others contend that it is of epigenetic origin [3,16–18,21] and a product of Triassic tectonic–hydrothermal processes. Due to the lack of precise geochronology data and comprehensive isotopic geochemistry studies, particularly the lack of in situ technique analysis, the metallogenic processes of the Dongtangzi Zn–Pb deposit remain poorly understood. Therefore, this study presents a comprehensive identification of its deposit geology, along with Rb–Sr and Sm–Nd geochronology and in situ S–Pb isotopic studies, aiming to further constrain the genesis of the Dongtangzi Zn–Pb deposit. The new results in this study, provide valuable information about the timing of Zn–Pb mineralization and the source of ore-forming materials. They also allow us to refine the origin of the Dongtangzi Zn–Pb deposit, which will be an essential factor for understanding the Zn–Pb metallogeny throughout the entire Fengtai ore cluster and the west Qinling Zn–Pb belt.

2. Regional Geology

The Qinling orogen was formed during the convergence and collision of the North China and Yangtze blocks (Figure 1a), resulting in a multi-stage composite orogenic belt composed of two suture zones and three tectonic belts [22]. The three tectonic units are, from north to south, the North Qinling belt, the South Qinling belt, and the north margin of the Yangtze block [22]. The northern suture zone is the Early Silurian Shangdan suture (Figure 1b), and the southern is the Late Triassic Mianlue suture (Figure 1b). The Fengtai ore cluster is located in the middle-west of the South Qinling belt (Figure 1c), which is bordered by the NWW-trending faults of the Xiangzihe–Huangbaiyuan fault (F_1 , part of the Shangdan suture) in the north and the Jiudianliang–Jiangkou fault (F_5) in the south (Figure 1c). There are three NWW-trending faults inside the ore cluster called the Xiushiyan–Guanyinxia (F_2), Wangjialeng–Erlangba (F_3), and Daohuigou–Zheliyuan (F_4) faults (Figure 1c). The basic tectonic setting of the Fengtai ore cluster is a compound fold with well-developed secondary folds and faults. The tectonic style is a large-scale transpressional strike–slip duplex system resulting from regional sinistral strike–slip faulting [23].

The Fengtai ore cluster is hosted by Middle–Upper Devonian siliciclastic and carbonate rocks (Figure 1c) deposited in a littoral–neritic depositional environment and subsequently metamorphosed under low greenschist facies conditions. This vertical succession comprises, from bottom to top, fine clastic rocks and metasandstone of the Middle Devonian Macaogou Formation (D_{2m}), followed by carbonate rocks of the Middle Devonian Guadaling Formation (D_{2g}), clastic–carbonate rocks of the Upper Devonian Xinghongpu Formation (D_{3x}), and fine clastic rocks of the Upper Devonian Jiuliping Formation (D_{3j}). Around the periphery of the ore cluster, high-grade meta-sedimentary rocks and volcanic rocks of the Proterozoic Qinling Group (P_{t1q}) and Danfeng Group (P_{t1d}) appear to the north; carbonate and clastic rocks of the Lower Carboniferous (C_1) period and breccia with siltstone of the Lower Cretaceous (K_1) period appear to the northwest (Figure 1c); and marine carbonate rocks with continental clastic rocks of the Carboniferous (C) period and limestone of the Lower Triassic Liufengguan Group (T_{1l}) appear to the southwest (Figure 1c).

Intense Triassic magmatic activity has been recorded in the ore cluster. The Xiba intermediate–felsic pluton, trending NWW, is positioned to the southeast of the cluster (Figure 1c), comprising medium-fine-grained granodiorite, monzogranite, quartz diorite, and tonalite, with transitional contact relations. A small Huahongshuping granodioritic intrusive stock is located in the north (Figure 1c). In addition, numerous dikes of diorite, granite porphyry, and lamprophyre commonly develop throughout the ore cluster (mainly concentrated adjacent to the Pb–Zn and Au deposits), filling the NE- or NWW-trending faults, with a thickness of tens of centimeters to several meters.

3. Ore Deposit Geology

3.1. Structures

The “M”-shaped Qiandongshan–Dongtangzi brachyanticline is the principal ore-hosting structure, striking about 280° (Figure 2). The hinge of the anticline plunges westwards at angles between 27° and 37°. There are EW-, NW-, and NE-trending faults in the mine area. The EW-trending reverse faults are the largest in scale and are developed mostly in the interface between the Gudaoling Formation and Xinghongpu Formation (Figure 2). The NW- and NE-trending faults are of smaller size but more abundant, belonging to the “X”-type conjugate shear faults formed under regional shearing events, cutting through the main orebody with small fault displacements.

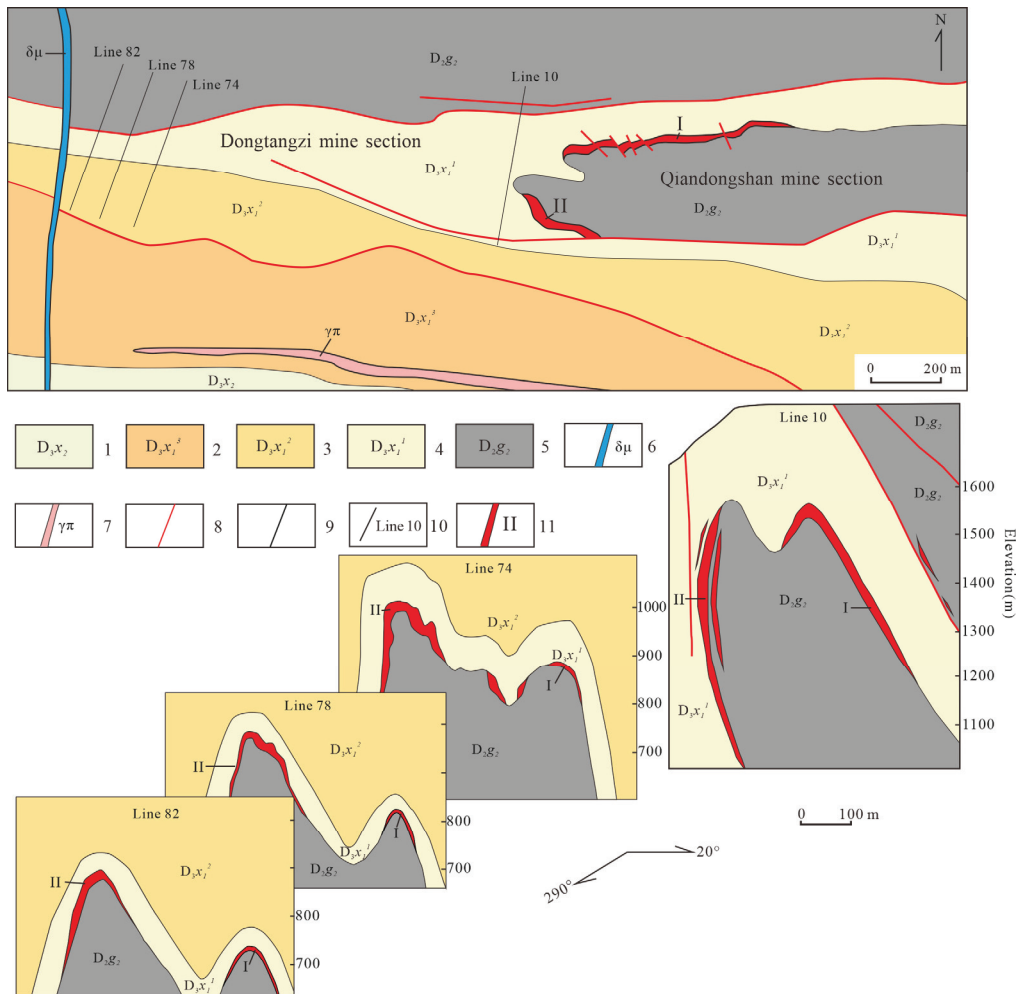


Figure 2. Geological map and composite cross-sections of the Dongtangzi Zn-Pb deposit (after Qi et al., 1993; Tang, 2013; Wu et al., 2016; Wang et al., 2023 [3,15,24]). Note: 1. The Upper Section of the Xinghongpu Formation ($D_{3 \times 2}$); 2. Upper member of the Lower Section of Upper Devonian Xinghongpu Formation (D_{3x1}^3); 3. Middle member of the Lower Section of Upper Devonian Xinghongpu Formation

- (D₃x₁²); 4. Lower member of the Lower Section of Upper Devonian Xinghongpu Formation (D₃x₁¹);
- 5. The Upper Section of the Middle Devonian Gudaoling Formation (D₂g₂); 6. Diorite porphyry dike;
- 7. Granite porphyry dike; 8. Fault; 9. Geological boundary; 10. Prospecting line and its number;
- 11. Zn-Pb orebody and its number.

3.2. Rocks

The strata within the mine area contain the Upper Section of the Middle Devonian Gudaoling Formation (D₂g₂) and the Upper Devonian Xinghongpu Formation (D₃x) (Figure 2). The EW-striking upper section of the Gudaoling Formation hosts the main orebody (Figures 2 and 3), which is comprised of microcrystalline biolithite and carbonaceous microcrystalline limestone, intensively silicified at the top by meters to tens of meters in thickness. The Xinghongpu Formation is comprised of two lithologic sections, namely the Lower Section (D₃x₁) and the Upper Section (D₃x₂), respectively. The Lower Section (D₃x₁) is comprised of three members, including the lower (D₃x₁¹) ferrodolomitic phyllite with sericite phyllite and thin layers of carbonaceous limestone, the middle (D₃x₁²) ferrodolomitic phyllite with thin layers of limestone and silty sericite phyllite, and the upper (D₃x₁³) carbonaceous phyllite with thin layers of carbonaceous biolithite. Among them, the carbonaceous limestone of the lower member (D₃x₁¹) hosts a small scale of Zn-Pb orebody (Figure 3). The Upper Section (D₃x₂) consists mainly of chlorite sericite phyllite, with less ferrodolomitic sericite phyllite at the bottom (Figure 3).

Rock units	Strata column	Lithologic description
The Upper section of the Upper Devonian Xinghongpu Formation (D ₃ x ₂)		Chlorite sericite phyllite, unmineralized, with thickness about 200 m
Upper member of the Lower section of the Upper Devonian Xinghongpu Formation (D ₃ x ₁ ³)		Carbonaceous calcareous sericite phyllite with thin layer of carbonaceous biolithite, unmineralized, with thickness about 300 m
Middle member of the Lower section of the Upper Devonian Xinghongpu Formation (D ₃ x ₁ ²)		Ferrodolomitic phyllite with thin layer of limestone and silty sericite phyllite, unmineralized, with thickness about 200 m
Lower member of the Lower section of the Upper Devonian Xinghongpu Formation (D ₃ x ₁ ¹)		Ferrodolomitic phyllite in the top, thin layer of carbonaceous limestone, sericite phyllite in the middle, with Zn-Pb mineralization in the bottom, with thickness about 100 m
The Upper Section of the Middle Devonian Gudaoling Formation (D ₂ g ₂)		Thick layered carbonaceous bioclastic limestone with calcareous phyllite and sericite carbonaceous phyllite in the top, containing the main Zn-Pb orebody; Thin layered fine grained limestone in the lower part with Zn-Pb mineralized veins, with thickness about 600 m

Figure 3. Stratigraphic column of the Dongtangzi Zn-Pb deposit. The thickness of the lithologic section is from Wang J.L. et al., 1996 [5].

The intrusive dikes occur throughout the mine area. There are several diorite porphyry dikes and granite porphyry dikes, filling the NE-trending and NWW-trending faults, respectively. The diorite porphyry dikes crosscut the main orebody, while the granite porphyry dikes—with zircon U-Pb ages of 226–221 Ma (LA-ICP-MS; [25])—are roughly parallel to the main orebody (Figures 3 and 4a). The main minerals of the granite porphyry dikes are plagioclase (30%), potash feldspar (35%), quartz (30%), biotite (3%), pyrite, zircon,

sphene, etc. (Figure 4b,c). The existence of cataclastic quartz suggests that the dike was deformed after its emplacement (Figure 4b,c).

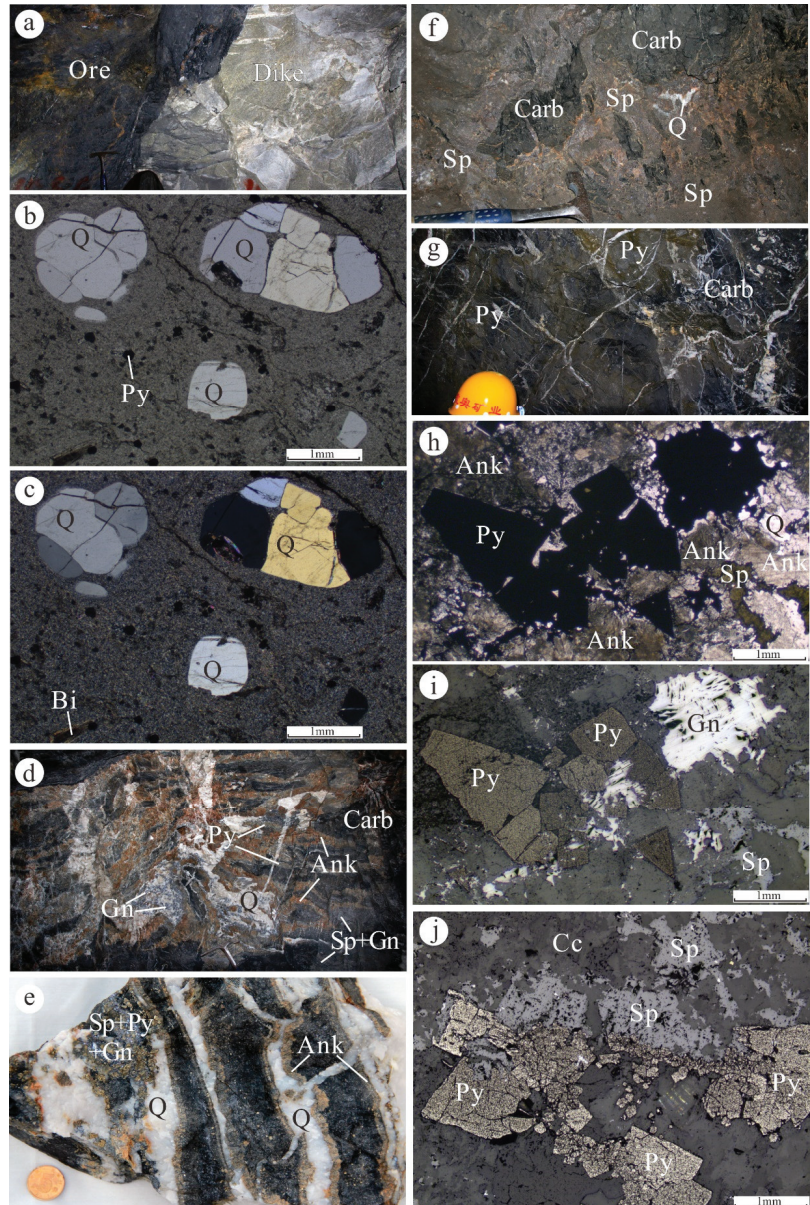


Figure 4. Rocks of the Dongtangzi Zn-Pb deposit. (a) The NWW-trending granite porphyry dike crosscutting the main orebody. (b,c) Subhedral granular quartz phenocrysts in the granite porphyry ((b): plane-polarized light; (c): cross-polarized light). (d) Breccia type ore. The brecciated carbonaceous limestone with disseminated sulfides inside and ankerite at the edges, cementing by medium-coarse-grained aggregates of quartz-dolomite-polymetallic sulfides. (e) Veinlet ore. Quartz-sulfide-ankerite veins crosscut the brecciated carbonaceous limestone. (f) Sphalerite-rich massive ore cement the breccia

of dolomitized rocks. (g) Pyrite-rich massive ore with metasomatic remnant of altered carbonates. (h,i) The euhedral granular pyrite was metasomatized by sphalerite and galena within the pyrite-rich ore ((h)—plane-polarized light; (i)—reflected light). (j) The fragmented pyrite metasomatized by sphalerite (reflected light). Abbreviations: Sp—sphalerite; Gn—galena; Py—pyrite; Q—quartz; Ank—ankerite; Cc—calcite; Carb—carbonate.

3.3. Orebodies

Controlled by the Qiandongshan–Dongtangzi anticline, the main orebody occurs at the contact zone between the Devonian Gudaoling Formation (D_2g) and the Xinghongpu Formation (D_3x) (Figures 2 and 3), which is composed of the No.1 orebody (north subsidiary anticline) and the No.2 orebody (south subsidiary anticline), accounting for more than 90% of the total Zn–Pb reserves. The No.1 orebody extends by 2.35 times its depth [26]. The other orebodies occur within the fault fracture zones and irregular tensile fractures in limestone, or within interlayer fractures in phyllite, on a relatively small scale with unstable occurrences (Figures 2 and 3). The eastern part of the No.1 orebody occurs in the northern flank of the anticline and the saddle of the northern subsidiary anticline, and there is a trend of pinching out westward (Figure 2). The No. 2 orebody, located on the southern flank of the anticline, is larger in scale in the west part within the Dongtangzi mine section (Figure 2). The orebodies in the north flank of the anticline are thinner and the wall rocks are strongly foliated, while the orebodies in the south flank of the anticline are thicker, without the preservation of any foliated structures. In addition, within the carbonaceous limestone near the footwall of the No. 2 orebody, a cryptoexplosive breccia pipe was discovered, with different sizes of angular–sub-angular breccias, composed of granite porphyry, quartz vein, altered rock, and massive sulfide ore, cemented with argillaceous and carbonaceous mineral aggregates (Figure 5a).

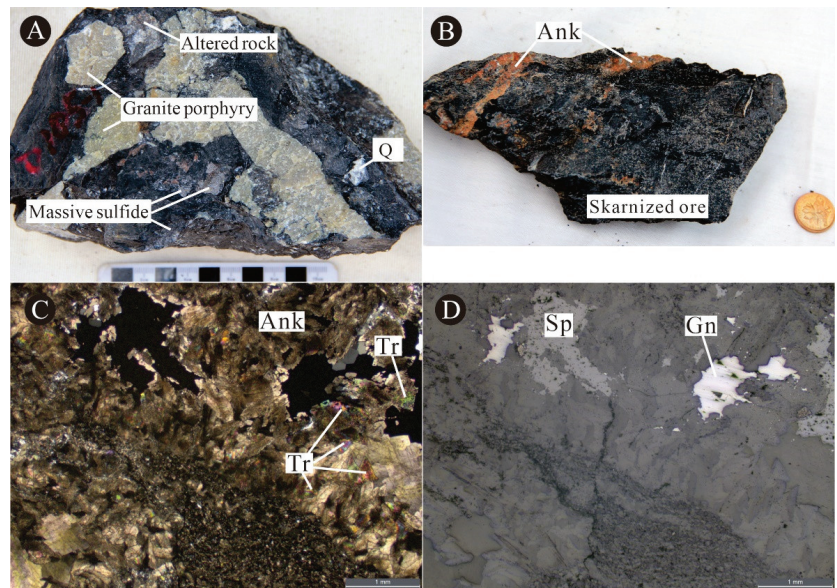


Figure 5. Cryptoexplosive breccia and skarn in the Dongtangzi Zn–Pb deposit. (A) Cryptoexplosive breccias, with different sizes of angular–sub-angular breccias, composed of altered granite porphyry, quartz aggregate, altered carbonaceous limestone, and massive sulfide ores, cemented by argillaceous

and carbonaceous mineral aggregates; (B) brecciated ore beside the granite porphyry dike; (C,D) ankerite is replaced by tremolite, which occurs at the edge of fine-grained disseminated sphalerite and galena aggregate ((C): cross-polarized light; (D): reflected light). Note: Sp—sphalerite; Q—quartz; Gn—galena; Ank—ankerite; Tr—tremolite.

The ore minerals mainly comprise sphalerite, galena, pyrite, chalcopyrite, and arsenopyrite. The gangue minerals include quartz, ankerite, dolomite, calcite, siderite, sericite, chlorite, and apatite. The ore structures are mainly veinlets (Figure 4e), banded, brecciated (Figure 4d,f), blocky (Figure 4g), banded, and disseminated. Extensive vein filling and metasomatic mineralization can be observed in all the orebodies. The ore textures include granular (Figure 4h,i), metasomatic (Figure 4h–j), fragmented (Figure 4j), and wrinkling pressure shadow texture. The wall rock alteration is widely and intensively developed throughout the floor and roof rocks, including silicification, dolomitization, calcitization, pyritization, sericitization, and graphitization. In addition, tremolitization is developed in the ore beside the granite porphyry dikes (Figure 5b–d).

3.4. Mineralogy Assemblage and Paragenetic Sequence

Based on a systematic observation of the mineral assemblages, ore structure and texture, hydrothermal alteration, and crosscutting relationships of the multistage veins in the Dongtangzi Zn-Pb deposit, the paragenetic association can be divided into two periods, namely the sedimentary period and the hydrothermal mineralization period. The hydrothermal mineralization period can be further divided into three stages (Figure 6): Stage I, a polymetallic sulfide–ankerite–quartz stage; Stage II, a quartz–pyrite-rich sulfide–ankerite stage; and stage III, a quartz–carbonate–sulfide stage.

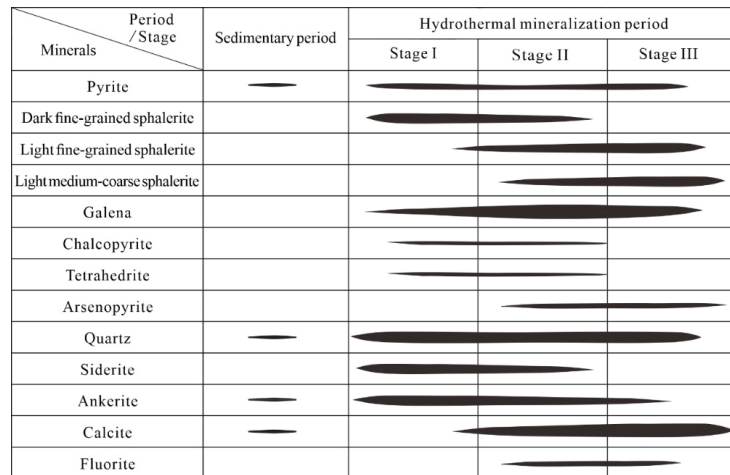


Figure 6. Mineral paragenetic sequence of the Dongtangzi Zn-Pb deposit.

3.4.1. Sedimentary Period

There is no obvious Zn-Pb mineralization in the sedimentary period, and syn-sedimentary pyrites (Py₀) are observed, which are mostly metasomatized by sulfides and quartz during the hydrothermal period (Figure 7a–c). The primary sedimentary textures are mostly destroyed by the structural deformation and metamorphism; syngenetic minerals are largely replaced, deformed, and cemented by hydrothermal minerals during the hydrothermal mineralization period.

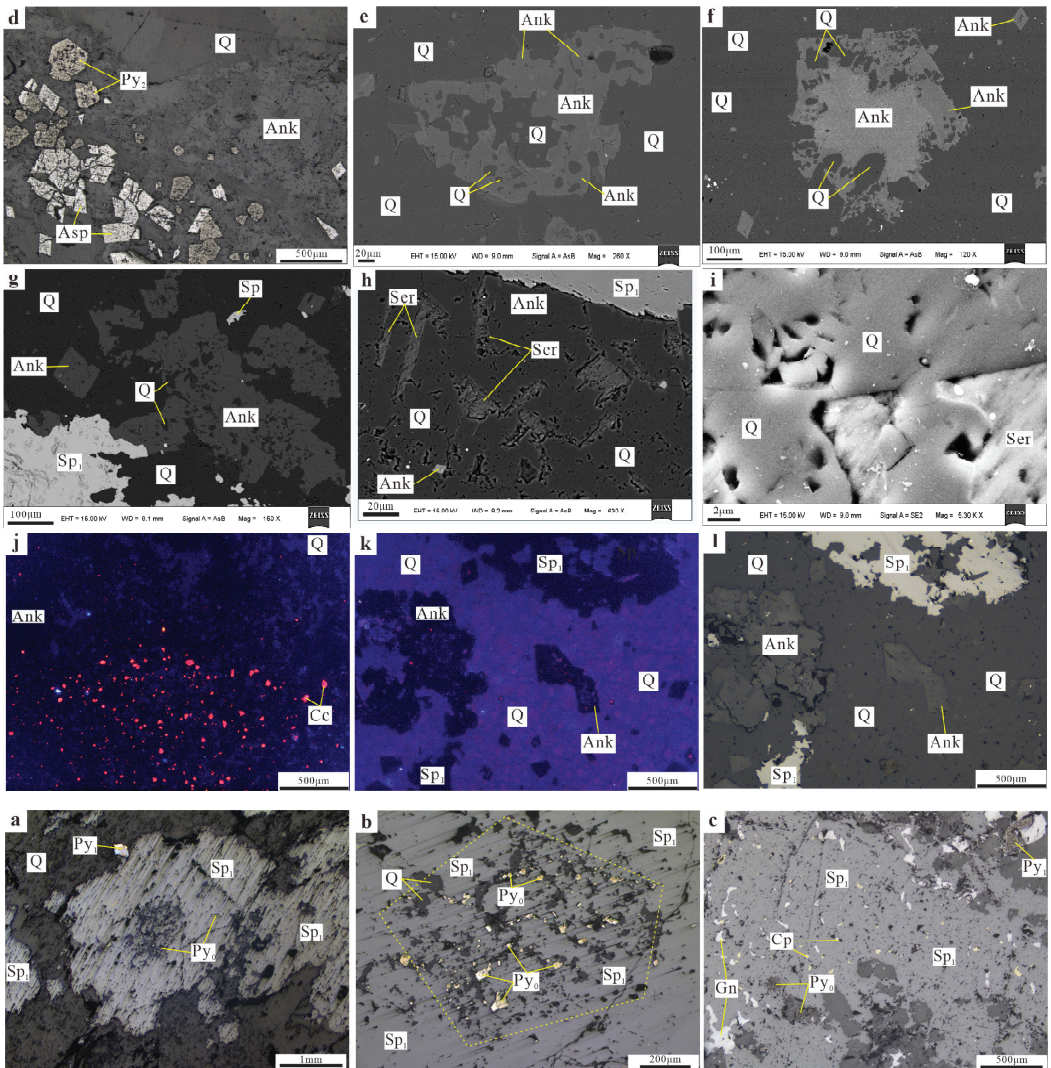


Figure 7. Microfabric characteristics of the ore in the Dongtangzi Zn-Pb deposit. (a,b) Metasomatic residual skeleton texture of pyrite (Py₀) replaced by the Stage I sphalerite (Sp₁), under reflected light. (c) Droplet chalcopyrite (Cp), irregular galena (Gn), and metasomatic residual Py₀ are developed in the massive sphalerite (Sp₁), under reflected light. (d) Densely disseminated pyrite (Py₂) + arsenopyrite (Asp₂) developed in the ferrodolomite siliceous rock, under reflected light. (e,f) The ankerite in the siliceous rock is replaced by quartz, forming skeletal crystal texture, back-scattered electron (BSE) image. (g) Ankerite (Ank) in the siliceous rocks are metasomatized by quartz (Q) and sphalerite, BSE image. (h) Micro-fine aggregates of quartz, sericite (Ser), and ankerite in the siliceous rocks, with sphalerite filling in cracks, BSE image. (i) Scanning electron microscopy (SEM) images show that the surface of the quartz developed triangular pores, with tightly cemented grains, flat edges, and crystal textures. (j) Cathode luminescence (CL) image of the ankerite siliceous rock. The residual of metasomatized calcite is orange colored, while the ankerite is black, and the quartz is deep bluish purple. (k,l) The silicate rocks are metasomatized by quartz and sphalerite (k)—cathode luminescence, (l)—reflected light).

3.4.2. Hydrothermal Mineralization Period

Stage I: A Polymetallic Sulfide–Ankerite–Quartz Stage

Stage I is rich in sphalerite and galena, with locally enriched pyrite, accompanied by less chalcopyrite, and is mainly hosted by silicified carbonaceous limestone. The sphalerite is fine-grained and mainly dark brown in color. The galena and pyrite are also fine-grained, cementing the breccia of the carbonaceous altered rock (Figure 8a). The Stage I ore developed silicification, dolomitization, chloritization, and local sericitization, replacing the banded marl along the bedding, or filling the tension fractures within the carbonaceous limestone (Figure 8g). Carbonates are extensively metasomatized by quartz and sulfides (Figure 7e–g), and some quartz and sulfides retain the skeletal crystal structure of carbonates (Figure 7e,f). Stage I is the main mineralization stage, which is generally affected by later tectonic deformation, developing fragmentation and local recrystallization (Figures 4d, 7f and 8a).

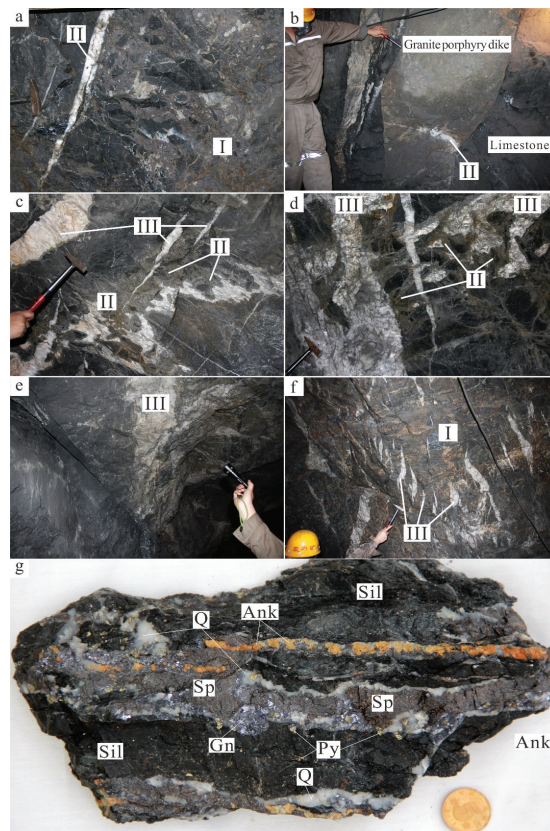


Figure 8. Ore of the different mineralization stages in the Dongtangzi Zn-Pb deposit. (a) The Stage I massive and brecciated ores intersected by the Stage II quartz–pyrite–ankerite veins. (b) The granite porphyry dike is crosscut by the Stage II quartz–pyrite–sphalerite vein. (c) The Stage II pyrite-rich ore is crosscut by Stage III quartz–calcite veins. (d) The Stage II pyrite–ankerite vein is crosscut by the Stage III calcite veins. (e) The Stage III coarse-grained calcite–pyrite vein. (f) The Stage III quartz–pyrite–sphalerite veins are arranged in echelon, crosscutting the Stage I ores. (g) The Stage I quartz–sphalerite–galena–pyrite–ankerite parallel veins crosscutting the carbonaceous altered rocks. Note: Sp: sphalerite; Q: quartz; Gn: galena; Ank: ankerite; Sil: siliceous rock.

No obvious sedimentary mineralization characteristics have been found in the ore of the Dongtangzi Zn-Pb deposit. The sheet-like sericite among the quartz grains is irregular (Figure 7h), without obvious orientation, and does not have the typical sedimentary texture of the directional arrangement of argillaceous minerals. The quartz grains are crystalline and there is tight cementation between grains (Figure 7i), with no obvious rounded grain texture, showing no syn-sedimentary characteristics, thereby indicating that the quartz in the altered rocks may occur as a result of hydrothermal fluid running through fracture systems of different scales. Most of the quartz in the altered rocks was obviously formed by metasomatism, as the calcite (the orange region in Figure 7j) is replaced by ankerite (the black region in Figure 7j) and quartz (the blue-purple region in Figure 7j), while the ankerite (Figure 7k,l) is replaced by quartz (the blue-purple region in Figure 7k) and sphalerite (Figure 7k,l). All of the above evidence suggests that the altered rocks were formed by epigenetic hydrothermal replacement of carbonate rocks, rather than by the sedimentary-exhalative processes suggested by some researchers [8,15,27,28].

Stage II: A Quartz–Pyrite-rich Sulfide–Ankerite Stage

The Zn-Pb mineralization scale of Stage II is smaller than that of Stage I, but is more enriched in pyrite, which locally intersects and replaces the Stage I ore, silicified carbonaceous limestone (Figure 8a), and silicified phyllite. Meanwhile, the granite porphyry dikes with scattered pyritization are crosscut by the stage II quartz vein (Figure 8b). The quartz–pyrite–ankerite veins are accompanied by polymetallic sulfides such as sphalerite, galena, chalcopyrite, and arsenopyrite, which are generally coarse-grained. The color of the Stage II sphalerite is obviously lighter than that of Stage I, being light yellowish brown in color, and medium-to-fine-grained. According to the interspersed relationship, the NWW-trending granite porphyry dike locally crosscuts the Stage I orebody and is cut through by the quartz–sulfide vein of Stage II, indicating that it was emplaced at a time between Stages I and II. No apparent replacement can be observed on the pyrite (Py₂) and arsenopyrite (Asp₂) in the altered rocks (Figure 7d). Dolomitization, pyritization, and silicification are well-developed in the wall rocks during Stage II (Figure 8c,d).

Stage III: A Quartz–Carbonate–Sulfide Stage

The Stage III quartz–carbonate–sulfide veins are widely developed in the whole deposit, forming NE-trending joint veins or en echelon veins (Figure 8f), hosted by carbonaceous limestone and phyllite. They mainly consist of coarse-grained quartz and calcite (Figure 8e), with coarse-to-medium-grained ankerite, pyrite, galena, and sphalerite. The Stage III veins are small in scale, which crosscut the wall rocks and the ore veins of the first two stages (Figure 8c,d). The wall rock alteration is weak, including silicification, pyritization, and carbonation.

4. Samples and Analytical Methods

All samples utilized in this work were collected from underground tunnels at diverse depths within the Dongtangzi Zn-Pb deposit. After making the polished thin sections, comprehensive microscopic observation was carried out to preliminarily characterize the morphology, textures, and paragenesis of ore-related minerals. Subsequently, representative samples were chosen for further analyses (Table 1). A subset of these samples underwent crushing, with sulfide minerals, including sphalerite, galena, and pyrite, meticulously hand-picked under a binocular microscope. The purity of individual mineral separations exceeded 99%, and all mineral isolations underwent thorough cleaning in an ultrasonic bath. Concurrently, other portions of the samples were polished into thin sections, facilitating high-precision *in situ* LA-MC-ICP-MS sulfur and lead isotope analyses.

Table 1. Samples description of the Dongtangzi Zn-Pb deposit.

No.	Sample	Position	Stage	Type	Description
1	D216.3-1	960 m elevation, north-south of the No.2 ore body	I	Siliceous rock	Siliceous rock with pyrite of the sedimentary period, intersected by the hydrothermal Stage I quartz-pyrite-galena veins
2	D22	1010 m elevation, south flank of the No.2 ore body	I	Disseminated ore	Lamellar carbonaceous altered rock, with disseminated medium-fine grained sphalerite
3	D28-4	960 m elevation, south flank of the No.2 ore body	I	Banded ore	Fine-grained quartz-ankerite-pyrite veins are zebra-striated in carbonaceous altered rocks
4	D29-1	960 m elevation, south flank of the No.2 ore body	I	Vein type ore	Quartz-dolomite-sphalerite-pyrite-galena veins developed in carbonaceous limestone
5	D45	960 m elevation, south flank of the No.2 ore body	I	Massive, brecciated ore	Medium-coarse-grained massive sphalerite-pyrite-dolomite aggregate, locally cementing breccias of carbonaceous altered rock
6	D48	860 m elevation, saddle part of the No.2 ore body	I	Disseminated ore	Fine-grained sphalerite, galena, pyrite, and dolomite are densely disseminated in altered rocks
7	DTZ-2-2	1060 m elevation, saddle part of the No.2 ore body	I	Mineralized carbonaceous limestone	Quartz-calcite veins are interspersed with carbonaceous limestone, with black aphanitic sphalerite developed at the edges
8	DTZ-1	1060 m elevation, south flank of the No.2 ore body	I	Mineralized carbonaceous phyllite	The carbonaceous phyllite contains lumpy, disseminated sphalerite, galena, and pyrite
9	DTZ-3-4	1060 m elevation, north flank of the No.2 ore body	I	Massive ore	Fine-grained black-brown lumpy sphalerite, with less quartz, pyrite, and galena
10	D41	860 m elevation, south flank of the No.2 ore body	I	Disseminated ore	Fine-grained sphalerite and ankerite are densely disseminated in grayish-black carbonaceous altered rocks
11	D213.2	960 m elevation, north flank of the No.2 ore body	I	Mineralized siliceous rock	Gray-black siliceous rock with disseminated fine-grained pyrite
12	D51-1	795 m elevation, south flank of the No.2 ore body	I	Disseminated ore	Fine-grained sphalerite, galena, pyrite, and dolomite are densely disseminated in altered rocks
13	D61-1	910 m elevation, saddle part of the No.2 ore body	I	Disseminated ore	Medium-fine-grained dense disseminated sphalerite, pyrite, and arsenopyrite are developed in silicified carbonaceous limestone
14	D229-1	960 m elevation, south flank of the No.2 ore body	I	Banded ore	Banded ankerite-sphalerite-pyrite-galena veins developed in altered carbonaceous limestone
15	D36	910 m elevation, south flank of the No.2 ore body		Granite porphyry dike	NWW-trending granite porphyry dike, nearly parallel to the ore body, with scattered pyrite
16	D55	960 m elevation, south flank of the No.1 ore body	II	Disseminated ore	Quartz-dolomite stockwork developed in the limestone, with fine-grained arsenopyrite and pyrite aggregate developed at the contact area

Table 1. Cont.

No.	Sample	Position	Stage	Type	Description
17	D58	960 m elevation, south flank of the No.1 ore body	II	Disseminated ore	Silicified limestone with disseminated pyrite, interspersed by quartz–dolomite stockwork
18	D107-3	795 m elevation, south flank of the No.2 ore body	II	Massive ore	The massive medium-fine-grained pyrite–sphalerite–arsenopyrite–ankerite aggregates, interspersed by the Stage III coarse-grained calcite and galena veins
19	D109	795 m elevation, south flank of the No.2 ore body	II	Massive ore	Pyrite-rich massive ore, micro-fine grained pyrite aggregates, cementing carbonaceous altered breccia
20	D205.2	795 m elevation, south flank of the No.2 ore body	II	Vein type ore	Veinlets composed of quartz, calcite, pyrite, sphalerite, and galena, crosscutting the altered rocks
21	D26	960 m elevation, saddle part of the No.2 ore body	III	Vein type ore	The medium-fine-grained lumpy sphalerite, galena, and calcite vein developed in the altered carbonatite
22	D230	960 m elevation, south flank of the No.2 ore body	III	Disseminated ore	Veinlet-disseminated ore, mineralized siliceous rock crosscutting by quartz–calcite–pyrite veins
23	D37-2	910 m elevation, north flank of the No.1 ore body	III	Gold bearing ore	The altered marl, with disseminated pyrite, interspersed with quartz–dolomite–pyrite vein
24	D223.3	795 m elevation, south flank of the No.2 ore body	III	Gold bearing ore	Dense disseminated pyrite is developed in the altered rock, with quartz–calcite aggregates

4.1. CL and SEM

Thin sections of samples collected from different mining levels, representing different stages of mineralization, were selected for cathodoluminescence (CL) and scanning electron microscopy (SEM) imaging. CL investigation was carried out at State Key Laboratory of Geological Processes and Mineral Resources, China University of Geosciences, using an FEI Quanta 600 (MLA) with EDX and Gatan CL detectors (Gatan, Inc., Warrendale, PA, USA). SEM investigation was carried out at the Institute of Geology, Chinese Academy of Geological Sciences, using a FEI NOVA nanoSEM (Thermo Fisher Scientific, Brno, Czech Republic) equipped with an Oxford X-Max 50 detector (Oxford Instruments, Oxford, UK).

4.2. In Situ S Isotope Analysis

Representative sphalerite, pyrite, and galena crystals of hydrothermal stage I to stage III, pyrite of sedimentary period, and pyrite of granite porphyry dike were selected for in situ LA-MC-ICP-MS sulfur isotope analysis by using a Resonetics-S155 excimer ArF laser ablation system with the Nu Plasma II multicollector ICP-MS (produced by Australian Scientific Instrument, Australia) at the State Key Laboratory of Geological Processes and Mineral Resources, China University of Geosciences, Wuhan. Detailed test methods followed Fu et al. (2016) and Zhu et al. (2016, 2017) [29–31]. The energy fluence of the laser was approximately 3 J/cm². For single spot analysis, the diameter was 33 μm with a laser repetition rate of 8 Hz. The true sulfur isotope ratio was calculated by correction for instrumental mass bias by linear interpolation between the biases calculated from two neighboring standard analyses. Isotope data are reported in delta notation (‰) in comparison with Vienna Cañon Diablo Troilite (V-CDT):

$$\delta^{34}\text{S}_{\text{V-CDT}} = [((^{34}\text{S}/^{32}\text{S})_{\text{sample}} / (^{34}\text{S}/^{32}\text{S})_{\text{V-CDT}}) - 1] \times 10^3$$

where $(^{34}\text{S}/^{32}\text{S})$ sample is the measured $^{34}\text{S}/^{32}\text{S}$ ratio in the sample and $(^{34}\text{S}/^{32}\text{S})_{\text{V-CDT}}$ is defined as 0.044163 [32]. The precision of $^{34}\text{S}/^{32}\text{S}$ analysis is less than 0.00003 (1 σ). An in-house pyrite standard named WS-1 was used to calibrate the mass bias for S isotopes [30]. This consists of a natural pyrite crystal from the Wenshan polymetallic skarn deposit, Yunnan Province, China. The $^{34}\text{S}_{\text{V-CDT}}$ value ($0.3 \pm 0.1\%$) for WS-1 natural pyrite was determined using the CF-IRMS method on a MAT 253 isotope ratio mass spectrometer (Thermo Finnigan, Bremen, Germany) at the Institute of Mineral Resources, Chinese Academy of Geological Sciences, Beijing. Standards were measured before and after every four spot analyses. We also use the pyrite standard to obtain the data of galena and sphalerite, and these data should be considered as rough results due to no proper standard.

4.3. In Situ Pb Isotope Analysis

Twenty-six analysis spots, including pyrite, galena, and sphalerite of hydrothermal stages I–III and pyrite of the granite porphyry dike, were selected for in situ LA-MC-ICP-MS lead isotope analysis. The examination was conducted utilizing a 193 nm laser ablation system (RESOLUTION M-50, ASI) interfaced with a Nu Plasma II multicollector ICP-MS (Wrexham, UK) at the State Key Laboratory of Continental Dynamics, Department of Geology, Northwest University, Xi'an. Homogeneous nano-particulate pressed sulfide powder tablets (PSPTs) served as reference materials to ensure measurement accuracy. Instrument parameters were optimized using the NIST610 standard ($\text{Pb} = 426 \mu\text{g/g}$) [33] to achieve maximal analytical sensitivity, signal stability, and optimal peak shape and alignment. Analytical signals were deduced using the Time Resolved Analysis (TRA) mode, with an integration time of 0.2 s. Each measurement spot encompassed a 30 s background measurement, followed by 50 s of ablation for signal collection, and an additional 120 s for wash time to mitigate memory effects. Galena laser ablation operated at a frequency of 2 Hz with a spot size of 9 μm , while for bismuthinite, the frequency was 6 Hz with a spot size of 30 μm , respectively. The ^{202}Hg , ^{203}Tl , $^{204}\text{Hg}+^{204}\text{Pb}$, ^{205}Tl , ^{206}Pb , ^{207}Pb , and ^{208}Pb ion beams were collected by corresponding Faraday cups. The $^{204}\text{Hg}/^{202}\text{Hg}$ natural abundance ratio (0.229883) was used to calculate and determine the interference from the ^{204}Hg species on the ^{204}Pb intensity obtained. Analytical procedures, reference material PSPTs, and data processing have been previously described in detail by Chen et al. (2014), Yuan et al. (2015), and Bao et al. (2017) [33–35].

4.4. Rb–Sr Isotope Analyses

The sulfide samples of Stage I were rinsed several times in distilled water, dried, and crushed to 40–60-mesh size. The individual minerals of sphalerite and pyrite were handpicked under a binocular microscope, with purity levels of >98% being used for analysis. Sulfide grains were crushed to <200 mesh using an agate ball mill, then washed in an ultrasonic bath and dried. For Rb–Sr isotope analyses, powder weighing 0.2–0.3 g of each sample were dissolved in Teflon beakers with a mix of HF and HNO₃ acids. Rb–Sr have been separated for isotopic analysis by adopting the resin of AG50W \times 8 and different eluent reagents. Firstly, REEs are separated from Rb–Sr by using the normal method of cation–exchange chromatography with eluent of HCl. Then, Rb and Sr were separated using a cation–ion exchange column.

Sulfide samples underwent Rb–Sr isotopic analyses using a VG 354 mass spectrometer (VG Instruments Group Limited from UK) equipped with five collectors at the Center of Modern Analysis, Nanjing University. The chemical separation and mass spectrometric procedures are outlined by Wang et al. (2006) [36]. $^{87}\text{Sr}/^{86}\text{Sr}$ is normalized to $^{86}\text{Sr}/^{88}\text{Sr} = 0.1194$, to correct for instrumental fractionation. During the period of this study, measurements for the American Standard Reference Material NBS 987 Sr standard gave $^{87}\text{Sr}/^{86}\text{Sr} = 0.710236 \pm 0.000007$ (2σ).

4.5. Sm–Nd Isotope Analyses

The carbonate minerals of ankerite, dolomite, and calcite in the Dongtangzi Zn–Pb deposit were systematically collected from hydrothermal mineralization period sphalerite–galena–pyrite–quartz–ankerite–dolomite–calcite veins within the main orebody, with six samples from Stage I, two from Stage II, and one from Stage III, respectively. These carbonate minerals were separated from the ore samples after crushing and were powdered in an agate mill before Sm–Nd isotopic analysis.

Powders of carbonate mineral specimens underwent dissolution utilizing purified 0.5 M dilute acetic acid at an ambient temperature over a four-hour duration. After centrifugation, acid-insoluble residues underwent digestion employing a mixture of HNO₃, HF, and HClO₄, rendering them amenable for Nd isotopic analyses. The Nd solutions were subjected to separation through conventional ion exchange techniques. The isotopic compositions of the refined Nd solutions were quantified utilizing a VG 354 mass spectrometer equipped with five collectors at the Center of Modern Analysis, Nanjing University. A comprehensive account of the experimental methodology can be found in the reports by Wang Y.X. et al. (2007) [37].

5. Results

5.1. In Situ S Isotopic Compositions

A total of 50 spots were assessed for the in situ sulfur isotope study, covering pyrite from the sedimentary period (n = 4); sulfides from the hydrothermal period in Stage I (n = 23), Stage II (n = 4), and Stage III (n = 15), and pyrite in the granite porphyry dike (n = 4). The results are listed in Table 2.

Table 2. In situ S isotopic composition of the sulfides from the Dongtangzi Zn–Pb deposit.

Sample/Point No.	Stage	Mineral	$\delta^{34}\text{S}$ (‰)
D216.3/1	Sedimentary period	Pyrite	16.9
D216.3/2		Pyrite	15.8
D216.3/5		Pyrite	19.9
D216.3/6		Pyrite	21.4
D216.3/3	Hydrothermal I	Sphalerite	7.3
D216.3/4		Sphalerite	8.7
D41/1		Sphalerite	9.1
D41/2		Pyrite	8.6
D41/3		Sphalerite	9.3
D41/4		Sphalerite	9.4
D41/5		Sphalerite	8.8
D51/1		Pyrite	8
D51/2		Galena	2.7
D51/3		Sphalerite	7.3
D51/4		Sphalerite	7
D51/5		Sphalerite	8
D51/6		Galena	1.4
D51/7		Galena	2.7
D51/8		Pyrite	7.1
D51/9		Sphalerite	7.1
D61/1		Pyrite	5.3
D61/2		Sphalerite	8.6
D61/3		Galena	1.1
D61/4		Sphalerite	8.8
D61/5		Sphalerite	8.9
D213.2/1		Sphalerite	8.3
D213.2/2		Sphalerite	8.8

Table 2. Cont.

Sample/Point No.	Stage	Mineral	$\delta^{34}\text{S}$ (‰)
D36.1/1	Granite porphyry dike	Pyrite	2.1
D36.1/2		Pyrite	4.3
D36.1/3		Pyrite	3.7
D36.1/4		Pyrite	2.5
D205.2/1	Hydrothermal II	Pyrite	7.4
D205.2/2		Chalcopyrite	6.4
D205.2/3	Hydrothermal III	Pyrite	7.3
D205.2/4		Chalcopyrite	6.5
D26/1		Sphalerite	9.9
D26/2		Galena	4.4
D26/3		Sphalerite	9.5
D26/4		Galena	4.8
D26/5		Sphalerite	9.9
D26/6		Pyrite	10.2
D26/7	Sphalerite	9.3	
D26/8	Galena	4.6	
D223.3/1		Pyrite	8.9
D223.3/2		Pyrite	3.8
D223.3/3		Pyrite	5
D223.3/4		Pyrite	4.4
D223.3/5		Pyrite	8.7
D223.3/6		Pyrite	7.2
D223.3/7		Pyrite	8.3

The measured $\delta^{34}\text{S}$ data of pyrite from the sedimentary period and the granite porphyry dike vary from 15.8 to 21.4‰ (averaging 18.5‰), and from 2.1 to 4.3‰ (averaging 3.2‰), respectively. On the other hand, those of the sulfides from the three hydrothermal mineralization stages vary from 1.1 to 9.4‰ (averaging 7.1‰), from 6.4 to 7.4‰ (averaging 6.9‰), and from 3.8 to 10.2‰ (averaging 7.3‰), respectively, showing a relatively restricted range, indicating that there are no significant differences in the source of the sulfur during the hydrothermal mineralization stages.

5.2. In Situ Pb Isotopic Compositions

All the sulfides analyzed have similar lead isotope values and the radioactive lead content is low (Table 3). The $^{206}\text{Pb}/^{204}\text{Pb}$, $^{207}\text{Pb}/^{204}\text{Pb}$, and $^{208}\text{Pb}/^{204}\text{Pb}$ ratios in Stage I are 18.074–18.107, 15.641–15.663, and 38.217–38.764, respectively. Those in Stage II are 18.073–18.082, 15.652–15.659, and 38.301–38.324, respectively. For the Stage III, the ratios are 18.078–18.265, 15.645–15.654, and 38.293–38.310, respectively. For the granite porphyry dike, the ratios are 18.091–18.101, 15.585–15.610, and 38.169–38.241, respectively.

Table 3. In situ Pb isotopic composition of the sulfides from the Dongtangzi Zn-Pb deposit.

Sample/Point No.	Stage	Mineral	$^{208}\text{Pb}/^{204}\text{Pb}$	$^{207}\text{Pb}/^{204}\text{Pb}$	$^{206}\text{Pb}/^{204}\text{Pb}$
D36/1	Granite porphyry dike	Pyrite	38.189 ± 0.010	15.595 ± 0.004	18.091 ± 0.011
D36/2		Pyrite	38.241 ± 0.009	15.61 ± 0.004	18.101 ± 0.003
D36/3		Pyrite	38.169 ± 0.005	15.585 ± 0.002	18.092 ± 0.002
D51/2	Hydrothermal I	Pyrite	38.448 ± 0.005	15.663 ± 0.002	18.076 ± 0.003
D51/3		Pyrite	38.286 ± 0.004	15.652 ± 0.001	18.078 ± 0.002
D51/4		Pyrite	38.324 ± 0.004	15.65 ± 0.002	18.074 ± 0.002
D51/1		Sphalerite	38.764 ± 0.026	15.662 ± 0.005	18.075 ± 0.001
D51/1		Galena	38.336 ± 0.008	15.661 ± 0.003	18.084 ± 0.001

Table 3. Cont.

Sample/Point No.	Stage	Mineral	$^{208}\text{Pb}/^{204}\text{Pb}$	$^{207}\text{Pb}/^{204}\text{Pb}$	$^{206}\text{Pb}/^{204}\text{Pb}$
D51/2		Galena	38.319 ± 0.007	15.654 ± 0.003	18.105 ± 0.002
D51/3		Galena	38.234 ± 0.006	15.647 ± 0.002	18.096 ± 0.002
D51/4		Galena	38.234 ± 0.009	15.646 ± 0.003	18.086 ± 0.002
D61/1		Galena	38.217 ± 0.004	15.643 ± 0.002	18.107 ± 0.005
D61/2		Galena	38.222 ± 0.007	15.642 ± 0.002	18.102 ± 0.003
D61/3		Galena	38.218 ± 0.005	15.641 ± 0.002	18.096 ± 0.002
D61/4		Galena	38.293 ± 0.001	15.647 ± 0.001	18.087 ± 0.002
D61/5		Galena	38.291 ± 0.004	15.645 ± 0.001	18.090 ± 0.003
D205-2/1	Hydrothermal II	Pyrite	38.307 ± 0.024	15.652 ± 0.009	18.074 ± 0.002
D205-2/2		Pyrite	38.324 ± 0.006	15.659 ± 0.002	18.074 ± 0.002
D205-2/3		Pyrite	38.314 ± 0.005	15.655 ± 0.002	18.073 ± 0.002
D205-2/4		Pyrite	38.321 ± 0.005	15.659 ± 0.002	18.082 ± 0.001
D205-2/5		Pyrite	38.301 ± 0.007	15.65 ± 0.003	18.080 ± 0.001
D26/1	Hydrothermal III	Galena	38.301 ± 0.007	15.646 ± 0.003	18.097 ± 0.002
D26/2		Galena	38.306 ± 0.005	15.649 ± 0.024	18.086 ± 0.003
D26/3		Galena	38.299 ± 0.006	15.646 ± 0.002	18.091 ± 0.004
D26/4		Galena	38.293 ± 0.003	15.645 ± 0.001	18.265 ± 0.005
D26/5		Galena	38.310 ± 0.003	15.654 ± 0.001	18.078 ± 0.002

5.3. Rb–Sr Isochron Age

The analytical data are listed in Table 4. The Rb contents of the samples are low, ranging from 0.235×10^{-6} to 1.207×10^{-6} , and the Sr contents are also low, ranging from 0.3105×10^{-6} to 5.218×10^{-6} . The $^{87}\text{Rb}/^{86}\text{Sr}$ values range from 0.528 to 6.971. The $^{87}\text{Sr}/^{86}\text{Sr}$ values have a wide range, from 0.71204 to 0.73148. Regression and age calculations of isochrons were performed using Isoplot/Ex Version 3.00 software [38] and with $\lambda = 1.42 \times 10^{-11} \text{ a}^{-1}$, using 1% errors for $^{87}\text{Rb}/^{86}\text{Sr}$ ratios and 0.05% errors for $^{87}\text{Sr}/^{86}\text{Sr}$ ratios at a confidence level of 95%. The analytical data yielded an isochron age of $211.6 \pm 2.6 \text{ Ma}$ for mineralization in Stage I, with an initial $^{87}\text{Sr}/^{86}\text{Sr}$ ratio of 0.71046 ± 0.00012 and an MSWD value of 0.31 (Figure 9a).

Table 4. Analytical data of Rb–Sr isotope ratios and Rb–Sr contents.

Sample No.	Mineral	Stage	Rb ($\mu\text{g/g}$)	Sr ($\mu\text{g/g}$)	$^{87}\text{Rb}/^{86}\text{Sr}$	$^{87}\text{Sr}/^{86}\text{Sr}$	2σ
DTZ-2-2	Spalerite	I	0.4932	2.7590	0.5278	0.712041	0.000008
DTZ-1	Pyrite	I	1.2070	5.2180	0.6794	0.712506	0.000008
DTZ-1	Galena	I	0.2347	0.3742	1.8150	0.715902	0.000009
DTZ-1	Spalerite	I	0.7834	1.6930	1.3620	0.714581	0.000010
DTZ-3-4	Galena	I	0.3728	0.3105	3.5470	0.721159	0.000008
DTZ-3-4	Spalerite	I	0.9346	0.3957	6.9710	0.731475	0.000009

Considering the potential for physical deformation of the ore, there exists a plausible scenario in which the determined ages might be influenced by tectonic overprint, necessitating further investigation of this aspect. The assessment of $1/\text{Rb}$ versus $^{87}\text{Rb}/^{86}\text{Sr}$ diagrams provides a way through which discern whether the initial $(^{87}\text{Sr}/^{86}\text{Sr})_i$ values remained constant throughout the sulfide growth process [39], thereby enabling an evaluation of data integrity. In the present investigation, the absence of covariation between $1/\text{Rb}$ values and $^{87}\text{Rb}/^{86}\text{Sr}$ (Figure 9b) signifies that the isochron age data are meaningful, offering a reliable age of the ore formation.

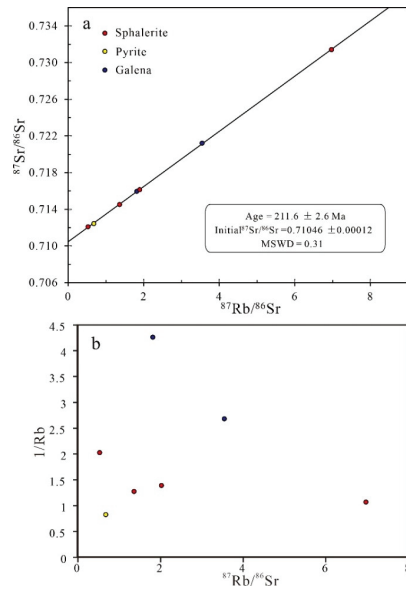


Figure 9. (a) Rb–Sr isochron age of sulfides from the Dongtangzi Zn–Pb deposit; (b) Diagram of $1/\text{Rb}$ versus $^{87}\text{Rb}/^{86}\text{Sr}$.

5.4. Sm–Nd Isochron Age

All $^{143}\text{Nd}/^{144}\text{Nd}$ ratios determined for the ankerite, dolomite, and calcite samples of the hydrothermal mineralization stages analyzed during this study were normalized to $^{146}\text{Nd}/^{144}\text{Nd} = 0.7219$, with results and analytical uncertainties (2σ) given in Table 5. The $^{147}\text{Sm}/^{144}\text{Nd}$ values for carbonate minerals from Stage I range from 0.0731 to 0.7195, with corresponding $^{143}\text{Nd}/^{144}\text{Nd}$ values ranging from 0.511851 and 0.512739.

Table 5. The Sm–Nd isotopic data of the stage I carbonates from the Dongtangzi Zn–Pb deposit.

Sample No.	Mineral	Stage	Sm ($\times 10^{-6}$)	Nd ($\times 10^{-6}$)	$^{147}\text{Sm}/^{144}\text{Nd}$	$^{143}\text{Nd}/^{144}\text{Nd}$
D22	Dolomite	I	0.1605	3.527	0.1351	0.511943 ± 9
D28-4	Ankerite	I	0.6537	2.678	0.7195	0.512739 ± 7
D29-1	Dolomite	I	0.4058	4.634	0.2586	0.512081 ± 8
D45-31	Dolomite	I	0.1325	5.336	0.0731	0.511851 ± 8
D45-32	Dolomite	I	0.3536	5.781	0.1803	0.511982 ± 7
D48	Dolomite	I	0.2953	4.013	0.2175	0.512024 ± 9
D55	Dolomite	II	0.4831	3.907	0.3656	0.512229 ± 14
D58	Calcite	II	0.5029	2.694	0.5498	0.512501 ± 8
D58	Dolomite	II	0.1847	5.325	0.1023	0.511875 ± 9

Regression and age calculations of isochrons were performed using Isoplot/Ex Version 3.00 software [38]. The ratio errors of $^{147}\text{Sm}/^{144}\text{Nd}$ and $^{143}\text{Nd}/^{144}\text{Nd}$ were 1% and 0.03%, respectively. The carbonate minerals yielded an isochron age of 211 ± 4 Ma (Figure 10a), with a mean square of weighted deviate (MSWD) value of 7.3 and an initial $^{143}\text{Nd}/^{144}\text{Nd}$ ratio of 0.511731 ± 0.000009 (Figure 10a). The nonlinear relationship between the plots on the $1/\text{Nd}$ vs. $^{143}\text{Nd}/^{144}\text{Nd}$ diagram (Figure 10b) excludes the possibility of a mixing line. Thus, the Sm–Nd isochron age may represent the mineralization age.

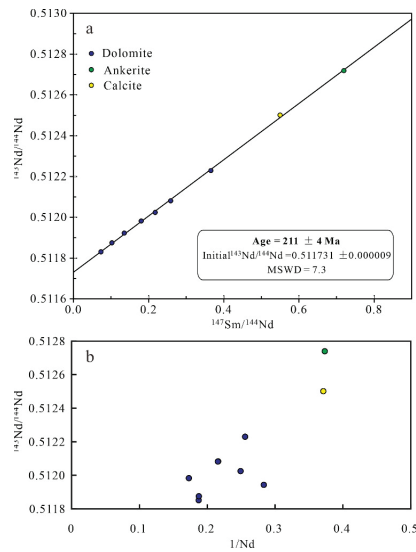


Figure 10. (a) Sm-Nd isochron age diagram of carbonates from the Dongtangzi Zn-Pb deposit; (b) Diagram of $1/\text{Nd}$ vs. $^{143}\text{Nd}/^{144}\text{Nd}$.

6. Discussion

6.1. Sources of Sulfur and Metals

6.1.1. Source of Sulfur

The sulfur isotopic compositions of sulfides extracted from mineral deposits traditionally serve as discerning indicators of sulfur sources, offering insights into ore formation conditions and genesis. Alterations in $\delta^{34}\text{S}$ values are commonly associated with shifts in source, temperature, pH, and oxygen fugacity ($f\text{O}_2$) [40–42]. The array of $\delta^{34}\text{S}$ values within a specific region furnishes valuable information regarding the dynamics of sulfide precipitation, sulfate reduction processes, and the extent of isotopic fractionation, as well as discerning whether the fluid system was open or closed, contingent on a limited or unlimited sulfate supply [41,43,44].

Many views about the sulfur source of Zn-Pb deposits in the Fengtai ore cluster have been proposed, such as (1) a mixed source of reduced sulfur in seawater sulfate and sulfur in deep-sea hydrothermal fluids, via the decomposition of metal sulfide complexes in hydrothermal fluids or a combination of metal chloride complexes in hydrothermal fluids with basinal H_2S [45]; (2) a mixture of ^{32}S -concentrated sulfur formed via a biological reduction with sulfur extracted from the sulfate and sulfide in the sedimentary formation [5]; and (3) seawater sulfate mixed with sulfur that leached from the basement rock [46]. However, previous works have not separately studied different sulfides from different mineralization stages, and no in situ analysis has been conducted, meaning that the mixing of sulfides from different stages and sources has been unavoidable.

Using the most advanced in situ LA-ICP-MS analysis method, in this work, sulfur isotopic compositions of sulfides from different episodes were obtained. Pyrite from the sedimentary period is ^{34}S enriched ($\delta^{34}\text{S}$ 15.8‰~21.4‰), which is identical to the seawater sulfate from the Middle Devonian period [47]. The sulfides from the hydrothermal mineralization period have $\delta^{34}\text{S}$ values ranging from 1.1‰ to 10.2‰, with peak values ranging from 6‰ to 10‰ (Figure 11), partly overlapping that of the granite porphyry dike pyrite (2.1‰~4.3‰) (Table 2, Figure 11). The $\delta^{34}\text{S}$ values obtained in this work can be divided into two main end members: magmatic source (2.1 to 4.3‰) and seawater sulfate source (15.8 to 21.4‰). Moreover, the $\delta^{34}\text{S}$ values of the ore sulfides are between the two end members (1.1‰~10.2‰), indicating a mixed source of magmatic sulfur and seawater

sulfate. Wilkinson and Hitzman (2014) [48] put forward the hypothesis that magmatic heat, originating from the sub-crustal emplacement of mid-crustal sills, may serve as a catalyst for the regional fluid flow associated with Irish-type deposits. Similarly, Slack et al. (2015) [49] demonstrated that the ore-forming fluid of the black shale-hosted Red Dog Zn-Pb-Ag deposit emanated from hydrothermal fluids that leached from mafic and ultramafic rocks at depth. Therefore, contemporaneous magmatic activities at depth could have functioned as a primary or partial source of sulfur in carbonate-hosted Pb-Zn deposits, including the Dongtangzi Zn-Pb deposit.

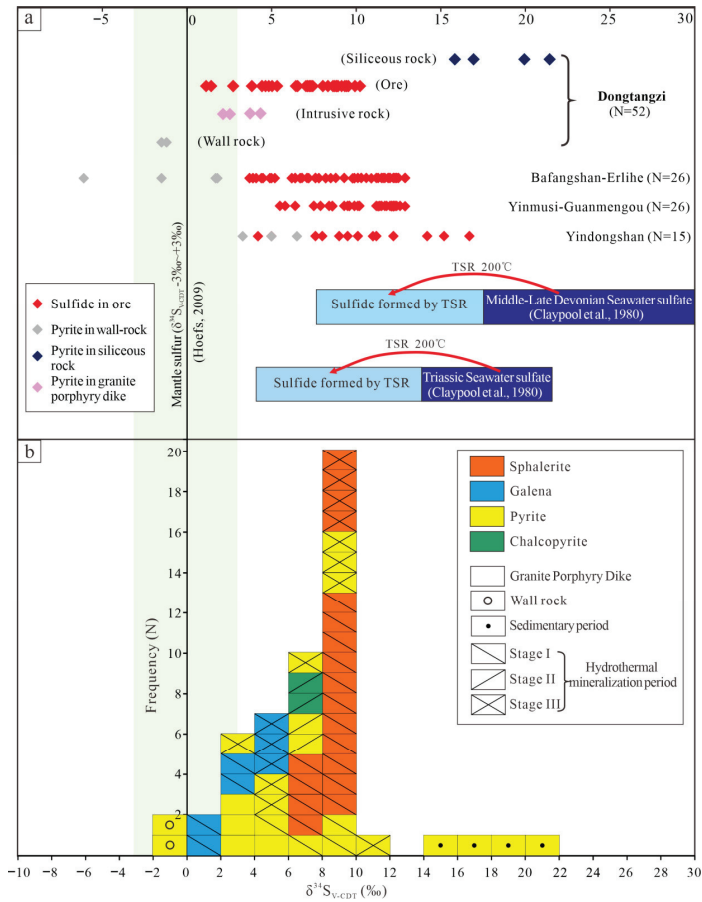


Figure 11. (a) Comparison diagram of sulfur isotope of the Pb-Zn deposits in the Fengtai ore cluster and (b) sulfur isotopic composition histogram of sulfides of the Dongtangzi Zn-Pb deposit. Note: The data of pyrite in the wall rock of the Dongtangzi deposit (gray dots) are from Wang J.L. et al. (1996) [5], and the others are obtained from this work. The data of the Bafangshan–Erlihe, Yinmushi–Guanmengou and Yindongshan deposits are from Hu Q.Q. (2015a) [21], and the data of the Middle–Late Devonian and Triassic Marine sulfate are from Claypool et al. (1980) [49].

Compared with pyrite from the hydrothermal mineralization period (averaging 7.2‰), pyrite from the sedimentary period is remarkably rich in heavy sulfur (averaging 18.5‰), showing a seawater sulfate source, while the values of pyrite in the granite porphyry dike (averaging 3.2‰) are closer to those of mantle-derived sulfur. The veined Stage I sphalerite in the siliceous rock ranges from 7.3 to 8.7‰ (sample D216.3), while the syngenetic

disseminated pyrites from the siliceous rock are the richest in heavy sulfur, ranging from 15.8 to 21.4‰ (sample D216.3), indicating that the sulfides from different stages had not reached isotopic equilibrium, even being hosted in the same thin section. In general, if $\delta^{34}\text{S}_{\text{pyrite}} > \delta^{34}\text{S}_{\text{sphalerite}} > \delta^{34}\text{S}_{\text{galena}}$, then the fractionation of S isotopes among minerals reached equilibrium [50]. The $\delta^{34}\text{S}$ values of the sulfides from the hydrothermal mineralization period show $\delta^{34}\text{S}_{\text{sphalerite}} > \delta^{34}\text{S}_{\text{pyrite}} > \delta^{34}\text{S}_{\text{galena}}$ (Table 2, mineral pairs from samples D51, D61, and D26), demonstrating that sphalerite and galena have reached equilibrium, but pyrite and sphalerite have not. This disequilibrium between pyrite and sphalerite could be explained by the mixing of magmatic sulfur during hydrothermal crystallization.

Wang X. et al. (1996) [19] obtained a range of 165–320 °C for the homogenization temperature of the fluid inclusions in quartz and sphalerite from the main mineralization stage of the Dongtangzi Zn-Pb deposit. Usually, the thermochemical sulfate reduction (TSR) reaction that occurs at around 200 °C will cause about 10‰ sulfur isotope fractionation between sulfates and reduced sulfurs [51,52]. As the temperature increases, the degree of sulfur isotope fractionation caused by the TSR reaction gradually decreases, and there is generally no obvious sulfur isotope fractionation between sulfide minerals and reduced sulfur during mineral precipitation [53]. Holser and Kaplan (1966) [54] first proposed that the $\delta^{34}\text{S}$ values of seawater reached a minimum in the Middle Devonian period and then rapidly reached a maximum in the late Devonian period (about 17‰ in the Middle Devonian VS. about 30‰ in the Late Devonian period). The rapid increase in global seawater sulfur isotope values during the Devonian and Early Triassic periods was possibly due to the rapid precipitation of pure sulfide minerals [47].

If the sulfur in the Pb-Zn sulfides of the Dongtangzi deposit mainly comes from Devonian seawater sulfate, then the $\delta^{34}\text{S}$ values of sulfides formed by the seawater sulfate TSR reaction at around 200 °C would be around 12‰ (the light blue area in Figure 11a), which is obviously higher than the measured $\delta^{34}\text{S}$ values (1.1‰~10.2‰, Figure 11a,b). A single TSR process in Devonian seawater sulfate would not result in such a low sulfur isotopic composition; hence, a great deal of light sulfur must have been involved during the mineralization processes. Possible sources include the following: (1) magmatic sulfur since some of the Pb-Zn sulfides have consistent sulfur isotope compositions, with pyrite in the granite porphyry dike (2.1 to 4.3‰, Figure 11), as obtained in this study; (2) sulfides enriched in light sulfur isotopes through a biogeochemical reduction reaction (BSR) in the seawater sulfate during sedimentation, which is supported by the light sulfur isotope enriched pyrite ($\delta^{34}\text{S} < 0\text{‰}$) found in the wall rock of the Dongtangzi deposit (−1.5~−1.1‰, Figure 11a); and (3) the seawater sulfate of the Triassic sedimentary basin distributed to the south of the Fengtai ore cluster, because Triassic seawater sulfate is relatively enriched in light sulfur isotopes, which could potentially generate sulfides via TSR (around 8‰; the light blue area in Figure 11a) with similar $\delta^{34}\text{S}$ ranges to the Pb-Zn sulfides in the Dongtangzi deposit (1.1‰~10.2‰, Figure 11a). During the Middle Triassic period, the west Qinling orogenic belt experienced a rapid transformation from Yangtze-type stable shallow carbonate sedimentation to Tethys-type deep-sea thick turbidite sedimentation. The Tethys-type rift basin opened in the Middle Triassic period, and rapidly closed between the Middle Triassic and early Late Triassic period, developing complexly folded deformation in the rigid massif, sandwiched between the two ancient blocks [55]. This rapid basin closure during Triassic is conducive to the deposition of evaporites, and the subsequent folding deformation provided the possibility of dissolution, infiltration, and long-distance transportation of these evaporites. To the southeast of the Fengtai ore cluster, abundant evaporites are developed in the sedimentary rocks of the Middle Triassic Jialingjiang Formation in the northern margin of the Yangtze Block, adjacent to the south Qinling belt, such as the Wadaozi, Huodigou, and Zuoxigou gypsum deposits [56,57].

In short, the sulfur associated with the Zn-Pb mineralization of the Dongtangzi deposit has a mixed source of magmatic sulfur and seawater sulfate of evaporites from regional sedimentary formation, precipitated by TSR.

6.1.2. Source of Lead

Given the markedly diminished concentrations of thorium (Th) and uranium (U) in sulfide minerals, particularly in galena, the accrued influence of U and Th on radiogenic lead (Pb) isotopes within sulfides is deemed negligible, as attested by previous studies [58–60]. Consequently, the lead isotopic ratios derived from galena, sphalerite, and pyrite in the Dongtangzi deposit could represent the isotopic composition of the associated hydrothermal fluids.

Earlier studies suggested that the metals of the Dongtangzi Zn-Pb deposit originated from host Devonian to Carboniferous carbonate rocks [19], and/or from deep magmatic hydrothermal fluid [11]. The lead isotopic composition of the major deposits in the Fengtai ore cluster (e.g., the Qiandongshan, the Yindongliang, the Bafangshan, and the Yinmusi) exhibit a relatively uniform and stable nature, with variations typically smaller than 1% [5]. These findings indicate the presence of stable and normal lead with a high μ -value, suggesting a mixed source of lead originating from the crust within the orogenic belt. Qi et al. (1993) [15] further noted that the sulfur and lead in the lead–zinc deposits of the Fengtai ore cluster originated from two distinct source regions; that is, the sulfur was derived from sea water while the lead originated from the basement rock. Wang X. et al. (1996) [19] proposed that the primary Pb-Zn source of the Pb-Zn deposits in the Fengtai ore cluster was the high-uranium crust rather than the mantle. This ore displayed characteristics of mixed lead, while the source region exhibited typical features associated with orogenic belts. Wang J.L. et al. (1996) [5] further postulated that the initially enriched lead in the ancient strata within the source region underwent leaching by subterranean hot water and was subsequently transported along growth faults to the seafloor, where mineralization occurred. The anomalous lead observed in the ore was attributed to the incorporation of crustal lead during later modification processes [5]. However, prior investigations failed to differentiate sulfides from different mineralization stages and were not conducted in situ, resulting in the unavoidable mixing of lead from various stages and sources within the same sample.

In this study, the in situ Pb isotope compositions of sulfides from different mineralization stages in the Dongtangzi deposit demonstrate a consistent and stable lead isotope composition across different hydrothermal mineralization stages. The narrow range of the bulk isotopic data suggests a single source or else a well-mixed source of Pb (Table 3, Figure 12) [61]. However, the lead isotopic composition of the ore sulfides is different from that of pyrite found in the granite porphyry dikes (Figure 12), indicating that they may have different source regions. In other words, the ore sulfides are close to the upper crust, while the pyrite of the granite porphyry dikes are close to the orogenic belt (Figure 12a). This suggests that the primary origin of the lead–zinc elements may be from upper-crust sources rather than from magmatic sources. The lead isotope composition diagram illustrates that the ore sulfides of the Dongtangzi deposit and Triassic granitic rocks such as the Xiba intrusion in the west Qinling orogen (Figure 12) have similar lead isotope compositions, indicating that they may share the same source area. Meanwhile, the lead isotope compositions of the ore sulfides partially overlap with those of the Neoproterozoic Yaolinghe Group and Bikou Group metamorphic basement rocks (Figure 12) beneath the Fengtai ore cluster. Such Pb isotopic signatures rule out contributions of Pb from the Paleozoic Mianlue oceanic crust (Figure 12).

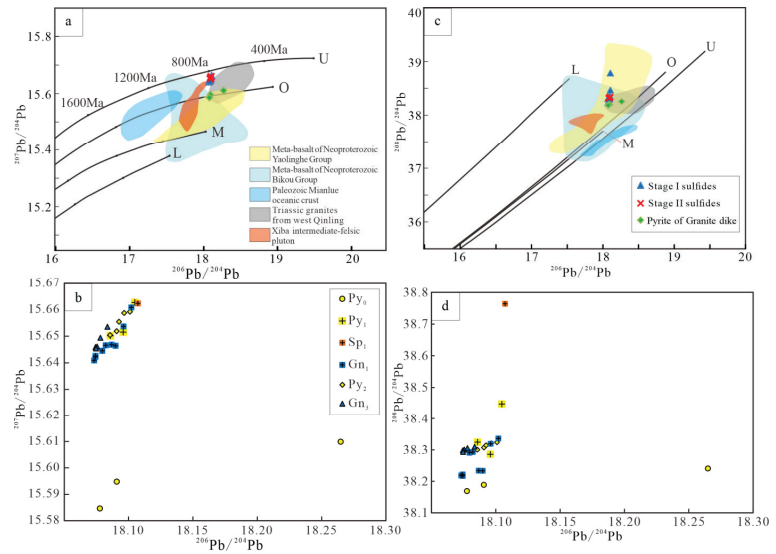


Figure 12. Comparison diagram of lead isotopes of the Dongtangzi Zn-Pb deposit. Plots of $^{206}\text{Pb}/^{204}\text{Pb}$ vs. $^{207}\text{Pb}/^{204}\text{Pb}$ (a,b) and $^{206}\text{Pb}/^{204}\text{Pb}$ vs. $^{208}\text{Pb}/^{204}\text{Pb}$ (c,d). Trends for the upper crust (U), orogenic belt (O), mantle (M), and lower crust (L) are taken from Zartman and Doe (1981) [62]. Data for the Triassic granites from west Qinling orogenic belt are from Zhang et al. (2006), Zhang et al. (2007a, b), Qin et al. (2007, 2008a, 2008b, 2010) [63–66]; the Neoproterozoic Yaolinghe and Bikou meta-volcanic rocks are from Xia et al. (2007, 2008) [67,68]; and the Paleozoic Mianlue oceanic crust are from Xu et al. (2002) [69]. Py₀: pyrite of sedimentary period; Py₁, Py₂: pyrite of the Stage I and Stage II; Sp₁: sphalerite of the Stage I; Gn₁, Gn₃: galena of the Stage III.

These findings suggest that the metallic materials involved in ore formation originate from a mixture of Triassic magmatic hydrothermal fluid and metamorphic basement. The remarkably homogeneous lead isotope composition of the ore sulfide (Table 3, Figure 12) mirrors that of global Mississippi Valley-type (MVT) or SEDEX-type Pb-Zn deposits [70,71], indicating the thorough mixing of ore-forming fluids within the source region.

6.2. Timing of the Ore Formation

The isotope dating of ore minerals is the best method through which to determine the age of a hydrothermal deposit. Obtaining the age of associated gangue minerals can further determine the metallogenic age. Since different mineral phases have different chemical potential, paragenetic minerals with different chemical properties precipitated from the same ore-forming fluid may have different Rb/Sr and Sm/Nd values. Consequently, for the dating of hydrothermal deposits, the hydrothermal mineral assemblage proves more advantageous than a single-mineral species [72]. The sulfide Rb-Sr isochron dating method has been widely used for dating Pb-Zn deposits [73–82]. Moreover, calcium-bearing minerals such as calcite and fluorite in hydrothermal deposits are ideal objects for Sm-Nd isotopic dating [83–88].

The temporal evolution within a hydrothermal deposit may span several million years, contrasting with a narrower timeframe of hundreds of thousands of years for a cohort of paragenetic hydrothermal minerals. Therefore, in the context of Rb-Sr or Sm-Nd isochron dating, the paragenetic minerals could be treated as having formed synchronously [72].

In order to eliminate submicroscopic fluid inclusions that might have contaminated the results, single sulfide mineral particles were ground to sizes below 200 mesh, followed by ultrasonic cleaning, effectively mitigating the interference from fluid inclusions within the minerals. Following the discriminant diagram proposed by Pettet et al. (1996) [89], the

constancy of the initial $^{87}\text{Sr}/^{86}\text{Sr}$ values during sulfide mineral growth can be determined by utilizing a $1/\text{Rb}\text{-}^{87}\text{Rb}/^{86}\text{Sr}$ relation diagram, thus assessing the validity of the data. The $1/\text{Rb}\text{-}^{87}\text{Rb}/^{86}\text{Sr}$ relation diagram (Figure 9b) demonstrates that the data points do not exhibit linear correlation. The Rb and Sr contents vary across distinct single-mineral sphalerite, galena, and pyrite samples, while the $^{87}\text{Sr}/^{86}\text{Sr}$ and $^{87}\text{Rb}/^{86}\text{Sr}$ values remain relatively stable. This observation indicates that the initial $^{87}\text{Sr}/^{86}\text{Sr}$ values of sphalerite, galena, and pyrite remain essentially unchanged during their growth, lending geological significance to the derived isochron ages, and effectively representing the primary mineralization age. The fundamental premise of Sm-Nd isochron dating for hydrothermal minerals is homogeneity, contemporaneity, and closure of the isotopic system. To ensure the basic conditions of contemporaneity and homogeneity of all samples, in this study, the samples were carbonates associated with the ore sulfides of the main ore-forming stage (mineralization Stages I and II). Additionally, there is no linear relationship between $1/\text{Nd}$ and $^{143}\text{Nd}/^{144}\text{Nd}$ (Figure 11b), indicating that the isochron formed by the nine data points (Figure 11a) has practical significance and could represent the primary ore-forming age.

The isochron ages of sulfides Rb-Sr (211.6 ± 2.6 Ma, Figure 10a) and carbonates Sm-Nd (211 ± 4 Ma, Figure 11a) are closely consistent within the error range, indicating that the main mineralization stage of the Dongtangzi Pb-Zn deposit occurred at about 211 Ma; that is, during the Late Triassic period.

The ages of some Zn-Pb and Au deposits in the Fengtai ore cluster have been reported. For instance, the Bafangshan–Erlihe Zn-Pb-Cu deposit has yielded a pyrite Re-Os isochron age of 226 ± 17 Ma [90] and a sphalerite Rb–Sr isochron age of 220.7 ± 7.3 Ma [91]. A quartz $^{40}\text{Ar}\text{-}^{39}\text{Ar}$ isochron age of 222.1 ± 3.5 Ma [92], a muscovite $^{40}\text{Ar}\text{-}^{39}\text{Ar}$ age of 209.5 ± 1.4 Ma, and Sm-Nd isochron ages of 209–208 Ma [93] have been obtained for the large Baguamiao gold deposit. Moreover, a sphalerite Rb-Sr isochron age of 210.2 ± 2.4 Ma [23] has been determined for the Chaima gold deposit. In addition, to the west of the Fengtai ore cluster, the giant Changba–Lijiagou Pb-Zn deposit has a sulfide Rb-Sr isochron age of 222.3 ± 2.2 Ma [77]. The large Liba gold deposit has yielded a mica $^{40}\text{Ar}\text{-}^{39}\text{Ar}$ age of 216.4 ± 1.5 Ma [94].

Similar ages have been obtained from the igneous rocks of the Fengtai ore cluster. For example, the NWW-trending granite porphyry dike of the Dongtangzi deposit has yielded a zircon U-Pb age of 221.3 ± 1.4 Ma [25]; the granite porphyry dike and the NE-trending diorite dikes crosscutting the main orebody of the Bafangshan–Erlihe deposit and those within the mine area have yielded zircon U-Pb ages of 217.9 ± 4.5 Ma and 221 ± 3 Ma [21], respectively. Furthermore, the monzonitic granite and granodiorite of the Xiba pluton (Figure 1c) yielded zircon U-Pb ages of 219 ± 1 Ma and 218 ± 1 Ma, respectively [95]. The ages of the Taibai and Baoji plutons to the north of the Fengtai ore cluster are 216 Ma [96] and 216 to 210 Ma [97], respectively. The main ages of the west Qinling magmatic belt lie within a similar age range of approximately 220 Ma to 205 Ma [63,98]. In summary, the ages of the polymetallic deposits in west Qinling range from 231 to 197 Ma and are concentrated at around 220–200 Ma. On the other hand, the ages of the magmatic rocks range from 248 to 195 Ma and are concentrated at around 230–200 Ma [16].

The ages described above indicate that the Zn-Pb metallogenic events, magmatic activities, and regional tectonic processes of the west Qinling orogenic belt are consistent in time [23,99] and are closely related to the collisional processes that occurred between the Qinling micro-block and the Yangtze block along the Mianlue suture zone during the Late Triassic to Middle Jurassic periods [99,100].

6.3. Ore Genesis

As mentioned above, the M-shaped anticline structure hosting the Dongtangzi Zn-Pb deposit could be regarded as the first-order ore-controlling factor. Structural deformation, hydrothermal fracture filling, hydrothermal replacement mineralization, and intense wall rock alteration occurred after sedimentation and diagenesis. Additionally, the foreland basin environment that formed the ore-hosting Devonian carbonate and clastic rocks [55] is

totally different from that of the SEDEX Pb-Zn deposits in the world, which formed in intra- and/or epicratonic rifts and passive margin environments [71,101]. Therefore, the Zn-Pb enrichment in this area should be dominated by epigenetic hydrothermal mineralization rather than syngenetic exhalative sedimentary processes.

By combining the results of the Rb-Sr and Sm-Nd chronology and in situ S-Pb isotopic research conducted in this study, the genesis of the Dongtangzi Zn-Pb deposit can be attributed to epigenetic hydrothermal fluid processes driven by Late Triassic regional tectono-magmatic activities. This work has promising implications for our understanding of the analogous Zn-Pb deposits of the west Qinling orogenic belt, given their similar geological settings and metallogenic characteristics.

7. Conclusions

The in situ S-Pb isotopic analysis of sulfides from different episodes indicates that the sulfur and Zn-Pb of the Dongtangzi Zn-Pb deposit originated from mixed sources of magmatic fluid and regional metamorphic basement via TSR reaction.

The Stage I ore sulfides and the associated carbonate minerals yielded Rb-Sr and Sm-Nd isochron ages of 211.6 ± 2.6 Ma and 211 ± 4 Ma, respectively.

The Dongtangzi Zn-Pb deposit is an epigenetic hydrothermal deposit driven by Late Triassic regional tectono-magmatic activities, corresponding with the collisional processes that occurred between the Qinling micro-block and the Yangtze block along the Mianlue suture zone.

Author Contributions: Investigation, Q.H., Y.W., S.C., R.W. (Ran Wei), X.L., C.W., M.T. and W.W.; data curation, Q.H., Y.W. and J.L.; writing—original draft preparation, Q.H. and Y.W.; writing—review and editing, Y.W. and Q.H.; project administration, R.W. (Ruiting Wang) and W.G. All authors have read and agreed to the published version of the manuscript.

Funding: This work was funded by the Ministry of Science and Technology of China (2016YFC0600106), the National Sciences Foundation of China (41372089), and the Fundamental Research Funds for the Central Public Welfare Research Institutes (K1607).

Data Availability Statement: Data that support the findings of this study are available from the corresponding author upon reasonable request.

Acknowledgments: We are grateful to the Baoji No.717 Corps Limited of Northwest Nonferrous Geological and Mining Group for their enthusiastic help with the field work. Thanks to the editors for their efforts and important advice. Many thanks to the three anonymous reviewers and the Academic Editor for their careful comments and constructive suggestions.

Conflicts of Interest: The authors declare that this study received funding from Ministry of Science and Technology of China, the National Sciences Foundation of China, and the Fundamental Research Funds for the Central Public Welfare Research Institutes. The funders were not involved in the study design, collection, analysis, interpretation of data, the writing of this article or the decision to submit it for publication. Ruiting Wang, Weihong Gao, Changan Wang, Minjie Tang and Wentang Wu are employees of Northwest Nonferrous Geological and Mining Group Co., Ltd. The paper reflects the views of the scientists and not the company.

References

1. Wang, R.T.; Wang, T.; Gao, Z.J.; Chen, E.H.; Liu, L.X. The main metal deposits metallogenic series and exploration direction in Feng-Tai Ore Cluster Region, Shaanxi Province. *West. Geol.* **2007**, *40*, 77–84. (In Chinese with English Abstract)
2. Li, J.H. Analysis on ore-controlling factors and prospecting potential of the Baguamiao-type gold deposits in Fengtai area, Shaanxi. *Miner. Resour. Geol.* **2008**, *22*, 62–64. (In Chinese with English Abstract)
3. Wu, X.D.; Song, S.K.; Gao, W.H.; Yang, S.W.; Zhang, X.G. Geological Characteristics and Prospecting Direction of Lead-Zinc Mine in Shaanxi Qiandongshan-Dongtangzi. *Gansu Metall.* **2016**, *38*, 87–94. (In Chinese with English Abstract)
4. Zhang, F.X. Characteristics and geological significance of the strawberry-like sulfide mineral in the lead-zinc deposit of Qiandongshan and Yinmusi in Shaanxi province. *Geol. Prospect.* **1986**, *22*, 40–42.
5. Wang, J.L.; He, B.C.; Li, J.Z.; He, D.R. *Qinling-Type Lead-Zinc Ore Deposits in China*; Geological Publishing House: Beijing, China, 1996; pp. 116–145. (In Chinese with English Abstract)

6. Wang, Y.T.; Hu, Q.Q.; Wang, R.T.; Gao, W.H.; Chen, S.C.; Wei, R.; Wang, C.A.; Wen, B.; Wen, S.W.; Tang, M.J. A new metallogenic model and its significance in search for Zn-Pb deposits in Fengtai (Fengxian-Taibai) polymetallic ore concentration area, Shaanxi Province. *Miner. Deposits* **2020**, *39*, 587–606. (In Chinese with English Abstract)
7. Fang, W.X. Research on mineral geochemistry of Qiandongshan Lead-Zinc deposit, a large-sized deposit in Fengxian County, Shaanxi. *Acta Mineral. Sinica* **1999**, *19*, 198–205. (In Chinese with English Abstract)
8. Fang, W.X. Characteristics of sedimentary facies of hydrothermal for the giant Qiandongshan Lead-zinc ore deposit, Feng County, Shaanxi Province. *Acta Sedimentol. Sinica* **1999**, *17*, 44–50. (In Chinese with English Abstract)
9. Huang, Z.Y.; Lu, R.A. Zoning characteristics and index of primary geochemical anomalies in Qiandongshan Pb-Zn deposit Shaanxi Province, China. *Geol. Prospec.* **2003**, *39*, 39–44. (In Chinese with English Abstract)
10. Ren, P.; Liang, T.; Liu, K.L.; Niu, L.; Lu, L.; Zhang, W.J. Geochemistry of Sulfur and Lead Isotopic Compositions of Sedex Lead-zinc Deposits in Fengtai Mineral Cluster Region of Qinling Mountains. *Northwest. Geol.* **2014**, *47*, 137–149. (In Chinese with English Abstract)
11. Zhang, G.L.; Tian, T.; Wang, R.T.; Gao, W.H.; Chang, Z.D. S, Pb isotopic composition of the Dongtangzi Pb–Zn deposit in the Fengtai ore concentration area of Shaanxi Province for tracing sources of ore-forming materials. *Geol. China* **2020**, *47*, 472–484. (In Chinese with English Abstract)
12. Li, H. Sulfides typomorphism and genesis of the Qiandongshan Pb–Zn deposit in Feng Country. *Geol. Prospect.* **1986**, *22*, 36–41. (In Chinese)
13. Yang, X.K. Comments on the genesis of the Qiandongshan Pb–Zn deposit in Fengtai area, Qinling. *Northwest Geol.* **1991**, *4*, 52–55. (In Chinese)
14. Li, J.Z.; He, D.R.; Wu, J.M. The Qinling-type Lead and Zinc ore deposit. *Acta Geol. Sinica* **1992**, *66*, 257–268.
15. Qi, S.J.; Li, Y. *The Types and Ore-Controlling Factors of Lead-Zinc Deposits in the Devonian Metallogenic Belt of Qinling Mountain*; Geological Publishing House: Beijing, China, 1993; pp. 1–178. (In Chinese with English Abstract)
16. Wang, Y.T.; Mao, J.W.; Hu, Q.Q.; Wei, R.; Chen, S.C. Characteristics and Metallogeny of Triassic polymetallic mineralization in Xicheng and Fengtai ore cluster zones, west Qinling, China and their implications for prospecting targets. *J. Earth Sci. Environ.* **2021**, *43*, 409–435. (In Chinese with English Abstract)
17. Shi, Y.H.; Wang, Y.; Chen, B.L.; Tan, R.W.; Gao, Y.; Shen, J.H. Characteristics of silicon-calcium surface ore-controlling in Fengtai ore-concentration areas, West Qinling Mountains: Examples from Qiandongshan Pb–Zn deposit. *Geol. China* **2022**, *49*, 226–240. (In Chinese with English Abstract)
18. Hu, Q.Q.; Wang, Y.T.; Mao, J.W.; Liu, X.L.; Chen, S.C.; Wei, R.; Zhang, J.; Wang, R.T.; Wang, C.A.; Dai, J.Z.; et al. Genesis of the Bafangshan-Erlihe Zn-Pb-Cu deposit in the Fengxian-Taibai ore cluster, west Qinling, China: Evidence from ore geology and ore-forming fluids. *Ore Geol. Rev.* **2020**, *126*, 103734. [CrossRef]
19. Wang, X.; Tang, R.Y.; Li, S.; Li, Y.X.; Yang, M.J.; Wang, D.S.; Guo, J.; Liu, P.; Liu, R.D.; Li, W.Q. *Qinling Orogeny and Metallogenesis*. Metallurgical Industry Press: Beijing, China, 1996; pp. 187–230. (In Chinese with English Abstract)
20. Zhang, F.X.; Wang, J.F. The submarine volcanic-exhalative-sedimentary origin of Lead-Zinc deposits in the Fengtai ore field, Shaanxi. *Geol. Rev.* **1988**, *34*, 157–168. (In Chinese with English Abstract)
21. Hu, Q.Q. *The Mineralization Features, Mechanism and Metallogenic Regularity of the Fengtai Pb-Zn Polymetallic Ore Cluster in West Qinling*. Ph.D. Thesis, Chinese Academy of Geological Sciences, Beijing, China, 2015.
22. Zhang, G.W.; Cheng, S.Y.; Guo, A.L.; Dong, Y.P.; Lai, S.C.; Yao, A.P. Mianlue paleo-suture on the southern margin of the Central Orogenic System in Qinling-Dabie— with a discussion of the assembly of the main part of the continent of China. *Geol. Bull. China* **2004**, *23*, 846–852. (In Chinese with English Abstract)
23. Wang, Y.T.; Liu, X.L.; Hu, Q.Q.; Zhang, J.; Chen, S.C.; Wang, R.T.; Dai, J.Z.; Gao, W.H.; Wen, S.W.; Chen, M.S.; et al. Rb-Sr isotopic Dating of Vein-like Sphalerites from the Chaima Au Deposit in Fengxian-Taibai Ore-concentration Area, Shaanxi Province and Its Geological Significance. *Northwest. Geol.* **2018**, *51*, 121–132. (In Chinese with English Abstract)
24. Wang, R.; Pang, Z.; Li, Q.; Zhang, G.; Zhang, J.; Cheng, H.; Wu, W.; Yang, H. Metallogenic Model and Prospecting Progress of the Qiandongshan–Dongtangzi Large Pb–Zn Deposit, Fengtai Orefield, West Qinling Orogeny. *Minerals* **2023**, *13*, 1163. [CrossRef]
25. Chen, S.C.; Wang, Y.T.; Yu, J.J.; Hu, Q.Q.; Zhang, J.; Wang, R.T.; Gao, W.H.; Wang, C.A. Petrogenesis of Triassic granitoids in the Fengxian-Taibai ore cluster, Western Qinling Orogen, central China: Implications for tectonic evolution and polymetallic mineralization. *Ore Geol. Rev.* **2020**, *123*, 103577. [CrossRef]
26. Zeng, L.G.; Zhang, J.; Hu, P. Spatio-temporal structure of the mineralization for Fengtai lead-zinc mineral cluster region, Shaanxi. *Geol. Sci. Technol. Inf.* **2009**, *28*, 84–90.
27. Lu, R.S.; Wei, H.M. Characteristics and Genesis of the Silicalites in Hot-Water Sedimentary Lead-Zinc Deposits in the Qinling Mountains. *Acta Petrol. Mineral.* **1992**, *11*, 14–21. (In Chinese with English Abstract)
28. Fang, W.X. Geochemical anomaly pattern and metallogenic model of the Bafangshan polymetallic deposit, Shaanxi. *Geol. Explor. Non-Ferrous Metals* **1997**, *6*, 167–171. (In Chinese with English Abstract)
29. Fu, J.L.; Hu, Z.C.; Zhang, W. In Situ Sulfur Isotopes ($\delta^{34}\text{S}$ and $\delta^{33}\text{S}$) Analyses in Sulfides and Elemental Sulfur Using High Sensitivity Cones Combined with the Addition of Nitrogen by Laser Ablation MC-ICP-MS. *Anal. Chim. Acta* **2016**, *911*, 14–26. [CrossRef]
30. Zhu, Z.Y.; Cook, N.J.; Yang, T.; Ciobanu, C.L.; Zhao, K.D.; Jiang, S.Y. Mapping of sulfur isotopes and trace elements in sulfides by LA-(MC)-ICP-MS: Potential analytical problems, improvements and implications. *Minerals* **2016**, *6*, 14. [CrossRef]

31. Zhu, Z.Y.; Jiang, S.Y.; Ciobanu, C.L.; Yang, T.; Cook, N.J. Sulfur isotope fractionation in pyrite during laser ablation: Implications for laser ablation multiple collector inductively coupled plasma mass spectrometry mapping. *Chem. Geol.* **2017**, *450*, 223–234. [CrossRef]
32. Ding, T.; Valkiers, S.; Kipphardt, H.; De Bievre, P.; Taylor, P.; Gonfiantini, R.; Krouse, R. Calibrated sulfur isotope abundance ratios of three IAEA sulfur isotope reference materials and V-CDT with a reassessment of the atomic weight of sulfur. *Geochim. Cosmochim. Acta* **2001**, *65*, 2433–2437. [CrossRef]
33. Chen, K.Y.; Yuan, H.L.; Bao, Z.A. Accurate and precise in situ determination of lead isotope ratios in NIST, USGS, MPI-DING and CGSG reference glasses using femtosecond laser ablation MC-ICP-MS. *Geostand. Geoanal. Res.* **2014**, *38*, 5–21.
34. Yuan, H.L.; Yin, C.; Chen, K.Y.; Bao, Z.A.; Zong, C.; Dai, M.N.; Lai, S.C.; Wang, R.; Jiang, S.Y. High precision in-situ Pb isotopic analysis of sulfide minerals by femtosecond laser ablation multicollector inductively coupled plasma mass spectrometry. *Sci. China Earth Sci.* **2015**, *58*, 1713–1721. [CrossRef]
35. Bao, Z.A.; Lu, C.; Zong, C.L.; Yuan, H.L.; Chen, K.Y.; Dai, M.N. Development of pressed sulfide powder tablets for in situ sulfur and lead isotope measurement using LA-MC-ICP-MS. *Int. J. Mass Spectrom.* **2017**, *421*, 255–262. [CrossRef]
36. Wang, Y.X.; Gu, L.X.; Zhang, Z.Z.; Wu, C.Z.; Zhang, K.J.; Li, H.M.; Yang, J.D. Geochronology and Nd–Sr–Pb isotopes of the bimodal volcanic rocks of the Bogda rift. *Acta Petrol. Sinica* **2006**, *22*, 1215–1224. (In Chinese with English Abstract)
37. Wang, Y.X.; Yang, J.D.; Chen, J.; Zhang, K.J.; Rao, W.B. The Sr and Nd isotopic variations of the Chinese Loess Plateau during the past 7Ma: Implications for the East Asian winter monsoon and source area of loess. *Palaeogeogr. Palaeoclimatol. Palaeoecol.* **2007**, *249*, 351–361. [CrossRef]
38. Ludwig, K.R. User’s Manual for Isoplot 3.70. A Geochronological Toolkit for Microsoft Excel. *Berkeley Geochronol. Center Spec. Publ.* **2008**, *4*, 1–74.
39. Li, W.B.; Huang, Z.L.; Xu, D.R.; Cheng, J.; Xu, C.; Guan, T. Rb-Sr Isotopic method on Zinc-Lead ore deposits: A review. *Geotecton. Metall.* **2002**, *26*, 436–441. (In Chinese with English Abstract)
40. Ohmoto, H. Systematics of sulfur and carbon isotopes in hydrothermal ore deposits. *Econ. Geol.* **1972**, *67*, 551–578. [CrossRef]
41. Ohmoto, H.; Rye, R.O. Isotopes of sulfur and carbon. In *Geochemistry of Hydrothermal Ore Deposits*; Barnes, H.L., Ed.; Wiley: New York, NY, USA, 1979; pp. 509–567.
42. Wilkin, R.T.; Barnes, H.L. Pyrite formation by reactions of iron monosulfides with dissolved inorganic and organic sulfur species. *Geochim. Cosmochim. Acta* **1996**, *60*, 4167–4179. [CrossRef]
43. Jørgensen, B.B. A theoretical model of the stable sulfur isotope distribution in marine sediments. *Geochim. Cosmochim. Acta* **1979**, *43*, 363–374. [CrossRef]
44. Ohmoto, H. Biogeochemistry of sulfur and the mechanisms of sulfide–sulfate mineralization in Archean oceans. In *Early Organic Evolution: Implications for Mineral and Energy Resources*; Schidlowski, M., Golubic, S., Kimberley, M.M., Mckirdy, D.M., Trudinger, P.A., Eds.; Springer: Berlin, Germany, 1992; pp. 378–397.
45. Wei, H.M.; Lu, R.S. An exploratory study of the source of mineralized materials in the stratabound Pb–Zn–(Cu) ore deposits of the Fengtai ore field in the Qinling Mountains. *J. Xi’an Coll. Geol.* **1990**, *12*, 28–39.
46. Ren, P. Occurrence State and Enrichment Mechanism of Dispersed Elements in Typical Lead-Zinc Deposits of Shaanxi. Master’s Thesis, Chang’an University, Xi’an, China, 2013; pp. 1–69.
47. Claypool, G.E.; Holser, W.T.; Kaplan, I.R.; Hitoshi, S.; Zak, I. The age curves of sulfur and oxygen isotopes in marine sulfate and their mutual interpretation. *Chem. Geol.* **1980**, *28*, 199–260. [CrossRef]
48. Wilkinson, J.; Hitzman, M. The Irish Zn–Pb ore field: The view from 2014. In *Irish Association for Economic Geology: Current Perspectives on Zinc Deposits*; Irish Association for Economic Geology: Dublin, UK, 2014; pp. 59–72.
49. Slack, J.F.; Dumoulin, J.A.; Schmidt, J.M.; Young, L.E.; Rombach, C.S. Paleozoic sedimentary rocks in the Red Dog Zn–Pb–Ag district and vicinity, western Brooks Range, Alaska: Provenance, deposition, and metallogenic significance. *Econ. Geol.* **2004**, *99*, 1385–1414. [CrossRef]
50. Zheng, Y.F.; Chen, J.F. *Steady Isotope Geochemistry*; Science Publishing House: Beijing, China, 2000; pp. 1–64. (In Chinese)
51. Kiyosu, Y.; Krouse, H.R. The role of organic acid in the abiogenic reduction of sulfate and the sulfur isotope effect. *Geochem. J.* **1990**, *24*, 21–27. [CrossRef]
52. Machel, H.G.; Krouse, H.R.; Sassen, R. Products and distinguishing criteria of bacterial and thermochemical sulfate reduction. *Appl. Geochem.* **1995**, *10*, 373–389. [CrossRef]
53. Fry, B.; Gest, H.; Hayes, J.M. Sulfur isotope effects associated with protonation of HS[−] and volatilization of H₂S. *Chem. Geol. Isot. Geosci. Sec.* **1986**, *58*, 253–258. [CrossRef]
54. Holser, W.T.; Kaplan, I.R. Isotope geochemistry of sedimentary sulfates. *Chem. Geol.* **1966**, *1*, 93–135. [CrossRef]
55. Dong, Y.P.; Santosh, M. Tectonic architecture and multiple orogeny of the Qinling orogenic Belt, Central China. *Gondwana Res.* **2016**, *29*, 1–40. [CrossRef]
56. Zheng, W.Z.; Cao, Z.Q.; Wei, Z.; Liu, Z.M.; Xu, S.K.; Deng, X.L. The characteristics, genesis and prospecting significance of “salt-soluble breccia” of Lower Middle Triassic in southern Shaanxi Province. *Geol. Chem. Miner.* **1988**, *2*, 37–43. (In Chinese)
57. Yang, B.; Tan, Y.T. Analysis of metallogenic regularity and prospecting potential of non-metallic minerals in Shaanxi Province. *China Non-Metall. Miner. Ind.* **2018**, *132*, 7–10. (In Chinese)

58. Carr, G.R.; Dean, J.A.; Suppel, D.W.; Heithersay, P.S. Precise lead isotope fingerprinting of hydrothermal activity associated with Ordovician to Carboniferous metallogenic events in the Lachlan fold belt of New South Wales. *Econ. Geol.* **1995**, *90*, 1467–1505. [CrossRef]
59. Muchez, P.; Heijlen, W.; Banks, D.; Blundell, D.; Boni, M.; Grandia, F. Extensional tectonics and the timing and formation of basin-hosted deposit in Europe. *Ore Geol. Rev.* **2005**, *27*, 241–267. [CrossRef]
60. Pass, H.E.; Cooken, D.R.; Davidson, G.; Maas, R.; Dipple, G.; Rees, C.; Ferreira, L.; Taylor, C.; Deyell, C.L. Isotope geochemistry of the northeast zone, Mount Polley alkali Cu-Au-Ag porphyry deposit, British Columbia: A case for carbonate assimilation. *Econ. Geol.* **2014**, *109*, 859–890. [CrossRef]
61. Zhou, J.X.; Wang, X.C.; Wilde, S.A.; Luo, K.; Huang, Z.L.; Wu, T.; Jin, Z.G. New insights into the metallogeny of MVT Zn-Pb deposits: A case study from the Nayongzhi in South China, using field data, fluid compositions, and in situ S-Pb isotopes. *Am. Mineral.* **2018**, *103*, 91–108. [CrossRef]
62. Zartman, R.E.; Haines, S.M. The plumbotectonic model for Pb isotopic systematics among major terrestrial reservoirs—A case for bi-directional transport. *Geochim. Cosmochim. Acta* **1981**, *52*, 1327–1339. [CrossRef]
63. Qin, J.F.; Lai, S.C.; Grapes, R.; Diwu, C.R.; Ju, Y.J.; Li, Y.F. Origin of Late Triassic high-Mg adakitic granitoid rocks from the Dongjiangkou area, Qinling orogen, central China: Implications for subduction of continental crust. *Lithos* **2010**, *120*, 347–367. [CrossRef]
64. Qin, J.F.; Lai, S.C.; Li, Y.F. Slab breakoff model for the Triassic post-collisional adakitic granitoids in the Qinling orogenic belt, central China: Zircon U-Pb ages, geochemistry and Sr-Nd-Pb isotopic constraints. *Int. Geol. Rev.* **2008**, *50*, 1080–1104. [CrossRef]
65. Qin, J.F.; Lai, S.C.; Wang, J.; Li, Y.F. Zircon LA-ICP MS U-Pb age, Sr-Nd-Pb isotopic compositions and geochemistry of the Triassic Wulong granodiorite (South Qinling, Central China) and their petrogenesis significance. *Acta Geologica Sinica* **2008**, *82*, 425–437.
66. Qin, J.F.; Lai, S.C.; Wang, J.; Li, Y.F. The high-Mg# adakite-like tonalites from Xichahe, South Qinling: Its petrogenesis and geological implication. *Int. Geol. Rev.* **2007**, *49*, 1145–1158.
67. Xia, L.Q.; Xia, Z.C.; Li, X.M.; Ma, Z.P.; Xu, X.Y. Petrogenesis of the Yaolinghe group, Wudang group volcanic rocks and basic dyke swarms from eastern part of the South Qinling Mountains. *Northwest Geology* **2008**, *41*, 1–29. (In Chinese with English Abstract)
68. Xia, L.Q.; Xia, Z.C.; Xu, X.Y.; Li, X.M.; Ma, Z.P. Petrogenesis of the Bikou Group volcanic rocks. *Earth Sci. Front.* **2007**, *14*, 84–101.
69. Xu, J.F.; Castillo, P.R.; Li, X.H.; Yu, X.Y.; Zhang, B.R.; Han, Y.W. MORB-type rocks from the Paleo-Tethyan Mian-Lueyang northern ophiolite in the Qinling Mountains, central China: Implications for the source of the low 206Pb/204Pb and high 143Nd/144Nd mantle component in the Indian Ocean. *Earth Planet. Sci. Lett.* **2002**, *198*, 323–337. [CrossRef]
70. Broadbent, G.C.; Myers, R.E.; Wright, J.V. Geology and origin of shale-hosted Zn-Pb-Ag mineralization at the Century deposit, northwest Queensland, Australia. *Econ. Geol.* **1998**, *93*, 1264–1294. [CrossRef]
71. Leach, D.L.; Sangster, D.; Kelley, K.; Large, R.R.; Garven, G.; Gutzmer, J.; Walters, S. Sediment-hosted lead-zinc deposits: A global perspective. *Econ. Geol.* **2005**, *100*, 561–607.
72. Liu, J.M.; Zhao, S.R.; Shen, J.; Jiang, N.; Huo, W.G. Review on direct isotopic dating of hydrothermal ore-forming processes. *Progress Geophys.* **1998**, *13*, 46–55. (In Chinese with English Abstract)
73. Nakai, S.; Halliday, A.N.; Kesler, S.E.; Jones, H.D.; Kyle, J.R.; Lane, T.E. Rb-Sr dating of sphalerites from Mississippi Valley (MVT) ore deposits. *Geochim. Cosmochim. Acta* **1993**, *57*, 417–427. [CrossRef]
74. Nakai, S.; Halliday, A.N.; Kesler, S.E.; Jones, H.D. Rb-Sr dating of sphalerites from Tennessee and the genesis of Mississippi Valley type ore deposits. *Nature* **1990**, *346*, 354–357. [CrossRef]
75. Zhang, R.B.; Liu, J.M.; Ye, J.; Chen, F.K. Chalcopyrite Rb-Sr isochron age dating and its ore-forming significance in Shouwangfen copper deposit, Hebei province. *Acta Petrol. Sinica* **2008**, *24*, 1353–1358. (In Chinese with English Abstract)
76. Zhang, C.Q.; Li, X.H.; Yu, J.J.; Mao, J.W.; Chen, F.K.; Li, H.M. Rb-Sr dating of single sphalerites from the Daliangzi Pb-Zn deposit, Sichuan, and its geological significances. *Geol. Rev.* **2008**, *54*, 532–538. (In Chinese with English Abstract)
77. Hu, Q.Q.; Wang, Y.T.; Mao, J.W.; Wei, R.; Liu, S.Y.; Ye, D.J.; Yuan, Q.H.; Dou, P. Timing of the formation of the Changba-Lijiagou Pb-Zn ore deposit, Gansu Province, China: Evidence from Rb-Sr isotopic dating of sulfides. *J. Asian Earth Sci.* **2015**, *103*, 350–359. [CrossRef]
78. Wang, J.; Duan, D.; Chen, X.; Kong, Z.; Zhang, C.; Zhou, J.; Wu, Y. Neoproterozoic Zn-Pb mineralization in the world-class Sichuan-Yunnan-Guizhou Zn-Pb triangle, southwest China: Insights from apatite geochemistry and in situ sericite Rb-Sr geochronology of the Daxiao deposit. *Ore Geol. Rev.* **2023**, *160*, 105569. [CrossRef]
79. Yu, H.; Gou, X.L.; Zhang, Y.C.; Dong, H.Y.; Tang, J.R.; Cui, Y.Y. Insights into ore genesis of the Beishan Pb-Zn deposit in Guangxi, South China: Evidence from Rb-Sr dating and in-situ S-Pb isotopes. *Ore Geol. Rev.* **2023**, *163*, 105779. [CrossRef]
80. Chen, C.; Lv, X.; Gun, M.; Yang, J. Metallogenic chronology and tectonic setting of the Erdaohe Pb-Zn-Ag deposit in Inner Mongolia, NE China: Constraints from sphalerite Rb-Sr dating, zircon U-Pb dating, and Hf isotope analysis. *Ore Geol. Rev.* **2021**, *134*, 104067. [CrossRef]
81. Yang, F.; Wang, G.; Cao, H.; Li, R.; Tang, L.; Huang, Y.; Zhang, H.; Xue, F.; Jia, W.; Guo, N. Timing of formation of the Hongdonggou Pb-Zn polymetallic ore deposit, Henan Province, China: Evidence from Rb-Sr isotopic dating of sphalerites. *Geosci. Front.* **2017**, *8*, 605–616. [CrossRef]
82. Rosa, D.; Schneider, J.; Chiaradia, M. Timing and metal sources for carbonate-hosted Zn-Pb mineralization in the Franklinian Basin (North Greenland): Constraints from Rb-Sr and Pb isotopes. *Ore Geol. Rev.* **2016**, *79*, 392–407. [CrossRef]

83. Zhou, J.; Huang, Z.; Yan, Z. The origin of the Maozu carbonate-hosted Pb–Zn deposit, southwest China: Constrained by C–O–S–Pb isotopic compositions and Sm–Nd isotopic age. *J. Asian Earth Sci.* **2013**, *73*, 39–47. [CrossRef]
84. Zhang, J.; Wen, H.; Qiu, Y.; Zhang, Y.; Li, C. Ages of sediment-hosted Himalayan Pb–Zn–Cu–Ag polymetallic deposits in the Lanping basin, China: Re–Os geochronology of molybdenite and Sm–Nd dating of calcite. *J. Asian Earth Sci.* **2013**, *73*, 284–295. [CrossRef]
85. Zhang, H.; Ji, W.; Yang, X.; Zhou, J.X.; Sun, C.; Jia, Z.; Hong, J.; Lv, P.; Zhao, Z.; Hou, Q. The origin of the Quemocuo carbonate-hosted Pb–Zn deposit in the Sanjiang Tethyan Belt, SW China: Constrained by Sm–Nd isochronic age and Sr–S–Pb isotope compositions. *Ore Geol. Rev.* **2020**, *117*, 103264. [CrossRef]
86. Xu, L.; Yang, J.H.; Zeng, Q.D.; Xie, L.W.; Zhu, Y.S.; Li, R.; Li, B. Pyrite Rb–Sr, Sm–Nd and Fe isotopic constraints on the age and genesis of the Qingchengzi Pb–Zn deposits, northeastern China. *Ore Geol. Rev.* **2020**, *117*, 103324. [CrossRef]
87. Halliday, A.N.; Shepherd, T.F.; Dickin, A.P.; Chesley, J.T. Sm–Nd evidence for the age and origin of a Mississippi Valley-type ore deposit. *Nature* **1990**, *344*, 54–56. [CrossRef]
88. Nie, F.J.; Bjorlykke, A.B.; Nilsen, K.S. The origin of the Proterozoic Bidjovagge gold–copper deposit, Finnmark, Northern Norway, as deduced from rare earth element and Nd isotope evidences on calcites. *Resour. Geol.* **1999**, *49*, 13–25. [CrossRef]
89. Pettko, T.; Diamond, L.W. Rb–Sr dating of sphalerite based fluid inclusion-host mineral isochrones: A certification of why it works. *Econ. Geol.* **1996**, *91*, 951–956. [CrossRef]
90. Zhang, F.; Liu, S.W.; Li, Q.G.; Sun, Y.L.; Wang, Z.Q.; Yan, Q.R.; Yan, Z. Re–Os and U–Pb Geochronology of the Erlihe Pb–Zn Deposit, Qinling orogenic belt, Central China, and constraints on its deposit genesis. *Acta Geol. Sinica* **2011**, *85*, 673–682. (In English) [CrossRef]
91. Hu, Q.Q.; Wang, Y.T.; Wang, R.T.; Li, J.H.; Dai, J.Z.; Wang, S.Y. Ore-forming time of the Erlihe Pb–Zn deposit in the Fengxian–Taibai ore cluster, Shaanxi Province: Evidence from the Rb–Sr isotopic dating of sphalerites. *Acta Petrol. Sinica* **2012**, *28*, 258–266. (In Chinese with English Abstract)
92. Feng, J.Z.; Wang, D.B.; Wang, X.M.; Shao, S.C.; Ma, Z.G.; Zhang, X.G. Geology and Metallogensis of the Baguamiao Giant Gold Deposit in Fengxian, Shaanxi Province. *Acta Geol. Sinica* **2003**, *77*, 387–398. (In Chinese with English Abstract)
93. Wang, Y.T.; Mao, J.W.; Zhang, J.; Wang, R.T.; Chen, G.M.; Hu, Q.Q.; Chen, S.C.; Liu, X.L. Geochronological constraints on the Baguamiao gold deposit, West Qinling orogen, central China: Implications for ore genesis and geodynamic setting. *Ore Geol. Rev.* **2020**, *122*, 103508. [CrossRef]
94. Zeng, Q.T.; McCuaig, T.C.; Hart, J.R.; Jourdan, F.; Muhling, J.; Bagas, L. Structural and geochronological studies on the Liba goldfield of the West Qinling Orogen, Central China. *Miner. Depos.* **2012**, *47*, 799–819. [CrossRef]
95. Zhang, F.; Liu, S.W.; Li, Q.G.; Wang, Z.Q.; Han, Y.G.; Yang, K.; Wu, F.H. LA–ICP–MS zircon U–Pb geochronology and geological significance of Xiba Granitoids from Qinling, Central China. *Acta Sci. Nat. Univ. Pekin.* **2009**, *45*, 833–840. (In Chinese with English Abstract)
96. Zhang, H.F.; Zhang, L.; Harris, N.; Jin, L.L. U–Pb zircon ages, geochemical and isotopic compositions of granitoids in Songpan–Graze fold belt, eastern Tibetan Plateau: Constraints on petrogenesis and tectonic evolution of the basement. *Contrib. Mineral. Petrol.* **2006**, *152*, 75–88. [CrossRef]
97. Liu, S.W.; Yang, P.T.; Li, Q.G. Indosinian Granitoids and Orogenic processes in the Middle Sagment of the Qinling Orogen, China. *J. Jinlin Univ. Earth Sci. Ed.* **2011**, *41*, 1928–1943. (In Chinese with English Abstract)
98. Sun, W.D.; Li, S.G.; Ya, D.C.; Li, Y.J. Zircon U–Pb dating of granitoids from South Qinling, Central China and their geological significance. *Geochimica* **2000**, *29*, 209–216. (In Chinese with English Abstract)
99. Mao, J.W.; Zhou, Z.H.; Feng, C.Y.; Wang, Y.T.; Zhang, C.Q.; Peng, H.J.; Yu, M. A preliminary study of the Triassic large-scale mineralization in China and its geodynamic setting. *Geol. China* **2012**, *39*, 1437–1471. (In Chinese with English Abstract)
100. Mao, J.W.; Qiu, Y.M.; Goldfarb, R.J.; Zhang, Z.C.; Ren, F.S. Geology, distribution, and classification of gold deposits in the Western Qinling belt, Central China. *Miner. Depos.* **2002**, *37*, 352–377. [CrossRef]
101. Leach, D.L.; Marsh, E.; Emsbo, P.; Rombach, C.; Kelley, K.D.; Reynolds, J.; Anthony, M. Nature of hydrothermal fluids at the shale-hosted Red Dog Zn–Pb–Ag deposits, Brooks Range, Alaska. *Econ. Geol.* **2004**, *99*, 1449–1480. [CrossRef]

Disclaimer/Publisher’s Note: The statements, opinions and data contained in all publications are solely those of the individual author(s) and contributor(s) and not of MDPI and/or the editor(s). MDPI and/or the editor(s) disclaim responsibility for any injury to people or property resulting from any ideas, methods, instructions or products referred to in the content.

Review

Metallogenic Model and Prospecting Progress of the Qiandongshan–Dongtangzi Large Pb–Zn Deposit, Fengtai Orefield, West Qinling Orogeny

Ruiting Wang^{1,*}, Zhenjia Pang¹, Qingfeng Li¹, Geli Zhang², Jiafeng Zhang², Huan Cheng¹, Wentang Wu³ and Hongbo Yang³

¹ Northwest Nonferrous Geological and Mining Group Co., Ltd., Xi'an 710054, China

² Baoji No. 717 Corps Limited of Northwest Nonferrous Geological and Mining Group, Baoji 721015, China

³ Shan'anxi Northwest Nonferrous Lead and Zinc Group Co., Ltd., Baoji 721015, China

* Correspondence: wrtyf@163.com; Tel.: +86-13659288199

Abstract: The Qiandongshan–Dongtangzi large Pb–Zn deposit is located in the Fengxian–Taibai (abbr. Fengtai) polymetallic orofield. The ore bodies primarily occur within and around the contact surface between the limestone of the Gudaoling Formation and the phyllite of the Xinghongpu Formation, which are clearly controlled by anticline and specific lithohorizon. Magmatic rocks are well developed in the mining area, consisting mainly of granitoid plutons and mafic–felsic dikes. Previous metallogenic geochronology studies have yielded a narrow range of ages between 226 and 211 Ma, overlapped by the extensive magmatism during the Late Triassic period in this region. The $\omega(\text{Co})/\omega(\text{Ni})$ ratio of pyrite in lead–zinc ore ranges from 4.44 to 15.57 (avg. 8.56), implying that its genesis is probably related to volcanic and magmatic–hydrothermal fluids. The δD and $\delta^{18}\text{O}$ values (ranging from -94.2‰ to -82‰ , and 18.89‰ to 20.72‰ , respectively) of the ore-bearing quartz indicate that the fluids were perhaps derived from a magmatic source. The $\delta^{34}\text{S}$ values of ore-related sulfides display a relatively narrow range of 4.29‰ to 9.63‰ and less than 10‰ , resembling those of magmatic–hydrothermal origin Pb–Zn deposits. The Pb isotopic composition of the sulfides from the Qiandongshan–Dongtangzi Pb–Zn deposit (with $^{206}\text{Pb}/^{204}\text{Pb}$ ratios of 18.06 to 18.14, the $^{207}\text{Pb}/^{204}\text{Pb}$ ratios of 15.61 to 15.71, and $^{208}\text{Pb}/^{204}\text{Pb}$ ratios of 38.15 to 38.50) is similar to that of the Late Triassic Xiba granite pluton, suggesting that they share the same Pb source. The contents of W, Mo, As, Sb, Hg, Bi, Cd, and other elements associated with magmatic–hydrothermal fluids are high in lead–zinc ores, and the contents of Sn, W, Co, and Ni are also enriched in sphalerite. The contents of trace elements and rare earth elements in the ore are similar to those in the Xiba granite pluton, and they may propose a magmatic–hydrothermal origin as well. As a result of this information, the Qiandongshan–Dongtangzi large Pb–Zn deposit may be classified as a magmatic hydrothermal stratabound type, with the Si/Ca contact area being the ore-forming structural plane. Thus, a mineralization model has been proposed based on a comparative analysis of the geological and geochemical properties of the lead–zinc deposit in the Fengtai orofield. It is considered that the secondary anticlines developed on both wings of the Qiandongshan–Dongtangzi composite anticline are the favorable sites for Pb–Zn deposition. Accordingly, the Si/Ca plane and secondary anticline are the major ore-controlling factors and prospecting targets. The verification project was first set up on the north wing of the composite anticline, and thick lead–zinc ore bodies were found in all verification boreholes, accumulating successful experience for deep exploration of lead–zinc deposits in this region.

Citation: Wang, R.; Pang, Z.; Li, Q.; Zhang, G.; Zhang, J.; Cheng, H.; Wu, W.; Yang, H. Metallogenic Model and Prospecting Progress of the Qiandongshan–Dongtangzi Large Pb–Zn Deposit, Fengtai Orefield, West Qinling Orogeny. *Minerals* **2023**, *13*, 1163. <https://doi.org/10.3390/min13091163>

Academic Editors: Yitian Wang, Changqing Zhang and Maria Boni

Received: 30 June 2023

Revised: 23 August 2023

Accepted: 27 August 2023

Published: 31 August 2023



Copyright: © 2023 by the authors. Licensee MDPI, Basel, Switzerland. This article is an open access article distributed under the terms and conditions of the Creative Commons Attribution (CC BY) license (<https://creativecommons.org/licenses/by/4.0/>).

Keywords: metallogenic model; prospecting progress; lead–zinc deposit; Qiandongshan–Dongtangzi; Fengtai orofield

1. Introduction

The Fengxian–Taibai (abbr. Fengtai) orefield in the Shaanxi Province, which belongs to the middle of the Qinling polymetallic metallogenic belt, is located in the northern margin of the South Qinling orogenic belt, and adjacent to the Shangdan suture zone. It is a famous place for the origin of mineral resources of lead, zinc, gold, etc. [1–3] The lead–zinc deposits were formed in the Late Triassic period and are mainly stratified and stratiform-like in the saddle and the two wings of the anticlinal fold. Since the beginning of this century, with the continuous discovery of shallow surface minerals in this region, the geological prospecting work in the orefield has shifted to the blind stage of depth exploration. Significant progress has been made over the past few decades in the exploration and metallogeny of the Fengtai orefield, represented by the Qiandongshan–Dongtangzi lead–zinc deposit. Exploration has been carried out in the region around the deep and peripheral parts of the known deposits, increasing the lead and zinc resources by approximately 2 million tons [4]. Research efforts on lead–zinc deposits have also deepened, with new understanding and achievements in deposit geology, geochemistry, geochronology, ore genesis, ore-controlling factors, and prospecting prediction. In particular, macro-prospecting and micro-metallogenic research have facilitated each other, which has led to a continuous improvement of the ore genesis and metallogenic model in the Fengtai orefield, showing great prospecting potential [4–8]. Based on this, combined with the prospecting experience, this paper makes a comprehensive study on the regional geological setting, geochemical characteristics, ore-controlling factors, ore-controlling rules, prospecting signs, ore genesis, and prospecting progress of the Qiandongshan–Dongtangzi lead–zinc deposit. A metallogenic model and prospecting targets were established, and exploration prediction and engineering verification were carried out, resulting in significant exploration breakthroughs.

2. Regional Geological Setting

The Fengtai orefield is known as the most developed lead–zinc deposit among the six orefields in the South Qinling metallogenic belt [3]. It is bounded in the north by the Xiangzihe fault (F_2^1), which is a part of the Lixian–Shanyang–Fengzhen fault, in the south by the Jiudianliang fault (F_2^2), which is a part of the west section of the Zhenan–Banyanzhen fault, and in the east by the Cretaceous rifted basin. The Fengtai orefield, as a part of the West Qinling orogeny, has experienced multiple tectono-magmatic activities, especially during the Indosinian period. Correspondingly, various structures are extremely developed, forming approximately rhomboid tectonic units composed of WNW-trending folds and WNW-trending faults (Figure 1).

The outcropping strata in the region are mainly the Middle Devonian Gudaoling Formation, the Late Devonian Xinghongpu Formation, and the Jiuliping Formation (Figure 1). The characteristics of each strata are shown in Figure 2.

The Gudaoling Formation occupies the core of regional WNW-trending anticline, and the Xinghongpu Formation is distributed on the two wings of the WNW-trending anticline. The Jiuliping Formation constitutes the core of regional WNW-trending Guchahe–Yinjiaba syncline (I level). In addition, the Triassic flysch Formation is exposed to the south of the compound fold, while the Cretaceous sedimentary is developed in the north. The WNW-trending faults are well developed in the Fengtai orefield, and the NE-trending faults are mostly post-mineralization faults with some degree of dislocations to the ore bodies.

The intermediate felsic dikes are well developed in the Fengtai orefield. The major intrusions are the Xiba and the Huahongshuping granitic plutons, which are distributed in the central part of the Fengtai orefield and are basically consistent with the direction of the main structural line (NW direction) within the area [6,9] (Zhang, 2010; Hu, 2015). The largest Xiba pluton is mainly composed of granodiorite, quartz diorite, and monzogranite, with hornstone and andalusite developed in the outer contact zone. A combination of previous zircon U–Pb ages indicate that the granitic complex intruded between 219 and 215 Ma [9–11]. The previous geochronological and geochemical data suggested that the Xiba pluton was formed in the Late Indosinian period, and was emplaced under the post-

collision setting after the collision between the North China Craton and the Yangtze Craton along the Mianlue suture zone [1,12,13] The Shuangwang large gold deposit is developed approximately 5 km north of the Xiba pluton, and the Yinmusi medium-sized lead–zinc deposit is developed approximately 15 km in the NW direction. It is believed that the Xiba pluton may provide heat energy and ore-forming material for mineralization [2,14–16]. The Huahongshuping pluton, which was emplaced in the Devonian strata, consists mainly of medium-fine granodiorite, with Late Triassic zircon U–Pb age (214.3 ± 2.7 Ma [8]. Hornfels, skarnization, and wolframite mineralization were locally formed in the contact zone between the Huahongshuping pluton and the wall-rock. Large quantities of marble have been found in the Changgou, Donggou, and other lead–zinc deposits to the south of the Huahongshuping pluton. Barite veins have been locally filled along faults, all of which should be genetically related to the Huahongshuping pluton. Moreover, many kinds of dikes are widely developed individually or in groups, filling in the WNW- and NE-trending faults, ranging from tens of centimeters to several meters in width and tens of meters to 3–4 km in length. Among them, the WNW-trending dikes are dominated by granite porphyry, and the NE-trending dikes are mainly diorite porphyrite and lamprophyre. In addition, there are the Hejiazhuang pluton and Taibai pluton to the northwest and northeast of the orefield.

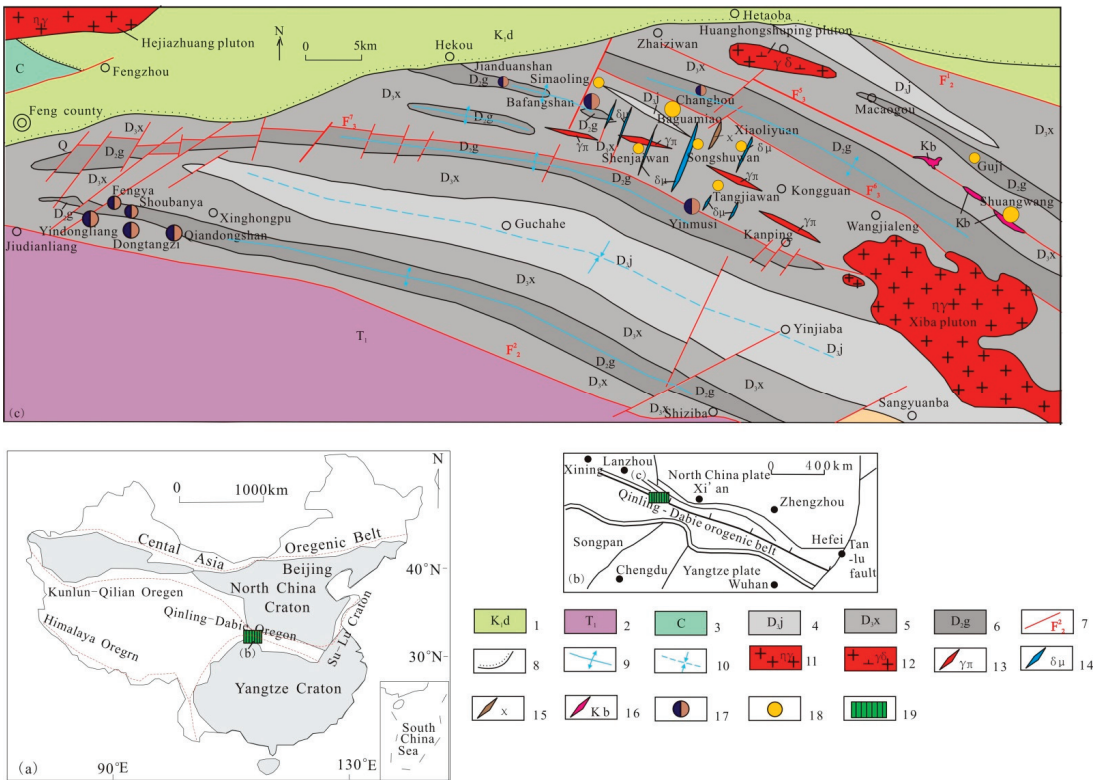


Figure 1. (a)—The location map of the study area in China; (b)—The location of the study area in the Qinling metallogenic belt; (c)—Geological Sketch Map of Mineral Deposits in Fengtai Polymetallic Orefield; 1—Cretaceous Donghe group; 2—Lower Triassic; 3—Carboniferous; 4—Upper Devonian Jiuliping formation; 5—Upper Devonian Xinghongpu Formation; 6—Middle Devonian Gudaoling Formation; 7—Faults and number; 8—Angular unconformity; 9—Axis of synclinorium; 10—Axis of anticline; 11—Monzogranite; 12—Granodiorite; 13—Granite-porphyry dike; 14—Diorite porphyrite dike; 15—Lamprophyre dike; 16—Albite breccia; 17—Lead–zinc deposit (the size is proportional to ore body mass); 18—Gold deposit (the size is proportional to ore body mass.); 19—Study region.







Formation	Code	Columnar section	Thickness	Description
Jiuliping	D _{1j}		1500–2500 (meter)	Metamorphic quartz sandstone and silty slate.
Xinghongpu	D _{3x³}		210–660 (meter)	Iron dolomitic silty phyllite, spotted iron dolomitic silty phyllite mixed with banded marlitized limestone, and the top is carbonaceous silty phyllite. There are gold deposits present.
	D _{3x²}		120–170 (meter)	Chlorite-bearing sericite phyllite with thin layers of microcrystalline limestone and ferruginous sericite phyllite. Irregular quartz veins are widely developed, and a few brachiopod fossils are contained in the thin layers of microcrystalline limestone.
	D _{3x¹} ²		300 (meter)	Ferridolomitic sericite phyllite, locally sandwiched with a small amount of calcareous sericite phyllite.
	D _{3x¹} ¹		90–180 (meter)	Carbonaceous calcareous sericite phyllite with lenticular, banded and thin-layer carbonaceous fine-grained limestone or thin-layer biological fine-grained limestone, followed by calcareous sericite phyllite. Local occurrences of coral, brachiopods, and a few crinoid stems fossils can be observed.
Gudaoling	D _{2g}		>500 (meter)	Thin to middle thick layered carbonaceous biocrystalline limestone, bioclastic limestone, crystalline limestone, and the biological fossils. At the top, there is a layer of silicified altered rock layers with a thickness of several meters to tens of meters, which means that the top is the main ore-bearing layer for lead-zinc deposits in the area. Currently, the large and medium-sized lead-zinc deposits that have been proven are allocated in this layer.

Figure 2. Bar Chart of Main Outcrop Strata in Fengtai Area (Main Bearing Strata of Lead, Zinc, and Gold).

The lead–zinc deposits in the Fengtai orefield are closely associated with anticline structure in this area. The lead–zinc ore bodies in the Fengtai orefield are primarily hosted in the carbon-bearing portion of the transition layer between the top of the Gudaoling Formation and the bottom of the Xinghongpu Formation, where the saddle and wings of the secondary anticline develop, as well as the WNW-trending fault. At present, the phenomenon of correlation between lead and zinc ore bodies and syncline has not been seen in the orefield. From north to south, there are six sub-anticlines (II level), corresponding to six lead–zinc ore belts: (1) the Changgou–Donggou lead–zinc ore belt, with the Baiyanggou, Changgou, Yindongshan, Liushugou, Donggou, Yafangwan, and other small lead–zinc deposits. (2) the Jianduanshan–Bafangshan–Erlihe lead–zinc polymetallic ore belt, with the Bafangshan–Erlihe super-large lead–zinc deposit and Jianduanshan small lead–zinc deposit. (3) the Sanjiaoya–Gangou lead–zinc ore belt, with the Gangou copper ore occurrence. (4) the Yinmusi–Daheigou lead–zinc ore belt, with the Yinmusi medium-sized lead–zinc deposit and Daheigou small-sized lead–zinc deposit. (5) the Magou–Tieluwan lead–zinc ore belt, with the lead–zinc ore occurrence in the contact zone between limestone and phyllite in Xinghongpu Formation. (6) the Qiandongshan–Shuibaigou lead–zinc ore belt is the largest metallogenic belt with the largest amount of proved resources in the area, with large-scale lead–zinc deposits such as Qiandongshan, Dongtangzi, and Yindongliang, as well as medium-sized deposits such as Fengya, Shoubanya, and Heiya.

3. Geology of Qiandongshan–Dongtangzi Lead–Zinc Deposit

3.1. Deposit Geology

3.1.1. Stratigraphy

The carbonate rocks of the Middle Devonian Gudaoling Formation (D_{2g}) and low-grade regionally metamorphosed argillaceous clastic rocks of the Upper Devonian Xinghongpu Formation (D_{3x}) are the dominant lithostratigraphic units in the mining area (Figure 3).

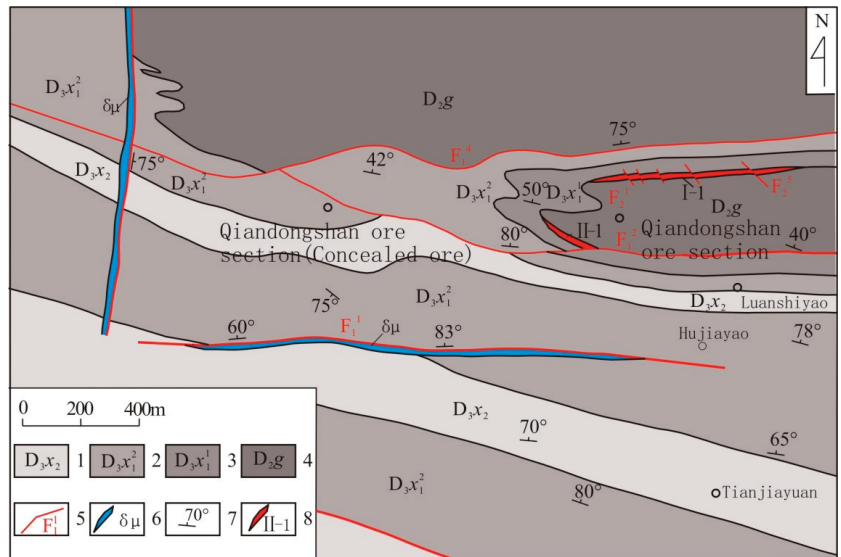


Figure 3. Geological Sketch Map of the Qiangdongshan–Dongtangzi Pb–Zn Deposit; 1—The second lithologic member of the Xinghongpu Formation; 2—The second layer of the first lithologic member of the Xinghongpu formation; 3—The first layer of the first lithologic member of the Xinghongpu Formation; 4—Gudaoling Formation; 5—Faults and number; 6—Diorite porphyrite dike; 7—Attitude of stratum; 8—Lead–zinc deposit and number.

The Middle Devonian Gudaoling Formation is the core unit of the anticlinal structure of the mining area, which is mostly distributed in the central and eastern parts of the mining area. The major lithology includes thin (generally 0.01 m to 0.1 m thick) to middle thick (generally 0.1 m to 0.5 m thick) layered carbonaceous bio-microcrystalline limestone, bio-clastic limestone, crystalline limestone, and fossils of coral, stromatoporoids, and a few brachiopods. The presence of advantageous rock formations such as biolimestone and the associated structural combinations between them often occur in the same mineral deposit, making them beneficial ore-forming structural surface combinations. This is the primary reason for the top layer becoming the main ore-bearing layer of lead–zinc deposition in the mining area. The ore-hosted rocks are silicified limestone, generally several meters to tens of meters thick, which is in integrated contact with the overlying Xinghongpu Formation.

The Upper Devonian Xinghongpu Formation is widely distributed in the mining area, consisting of a set of fine clastic rocks interbedded with carbonate rocks, forming the wings of the anticlinal structure. According to the lithological combination characteristics, it can be divided into three lithological sections (Figure 2), and only the first and second lithologic sections are exposed in the mining area. The first lithological section ($D_3x_1^1$) is distributed nearly in an EW direction. The lower part ($D_3x_1^1$) mainly composed of carbonaceous calcareous sericite phyllite with lenticular, banded, and thin-layer carbonaceous fine-grained limestone or thin-layer biological fine-grained limestone, followed by calcareous sericeous phyllite. Local occurrences of coral, brachiopods, and a few crinoid stems fossils can be observed; The upper part ($D_3x_1^2$) mainly consists of ferridolomitic sericite phyllite, locally sandwiched with a small amount of calcareous sericite phyllite. The second lithological section (D_3x_2) is mainly distributed in the southern part of the mining area. It is composed of chlorite-bearing sericite phyllite with thin layers of microcrystalline limestone and ferruginous sericite phyllite. Irregular quartz veins are widely developed, and a few brachiopod fossils are contained in the thin layers of microcrystalline limestone. It has integrated contact with the overlying formation.

3.1.2. Structure Geology

(1) Fold structure

The fold structures in the mining area are mainly composed of a compound anticline consisting of Qiandongshan–Dongtangzi (III level). The secondary anticline structures (IV level) are well developed and often exhibit tight closures and overturned folds, i.e., overturned southern limb and normal northern limb.

The Qiandongshan–Dongtangzi complex anticline (III level) is located on the southwestern end of the Qiandongshan–Shangtianba–Shuibaigou complex anticline (II level), near the EW direction. The Qiandongshan–Dongtangzi complex anticline (III level) core is only exposed on the surface of Qiandongshan, with an exposed length of more than 11 km in the east–west direction and a width of approximately 120–460 m in the north–south direction. The Qiandongshan–Dongtangzi complex anticline (III level) slopes westward to the Dongtangzi and is a concealed anticline. The strike of the axial plane is oriented between 275° and 285° , with the upper portion approaching a vertical orientation and the lower portion steeply dipping towards the north. The northern wing is normal, with a dip direction angle of $354^\circ-7^\circ$ and a dip angle of $55^\circ-79^\circ$; the southern wing is nearly vertical, with a dip direction angle of $195^\circ-220^\circ$ and a dip angle of $72^\circ-88^\circ$. The lower part is overturned and inclined to the north, with a dip angle of 75° .

In the anticlinal hinge zone, a complex “M”-shaped double-folded structure is formed by the subordinated primary anticline structures (IV level) in the south and north, which is known as the Qiandongshan–Dongtangzi structure (III level). The northern subordinate anticline (IV level) develops on the north side of the transition end of the Qiandongshan–Dongtangzi complex anticline (III level). The strike of the northern subordinate anticlinal ridge is 288° , and the dip angle ranges from 19° to 44° . The southern subordinate anticline (IV level) is developed in the southern side of the transition end of the Qiandongshan–Dongtangzi compound anticline (III level). The southern subordinate anticline dips to the west, with a strike of 282° , and a dip angle ranging from 10° to 38° .

(2) Fault structure

The fault structure in the mining area is well developed and can be divided into two groups based on their distribution orientation: longitudinal fault and transverse fault.

① Longitudinal fault

The longitudinal faults spread in a WNW direction, and most of them developed between the interface of the Gudaoling Formation and the Xinghongpu Formation on both sides of the anticline structure, demonstrating a reverse faulting nature. These structures mainly refer to interlayer detachment faults formed prior to mineralization, which also underwent activity after mineralization, often disrupting the integrity of anticline and syncline structures. The occurrence of faults is consistent with that of the fold axial plane, and locally cut across the bedding planes. Two major longitudinal faults are the F_1^2 and F_1^4 . Among them, the F_1^2 fault is a compression torsional fault, developed in the southwestern part of the mining area, and the southern limb of the Qiandongshan–Dongtangzi compound anticline. The fault has a length of over 1000 m in the surface, dipping direction from 275° to 295° , with a dip direction of north–northeast and a dip angle ranging from 61° to 88° . The fault exhibits a wavy and curved pattern, with a fracture zone width ranging from 0.05 to 3 m. This fault causes the lower part of the first lithological section of the Xinghongpu Formation ($D_3x_1^1$) into direct contact with the second lithological section (D_3x^2), resulting in a vertical drop of approximately 270 m and a horizontal displacement of 14 m in the footwall of the No. II ore body in the Qiandongshan area.

② Transverse fault

The transverse faults occur near the No. I-1 ore body, mainly in the NW direction and secondarily in the NE direction. They are relatively small in size but numerous, appearing at approximately equal intervals along the trend of the ore body, with spacing ranging from several tens of meters to approximately 100 m. These faults formed after the ore-forming period and often cut across the northern limb of the northern subordinate anticline, causing displacement of the strata and the ore body, and are part of the ore-breaking structure. They

mostly exhibit sub-horizontal displacement, accompanied by a small amount of vertical displacement, with horizontal displacement generally ranging from a few meters to over ten meters. This group of faults belongs to a set of the X-conjugated faults caused by shear stress.

3.1.3. Magmatic Phenomena and Hydrothermal Activity

There is no large-scale outcrop of magmatic rocks in the mining area, with only an EW-trending Indosinian diorite dike developed on the surface of the Songjiashan, intruded into the Upper Devonian Xinghongpu Formation, with approximately 1500 m in length and 1–4 m in width. The deep exploration project also revealed the presence of diorite dikes and granite porphyry dikes. The diorite dikes are spread in a NE direction, while the granite porphyry dikes exhibit an almost EW direction. The dikes mostly developed in the southern limb of the Qiandongshan–Dongtangzi compound anticline, and these dikes are intersecting with the No. II-1 ore body.

The quartz veins are very developed in the Dongtangzi lead–zinc deposit, mainly occurring along the stratiform layers. Laterally striking quartz veins are superimposed on them, and large-scale calcite–quartz veins produced in the stratiform layer are developed in the late stage. The entire mineralization process is accompanied by intense hydrothermal activity (Figure 4). Therefore, the mineralization processes of the deposit can be divided into four stages [17]: the sulphide–iron carbonate–quartz vein stage, and the massive sulfide-carbonate stage, and the low-sulfide quartz–calcite vein stage, and thick quartz–carbonate vein stage. The deep drilling control of the Dongtangzi ore section reveals a locally inclined and thick granite porphyry dike exceeding 60 m (true thickness of 30–40 m). The widespread occurrence of dikes suggests the possible existence of concealed intrusive bodies in the deep part.



Figure 4. Network quartz–sulfide veins in the Qiandongshan–Dongtangzi Pb–Zn deposit.

3.2. Geological Characteristics of Ore Body

The large lead–zinc deposit of Qiandongshan–Dongtangzi can be divided into two sections: the Qiandongshan ore section and the Dongtangzi ore section. A total of five lead–zinc bodies have been delineated in the large lead–zinc deposit of Qiandongshan–Dongtangzi, of which No. I-1 and No. II-1 ore bodies are the main ore bodies (Figure 5). The two main ore bodies currently have an estimated resource of approximately 2 million tons of lead and zinc. The ore bodies mainly occur near the Si/Ca interface in the contact zone of the biocrystalline limestone of Gudaoling Formation and the carbonaceous calcareous phyllite of Xinghongpu Formation. The ore body is strictly controlled by the “M”-shaped secondary anticline, resulting in the formation of thick ore bodies in the silicocalcium layer, that is, the size, shape, and occurrence of the ore body are controlled by the Si/Ca structural

plane. The ore body dips to the west of the fold, with its outcrop exhibiting a horizontally positioned “eight” shape at the surface of the Qiandongshan ore section. It becomes a concealed ore body dipping to the eastern side of the Dongtangzi ore section, following the structure of the fold.

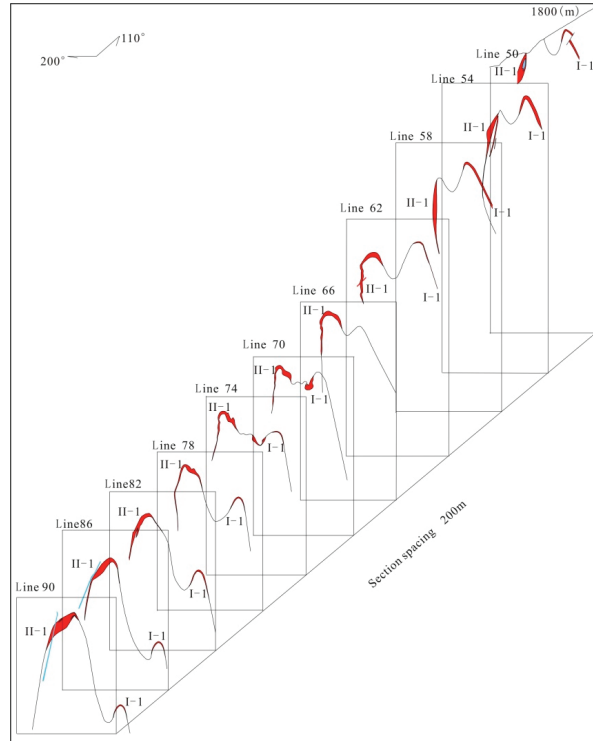


Figure 5. Joint Geological Section Map of the Qiandongshan–Dongtangzi Pb-Zn Deposit.

The No. I-1 ore body is located on both wings and the saddle of the northern secondary fold of the “M” complex anticline, and is strictly controlled by the northern secondary fold. The total length of ore body control exceeded 1700 m (402 m in the Dongtangzi ore section and 1304 m in the Qiandongshan ore section), with thicknesses ranging from 0.91 m to 9.36 m, and an average thickness of 8.14 m. The Pb grade varies from 0.17% to 3.93%, with an average of 1.21%, while the Zn grade ranges from 0.27% to 7.61%, with an average of 5.68%. The ore body is stratified and stratiform-like in shape, consistent with the common occurrences of the medium-low temperature hydrothermal lead–zinc deposit [18], and is not closed to the west. The ore body only appears on the surface (Qiandongshan ore section) with a length of approximately 550 m, but extends to a depth extension of 1350 m. The dip direction of the ore body is 288° , with an upper dip angle of 31° to 39° and a lower dip angle of 33° to 19° . The engineering control extends the ore body inclination to a maximum of 450 m. The dip direction angle of the ore body is oriented between 345° and 7° , with a dip angle of 56° – 79° . The overall continuity of the ore body is good, but there is a barren section of approximately 80–150 m of silicified limestone and biogenic limestone interbedded below the elevation of 1280 m, which separates it into two sub-ore bodies.

The No. II-1 ore body is located on both wings and the saddle of the southern secondary fold of the “M” complex anticline and is strictly controlled by the southern secondary fold. The total length of ore body control is 2300 m (1400 m in the Dongtangzi ore section and 900 m in the Qiandongshan ore section), with a thickness ranging from 0.48 to 40.29 m and maximum thickness in the saddle portion. The average thickness is 12.23 m.

The Pb grade ranges from 0.21% to 4.60%, with an average of 1.44%, while the Zn grade ranges from 0.21% to 11.88%, with an average of 5.51%. The ore body is saddle-shaped in the profile, and the layered and layer-like output on the plane, which is a common form of magmatic hydrothermal ore bodies deposited in carbonate formation [18] and is also a common form of low-temperature hydrothermal lead–zinc ore body controlled by anticline structure and Si/Ca surface. The ore body extends towards the west without being enclosed by a boundary, exhibiting good continuity. Its outcropping length at the surface (in the Qiandongshan mine section) is 65 m, while its length extends to 2000 m in depth. The dip direction of the ore body is between 280° and 288°. The dip angle of the Qiandongshan ore section is between 28° and 34°, while the dip angle of the Dongtangzi ore section is between 22° and 10°. The dip angle of the II-1 ore body becomes more shallow along with the orientation of the ore body to the west. The maximum depth of the ore body by the engineering control is 475 m. The dip direction angle of the northern wing of the ore body is oriented between 0° and 19°, with a dip angle of 48°–75°, while the dip direction angle of the southern wing of the ore body is oriented between 195° and 220°, with a dip angle of 55°–88°, gradually changing from a gentle to steep inclination and ultimately reversing.

According to the exploration data, there is a transition in the proportion of reserves between the I-1 and II-1 ore bodies above an elevation of 1380 m. In the Qiandongshan ore section, the area above the elevation of 1380 m is mainly dominated by the No. I-1 ore body, which accounts for 71% of the total reserves of the entire deposit. Below 1380 m, the No. II-1 ore body gradually becomes the main ore body, where the thickness and grade begin to change. The thickness of No. II-1 ore body increased and the grade becomes higher. Below the elevation of 1080 m, the No. II-1 ore body is the major ore body, and the resource of No. II-1 ore body is more than three times that of No. I-1 ore body.

The deposit exhibits zonation of Pb, Zn–Zn, and Pb–Au from east to west on the plane of the deposit. The Pb–Zn grade decreases from east to west along the trend of the ore body and correlates closely with the variation in thickness of the ore body. The thickness and grade of the ore body at the anticline saddle are the highest and gradually decrease towards the edges until it disappears. In addition to the two main useful elements of lead and zinc, Ag, Cd, Au, and Hg are also associated with the large lead–zinc deposit of Qiandongshan–Dongtangzi, and the amount of Cd resources reaches a large scale.

3.3. Ore Characteristics and Surrounding Rock Alteration

The mineral composition of lead–zinc ore comprises sphalerite, galena, pyrite, chalcopyrite, siderite, tetradymite, pyrolusite, hematite, followed by arsenopyrite, and jamesonite. Gangue minerals include calcite, ankerite, quartz, a small amount of sericite, graphite, chlorite, montmorillonite, organic carbon, etc. The minerals' assemblages in the mining area show obvious characteristics of intermediate- to low-temperature mineralization. The microstructure of ore samples reveals the presence of banded pyrite (Figure 6a), and chalcopyrite replacing galena and sphalerite and galena replacing pyrite (Figure 6b,c).

The structure of ore mainly includes crystal structure, metasomatic structure, fragmentation structure, pressure shadow structure, followed by emulsion structure, corrosion structure, skeleton crystal structure, etc. The ore structure is mainly massive, lenticular, disseminated, and patchy, followed by vein, network vein, and strip. The ore has the structural characteristics of hydrothermal ore deposits.

The natural types of lead–zinc sulfide ore can be divided into disseminated, banded, massive, and vein type sulfide ore according to the structure and mineral combination characteristics of ores.

Overall, the degree of alteration of the wall-rocks in the mining area is relatively weak, with a limited scope of alteration influence. The alteration related to mineralization is extensively developed in the near-ore wall rocks ranging from a few centimeters to 1–2 m in the roof and floor, and could extend up to 3–4 m in the saddle zone. The alteration types are mainly silicification, pyritization, and dolomitization, followed by sericitization and graphitization. The wall-rock alteration has obvious zonation, with silicification occurring

in the central part, while the sides are mainly altered to sericite, showing characteristics of medium- to low-temperature hydrothermal alteration.

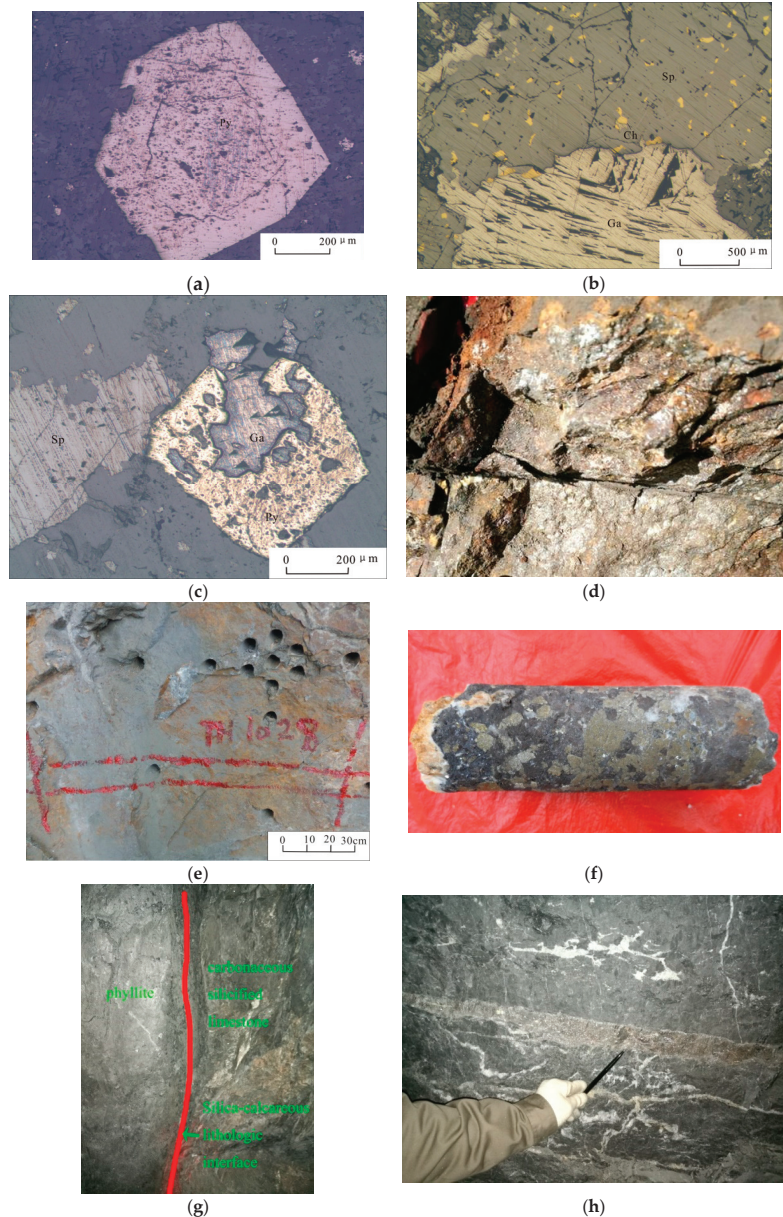


Figure 6. Outcrops and Microscopic Mineralization Characteristics of Pb-Zn Ores in the Qiangongshan–Dongtangzi Pb-Zn Deposit. (a) Ring-banded pyrite occurs in lead-zinc ores; (b) chalcopyrite replacing galena and sphalerite; (c) the skeleton crystal structure formed by galena metasomatism with pyrite; (d) Shuibogou massive sulfide outcrops. (Ag 4.5 g/t, TFe 33.69%); (e) Hetaogou massive sulfide outcrops (Au 10.81 g/t, Ag 3.39 g/t, TFe 31.72%); (f) sulfide aggregate core at 74.33 m of a borehole (Au 3.40 g/t, Ag 47 g/t, Pb 1.06%, Zn 16.5%, Cu 0.18%); (g) main metallogenic structural plane of lead-zinc ore body; (h) the Secondary metallogenic structural plane of lead-zinc ore body.

3.4. Mineralization and Metallogenic Structure

The lead–zinc ore bodies in the Fengtai orefield mainly occur in the depleted space of the contact zone between the limestone of the Gudaoling Formation and the phyllite of the Xing Formation in the anticline core. In addition, vein-like and network-like ore bodies were also found in the internal faults and fissures of limestone in the lower section of the Gudaoling Formation, such as the small-scale ore bodies in the Qiandongshan and Dongtangzi sections. In the lower member of the Xinghongpu Formation, the ore bodies occur in the interbedded fissure of phyllite, such as ore bodies in Bafangshan–Erlihe. The vein-like and layer-like ore bodies in the limestone lens body of the middle section of the Xinghongpu Formation, such as the small lead–zinc deposits in Yafangwan.

Although the magmatic rocks in the Fengtai orefield, where the large Qiandongshan–Dongtangzi lead–zinc deposit is located, are not very developed, in addition to the industrial deposits of lead, zinc, and gold, there are still a number of hydrothermal-related ore (mineralization) points, such as Jiuzigou copper (mineralization) points and Wangjialeng iron point. These iron and copper mineralizations often have a transitional relationship with the lead–zinc deposit in space, forming a metallogenic system related to magmatic hydrothermal fluid. The lead–zinc–copper polymetallic metallogenic belt of Qiandongshan–Weiziping–Tongpaigou, in which Qiandongshan–Dongtangzi Pb–Zn Deposit is located, exhibits obvious mineralization zoning: the west section of Yindongliang–Qiandongshan is mainly lead–zinc mineralization; the middle section of Tieluwan–Jiuzigou is mainly lead–zinc–copper mineralization; and the east section of Wangjiagou–Tongpaigou is dominated by copper mineralization [19]. During surface exploration around the Xiba pluton which extends eastward from the Pb–Zn–Cu polymetallic mineralization zone of Qiandongshan–Weiziping–Tongpaigou, massive sulfide mineralization was observed (Figure 6d,e). Similar rocks were also encountered in shallow drilling (Figure 6f).

The large Pb–Zn deposit is controlled by the anticlinal structure (III level) and the interface of lithology, and the ore body occurs in the contact area between Gudaoling Formation and Xinghongpu Formation. The ore-forming structure of the deposit is a fold-fault tectonic system, that is, the anticlinal and fault compound ore-forming tectonic system, which is the main form controlling the ore belt (orefield) output. Fold structure mainly controls the distribution of deep buried metallogenic geological bodies. The ore-controlling fold structure is Qiandongshan–Dongtangzi complex's anticline and its secondary anticline fold. The ore body is controlled by the WNW fold (III and IV level) and the interlayer fault zone. The anticlinal metallogenic structure and the interface between shallow metamorphic mudstone–clastic carbonate rock formations together form the geochemical barrier for mineralization in the mining area. The main metallogenic structural plane is the lithologic contact interface of Gudaoling Formation limestone and Xinghongpu Formation phyllite, namely the silica–calcium plane (Figure 6g). The secondary structural plane is the fractures in limestone and phyllite near the contact zone (Figure 6h). The main ore bodies occur in the interbedded tectonic belt within the contact zone between the limestone of Gudaoling Formation and the phyllite of Xinghongpu Formation in the saddle part of anticline and the extension part of the two wings. The direct ore-bearing rocks are silicified limestone, silicified phyllite, and quartz veins. The ore body is deposited to the west, the surface section of the surface is stratiform in the plane and section, and the hidden section is parabolic. In the interlayer, faults and fissures locally developed in limestone and phyllite near the contact zone, and there are vein-shaped secondary ore bodies formed by hydrothermal filling. They are controlled by faults, and their scale is generally small, which is a manifestation of the surface ore-controlling characteristics of secondary faults formed by regional tectonic movements.

4. Geochemical Anomaly Characteristics

The 1:50,000 geochemical exploration dispersive flow and stream sediments of the Qiandongshan–Dongtangzi lead–zinc deposit show that seven elements of Pb, Zn, Ag, Au, As, Hg, and Sb are enriched in the area, followed by Cu and Bi relatively enriched,

while eight elements of Ni, Co, Cr, V, Mn, Ti, Mo, and B are relatively depleted. The anomalous element combination of Pb-Zn-Ag-Cu-Au-As-Hg has obvious characteristics of hydrothermal lead-zinc deposit, and the anomalous element combination is basically consistent with the typical hydrothermal lead-zinc deposit in the southeast Guizhou Province [20].

5. Geochemical Characteristics of Deposits

5.1. Pyrite Genesis

The electron probe analysis of the ore samples in the Qiandongshan–Dongtangzi lead–zinc deposit is shown in Table 1. The analysis results of the samples showed that the $\omega(\text{Co})/\omega(\text{Ni})$ values of pyrrhotite were in the range of 4.44 to 15.57, with an average of 8.56. The $\omega(\text{Co})/\omega(\text{Ni})$ values of the vein lead–zinc ore were in the range of 8.25 to 29.20, with an average of 18.70. In the discrimination diagram of Co/Ni ratio, the plots are all located near the evolution line of $\omega(\text{Co})/\omega(\text{Ni}) = 10$, far exceeding the evolutionary line of $\omega(\text{Co})/\omega(\text{Ni}) = 1$. This indicates that it is a magmatic–hydrothermal–origin pyrite [21]. The content of As, Co, and Ni in pyrite are important indicators for determining the genesis of pyrite and distinguishing ore deposit types [22]. In the As-Co-Ni ternary phase diagram, the plots are all located in the volcanic–magmatic–hydrothermal origin area, indicating that pyrite in lead–zinc ores has a volcanic–magmatic–hydrothermal origin.

Table 1. Electron Microprobe Analysis Results of Pyrite in the Qiandongshan–Dongtangzi Pb–Zn Deposit.

Sample Type	Number of Samples	w(Fe)/%	w(S)/%	w(Pb)/ 10^{-6}	w(As)/ 10^{-6}	w(Co)/ 10^{-6}	w(Ni)/ 10^{-6}	w(Cu)/ 10^{-6}	w _{total} /%
Massive ore pyrite	6	46.55	53.31	440.00	3441.67	750.00	41.67	131.67	100.34
The veined ore pyrite	6	46.21	52.69	941.67	7971.67	778.33	21.67	745.00	99.94

Note: Data from [17]; w(.) is the content of elements or compounds; w_{total} indicates the total content.

Previous studies have conducted a statistical analysis on the content of trace elements in sphalerite and pyrite from two types of deposits, i.e., stratiform and hydrothermal type [23,24]. The values obtained from the analysis can be used to distinguish the genetic type of the deposit: The stratiform lead–zinc deposits are characterized by $\omega(\text{Ga}) > 30 \times 10^{-6}$, $\omega(\text{Zn})/\omega(\text{Cd}) > 300$, and $\omega(\text{Co})/\omega(\text{Ni}) < 1.5$, while the hydrothermal lead–zinc deposits exhibit $\omega(\text{Ga}) < 40 \times 10^{-6}$, $\omega(\text{Zn})/\omega(\text{Cd}) < 300$, and $\omega(\text{Co})/\omega(\text{Ni}) > 1.5$. The average content of Ga elements in the ore samples of the Dongtangzi lead–zinc deposit is 13.23×10^{-6} , the average content of $\omega(\text{Zn})/\omega(\text{Cd})$ is 14.65, and the average content of $\omega(\text{Co})/\omega(\text{Ni})$ is 6.17, which also probably proves that the Qiandongshan–Dongtangzi lead–zinc deposit is of magmatic–hydrothermal origin.

5.2. Geochemical Characteristics of Elements

5.2.1. Geochemical Characteristics of Trace Elements

Statistical analysis shows that the Sb content of ore from the Dongtangzi ore section, the Qiandongshan ore section, the Fengya ore section, the Yindongliang ore section, and the Bafangshan–Erlihe lead–zinc mining area ranges from $(9.7\text{--}35) \times 10^{-6}$, while the As $(29.1\text{--}135.5) \times 10^{-6}$, the Hg $(8.22\text{--}135) \times 10^{-6}$, and the Cd $(815\text{--}1000) \times 10^{-6}$ (Table 2) [17,25]. Among them, the content of Sb, Hg, and Cd in lead–zinc ore is significantly higher than that of phyllite, which is two–three orders of magnitude higher than of silicified/mineralized limestone. Furthermore, it is far higher than the average abundance of sedimentary rocks [26]. Since Sb is an indicator element for hydrothermal activity, it indicates that ore-forming materials may be enriched through the hydrothermal process. The content of elements such as, Ag, As, and Bi related to magmatic–hydrothermal activity are significantly higher in lead–zinc ores, reflecting strong hydrothermal activity during mineralization [5]. The content of W and Mo in lead–zinc ore and mineralized limestone are significantly higher than those in bioclastic limestone. These elements, including W,

Mo, As, Sb, Hg, Bi, and Cd are indicator elements of magmatic–hydrothermal activity. The contents of W, Mo, As, Sb, Hg, Bi, and Cd in lead–zinc ore are significantly higher than those in surrounding rocks, indicating a close correlation between magmatic–hydrothermal activity and the lead–zinc mineralization process.

Table 2. Analysis Results of Trace Elements and REE of different Rock types and ore in the Fengtai orefield.

Number of Samples	Dongtangzi Lead Zinc Deposit					Bafangshan—Erlihe Lead—Zinc Deposit					Xiba Pluton			
	3	3	2	2	4	9	2	1	8	3	3	3	3	
Lithology	Rock1	Rock2	Rock3	Rock4	Rock5	Rock6	Rock1	Rock7	Rock5	Rock8	Rock9	Rock10	Rock11	
Au							0.34	0.035	0.038					
Ag							10.57	0.04	0.04					
As							135.5	0.20	0.39					
Cd	682.7	2.37	0.95	0.85	0.15									
Bi							8.22	0.39	3.87					
Cr	4.67	4.03	9.45	7.15	103.6									
Co	51.03	2.53	4.70	16.55	21.80									
Ni	8.27	23.70	9.60	8.70	42.85									
Cu	298.7	3.93	47.45	68.25	15.23									
Zn	>10,000	156.7	12,757	54,050	75.25		222.0	38.00	320.0					
Ga	13.23	0.77	2.40	3.40	22.30									
Rb	6.73	6.03	10.75	8.40	221.2					106.0	74.43	127.3	172.3	
Sr	19.67	344.3	85.30	36.95	97.95					724.3	701.7	542.7	332.3	
Mo	0.37	2.53	4.60	4.30	0.38					0.18	0.59	0.77	0.24	
Cd	682.7	2.37	0.95	0.85	0.15									
In	0.20	0.50	58.15	183.0	0.10									
Sb	9.70	0.00	0.00	0.00	3.55		27.10	0.28	0.06					
Hg							8.22	0.02	0.03					
Ba	250	0.50	0.95	0.75	720.9					1344.3	227.7	419.7	880.7	
W	4.20	0.87	3.35	4.30	4.45									
Tl	0.10	0.10	0.15	0.30	1.00					3552.7	5566	5047.7	1281	
Pb	6422	149.8	1387	36,945	53.30		250.5	9.93	38.70					
La	0.87	2.23	1.65	1.60	42.88	20.77	22.05	25.00	127.2	30.03	24.37	31.57	38.30	
Ce	1.40	3.70	3.15	2.95	75.03	38.20	46.40	56.10	267.1	50.28	46.60	57.80	65.03	
Pr	0.17	0.53	0.45	0.40	9.28	4.35	4.87	6.17	29.70	6.08	5.95	6.94	7.44	
Nd	0.73	1.93	2.10	1.85	33.65	15.63	19.20	23.3	107.4	20.33	23.67	25.77	25.03	
Sm	0.13	0.40	0.70	0.60	4.95	3.01	3.59	4.57	20.53	3.39	4.53	4.56	4.05	
Eu	0.07	0.10	0.15	0.10	1.03	0.60	1.04	1.09	4.00	1.35	1.26	1.19	1.21	
Gd	0.13	0.37	0.60	0.50	4.63	2.39	3.84	4.69	14.84	3.00	3.87	4.09	3.58	
Tb	0.03	0.10	0.15	0.15	0.63	0.35	0.54	0.71	1.96	0.42	0.62	0.60	0.48	
Dy	0.23	0.47	0.90	0.90	3.10	2.53	2.98	3.73	11.90	2.13	3.44	3.24	2.31	
Ho	0.07	0.10	0.20	0.20	0.73	0.38	0.56	0.76	1.60	0.46	0.78	0.73	0.47	
Er	0.17	0.27	0.50	0.55	2.23	1.17	1.77	2.28	5.16	1.20	2.10	1.98	1.43	
Tm	0.00	0.03	0.10	0.15	0.40	0.16	0.25	0.37	0.81	0.21	0.35	0.33	0.21	
Yb	0.23	0.30	0.55	0.70	2.73	1.05	1.70	2.28	6.03	1.36	2.27	2.15	1.43	
Lu	0.00	0.00	0.10	0.10	0.45	0.16	0.23	0.33	0.95	0.21	0.35	0.34	0.23	
Y	1.57	2.53	4.60	4.30	19.78					12.63	21.93	20.83	13.93	
REE	4.23	10.47	11.3	10.75	181.8	90.74	109.0	131.4	599.1	120.5	120.2	141.3	151.2	
LREE	3.37	8.87	8.20	7.50	166.9		97.14	116.2		111.5	106.4	127.9	141.1	
HREE	0.86	1.57	3.10	3.25	14.83		11.86	15.15		8.99	13.78	13.46	10.14	
LREE/HREE	3.92	5.53	2.65	2.31	11.58	3.91	8.19	7.67	5.01	12.40	7.72	9.50	13.91	
(La) _N /(Yb) _N	2.73	5.53	2.10	2.10	11.70	20.38	10.56	10.99	21.40	15.96	7.72	10.64	19.16	
δEu	1.00	0.53	0.75	0.60	0.65	0.68	0.94	0.72	0.66	1.28	0.90	0.83	0.96	
δCe	0.90	0.87	0.90	0.90	0.90	0.93	1.06	1.06	1.01					

Note: Element content unit is 10⁻⁶; Dongtangzi data came from [17]; the data of Bafangshan—Erlihe came from [25]; Xiba rock mass data from [27]; Rock1 is Lead–Zinc ore; Rock2 is Bioclastic limestone; Rock3 is Silicified limestone; Rock4 is Mineralized Silicified limestone; Rock5 is Phyllite; Rock6 is Limestone; Rock7 is Mineral-bearing siliceous rock; Rock8 is Granodiorite; Rock9 is Quartz diorite; Rock10 is Monzonite diorite; and Rock11 is Monzogranite.

The sphalerite in the lead–zinc ore of Dongtangzi ore section is relatively rich in Sn, W, Co, and Ni elements. Sn and W are highly active elements during magmatic–hydrothermal processes, indicating that mineralization is closely related to hydrothermal activities [28]. The galena in the Bafangshan—Erlihe lead–zinc deposit has high contents of Ag, Sb, Bi, and Se. The amounts of Au, Pt, and Pd in the ore samples are much higher than the

crustal average, with a Pt/Pd ratio of 0.34–0.58, which is less than the crustal average value (Pt/Pd = 1). This observation indicates that late-stage hydrothermal activities were relatively intense [25]. The enrichment characteristics of these elements are consistent with the development of quartz and calcite veins formed in the deposit.

On the spider diagram for primitive mantle normalized trace elements (Figure 7), lead–zinc ores and mineralized rocks have similar trace element patterns with granodiorite, quartz diorite, quartz monzonite diorite, and monzonite granite of Xiba pluton, all of which are right-trending. Except for the lead–zinc ores of the Dongtangzi section, the elements in all samples were higher than those in the primitive mantle. The rocks were obviously enriched in large ion lithophile elements such as Rb and relatively depleted in Ti and Ba. The depletion of Ti was caused by the separation and crystallization of plagioclase in the magma, while the depletion of Ba was a result of the residual state of granitic magma. In general, the enrichment characteristics of trace elements in the Qiandongshan–Dongtangzi Pb–Zn deposit are highly similar to those of the Xiba pluton, indicating that this deposit is associated with magmatic–hydrothermal fluids.

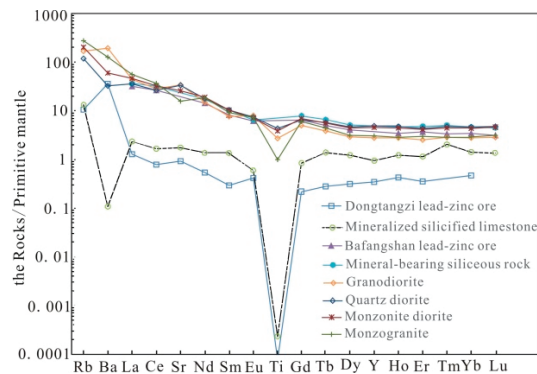


Figure 7. Chondrite-normalized rare earth element and other elements patterns of the Qiandongshan–Dongtangzi rocks.

5.2.2. Geochemical Characteristics of Rare Earth Elements

The average content of total rare earth elements in phyllite from the Dongtangzi ore section is 181.46×10^{-6} , with a LREEs/HREEs ratio of 11.59. LREEs are enriched and there is significant fractionation of rare earth elements, with a negative anomaly of Eu (0.65) and a weak negative anomaly of Ce (0.93). The mean value of the total REE content in bioclastic limestone is 10.47×10^{-6} , with a ratio of LREEs/HREEs is 5.53. LREEs are enriched and there is significant fractionation of rare earth elements, with a negative anomaly of Eu (0.53) and a weak negative anomaly of Ce (0.87). The mean value of the total REE content in silicified limestone is 11.28×10^{-6} . The Eu exhibits a negative anomaly with a value of 0.75, while Ce shows a weak negative anomaly with a value of 0.89. The total content of rare earth elements, as well as the fractionation of light and heavy rare earth elements, in ore-bearing silicified limestone is similar to that in silicified limestone. However, the negative anomaly of Eu in ore-bearing silicified limestone is more prominent. The content of total rare earth elements in lead–zinc ores is 4.33×10^{-6} , with a ratio of LREEs/HREEs is 3.61. The fractionation of light and heavy rare earth elements is small, with an average value of Eu anomaly at 0.97 and Ce anomaly at 0.88. [17]. The composition of rare earth elements suggests that lead–zinc ore is more closely related to hydrothermal origin, and these characteristics are basically consistent with the characteristics of rare earth elements in the Bafangshan–Erlihe mining area [25] (Wang, 2011).

The chondrite normalized REE partition patterns of Pb–Zn ores, ore-bearing siliceous rocks, and Xiba granodiorite, quartz diorite, monzonite diorite, and monzonite granite are very similar (Figure 8), indicating that they have the same material source, all of which are

related to magmatic–hydrothermal fluid. The rare earth element model is characterized by enrichment in light REE, showing no Eu anomaly and negative Ce anomaly, indicating that it is not the product of normal seawater deposition. Furthermore, it also shows a distinct difference in positive Eu anomaly characteristics compared to near-source sulfide ores and volcanic rocks in typical submarine hydrothermal sedimentary deposits [29,30]. There are significant differences in the rare earth element patterns between limestone and other types of rocks, indicating different sources of materials. The rare earth element patterns in lead–zinc ores exhibit weak Eu anomalies, suggesting that they are not the products of normal seawater sedimentation [31]. Additionally, the significant differences in the Eu positive anomaly characteristics between lead–zinc ores and seafloor hydrothermal sedimentary rocks indicate that lead–zinc ores are of hydrothermal origin.

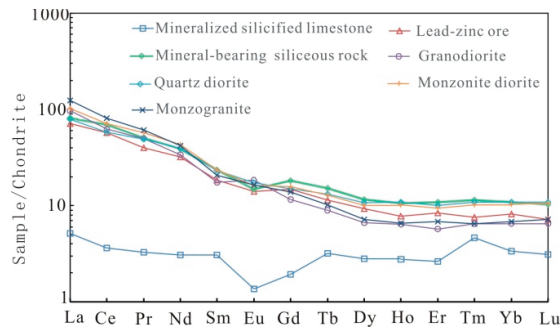


Figure 8. Chondrite REE patterns of the Qiandongshan–Dongtangzi rocks.

5.3. Isotopic Geochemical Characteristics

5.3.1. H–O Isotopic Composition

Studies on hydrogen and oxygen isotopes of the Qiandongshan–Dongtangzi lead–zinc deposit (Table 3) suggests that the ore-forming fluids were mainly derived from magmatic water in the early stage, and later mixed with groundwater and atmospheric water [17] (Figure 9). The hydrogen and oxygen isotopic ratios of 37 quartz samples from Bafangshan–Erlihe Pb–Zn deposit (the Jianduduananshan–Bafangshan–Erlihe lead–zinc polymetallic ore belt in which the Bafangshan–Erlihe lead–zinc deposit is located is 12 km apart from the Qiandongshan–Shuibaigou lead–zinc ore belt in which the Dongtangzi–Qiandongshan lead–zinc deposit is located.) in the Fengtai orefield are all in the area of magmatic water and organic water, it is considered that the ore-forming fluids have the characteristics of multiple sources. And the $\delta^{18}\text{O}_{\text{H}_2\text{O}}$ ratio ranges are close to the range of magmatic water defined by Ohmoto (1986) [32], which reflects the contribution of magmatic water during the mineralization process [6]. The δD values in two sphalerite samples and five quartz samples in the Bafangshan–Erlihe lead–zinc deposit indicate a mixing characteristic of atmospheric water and magmatic water, suggesting that ore-forming fluids were of mixed origin [25]. The results of hydrogen–oxygen isotope studies on the Yafangwan lead–zinc deposit in the southern limb of the Changgou–Donggou anticline in the Fengtai orefield indicate that the ore-forming fluids were a mixture of magmatic water and metamorphic water. The high homogenization temperature of fluid inclusions may be related to the intrusion of the Xiba pluton [33]. The ore-forming fluid in the main ore-forming stage of the magmatic hydrothermal lead–zinc deposit has the characteristics of a mixture of atmospheric water and magmatic water [18]. The hydrogen and oxygen isotopic composition characteristics of the lead–zinc deposit in the Fengtai orefield indicate that the main component of the ore-forming fluid lie between metamorphic and formation water, while the participation metamorphic water and atmospheric water are in the later stage. This fully indicates that the lead–zinc deposit in the Fengtai orefield

is likely of magmatic–hydrothermal origin, which is consistent with the extensive outcrops of Indosinian granites in the orefield.

Table 3. H-O Isotopic Compositions of Pb-Zn Ores in the Fengtai orefield.

Name of Mine	No.	Number of Amples	Mineral	$\delta D/\text{‰}$	$\delta^{18}O/\text{‰}$	T/°C	$\delta^{18}O_{H_2O}/\text{‰}$	References
Dongtangzi	1	7	quartz	−87.91	20.56	215.00	9.76	[17]
	2	5	quartz	−86.26	20.72	225	10.52	
	3	4	quartz	−86.13	20.50	200.00	8.80	
	average	16	quartz	−86.77	20.59	213.33	9.69	
Bafangshan–Erlihe	4	37	quartz	−87.49	18.89	218.95	8.31	[6]
Qiandongshan	5	5	quartz	−94.2			−13.04	[34]
	6	3	quartz	−82			−10.56	[1]

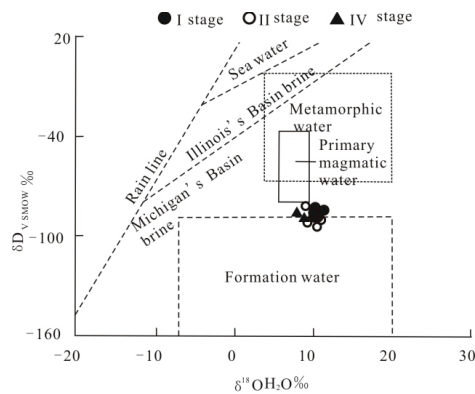


Figure 9. Diagram of $\delta D_{V-SMOW}-\delta^{18}O_{H_2O}$ in Qiandongshan–Dongtangzi Pb-Zn Deposit.

In conclusion, numerous H-O isotope data indicate that the source of ore-forming fluid is closely related to magmatism and metamorphism, which is also consistent with the magmatism and metamorphism the Fengtai orefield during the Indosinian period.

5.3.2. Sulfur Isotope Characteristics

The $\delta^{34}S$ values of sulfides in Sedex-type lead–zinc deposit often exhibit a large range of variation, with most falling within the interval of 20‰–30‰ [1]. In contrast, the $\delta^{34}S$ values of lead–zinc deposits associated with magmatic activity are generally small and vary from −5‰ to 10‰ (Table 4). The $\delta^{34}S$ values of sulfides from the Qiandongshan–Dongtangzi lead–zinc deposit range from 4.29‰ to 9.63‰. The $\delta^{34}S$ values of sulfides in the Qiandongshan–Dongtangzi lead–zinc deposit have smaller and homogeneous ranges, all of which are less than 10‰. These characteristics are significantly different from those of the Sedex-type lead–zinc deposits with larger $\delta^{34}S$ value ranges. However, they share similarities with the $\delta^{34}S$ values of lead–zinc deposits related to magmatic activities, such as Dongzhongla, Tibet, and Qixiashan, in the Jiangsu Province. These $\delta^{34}S$ values indicate that the Qiandongshan–Dongtangzi lead–zinc deposit was probably formed by magmatic–hydrothermal processes and suggest that magmatic activities in the region played a role in mineralization.

Table 4. Sulfur Isotope Compositions of the Qiandongshan–Dongtangzi Pb–Zn Deposit.

Type of Deposit	Ore Deposit	Number of Samples	$\delta^{34}\text{S}$	References
Sedex type	Huogeqi lead–zinc deposit in langshan area, neimenggu Province		3.6‰~23.5‰	[35]
	Jiashengpan lead–zinc deposit		17‰~31.4‰	[36]
	Dongshengmiao lead–zinc deposit		21.7‰~41.84‰	[37]
	Changba lead–zinc mine in Gansu Province		11.4‰~27.81‰	[12]
Magmatic hydrothermal type	Dongzhongla lead–zinc deposit in Tibet		2.2‰~4.8‰	[38]
	Qixiashan lead zinc–deposit, Jiangsu Province		−4.6‰~−3.8‰	[37]
	Dongtangzi mine section	14	4.29‰~9.63‰	[17]
	Qiandongshan mine section	11	5.25‰~9.35‰	[39]
	Bafangshan–Erlihe	57	3.70‰~12.90‰	[6]
	Shoubanya–Yindongliang	6	2.3‰~8.0‰	[40]

The sulfur isotope results of sulfides from the Qiandongshan–Dongtangzi deposit show that the sulfur $\delta^{34}\text{S}$ value is much lower than that of global Devonian seawater, with the minimum value in the Middle Devonian being 17‰, which may indicate the addition of magmatic sulfur [6]. Wang et al. [25] argue that the sulfur isotopic composition of the Bafangshan–Erlihe Pb–Zn deposit is different from both magmatic hydrothermal deposit and sedimentary deposit, showing characteristics of mixed sulfur sources. The vein-like and disseminated sphalerite and pyrite within the diorite porphyrite dikes in the Bafangshan–Erlihe Pb–Zn deposit has typical characteristics of magmatic sulfur, providing direct evidence that magmatic activity contributes to some of the sulfur source.

5.3.3. Lead Isotope Characteristics

The Pb isotope compositions of the main lead–zinc deposits in the Fengtai orefield are shown in Table 5. The $^{206}\text{Pb}/^{204}\text{Pb}$ ratios of each ore deposits range from 18.02 to 18.14, the $^{207}\text{Pb}/^{204}\text{Pb}$ ratios range from 15.60 to 15.71, and the $^{208}\text{Pb}/^{204}\text{Pb}$ ratios range from 38.07 to 38.50. The Pb isotope ratios of individual lead–zinc deposit in the mining area are very stable, with a variation range generally less than 1%. The Pb isotopic composition of the largest Xiba granite in the mining area is 17.77–17.94 for $^{206}\text{Pb}/^{204}\text{Pb}$, 15.47–15.52 for $^{207}\text{Pb}/^{204}\text{Pb}$, and 37.85 ~ 37.89 for $^{208}\text{Pb}/^{204}\text{Pb}$. It is evident that the Pb isotopic compositions of the Fengtai Pb–Zn deposits and the Xiba pluton are quite similar, suggesting that the various ore deposits in the Fengtai orefield and the Xiba pluton have the same lead source. This suggests a close relationship between mineralization of lead–zinc ore deposits in the Fengtai and magmatic activity.

Table 5. Lead isotope compositions of Pb–Zn deposits in Fengtai orefield.

No.	Location	Number of Samples	Mineral	$^{206}\text{Pb}/^{204}\text{Pb}$	$^{207}\text{Pb}/^{204}\text{Pb}$	$^{208}\text{Pb}/^{204}\text{Pb}$	References
1	Dongtangzi	10	Galena	18.14	15.71	38.50	[17]
2	Qiandongshan	11	Galena	18.06	15.61	38.15	[39]
3	Bafangshan–Erlihe	9	Galena	18.08	15.63	38.34	[25]
4	Fengya	4	Ore	18.09	15.61	38.27	[24]
5	Shoubanya	6	Ore	18.02	15.60	38.07	[34]
6	Yindongliang	5	Ore	18.11	15.67	38.33	[41]
7	Xiba pluton	1	Quartz diorite	17.94 ± 29	15.47 ± 25	37.85 ± 64	[42]
		4	Potassium feldspar	17.77	15.52	37.89	[41]

The results show that the Pb isotopic composition of sulfides in the Pb–Zn deposits in the Fengtai orefield mainly falls within the upper crust and mantle mixing zone (magma-tism) on the $\Delta\beta$ – $\Delta\gamma$ diagram, indicating that the Pb source of the ore may be the mixture of

mantle-derived lead and upper crust lead (Figure 10). This suggests that the ore deposit formed in a tectonic environment transitioning from a subduction zone to an orogenic belt, rather than a hydrothermal sedimentary environment, indicating that magmatic activity originating from crust-mantle interactions may have provided some of the ore-forming elements [6,39].

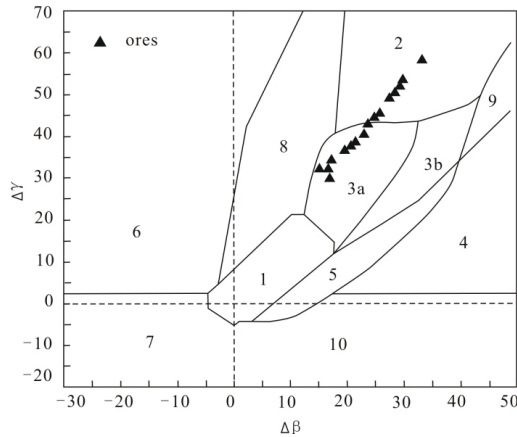


Figure 10. $\Delta\beta$ - $\Delta\gamma$ genetic discriminate diagram of galena from the Fengtai orefield (after [41]). 1—Lead sourced from mantle; 2—Lead sourced from upper crust; 3—Subducting lead sourced from upper crust and mantle (3a—magmatism; 3b—sedimentation); 4—Lead of chemical deposition; 5—Lead of submarine hot-water; 6—Mesometamorphism; 7—Lead of kata-metamorphism; 8—Lead of orogenic belt; 9—Lead of upper crust in ancient shale; 10—Lead of retrograde metamorphism.

5.4. Metallogenic Age

The understanding process of the formation age of lead–zinc deposits in the Fengtai orefield can be divided into two stages. The first stage, before 2011, involved a viewpoint attributing the lead–zinc deposits within the region to a volcanogenic sedimentary origin. As a result, it was indirectly considered that the period of mineralization was consistent with the period of rock formation, specifically during the Middle–Late Devonian period [1,40]. Another viewpoint suggests that it is a sedimentary metamorphic type. The early sedimentation represents the lithification stage of the surrounding rock, and the later metamorphism occurred during the Indosinian period [12,43,44]. The second stage is after 2011, when isotopic dating results showed that the mineralization age of the lead–zinc deposits in the Fengtai orefield mainly ranged from 226–212 Ma, leading many scholars to have a relatively unified understanding that the mineralization age of these lead–zinc deposits belongs to the Late Triassic period (Table 6).

Table 6. Isotopic Age Data of Ore and Igneous Rock Samples from the Fengtai orefield.

	Location	Test Sample	Test Method	Age	References
1	Bafangshan—Erlihe lead—zinc deposit	pyrite	Re-Os isochron	226 ± 17 Ma	[45]
2	Bafangshan—Erlihe lead—zinc deposit	sphalerite	Rb-Sr isochron	220.7 ± 7.3 Ma	[46]
3	Bafangshan—Erlihe lead—zinc deposit	pyrite	Re-Os isochron	226 ± 17 Ma	[47]
4	Qiandongshan—Dongtangzi lead—zinc deposit	Sphalerite, galena, pyrite	Rb-Sr isochron	211.6 ± 2.6 Ma 215.3 ± 3.2 Ma	[6]
5	Changba—Lijiagou lead—zinc deposit average	sulfide	Rb-Sr isochron	222.3 ± 2.2 Ma 220.3 ± 6.55 Ma	[48]
6	Bafangshan—Erlihe lead—zinc deposit	Diorite porphyrite veins	Zircon U-Pb	214 ± 2 Ma	[45]
7	Bafangshan—Erlihe lead—zinc deposit	Diorite porphyrite veins	Zircon U-Pb	221 ± 3 Ma	[45]
8	Bafangshan—Erlihe lead—zinc deposit	Diorite porphyrite veins	Zircon U-Pb	214 ± 2 Ma	[25]

Table 6. Cont.

	Location	Test Sample	Test Method	Age	References
9	Bafangshan—Erlihe lead—zinc deposit	Granite porphyry dikes	Zircon U-Pb	217.9 ± 4.5 Ma	[25]
10	Bafangshan—Erlihe lead—zinc deposit	Diorite porphyrite veins	Zircon U-Pb	220 ± 2.5 Ma	[47]
11	Dongtangzi lead—zinc deposit	Granite porphyry dikes	Zircon U-Pb	221.8 ± 1.1 Ma	[16]
12	Dongtangzi lead—zinc deposit	Granite porphyry dikes	Zircon U-Pb	226.7 ± 1.2 Ma	[16]
13	Dagou pluton	Diorite porphyrite veins	Zircon U-Pb	225.0 ± 1.0 Ma	[16]
	Dagou pluton	Granodiorite dikes	Zircon U-Pb	217.4 ± 2.0 Ma	[16]
14		average		219.8 ± 2.14 Ma	
15	Duji pluton	Biotite granite	Zircon U-Pb	223.7 ± 1.0 Ma	[16]
16	Xiba pluton	monzogranite	Zircon U-Pb	219 ± 1 Ma	[47]
17	Xiba pluton	granodiorite	Zircon U-Pb	218 ± 1 Ma	[47]
18	Xiba pluton	monzogranite		214.9 ± 1.1 Ma	[49]
19	Hejiazhuang pluton			248 ± 2 Ma	[50]
20	Hejiazhuang pluton	granodiorite	LA-ICP-MS	246 ± 3 Ma	[51]
21	Hejiazhuang pluton	granodiorite	LA-ICP-MS	248 ± 2 Ma	[50]
22	Huahongshuping pluton	granodiorite	Zircon U-Pb	214.3 ± 2.7 Ma	[7]
23	Huahongshuping pluton	granodiorite	Zircon U-Pb	225.3 ± 1.4 Ma	[16]
24	Taibai pluton			216 Ma	[52]
25	Taibai pluton	Biotite monzogranite		214 ± 2 Ma	[53]
26	Baoji pluton			216~210 Ma	[51]
27	Huayang Rock mass	monzogranite	LA-ICP-MS	214 ± 2 Ma	[54]
		average		224.4~225.1 ± 1.94 Ma	

The Fengtai orefield is extensively developed with magmatic rocks, such as the largest Xiba pluton and Huahongshuping pluton. The granite plutons have concentrated ages of 248–214 Ma [55], and the granite dikes have concentrated ages of 226–214 Ma [55]. The dating results show that the magmatic activity of the Fengtai orefield occurred in the Late Triassic period, and its formation age roughly corresponds to the mineralization age of lead–zinc deposit.

Wang et al. [8] proposed that the Devonian carbonate and clastic rocks in the Fengtai orefield are sedimentary products of the littoral-shallow sea facies in the foreland basin, formed under compression environment. This mineralization dynamic background is completely different from the typical Sedex Pb-Zn deposits. Therefore, the Devonian period in the Fengtai orefield is not suitable for hydrothermal sedimentation or SEDEX mineralization, and the Pb-Zn deposits are products of large-scale tectonic deformation, metamorphism, magmatism, and fluid activity in the collision stage of the Qinling orogenic belt after the Late Triassic period.

In summary, the geochronology data of the Fengtai orefield show that the mineralization age of Pb-Zn deposit is concentrated in 226–211 Ma. The emplacement of granite dikes and Pb-Zn deposit appears to be roughly equivalent to the formation age of the lead–zinc deposits (Figure 11), while the granite pluton formed slightly earlier than the granite dikes and lead–zinc deposits. The lead–zinc mineralization activity occurred slightly later than the magmatic activity in the region, and the lead–zinc deposits likely formed during the Late Triassic period.

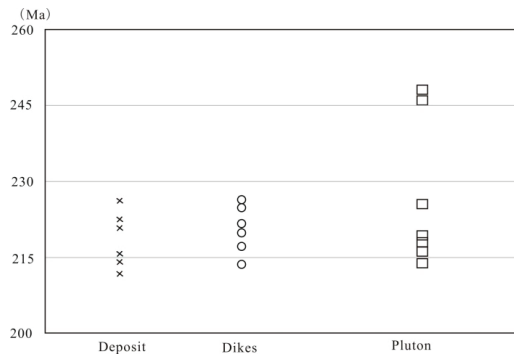


Figure 11. Distribution map of diagenetic and metallogenic ages in the Fengtai orefield.

6. Ore Genesis and Prospecting Model

6.1. Ore Genesis

We carried out the project of “Prospecting and Prediction of FengTai” orefield on the typical lead–zinc deposits. Combined with the analysis of isotopic ages and trace element data, it is suggested that the Qinling Orogenic Belt was in the post-collision extensional stage after collision during the Indosinian period. Intense magmatic activity and mineralization occurred in this tectonic setting [13,27,56–59], which formed the basis for the formation of the Qiandongshan–Dongtangzi lead–zinc deposit. It shows obvious difference from typical Sedex lead–zinc deposit in the geological characteristics, the macroscopic and microscopic structural of lead–zinc ores, H-O-S-Pb isotopes, trace and rare earth element characteristics, mineralization age, and the relationship between ore body and granite, but they are closely related to magmatic–hydrothermal processes. In addition, there are developed skarnified minerals such as tremolite, chlorite, and biotite in the Yafangwan deposit. Silicification, ferrodolomitization, ferrocalcite, pyritization, marbleization, and sericization are developed in the hanging wall and footwall of the main ore bodies of the Yafangwan deposit, and these characteristics show the close relationship between Pb–Zn mineralization and magmatic activity.

During the Devonian period, the Fengtai orefield was situated in an active continental margin sedimentary environment. Stable isotope studies have shown that the initial enrichment of ore-forming materials in the strata constitutes the foundation of final mineralization [6]. In the Late Indosinian period, the high-temperature, acidic and lead-zinc-chloride-rich supercritical fluid exsolved from the intermediate-acidic intrusions exhibits along channels formed by WNW-trending faults, driven by structural stress and temperature gradients, and diagonally progressing from SE to NW. Organic matter often forms stable complexes with lead, zinc, and other metals in intermediate- to low-temperature hydrothermal fluids, which facilitates the transportation of ore-forming metals. Among them, the lead complexing ability is several orders of magnitude higher than that of Cl^- and CO_3^{2-} [60], and organic lead complexes make a significant contribution to the transport of lead [61,62]. The solubility of sphalerite is several times to tens of times higher in fluid media containing organic compounds compared to those without organic compounds [63]. During upward migration, the fluid extracted a large amount of SiO_2 when passing through sandstone and siltstone [18], and when entering carbonate rocks, CaCO_3 was converted into Ca^{2+} and HCO_3^- that dissolved in the fluid, releasing HO^- ions, causing the fluid to shift towards alkalinity and leading to the precipitation of a large amount of SiO_2 . As pH increased, the solubility of lead and zinc chloride complexes decreased by two orders of magnitude with each a one-unit increase in pH. As the pressure and temperature decrease and water–rock reactions occur, the stability of metal elements migrating in the form of chloride complexes is greatly reduced [64]. They are then converted into hydrosulfide complexes and begin to precipitate in large quantities due to the

decrease in solubility with increasing pH, eventually forming sulfide minerals of lead and zinc. The ore-forming metals suffered the metasomatism mineralization near the acid-base geochemical barrier (the Si/Ca interface), especially in the saddle detachment part of the anticline and the limb contact zone. Mineralization results in ore bodies occurring on the side of carbonate rocks [18]. According to the study results of Tagirov and Seward [64,65] and Ye Tianzhu et al. [18] on the transport conditions of zinc, the overall zinc grade of the lead–zinc ore body in the mining area is generally higher than that of lead, which may be caused by the difference in the transport effects of chloride complexes on lead and zinc in the ore-forming fluid.

Ye et al. [18] concluded that the metallogenic geological bodies of magmatic–hydrothermal origin lead–zinc deposits are intermediate-acidic intrusions, with various lithology including quartzite diorite, plagioclase granite porphyry, granite porphyry, granodiorite porphyry, granite, and quartz porphyry. Examples of such deposits include the Mengentaolegai Pb–Zn–Ag deposit in the Neimenggu Province, the Gaocheng Pb–Zn–Ag deposit in the Guangdong Province, and the Xinhua the deposit in Guangxi Province. At present, no granite intrusion has been found within a certain exploration depth in these deposits, which is the main reason for the controversy over the existence of their mineralization geological bodies. The discovery of intermediate-acidic dikes in the Qiandongshan–Dongtangzi mining area suggests that the hidden intrusions in the deeper parts of the mining area may be the metallogenic geological body. Meanwhile, the undiscovered hidden intrusions also contribute to the uncertainty surrounding the origin of the Qiandongshan–Dongtangzi lead–zinc deposit.

In summary, the formation of the Qiandongshan–Dongtangzi lead–zinc deposit is likely related to magmatic–hydrothermal activity. It is supported by the evidence that magmatic activity not only provided the heat energy, but also supplied some ore-forming materials for lead–zinc mineralization. The Qiandongshan–Dongtangzi lead–zinc deposit is perhaps a stratabound magmatic hydrothermal lead–zinc deposit developed in the Late Triassic period of the Qinling orogenic belt. The mineralization mother rock is likely a concealed granite body, with the ore-forming structural plane in the contact surface between the limestone of the Gudaoling Formation and the phyllite of the Xinghongpu Formation. The ore-forming fluid is driven from magmatic–hydrothermal fluid, which constitutes a perfect mineralization system integrating ore-forming geological body, ore-forming structural plane, metallogenesis, and ore-forming fluid [18].

6.2. Prospecting Model

During the Indosinian period, the Qinling orogeny was triggered by the subduction collision of the Yangtze Craton, leading to extensive intermediate-felsic magmatic activity [16,66–68]. At the same time, a large-scale compressional-shear deformation system was formed due to a series of WNW-oriented composite folds, brittle-ductile shear zones, faults and joints, as well as NEN- and NE-oriented faults and joints [42,69].

The extensive magmatic activity that occurred on a large scale not only served as a heat energy but also facilitated the mobilization of ore-forming elements (e.g., Pb and Zn) during their migration process. This, in turn, led to the release of ore-forming fluids and materials, resulting in the transport of significant amounts of zinc and lead-rich fluids. Driven by the temperature–pressure gradient and buoyancy effect [70], these fluids migrated towards the lower temperature and pressure regions along the WNW-trending fault structure that extended from the basement rock to the Devonian strata, and subsequently mixed with meteoric water infiltrating the Devonian strata and organic water present in the shallow part, thereby enhancing the mineralization process. As a result, a filling saddle-shaped main ore body was formed in the detachment space of the contact zone between the Gudaoling Formation limestone and the Xinghongpu Formation phyllite within the core of the anticline (Figure 12). Additionally, a small-scale vein-type lead–zinc ore body was formed as part of the ore-forming fluid, flowed through the axial faults and fissures present in the limestone. In the process of mineralization fluid, biolimestone and other rock formations have a

neutralization reaction with carbonate rocks due to their chemical activity, porous and permeable, or provide reducing agents and adsorption, the weakly acidic mineralizing fluid has a neutralization reaction with carbonate rocks, and carbonate rocks dissolve to promote sulfide precipitation, thereby facilitating mineralization [62]. It is worth noting that the lead–zinc mineralization observed in various locations and decompression–expansion sites within the ore cluster region can be attributed to mineralization occurring in different spatial structures during the same process [3,4,8,55].

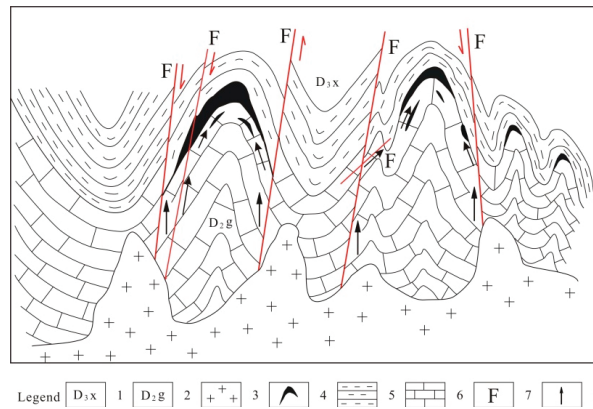


Figure 12. Metallogenic model of Qiandongshan–Dongtangzi Pb–Zn deposit. 1—Upper Devonian Xinghongpu Formation; 2—Middle Devonian Gudaoling Formation; 3—Triassic intermediate-acid rock mass; 4—Pb–Zn ore body; 5—Phyllite; 6—Limestone; 7—Faults; 8—Direction of magmatic hydrothermal fluid migration.

7. Ore-Controlling Factors and Prospecting Criteria

7.1. Ore-Controlling Factor

From the perspective of spatial occurrence characteristics of lead–zinc deposits, the ore-controlling factors of the lead–zinc deposits in the Fengtai orefield are basically the same, that is, they are controlled by the trinity “stratigraphy + stratigraphic position + structure”.

The lead–zinc ore body in the Qiandongshan–Dongtangzi large lead–zinc deposit is located on the limestone side of the contact zone between the Middle Devonian Gudaoling Formation and the Upper Devonian Xinghongpu Formation, which is at the top of the Gudaoling Formation. This demonstrates that the occurrence of the lead–zinc ore body is controlled by stratigraphy.

The ore-hosted rock is dominated by silicified limestone, which is present in specific layers and macroscopically demonstrates the control of specific layers on lead–zinc deposits. This particular layer is the lithological interface (Si/Ca interface) and the carbonaceous rock layer [71,72] (Zhang, 2012; Shi et al., 2022). The interface between limestone and phyllite is the main ore-forming structural plane of lead–zinc ore body in Qiandongshan–Dongtangzi large lead–zinc deposits, serving as the transition boundary for physical and chemical conditions and a weak zone for tectonic activities. The occurrence of lead–zinc ore bodies often have high carbonaceous content. This is due to the occurrence of lithological interface sliding and thermal metamorphism during mineralization which leads to the precipitation of carbonaceous materials in the wall-rock, often resulting in the development of carbonaceous layers in the hanging wall of the ore body, forming a distinctive lithological layer.

The most obvious occurrence feature of lead–zinc ore bodies in the Fengtai orefield is that they are controlled by anticline structure. The Qiandongshan–Dongtangzi large lead–zinc deposit is controlled by the Qiandongshan–Dongtangzi complex anticline (level III) on the south side of the western end of the Qiandongshan–Shangtianba–Shuibagou complex

anticline (level II). The secondary anticlines in the north branch anticline and the south branch anticline (level IV), respectively, control the No. I ore body and No. II ore body in the mining area. In addition, the fault structural plane controls the ore body, and the veined Pb-Zn ore body found along the inter-layer fracture zone within the limestone of Gudaoling Formation or the phyllite of the Xinghongpu Formation is the manifestation of structural ore control.

7.2. Prospecting Criteria

The contact interface between the limestone of the Middle Devonian Gudaoling Formation and the phyllite of the Upper Devonian Xinghongpu Formation is the stratigraphic marker for prospecting the Qiandongshan–Dongtangzi large Pb-Zn deposit. The anticlinal structures, especially the turning end and the wing of the secondary fold, serve as important structural indicators for mineral exploration. Silicified limestone serves as an indicator for direct lithology exploration in the field. Silicification and dolomitization serve as the alteration indicators for mineral exploration. The development of lead–zinc mineralization mainly is often associated with low-resistance, high-polarization induced electrical anomalies, self-potential anomalies, and geochemical anomalies characterized by combinations of elements such as Pb, Zn, Au, Ag, As, and Sb. These anomalies serve as indirect indicators for mineral exploration from a physical and chemical perspective.

8. Prospecting Prediction and Verification

Based on the metallogenic model outlined above, the prospecting predictions primarily rely on the Si/Ca interface and the secondary anticline structure. A series of WNW-trending tight folds formed in the Fengtai orefield during the Indosinian period, which is the most favorable location for prospecting prediction. It is considered that the secondary anticlines (IV level) developed on both limbs of the Qiandongshan–Dongtangzi anticline (III level) favorable mineralization sites. Accordingly, we propose a novel prospecting verification strategy targeting the saddle of the secondary anticline in the Dongtangzi lead–zinc deposit section. Specifically, we have developed a prospecting verification scheme for the CZK8205 drill hole in the 82nd exploration line (Figure 13). It has been confirmed that a thick and extensive industrial ore body, containing Pb at a grade of 4.0% and Zn at a grade of 6.28%, with a true thickness of 5.35 m was discovered on the phyllite of the contact zone between bioclastic limestone and phyllite within the saddle of the secondary anticline. Subsequently, two additional drill holes, CZK8206 and CZK8207, were carried out on the south and north sides of the CZK8205 drill hole, respectively, in the two limbs of the secondary anticline. In the CZK8207 drill hole, a thick and rich industrial ore body with a Pb grade of 2.44%, a Zn grade of 6.82%, and a true thickness of 8.46 m was discovered. Exploration and mining activities have demonstrated that the known ore bodies exhibit a westward inclination with the Qiandongshan–Dongtangzi ore-controlling anticline. Moreover, the secondary anticline, which is similar to the primary ore-controlling anticline, is also inclined to the west and extends stably in a concealed mode. It is suggested that the extension of the ore body towards the west is highly probable, as supported by comprehensive research. To verify this hypothesis, two verification drill holes, CZK8604 and CZK8605, were conducted in the 86th line of the western extension of the ore body. The results of these drill holes revealed lead–zinc ore bodies with a Pb grade of 0.06%, a Zn grade of 6.59%, and a true thickness of 1.92 m for CZK8604, and a Pb grade of 0.89%, a Zn grade of 6.77%, and a true thickness of 2.64 m for CZK8605. Remarkably, the scale, thickness, and grade of this ore body is comparable to that of the II-1 main ore body.

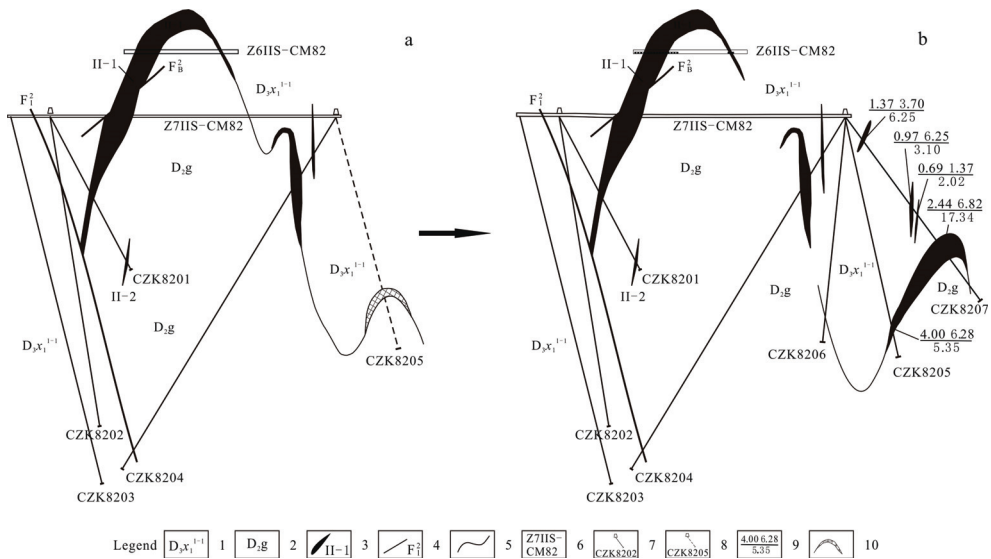


Figure 13. The Geological Profiles 82 Exploration Line of the Dongtangzi Lead-Zinc section. (a)—Prediction diagram; (b)—Verification diagram; 1—Calcareous phyllite intercalated with thin limestone in the first lithologic substratum of the first lithologic member of the Xinghongpu Formation in the upper Devonian; 2—Thin–medium–thick bedded bioclastic microcrystalline limestone and crystalline limestone of the Gudaoling Formation in the Middle Devonian; 3—Lead–zinc deposit and number; 4—Faults and number; 5—Geological boundary; 6—Location and number of the tunnel; 7—Number of completed drilling; 8—Number of design drilling; 9—Lead grade(%) Zinc grade(%)/true thickness(m); 10—Prediction of ore body location approach of integrating a ‘metallogenic model + prospecting prediction + drill hole verification’ has proven to be a successful method for deep geological prospecting, which has accumulated successful experience for the discovery of a new lead–zinc deposit.

9. Conclusions

- (1) The genesis of the Qiangongshan–Dongtangzi deposit should be probably attributed to a stratiform magmatic–hydrothermal origin. The deposit contains stratabound ore bodies in the anticlinal core, as well as vein-like and network-like ore bodies in the faults and fissures within the limestone. The ore bodies are controlled by the Si/Ca interface and the anticline structure.
- (2) The Qiangongshan–Dongtangzi lead–zinc deposit formed in two stages. During the Indosinian period, a series of WNW-trending folds formed due to plate subduction and collision. This event also triggered large-scale intermediate-felsic magmatic activity that created structures for ore transportation and provided space for mineralization. In the late- to post-collision stage, magmatic fluids carrying ore-forming elements were deposited on the Si/Ca interface of the physical-chemical mutation. This interface formed in the contact zone between limestone of the Gudaoling Formation and phyllite of the Xinghongpu Formation at the core of an anticline.
- (3) The detachment space created by the intersection of the anticline structure and the Si/Ca interface plays a critical role in metallogenic prediction. In particular, a series of WNW-trending secondary anticlines that have developed on the two limbs of the main ore-controlling anticline of the Qiangongshan–Dongtangzi large-scale lead–zinc deposit are the most favorable metallogenic sites and the preferred target for prospecting prediction. The drilling verification scheme was designed for the secondary anticline on the north limb of the main ore-controlling anticline in the Dongtangzi lead–zinc deposits based on this method.

- (4) The drilling verification of the secondary anticline located on the north limb of the Qiandongshan–Dongtangzi ore-controlling anticline has led to the discovery of a thick and rich industrial lead–zinc ore body. The success of this example sets a precedent for prospecting and prediction in the Qiandongshan–Dongtangzi mining area, and contributes to the accumulation of successful experience in deep exploration and blind prospecting within the Fengtai orefield.

Author Contributions: Conceptualization, R.W. and G.Z.; validation, R.W., W.W. and H.Y.; investigation, G.Z. and J.Z.; resources, R.W. and G.Z.; data curation, Z.P., Q.L., G.Z. and J.Z.; writing—original draft preparation, R.W., Z.P., Q.L. and H.C.; writing—review and editing, R.W., Z.P. and Q.L.; supervision, W.W. and H.Y.; project administration, W.W. and H.Y.; funding acquisition, Y.W. and H.Y. All authors have read and agreed to the published version of the manuscript.

Funding: Prospecting predictor of Fengtai ore concentration area in Shaanxi province (No. DD2016005213).

Data Availability Statement: The data are derived from our team work or the references, and is available.

Conflicts of Interest: The authors declare no conflict of interest. The funders had no role in the design of the study; in the collection, analysis, or interpretation of data; in the writing of the manuscript; or in the decision to publish the results.

References

- Qi, S.J.; Li, Y. *Lead-Zinc Metallogenic Belt of Devonian System in Qinling Mountains*; Geological Publishing House: Beijing, China, 1993.
- Jia, R.X.; Han, S.S.; Wei, H.M. Main Metallogenic Characteristics and Genetic Analysis of Gold Deposit in Fengtai Ore Field Qinling. *J. Xi'an Eng. Univ.* **1999**, *21*, 67–75. (In Chinese with English Abstract)
- Wang, R.T.; Wang, D.S.; Dai, J.Z. *Study on Synthetical Exploration Technology for Pb-Zn-Ag-Cu-Au Deposits in Major Mineralization Concentrated Region of Shannxi Area in Qinling Orogenic Belt*; Geological Publishing House: Beijing, China, 2012; pp. 1–262.
- Wang, R.T.; Zhang, G.L.; Li, Q.F.; Zhang, B.; Cheng, H.; Ji, Y.F. Metallogenic Regularity and Prospecting Prediction of Fengtai Pb-Zn-Au Ore Concentration Area in Qinling Mountains. *J. Earth Sci. Environ.* **2021**, *43*, 528–548. (In Chinese with English Abstract)
- Fang, W.X. Research on Mineral Geochemistry of Qiandongshan Large-sized Lead-zinc Deposit in Fengxian County, Shaanxi. *Acta Miner. Sin.* **1999**, *19*, 198–205. (In Chinese with English Abstract)
- Hu, Q.Q. The Mineralization Features, Mechanism and Metallogenic Regularity of the Fengtai Pb-Zn Polymetallic Ore Cluster in West Qinling, China. Ph.D. Thesis, Chinese Academy of Geological Sciences, Beijing, China, 2015.
- Zhang, Y.F.; Yang, T.; Yi, P.F.; Yao, Z.; He, Y.F. LA-ICP-MS Zircon Geochronology and Geochemistry of the Huahongshuping Granodiorite Pluton in South Qinling. *Geol. Explor.* **2018**, *54*, 300–314. (In Chinese with English Abstract)
- Wang, Y.T.; Hu, Q.Q.; Wang, R.T.; Gao, W.H.; Chen, S.C.; Wei, R.; Wang, C.A.; Wei, B.; Wei, S.W.; Tang, M.J. A New metallogenic model and its Significance in Search for Zn-Pb Deposits in Fengtai (Fengxian-Taibai) Polymetallic Ore Concentration Area, Shannxi Province. *Miner. Depos.* **2020**, *39*, 587–606. (In Chinese with English Abstract)
- Zhang, F. Magmatism and Mineralization of the Indosinian Period in the Fengtai Area, Qinling Mountains: Evidence of Geological Chronology and Geochemistry. Ph.D. Thesis, Peking University, Beijing, China, 2010.
- Wang, H.; Wang, J.P.; Liu, J.J.; Cao, R.R.; Hui, D.F.; Cheng, J.J. Mineralogy of the Xiba Granitoid Pluton in the Southern Qinling Orogenic Belt and Its Implications for Petrogenesis. *Geoscience* **2011**, *3*, 489–502. (In Chinese with English Abstract)
- Li, Q.F.; Wang, B.W.; Zhang, B. *A Summary of 1:50000 Jiingkou (I48E013012), Jiangkou (I48E014021) and Guanshan (I48E012021), Mineral Geological Survey for Shaanxi*; Baoji 717 Corps Limited of Northwest Nonferrous Geological and Mining Group: Baoji, China, 2019. (In Chinese)
- Wang, J.L.; He, B.C.; Li, J.Z. *Qinling Type Lead and Zinc Mineral Deposits in China*; Geological Publishing House: Beijing, China, 1996; pp. 1–264. (In Chinese)
- Zhang, F.X.; Du, X.H.; Wang, W.T.; Qi, Y.L. Mineralization responded to mesozoic geological evolution of the Qinling orogen and its environs. *Chin. J. Geol.* **2004**, *39*, 486–495. (In Chinese with English Abstract)
- Wang, R.T. Study on Metallogenic Model for Typic Metal Ore Deposits and Exploration Predicting of Qinling Orogenic Belt in Shannxi Province, China. Ph.D. Thesis, University of Geosciences, Beijing, China, 2005; pp. 1–158.
- Feng, J.Z.; Wang, D.B.; Wang, X.M.; Shao, S.C. Stable Isotope Geochemistry of Three Typical Gold Deposits in the West Qinling. *Geol. China* **2004**, *31*, 78–84. (In Chinese with English Abstract)
- Chen, S.C.; Wang, Y.T.; Yu, J.J.; Hu, Q.Q.; Zhang, J.; Wang, R.T.; Gao, W.H.; Wang, C.A. Petrogenesis of Triassic granitoids in the Fengxian-Taibai ore cluster, Western Qinling Orogen, central China: Implications for tectonic evolution and polymetallic mineralization. *Ore Geol. Rev.* **2020**, *123*, 103577. [CrossRef]

17. Zhang, G.L.; Wang, R.T.; Tian, T.; Ding, K.; Gao, W.H.; Guo, Y.Y. Geological-geochemical Characteristics and Genesis of Dongtangzi Pb-Zn Deposit in Fengxian-Taibai Ore Concentration Area of Shaanxi, China. *J. Earth Sci. Environ.* **2018**, *40*, 520–534. (In Chinese with English Abstract)
18. Ye, T.Z.; Lu, Z.C.; Pang, Z.S. *Theory and Method of Prospecting Prediction in Exploration Area (Pandect)*; Geological Publishing House: Beijing, China, 2015. (In Chinese with English Abstract)
19. Li, Y.Q.; Wang, R.T.; Meng, D.M.; Dai, J.Z.; Huang, C.Q. Geological Characteristics and Prospecting Direction of Taishanmiao Copper Deposits in Fengxian County, Shaanxi Province. *Northwest. Geol.* **2015**, *48*, 169–175. (In Chinese with English Abstract)
20. Huang, Z.Y.; Lu, R.N. Zoning Characteristics and Index of Primary Geochemical Anomalies in Qiandongshan Pb-Zn Deposit, ShanXi Province, China. *Geol. Prospect.* **2003**, *3*, 39–44. (In Chinese with English Abstract)
21. Long, H.S.; Luo, T.Y.; Huang, Z.L.; Zhou, M.Z.; Yang, Y.; Qian, Z.K. Rare Earth Element and Trace Element Geochemistry of Pyrite Ores in the Laochang Large Size Silver Polymetallic Deposit of Lancang, Yunnan Province, China. *Acta Miner. Sin.* **2011**, *31*, 462–473. (In Chinese with English Abstract)
22. Yan, Q.J.; Wei, X.Y.; Ye, M.F.; Zhou, H.B.; Zhou, N.C. Determination of Composition of Pyrite in the Baishantang Copper Deposit by Laser Ablation-inductively Coupled Plasma-mass Spectrometry and Electron Microprobe. *Rock Miner. Anal.* **2016**, *35*, 658–666. (In Chinese with English Abstract)
23. Zeng, Y.C.; Huang, S.J.; Jia, G.X.; Chen, Y.R. Eigenlements of Some Metallic Minerals in the Magmatic Hydrothermal and Stratabound Pb-Zn Deposits and Their Geological Significance. *Geol. Prospecting* **1985**, *21*, 28–33. (In Chinese)
24. Han, Z.X. The Typomorphic Characteristic of the Sphalerite in the Qinling Devonian System Lead-zinc Metallogenic Belt. *J. Xi'an Coll. Geol.* **1994**, *16*, 12–17. (In Chinese with English Abstract)
25. Wang, R.T.; Li, F.L.; Chen, E.H.; Dai, J.Z.; Wang, C.A.; Xu, X.F. Geochemical Characteristics and Prospecting Prediction of the Bafangshan-Erlihe Large Lead-zinc Ore Deposit, Feng County, Shaanxi Province, China. *Acta Petrol. Sin.* **2011**, *27*, 779–793. (In Chinese with English Abstract)
26. Li, T. Application of the elemental abundance. *Geol. Explor.* **1981**, *6*, 1–6. (In Chinese)
27. Wang, L.; Tian, T.; Li, W.; Zhang, B.; Zhang, G.L.; Wang, F.; Zheng, S.X. Discussion on the geochemistry and evolution of Xiba rock mass in the central part of Fengtai high ore concentration area. *Gold* **2021**, *42*, 25–30. (In Chinese with English Abstract)
28. Zhang, G.L.; Wang, L.; Tian, T. *Achievement Report of Sub-Project of Prospecting and Prediction in Fengtai Ore Gathering Area of Shaanxi Province*; Baoji 717 Corps Limited of the Northwest Nonferrous Geological and Mining Group: Baoji, China, 2019.
29. Han, F.; Sun, H.T. Metallogenic system of sedex type deposits: A review. *Earth Sci. Front.* **1999**, *6*, 139–157. (In Chinese)
30. Leach, D.L.; Sangster, D.F.; Kelley, K.D.; Large, R.R.; Garven, G.; Allen, C.R.; Gutzmer, J.; Wahers, S. Sediment-hosted lead-zinc deposits: A global perspective. *Economic Geol.* **2005**, *100*, 561–607.
31. Li, H.Z.; Zhou, Y.Z.; Yang, Z.J.; Gu, Z.H.; Lv, W.C.; He, J.G.; Li, W.; An, Y.F. Geochemical Characteristics and Their Geological Implications of Cherts from Bafangshan-Erlihe Area in Western Qinling Orogen. *Acta Petrol. Sin.* **2009**, *25*, 3094–3102. (In Chinese with English Abstract)
32. Ohmoto, H. Stable Isotope Geochemistry of Ore Deposits. *Rev. Miner. Geochem.* **1986**, *16*, 491–559.
33. Liu, B.Z.; Wang, J.P.; Zeng, X.T.; Wang, K.X.; Cao, R.R.; Cheng, J.J. Ore fluid and geochemical characteristics of Yanfangwan Pb-Zn deposit in Shaanxi Province. *Contrib. Geol. Miner. Resour. Res.* **2013**, *28*, 50–57. (In Chinese with English Abstract)
34. Wang, X.; Tang, R.Y.; Li, S.; Li, Y.X.; Yang, M.J.; Wang, D.S.; Guo, J.; Liu, P.; Liu, R.D.; Li, W.Q. *Oro-Geny and Metal Mineralization of Qinling Area*; Metallurgical Industry Press: Beijing, China, 1996. (In Chinese)
35. Jiang, X.M. A Discussion on the Genesis and Oreforming Mechanism of the Hogeqi Cu-Pb-Zn Deposit. *J. Miner. Deposits.* **1983**, *4*, 1–10. (In Chinese with English Abstract)
36. Fu, C.; Wang, J.P.; Peng, R.M.; Liu, J.J.; Liu, Z.J.; Liu, Z.M. Features of Sulfur Isotope of the Jiashengpan Lead-Zinc-Sulfur Dposit in Inner Mongolia and Its Genesis Significance. *J. Geosci.* **2010**, *24*, 34–41. (In Chinese with English abstract)
37. Zhang, M.C.; Chen, R.Y.; Ye, T.Z.; Li, J.C.; Lü, Z.C.; He, X.; Chen, H.; Yao, L. Genetic study on the Qixiashan Pb-Zn polymetallic deposit in Jiangsu Province: Evidence from fluid inclusions and H-O-S-Pb isotopes. *J. Acta Petrol. Sin.* **2017**, *33*, 3453–3470. (In Chinese with English Abstract)
38. Liu, T.T.; He, Z.W.; Cui, X.L.; Ni, Z.Y.; Liu, H.F.; Zhang, J.S. Model Construction and Prospecting Prediction of Lead-Zinc Polymetallic Ore Deposits Based on GIS Information Method. *J. Guilin Univ. Technol.* **2011**, *4*, 511–515. (In Chinese with English Abstract)
39. Ren, P.; Liang, T.; Liu, K.L.; Liu, L.; Lu, L.; Zhang, W.J. Geochemistry of Sulfur and Lead Isotopic Compositions of Sedex Lead-zinc Deposits in Fengtai Mineral Cluster Region of Qinling Mountains. *J. Northwestern Geol.* **2014**, *47*, 137–149. (In Chinese with English Abstract)
40. Wei, H.M.; Zhang, Z.F. Lithofacies during the ore-forming period and their prospecting significance in the Qiandongshan-Tanjiagou area of the Fengtai lead-zinc ore field. *Northwest Geol.* **1987**, *5*, 6–11. (In Chinese)
41. Zhang, F.X.; Wang, J.F. Devonian syn-genetic faults and lith of acies in relation to submarine exhalative sedimentary lead- zinc deposits in Qinling area, Shaanxi Province. *J. Miner. Deposits.* **1991**, *3*, 217–231. (In Chinese with English Abstract)
42. Zhang, H.F.; Ouyang, J.P.; Lin, W.L.; Chen, Y.L. Pb, Sr, Nd, Isotope Composition of Ningshan Granitoids, South Qinling and their Deep Geological Information. *Acta Petrologica Miner.* **1997**, *16*, 22–31. (In Chinese with English Abstract)
43. Wang, R.T.; Wang, T.; Gao, Z.J.; Chen, E.H.; Liu, L.X. The Main Metal Deposits Metallogenic Series and Exploration Direction in Feng-Tai Ore Cluster Region, Shaanxi Province. *Northwest Geol.* **2007**, *40*, 77–84. (In Chinese with English Abstract)

44. Wang, D.S.; Wang, R.T.; Dai, J.Z.; Wang, C.A.; Li, J.H.; Chen, L.X. “Dual Ore controlling Factors” Characteristics of Metallic Deposits in the Qinling Orogenic Belt. *Acta Geol. Sin.* **2009**, *83*, 1719–1729. (In Chinese with English Abstract)
45. Zhang, F.; Liu, S.W.; Li, Q.G.; Sun, Y.L.; Wang, Z.Q.; Yan, Q.R.; Yan, Z. Re-Os and U-Pb Geochronology of the Erlihe Pb-Zn Deposit Qinling Orogenic Belt, Central China and Constraints on Its Deposit Genesis. *Acta Geol. Sin. (Engl. Ed.)* **2011**, *85*, 673–682. [CrossRef]
46. Hu, Q.Q.; Wang, Y.T.; Wang, R.T.; Li, J.H.; Dai, J.Z.; Wang, S.Y. Ore-forming time of the Erlihe Pb-Zn deposit in the Fengxian-Taibai ore concentration area, Shaanxi Province: Evidence from the Rb-Sr isotopic dating of sphalerites. *Acta Petrol. Sin.* **2012**, *28*, 258–266. (In Chinese with English Abstract)
47. Zhang, F.; Liu, S.W.; Li, Q.G.; Wang, Z.Q.; Han, Y.G.; Yang, K.; Wu, F.H. LA-ICP-MS Zircon U-Pb Geochronology and Geological Significance of Xiba Granitoids from Qinling, Central China. *Acta Sci. Nat. Univ. Pekin.* **2009**, *45*, 833–840. (In Chinese with English Abstract)
48. Hu, Q.Q.; Wang, Y.T.; Mao, J.W.; Liu, S.W. Timing of the Formation of the Changba-Lijiagou Pb-Zn Ore Deposit, Gansu Province, China: Evidence from Rb-Sr Isotopic Dating of Sulfides. *J. Asian Earth Sci.* **2015**, *103*, 350–359. [CrossRef]
49. Wang, H. The Features of Magmatic Rocks in Shangwang Gold Mine, Shanxi Province and Its Implication on Gold Mineralization. Ph.D. Thesis, China University of Geosciences, Beijing, China, 2012.
50. Yang, P.T.; Liu, S.W.; Li, Q.G.; Wang, Z.Q.; Zhang, F.; Wang, W. Chronology and Petrogenesis of the Hejiazhuang Granitoid Pluton and Its Constraints on the Early Triassic Tectonic Evolution of the South Qinling Belt. *Sci. China Earth Sciences* **2013**, *43*, 1874–1892. (In Chinese) [CrossRef]
51. Liu, S.W.; Yang, P.T.; Li, Q.G.; Wang, Z.Q.; Zhang, W.Y.; Wang, W. Indosinian Granitoids and Orogenic Processes in the Middle Segment of the Qinling Orogen, China. *J. Jilin Univ. (Earth Sci. Ed.)* **2011**, *41*, 1928–1943. (In Chinese with English Abstract)
52. Zhang, Z.Q.; Zhang, G.W.; Liu, D.Y. *Isotopic Geochronology and Geochemistry of Ophiolites, Granites and Clastic Sedimentary Rocks in the Qinling-Dabie Orogenic Belt*; Geological Publishing House: Beijing, China, 2006.
53. Lü, X.Q.; Wang, X.X.; Ke, C.H.; Li, J.B.; Yang, Y.; Meng, X.Y.; Nie, Z.R.; Zhang, P.F. LA-ICP-MS zircon U-Pb dating of Taibai pluton in North Qinling Mountains and its geological significance. *Miner. Depos.* **2014**, *33*, 37–52. (In Chinese with English Abstract)
54. Meng, X.Y.; Wang, X.X.; Ke, C.H.; Li, J.B.; Yang, Y.; Lü, X.Q. LA-ICP-MS zircon U-Pb age, geochemistry and Hf isotope of the granitoids from Huayang pluton in South Qinling orogen: Constraints on the genesis of Wulong plutons. *Geol. Bull. China* **2013**, *32*, 1704–1719. (In Chinese with English Abstract)
55. Wang, Y.T.; Mao, J.W.; Hu, Q.Q.; Wei, R.; Chen, S.C. Characteristics and Metallogeny of Triassic Polymetallic Mineralization in Xicheng and Fengtai Ore Cluster Zones, West Qinling, China and Their Implications for Prospecting Targets. *J. Earth Sci. Environ.* **2021**, *43*, 409–435. (In Chinese with English Abstract)
56. Wang, J.H.; Zhang, F.X.; Yu, Z.P.; Yu, L. Minerogenetic series of metallic ore deposits in the Qinling Mountains and tectonodynamic background of the continental orogenic belts. *Geol. China* **2002**, *29*, 192–196. (In Chinese with English Abstract)
57. Lu, X.X.; Li, M.L.; Wang, W.; Yu, Z.P.; Shi, Y.Z. Indosinian movement and metallogenesis in Qinling orogenic belt. *Miner. Depos.* **2008**, *27*, 762–773. (In Chinese with English Abstract)
58. Chen, Y.J. Indosinian tectonic setting, magmatism and metallogenesis in Qinling Orogen, central China. *Geol. China* **2010**, *37*, 854–865. (In Chinese with English Abstract)
59. Shi, K.; Du, J.G.; Wan, Q.; Chen, F.; Cai, Y.; Cao, J.Y.; Wu, L.B.; Wang, L.M.; Tan, D.X. Chronology study of the Mesozoic intrusive rocks in the Tongling ore-cluster region, Anhui, and its metallogenic significance. *Acta Geol. Sin.* **2019**, *93*, 1096–1112. (In Chinese with English Abstract)
60. Hennet, R.J.C.; Crerar, D.A.; Schwartz, J. Organic complexes in hydrothermal systems. *Econ. Geol.* **1988**, *83*, 742–764. [CrossRef]
61. Giordano, T.H.; Barnes, H.L. Lead transport in Mississippi Valley-type ore solutions. *Economic Geol.* **1981**, *76*, 2200–2211. [CrossRef]
62. Barmes, H.L.; Gould, W.W. Hydrothermal replacement of carbonates by sulfides. In Proceedings of the 7th International Symposium on Water-Rock Interaction, Park City, UT, USA, 13–18 July 1992; pp. 1565–1567.
63. Lu, J.C.; Yuan, Z.Q. Experimental Studies of Organic–An Complexes and their Stability. *Geochimica* **1986**, *1*, 66–77. (In Chinese)
64. Seward, T.M.; Barnes, H.L. Metal transport by hydrothermal ore fluids. In *Geochemistry of Hydrothermal Ore Deposits*; Barnes, H.L., Ed.; John Wiley & Sons, Inc.: New York, NY, USA, 1997.
65. Tagirov, B.R.; Seward, T.M. Hydrosulfide/sulfide complexes of zinc to 250 °C and the thermodynamic properties of sphalerite. *Chem. Geol.* **2010**, *269*, 301–311. [CrossRef]
66. Deng, Z.B.; Liu, S.W.; Zhang, W.Y.; Hua, F.Y.; Li, Q.G. Petrogenesis of the Guangtoushan granitoid suite, central China: Implications for Early Mesozoic geodynamic evolution of the Qinling Orogenic Belt. *Gondwana Res.* **2016**, *30*, 112–131. [CrossRef]
67. Hu, F.Y.; Liu, S.W.; Zhang, W.Y.; Deng, Z.B.; Chen, X.A. Westward propagating slab tear model for Late Triassic Qinling Orogenic Belt geodynamic evolution: Insights from the petrogenesis of the Caoping and Shahewan intrusions, central China. *Lithos* **2016**, *262*, 486–506. [CrossRef]
68. Xiong, X.; Zhu, L.M.; Zhang, G.W.; Santosh, M.; Jiang, H.; Zheng, J.; Guo, A.L.; Ding, L.L. Petrogenesis and tectonic implications of Indosinian granitoids from Western Qinling Orogen, China: Products of magma-mixing and fractionation. *Geosci. Front.* **2020**, *11*, 1305–1321. [CrossRef]
69. Wang, Y.T.; Chen, S.C.; Hu, Q.Q.; Zhang, J.; Liu, X.L.; Huang, S.K. Tectonic controls on polymetallic mineralization in the Fengxian-Taibai ore cluster zone, western Qinling, Shanxi Province. *Acta Petrol. Sin.* **2018**, *34*, 1959–1976. (In Chinese with English Abstract)

70. Cox, S.F. Structural and isotopic constraints on fluid flow regimes and fluid pathways during upper crustal deformation: An example from the Taemas area of the Lachlan Orogen, SE Australia. *J. Geophys. Res.* **2007**, *112*, B08208. [CrossRef]
71. Zhang, C.Q.; Ye, T.Z.; Wu, Y.; Wang, C.H.; Ji, H.; Li, L.; Zhang, T.T. Discussion on controlling role of Si-Ca boundary in locating Pb-Zn deposits and its prospecting significance. *Miner. Depos.* **2012**, *31*, 405–416. (In Chinese with English Abstract)
72. Shi, Y.H.; Wang, Y.; Chen, B.L.; Tan, R.W.; Gao, Y.; Shen, J.H. Characteristics of silicon-calcium surface ore-controlling in Fengtai ore-concentration areas, West Qinling Mountains: Examples from Qiandongshan Pb-Zn deposit. *Geol. China* **2022**, *49*, 226–240. (In Chinese with English Abstract)

Disclaimer/Publisher’s Note: The statements, opinions and data contained in all publications are solely those of the individual author(s) and contributor(s) and not of MDPI and/or the editor(s). MDPI and/or the editor(s) disclaim responsibility for any injury to people or property resulting from any ideas, methods, instructions or products referred to in the content.

Article

Mixing in Two Types of Fluids Responsible for Some Carbonate-Hosted Pb–Zn Deposits, SW China: Insights from the Maoping Deposit

Lei Wang ^{1,2}, Runsheng Han ^{1,2,*}, Yan Zhang ^{1,2,*} and Xiaodong Li ^{1,2}

¹ Faculty of Land Resources Engineering, Kunming University of Science and Technology, Kunming 650093, China; wanglei880813@yeah.net (L.W.); 13474046051@163.com (X.L.)

² South-West Institute of Geological Survey, Geological Survey Center for Nonferrous Metals Resources, Kunming 650093, China

* Correspondence: 11301124@kust.edu.cn (R.H.); m15925201825@163.com (Y.Z.)

Abstract: Carbonate-hosted Pb–Zn deposits are of major economic importance. The Sichuan–Yunnan–Guizhou metallogenic belt (SYGMB), located on the western margin of the Yangtze Block, comprises over 400 carbonated-hosted Pb–Zn deposits. However, ore-forming fluids recorded in these deposits have led to controversy regarding ore genesis. We investigated a fluid system for the Maoping deposit in the SYGMB, based on fluid inclusions, and H–O–He–Ar isotopic studies. The results showed that ore-forming fluids in the Maoping deposit are characterized by mixing of high-temperature and low-salinity metamorphic fluids and low-temperature and high-salinity basinal brines. The Precambrian basement is considered to produce metamorphic fluids, while the basinal brines are said to originate from the Youjiang Basin. The mineralization at the depositional site appears to reflect the coincidence of the metamorphic fluids, basinal brines, Carboniferous coal seams, and structural-stratigraphic traps. Regional-scale data show large-scale heterogeneity in fluid properties, including basinal brines, metamorphic fluids, and organic fluids. Furthermore, the data suggest a precipitation model for some high-grade Pb–Zn deposits in the SYGMB. These findings will contribute to an understanding of deposit types in the SYGMB.

Keywords: fluid inclusions; isotope; fluid mixing; carbonate-hosted Pb–Zn deposits; Southwest China

Citation: Wang, L.; Han, R.; Zhang, Y.; Li, X. Mixing in Two Types of Fluids Responsible for Some Carbonate-Hosted Pb–Zn Deposits, SW China: Insights from the Maoping Deposit. *Minerals* **2023**, *13*, 600. <https://doi.org/10.3390/min13050600>

Academic Editors: Yitian Wang, Changqing Zhang and Pierre Schiano

Received: 25 March 2023

Revised: 11 April 2023

Accepted: 24 April 2023

Published: 26 April 2023



Copyright: © 2023 by the authors. Licensee MDPI, Basel, Switzerland. This article is an open access article distributed under the terms and conditions of the Creative Commons Attribution (CC BY) license (<https://creativecommons.org/licenses/by/4.0/>).

1. Introduction

Most ore deposits form from aqueous fluids that are the main agent for the movement of mass in the crust [1]. These ore-forming fluids are commonly divided into meteoric water, sea water, basinal brines, metamorphic fluids, and magmatic fluids based on mainly their compositional variations related to different geological environments [2–4].

Carbonate-hosted Pb–Zn deposits play an important role in the supply of base metals to the world [5]. They occur in limestones or dolostones, with clearly epigenetic characteristics, and are generally not associated with or genetically related to igneous rocks [6–10]. This type of Pb–Zn deposit is best known for Mississippi-Valley-type (MVT) deposits [6,11–13]. In terms of fluid properties, the fluids associated with MVT deposits are distinct. It is widely accepted that MVT deposits precipitated from basinal brines, characterized by low temperatures (50° to 200 °C) and high salinities (10 to 30 wt.% NaCl eqv.) [13,14].

The Sichuan–Yunnan–Guizhou metallogenic belt (SYGMB) in Southwest China comprises over 400 variably sized Pb–Zn deposits that are hosted in the late Ediacaran to early Permian carbonate sequences [15]. These Pb–Zn deposits contain total sulfur ore reserves of >200 Mt, with average grades of 10 wt.%–35 wt.% Pb + Zn [15–21]. Such extensive mineralization means the operation of a huge fluid system, with economic significance and academic value to attract the attention of many scholars. However, there are some debates on fluid properties and related deposit types in the SYGMB. Given that

these deposits are similar to typical MVT deposits, they have been generally classified as MVT deposits [22–25]. However, some of their geological characteristics (e.g., high grades, ore-controlled compressive structure, high temperatures, low salinities) differ from the typical MVT deposits, suggesting Huize-style [26–29] or SYG-type deposits [18,30]. In addition, deposits in the SYGMB have a close spatial relationship with Permian Emeishan flood basalts (EFBs), which leads to a consideration of magmatic fluids being associated with the Emeishan mantle plume for ore genesis [31].

The Maoping Pb–Zn carbonate-hosted deposit in the SYGMB has ~14 Mt of sulfide ores at mean grades of 6.1 wt.% Pb and 20.2 wt.% Zn [25,29]. We provide a detailed description of the geology in this deposit based on field investigations and petrographic observations. Fluid inclusions, traditional stable isotopes (H–O), and noble gas isotopes (He–Ar) are used to constrain the properties and sources of Maoping ore formation. The contribution of these data to the development of a genetic model for the Maoping deposit is emphasized. Previous data in the SYGMB are also presented to impact our understanding of carbonate-hosted Pb–Zn deposits in the SYGMB.

2. Regional Geology

The Sichuan–Yunnan–Guizhou metallogenic belt (SYGMB), located in the southwestern part of the Yangtze Block (Figure 1A), is limited by a triangular area bounded by the N-trending Anninghe–Lvzhijiang, SE-trending Mile–Shizong, and SW-trending Ziyun–Yadu faults (Figure 1B). The strata of the SYGMB are composed of basement metamorphic rocks, cover sedimentary rocks, and the Emeishan large igneous province (basalts); see Figure 1B. The basement comprises Archean (e.g., the Kangding group of ~3.3–2.9 Ga [32,33]), Mesoproterozoic (e.g., the Dongchuan group of ~1.7–1.5 Ga [34]), and Neoproterozoic (e.g., the Kunyang/Huili group of ~1.1–0.9 Ga [35,36]) metamorphic rocks. The cover overlies the basement by an angular unconformity. It consists of Ediacaran-to-Triassic sedimentary series, which are mainly marine carbonate rocks. The Late Permian Emeishan basalts (259 ± 3 Ma [37]) occupy a large part of the SYGMB (Figure 1B).

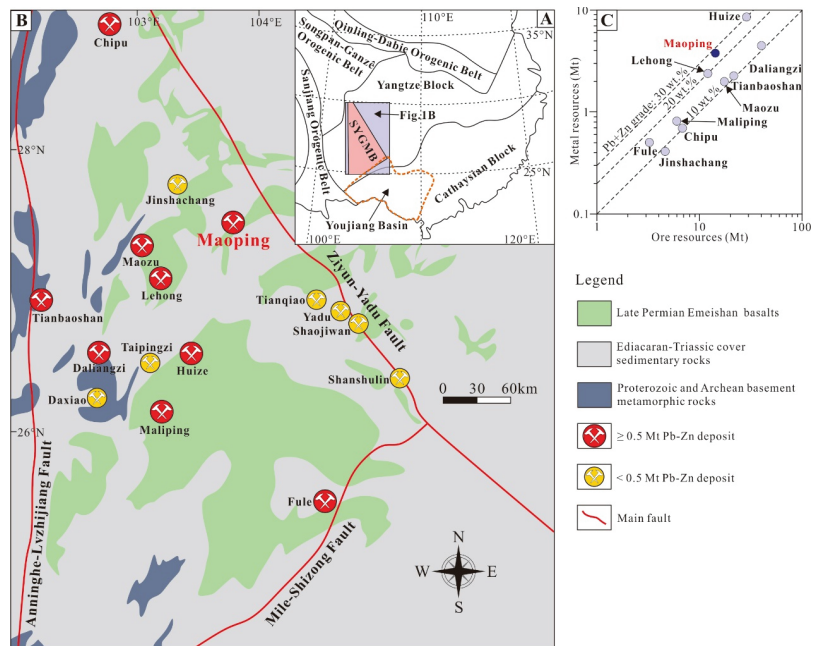


Figure 1. (A) Location of the SYGMB and Youjiang Basin in Southwest China (modified from Luo et al. [38] and Wang et al. [39]). (B) Simplified geological map of the SYGMB, showing Pb–Zn deposits

mentioned in the text (modified from Liu and Lin [15] and Han et al. [21]). (C) Pb + Zn ore resources versus Pb + Zn metal resources, showing some deposits in Figure 2b. Data from Leach and Song [25], Han et al. [29], Luo et al. [38,40], Zhou et al. [41], Ren et al. [42], Li et al. [43], and Zhao et al. [44].

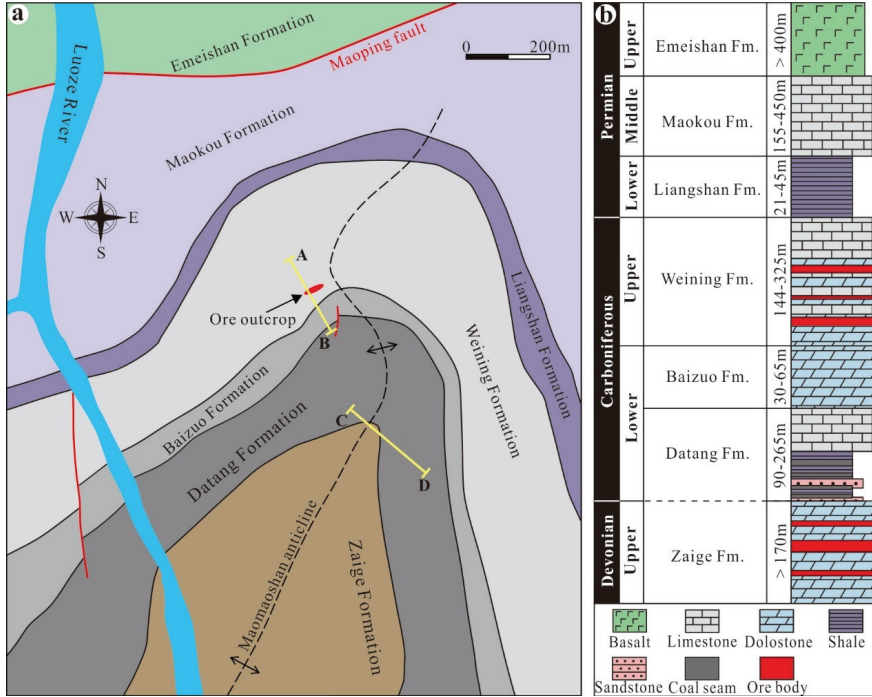


Figure 2. (a) Geological map of the Maoping mining district (modified from Wei et al. [45]). A–B and C–D cross sections are presented in Figure 3. (b) Stratigraphic column of the Maoping mining district, showing lithologies and ore-bearing stratum (modified from Xiang et al. [46]).

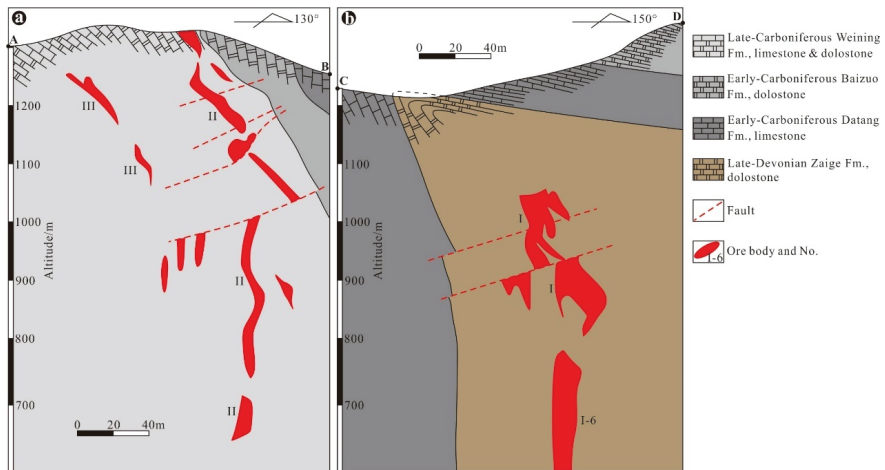


Figure 3. (a) A–B and (b) C–D cross sections, showing the characteristics of ore bodies in the Maoping deposit (modified after Han et al. [47]). The cross-section locations are in Figure 2.

The SYGMB comprises over 400 carbonate-hosted Pb–Zn deposits [15,40,48], which occur in limestone or dolostone of Late Ediacaran to Middle Permian. There are nine known deposits of Pb + Zn metal > 0.5 Mt in the SYGMB, including Huize, Maoping, Lehong, Fule, Maliping, Maozu, Daliangzi, Tianbaoshan, and Chipu (Figure 1B,C).

3. Ore Deposit Geology

3.1. Stratigraphy and Lithology

The strata exposed in the Maoping mining district includes the Upper Devonian Zaige Formation, the Lower Carboniferous Datang and Baizuo Formation, the Upper Carboniferous Weining Formation, the Lower Permian Liangshan Formation, the Middle Permian Maokou Formation, and the Upper Permian Eeimeishan Formation (Figure 2a). The Zaige Formation, generally comprising dolostones, is the main ore-bearing strata of the Maoping deposit (Figure 2b). The Datang Formation is subdivided into two members: dark shales interlayered with sandstones and coal seams in the lower member and limestones in the upper member (Figure 2b). The Baizuo Formation is medium-bedded dolostones (Figure 2b). The Weining Formation, generally comprising limestones interbedded with dolostones, is the secondary ore-bearing strata of the Maoping deposit (Figure 2b). The Liangshan and Maokou Formations are shales and limestones, respectively (Figure 2b). The Emeishan Formation is composed of flood basalts (Figure 2b).

3.2. Structure

Structurally, the Maoping fault and Maomaoshan anticline are the main structures of the Maoping mining district (Figure 2a). The Maoping fault, a reverse fault, is approximately 30 km in length and 10–40 m in width, strikes NE trending at 10°–80°, and dips to the SE at an angle of 70°–85° [49]. This fault, which considered the migration pathway of ore-forming fluids [50,51], restricts the location of a series of Pb–Zn deposits with a certain range [47]. The Maomaoshan anticline is a locally overturned anticline, striking NE at a bearing of 20°–45°, and whose NW limb is partially overturned with a dipping angle of 65°–86° and SE limb gently dips an angle of 17°–35° [52]. The known ore bodies of the Maoping deposit occur in the NW wing and plunging end of this anticline.

3.3. Ore Body Characteristics

The Maoping deposit is composed of numerous ore bodies, and almost all ore bodies are concealed. These ore bodies are divided into three main groups (Groups I, II, and III; Figure 3). Group I is hosted in the dolostone of the Late Devonian Zaige Formation, while Groups II and III are hosted within the limestone and dolostone of the Early Carboniferous Weining Formation (Figure 3). They are structurally controlled by bedding fractures [46,50,51] and occur as irregular-thickness veins roughly parallel to stratigraphic bedding (Figure 3). The No. I-6 ore body (Figure 3) is the largest-known ore body, with more than 0.5 Mt of Pb + Zn metal reserves. This ore body's dimensions are 370 m length, 280 m width, and 36.98 m average thickness, containing an average of 7.02 wt.% Pb and 16.93 wt.% Zn [51].

3.4. Mineralogy

The ores are composed of sphalerite, galena, and pyrite as ore minerals, with calcite, dolomite, quartz, and bitumen as gangue minerals (Figures 4 and 5). Massive ores made up of sulfide (sphalerite, galena, and/or pyrite; Figure 4a,b) are predominant, followed by brecciated ores (Figure 4c,d), which consist of sulfide breccias cemented by calcite. Minerals in the ores have replacement (Figure 5a–c), veinlet–vein filling (Figure 5d,e,g), fragmented (Figure 5e), co-dissolved (Figure 5f), euhedral-subhedral granular (Figure 5g), enclosed (Figure 5h), and emulsion (Figure 5i) textures.

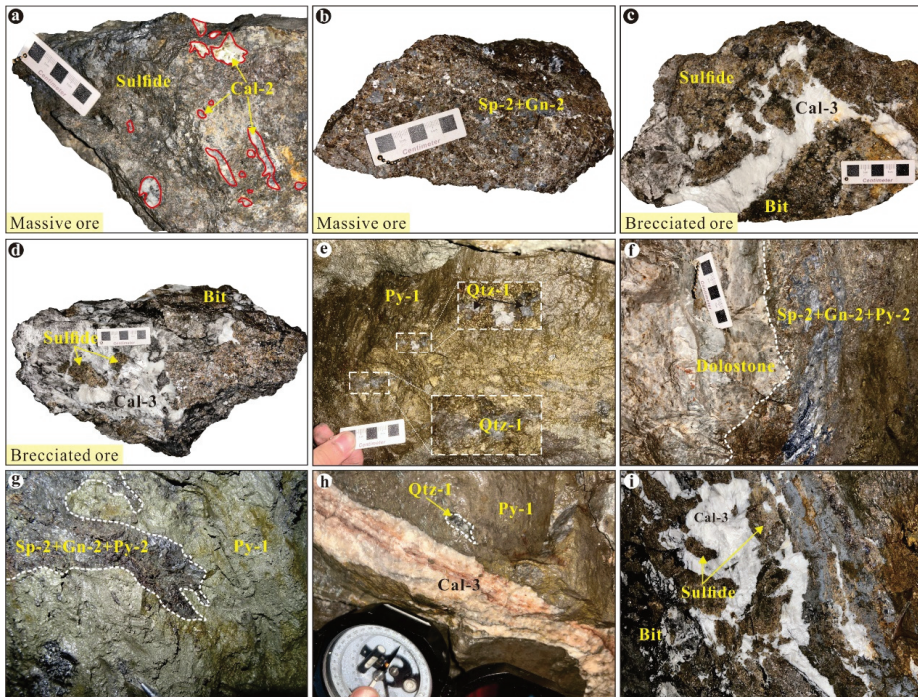


Figure 4. Photographs of field outcrops and hand specimens from the Maoping deposit. (a) Massive ore with an irregular Cal-2 block. (b) Massive ore made up of Sp-2 and Gn-2. (c,d) Brecciated ore made up of sulfide that is cemented by Cal-3. (e) Abundant Py-1 containing minor Qtz-1. (f) Coexisting Sp-2, Gn-2, and Py-2, with a clear boundary with host rock (dolostone). (g) Py-1 invaded by Sp-2+Gn-2+Py-2 veins. (h) Cal-3 vein crosscutting pre-existing Py-1 containing Qtz. (i) Sulfide breccias cemented by late Cal-3. Abbreviations: Py = pyrite; Sp = sphalerite; Gn = galena; Cal = calcite; Qtz = quartz; Bit = bitumen.

3.5. Mineral Paragenesis

Based on the mineral assemblages and crosscutting relationships, the hydrothermal period of the Maoping deposit can be subdivided into three stages of mineralization: (I) early ore stage, (II) main ore stage, and (III) late ore stage (Figure 6).

Stage I (pyrite + quartz stage): Abundant pyrites (Py-1) occur in this stage (Figure 4e,g,h). They are characterized by coarse grains (Figure 5a,e). In addition, minor quartz (Qtz-1) can be observed in dense, massive Py-1 (Figure 4e), and sphalerite, galena, and dolomite can be seen occasionally. Stage II (sphalerite + galena stage): Major sphalerite and galena (Sp-2 and Gn-2) with minor calcite (Cal-2; Figure 4a) and euhedral-subhedral fine-grained pyrite (Py-2; Figure 5g) are precipitated in this stage, which formed the massive ores (Figure 4f). There are significant crosscutting relationships of mineral assemblages between this stage and Stage I, such as Py-1 invaded by Sp-2 + Gn-2 + Py-2 veins at the macroscopic scale (Figure 4g) and Gn-2 veinlets crosscutting Py-1 at the microscale (Figure 5e). Additionally, quartz and dolomite are rarely seen. Stage III (calcite stage): This stage is characterized by the appearance of abundant calcite (Cal-3). It cuts through the mineral assemblages of Stages I and II (Figures 4h and 5g). Notably, early sulfide breccias are frequently cemented by Cal-3, forming brecciated ores (Figure 4i). In this stage, sphalerite, galena, dolomite, and bitumen can be occasionally observed.

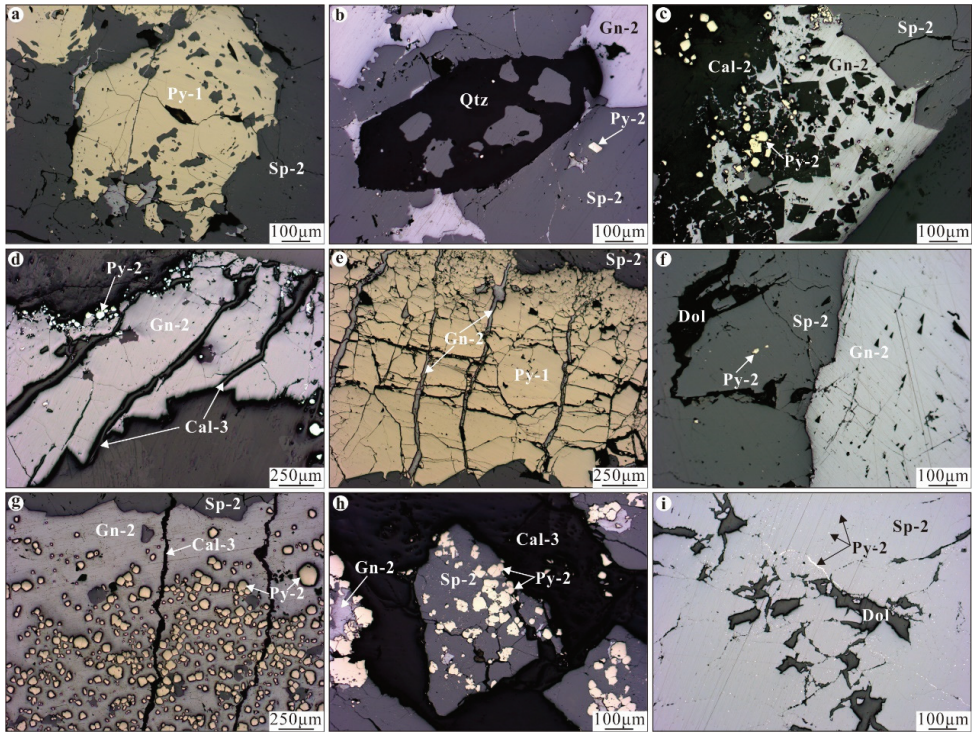


Figure 5. Microphotographs of ore textures observed at the Maoping deposit. (a) Coarse-grained Py-1 replaced by Sp-2. (b) Replacement of hexagonal prism Qtz by Sp-2. (c) Cal-2 replaced by Gn-2. (d) Cal-3 veinlets cutting through pre-existing Gn-2. (e) Late Gn-2 veinlets crosscutting fragmented Py-1. (f) Sp-2 coexisting with Gn-2. (g) Euhedral-subhedral fine-grained Py-2 distributed in Gn-2 and Cal-3 veinlets cutting through pre-existing Gn-2. (h) Sp-2 and Py-2 chips enclosed and cemented by late Cal-3. (i) Inclusions of Py-2 in Sp-2 and Sp-2 fractures filled with Dol. Abbreviations: Py = pyrite; Sp = sphalerite; Gn = galena; Cal = calcite; Qtz = quartz; Dol = dolomite.

Mineral	Hydrothermal period		
	Early ore stage (I)	Main ore stage (II)	Late ore stage (III)
Pyrite	Py-1	Py-2	
Quartz	Qtz-1		
Sphalerite		Sp-2	
Galena		Gn-2	
Calcite		Cal-2	Cal-3
Dolomite			
Bitumen			

Major phase
 Minor phase
 Local phase

Figure 6. Mineral paragenesis of the Maoping deposit.

4. Materials and Methods

4.1. Sampling and Sample Preparation

The sample suite was collected from the underground galleries and drill cores of three main ore body groups (Figure 3). Double-polished thin sections (~200 μm) for fluid-inclusion studies were prepared from the sample suite. Pyrite, calcite, and sphalerite grains (40–80 meshes) were screened from the sample suite for more than 99% purity under a stereomicroscope. Quartz-1, sphalerite-2, calcite-2, and calcite-3 were chosen for fluid-inclusion petrography and microthermometry. One pyrite-2 sample and seven sphalerite-2 samples were selected for cationic compositions of fluid-inclusion extracts. In addition, 10 calcite-2 samples and 17 calcite-3 samples were chosen for H–O isotopic analyses. Five pyrite-1 samples were selected for He–Ar isotopic analyses.

4.2. Analytical Methods

Fluid-inclusion petrography was performed according to Roedder [53] and Lu et al. [54]. Fluid inclusions were classified as primary, pseudosecondary, secondary, or isolated inclusions, with no clear spatial relation to growth zones or fractures (cf. [55]). A Linkam TMS94/1500 heating-freezing system coupled to a Leitz1350 was used for microthermometric measurements at the Institute of Geochemistry, Chinese Academy of Sciences, Guiyang, China. Calibration of the heating and freezing stages was performed by analyzing fluid-inclusion standards before and after each measurement campaign. The range of temperature for the microthermometric measurements was -195 to $+600$ $^{\circ}\text{C}$. The estimated accuracy of the freezing and heating measurements was ± 0.1 $^{\circ}\text{C}$ for temperatures lower than 25 $^{\circ}\text{C}$, ± 1 $^{\circ}\text{C}$ for temperatures ranging from 25 $^{\circ}\text{C}$ to 300 $^{\circ}\text{C}$, and ± 2 $^{\circ}\text{C}$ for temperatures higher than 300 $^{\circ}\text{C}$. Salinities were calculated using the final melting temperatures of ice [56].

The extraction of the liquid phase from fluid inclusions was conducted using the thermal explosion method. The explosive conditions of fluid inclusions in pyrite and sphalerite were 700 $^{\circ}\text{C}$ for 10 min and 500 $^{\circ}\text{C}$ for 10 min, respectively. K^+ , Na^+ , Ca^{2+} , and Mg^{2+} in the liquid phase were measured using an ion chromatograph (ICS-600) at the Beijing Research Institute of Uranium Geology, Beijing, China (BRIUG). The minimum detection limit was 0.01 mg/L.

Hydrogen and oxygen isotopic analyses were carried out at BRIUG using a MAT-253 mass spectrometer. Fluid inclusions hosted in calcite were thermally decrepitated in vacuum at 550 $^{\circ}\text{C}$ to produce H_2O , which was subsequently reduced to H_2 with a zinc reagent for H isotope study. Oxygen isotopic compositions were analyzed from calcite using the BrF_5 technique. Outcome data were presented as δD and $\delta^{18}\text{O}$ values in relation to Vienna Standard Mean Ocean Water (V-SMOW). The analytical precisions were better than $\pm 0.1\text{‰}$ and $\pm 0.2\text{‰}$ for δD and $\delta^{18}\text{O}$, respectively.

Helium and argon isotopic analyses were performed using a Helix-SFT noble gas isotope mass spectrometer at BRIUG. Noble gases were extracted from pyrite using a one-step or a multi-step crushing process in a vacuum crusher at $20,000$ psi pressure. He and Ar trapped in the cold finger were introduced separately into the mass spectrometer and analyzed in static mode. Line blanks were run before each measurement, producing negligible He blanks ($^3\text{He} < 3 \times 10^{17}$ ccSTP) and low Ar blanks ($^{40}\text{Ar} < 4 \times 10^{-11}$ ccSTP), about 0.1% of the signals from samples. Outcome data were calibrated using Helium HESJ standards [57]. Detailed measurement procedures are described by He et al. [58].

5. Results

5.1. Fluid-Inclusion Petrography

Isolated fluid inclusions, with no clear spatial relation to growth zones or fractures, were the empirical criteria for discerning primary fluid inclusions [53,59]. Consequently, isolated inclusions in quartz-1, sphalerite-2, calcite-2, and calcite-3 were interpreted as primary fluid inclusions. In addition, these minerals were also found to contain primary fluid-inclusion assemblages (FIAs) along growth zones, although they also contained

secondary fluid inclusions along healed fractures. Three major types of primary fluid inclusions were observed in these minerals based on the phase present at room temperature: (1) liquid-rich fluid inclusions (LV type) with 5 to 40 vol.% vapor in all minerals (Figure 7), (2) liquid fluid inclusions (L type) in quartz-1 (Figure 7a), and (3) daughter mineral-bearing fluid inclusions (SLV type) in quartz-1 (Figure 7a) and calcite-3 (Figure 7g). Only the LV-type fluid inclusions were analyzed microthermometrically in this study.

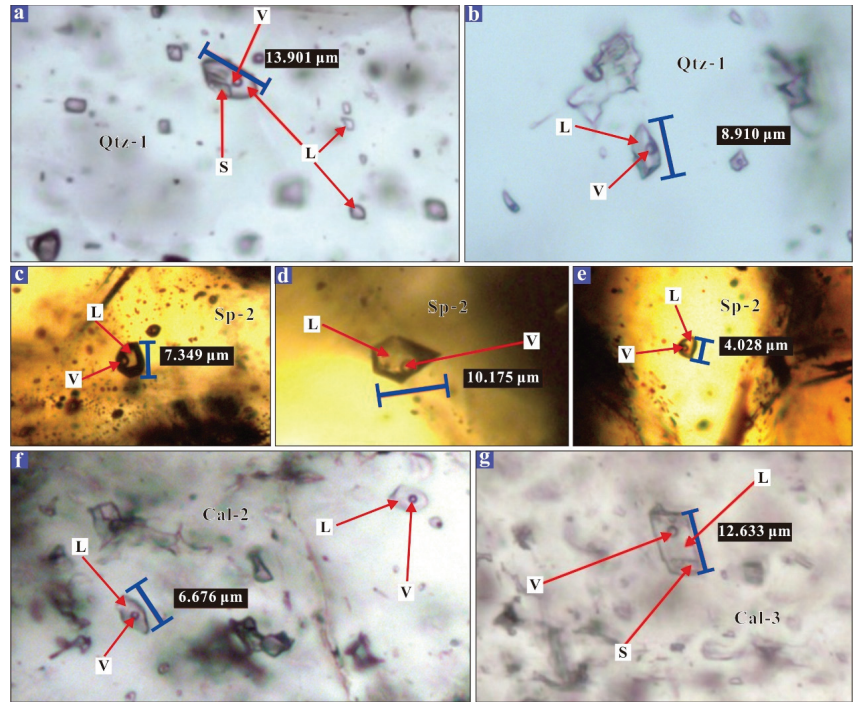


Figure 7. Photomicrographs of primary fluid inclusions from the Maoping deposit samples. (a) SLV- and L-type fluid inclusions in Qtz-1. (b) LV-type fluid inclusions in Qtz-1. (c–e) LV-type fluid inclusions in Sp-2. (f) LV-type fluid inclusions in Cal-2. (g) SLV-type fluid inclusion in Cal-3. Abbreviations: L = liquid; V = vapor; S = solid; Qtz = quartz; Sp = sphalerite; Cal = calcite.

5.2. Microthermometry

Microthermometric data collected from the different stages are summarized in Table 1. The complete dataset is included in Supplementary Table S1. The fluid inclusions in quartz-1 showed homogenization temperatures (T_h) ranging from 290 to 390 °C, with the majority falling between 300 and 340 °C (Figure 8a), and had salinities varying between 0.2 and 7.6 wt.% NaCl eqv., with the majority falling between 2 and 6 wt.% NaCl eqv. (Figure 8b). The fluid inclusions in sphalerite-2 had a T_h of 217 to 314 °C, with a peak range of 240 to 300 °C (Figure 8a), and salinities of 3.9 to 14.1 wt.% NaCl eqv., with a peak range of 6 to 10 wt.% NaCl eqv. (Figure 8b). The fluid inclusions in calcite-2 had a T_h of 217 to 278 °C, with a peak range of 220 to 260 °C (Figure 8a), and salinities of 5.3 to 13.4 wt.% NaCl eqv., with a peak range of 6 to 10 wt.% NaCl eqv. (Figure 8b). The T_h and salinities of the fluid inclusions in calcite-3 ranged from 135 to 214 °C (160 to 200 °C peak value; Figure 8a) and 8.9 to 21.3 wt.% NaCl eqv. (12 to 16 wt.% NaCl eqv. peak value; Figure 8b), respectively.

Table 1. Summary of microthermometric data on fluid inclusions from the Maoping deposit.

Stage	Host	N	T _m (°C)		T _h (°C)		Salinity (wt.% NaCl Eqv.)	
			Range	Mean	Range	Mean	Range	Mean
I	Quartz	34	−4.8 to −0.1	−2.3	290 to 390	329	0.2 to 7.6	3.8
II	Sphalerite	21	−10.2 to −2.3	−5.7	217 to 314	268	3.9 to 14.1	8.7
II	Calcite	19	−9.5 to −3.2	−6.4	217 to 278	241	5.3 to 13.4	9.6
III	Calcite	35	−18.4 to 5.8	−10.7	135 to 214	178	8.9 to 21.3	14.5

Note: Salinity = 0.00 + (1.78 × A) − (0.0442 × A²) + (0.000557 × A³), where A is the absolute value of the last ice-melting temperature (T_m) [56].

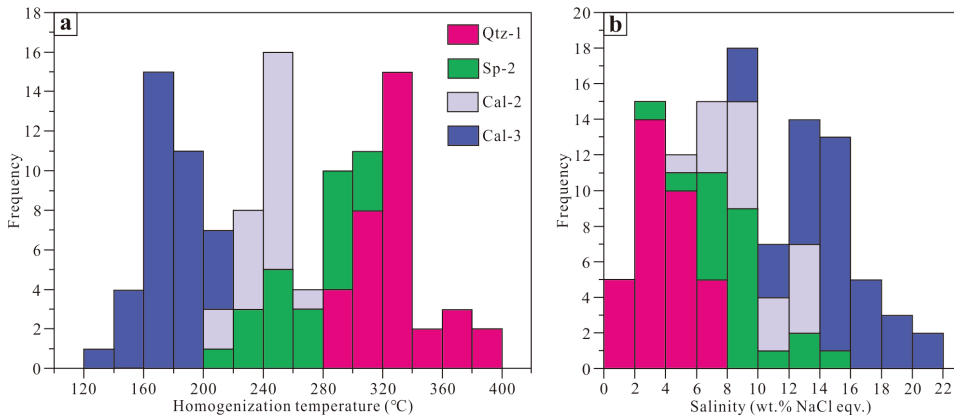


Figure 8. Stacked histograms of the homogenization temperatures (a) and salinities (b) of fluid inclusions in the Maoping deposit. Abbreviations: Qtz = quartz; Sp = sphalerite; Cal = calcite.

5.3. H–O Isotopic Compositions

Hydrogen and oxygen isotopic compositions obtained from calcite of Stages II and III are presented in Table 2. The δD_{V-SMOW} and δ¹⁸O_{V-SMOW} values of calcite from Stage II ranged from −71.4 to −50.0‰ (mean −65.1‰) and +11.4 to +13.7‰ (mean + 12.2‰), respectively, while those of calcite from Stage III varied from −78.7 to −50.3‰ (mean −66.4‰) and +7.4 to +9.9‰ (mean + 8.5‰), respectively.

Table 2. Compositions of hydrogen and oxygen isotopes in calcite from the Maoping deposit.

Sample No.	Stage	Mineral	δD _{V-SMOW} /‰	δ ¹⁸ O _{V-SMOW} /‰	T/°C	δ ¹⁸ O _{H2O} /‰
KGR02	II	Calcite	−50.0	21.3	241	13.7
KHr-13		Calcite	−58.9	19.0	241	11.4
KGr-11-1		Calcite	−66.4	19.4	241	11.8
KHr-21-1		Calcite	−70.8	21.0	241	13.4
KHr-21-3		Calcite	−67.9	19.2	241	11.6
KHr-21-4		Calcite	−71.9	19.7	241	12.1
KHr-23		Calcite	−59.6	19.5	241	11.9
KZr-11		Calcite	−63.9	19.3	241	11.7
KZr-13		Calcite	−74.1	20.1	241	12.5
KPr-11-2		Calcite	−67.0	19.6	241	12.0

Table 2. Cont.

Sample No.	Stage	Mineral	$\delta D_{V-SMOW}/\text{‰}$	$\delta^{18}O_{V-SMOW}/\text{‰}$	T/°C	$\delta^{18}O_{H_2O}/\text{‰}$
KHr5-2		Calcite	−64.3	19.0	178	8.2
KHr5-3		Calcite	−72.6	19.0	178	8.2
KPr-2		Calcite	−69.3	19.2	178	8.4
KPr-504-3		Calcite	−78.7	19.1	178	8.3
KLR6-3		Calcite	−73.8	19.0	178	8.2
KLR-7		Calcite	−74.8	19.2	178	8.4
KHr-11		Calcite	−70.3	18.9	178	8.1
KHr-12		Calcite	−77.3	18.2	178	7.4
KZr-12	III	Calcite	−70.7	19.1	178	8.3
KZr-13-1		Calcite	−56.5	19.3	178	8.5
KGR-66-1		Calcite	−60.8	20.7	178	9.9
KGR-72-2		Calcite	−61.9	20.6	178	9.8
KG-303		Calcite	−61.3	18.4	178	7.6
KPr-601		Calcite	−68.4	19.4	178	8.6
KZ-HX-1r		Calcite	−52.1	18.2	178	7.4
KZ-HX-2r		Calcite	−65.8	19.9	178	9.1
HX-850		Calcite	−50.3	19.9	178	9.1

Note: $1000 \ln \alpha_{(\text{calcite-H}_2\text{O})} = 2.78 \times 10^6 / (T + 273.15)^2 - 2.89$ [60]; temperature (T) is based on the mean value of homogenization temperatures yielded by fluid inclusions in calcite from the Maoping deposit (Table 1).

5.4. He–Ar Isotopic Compositions

The analytical results of He and Ar isotopic compositions of fluid inclusions hosted in pyrite from the Maoping deposit are exhibited in Table 3. The ⁴He concentrations ranged from 1.33×10^{-7} to 10.4×10^{-7} ccSTP/g, and the ³He/⁴He ratios were between 0.05 and 0.08 Ra, where Ra is the ³He/⁴He ratio of air, with a value of 1.40×10^{-6} [61]. The ⁴⁰Ar concentrations ranged from 4.12×10^{-7} to 26.8×10^{-7} ccSTP/g, with ⁴⁰Ar/³⁶Ar ratios of 309.7 to 746.9. The ⁴⁰Ar* was radiogenic ⁴⁰Ar, and the ⁴⁰Ar*/⁴He ratios were between 0.53 and 0.96, using the formula $^{40}\text{Ar}^*/^4\text{He} = (^{40}\text{Ar} - 295.5 \times ^{36}\text{Ar})/^4\text{He}$ [62]. Pyrite samples in this study were collected underground, so cosmogenic He was not considered a source of ³He [63–65]. The F⁴He values, defined as the ⁴He/³⁶Ar ratios of samples compared to those of the atmosphere (0.1655; [66]), ranged from 181 to 4797, indicating that the volatiles released from the pyrite samples contain negligible atmospheric He (cf. [66]). Consequently, the He and Ar isotopic compositions of fluid inclusions in these samples can represent those of ore-forming fluid.

Table 3. Helium and argon isotopic compositions of fluid inclusions in pyrite from the Maoping deposit.

Sample No.	Host	⁴ He (10 ^{−7})	³ He/ ⁴ He (Ra)	⁴⁰ Ar (10 ^{−7})	⁴⁰ Ar*/ ⁴ He	⁴⁰ Ar/ ³⁶ Ar	F ⁴ He
KHr5-6	Pyrite-1	7.23	0.05	11.4	0.58	467.6	1790
KHr6	Pyrite-1	10.4	0.05	9.80	0.57	746.9	4797
KHr8-1	Pyrite-1	7.50	0.05	10.1	0.53	486.8	2189
KHr8-2	Pyrite-1	2.59	0.07	26.8	0.48	309.7	181
KHr43-3	Pyrite-1	1.33	0.08	4.12	0.96	427.7	837

Note: The unit for ⁴He and ⁴⁰Ar is ccSTP/g; Ra is the ³He/⁴He ratio of air (1.4×10^{-6}).

6. Discussion

6.1. Reliability of Fluid-Inclusion Data

There is an assumption in fluid-inclusion studies that the integrity of fluid inclusions since their time of formation has been preserved [53]. Fluid-inclusion re-equilibration toward greater volumes (lower densities) caused by plastic deformations or the partial leakage of fluid inclusions caused by overheating can result in anomalously high T_h values and an overestimate of ore-forming temperatures [67]. The fluid-inclusion microthermome-

try of some deposits (e.g., Huize) in the SYGMB exhibit widely variable and abnormally high T_h (data concentrated 150 to 221 °C and 320 to 364 °C [68,69]) for an MVT deposit, which has been questioned by some authors. Here, it is necessary to estimate the reliability of fluid-inclusion data for the Maoping deposit, although no post-mineralization plastic deformations have been observed in this deposit.

The potential for fluid inclusions' re-equilibration during overheating largely depends on the fluid inclusions' size and host mineral strength [70,71]. Consequently, the plot of fluid-inclusion size (maximum dimension) against T_h has been used to evaluate whether fluid inclusions were re-equilibrated [67,72]. A positive correlation should be displayed in this plot if re-equilibration has occurred, and this effect would be significant for softer minerals (e.g., calcite) [67]. For all datasets, there was no positive correlation in any host minerals (Figure 9). In addition, quartz had the highest T_h values, followed by sphalerite and then calcite, which is opposite to the higher T_h of softer minerals after re-equilibration. The last evidence for preservation of fluid-inclusion integrity is that fluid inclusion in the same minerals typically showed a relatively narrow range of T_h values that was much less than that between different minerals (Figure 9). Certainly, this would also be interpreted as different precipitation temperatures of these minerals.

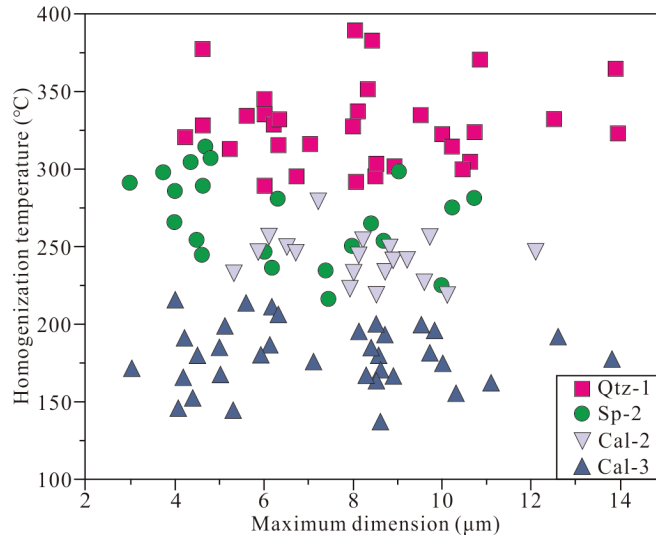


Figure 9. Plot of homogenization temperatures as a function of maximum inclusion dimensions for the Maoping deposit. Abbreviations: Qtz = quartz; Sp = sphalerite; Cal = calcite.

6.2. Definition for Two Types of Fluids

Fluid inclusions in minerals from the Maoping deposit showed a large variation in temperatures (135 to 390 °C; Figure 8a) and salinities (0.2 to 21.3 wt.% NaCl eqv.; Figure 8b). This variation can be commonly explained by the mixing of multiple fluids during ore deposition [67,73]. In addition, there are three groups of fluid inclusions with distinct T_h and salinities in the Maoping deposit (Figure 10a). The Stage I group has the characteristics of metamorphic fluids in temperature and salinity. Most of the Stage III group falls into the basinal brine field. The Stage II group is between Stage I and Stage III, which seems to indicate the mixing of metamorphic fluids and basinal brines.

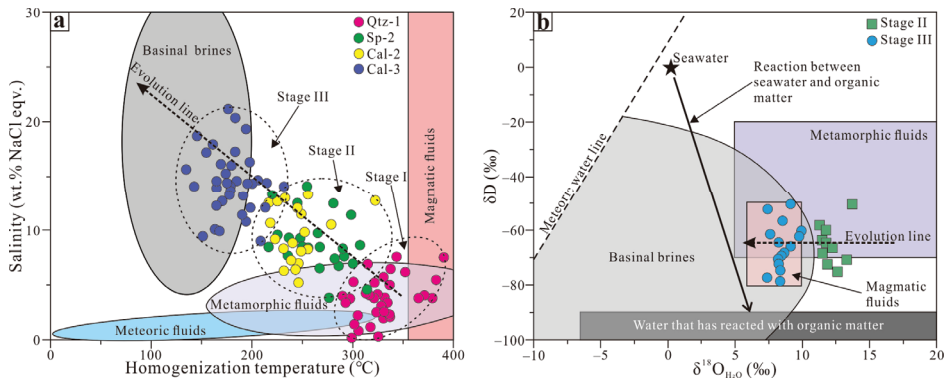


Figure 10. (a) Plot of homogenization temperatures and salinities of fluid inclusions in different ore stages of the Maoping deposit (base map from Kesler [1]). Abbreviations: Qtz = quartz; Sp = sphalerite; Cal = calcite. (b) Plot of δD versus $\delta^{18}OH_2O$ for calcite in the Maoping deposit (base map from Taylor [74]). The field of basinal brines is from Kesler [1].

The fluid δD (obtained by direct measurement of fluid inclusions) and fluid $\delta^{18}O$ values (based on mineral compositions and mineral–water fractionation factors) from hydrothermal period samples were widely used to trace the fluid sources [59,75–79]. The $\delta^{18}OH_2O$ values of fluids for Stage II (+11.4 to +13.7‰; Table 3) were significantly higher than those of magmatic fluids (+7 to +9‰; [74]) and were similar to those of metamorphic fluids (+5 to +25‰; [74]). The $\delta^{18}OH_2O$ values of fluids for Stage III ranged from +7.4 to +9.9‰ (Table 2), which overlap those of magmatic fluids. Nevertheless, Stage III fluids with low temperature and high salinity are more likely to be basinal brines (Figure 10a). In the δD versus $\delta^{18}OH_2O$ plot (Figure 10b), moreover, the H–O isotopic data of fluids for Stages III can all fall into the basinal brine field identified by Kesler [1], while those of fluids for Stages II fall between the metamorphic fluid field and the basinal brine field (Figure 10b), which can be explained by a mixing of these two fluids.

Although fluids for Stage I are characterized by metamorphic fluids (Figure 10a), their high temperatures can also be suspected to be due to mantle fluids (or magmatic fluids), especially in the case of the presence of EFBs in SYGMB (Figure 1B). The EFBs (c. 260 Ma [37]) are spatially associated with Pb–Zn deposits in the SYGMB but are much older than these deposits (194–230 Ma; see [21] and references therein). However, stable isotope studies suggest that magmatic fluids originating from EFBs should be partly responsible for these deposits ([18] and references therein).

Isotopic compositions of noble gases in paleofluids are being intensively used to track the sources of volatiles and heat in ore-forming fluids [61,80–83]. Pyrite is a suitable noble gas carrier due to the negligible He and Ar diffusion coefficients of its fluid inclusions [62]. Here, pyrite from Stage I was used to analyze the He–Ar isotopic compositions to reflect the origin of high-temperature fluids for Stage I. In the 4He versus 3He plot (Figure 11a), the $^3He/^4He$ ratios (0.05–0.08 Ra) were slightly higher compared to crust lines (0.01–0.05 Ra) and notably lower compared to the mantle line (6–9 Ra), indicating that the high-temperature fluids are dominated by crust fluids. The He_{mantle} (%) values (proportion of mantle-derived He) varied between 0.67% and 1.17%, as calculated by the formula [66] $He_{mantle}(\%) = [(^3He/^4He)_{sample} - (^3He/^4He)_{crust}] / [(^3He/^4He)_{mantle} - (^3He/^4He)_{crust}]$, where $(^3He/^4He)_{mantle} = 0.01$ Ra, $(^3He/^4He)_{crust} = 6.00$ Ra, and $(^3He/^4He)_{sample} = 0.05 - 0.08$ Ra. These values indicate a negligible proportion of mantle-derived He in the high-temperature fluids. In the plot of $^{40}Ar/^{36}Ar$ versus $^3He/^4He$ (Figure 11b), similarly, the data points suggest a negligible mantle source component.

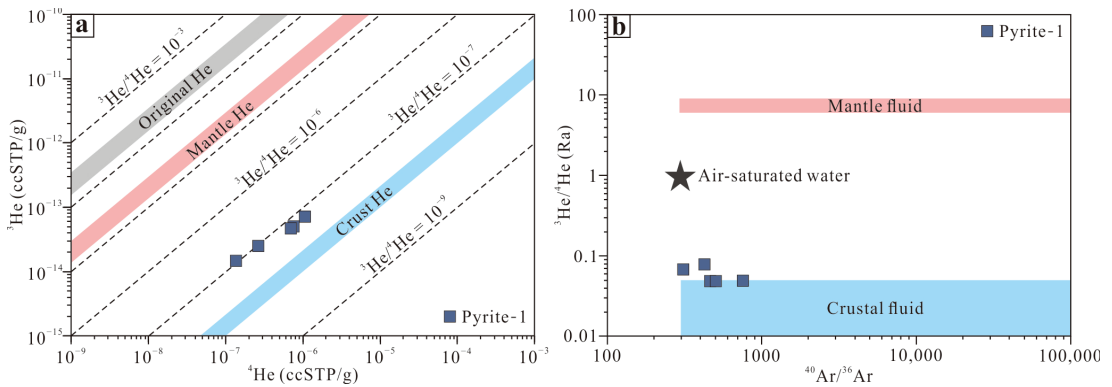


Figure 11. Plots of (a) ^4He versus ^3He and (b) $^{40}\text{Ar}/^{36}\text{Ar}$ versus $^3\text{He}/^4\text{He}$ for fluid inclusions in pyrite from the Maoping deposit (base map from Mamyin and Tolstikjin [84]).

6.3. A Genetic Model for the Maoping Deposit

The continental basin and its distal parts are a common tectonic setting for carbonate-hosted Pb–Zn deposits [11,13,25,67]. The Youjiang foreland basin, located along the SE border of the SYGMB (Figure 1A), was uplifted into a fold belt during the Late Triassic to Early Jurassic [39,85,86]. The Pb–Zn mineralization ages for the SYGMB (such as c. 203 Ma yielded by Maoping sphalerite Rb–Sr isotope geochronology [48]) coincide with the well-constrained episode of the evolution of the Youjiang foreland basin, suggesting basinal brines originating from the basin are related to the mineralization [24,48,87].

High maturation values are observed in the Youjiang Basin, where the vitrinite reflectance values ($R_m > 3\%–4\%$ [88,89]) and conodont alteration indices ($CAI > 3–5$ [90]) imply paleogeotemperatures of 200–350 °C during the Late Permian to Middle Triassic. Given the thermal anomaly, medium- to high-temperature basinal brines are considered to contribute to Pb–Zn mineralization in the SYGMB [48,86]. The contradiction between moderate- to high-temperature basinal brines identified by paleogeotemperatures and low-temperature basinal brines identified by fluid-inclusion data is problematic. The basinal brines with long-distance migration (>400 km from the thermal center of the Youjiang Basin to the Maoping deposit) will result in the temperature falling significantly due to the water–rock reaction. Furthermore, the paleogeothermal value does not seem to reflect the true temperature of fluids, especially in the Irish Midlands basin, where the R_m and CAI values indicate abnormal temperatures (300 to 550 °C) that are difficult to compare with fluid-inclusion data (100 to 250 °C) [67,91,92]. Lastly, the R_m and CAI values recorded in the Upper Permian and Middle Triassic series of the Youjiang Basin are also likely due to magmatic hydrothermal overprinting during the Early Cretaceous, with extensive magmatic activity [39,93]. Consequently, low-temperature basinal brines originating from the Youjiang Basin are more likely to contribute to the Maoping deposit, considering the aforementioned points. However, the basement containing a series of low- to high-grade metamorphic rocks [33,34] is a potential source of high-temperature metamorphic fluids, which is supported by isotopic evidence. The tracing of Pb–Zn–Cd–Sr isotopes indicates that the basement is an important source of ore-forming materials in the Maoping deposit [46,48,94].

Based on these findings, a possible genetic model for Maoping was proposed in Figure 12. During the Late Triassic to Early Jurassic, a large number of thrust fold belts, including the Youjiang fold belt and the Maoping thrust fold belt (Maomaoshan anticline and Maoping fault; Figure 2a), occurred in the southwestern part of the Yangtze Block due to intense tectonic compression (Indosinian Orogeny) [21,95–97]. Because the Youjiang foreland basin was uplifted over the Youjiang fold belt, basinal brines originating from the Youjiang Basin migrated to the northwest (Sichuan–Yunnan–Guizhou region) as a result

of gravity and/or tectonic dynamics [24,48]. During the basal brines' migration, Pb and Zn were extracted from cover sedimentary rocks and SO_4^{2-} was obtained from the sulfate evaporate (gypsum) layers distributed not far from the Maoping mining district [98]. Afterward, coalbed methane (CH_4) in the Carboniferous coal seam (Figure 2b) of the Maoping mining district acted as a reducing agent and transformed the SO_4^{2-} in the basal brine into H_2S through thermochemical sulfate reduction (TSR). However, the metamorphic fluids extracting Pb and Zn from basement metamorphic rocks migrated upward along the Maoping fault, which was a response to tectonic compression. These rising fluids were more buoyant due to their higher temperatures and lower salinities and were consequently able to punch through cover sedimentary rocks to reach the mineralization site. Finally, the low-temperature and medium-high salinity basal brines and high-temperature and low-salinity metamorphic fluids were mixed in the bedding fractures of the sedimentary rock cover and mineralization occurred. In the early ore stage (Stage I), metamorphic fluids were predominant in the mixed fluids, showing high temperature and low salinity. With the evolution of mixed fluids, the proportion of basal brines was higher in the late ore stage (Stage III), and the mixed fluids had the characteristics of low temperature and high salinity.

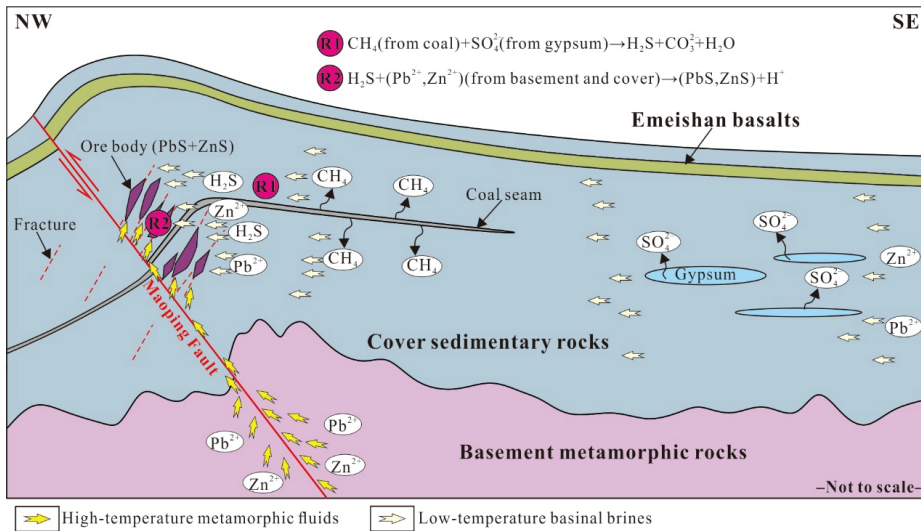


Figure 12. Fluid-mixing model for the Maoping deposit.

6.4. Implications for Carbonate-Hosted Deposits in the SYGMB

In terms of T_h -salinity properties (Figure 13A), the fluids associated with MVT deposits (temperatures of 50 to 200 °C and salinities of 10 to 30 wt.% NaCl eqv. [13]) do not clearly fit the regional pattern in the SYGMB (temperatures of 100 to 400 °C and salinities of 0 to 20 wt.% NaCl eqv.; Figure 13A). In the $\delta\text{D}-\delta^{18}\text{O}_{\text{H}_2\text{O}}$ diagram (Figure 13B), furthermore, the SYGMB Pb-Zn metallogenic hydrothermal system shares much of the complexity. Although the H-O isotopes of fluids in the most deposits are either in the field of the Youjiang Basin brines or in the field of metamorphic fluids, those in the Jinshachang and Chipu deposits fall more into the field of organic water. It is noteworthy that plotting the principal modal T_h and salinity data from the SYGMB (Figure 13A) shows that the high-grade Pb-Zn deposits (e.g., Huize, Maoping, and Lehong with an average grade of Pb + Zn \geq 20 wt.%; Figure 1C) are characterized by a wide range of T_h and salinities.

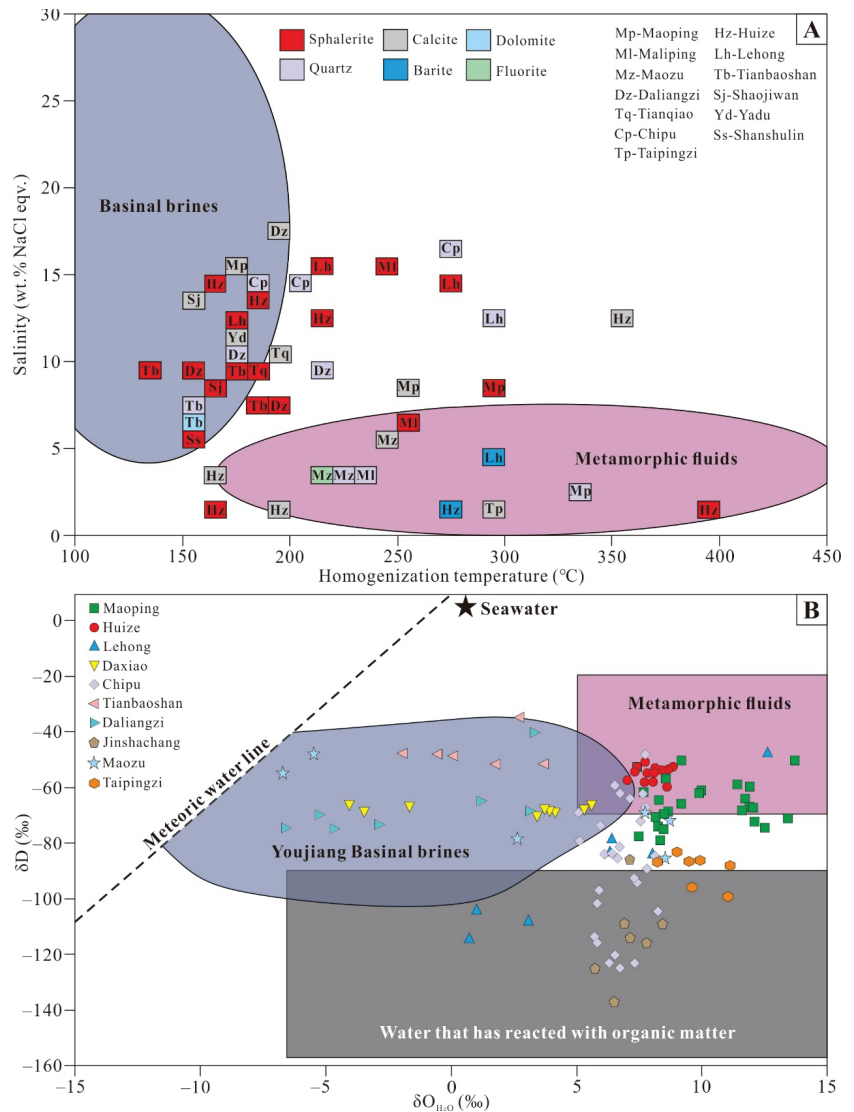


Figure 13. (A) Modal homogenization temperature–salinity plot for carbonate-hosted Pb–Zn deposits in the SYGMB (base map from Kesler [1]). Data from Han et al. [20,68], Luo et al. [38], Wang et al. [69], Zhang et al. [99], Zhao et al. [100], Wang [101], Yang [102], Wang et al. [103], and Ding et al. [104]. See Supplementary Table S2 for details. (B) δD versus $\delta^{18}O_{H_2O}$ plot for minerals from carbonate-hosted Pb–Zn deposits in the SYGMB (base map and field of Youjiang basinal brines from Taylor [74] and Wang et al. [105], respectively). Data from Zhou et al. [41], Zhao et al. [44], Liu et al. [97], Wang et al. [103], Ding et al. [104], Li et al. [106], Wu et al. [107], Yuan et al. [108], and Yang et al. [109]. See Supplementary Table S3 for details.

Such high-grade deposits require the fluids to carry abundant metals for ore deposition. There are three commonly proposed depositional processes in carbonate-hosted Pb–Zn deposits: (1) The reduced sulfur model is identified as reduced sulfur and metals to be transported together to the mineralization site [110,111], (2) the local sulfate reduction model calls upon migrating sulfate and metals to the mineralization site, where CH_4 or

other organic matter reduces sulfate and precipitates Pb–Zn sulfide [112,113], and (3) the mixing model is described as the mixing of metal-rich fluids with H₂S-rich fluids at the depositional site [114,115].

The effect of the activity of reduced sulfur is considered the most important factor that controls the solubility of Pb and Zn in the fluids [116]. The occurrence of reduced sulfur in the fluids limits the base metal concentrations in the fluids to only a few ppm [73]. Thus, the reduced sulfur model is not suitable for high-grade deposits. It is proposed that the combination of models 1 and 2 is a possible mechanism of ore deposition for some high-grade deposits in the SYGMB. We can describe it as the mixing of metal-rich but reduced sulfur-poor metamorphic fluids with basinal brines rich in metals and sulfate at the depositional site, where organic matter (e.g., CH₄) reduces sulfate and precipitates sulfide. This model requires that the basinal brines carry a large amount of sulfate to provide enough reduced sulfur to precipitate abundant Pb–Zn sulfide. The SYGMB high-grade deposits where organic matter appears can be explained by this model.

7. Conclusions

Three mineralization stages are recognized in the Maoping deposit based on the mineral assemblages and crosscutting vein relationships, i.e., (I) the pyrite + quartz stage, (II) the sphalerite + galena stage, and (III) the calcite stage. Stage I forms in high-temperature (300 to 340 °C) and low-salinity (2 to 6 wt.% NaCl eqv.) fluids. Moderate-temperature (220 to 260 °C) and moderate-salinity (6 to 10 wt.% NaCl eqv.) fluids are observed in Stage II. Fluids in Stage III are characterized by low temperature (160 to 200 °C) and high salinity (12 to 16 wt.% NaCl eqv.).

Metamorphic fluids and basinal brines are identified by fluid-inclusion measurements, together with hydrogen and oxygen isotope data. Helium and argon isotope data show a negligible mantle source component, suggesting magmatic fluids derived from Permian Emeishan basalts have no contribution to ore-forming fluids. The high-temperature and low-salinity metamorphic fluids originating from the Precambrian basement mixed with the low-temperature and high-salinity basinal brines in the Maoping district, and Pb–Zn mineralization occurred.

Regional-scale data show large-scale heterogeneity in fluid properties, including basinal brines, metamorphic fluids, and organic fluids. A possible precipitation model for high-grade Pb–Zn deposits in the SYGMB is described as the mixing of metal-rich but reduced sulfur-poor metamorphic fluids with basinal brines rich in metals and sulfate at the depositional site, where organic matter reduces sulfate and precipitates sulfide.

Supplementary Materials: The following supporting information can be downloaded at <https://www.mdpi.com/article/10.3390/min13050600/s1>: Table S1: Complete dataset for microthermometry on fluid inclusions from the Maoping deposit. Table S2: Microthermometric data on fluid inclusions for carbonate-hosted Pb–Zn deposits in the SYGMB. Table S3: Hydrogen and oxygen isotope data for carbonate-hosted Pb–Zn deposits in the SYGMB.

Author Contributions: Conceptualization, L.W. and R.H.; methodology, L.W. and X.L.; software, L.W.; validation, R.H. and Y.Z.; formal analysis, L.W. and Y.Z.; investigation, L.W., R.H., Y.Z. and X.L.; resources, R.H. and Y.Z.; data curation, L.W. and X.L.; writing—original draft preparation, L.W.; writing—review and editing, R.H. and Y.Z.; visualization, L.W.; supervision, R.H. and Y.Z.; project administration, R.H. and Y.Z.; funding acquisition, R.H. and Y.Z. All authors have read and agreed to the published version of the manuscript.

Funding: This work was jointly supported by the National Natural Science Foundation of China (grant nos. 41802089, 42172086, 41572060, and U1133602), the China Postdoctoral Science Foundation (grant no. 2017M610614), the Yunnan Major Scientific and Technological Projects (grant no. 202202AG050014), the Ten Thousand Talent Program of Yunnan Province (grant no. YNWR-QNBJ-2019-157), the Projects of the YM Lab (2011), and the Innovation Team of the Yunnan Province (2008 and 2012).

Data Availability Statement: All data are contained within the article and Supplementary Materials.

Conflicts of Interest: The authors declare no conflict of interest.

References

1. Kesler, S.E. Ore-forming fluids. *Elements* **2005**, *1*, 13–18. [CrossRef]
2. Yardley, B.W.D. Metal concentrations in crustal fluids and their relationship to ore formation. *Econ. Geol.* **2005**, *100*, 613–632. [CrossRef]
3. Liebscher, A.; Heinrich, C.A. Fluid-fluid interactions in Earth’s lithosphere. *Rev. Mineral. Geochem.* **2007**, *65*, 1–13. [CrossRef]
4. Zhang, D.H.; Jin, X.D.; Mao, S.D.; Wang, L.L. The classification of ore-forming fluid and the efficiency of ore formation of magmatic hydrothermal solution. *Earth Sci. Front.* **2011**, *18*, 90–102, (In Chinese with English Abstract).
5. Kucha, H.; Schroll, E.; Raith, J.; Halas, S. Microbial sphalerite formation in carbonate-hosted Zn-Pb ores, Bleiberg, Austria: Micro-to nanotextural and sulfur isotope evidence. *Econ. Geol.* **2010**, *105*, 1005–1023. [CrossRef]
6. Leach, D.L.; Bradley, D.C.; Lewchuk, M.; Symons, D.T.A.; Brannon, J.; Marsily, G. Mississippi Valley-type lead-zinc deposits through geological time: Implications from recent age-dating research. *Miner. Depos.* **2001**, *36*, 711–740. [CrossRef]
7. Wilkinson, J.J.; Weiss, D.J.; Mason, T.; Coles, B.J. Zinc isotope variation in hydrothermal systems: Preliminary evidence from the Irish Midlands ore field. *Econ. Geol.* **2005**, *100*, 583–590. [CrossRef]
8. Höll, R.; Kling, M.; Schroll, E. Metallogenesis of germanium—A review. *Ore Geol. Rev.* **2007**, *30*, 145–180. [CrossRef]
9. Han, R.S.; Zhang, Y.; Ren, T.; Qiu, W.L.; Wei, T.P. A summary of research on carbonate-hosted, non-magmatic, epigenetic, hydrothermal type Pb-Zn deposits. *J. Kunming Univ. Sci. Technol. (Nat. Sci.)* **2020**, *45*, 29–40. (In Chinese with English Abstract)
10. Giorno, M.; Barale, L.; Bertok, C.; Frenzel, M.; Looser, N.; Guillong, M.; Bernasconi, S.M.; Martire, L. Sulfide-associated hydrothermal dolomite and calcite reveal a shallow burial depth for Alpine-type Zn-(Pb) deposits. *Geology* **2022**, *50*, 853–858. [CrossRef]
11. Sangster, D.F. Mississippi Valley-type and SEDEX lead-zinc deposits: A comparative examination. *Trans. Inst. Min. Metall.* **1990**, *99*, B21–B42.
12. Leach, D.L.; Sangster, D.F. Mississippi Valley-type lead-zinc deposits. In *Mineral Deposit Modelling*; Special Paper 40; Kirkham, R.V., Sinclair, W.D., Thorpe, R.I., Duke, J.M., Eds.; Geological Association of Canada: St. John’s, NL, Canada, 1993; pp. 289–314.
13. Leach, D.L.; Sangster, D.F.; Kelley, K.D.; Large, R.R.; Walters, S.G. Sediment-host lead-zinc deposits: A global perspective. *Econ. Geol.* **2005**, *100*, 561–607.
14. Kesler, S.E.; Martini, A.M.; Appold, M.S.; Walter, L.M.; Huston, Y.J.; Furman, F.C. Na-Cl-Br systematics of fluid inclusions from Mississippi Valley-type deposits, Appalachian Basin: Constraints on solute origin and migration paths. *Geochim. Cosmochim. Acta* **1996**, *60*, 225–233. [CrossRef]
15. Liu, H.C.; Lin, W.D. *Regularity Research of Lead-Zinc-Silver Deposits in Northeastern Yunnan Province*; Yunnan University Press: Kunming, China, 1999; pp. 1–468. (In Chinese)
16. Huang, Z.L.; Chen, J.; Han, R.S.; Li, W.B.; Liu, C.Q.; Zhang, Z.L.; Ma, D.Y.; Gao, D.R.; Yang, H.L. *Geochemistry and Ore-Formation of the Huize Giant Lead-Zinc Deposit, Yunnan Province, China: Discussion on the Relationship between the Emeishan Flood Basalts and Lead-Zinc Mineralization*; Geological Publishing House: Beijing, China, 2004; pp. 1–214. (In Chinese)
17. Zhou, J.X.; Huang, Z.L.; Gao, J.G.; Yan, Z.F. Geological and C-O-S-Pb-Sr isotopic constraints on the origin of the Qingshan carbonate-hosted Pb-Zn deposit, Southwest China. *Int. Geol. Rev.* **2013**, *55*, 904–916. [CrossRef]
18. Zhou, J.X.; Xiang, Z.Z.; Zhou, M.F.; Feng, Y.X.; Luo, K.; Huang, Z.L.; Wu, T. The giant Upper Yangtze Pb–Zn province in SW China: Reviews, new advances and a new genetic model. *J. Asian Earth Sci.* **2018**, *154*, 280–315. [CrossRef]
19. Zhang, Y.; Han, R.S.; Ding, X.; Wang, Y.R.; Wei, T.P. Experimental study on fluid migration mechanism related to Pb-Zn super-enrichment: Implications for mineralisation mechanisms of the Pb-Zn deposits in the Sichuan-Yunnan-Guizhou, SW China. *Ore Geol. Rev.* **2019**, *114*, 103110. [CrossRef]
20. Han, R.S.; Zhang, Y.; Wang, F.; Wu, P.; Qiu, W.L.; Li, W.Y. *Metallogenic Mechanism of Germanium Rich Lead-Zinc Deposits and Prediction of Concealed Ore Location in Northeast Yunnan*; Science Press: Beijing, China, 2019; pp. 1–501. (In Chinese with English Abstract)
21. Han, R.S.; Wu, P.; Zhang, Y.; Huang, Z.L.; Wang, F.; Jin, Z.G.; Zhou, G.M.; Shi, Z.L.; Zhang, C.Q. New research progresses of metallogenic theory for rich Zn-Pb-(Ag-Ge) deposits in the Sichuan-Yunnan-Guizhou Triangle (SYGT) area, southwestern Tethys. *Acta Geol. Sin.* **2022**, *96*, 554–573. (In Chinese with English Abstract)
22. Ye, L.; Cook, N.J.; Ciobanu, C.L.; Liu, Y.P.; Zhang, Q.; Liu, T.G.; Wei, G.; Yang, Y.L.; Danyushevskiy, L. Trace and minor elements in sphalerite from base metal deposits in South China: A LA-ICPMS study. *Ore Geol. Rev.* **2011**, *39*, 188–217. [CrossRef]
23. Zhang, C.Q.; Xu, J.J.; Mao, J.W.; Rui, Z.Y. Advances in the study of Mississippi Valley-type deposits. *Miner. Depos.* **2009**, *28*, 195–210. (In Chinese with English Abstract)
24. Zhang, C.Q.; Wu, Y.; Hou, L.; Mao, J.W. Geodynamic setting of mineralization of Mississippi Valley-type deposits in world-class Sichuan-Yunnan-Guizhou Zn-Pb triangle, southwest China: Implications from age-dating studies in the past decade and the Sm-Nd age of the Jinshachang deposit. *J. Asian Earth Sci.* **2015**, *103*, 103–114. [CrossRef]
25. Leach, D.L.; Song, Y.C. Sediment-hosted zinc-lead copper deposits in China. In *Mineral Deposits of China*; Special Publication Number, 22; Chang, Z., Goldfarb, R.J., Eds.; Society of Economic Geologist, Inc.: Lawrence, KS, USA, 2019; pp. 325–409.

26. Han, R.S.; Hu, Y.Z.; Wang, X.K.; Hou, B.H.; Huang, Z.L.; Chen, J.; Wang, F.; Wu, P.; Li, B.; Wang, H.J.; et al. Mineralization model of rich Ge-Ag-bearing Zn-Pb polymetallic deposit concentrated district in northeastern Yunnan, China. *Acta Geol. Sin.* **2012**, *86*, 280–294. (In Chinese with English Abstract)
27. Han, R.S.; Wang, F.; Hu, Y.Z.; Wang, X.K.; Ren, T.; Qiu, W.L.; Zhong, K.H. Metallogenic tectonic dynamics and chronology constrains on the Huize-type (HZE) germanium-rich silver-zinc-lead deposits. *Geotecton. Metallog.* **2014**, *38*, 759–771. (In Chinese with English Abstract)
28. Han, R.S.; Chen, J.; Wang, F.; Wang, X.K.; Li, Y. Analysis of metal-element association halos within fault zones for the exploration of concealed ore-bodies—A case study of the Qilinchang Zn-Pb-(Ag-Ge) deposit in the Huize mine district, northeastern Yunnan, China. *J. Geochem. Explor.* **2015**, *159*, 62–78. [CrossRef]
29. Han, R.S.; Zhang, Y.; Qiu, W.L.; Ding, T.Z.; Wang, M.Z.; Wang, F. Geology and geochemistry of Zn-Pb-(Ge-Ag) deposits in the Sichuan-Yunnan-Guizhou Triangle area, China: A review and a new type. *Front. Earth Sci.* **2023**, *11*, 1136397. [CrossRef]
30. Zhou, J.X.; Huang, Z.L.; Yan, Z.F. The origin of the Maozu carbonate-hosted Pb-Zn deposits, southwest China: Constrained by C-O-S-Pb isotopic compositions and Sm-Nd isotopic age. *J. Asian Earth Sci.* **2013**, *73*, 39–47. [CrossRef]
31. Xu, Y.; Huang, Z.L.; Zhu, D.; Luo, T.Y. Origin of hydrothermal deposits related to the Emeishan magmatism. *Ore Geol. Rev.* **2014**, *63*, 1–8. [CrossRef]
32. Qiu, Y.M.; Gao, S.; McNaughton, N.J.; Groves, D.I.; Ling, W.L. First evidence of > 3.2Ga continental crust in the Yangtze craton of South China and its implications for Archean crustal evolution and Phanerozoic tectonics. *Geology* **2000**, *28*, 11–14. [CrossRef]
33. Gao, S.; Yang, J.; Zhou, L.; Li, M.; Hu, Z.; Guo, J.; Yuan, H.; Gong, H.; Xiao, G.; Wei, J. Age and growth of the Archean Kongling terrain, South China, with emphasis on 3.3 Ga granitoid gneisses. *Am. J. Sci.* **2011**, *311*, 153–182. [CrossRef]
34. Zhao, X.F.; Zhou, M.F.; Li, J.W.; Sun, M.; Gao, J.F.; Sun, W.H.; Yang, J.H. Late Paleoproterozoic to Early Mesoproterozoic Dongchuan Group in Yunnan, SW China: Implications for tectonic evolution of the Yangtze Block. *Precambrian Res.* **2010**, *182*, 57–69. [CrossRef]
35. Sun, W.H.; Zhou, M.F.; Yan, D.P.; Li, J.W.; Ma, Y.X. Provenance and tectonic setting of the Neoproterozoic Yanbian group, western Yangtze block (SW China). *Precambrian Res.* **2008**, *167*, 213–236. [CrossRef]
36. Wang, L.J.; Yu, J.H.; Griffin, W.L.; O'Reilly, S.Y. Early crustal evolution in the western Yangtze Block: Evidence from U-Pb and Lu-Hf isotopes on detrital zircons from sedimentary rocks. *Precambrian Res.* **2012**, *222*, 368–385. [CrossRef]
37. Zhou, M.F.; Malpas, J.; Song, X.Y.; Robinsin, P.T.; Sun, M.; Kennedy, K.K.; Leher, C.M.; Keays, R.R. At temporal link between the Emeishan large igneous province (SW China) and the end-Guadalupean mass extinction. *Earth Planet. Sci. Lett.* **2002**, *196*, 113–122. [CrossRef]
38. Luo, K.; Zhou, J.X.; Huang, Z.L.; Wang, X.K.; Wilde, S.A.; Zhou, W.; Tian, L.Y. New insights into the origin of early Cambrian carbonate-hosted Pb-Zn deposits in South China: A case study of the Maliping Pb-Zn deposit. *Gondwana Res.* **2019**, *70*, 88–103. [CrossRef]
39. Wang, Q.F.; Yang, L.; Xu, X.J.; Santosh, M.; Wang, Y.N.; Wang, T.Y.; Chen, F.G.; Wang, R.X.; Gao, L.; Liu, X.F.; et al. Multi-stage tectonics and metallogeny associated with Phanerozoic evolution of the South China Block: A holistic perspective from the Youjiang Basin. *Earth-Sci. Rev.* **2020**, *211*, 103405. [CrossRef]
40. Luo, K.; Zhou, J.X.; Ju, Y.W. A shift from BSR to TSR caused the formation of the Chipu Pb-Zn deposit, South China. *Ore Geol. Rev.* **2022**, *144*, 104845. [CrossRef]
41. Zhou, J.X.; Bai, J.H.; Huang, Z.L.; Zhu, D.; Yan, Z.F.; Lv, Z.C. Geology, isotope geochemistry and geochronology of the Jinshachang carbonate-hosted Pb-Zn deposit, southwest China. *J. Asian Earth Sci.* **2015**, *98*, 272–284. [CrossRef]
42. Ren, T.; Zhou, J.X.; Wang, D.; Yang, G.S.; Lv, C.L. Trace elemental and S-Pb isotopic geochemistry of the Fule Pb-Zn deposit, NE Yunnan Province. *Acta Petrol. Sin.* **2019**, *35*, 3493–3505. (In Chinese with English Abstract)
43. Li, Z.L.; Ye, L.; Hu, Y.S.; Wei, C.; Huang, Z.L.; Yang, Y.L.; Danyushevsky, L. Trace elements in sulfides from the Maozu Pb-Zn deposit, Yunnan Province, China: Implications for trace-element incorporation mechanisms and ore genesis. *Am. Mineral.* **2020**, *105*, 1734–1751. [CrossRef]
44. Zhao, D.; Han, R.; Wang, L.; Ren, T.; Wang, J.S.; Zhang, X.P. Genesis of the Lehong large zinc-lead deposit in northeastern Yunnan, China: Evidences from geological characteristics and C-H-O-S-Pb isotopic compositions. *Ore Geol. Rev.* **2021**, *135*, 104219. [CrossRef]
45. Wei, A.Y.; Xue, C.D.; Xiang, K.; Li, J.; Liao, C.; Akhter, Q.J. The ore-forming process of the Maoping Pb-Zn deposit, northeastern Yunnan, China: Constraints from cathodoluminescence (CL) petrography of hydrothermal dolomite. *Ore Geol. Rev.* **2015**, *70*, 562–577. [CrossRef]
46. Xiang, Z.Z.; Zhou, J.X.; Luo, K. New insights into the multi-layer metallogenesis of carbonated-hosted epigenetic Pb-Zn deposits: A case study of the Maoping Pb-Zn deposit, South China. *Ore Geol. Rev.* **2020**, *122*, 103538. [CrossRef]
47. Han, R.S.; Wu, P.; Wang, F.; Zhou, G.M.; Li, W.Y.; Qiu, W.L. 'Four Steps Type' ore-prospecting method for deeply concealed hydrothermal ore deposits—A case study of the Maoping Zn-Pb-(Ag-Ge) deposit in Southwestern China. *Geotecton. Metallog.* **2019**, *43*, 246–257. (In Chinese with English Abstract)
48. Yang, Q.; Liu, W.H.; Zhang, J.; Wang, J.; Zhang, X.J. Formation of Pb-Zn deposits in the Sichuan-Yunnan-Guizhou triangle linked to the Youjiang foreland basin: Evidence from Rb-Sr age and in situ sulfur isotope analysis of the Maoping Pb-Zn deposit in northeastern Yunnan Province, southeast China. *Ore Geol. Rev.* **2019**, *107*, 780–800. [CrossRef]

49. Tan, S.C.; Zhou, J.X.; Luo, K.; Xiang, Z.Z.; He, X.H.; Zhang, Y.H. The sources of ore-forming elements of the Maoping large-scale Pb-Zn deposit, Yunnan Province: Constrains from in-situ S and Pb isotopes. *Acta Petrol. Sin.* **2019**, *35*, 3461–3476. (In Chinese with English Abstract)
50. Hu, X.Y.; Chen, Y.H.; Liu, G.X.; Yang, H.; Luo, J.H.; Ren, K.Y.; Yang, Y.G. Numerical modeling of formation of the Maoping Pb-Zn deposit within the Sichuan-Yunnan-Guizhou Metallogenic Province, Southwestern China: Implications for the spatial distribution of concealed Pb mineralization and its controlling factors. *Ore Geol. Rev.* **2022**, *140*, 104573. [CrossRef]
51. Wang, L.; Han, R.S.; Zhang, Y.; Zhou, G.M.; Zhong, H.; Zuo, J.G.; Deng, P. Spatial structure orebodies and prediction of deep orebodies of Maoping lead-zinc deposit, northeastern Yunnan Province. *Miner. Depos.* **2022**, *41*, 207–224. (In Chinese with English Abstract)
52. Wei, C.; Ye, L.; Hu, Y.S.; Huang, Z.L.; Danyushevsky, L.; Wang, H.Y. LA-ICP-MS analyses of trace elements in base metal sulfides from carbonate-hosted Zn-Pb deposits, South China: A case study of the Maoping deposit. *Ore Geol. Rev.* **2021**, *130*, 103945. [CrossRef]
53. Roedder, E. Fluid inclusions. *Rev. Mineral.* **1984**, *12*, 644.
54. Lu, H.Z.; Fan, H.R.; Ni, P.; Ou, G.X.; Shen, K.; Zhang, W.H. *Fluid Inclusions*; Science Press: Beijing, China, 2004; pp. 1–487. (In Chinese)
55. Bauer, M.E.; Burisch, M.; Ostendorf, J.; Krause, J.; Frenzel, M.; Seifert, T.; Gutzmer, J. Trace element geochemistry of sphalerite in contrasting hydrothermal fluid systems of the Freiberg district, Germany: Insights from LA-ICP-MS analysis, near-infrared light microthermometry of sphalerite-hosted fluid inclusions, and sulfur isotope geochemistry. *Miner. Depos.* **2019**, *54*, 237–262.
56. Bodnar, R.J. Revised equation and table for determining the freezing point depression of H₂O-NaCl solutions. *Geochim. Cosmochim. Acta* **1993**, *57*, 683–684. [CrossRef]
57. Matsuda, J.; Matsumoto, T.; Sumino, H.; Nagao, K.; Yamamoto, J.; Miura, Y.; Kaneoka, I.; Takahata, N.; Sano, Y. The ³He/⁴He ratio of the new internal He standard of Japan (HESJ). *Geochem. J.* **2002**, *36*, 191–195. [CrossRef]
58. He, H.Y.; Zhu, R.X.; Saxton, J. Noble gas isotopes in corundum and peridotite xenoliths from the eastern North China Craton: Implication for comprehensive refertilization of lithospheric mantle. *Phys. Earth Planet Inter.* **2011**, *189*, 185–191. [CrossRef]
59. Zhang, P.; Kou, L.L.; Zhao, Y.; Sha, D.M. Genesis of the Maoling gold deposit in the Liaodong Peninsula: Constraints from a combined fluid inclusion, C-H-O-S-Pb-He-Ar isotopic and geochronological studies. *Geosci. Front.* **2022**, *13*, 101379. [CrossRef]
60. O’Neil, J.R.; Clayton, R.N.; Mayeda, T.K. Oxygen isotope fractionation in divalent metal carbonates. *J. Chem. Phys.* **1969**, *51*, 5547–5558. [CrossRef]
61. Stuart, F.M.; Burnard, P.G.; Taylor, R.P.; Turner, G. Resolving mantle and crustal contributions to ancient hydrothermal fluids: He-Ar isotopes in fluid inclusions from Dae Hwa W-Mo mineralization, South Korea. *Geochim. Cosmochim. Acta* **1995**, *59*, 4663–4673. [CrossRef]
62. Burnard, P.G.; Hu, R.; Turner, G.; Bi, X.W. Mantle, crustal and atmospheric noble gases in Ailaoshan Gold deposits, Yunnan Province, China. *Geochim. Et Cosmochim. Acta* **1999**, *63*, 1595–1604. [CrossRef]
63. Liu, J.C.; Wang, Y.T.; Hu, Q.Q.; Wei, R.; Huang, S.K.; Sun, Z.H.; Hao, J.L. Ore genesis of the Fancha gold deposit, Xiaoqinling goldfield, southern margin of the North China Craton: Constraints from pyrite Re-Os geochronology and He-Ar, in-situ S-Pb isotopes. *Ore Geol. Rev.* **2020**, *119*, 103373. [CrossRef]
64. Yu, D.S.; Xu, D.R.; Wang, Z.L.; Xu, K.; Huang, Q.Y.; Zou, S.H.; Zhao, Z.X.; Deng, T. Trace element geochemistry and O-S-Pb-He-Ar isotopic systematics of the Lishan Pb-Zn-Cu hydrothermal deposit, NE Hunan, South China. *Ore Geol. Rev.* **2021**, *133*, 104091. [CrossRef]
65. Gao, Y.; Liu, J.; Li, T.G.; Zhang, D.D.; Yang, Y.C.; Han, S.J.; Ding, Q.F.; Zhang, S. Multiple isotope (He-Ar-Zn-Sr-Nd-Pb) constraints on the genesis of the Jiawula Pb-Zn-Ag deposit, NE China. *Ore Geol. Rev.* **2021**, *134*, 104142. [CrossRef]
66. Kendrick, M.A.; Burgess, R.; Patrick, R.A.D.; Turner, G. Fluid inclusion noble gas and halogen evidence on the origin of Cu-porphyry mineralizing fluids. *Geochim. Cosmochim. Acta* **2001**, *65*, 2651–2668. [CrossRef]
67. Wilkinson, J.J. A review of fluid inclusion constraints on mineralization in the Irish ore field and implications for the genesis of sediment-hosted Zn-Pb deposits. *Econ. Geol.* **2010**, *105*, 417–442. [CrossRef]
68. Han, R.S.; Li, B.; Ni, P.; Qiu, W.L.; Wang, X.D.; Wang, T.G. Infrared micro-thermometry of fluid inclusions in sphalerite and geological significance of Huize super-lager Zn-Pb-(Ge-Ag) deposit, Yunnan Province. *J. Jilin Univ. (Earth Sci. Ed.)* **2016**, *46*, 91–104. (In Chinese with English Abstract)
69. Wang, J.; Zhang, J.; Zhong, W.B.; Yang, Q.; Li, F.K.; Zhu, Z.K. Sources of ore-forming fluids from Tianbaoshan and Huize Pb-Zn deposits in Yunnan-Sichuan-Guizhou region, Southwest China: Evidence from fluid inclusions and He-Ar isotopes. *Earth Sci.* **2018**, *43*, 2076–2099. (In Chinese with English Abstract)
70. Burruss, R.C. Diagenetic palaeotemperatures from aqueous fluid inclusions: Re-equilibration of inclusions in carbonate cements by burial heating. *Mineral. Mag.* **1987**, *51*, 477–481. [CrossRef]
71. Bodnar, R.J.; Binns, P.R.; Hall, D.L. Synthetic fluid inclusions. VI. Quantitative evaluation of the decrepitation behavior of fluid inclusions in quartz at one atmosphere confining pressure. *J. Metamorph. Geol.* **1980**, *7*, 229–242. [CrossRef]
72. Li, D.F.; Chen, H.Y.; Zhang, L.; Hollings, P.; Chen, Y.J.; Lu, W.J.; Zheng, Y.; Wang, C.M.; Fang, J.; Chen, G.; et al. Ore geology and fluid evolution of the giant Caixiashan carbonate-hosted Zn-Pb deposit in the Eastern Tianshan, NW China. *Ore Geol. Rev.* **2016**, *72*, 355–372. [CrossRef]

73. Nejadhadad, M.; Taghipour, B.; Lentz, D.R. Implications of multiple fluids in the deposition of Pb-Zn-Ba deposits in the Alvand Mountain, Golpayegan, Iran: Evidence from fluid inclusions and O, C, S isotopes. *Ore Geol. Rev.* **2023**, *153*, 105300. [CrossRef]
74. Taylor, H.P. The application of oxygen and hydrogen isotope studies to problems of hydrothermal alteration and ore deposition. *Econ. Geol.* **1974**, *69*, 843–883. [CrossRef]
75. Samson, I.M.; Russell, M.J. Genesis of the Silvermines zinc-lead-barite deposit, Ireland: Fluid inclusion and stable isotope evidence. *Econ. Geol.* **1987**, *82*, 371–394. [CrossRef]
76. Kesler, S.E.; Vennemann, T.W.; Frederickson, C.; Breithaupt, A.; Vazquez, R.; Furman, F.C. Hydrogen and oxygen isotope evidence for origin of MVT-forming brines, southern Appalachians. *Geochim. Cosmochim. Acta* **1997**, *61*, 1513–1523. [CrossRef]
77. Meinert, L.D.; Hedenquist, J.W.; Satoh, H.; Matsuhisa, Y. Formation of anhydrous and hydrous skarn in Cu-Au ore deposits by magmatic fluids. *Econ. Geol.* **2003**, *98*, 147–156. [CrossRef]
78. Xu, R.; Li, W.C.; Deng, M.G.; Zhou, J.X.; Ren, T.; Yu, H.J. Genesis of the superlarge Luziyuan Zn-Pb-Fe(-Cu) distal skarn deposit in western Yunnan (SW China): Insights from ore geology and C-H-O-S isotopes. *Ore Geol. Rev.* **2019**, *107*, 944–959. [CrossRef]
79. Wang, K.; Wang, Y.H.; Xue, C.J.; Liu, J.J.; Zhang, F.F. Fluid inclusions and C-H-O-S-Pb isotope systematics of the Caixiashan sediment-hosted Zn-Pb deposit, eastern Tianshan, northwest China: Implication for ore genesis. *Ore Geol. Rev.* **2020**, *119*, 103404. [CrossRef]
80. Hu, R.Z.; Burnard, P.G.; Bi, X.W.; Zhou, M.F.; Pen, J.T.; Su, W.C.; Wu, K.X. Helium and argon isotope geochemistry of alkaline intrusion-associated gold and copper deposits along the Red River-Jinshajiang fault belt, SW China. *Chem. Geol.* **2004**, *203*, 305–317. [CrossRef]
81. Hu, R.Z.; Bi, X.W.; Jiang, G.H.; Chen, H.W.; Peng, J.T.; Qi, Y.Q.; Wu, L.Y.; Wei, W.F. Mantle-derived noble gases in ore-forming fluids of the granite-related Yaogangxian tungsten deposit, Southeastern China. *Miner. Depos.* **2012**, *47*, 623–632. [CrossRef]
82. Kendrick, M.A.; Burnard, P.G. Noble gases and halogens in fluid inclusions: A journey through the earth's crust. In *The Noble Gases as Geochemical Tracers*; Burnard, P.G., Ed.; Springer: Heidelberg, Germany, 2013; pp. 319–369.
83. Bouabdellah, M.; Niedermann, S.; Velasco, F. The Touissit-Bou Beker Mississippi Valley-Type District of Northeastern Morocco: Relationships to the Messinian salinity crisis, Late Neogene-Quaternary Alkaline magmatism, and buoyancy-driven fluid convection. *Econ. Geol.* **2015**, *110*, 1455–1484. [CrossRef]
84. Mamyin, B.A.; Tolstikhin, I.N. *Helium Isotopes in Nature*; Elsevier: Amsterdam, The Netherlands, 1984; p. 273.
85. Yang, J.H.; Cawood, P.A.; Du, Y.S.; Huang, H.; Hu, L.S. Detrital record of Indosinian mountain building in SW China: Provenance of the Middle Triassic turbidites in the Youjiang Basin. *Tectonophysics* **2012**, *574*, 105–117. [CrossRef]
86. Liu, Y.; Hu, K.; Han, S.C.; Sun, Z.H. Structural evolution of the Youjiang Basin and its controlling effects on the formation of Carlin-type gold deposits. *Geol. J. China Univ.* **2015**, *21*, 1–14. (In Chinese with English Abstract)
87. Liu, W.H.; Zhang, J.; Wang, J. Sulfur isotope analysis of carbonate-hosted Zn-Pb deposits in Northwestern Guizhou Province, Southwest China: Implications for the source of reduced sulfur. *J. Geochem. Explor.* **2017**, *181*, 31–44. [CrossRef]
88. Luo, H.Z. A regressive correlation between volatility and reflectance of vitrinite in the coal beds in Upper Permian formations in Dian-Qian-Gui region and a discussion on their degree of metamorphism. *Pet. Explor. Dev.* **1983**, *6*, 43–50. (In Chinese with English Abstract)
89. Zhuang, X.G. The paleogeothermal field of northwestern Guangxi: Characteristics and its role in the formation of micro-disseminated gold deposits. *Miner. Depos.* **1995**, *14*, 83–89. (In Chinese with English Abstract)
90. DIPG (Dian-Qian-Gui Institute of Petroleum Geology). Research Report on Oil Potential of the Stratum of Yunnan-Guizhou-Guangxi Border Area. 1983; unpublished. (In Chinese)
91. Hitzman, M.W.; Beaty, D.W. The Irish Zn-Pb-(Ba) ore field. *Soc. Econ. Geol. Spec. Publ.* **1996**, *4*, 112–143.
92. Reed, C.P.; Wallace, M.W. Diagenetic evidence for an epigenetic origin of the Courtbrown Zn-Pb deposit, Ireland. *Miner. Depos.* **2001**, *36*, 428–441. [CrossRef]
93. Li, J.H.; Zhang, Y.Q.; Dong, S.W.; Johnston, S.T. Cretaceous tectonic evolution of South China: A preliminary synthesis. *Earth-Sci. Rev.* **2014**, *134*, 98–136. [CrossRef]
94. Wu, T.; Huang, Z.L.; He, Y.F.; Yang, M.; Fan, H.F.; Wei, C.; Ye, L.; Hu, Y.S.; Xiang, Z.Z.; Lai, C. Metal source and ore-forming process of the Maoping carbonate-hosted Pb-Zn deposit in Yunnan, SW China: Evidence from deposit geology and sphalerite Pb-Zn-Cd isotopes. *Ore Geol. Rev.* **2021**, *135*, 104214. [CrossRef]
95. Wang, C.; Bagas, L.; Lu, Y.; Santosh, M.; Du, B.; McCuaig, T.C. Terrane boundary and spatio-temporal distribution of ore deposits in the Sanjiang Tethyan Orogen: Insights from zircon Hf-isotopic mapping. *Earth-Sci. Rev.* **2016**, *156*, 39–65. [CrossRef]
96. Wu, Y.; Kong, Z.G.; Chen, M.H.; Zhang, C.Q.; Cao, L.; Tang, Y.J.; Yuan, X.; Zhang, P. Trace elements in sphalerites from the Mississippi Valley-type lead-zinc deposits around the margins of Yangtze Block and its geological implications: A LAICPMS study. *Acta Petrol. Sin.* **2019**, *35*, 3443–3460. (In Chinese with English Abstract)
97. Liu, X.K.; Chen, F.C.; Chang, H.; Gao, J.G.; Wu, P.; Tan, J. The mineralization of Daxiao carbonate-hosted Pb-Zn deposit, northeast Yunnan province, SW China: Constraints from Rb-Sr isotopic dating and H-O-S-Pb isotopes. *Ore Geol. Rev.* **2022**, *147*, 104956. [CrossRef]
98. Ren, S.L.; Li, Y.H.; Zeng, P.S.; Qiu, W.L.; Fan, C.F.; Hu, G.Y. Effect of sulfate evaporate salt layer in mineralization of the Huize and Maoping lead-zinc deposits in Yunnan: Evidence from sulfur isotope. *Acta Geol. Sin.* **2018**, *92*, 1041–1055. (In Chinese with English Abstract)

99. Zhang, C.Q.; Mao, J.W.; Yu, J.J.; Li, H.M. Study on fluid inclusion and the metallogenic mechanism of Chipu Pb-Zn deposit in Sichuan, China. *Acta Petrol. Sin.* **2007**, *23*, 2541–2552. (In Chinese with English Abstract)
100. Zhao, D.; Han, R.S.; Ren, T.; Wang, J.S.; Wu, H.Z.; Zhang, X.P.; Cui, J.H. Characteristics of fluid inclusions geochemistry of Lehong large-sized Pb-Zn ore deposit, northeastern Yunnan Province. *Miner. Depos.* **2018**, *37*, 1018–1036. (In Chinese with English Abstract)
101. Wang, H. Metallogenic of MVT Lead-Zinc Deposits in Huili-Huidong, Sichuan Province: A Case Study of Daliangzi and Tianbaoshan Pb-Zn Deposits. Ph.D. Dissertation, Kunming University of Science and Technology, Kunming, China, 2019; pp. 1–140. (In Chinese with English Abstract)
102. Yang, Q. Study on Mineralization of Lead-Zinc Deposits in Northeastern Yunnan and Northwestern Guizhou Province, China. Ph.D. Dissertation, China University of Geosciences, Wuhan, China, 2021; pp. 1–183. (In Chinese with English Abstract)
103. Wang, H.; Zhu, X.Y.; Wang, J.B.; Jia, D.L.; Shi, Y.; Chen, L.; Xu, Z.F. Sources of metallogenic materials and metallogenic mechanism of Tianbaoshan Pb-Zn deposit in Sichuan Province: Constraints from fluid inclusions and isotopic evidences. *Acta Petrol. Sin.* **2021**, *37*, 1830–1846. (In Chinese with English Abstract)
104. Ding, W.P.; Xie, C.F.; Huang, C.; Zhang, B.; Xin, Z.; Zhan, H.S.; Zheng, L.L.; Kong, F.Q.; Wang, H.B.; Huang, L.F. Sources of Permian lead-zinc ore-forming materials in Sichuan-Yunnan-Guizhou area: C-H-O-S-Pb isotope constraint—An example from Taipingzi lead-zinc deposit in Yunnan Provinces. *Geol. China* **2022**, *49*, 1845–1861. (In Chinese with English Abstract)
105. Wang, G.Z.; Hu, R.Z.; Su, W.C.; Zhu, L.M. Basin fluid flow and mineralization in Youjiang Basin, Yunnan-Guizhou-Guangxi Provinces. *Sci. China (Ser. D)* **2003**, *46*, 99–109.
106. Li, W.B.; Huang, Z.L.; Zhang, G. Sources of the ore metals of the Huize ore field in Yunnan province: Constraints from Pb, S, C, H, O and Sr isotope geochemistry. *Acta Petrol. Sin.* **2006**, *22*, 2567–2580. (In Chinese with English Abstract)
107. Wu, Y.; Zhang, C.Q.; Mao, J.W.; Ouyang, H.G.; Sun, J. The genetic relationship between hydrocarbon systems and Mississippi Valley-type Zn-Pb deposits along the SW margin of Sichuan Basin, China. *Int. Geol. Rev.* **2012**, *55*, 941–957. [CrossRef]
108. Yuan, B.; Mao, J.W.; Yan, X.H.; Wu, Y.; Zhang, F.; Zhao, L.L. Sources of metallogenic materials and metallogenic mechanism of Daliangzi Ore Field in Sichuan Province: Constraints from geochemistry of S, C, H, O, Sr isotope and trace element in sphalerite. *Acta Petrol. Sin.* **2014**, *30*, 209–220. (In Chinese with English Abstract)
109. Yang, Q.; Zhang, J.; Wang, J.; Zhong, W.B.; Liu, W.H. Study of ore-forming fluid geochemistry of Maozu large-scale lead-zinc deposit in northeast Yunnan. *Miner. Resour. Geol.* **2017**, *31*, 854–863. (In Chinese with English Abstract)
110. Anderson, G.M. Precipitation of Mississippi Valley-type ores. *Econ. Geol.* **1975**, *70*, 937–942. [CrossRef]
111. Symons, D.A. Genesis of Mississippi Valley-type lead-zinc deposits. *Annu. Rev. Earth Planet. Sci.* **1986**, *14*, 177–199.
112. Barton, P.B. Possible role of organic matter in the precipitation of the Mississippi Valley ores: Genesis of strata-bound lead-zinc-barite-fluorite deposits in carbonate rocks. *Econ. Geol. Monogr.* **1967**, *3*, 371–377.
113. Anderson, G.M. Organic maturation and ore precipitation in Southeast Missouri. *Econ. Geol.* **1991**, *86*, 909–926. [CrossRef]
114. Corbella, M.; Ayora, C.; Cardellach, E. Hydrothermal mixing, carbonate dissolution and sulfide precipitation in Mississippi Valley-type deposit. *Miner. Depos.* **2004**, *39*, 344–357. [CrossRef]
115. Anderson, G.M. The mixing hypothesis and the origin of Mississippi Valley-type ore deposits. *Econ. Geol.* **2008**, *103*, 1683–1690. [CrossRef]
116. Plumlee, G.S.; Leach, D.L.; Hofstra, A.H.; Landis, G.P.; Rowan, E.L.; Viets, J.G. Chemical reaction path modeling of ore deposition in Mississippi Valley-type Pb-Zn deposits of the Ozark region, U.S. midcontinent. *Econ. Geol.* **1994**, *89*, 1361–1383. [CrossRef]

Disclaimer/Publisher’s Note: The statements, opinions and data contained in all publications are solely those of the individual author(s) and contributor(s) and not of MDPI and/or the editor(s). MDPI and/or the editor(s) disclaim responsibility for any injury to people or property resulting from any ideas, methods, instructions or products referred to in the content.

Article

Metallogenesis and Formation of the Maliping Pb-Zn Deposit in Northeastern Yunnan: Constraints from H-O Isotopes, Fluid Inclusions, and Trace Elements

Yongsheng Yao ¹, Hongsheng Gong ^{1,2,*}, Runsheng Han ^{1,2,*}, Changqing Zhang ³, Peng Wu ^{1,2} and Gang Chen ¹

¹ Faculty of Land Resources Engineering, Kunming University of Science and Technology, Kunming 650093, China; yaoyongsheng2021@163.com (Y.Y.); wupeng8104@163.com (P.W.); chengang@kust.edu.cn (G.C.)

² Southwest Institute of Geological Survey, Geological Survey Center for Non-Ferrous Metals Resources, Kunming 650093, China

³ MNR Key Laboratory of Metallogeny and Mineral Assessment, Institute of Mineral Resources, Chinese Academy of Geological Sciences, Beijing 100037, China; zcqchangqing@163.com

* Correspondence: ghs7633@163.com (H.G.); 11301124@kust.edu.cn (R.H.); Tel.: +86-139-0886-1618 (H.G.)

Abstract: The Maliping large-scale Pb-Zn deposit is located in the Sichuan-Yunnan-Guizhou Pb-Zn polymetallic metallogenic triangle area (SYGT), where the Pb-Zn ore body is hosted in the interlayer fracture zone at the interface between siliceous cataclastic dolomite and clastic rocks in the Lower Cambrian Yuhucun Formation and is tectonically driven. Unlike other Pb-Zn deposits hosted in the Sinian and Carboniferous carbonate rocks in the area, the metallogenic mechanism and deep and peripheral ore prospecting prediction research require further exploration. In this study, representative samples of a typical orebody profile were systematically collected, and microthermometry of fluid inclusions and H-O isotopes and metal sulfide trace element analyses were performed. The main findings were as follows: (1) The fluid inclusion study showed that the ore-forming fluids have vapor-rich phase reduction characteristics of medium-low temperature, salinity, and density. (2) H-O isotopic studies showed that the ore-forming fluids are derived from the mixing of deep-source fluids flowing through the deep fold basement (Kunyang Group) and organic containing basin brine. (3) Rare earth element (REE) characteristics indicate that the ore-forming materials were primarily derived from the folded basement (Kunyang Group). (4) The trace element study showed that sphalerite is relatively enriched in Cu, Cd, Ga, and Ge, while depleted in Fe, Mn, Sn, and Co, similar to the typical Huize-type (HZT) Pb-Zn deposit in the area. Therefore, it is suitable to explore the deposit using a large-scale “four step style” ore prospecting method for ore prospecting and prediction. Moreover, the results provide a reference for the study of Pb-Zn metallogenic systems and new ideas for the deep and peripheral prospecting of Pb-Zn deposits in this area.

Keywords: H-O isotopes; fluid inclusions; trace elements; ore-forming materials sources; metallogenic mechanism; Maliping Pb-Zn deposit; Sichuan-Yunnan-Guizhou Pb-Zn polymetallic metallogenic triangle area

Citation: Yao, Y.; Gong, H.; Han, R.; Zhang, C.; Wu, P.; Chen, G. Metallogenesis and Formation of the Maliping Pb-Zn Deposit in Northeastern Yunnan: Constraints from H-O Isotopes, Fluid Inclusions, and Trace Elements. *Minerals* **2023**, *13*, 780. <https://doi.org/10.3390/min13060780>

Academic Editor: George M. Gibson

Received: 9 May 2023

Revised: 31 May 2023

Accepted: 2 June 2023

Published: 7 June 2023



Copyright: © 2023 by the authors. Licensee MDPI, Basel, Switzerland. This article is an open access article distributed under the terms and conditions of the Creative Commons Attribution (CC BY) license (<https://creativecommons.org/licenses/by/4.0/>).

1. Introduction

The Sichuan-Yunnan-Guizhou Pb-Zn polymetallic metallogenic triangle area (SYGT) is situated on the southwestern margin of the Yangtze Block (Figure 1a) and is an important component of the large low-temperature metallogenic domains in southwest China [1–3]. The SYGT is the largest Pb-Zn metallogenic area in China, with over 500 Pb-Zn deposits (spots) distributed in the area [4,5]. These are controlled by fault structures and distributed in a beaded shape along larger-scale fault zones. Most deposits exhibit an average Pb + Zn grade exceeding 15% [6] and are rich in valuable elements, such as Ag and Ge [7–12]. In recent years, a large number of geologists have conducted research and development studies on Pb-Zn deposits in the area, but insufficient reserves in old mines and the

challenges of deep ore prospecting remain issues. Therefore, there is an urgent need to innovate and improve the metallogenic theory and ore prospecting methods and to identify deep replacement resources.

The ore body of the Maliping Pb-Zn deposit is a large-scale Pb-Zn deposit newly discovered in northeast Yunnan. It is hosted in the Lower Cambrian Yuhucun Formation (to facilitate comparison with previous research results, the stratigraphic division in this study still follows the original stratigraphic criteria), within the interlayer fracture zone of the interface between siliceous cataclastic dolomite and clastic rocks (Yunnan Nonferrous Geological, Geophysical, and Geochemical Exploration Survey, 2011 internal data). Although numerous studies have been conducted on carbonate-hosted Pb-Zn deposits in the SYGT, relatively few investigations have been conducted on Pb-Zn deposits hosted in the interlayer fracture zone of the interface between the siliceous cataclastic dolomite and clastic rocks. Previous studies have examined the genesis of the Maliping Pb-Zn deposit from different perspectives and proposed varying views: (1) Based on field geological characteristics and analysis of major and trace elements in the ore, Shen et al. [13] and He et al. [14] suggested that the deposit was based on the original ore layer formed by hydrothermal deposition and was driven and transformed mineralization by the eruption of the later Emeishan basalt, which had a submarine (volcanic) hydrothermal exhalative sedimentation + later (hydrothermal) superimposed transformation genesis. (2) Luo et al. [15] and Hu et al. [16] suggested that the deposit was of the Mississippi Valley type (MVT) through the study of dispersed elements in ore minerals and C-O-S-Pb isotopes. Luo et al. [17] suggested that the major metal source of the Maliping deposit was Proterozoic basement rocks (e.g., the Kunyang Group), whereas Early Cambrian black shales and phosphate rocks acted as secondary sources. The previous understanding of the genesis of the deposit remains controversial, and the research on the metallogenic mechanism and ore prospecting prediction of Pb-Zn deposits hosted in the interlayer fracture zone at the interface between siliceous cataclastic dolomite and clastic rock needs to be in-depth.

In this study, we performed microthermometry of fluid inclusions, microscopic laser Raman spectroscopy, H-O isotopic composition analysis, metal sulfide trace element analysis, and electron probe micro-analysis (EMPA)-mapping analysis to trace the characteristics and sources of ore-forming fluids in the Maliping Pb-Zn deposit. In addition, we conducted a comparative analysis with typical Pb-Zn deposits in the area to determine the genesis of the deposit and propose a metallogenic mechanism. These findings offer a new basis for the study of the regional Pb-Zn mineralization system and the ore prospecting prediction of deep and peripheral parts of the deposit.

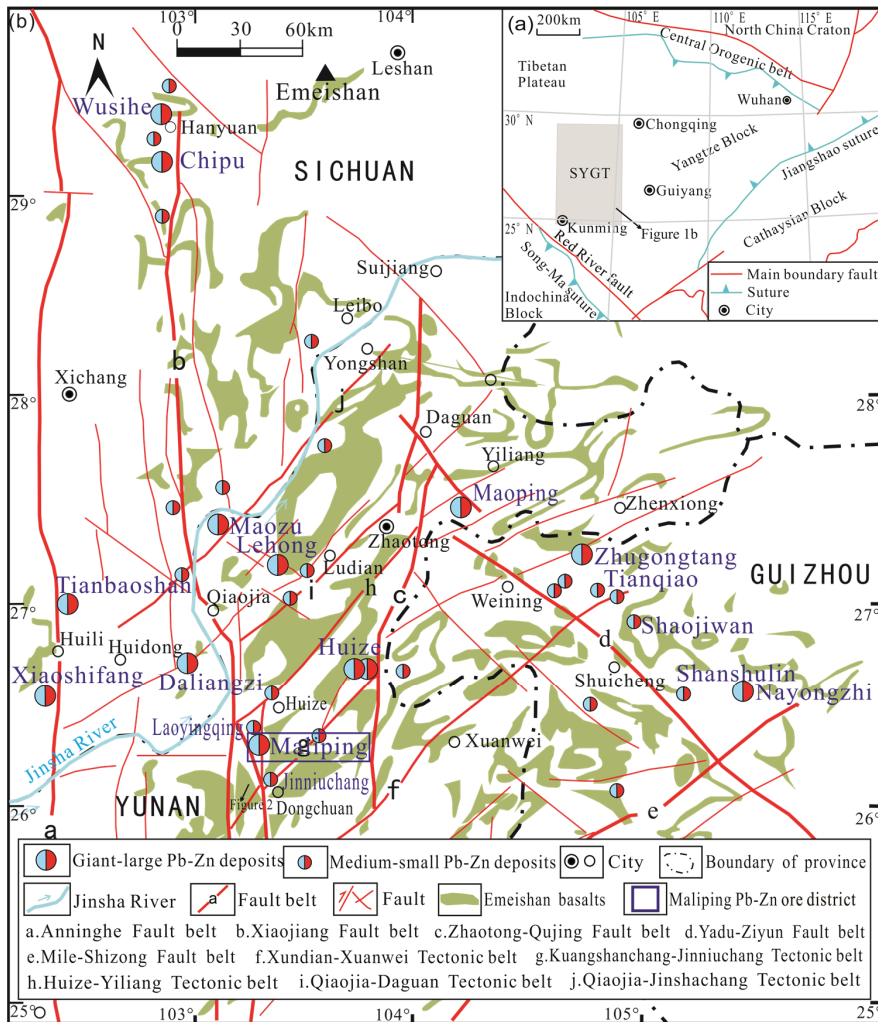


Figure 1. (a) Simplified tectonic map of southwest China [18]; (b) Distribution map of main faults and deposits in the SYGT [18].

2. Metallogenic Geological Background

The SYGT is located on the southwestern margin of the Yangtze Block (Figure 1a) and is controlled by three deep boundary faults: the NW-trending Yadu-Ziyun (Kangding-Yiliang-Shuicheng), NE-trending Mile-Shizong, and the NS-trending Anninghe fault belts (Figure 1b). The strata in the area mainly include basement and sedimentary cover, with an angular unconformity between them. Since the Archean, multiple stages of tectonic evolutions have occurred in the area, with the crystalline basement constituted by the Paleoproterozoic Kangding Group and the folded basement constituted by the Mesoproterozoic Kunyang and Huili groups [6,19].

The ore concentration area of northeastern Yunnan has formed eight NE-trending “Xi-type” tectonic mineralization belts from south to north (sinistral oblique thrust strike-slip fault-fold belt, controlling the spatial distribution of Pb-Zn deposits in the region), which are typical structures in the area [20,21]. The Maliping Pb-Zn deposit is located on

the eastern side of the Xiaojiang fault belt in northeastern Yunnan and is controlled by an interlayer fault on the eastern wing of the Wuxing anticline. Within the ore district, there is a monoclinic structure, developing NW- and nearly NS-trending faults. The NE-trending bedding fault was the main ore-controlling and ore-bearing fault. The strata in the ore district are distributed in a nearly NS-trending manner, trending eastward and exposing the Kunyang Group, Heishantou Formation, Sinian, Cambrian, Devonian, Carboniferous, Permian, and Quaternary (Figure 2a). No magmatic rock outcrops are observed in the ore district (Figure 2b).

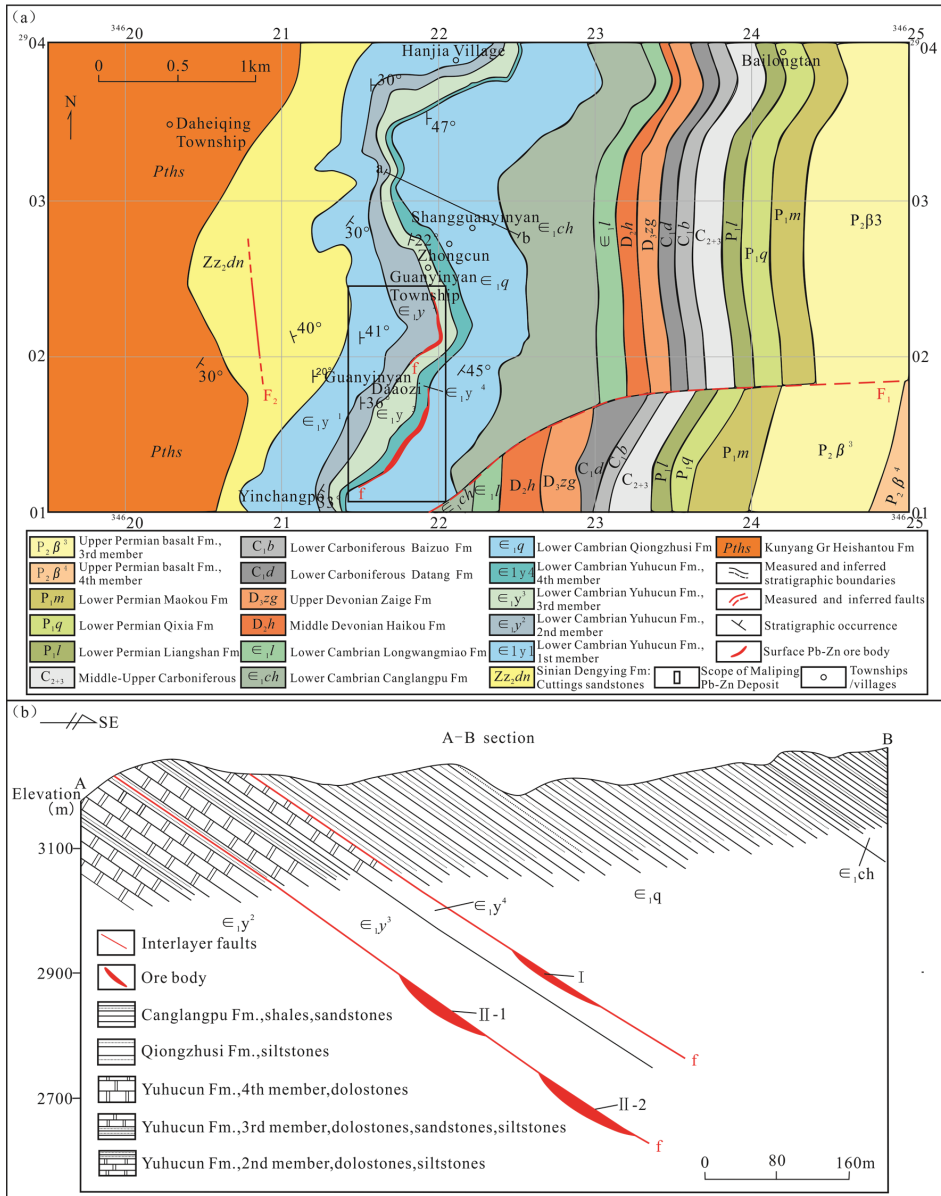


Figure 2. (a) Geological sketch map of the Maliping Pb-Zn deposit; (b) Geological section map of the Maliping Pb-Zn Deposit [16].

The ore bodies (I, II-1, and II-2) are hosted in the NEE-trending interlayer fracture zone at the interface between the siliceous cataclastic dolomite and clastic rocks in the Lower Cambrian Yuhucun Formation; however, a small portion also occurs along the NW-trending fault (Figure 3a,b), which is lenticular and stratoid (Figure 3b). The ore body strikes $68\text{--}156^\circ$ and dips $15\text{--}42^\circ$, with an average true thickness of 1.63–2.69 m and an average Pb + Zn grade of 12.69%–15.89% (Yunnan Nonferrous Geological, Geophysical, and Geochemical Exploration Survey, 2011 internal data). The ore minerals are primarily sphalerite and galena, followed by pyrite and limonite; gangue minerals are mainly quartz. The ore textures are granular, mosaic, and porphyritic. The ore structure is primarily disseminated and brecciated but also includes banded, taxitic, veinlet, and laminated structures (Figure 3c,d). Pyrite and sphalerite are symbiotic (Figure 3e,g), galena metasomatic pyrite and sphalerite, quartz metasomatic galena, sphalerite, and pyrite (Figure 3e,f,h,i). Wall-rock alteration is primarily characterized by silicification.

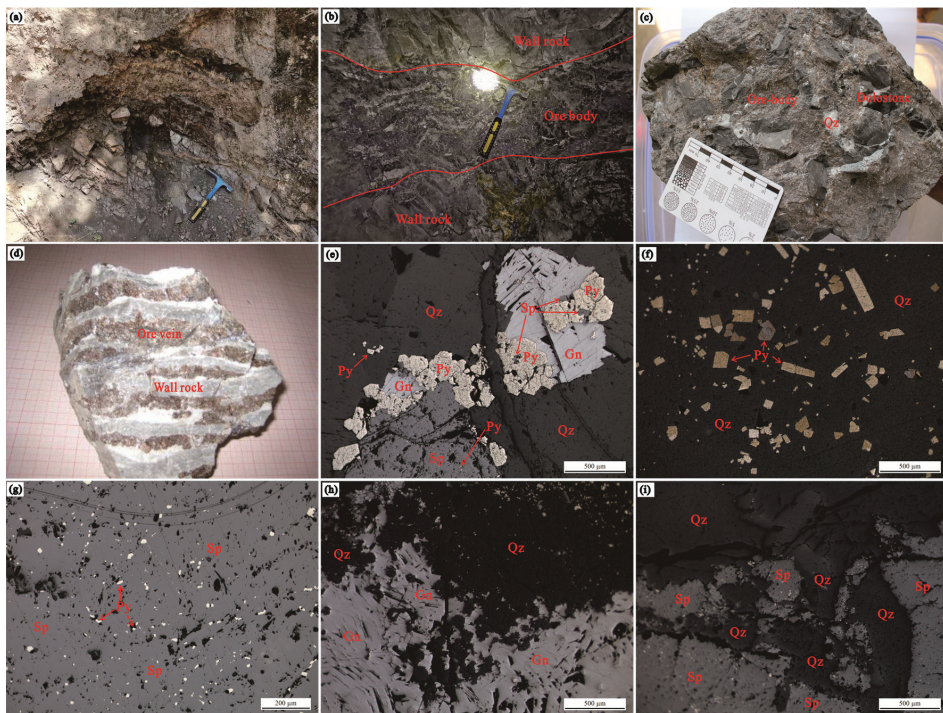


Figure 3. Ore mineralization characteristics and microscopic photos of the Maliping Pb-Zn deposit. (a) Interlayer sliding zone in the Maliping Pb-Zn deposit; (b) Stratoid ore body controlled by interlayer fault; (c) Brecciated ore; (d) Banded ore; (e) Pyrite and sphalerite are symbiotic, galena metasomatic pyrite and sphalerite, quartz metasomatic galena, sphalerite and pyrite; (f) Quartz metasomatic pyrite; (g) Pyrite and sphalerite are symbiotic; (h) Quartz metasomatic galena; (i) Quartz metasomatic sphalerite. (Gn = Galena; Py = Pyrite; Sp = Sphalerite; Qz = Quartz).

3. Research Methods

3.1. Sample Collection

Eight representative primary metal sulfide ores were collected from different middle sections, with six II-1 and two II-2 orebodies. Six single-mineral sphalerite and seven quartz samples were selected from among the collected samples. Seven quartz samples were analyzed for H-O isotopes, and six sphalerite samples were analyzed for trace elements and rare earth elements (REEs). We utilized eight metal sulfide ore samples and ground double-

sided polished fluid inclusion slices (thickness of approximately 200 μm). By comparing the petrography of the fluid inclusions, a microscopic thermodynamic analysis was conducted on 71 inclusions from 2 representative inclusion slices.

3.2. Analytical Methods

Single metal sulfide minerals were ground manually to 40–60 mesh, cleaned, and dried. Single minerals with a purity of over 99% were selected under binocular conditions. Subsequently, six single sphalerite minerals were crushed to less than 200 mesh in an agate mortar, and seven single quartz minerals were crushed to 60 mesh in an agate mortar for instrument analysis.

H–O isotopic testing was performed at Beijing Createch Testing Technology Co., Ltd. The hydrogen isotope testing procedures were as presented by Gong et al. [22]. The testing equipment used was a pyrolysis furnace (FlashEA, Thermo, Waltham, MA, USA) and a mass spectrometer (253 plus, Thermo, Waltham, MA, USA). The international standard material (polyethylene, IAEA-CH-7, $\delta\text{DV-SMOW} = -100.3\text{‰}$) had a test accuracy of better than 1‰ [22]. For oxygen isotope testing, the sample was ground to 200 mesh, and 6 mg of pure quartz sample was weighed. The analysis adopted the traditional BrF5 method [23] with a standard sample analysis accuracy exceeding $\pm 0.2\%$ and a relative standard of V-SMOW. A 253-plus gas isotope ratio mass spectrometer was used as the testing instrument.

Single-mineral trace and REE content analyses were completed at the South China Mineral Resources Supervision and Inspection Center, China. The testing instrument was an inductively coupled plasma mass spectrometer (ICP-MS), with a standard sample analysis accuracy of better than 5% and a lower detection limit of $(0.n-n) \times 10^{-9}$. The analysis and operating procedures were as presented by Qi et al. [24]. EPMA-mapping was completed at the Research Center for Analysis and Measurement, Kunming University of Science and Technology, using an EPMA-1720 with an accelerating voltage of 15 kV, current of 10 nA, and analytical accuracy of 0.01%.

Microthermometry of the inclusions and laser Raman microprobe testing of individual inclusion components were performed at the Southwest Institute of Geological Survey, Geological Survey Center for Nonferrous Metals Resources. The testing equipment used was a THMS 600 standard microscope and a Renishawin Via micro confocal laser Raman spectrometer. During microthermometry, the fluid inclusions standard sample was used to calibrate the cold and hot platform and determine the error at high ($>200\text{ }^\circ\text{C}$) $\pm 2\text{ }^\circ\text{C}$ and low temperatures ($<0\text{ }^\circ\text{C}$) $\pm 0.1\text{ }^\circ\text{C}$. The analysis and operating procedure are shown in Goldstein and Reynolds [25]. The laser Raman microprobe test light source was 514.5 μm , with a counting time of 10 s, counting once every 1 cm^{-1} (wave number), over 100–4000 cm^{-1} all-band Qu wave peaks. The laser beam spot was 2 μm , and the spectral resolution was 2 cm^{-1} .

4. Analytical Results

4.1. Petrographic Characteristics of Fluid Inclusions

The fluid inclusions in quartz were all primary inclusions distributed in dispersed and isolated irregular shapes, such as triangular and flat. Their sizes were usually 4–10 μm , with a few were over 10 μm . The inclusions are vapor–liquid two-phase inclusions, most of which are rich in liquid-phase inclusions, with the vapor phase accounting for approximately 10%–35% (Figure 4).

4.2. Microthermometry Results of Fluid Inclusions

The salinities and homogenization temperatures of 71 primary vapor–liquid two-phase inclusions in gangue mineral quartz from the metallogenic period were determined (Figure 5). The homogenization temperatures of fluid inclusions ranged from 220 to 297 $^\circ\text{C}$ (mean 254 $^\circ\text{C}$). The salinities ranged from 5.6 to 15.7 wt% NaCl_{eqv} (mean 12.4 wt% NaCl_{eqv}).

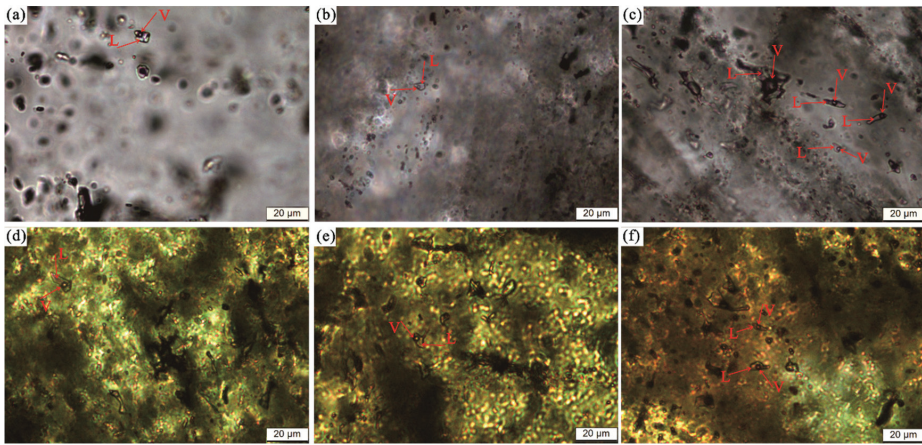


Figure 4. (a–f) Petrographic Photos of fluid inclusions in quartz of the Maliping Pb–Zn deposit. (L = Liquid, V = Vapor).

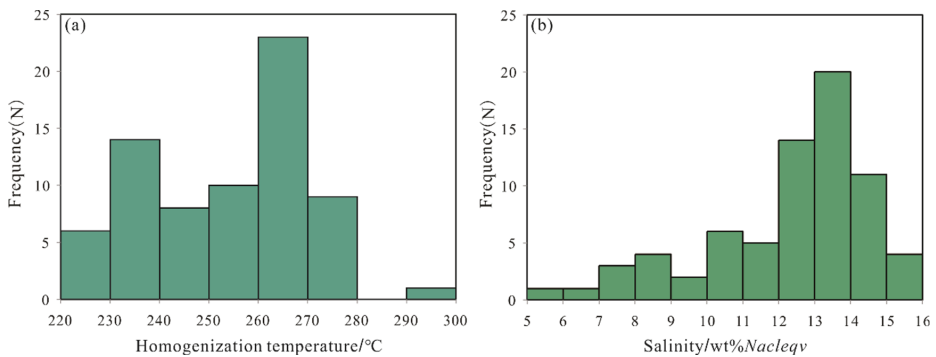


Figure 5. Histogram of homogenization temperature (a) and salinity (b) of fluid inclusions in quartz of the Maliping Pb–Zn deposit.

4.3. Laser Raman Spectroscopic Analysis

Based on microscopic laser Raman spectroscopic peak scanning of fluid inclusions (in quartz), the liquid of the measured inclusions all contain H₂O, while the vaporous parts of certain inclusions contain H₂S (2611 cm⁻¹) and N₂ (2331 cm⁻¹) (Figure 6).

4.4. Trace Elements

4.4.1. Trace Element Contents

The sphalerite is mainly dark brown and rich in various trace elements. The primary characteristics are listed as follows (Table 1).

- (1) Sphalerite is rich in Cd and Cu. The content of Cd is relatively higher than that of Cu, and there is a slight variation in Cd, at 1570×10^{-6} – 2160×10^{-6} (mean 1933.3×10^{-6} , n = 6). In contrast, the stability of Cu is low, with a large range of variation, at 498×10^{-6} – 1860×10^{-6} (mean 925.3×10^{-6} , n = 6).
- (2) Sphalerite is also relatively enriched in Pb, Sb, Hg, Ga, Ge, Ti, and Ba. The content of Pb varies greatly, at 17.7×10^{-6} – 3760×10^{-6} (mean 833.6×10^{-6} , n = 6), while the contents of Ga and Ge are relatively stable, 93.8×10^{-6} – 185×10^{-6} (mean 138.9×10^{-6} , n = 6) and 45.9×10^{-6} – 68.8×10^{-6} (mean 57.1×10^{-6} , n = 6), respectively.

- (3) The Ni, Co, As, Sn, Ag, Cr, and Mn contents are relatively low. The contents of Co and Mn are 4.77×10^{-6} – 18.4×10^{-6} (mean 14.4×10^{-6} , $n = 6$) and 12.9×10^{-6} – 73.3×10^{-6} (mean 42.1×10^{-6} , $n = 6$), respectively.
- (4) The contents of Li, Rb, W, Mo, Sr, Sc, Nb, Zr, Hf, Tl, U, and Th are the lowest, below 5.0×10^{-6} .

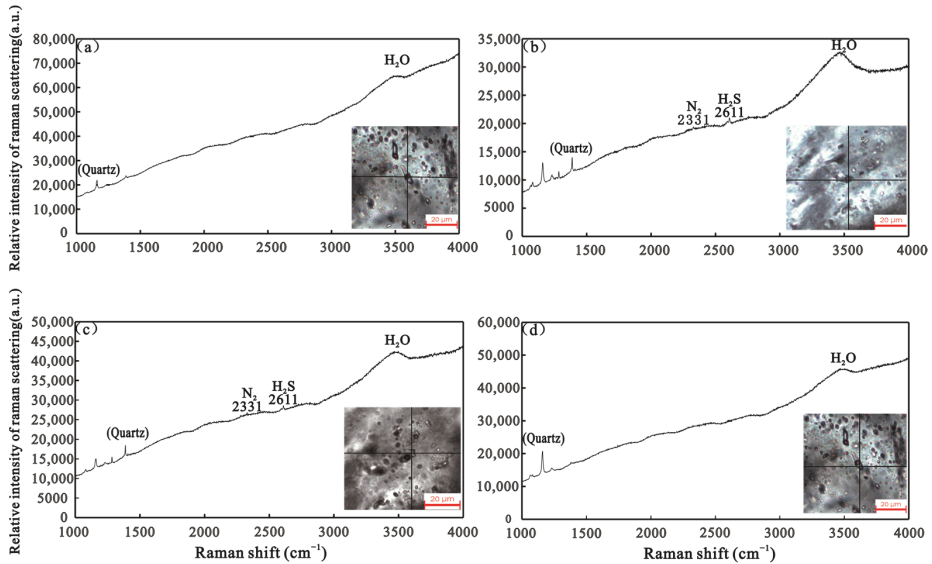


Figure 6. (a–d) Representative Raman spectra of fluid inclusions in quartz of the Maliping Pb–Zn Deposit.

Table 1. Trace element contents of sphalerite in the Maliping ore (ppm).

Element/Sample Number	MLP-1	MLP-2	MLP-3	MLP-5	MLP-6	MLP-7
Cu	498	664	868	1100	1860	562
Pb	17.7	251	755	106	3760	112
Ni	3.41	1.78	4.72	9.11	12.3	3.65
Co	14.2	18.4	16.2	17.6	15.4	4.77
Cd	1630	2070	2080	2090	2160	1570
Li	0.018	<0.01	<0.01	<0.01	<0.01	<0.01
Rb	0.6	0.75	0.67	0.73	1.96	1.24
W	0.035	0.12	0.41	0.35	1.13	3.04
Mo	0.11	0.14	0.18	0.14	2.55	0.68
As	16.1	14.3	28.9	25.3	22.7	19.6
Sb	157	305	386	411	602	295
Hg	73.9	275	198	147	212	160
Sr	0.89	1.26	12.1	1.64	3.72	2.19
Sc	0.31	0.28	0.26	0.2	0.44	0.35
Nb	<0.05	0.057	0.28	0.22	0.6	0.051
Zr	0.3	0.57	1.38	1.53	1.11	1
Hf	<0.01	0.013	0.043	0.046	0.043	0.025
Ga	97.7	142	185	154	161	93.8
Sn	12.6	33.3	31.7	37.8	18.9	5.43
Ge	60.8	45.9	55.5	52.8	58.7	68.8
Tl	0.06	0.17	0.33	0.1	0.17	0.05
Ag	6.18	20.4	44.2	16.2	44.4	17.4

Table 1. Cont.

Element/Sample Number	MLP-1	MLP-2	MLP-3	MLP-5	MLP-6	MLP-7
U	0.036	0.01	0.035	0.036	0.82	0.08
Th	0.098	0.095	0.14	0.082	0.4	0.23
Ti	5.01	14.7	644	361	240	18.9
Mn	12.9	73.3	60.1	40.3	52.2	14
Cr	2.77	2.99	3.57	3.84	18.08	7
Ba	6.29	49.64	77.04	27.13	504.86	47.57

4.4.2. REE Contents

The REE content and characteristic analysis results for the sphalerite are listed in Table 2. The total REE content (Σ REE) ranges from 0.24×10^{-6} to 0.78×10^{-6} (mean 0.39×10^{-6}). The light-to-heavy REE ratio (LREE/HREE) ranges from 5.67×10^{-6} to 8.48×10^{-6} (mean 6.87×10^{-6}); $(\text{La}/\text{Yb})_{\text{N}}$ (N denotes the normalized value of chondrites) ranges from 9.39×10^{-6} to 27.40×10^{-6} (mean 14.97×10^{-6}); $(\text{La}/\text{Sm})_{\text{N}}$ ranges from 2.33×10^{-6} to 3.47×10^{-6} (mean 2.87×10^{-6}); $(\text{Gd}/\text{Yb})_{\text{N}}$ ranges from 2.38×10^{-6} to 6.29×10^{-6} (mean 3.50×10^{-6}); δ Eu (δ denotes the degree of anomaly) ranges from 1.25×10^{-6} to 2.25×10^{-6} (mean 1.84×10^{-6}), and δ Ce ranges from 0.56×10^{-6} to 0.95×10^{-6} (mean 0.71×10^{-6}).

Table 2. Characteristics of REE in sphalerite from the Maliping ore (ppm; characteristic value is dimensionless unit).

Element/Sample Number	MLP-1	MLP-3	MLP-5	MLP-6
La	0.05204519	0.15922395	0.0811368	0.11615857
Ce	0.08870712	0.21635529	0.09672696	0.11322446
Pr	0.01013269	0.03578948	0.0178416	0.0209005
Nd	0.04651827	0.17652377	0.0845352	0.09606193
Sm	0.00967212	0.04376188	0.0225144	0.02250824
Eu	0.00414519	0.03122491	0.01062	0.01487151
Gd	0.01059327	0.04116564	0.0161424	0.01969471
Tb	0.00138173	0.00600775	0.002124	0.00281353
Dy	0.00782981	0.03041702	0.0101952	0.01406765
Ho	0.00230288	0.00644108	0.002124	0.00361739
Er	0.00644808	0.01681144	0.0033984	0.00683286
Tm	0.00046058	0.00216661	0.0004248	0.00080387
Yb	0.00368462	0.01216241	0.002124	0.00643092
Lu	0.00046058	0.00173329	0.0004248	0.00080387
Y	0.05158462	0.23143821	0.0458784	0.07877882
Σ REE	0.24	0.78	0.35	0.44
LREE	0.21	0.66	0.31	0.38
HREE	0.03	0.12	0.04	0.06
LREE/HREE	6.37	5.67	8.48	6.97
$(\text{La}/\text{Yb})_{\text{N}}$	10.13	9.39	27.4	12.96
$(\text{La}/\text{Sm})_{\text{N}}$	3.47	2.35	2.33	3.33
$(\text{Gd}/\text{Yb})_{\text{N}}$	2.38	2.8	6.29	2.53
δ Eu	1.25	2.25	1.7	2.16
δ Ce	0.95	0.7	0.62	0.56

4.5. H and O Isotopes

The H and O isotope analysis results for quartz are listed in Table 3. The $\delta^{18}\text{O}_{\text{Quartz}}\text{‰}$ ranges from 14.99‰ to 19.79‰ (mean 18.21‰), and the $\delta\text{D}\text{‰}$ ranges from -98.2‰ to -57.8‰ (mean -79.10‰). By combining fluid inclusions microthermometry data with the formula of Clayton et al. [26], $1000 \ln a = \delta^{18}\text{O}_{\text{Quartz}} - \delta^{18}\text{O}_{\text{H}_2\text{O}} = 3.38 \times 10^6 \text{ T}^{-2} - 3.4$ [$\text{T} = (254 + 273.15) \text{ °C}$], the $\delta^{18}\text{O}_{\text{H}_2\text{O}}$ in ore-forming fluids was found to range from 6.23 to 11.03‰ (mean 9.44‰) (Table 3).

Table 3. H and O isotopic composition of quartz in the Maliping Pb-Zn deposit.

Sample Number	$\delta D\text{‰}$	$\delta^{18}O_{\text{Quartz}}\text{‰}$	$\delta^{18}O_{\text{H}_2\text{O}}\text{‰}$
MLP-1-3	−67.4	19.79	11.03
MLP-3-3	−81.3	18.52	9.76
MLP-4-3	−73.0	18.27	9.51
MLP-5-3	−86.5	18.37	9.61
MLP-6-3	−98.2	18.23	9.47
MLP-7-3	−57.8	19.28	10.52
MLP-8-3	−89.5	14.99	6.23

4.6. EPMA-Mapping

The results of the EPMA-mapping for the sphalerite are shown in Figure 7. Pb and Fe have dense optical density clusters, with Fe having more such clusters. Zn is enriched but lacking in Pb and Fe dense optical density clusters, and Cd, Cu, Ga, Ge, and Mn are uniformly distributed in sphalerite.

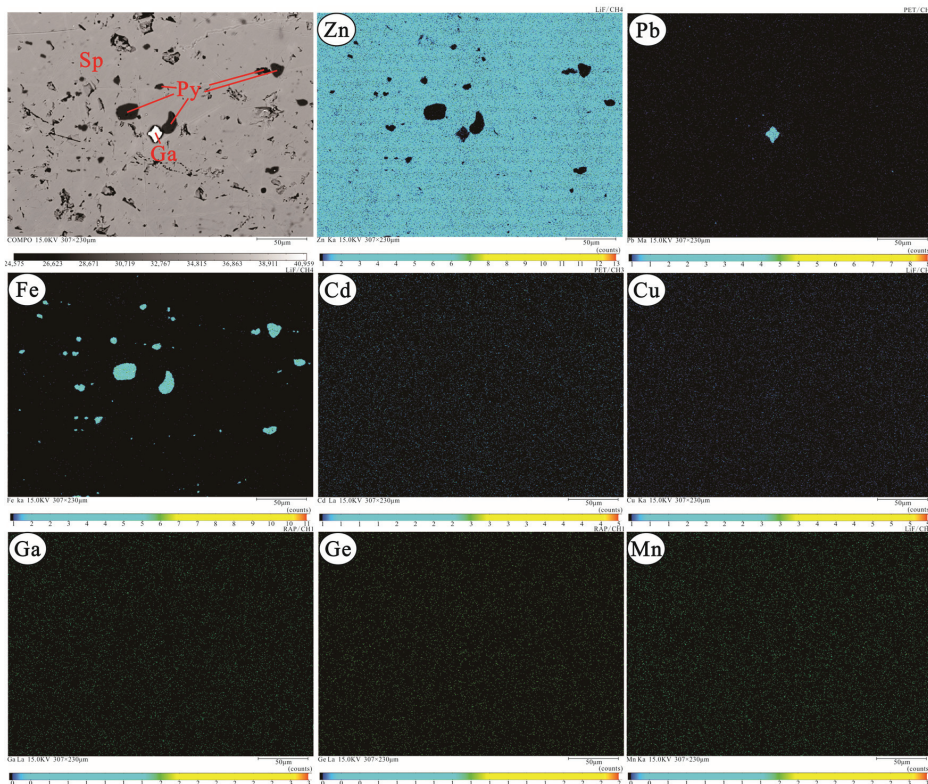


Figure 7. EPMA-mapping of sphalerite from the Maliping Pb-Zn deposit.

5. Discussion

5.1. Properties and Sources of Ore-Forming Fluids

5.1.1. Properties of Ore-Forming Fluids

(1) Fluid density

The density of ore-forming fluids can be obtained by converting the homogenization temperature and salinity of the fluid inclusions; the density formula is [27]:

$$D = A + BT + CT^2$$

D—Fluid density (g/cm^3); T—homogenization temperature ($^{\circ}\text{C}$); A, B, and C are dimensionless parameters, which are functions of salinity:

$$A = A_0 + A_1W + A_2W^2$$

$$B = B_0 + B_1W + B_2W^2$$

$$C = C_0 + C_1W + C_2W^2$$

W—Salinity (NaCl% weight); $A_0, A_1, A_2, B_0, B_1, B_2, C_0, C_1,$ and C_2 are dimensionless parameters with the following values:

$$A_0 = 0.993531, A_1 = 8.72147 \times 10^{-3}, A_2 = -2.43975 \times 10^{-5}$$

$$B_0 = 7.11652 \times 10^{-5}, B_1 = -5.2208 \times 10^{-5}, B_2 = 1.26656 \times 10^{-6}$$

$$C_0 = -3.4997 \times 10^{-6}, C_1 = 2.12124 \times 10^{-7}, C_2 = -4.52318 \times 10^{-9}$$

The calculation shows that the density of ore-forming fluids in Maliping is between 0.78 and 0.95 g/cm^3 (mean 0.90 g/cm^3).

(2) Ore-forming pressure

The ore-forming pressure estimation formula is given by $P = (219 + 2620 \times W) \times T \div (374 + 920 \times W)$ [28]

P—pressure (10^5 Pa); T—homogenization temperature ($^{\circ}\text{C}$); W—Salinity (NaCl% weight);

The calculation shows that the pressure of the ore-forming fluids in Maliping is between 60 and 81 MPa (mean 70 MPa).

(3) Ore-forming depth

$$H = P \times 10^{-5} / 300$$
 [28]

H—ore-forming depth (km); P—ore-forming pressure (10^5 Pa);

The calculation shows that the depth of the ore-forming fluids in Maliping is between 2.0 and 2.7 km (mean 2.3 km).

5.1.2. Sources of Ore-Forming Fluids

In the $\delta\text{D}-\delta^{18}\text{O}_{\text{H}_2\text{O}}$ relationship diagram (Figure 8), H and O isotopes are mainly distributed among metamorphic water, primary magmatic water, and organic matter fluid, with a tendency towards organic matter fluid. However, the magmatic rocks around the ore district are mainly Emeishan basalt (approximately 260 Ma) [29–34], which is 50 Ma older than the main ore-forming age of the Pb-Zn deposits in the region (approximately 200 Ma) [35–37]. Therefore, magmatic water cannot be used as a direct source of the ore-forming fluids. Hence, the ore-forming fluids may be a mixed source of metamorphic water and organic matter fluid.

The variation range of $\delta^{18}\text{O}_{\text{H}_2\text{O}}$ in the deposit fluid is between 6.18‰ and 10.98‰, and the range of δD is from -98.2 ‰ to -57.8 ‰ (Table 3), indicating that the lateral drift of $\delta^{18}\text{O}_{\text{H}_2\text{O}}$ is not large, while the vertical drift of δD is extremely large. This pattern is similar to that of the Chipu Pb-Zn deposit, which has significant organic matter involved in mineralization [38,39]. Microscopic Raman testing results of the fluid inclusions in the deposit indicated that the vapor components were mainly H_2S and N_2 , and the REE distribution pattern of the deposit exhibited negative Ce anomalies, indicating that the fluids were reducible [40]. Hence, based on the test results and comparative analysis, the ore-forming fluids have reducibility; there is organic matter involved in the mineralization, and the participation of organic matter hydrogen ($\delta\text{D}_{\text{H}_2\text{O}}$) leads to a large vertical “drift” in δD .

Compared with the basin brine of Illinois, California, and Sichuan, the ore-forming fluids of the Maliping Pb-Zn deposit exhibit lower δD and higher $\delta^{18}\text{O}_{\text{H}_2\text{O}}$ (Figure 8). Within the deep source of the Maliping ore district, a series of metamorphic rocks exists in the folded basement (Kunyang Group), and REE tracing analysis suggests that the deep source fluid flowing through these rocks is mixed with the organic-containing brine, resulting in lower δD . Deep source fluids react with carbonate rocks during their ascent, resulting in higher $\delta^{18}\text{O}_{\text{H}_2\text{O}}$.

In summary, the ore-forming fluids of the Maliping Pb-Zn deposit were mainly derived from the mixing of deep source fluids flowing through the deep folded basement (Kunyang

Group) and organic-containing basin brine. Based on the homogenization temperature and salinity test results of the fluid inclusions and the aforementioned ore-forming fluids properties, the ore-forming fluids has medium-low temperature, medium-low salinity, medium-low density, and deep source reducibility.

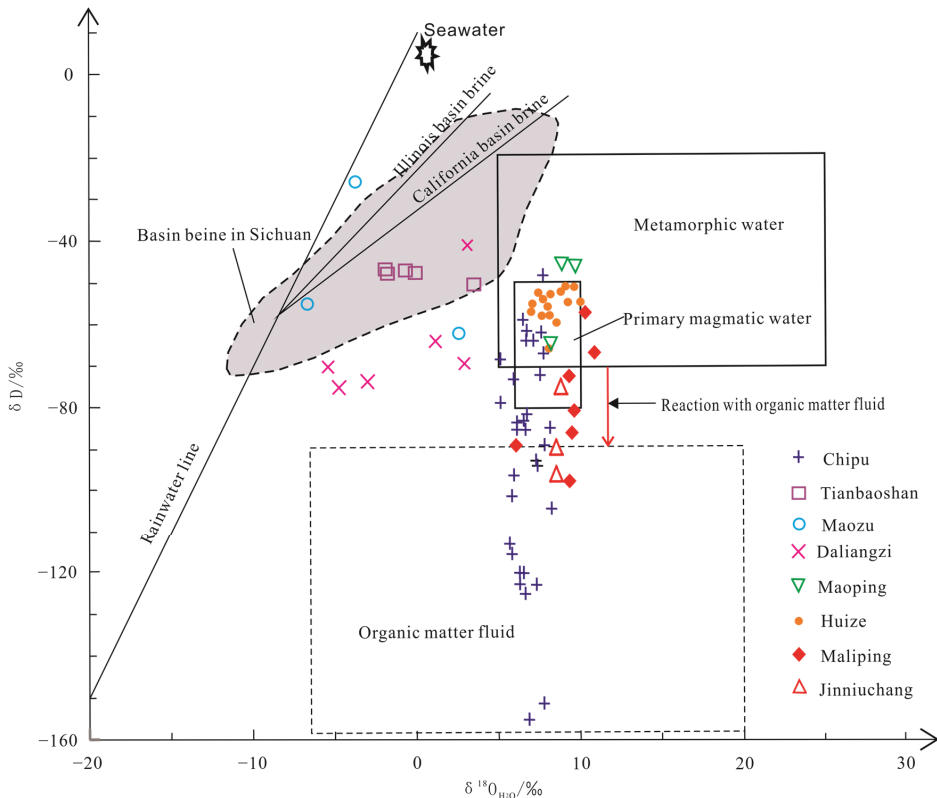


Figure 8. Diagram of δD - $\delta^{18}O_{H_2O}$ for quartz separates from the Maliping Pb-Zn deposit. (Huize [41,42]; Chipu [38]; Tianbaoshan [43,44]; Maozu [18,45]; Daliangzi [46]; Maoping [47]; Jinniuchang [48]; Base map [49]).

5.2. Sources of Ore-Forming Materials

REEs can be used to trace the sources of ore-forming materials, among which Eu and Ce anomalies can identify the ore-forming environment and indicate the sources of ore-forming fluids to a certain extent [50,51]. The vast majority of Pb-Zn deposits in the SYGT are hosted in carbonate rocks, and there is a large range of Emeishan basalt and basement rocks (e.g., the Kunyang and Huili groups). Previous scholars have fiercely debated whether these provide material sources for the ore-forming process, with the main viewpoints being: (1) they are provided by carbonate rock strata and Emeishan basalt in coordination [18,52,53]; (2) the main ore-forming elements are provided by a mixture of Mesoproterozoic basement strata and the Sinian-Carboniferous sedimentary rock strata [41,54,55]; (3) they are mainly provided by Mesoproterozoic basement rocks [21,56–59]. Thus, the sources of ore-forming materials for the Pb-Zn deposits in the area require further investigation.

Figure 9 shows that the REE distribution pattern in fresh wall rocks of the ore district are enriched LREE, depleted HREE, weak negative Ce anomalies, and medium negative Eu anomalies. These characteristics are similar to the REE distribution pattern curve in

the upper crust, indicating that the migration amount of REEs in the fresh wall rocks was extremely small, further indicating that the REEs in the fresh wall rocks contributed little to ore-forming materials [60]. The REE distribution pattern of altered wall rocks in the ore district is consistent with that of sphalerite in the Maliping deposit, with both exhibiting right-dipping positive Eu anomalies, negative Ce anomalies, and relative enrichment of LREEs, indicating a certain genetic connection. Additionally, they had similar Σ REE contents, indicating that they had similar sources. Both exhibited positive Eu anomalies, indicating that a water–rock reaction occurred during the ore-forming process [61], and a small amount of REEs in the altered wall rocks migrated and participated in the mineralization process.

The REE distribution pattern of the Emeishan Basalt is also a relatively enriched right-dipping type for LREEs, but the regional Pb–Zn ore-forming age occurred later than the Emeishan Basalt (see above), reflecting the likelihood that ore-forming materials were provided because of the activation of the Emeishan Basalt by later ore-forming fluids [55].

The REE distribution pattern of the Kunyang Group is a relatively enriched right-dipping type of LREEs, which is consistent with the sphalerite of the Maliping deposit, indicating a certain genetic connection between the two. Additionally, the higher Σ REE contents of the Kunyang Group provided favorable conditions for sourcing REEs for the ore-forming process.

The sphalerites of the Huize, Lehong, and Maliping deposits in northeastern Yunnan have similar REE distribution patterns and Σ REE contents, indicating similar sources of ore-forming materials. The ore-forming materials for the Huize Pb–Zn deposit were mainly derived from basement rocks (Kunyang Group) and cover sedimentary rocks, whereas the Emeishan basalt may provide a small amount of material for mineralization [62]. The ore-forming materials for the Lehong Pb–Zn deposit were mainly derived from Proterozoic Eon basement rocks (Kunyang Group), with a possible contribution from sedimentary strata [9,62].

In summary, the ore-forming materials for the Maliping Pb–Zn deposit were mainly derived from the basement rocks (Kunyang Group). The altered wall rocks that underwent water–rock reactions and the Emeishan basalt, which underwent fluid activation may have provided a small amount of ore-forming materials.

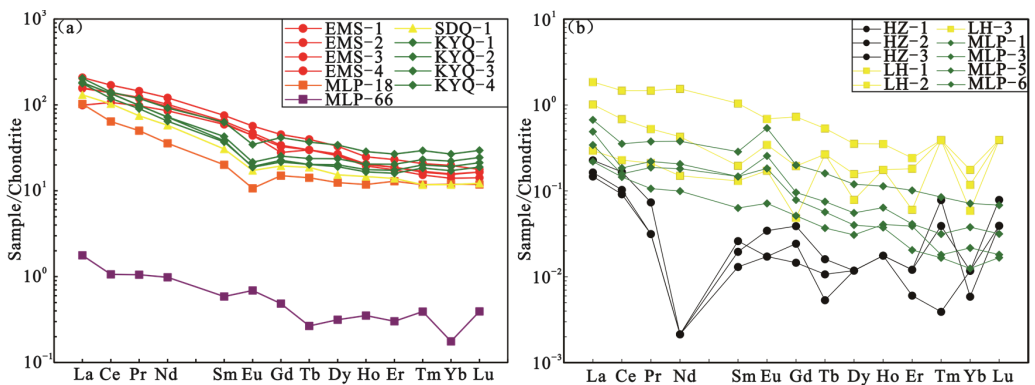


Figure 9. (a,b) Distribution pattern of REE in the Maliping Pb–Zn deposit. [(a): EMS-1,2,3,4 = Emeishan basalt [63]; SDQ-1 = Valuation of rare earth element abundance in the upper crust [64]; MLP-18, 66 = Fresh wall rock and altered wall rock in Maliping deposit [61]; KYQ-1, 2, 3, 4 = Metamorphic rocks of the Kunyang Group [65]; (b): HZ-1, 2, 3 = Sphalerite in Huize deposit [66]; LH-1, 2, 3 = Sphalerite in Lehong deposit [21]; MLP-1, 3, 5, 6 = Sphalerite in Maliping deposit].

5.3. Deposit Genesis

Trace elements of different genetic types of sphalerite have different characteristic element compositions, which can reveal the genetic type of the deposit to a certain extent [67–72]. Trace elements present in the form of isomorphic substitutions are more important typomorphic features [73]. Ye et al. [68] suggested that sphalerite in the sedimentary exhalative (SEDEX) Pb–Zn deposits in southern China are relatively rich in In, Fe, and Mn and poor in Ga, Ge, and Cd. The sphalerite in the magmatic hydrothermal Pb–Zn deposits is relatively rich in Mn, Fe, Sn, Co, and In and poor in Ga, Ge, and Cd. Most SEDEX and magmatic hydrothermal deposits contain Fe and Mn contents greater than 10% and 2000×10^{-6} , respectively. The results of the EPMA-mapping (Figure 7) showed that Cd, Cu, Ga, Ge, and Mn are uniformly distributed in sphalerite, indicating that they primarily exist in the form of isomorphism. Pb and Fe have dense optical density clusters, with Fe having a greater number of clusters, indicating that Pb and Fe exist in at least two forms—mineral inclusions (galena and pyrite) and isomorphic—within the sphalerite. Fe mainly exists in mineral inclusions of pyrite. These characteristics coincided with the corresponding trace element contents and variations (Table 1). Combining these findings, the sphalerite in the Maliping Pb–Zn deposit is found to be relatively rich in Cd, Cu, Ga, and Ge and poor in Fe, Mn, Sn, and Co, which significantly differs from the previous understanding that the deposit belonged to the SEDEX and magmatic-hydrothermal Pb–Zn deposits.

Based on significant differences in the types of ore-forming geological processes, ore-forming temperatures, ore-forming modes, genetic types of ore-bearing carbonate rocks, and exploration directions between Pb–Zn deposits in the SYGT and MVT Pb–Zn deposits, Han et al. [21] divided the carbonate-hosted non-magmatic epigenetic hydrothermal type Pb–Zn deposits into two sub-types: typical MVT and Huize type (HZT) deposits. Most carbonate-hosted non-magmatic epigenetic hydrothermal Pb–Zn deposits worldwide are intermediate transitional types between the two sub-type member deposits. Among them, HZT is an epigenetic Pb–Zn deposit dominated by fluid “penetration” metasomatism and is controlled by strike-slip fault-fold structure and altered carbonate rocks. It is characterized by a high Pb–Zn grade, large deposit scale, and high metallogenic temperature (200–350 °C) [21]. By comparing trace elements in sphalerite in the Maliping, typical MVT, and typical HZT deposits (Table 4, Figure 10), the Maliping deposit was found to be rich in Cd, Cu, Ga, and Ge, similar to typical MVT and HZT deposits. However, there are also a number of differences: (i) poor Cr and Ni (Table 1), which is significantly different from the Cr-enrichment in typical HZT deposits, where the content of Cr typically exceeds 1000×10^{-6} [21], and from the relatively high content of Ni in the MVT (Upper Mississippi Valley district) deposits [74]; (ii) the Maliping deposit is hosted in the interlayer fracture zone at the interface between siliceous cataclastic dolomite and clastic rocks in the Lower Cambrian Yuhucun Formation, belonging to the interlayer detachment fracture zone and its lateral pinnate crack structural ore-control type [75], which is different from the Pb–Zn deposits hosted by carbonate rocks in typical MVT and HZT deposits.

In the Mn–Cd and Ge–Mn relationship diagrams (Figure 11), most data points of the Maliping deposit fall within the typical HZT deposit area. The content of Fe in the sphalerite (mean 6443×10^{-6} , $n = 43$) [16] is between HZT Pb–Zn deposits such as Huize (855.25×10^{-6}) and Maoping (21275.65×10^{-6}), and the content of Sn (mean 23.3×10^{-6} , $n = 6$) is slightly higher than that of Pb–Zn deposits, such as Huize (2.35×10^{-6}) and Maoping (2.78×10^{-6}) [21], implying that the Fe and Sn trace element contents in the Maliping Pb–Zn deposit are consistent with those in typical HZT deposits. The microthermometry results of the ore inclusions range from 220 to 297 °C (mean 254 °C) (slightly higher than that measured by Luo [61]), which is consistent with typical HZT deposits (200–350 °C) [21] and significantly higher than the typical MVT deposits (50–200 °C) [76,77]. The ore grade of the deposit exceeded 10%, which is significantly different from the characteristics of typical MVT deposits, where the Pb + Zn grade is usually less than 10% [21,37].

Table 4. Characteristics of some trace elements of sphalerite in the Maliping, typical MVT and HZT deposits (ppm).

Deposit Name	Deposit Type	Element	Sample Quantity	Range	Mean	Source
Upper Mississippi Valley district	Typical MVT	Mn	6	2.00~140.00	48.50	[74]
		Ag	6	2.00~46.00	21.33	
		Co	6	8.00~29.00	15.33	
		Cd	6	390.00~4000.00	1678.33	
		Cu	6	10.00~150.00	75.50	
		Ga	6	10.00~250.00	95.00	
		Ge	6	20.00~250.00	101.70	
Xiangxi Huayuan	Typical MVT	Mn	46	0.67~1305.74	132.02	[78]
		Ag	46	0.79~4.28	2.10	
		Co	38	0.00~5.03	0.50	
		Cd	46	813.00~15,964.00	7609.67	
		Cu	46	1.00~485.00	163.59	
		Ga	46	1.37~172.21	34.28	
		Ge	46	2.04~245.63	29.42	
Huize	Typical HZT	Mn	20	0.46~20.82	9.31	[21]
		Ag	20	1.39~27.39	7.06	
		Co	20	0.03~1.33	0.31	
		Cd	20	1053.97~3518.87	1881.32	
		Cu	20	7.46~319.13	137.14	
		Ga	20	0.12~65.16	11.63	
		Ge	20	3.06~231.15	80.55	
Maoping	Typical HZT	Mn	20	5.08~19.68	12.67	[21]
		Ag	20	2.29~17.10	6.76	
		Co	20	0.03~0.05	0.04	
		Cd	20	811.21~1809.66	1315.96	
		Cu	20	5.48~782.08	169.94	
		Ga	20	0.14~8.69	1.80	
		Ge	20	0.63~814.31	146.77	
Lehong	Typical HZT	Mn	9	19.13~30.86	24.19	[21]
		Ag	9	30.50~57.24	41.36	
		Co	9	0.41~41.2	7.43	
		Cd	9	1900.00~3830.00	3081.89	
		Cu	9	110.00~2480.00	658.33	
		Ga	9	9.30~158.00	51.91	
		Ge	5	11.30~59.20	34.71	
Maliping	Typical HZT	Mn	6	12.90~73.3	42.13	This study
		Ag	6	6.18~44.40	24.80	
		Co	6	4.77~18.40	14.43	
		Cd	6	1570.00~2160.00	1933.33	
		Cu	6	498.00~1860.00	925.33	
		Ga	6	93.80~185.00	138.92	
		Ge	6	45.90~68.80	57.08	

In summary, combined with the REE distribution pattern and ore-forming material sources of the above-mentioned deposit having more similar characteristics to typical HZT deposits (Huize and Lehong Pb-Zn deposits), the genetic type of the Maliping deposit is significantly different from the SEDEX and magmatic hydrothermal types. Despite having certain similarities with typical MVT Pb-Zn and HZT Pb-Zn deposits, it is a transitional type between the two sub-type members and is more inclined to the latter. Therefore, its genetic type was defined as an HZT-like deposit.

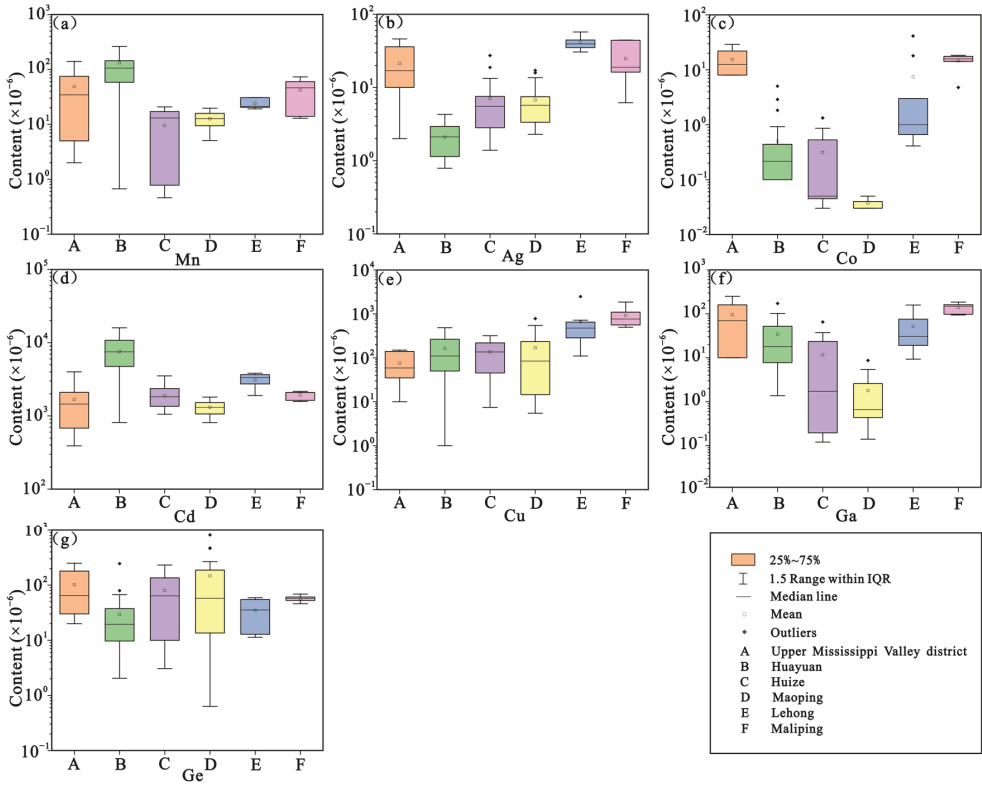


Figure 10. (a–g) Comparison of some trace elements in sphalerite in Maliping, typical MVT and HZT deposits.

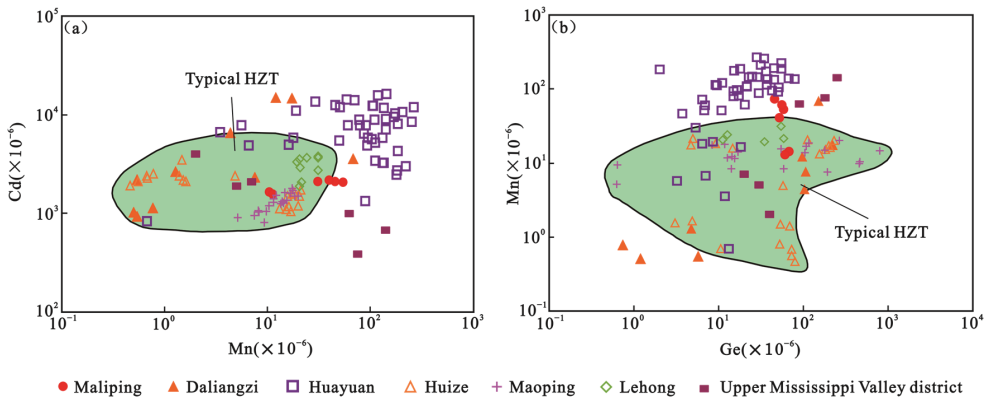


Figure 11. Relationship diagram of different types of Pb-Zn ore Mn-Cd (a) and Ge-Mn (b). (DaLiangzi [79]).

5.4. Metallogenic Mechanism and Ore Prospecting Indicative Significance

5.4.1. Metallogenic Mechanism

The genetic type of the Maliping Pb-Zn deposit was HZT-like. Considering the results of Han et al. [20] with regard to the ore-forming dynamic background of the HZT Pb-Zn deposit, Luo et al. [17] proposed that the reduced sulfur of the Maliping Pb-Zn deposit

was mainly derived from the thermal-chemical sulfate reduction (TSR) of seawater sulfate. The metallogenic mechanism of the deposit can be described as follows. During the Triassic period (230–200 Ma), the collision between the Indochina and Yangtze blocks led to the closure of the Paleo-Tethys Ocean, forming the Nanpanjiang-Youjiang orogenic belt, with regional tectonic stress conducted into the Yangtze Block, forming a series of strike-slip fault-fold structural belts in the SYGT and the Wuxing anticline. Tectonic dynamics drove high temperature and low salinity deep fluids upward along the Xiaojiang and branch faults, gradually extracting the major ore-forming metal ions such as Pb and Zn from the basement (Kunyang Group) and forming a large number of medium salinity fluids rich in ore-forming materials. In addition, under strong extrusion stress and/or orogenic uplift gravity, basin fluids containing organic matter exhibited large-scale and long-distance migration along the stratigraphic carbonate karst, gradually extracting the gypsum-salt layer sulfates in the marine carbonate rocks of the Lower Cambrian Yuhucun Formation and forming a medium-high salinity acidic fluid containing SO_4^{2-} . When the two fluids migrated to the tensile space of the interlayer detachment fracture zone of the Lower Cambrian Yuhucun Formation in the SE limb of the Wuxing anticline, they mixed and experienced homogenization. Simultaneously, the ore-forming fluid dissolved the carbonate rock to expand the ore-bearing space. The thermal energy brought by extensive hydrothermal flow and circulation initiated the TSR process, converting SO_4^{2-} into H_2S . With changes in physical, chemical, etc., ore-forming conditions, metal sulfides precipitated in a reducing environment to form the large-scale Maliping Pb-Zn deposit.

5.4.2. Ore Prospecting Indicative Significance

Han et al. [21] proposed a large-scale “four step style” deep ore prospecting method ((i) using deposit models to optimize ore prospecting direction; (ii) predicting favorable zones through tectonic-altered lithofacies; (iii) delineation of key target areas through structural geochemical exploration; (iv) applying geophysical prospecting technology to locate concealed ore body), which successfully combined the deposit model and ore prospecting exploration technology and achieved significant demonstration results in deep and peripheral ore prospecting on the Huize and Maoping Pb-Zn deposits in northeastern Yunnan. This study determined that the genetic type of the Maliping Pb-Zn deposit is HZT-like and constructed a metallogenic mechanism for the deposit. Thus, we can modify the “four step style” deep ore prospecting method and establish the exploration technical methods that are conformed to the actual ore prospecting of the deposit, thereby further delineating key ore prospecting target areas at the deep and peripheral areas of the deposit.

6. Conclusions

- (1) The ore-forming fluids of the Maliping Pb-Zn deposit were a medium-low temperature, medium-low salinity, medium-low density, and deep source reducing fluid, mainly derived from the mixing of deep source fluid flowing through the deep folded basement (Kunyang Group) and organic-containing basin brine. The ore-forming materials were mainly derived from the basement rocks (Kunyang Group).
- (2) The deposit is a transitional type between two sub-type members of the typical MVT and HZT Pb-Zn deposits and is more similar to the latter. Thus, it is an HZT-like deposit, and it is suitable to use a large-scale “four step style” deep ore prospecting method to delineate the deep and peripheral ore prospecting target areas of the deposit.

Author Contributions: Conceptualization, Y.Y. and H.G.; formal analysis, Y.Y.; investigation, Y.Y., H.G. and R.H.; writing—original draft preparation Y.Y.; writing—review and editing, H.G., R.H., C.Z., P.W. and G.C.; supervision, C.Z. and P.W.; funding acquisition, H.G. and R.H. All authors have read and agreed to the published version of the manuscript.

Funding: This research was funded by the National Natural Science Foundation of China (42172086, 41572060, U1133602), Yunling scholars (2015), Mineral Resources Prediction and Evaluation Engineering Laboratory of Yunnan Province (2010), and Innovation Team of Yunnan province (2012).

Data Availability Statement: Not applicable.

Conflicts of Interest: The authors declare no conflict of interest.

References

- Li, L.J.; Han, R.S.; Zhang, Y.; Wu, J.B.; Feng, Z.X. Trace element signatures of sphalerite in the Sichuan Daliangzi Ge-rich Pb-Zn deposit and its implications for deep ore prospecting. *Front. Earth Sci.* **2022**, *10*. [CrossRef]
- Li, Z.L.; Ye, L.; Hu, Y.S.; Huang, Z.L. Geological significance of nickelifferous minerals in the Fule Pb-Zn deposit, Yunnan Province, China. *Acta Geochim.* **2018**, *37*, 684–690. [CrossRef]
- Tu, G.Z.; Hu, R.Z. Characteristic features of the vast low-temperature mineralization province in Southwest China. *Chin. Sci. Bull.* **1999**, *44*, 260.
- Tan, S.C.; Zhou, J.X.; Luo, K.; Xiang, Z.Z.; He, X.H.; Zhang, Y.H. The sources of ore-forming elements of the Maoping large-scale Pb-Zn deposit, Yunnan Province: Constrains from in-situ S and Pb isotopes. *Acta Petrol. Sin.* **2019**, *35*, 3461–3476.
- Jian, L.; Gao, J.G.; Dao, Y.; Tan, Q.L. Wallrock Alteration and Metallogenic Stages of Pb-Zn Deposits in the Sichuan-Yunnan-Guizhou Border Area Southwest China. *Adv. Mater. Res.* **2013**, *2695*, 2120–2124. [CrossRef]
- Ren, T.; Zhou, J.X.; Wang, D.; Yang, G.S.; Lv, C.L. Trace elemental and S-Pb isotopic geochemistry of the Fule Pb-Zn deposit, NE Yunnan Province. *Acta Petrol. Sin.* **2019**, *35*, 3493–3505.
- Zhang, C.Q.; Wu, Y.; Hou, L.; Mao, J.W. Geodynamic setting of mineralization of Mississippi Valley-type deposits in world-class Sichuan-Yunnan-Guizhou Zn-Pb triangle, southwest China: Implications from age-dating studies in the past decade and the Sm-Nd age of Jinshachang deposit. *J. Asian Earth Sci.* **2015**, *103*, 103–114. [CrossRef]
- Liang, X.Y.; Li, B.; Zhang, C.N.; Qin, H.K.; Li, G.; Zhang, X.Y. Mineralogical and Geochemical Characteristics of Carbonates and Their Geological Significance to the Fuli Pb-Zn Deposit, Yunnan Province. *Minerals* **2022**, *12*, 1317. [CrossRef]
- Zhao, D.; Han, R.S.; Wang, L.; Ren, T.; Wang, J.S.; Zhang, X.P.; Cui, J.H.; Ding, J.J. Genesis of the Lehong Large Zinc-Lead Deposit in Northeastern Yunnan, China: Evidence from Geological Characteristics and C-H-O-S-Pb Isotopic Compositions. *Ore Geol. Rev.* **2021**, *135*, 104219. [CrossRef]
- Zhu, C.W.; Wang, J.; Zhang, J.W.; Chen, X.C.; Fan, H.F.; Zhang, Y.X.; Yang, T.; Wen, H.J. Isotope geochemistry of Zn, Pb and S in the Ediacaran strata hosted Zn-Pb deposits in Southwest China. *Ore Geol. Rev.* **2020**, *117*, 103274. [CrossRef]
- He, Z.W.; Li, B.; Wang, X.F.; Xiao, X.G.; Wan, X.; Wei, Q.X. The Origin of Carbonate Components in Carbonate Hosted Pb-Zn Deposit in the Sichuan-Yunnan-Guizhou Pb-Zn Metallogenic Province and Southwest China: Take Lekai Pb-Zn Deposit as an Example. *Minerals* **2022**, *12*, 1615. [CrossRef]
- Zhu, C.W.; Wen, H.J.; Zhang, Y.X.; Huang, Z.L.; Cloquet, C.; Luais, B.; Yang, T. Cadmium isotopic constraints on metal sources in the Huize Zn-Pb deposit, SW China. *Geosci. Front.* **2021**, *12*, 101241. [CrossRef]
- Shen, L.; Rao, X.H.; Wei, W.B.; Zhang, M.H.; Tao, Y.L. Geological characteristics and its genesis of Guanyingyan ore section in Maliping Pb-Zn deposit, Huize, Yunnan. *Sci. Technol. Eng.* **2014**, *14*, 149–155+172.
- He, S.H.; Chen, X.S.; Rong, H.F. Geological characteristics and genesis of the Maliping lead-zinc deposit in Huize County, Yunnan Province. *China Min. Mag.* **2014**, *23*, 80–87.
- Luo, K.; Zhou, J.X.; Huang, Z.L.; Cui, Y.L.; Jin, Z.G. Geochemistry and genesis of the Maliping lead-zinc deposit in Dongchuan, Yunnan. In Proceedings of the 8th National Colloquium on Mineralization Theory and Prospecting Methods, Nanchang, China, 9–12 December 2017; p. 145. (In Chinese)
- Hu, Y.S.; Ye, L.; Huang, Z.L.; Li, Z.L.; Wei, C.; Danyushevsky, L. Distribution and existing forms of trace elements from Maliping Pb-Zn deposit in Northeastern Yunnan, China: A LA-ICPMS study. *Acta Petrol. Sin.* **2019**, *35*, 3477–3492.
- Luo, K.; Zhou, J.X.; Huang, Z.L.; Wang, X.C.; Wilde, S.A.; Zhou, W.; Tian, L.Y. New insights into the origin of early Cambrian carbonate-hosted Pb-Zn deposits in South China: A case study of the Maliping Pb-Zn deposit. *Gondwana Res.* **2019**, *70*, 88–103. [CrossRef]
- Liu, H.C.; Lin, W.D. *Regularity Research of Pb-Zn-Ag Ore Deposits Northeastern Yunnan*; Yunnan University Press: Kunming, China, 1999; pp. 1–468. (In Chinese)
- Yang, Q.; Liu, W.H.; Zhang, J.; Wang, J.; Zhang, X.J. Formation of Pb-Zn deposits in the Sichuan-Yunnan-Guizhou triangle linked to the Youjiang foreland basin: Evidence from Rb-Sr age and in situ sulfur isotope analysis of the Maoping Pb-Zn deposit in northeastern Yunnan Province, southeast China. *Ore Geol. Rev.* **2019**, *107*, 780–800. [CrossRef]
- Han, R.S.; Wang, F.; Hu, Y.Z.; Wang, X.K.; Ren, T.; Qiu, W.L.; Zhong, K.H. Metallogenic tectonic dynamics and chronology constrains on the Huize-type (HZT) Germanium-rich Silver-Zinc-Lead deposits. *Geotecton. Metallog.* **2014**, *38*, 758–771.
- Han, R.S.; Zhang, Y.; Wang, F.; Wu, P.; Qiu, W.L.; Li, W.Y. *The Metallogenic Mechanism of the Germanium-Rich Lead-Zinc Deposit and Prediction of Concealed Ore Location in the Ore Concentration Area of Northeastern Yunnan*; Science Press: Beijing, China, 2019; pp. 1–510. (In Chinese)

22. Gong, B.; Zheng, Y.F.; Chen, R.X. An online method combining a thermal conversion elemental analyzer with isotope ratio mass spectrometry for the determination of hydrogen isotope composition and water concentration in geological samples. *Rapid Commun. Mass Spectrom. RCM* **2007**, *21*, 1386–1392. [CrossRef]
23. Clayton, R.N.; Mayeda, T.K. The use of bromine pentafluoride in the extraction of oxygen from oxides and silicates for isotopic analysis. *Geochim. Cosmochim. Acta* **1963**, *27*, 43–52. [CrossRef]
24. Qi, L.; Hu, J.; Gregoire, D.C. Determination of trace elements in granites by inductively coupled plasma mass spectrometry. *Talanta* **2000**, *51*, 507–513.
25. Goldstein, R.H.; Reynolds, T.J. *Systematics of Fluid Inclusions in Diagenetic Minerals*; Society for Sedimentary Geology: Tulsa, OK, USA, 1994; pp. 1–199.
26. Clayton, R.N.; O’Neil, J.R.; Mayeda, T.K. Oxygen isotope exchange between quartz and water. *J. Geophys. Res.* **1972**, *77*, 3057–3067. [CrossRef]
27. Liu, B.; Duan, G.X. The density and isochoric formulae for NaCl-H₂O fluid inclusions (salinity ≤ 25 wt%) and their applications. *Acta Mineral. Sin.* **1987**, *7*, 345–352.
28. Shao, J.L.; Mei, J.M. On the study of typomorphic characteristics of mineral inclusion in the gold deposits from volcanic terrain in Zhejiang and its genetic and prospecting significance. *Mineral. Petrol.* **1986**, *6*, 103–111.
29. Zhou, M.F.; Malpas, J.; Song, X.Y.; Robinson, P.T.; Sun, M.; Kennedy, A.K.; Leshner, C.M.; Keays, R.R. A temporal link between the Emeishan large igneous province (SW China) and the end-Guadalupian mass extinction. *Earth Planet. Sci. Lett.* **2002**, *196*, 113–122. [CrossRef]
30. Meng, F.C.; Tian, Y.L.; Kerr, A.C.; Wang, W.; Wu, Z.P.; Xu, Q.; Du, Q.; Zhou, Y.Q.; Liu, J.Q. Geochemistry and petrogenesis of Late Permian basalts from the Sichuan Basin, SW China: Implications for the geodynamics of the Emeishan mantle plume. *J. Asian Earth Sci.* **2023**, *241*, 105477. [CrossRef]
31. Shellnutt, J.G.; Denyszyn, S.W.; Mundil, R. Precise age determination of mafic and felsic intrusive rocks from the Permian Emeishan large igneous province (SW China). *Gondwana Res.* **2012**, *22*, 118–126. [CrossRef]
32. Shellnutt, J.G. The Emeishan large igneous province: A synthesis. *Geosci. Front.* **2014**, *5*, 369–394. [CrossRef]
33. Ali, J.R.; Thompson, G.M.; Zhou, M.F.; Song, X.Y. Emeishan large igneous province, SW China. *Lithos* **2005**, *79*, 475–489. [CrossRef]
34. Saunders, A.D.; Jones, S.M.; Morgan, L.A.; Pierce, K.L.; Widdowson, M.; Xu, Y.G. Regional uplift associated with continental large igneous provinces: The roles of mantle plumes and the lithosphere. *Chem. Geol.* **2007**, *241*, 282–318. [CrossRef]
35. Tang, Y.Y.; Bi, X.W.; Zhou, J.X.; Liang, F.; Qi, Y.Q.; Leng, C.B.; Zhang, X.C.; Zhang, H. Rb-Sr isotopic age, S-Pb-Sr isotopic compositions and genesis of the ca. 200 Ma Yunluheba Pb-Zn deposit in NW Guizhou Province, SW China. *J. Asian Earth Sci.* **2019**, *185*, 104054. [CrossRef]
36. Bao, M.; Zhou, J.X.; Huang, Z.L.; Jin, Z.G. Dating methods for Pb-Zn deposits and chronology research progress of Sichuan-Yunnan-Guizhou Pb-Zn metallogenic province: A review. *Acta Mineral. Sin.* **2011**, *31*, 391–396.
37. Zhou, J.X.; Bai, J.H.; Huang, Z.L.; Zhu, D.; Yan, Z.F.; Lv, Z.C. Geology, isotope geochemistry and geochronology of the Jinshachang carbonate-hosted Pb–Zn deposit, southwest China. *J. Asian Earth Sci.* **2015**, *98*, 272–284. [CrossRef]
38. Wu, Y. The Age and Ore-Forming Process of MVT Deposits in the Boundary Area of Sichuan-Yunnan-Guizhou Provinces, Southwest China. Ph.D. Thesis, China University of Geosciences Beijing, Beijing, China, 2013.
39. Wu, Y.; Zhang, C.Q.; Mao, J.W.; Ouyang, H.G.; Sun, J. The genetic relationship between hydrocarbon systems and Mississippi Valley-type Zn–Pb deposits along the SW margin of Sichuan Basin, China. *Int. Geol. Rev.* **2013**, *55*, 941–957. [CrossRef]
40. Zhao, Y.Y.; Li, S.Z.; Li, D.; Guo, L.L.; Dai, L.M.; Tao, J.L. Rare earth element geochemistry of carbonate and its paleoenvironmental implications. *Geotecton. Metallog.* **2019**, *43*, 141–167.
41. Li, W.B.; Huang, Z.L.; Zhang, G. Sources of the ore metals of the Huize ore field in Yunnan Province: Constraints from Pb, S, C, H, O and Sr isotope geochemistry. *Acta Petrol. Sin.* **2006**, *22*, 2567–2580.
42. Guo, X. Mineralization and Metallogenic Pattern of Lead-Zinc Deposits in Northeast Yunnan. Ph.D. Thesis, China University of Geosciences Beijing, Beijing, China, 2011.
43. Zhou, J.X.; Gao, J.G.; Chen, D.; Liu, X.K. Ore genesis of the Tianbaoshan carbonate-hosted Pb–Zn deposit, Southwest China: Geologic and isotopic (C–H–O–S–Pb) evidence. *Int. Geol. Rev.* **2013**, *55*, 1300–1310. [CrossRef]
44. Wang, X.C. Genesis analysis of the Tianbaoshan Pb-Zn deposit. *J. Chengdu Coll. Geol.* **1992**, *19*, 10–20.
45. Que, M.Y.; Luo, A.P.; Zhang, L.S. *Upper Sinian and Lower Cambrian Stratified Lead-Zinc Deposits in Northeastern Yunnan*; Chengdu University of Science and Technology Press: Chengdu, China, 1993; pp. 1–169. (In Chinese)
46. Yang, Y.X.; Ke, C.X.; Lin, F.C. *Metallogeny of lead-Zinc Deposit the Eastern Margin of Kangdian Axis*; Sichuan Science and Technology Publishing House: Chengdu, China, 1994; pp. 1–175. (In Chinese)
47. Han, R.S.; Zou, H.J.; Hu, B.; Hu, Y.Z.; Xue, C.D. Features of fluid inclusions and sources of ore-forming fluid in the Maoping carbonate-hosted Zn-Pb-(Ag-Ge) deposit, Yunnan, China. *Acta Petrol. Sin.* **2007**, *23*, 2109–2118.
48. Gong, H.S.; Han, R.S.; Wu, P.; Ma, L.; Chen, G. Constraints of fluid inclusion and H-O-S-Pb isotope compositions on metallogenic model of Jinniuchang Pb-Zn deposit, SW China. *Chin. J. Nonferrous Met.* **2022**, *32*, 3206–3226.
49. Kesler, S.E.; Vennemann, T.W.; Frederickson, C.; Breithaupt, A.; Vazquez, R.; Furman, F.C. Hydrogen and oxygen isotope evidence for origin of MVT-forming brines, southern Appalachians. *Geochim. Cosmochim. Acta* **1997**, *61*, 1513–1523. [CrossRef]
50. Hanson, G.N. Rare earth elements in petrogenetic studies of igneous systems. *Annu. Rev. Earth Planet. Sci.* **1980**, *8*, 371–406. [CrossRef]

51. Lottermoser, B.G. Rare earth elements and hydrothermal ore formation processes. *Ore Geol. Rev.* **1992**, *7*, 25–41. [CrossRef]
52. Huang, Z.L.; Li, W.B.; Chen, J.X.; Han, R.S.; Liu, C.Q.; Xu, C.; Guan, T. Carbon and oxygen isotope constraints on mantle fluid involvement in the mineralization of the Huize super-large Pb-Zn deposits, Yunnan Province, China. *J. Geochem. Explor.* **2003**, *78*, 637–642. [CrossRef]
53. Shen, X.L.; Lin, H.H.; Zhang, B.L.; Du, Q.X. The genesis of Guanting Pb–Zn deposits in the Jianshui area, Yunnan Province, SW China: Constraints from geochronology, S isotopes and trace elements. *Mineral. Petrol.* **2021**, *116*, 47–69. [CrossRef]
54. He, Y.F.; Wu, T.; Huang, Z.L.; Ye, L.; Deng, P.; Xiang, Z.Z. Genesis of the Maoping carbonate-hosted Pb–Zn deposit, northeastern Yunnan Province, China: Evidences from geology and C–O–S–Pb isotopes. *Acta Geochim.* **2020**, *39*, 782–796. [CrossRef]
55. Zhou, J.X.; Huang, Z.L.; Zhou, M.F.; Li, X.B.; Jin, Z.G. Constraints of C–O–S–Pb isotope compositions and Rb–Sr isotopic age on the origin of the Tianqiao carbonate-hosted Pb–Zn deposit, SW China. *Ore Geol. Rev.* **2013**, *53*, 77–92. [CrossRef]
56. Bao, Z.W.; Li, Q.; Wang, C.Y. Metal source of giant Huize Zn–Pb deposit in SW China: New constraints from in situ Pb isotopic compositions of galena. *Ore Geol. Rev.* **2017**, *91*, 824–836. [CrossRef]
57. Zhou, C.X.; Wei, C.S.; Guo, J.Y.; Li, C.Y. The source of metals in the Qilinchang Zn–Pb deposit, Northeastern Yunnan, China: Pb–Sr isotope constraints. *Econ. Geol. Bull. Soc. Econ. Geol.* **2001**, *96*, 583–598. [CrossRef]
58. Zhou, J.X.; Huang, Z.L.; Yan, Z.F. The origin of the Maozu carbonate-hosted Pb–Zn deposit, southwest China: Constrained by C–O–S–Pb isotopic compositions and Sm–Nd isotopic age. *J. Asian Earth Sci.* **2013**, *73*, 39–47. [CrossRef]
59. Oyebamiji, A.; Falae, P.; Zafar, T.; Rehman, H.U.; Oguntuase, M. Genesis of the Qilinchang Pb–Zn deposit, southwestern China: Evidence from mineralogy, trace elements systematics and S–Pb isotopic characteristics of sphalerite. *Appl. Geochem.* **2023**, *148*, 105545. [CrossRef]
60. Qi, X.X.; Li, T.F.; Yu, C.L. Rare earth element and trace element Geochemistry of Shalagang antimony deposit in the southern Tibet and its tracing significance for the origin of metallogenic elements. *Geoscience* **2008**, *22*, 162–172.
61. Luo, K. Metallogenesis of Pb–Zn Deposits in the Upper Ediacaran to Lower Cambrian in the Sichuan–Yunnan–Guizhou Pb–Zn Metallogenic Province: A Case Study of the Wusihe and Maliping Deposits. Ph.D. Thesis, University of Chinese Academy of Sciences, Beijing, China, 2019.
62. Kong, Z.G.; Wu, Y.; Liang, T.; Zhang, F.; Meng, X.Y.; Lu, L. Sources of ore-forming material for Pb–Zn deposits in the Sichuan–Yunnan–Guizhou triangle area: Multiple constraints from C–H–O–S–Pb–Sr isotopic compositions. *Geol. J.* **2018**, *53*, 159–177. [CrossRef]
63. Gong, W.M. Research of Characteristics and Petrogenesis of Emeishan Basalt in Huize Area of Yunan. Master’s Thesis, East China University of Technology, Nanchang, China, 2017.
64. Rudnick, R.L.; Gao, S. Composition of the continental crust. *Treatise Geochem.* **2003**, *3*, 1–64.
65. Miao, Y.; Wei, S.G.; Lü, X.C.; Song, W.T.; Wan, L.W. Geochemical characteristics and formation environment of metamorphic rocks in Etouchang formation of middle proterozoic lower Kunyang Group in Northeastern Yunnan. *Geol. Bull. China* **2020**, *39*, 1538–1548.
66. Han, R.S.; Chen, J.; Huang, Z.L.; Ma, D.Y.; Xue, C.D.; Li, Y.; Zou, H.J.; Li, B.; Hu, Y.Z.; Ma, G.S.; et al. *Dynamics of Tectonic Ore-Forming Processes and Localization-Prognosis of Concealed Orebodies—As Exemplified by the Huize Super-large Zn–Pb–(Ag–Ge) District, Yunnan*; Science Press: Beijing, China, 2006; pp. 1–200.
67. Zhang, Q. Trace elements in galena and sphalerite and their geochemical significance in distinguishing the genetic types of Pb–Zn ore deposits. *Chin. J. Geochem.* **1987**, *6*, 177–190.
68. Ye, L.; Cook, N.J.; Ciobanu, C.L.; Liu, Y.P.; Zhang, Q.; Liu, T.G.; Gao, W.; Yang, Y.L.; Danyushevskiy, L. Trace and minor elements in sphalerite from base metal deposits in South China: A LA–ICPMS study. *Ore Geol. Rev.* **2011**, *39*, 188–217. [CrossRef]
69. Cook, N.J.; Ciobanu, C.L.; Pring, A.; Skinner, W.; Danyushevsky, L.; Shimizu, M.; SainiEidukat, B.; Melcher, F. Trace and minor elements in sphalerite: A LA–ICPMS study. *Geochim. Cosmochim. Acta* **2009**, *73*, 4761–4791. [CrossRef]
70. Belissant, R.; Boiron, M.C.; Luais, B.; Cathelineau, M. LA–ICP–MS analyses of minor and trace elements and bulk Ge isotopes in zoned Ge-rich sphalerites from the Noailhac–Saint-Salvy deposit (France): Insights into incorporation mechanisms and ore deposition processes. *Geochim. Cosmochim. Acta* **2014**, *126*, 518–540. [CrossRef]
71. Frenzel, M.; Hirsch, T.; Gutzmer, J. Gallium, germanium, indium, and other trace and minor elements in sphalerite as a function of deposit type—A meta-analysis. *Ore Geol. Rev.* **2016**, *76*, 52–78. [CrossRef]
72. Mishra, B.P.; Pati, P.; Dora, M.L.; Baswani, S.R.; Meshram, T.; Shareef, M.; Pattanayak, R.S.; Suryavanshi, H.; Mishra, M.; Raza, M.A. Trace-element systematics and isotopic characteristics of sphalerite-pyrite from Volcanogenic Massive Sulfide deposits of Betul belt, Central Indian Tectonic Zone: Insight of ore genesis to exploration. *Ore Geol. Rev.* **2021**, *134*, 104149. [CrossRef]
73. Wang, R.K. *Earth and Cosmogenic Mineralogy*; Anhui Publishing House: Hefei, China, 1989; pp. 100–108. (In Chinese)
74. Hall, W.E.; Heyl, A.V. Distribution of minor elements in ore and host rock, Illinois–Kentucky fluorite district and Upper Mississippi Valley zinc–lead district. *Econ. Geol.* **1968**, *63*, 655–670. [CrossRef]
75. Gong, H.S. Structural Ore–Controlling Characteristics and Metallogenic Mechanism of Lead–Zinc Deposits Clastic Rocks–Hosted in the Dahai Mining Area, Northeast Yunnan. Ph.D. Thesis, Kunming University of Science and Technology, Kunming, China, 2022.
76. Leach, D.L.; Sangster, D.F. Mississippi valley-type lead–zinc deposits. *Geol. Assoc. Can. Spec. Pap.* **1993**, *40*, 289–314.
77. John, R. Mississippi Valley-Type Deposits. *Rocks Miner.* **2006**, *81*, 69–71.

78. Wei, H.T.; Shao, Y.J.; Ye, Z.; Zhou, H.D. Geochemical characteristics of trace elements of sphalerite from Huayuan Pb-Zn ore field, Western Hunan, China. *J. Chengdu Univ. Technol.* **2021**, *48*, 142–153.
79. Wu, Y.; Kong, Z.G.; Chen, M.H.; Zhang, C.Q.; Cao, L.; Tang, Y.J.; Yuan, X.; Zhang, P. Trace elements in sphalerites from the Mississippi Valley-type lead-zinc deposits around the margins of Yangtze Block and its geological implications: A LAICPMS study. *Acta Petrol. Sin.* **2019**, *35*, 3443–3460.

Disclaimer/Publisher’s Note: The statements, opinions and data contained in all publications are solely those of the individual author(s) and contributor(s) and not of MDPI and/or the editor(s). MDPI and/or the editor(s) disclaim responsibility for any injury to people or property resulting from any ideas, methods, instructions or products referred to in the content.

Article

Geology, Fluid Inclusions, and C–H–O–S–Pb Isotope Geochemistry of Pb–Zn Deposits within the Tuotuohe Region of the Tibetan Plateau: Implications for Ore Genesis

Ye Qian ^{1,2,*}, Lixiang Zhao ¹ and Jinlei Sun ^{1,3}

¹ College of Earth Sciences, Jilin University, Changchun 130061, China; zhaolx21@mails.jlu.edu.cn (L.Z.); jinleisun123@163.com (J.S.)

² Shandong Provincial Engineering Laboratory of Application and Development of Big Data for Deep Gold Exploration, Weihai 264209, China

³ State Key Laboratory of Ore Deposit Geochemistry, Institute of Geochemistry, Chinese Academy of Sciences, Guiyang 550081, China

* Correspondence: qianye@jlu.edu.cn

Abstract: The Tuotuohe region is a highly prospective area for Pb and Zn mineral exploration. This paper contributes to our comprehension of the ore-controlling structures, fluid inclusions, and C–H–O–S–Pb isotope geochemistry of Pb–Zn deposits in this region. These deposits are generally hosted by carbonates and controlled by fractures. The principal homogenization temperatures of quartz- and calcite-hosted inclusions ranged predominantly between 120 and 220 °C, with salinities varying from 6 to 16 wt.% NaCl equivalent. The Pb isotope compositions of the ore deposits are comparable to those of Cenozoic volcanic rocks in the region but differ significantly from those of the host rocks, indicating that the Pb within these deposits was derived from the mantle. The C, O, and S isotope compositions of samples exhibit a bimodal distribution based on whether they were derived from magma or host rocks, implying that magma-derived fluids underwent an isotopic exchange with the host rocks. The H–O isotope compositions of samples also indicate that ore-forming fluids were originally magmatic but were depleted by combining with meteoric water. These findings are also supported by variations in fluid inclusion homogenization temperatures and salinities. Taken together, these findings suggest that the Pb–Zn deposits of the Tuotuohe region developed from magma to hydrothermal fluids at medium–low temperatures.

Keywords: fluid inclusions; isotope geochemistry; Pb–Zn deposits; ore genesis; Tuotuohe region; Tibetan Plateau

Citation: Qian, Y.; Zhao, L.; Sun, J. Geology, Fluid Inclusions, and C–H–O–S–Pb Isotope Geochemistry of Pb–Zn Deposits within the Tuotuohe Region of the Tibetan Plateau: Implications for Ore Genesis. *Minerals* **2023**, *13*, 762. <https://doi.org/10.3390/min13060762>

Academic Editors: Maria Boni, Yitian Wang and Changqing Zhang

Received: 12 April 2023

Revised: 22 May 2023

Accepted: 30 May 2023

Published: 31 May 2023



Copyright: © 2023 by the authors. Licensee MDPI, Basel, Switzerland. This article is an open access article distributed under the terms and conditions of the Creative Commons Attribution (CC BY) license (<https://creativecommons.org/licenses/by/4.0/>).

1. Introduction

The nearly north–south-trending Nujiang, Lancangjiang, and Jinshajiang drainage area of western Yunnan, eastern Tibet, western Sichuan, and southeast Qinghai in the southwest of China is collectively termed the Sanjiang or Southwest Sanjiang area. This area represents a complex tectonomagmatic belt that contains a significant amount of polymetallic mineralization and is the most prospective area for mineral exploration and development in western China [1–3]. This metallogenic belt hosts more than 100 large- to small-sized Pb–Zn–Ag deposits (e.g., the Jinding, Huize, and Nanping deposits in Yunnan) and more than 400 Pb–Zn–(Ag) prospects [4–6].

The Southwest Sanjiang structural zone extends to the northwest to an area termed North Sanjiang, which includes the Tuotuohe region that is the focus of this study. Both Southwest and North Sanjiang are geologically similar and have similar tectonic and structural histories, with both areas undergoing late Paleozoic to Mesozoic Tethyan tectonism and Cenozoic continental collisional orogenesis, both of which were associated with the formation of numerous ore deposits.

Dozens of valuable Pb–Zn deposits and prospects have been identified within the Yushu and Tuotuohe regions of the North Sanjiang area, including a number of large deposits, such as the Duocaima [7], Dongmozhaohua [8–11], and Mohailahen deposits [10]. The identification of these deposits and prospects means that the North Sanjiang area is highly prospective for further mineral exploration, and these discoveries indicate that North Sanjiang could be as well-endowed as the Southwest Sanjiang area, suggesting that the North Sanjiang area could be an extension of the Southwest Sanjiang metallogenic belt. This hypothesis is corroborated by Hou [1], who suggested that a giant belt of Pb–Zn–Cu–Ag mineralization is present within the Sanjiang area, which surrounds the eastern and northern edges of the Tibetan Plateau.

However, the North Sanjiang area, including the Tuotuohe region, is relatively unexplored and unresearched, especially when compared with the Southwest Sanjiang area. This is exemplified by the fact that there is little or no knowledge of the tectonic setting of mineralization, the type and composition of ore-forming fluids, or the source of mineralization in the North Sanjiang area. This lack of knowledge hinders future mineral exploration and means that exploration targeting may be ineffective.

This paper focuses on the geology, ore-forming fluids, and isotope geochemistry of five Pb–Zn deposits and prospects within the Tuotuohe region, namely mineralization within the Duocaima (DCM), Kongjie (KJ), Nabaozhalong (NBZL), Chuduoqu (CDQ), and Quemocuo (QMC) areas, and discusses (1) the tectonic setting of mineralization, (2) the source of ore-forming fluids and the metals deposited in these mineralized areas, and (3) the ore-forming processes that generated this mineralization. These new data indicate that the deposits in the study area represent a medium- to low-temperature hydrothermal vein type of mineralization, and this new information may provide a firm scientific foundation for future mineral exploration in this area.

2. Geological Setting

The Tuotuohe region is located within the hinterland of the Tibetan Plateau; is geologically within the northern Qiangtang Block [12]; and is bounded by the Jinshajiang suture belt to the north, the Tanggulasan Mountains Fault to the south, the line of 94°30′ longitude to the east, and a large bend of the Tuotuohe River to the west [13,14] (Figure 1). The Qiangtang Block records the Carboniferous–Permian development, evolution, and closure of the Tethys Ocean; the Early Triassic amalgamation with the Kunlun Block; the Early Cretaceous conjoining with the Lhasa Block as a result of southward subduction of the Bangonghu–Nujiang Ocean [15,16]; and the far-field effects of the Late Cretaceous subduction of the Indian Plate beneath the Eurasian Plate [17], which caused a fundamental transition in the crust–mantle dynamics of the region. The associated detachment and delamination, thinning of the lithosphere, and rapid uplift of the Tibetan Plateau [15,18–20] during this latest event all influenced the formation of mineral deposits in the study area during the Cenozoic.

Sedimentary and volcanic rocks are widespread within the Tuotuohe Basin. Marine units dominate the Carboniferous–Permian section of the basin, with marine and marine-terrestrial units deposited between the Triassic and the Jurassic. These units are generally divided by the Tuotuohe River, and the Cenozoic evolution of the basin involved the formation of imbricate thrust structures [13,14] (Figure 1b). The deposition of marine units ceased during the Cretaceous and was superseded by a period of intra-continental tectonism, although Lower Triassic and Paleocene sediments are absent from the Tuotuohe region as a result of Tethyan and Himalayan collisional orogenesis and the formation of two regional angular unconformities [6,14,21].

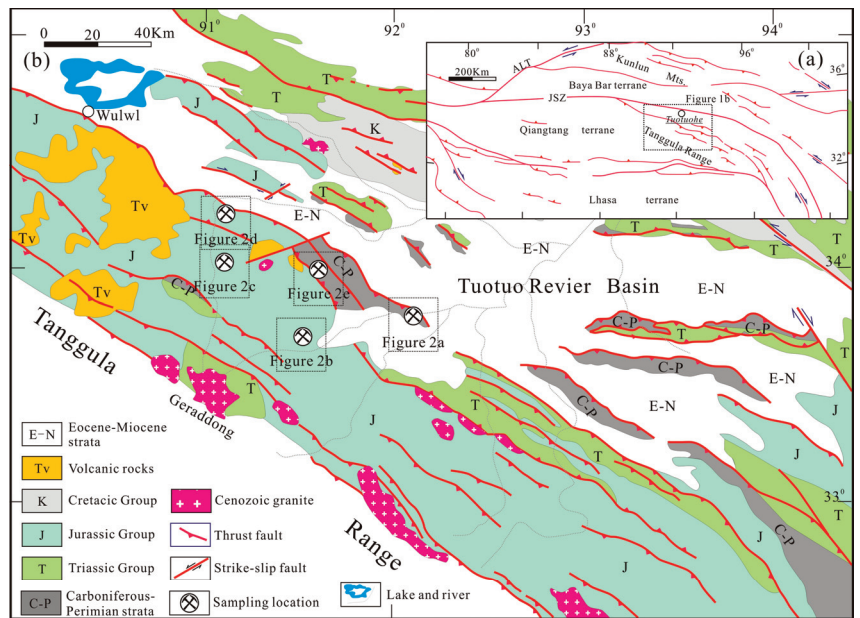


Figure 1. Simplified tectonic map of the Tibetan Plateau (a) and Tuotuohe region (b) (adapted from [13]). JSZ, Jinshajiang suture; BSZ, Banggongcuo-Nujiang suture; ALT, Altyn Tagh Fault.

The active continental margin and intra-continental orogenic activities suggest that units in the study area are intensively and extensively folded. The oldest fold structures in the area are within segments of a complexly folded island arc belt of the early Permian and continental marginal orogenic belt in the Qiangtang Block, with faults in these areas characterized by a WNW–ESE-trending thrust belt. These thrusts and other major faults in the study area usually delineate boundaries between the basin and orogenic belt and control both outcrop patterns and the location of mineralization.

The Tuotuohe region contains a significant volume of volcanic rocks, the most distinctive of which are Cenozoic alkaline volcanic rocks that have a zircon U–Pb age of 32–40 Ma [22] (Figure 1b). These alkaline volcanics are associated with the crustal thickening of the Tibetan Plateau that occurred from 65 Ma onward. The magmas that formed these volcanics were generated by a low degree of partial melting of mafic eclogite materials at the base of the thickened crust, and these magmas were also subsequently contaminated by lithospheric mantle materials. The Duocaima and Nabaozhalong areas of the study area also contain the late Permian to the early Triassic crystal tuffs that yield zircon U–Pb ages of 256 and 245 Ma [23] (Figure 2). The magmas that formed these tuffs were generated during the subduction of the Jinshajiang Ocean to the south of the study area.

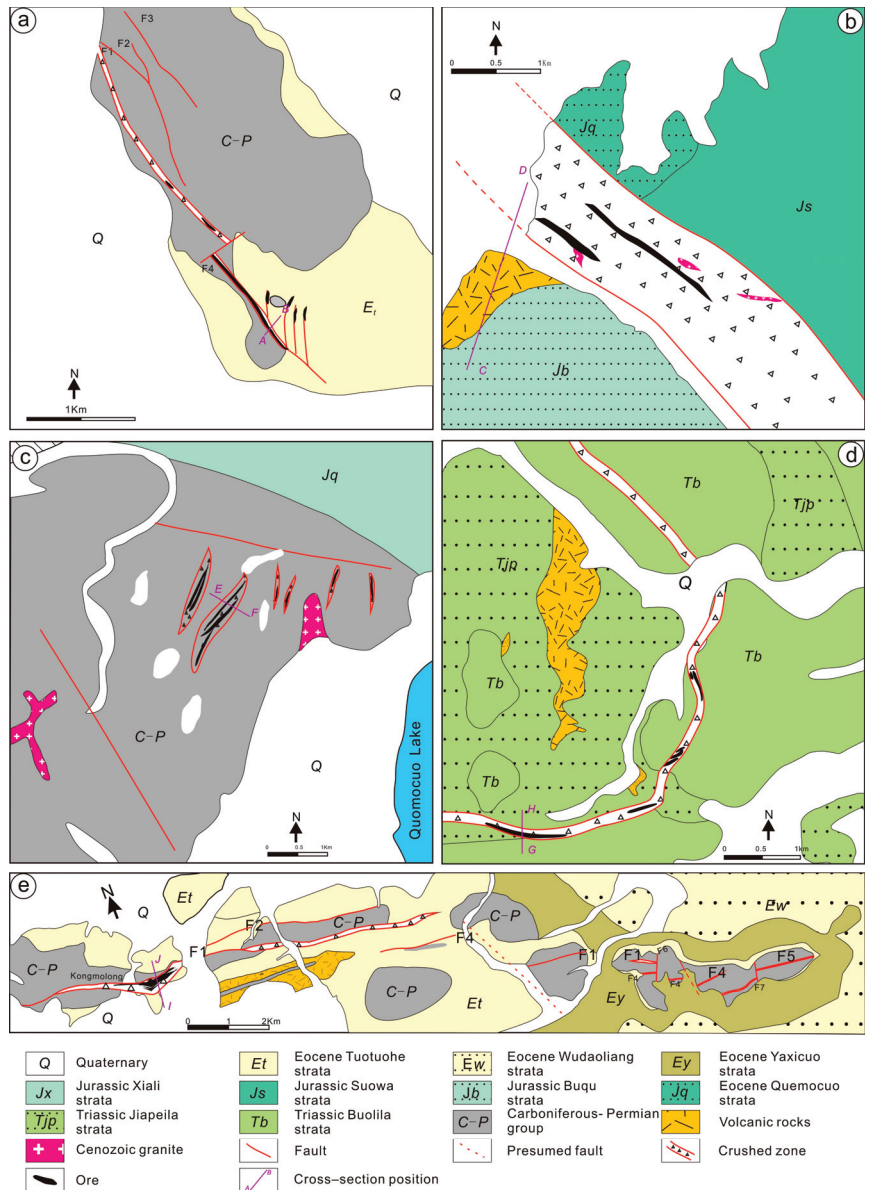


Figure 2. Schematic map showing regional and ore geology of the Pb–Zn deposits in Tuotuohe region. (a) Geology of the KJ Pb–Zn deposit. (b) Geology of the CDQ Pb–Zn deposit. (c) Geology of the QMC Pb–Zn deposit. (d) Geology of the NBZL Pb–Zn deposit. (e) Geology of the DCM Pb–Zn deposit.

3. Ore Deposits Geology

3.1. Host Rocks for Pb–Zn Mineralization

Sporadic bands of Carboniferous and Permian units outcrop between the Mesozoic and Cenozoic units within the Tuotuohe region and significant amounts of Triassic and Cretaceous units are exposed in the northwest of the study area, whereas Jurassic units dominate the southwest and Cenozoic units are concentrated in the interior of the basin. The outcropping of all of these entities is controlled by regional structures [13].

The Kongjie (KJ), Duocaima (DCM), Nabaozhalong (NBZL), Chuduoqu (CDQ), and Quemocuo (QMC) deposits are typical examples of Pb–Zn mineralization within the study area. They are generally located in the southern and western Tuotuohe Basin and are hosted by carbonate sediments, including Triassic limestones of the Zarigen (Kongjie), Jiushidaoban (Duocaima), Labuchari (Quemocuo), and Bolila (Nabaozhalong) formations, Jurassic limestones within the Buqu Formation (Chuduoqu), and Cenozoic limestones of the Wudaoliang Formation (Duocaima; Table 1; Figure 2).

Table 1. The geological characteristics of the deposits in Tuotuohe region.

	Ore-Bearing Wallrock	Ore Bodies	Ore-Controlling Structure	Ore Types and Mineral Assemblages	Wallrock Alteration
Duocaima	The Jiushidaoban Formation limestones, the Wudaoliang Formation limestones	Veined, lenticular	The NW fault fracture zone	Brecciated, veinlet, poikilitic, and impregnation structures; galena, sphalerite, pyrite, sardinianite, smithsonite, limonite, etc.	Carbonation, silicification, argillization
Chuduoqu	The Buqu Formation limestones	Veined	The NW fault fracture zone primarily, and near NS interformational fracture zone secondly	Galena, chalcopyrite, sphalerite, cerusite, limonite, pyrite, covellite, etc.; veinlet, massive, and brecciated structures	Baratization, carbonation, silicification, argillization
Nabaozhalong	The Bolila Formation grain limestones	Veined	The circular structure	Massive, brecciated, veinlet, and impregnation structures; galena, sphalerite, pyrite, malachite, etc.	Carbonation, silicification, kaolinization
Kongjie	The Zharigen Formation bioclastic limestones	Veined	The NW fault fracture zone	Galena, sphalerite, limonite, pyrite, etc.; massive, and impregnation structures	Carbonation, silicification
Quemocuo	The Labochari Formation micrite and bioclastic limestones	Veined, lenticular	The NNE fault fracture zone	Galena, sphalerite, etc.; massive, brecciated, veinlet, and impregnation structures	Carbonation, silicification, baratization

Some mineralization in the study area is hosted by sandstones, including mineralization within the Jurassic Jiabila (Nabaozhalong) and Xili (Duocaima) formations and the Cenozoic Tuotuohe Formation (Duocaima, Kongjie; Figure 2), although it should be noted that the majority of significant mineralization is hosted by carbonate formations rather than sandstones.

3.2. Ore-Controlling Structures

The most important ore-controlling structures in the study area are NW–SE-trending faults [13], which generally control the location of individual deposits and ore bodies, including those within the DCM, KJ, and CDQ deposits (Table 1, Figure 2).

The faults associated with the KJ deposit are small-scale, descend to the NE at 50°–70°, and cover a length of 3.4 km with a fragmentation width of 50–200 m. From the northwest to the southeast, the width is gradually decreasing. In addition, the Pb–Zn ore bodies that

comprise the KJ deposit are dominated by fragmentation associated with the development of extensional breccias (Figure 2a).

The CDQ deposit strikes SE–NW, leading some researchers to suggest that the deposit is controlled by an interformational fracture zone, and previous research suggests that ore bodies within the deposit trend S–N. However, fieldwork undertaken during this study indicates that this deposit is associated with a NW–SE-trending structure (Figure 2b) that is a more essential control on the location of mineralization than the previously identified S–N structure. Field geological investigation and cataloging of the mine (Figure 3) revealed that the main ore-controlling structure is an EW-oriented alteration and fragmentation zone, within which multiple EW-oriented ore bodies can be circled. The above-mentioned near-SN-oriented structure is a series of parallel distribution of interstratified fracture zones, which contains ore but are secondary ore-bearing structures, in which mineralization is intermittently distributed, and the mineralization is weakened to disappear away from the EW main structure zone. The NW–SE-trending structure is concordant with regional bedding, is over 500 m wide, has a length of more than several thousand meters, and extends to the west of the study area where it is covered by Quaternary sediments. This structure hosts a significant number of ore bodies, with intermittent mineralization of the CDQ deposit located in an interformational fracture zone. However, all of these ore bodies dissolve outside the NW–SE-trending structure. The interformational fracture zone slightly displaces the NW–SE-trending mineralization-rich veins, indicating that the former predates the latter, although both faults formed in the same overall period. The new ore-controlling NW–SE structure discovered during this study has altered the approach to mineral exploration in this area, and the total Pb–Zn metal reserves for the deposit are greater than 510,000 tons [24].

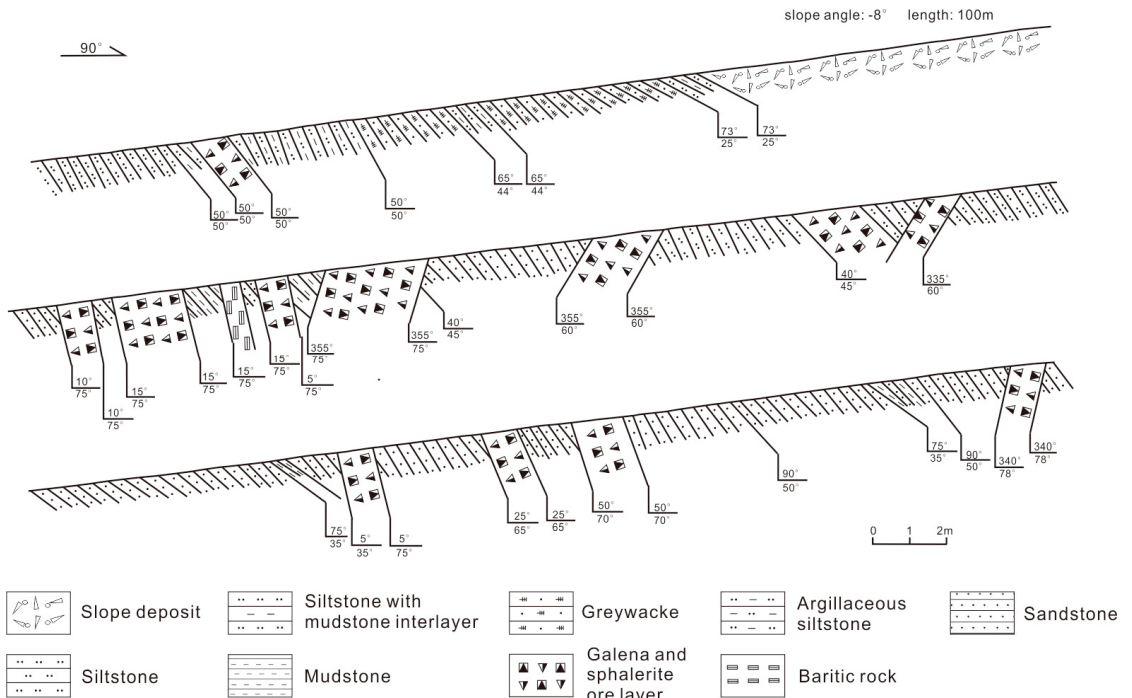


Figure 3. Measured profile of the CDQ Pb–Zn deposit.

The QMC Pb–Zn prospect is associated with lenticular ore-controlling structures that trend ENE–WSW, are brecciated, and are dominated by limestone components; these structures are common within this portion of the study area (Figure 2c). Breccias in this area have an angular shape, vary in diameter, and were formed during tensional tectonism. The QMC Pb–Zn mineralized prospect is hosted by one of these ENE–WSW-oriented structures and is a minor prospect. Through the geological compilation and route geological investigation of TC1 and TC5 (Figure 4a,b), the main control tectonic zone is in the NWW direction, and the NWW and NW direction fractures control a group of NE-direction-distributed ore (chemical) bodies distributed in a subparallel lateral row. The NWW-oriented fractures have left-rotation tensegrity, while the NE-oriented lateral ore bodies are controlled by right-going tensegrity.

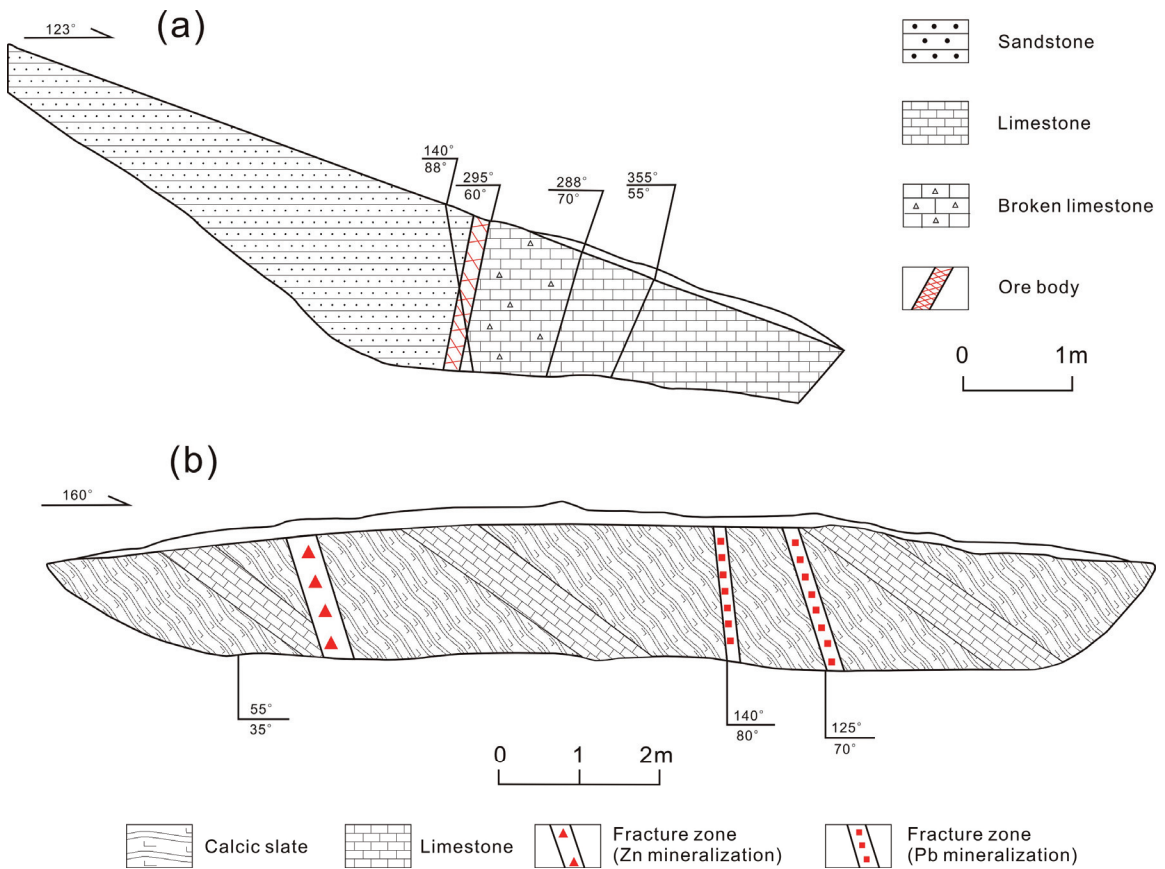


Figure 4. Geological compilation maps of (a) TC1 trench and (b) TC5 trench of M1 ore body within the QMC deposit.

The structure that controls the location of Pb–Zn mineralization within the NBZL deposit is circular in geometry, centered on volcanic and dike units within the west of the mine (Figure 2d). This structure descends outwards at an angle of 30° and is the primary host for fault gouges, breccias, and ore bodies in the area. However, only the eastern half of the circular structure has been identified to date, and no specific research has been undertaken on the western half, primarily as a consequence of mining rights issues. Drilling has identified that Pb–Zn mineralization predominantly occurs along the contact between the hanging wall of the circular structure and the limestones of the Bolila

Formation, with mineralization controlled by both the location of the structure and the presence of limestone.

The fault that hosts the ore bodies within the DCM deposit is about 20 km long, 40–400 m wide, trends NW–SE, and descends 60–80° to the NE. The deposit is divided into three ore blocks (from west to east): the Kongmolong, Chaqupacha, and Duocaima blocks. Fractures within the deposit contain tectonic breccias and fault gouges, both of which are suitable sites for mineralization, indicating that the mineralization within the deposit is preferentially fracture-hosted (Figure 2e). The field trenching and geological compilation of drill holes show that the interstratified fracture zone does have a certain degree of mineralization, but the main part of the mineralization is controlled by the steeply dipping interlayer fracture, and the mineralization is more abundant at the superposition of the two structures. In other words, the main ore-holding structure is a steeply dipping interlayer fracture rather than an interstratified fracture zone (Figure 5).

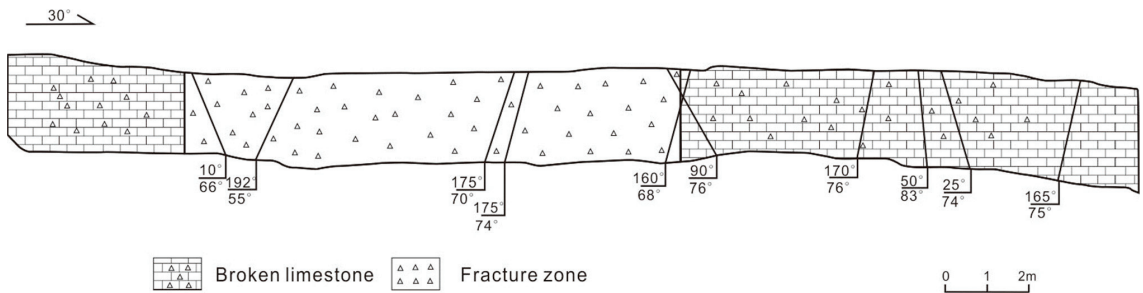


Figure 5. Geological compilation map of TC01 trench in the Kongmolong section of the DCM Pb–Zn deposit.

From the geological phenomena revealed by the field geological work, the Kongjie Pb–Zn ore is mainly Zn mineralization, and the quantity of galena is greatly reduced compared with other deposits, which is consistent with the results of chemical analysis ($Pb/Zn = 0.01\sim 0.3$) (Figure 6a), indicating that this deposit has a deep stripping depth; the Pb–Zn ore of Quemucuo has a large amount of galena and less sphalerite due to the low mineralization temperature and mineral assemblage, and its Pb/Zn ratio is 6~15, indicating that the surface position at this stage is close to the head of the deposit, and this deposit has a shallow stripping and better preservation conditions (Figure 6c); the Pb/Zn ratio of the Duocaima deposit is high (0.1~150), showing a strong Pb mineralization (Figure 6e), which is consistent with the small depth of mineralization and low temperature of mineralization, and the shallow denudation of the deposit; the Pb/Zn ratio of Chuduocu is between 0.1 and 10 (Figure 6b), with relatively good Pb–Zn mineralization potential and shallow stripping; the Pb/Zn ratio of Nabozhalong is low (the main body is around 0.1) (Figure 6d), which is equivalent to the central Pb–Zn zone in the vertical zone of Pb–Zn, indicating a deep stripping.

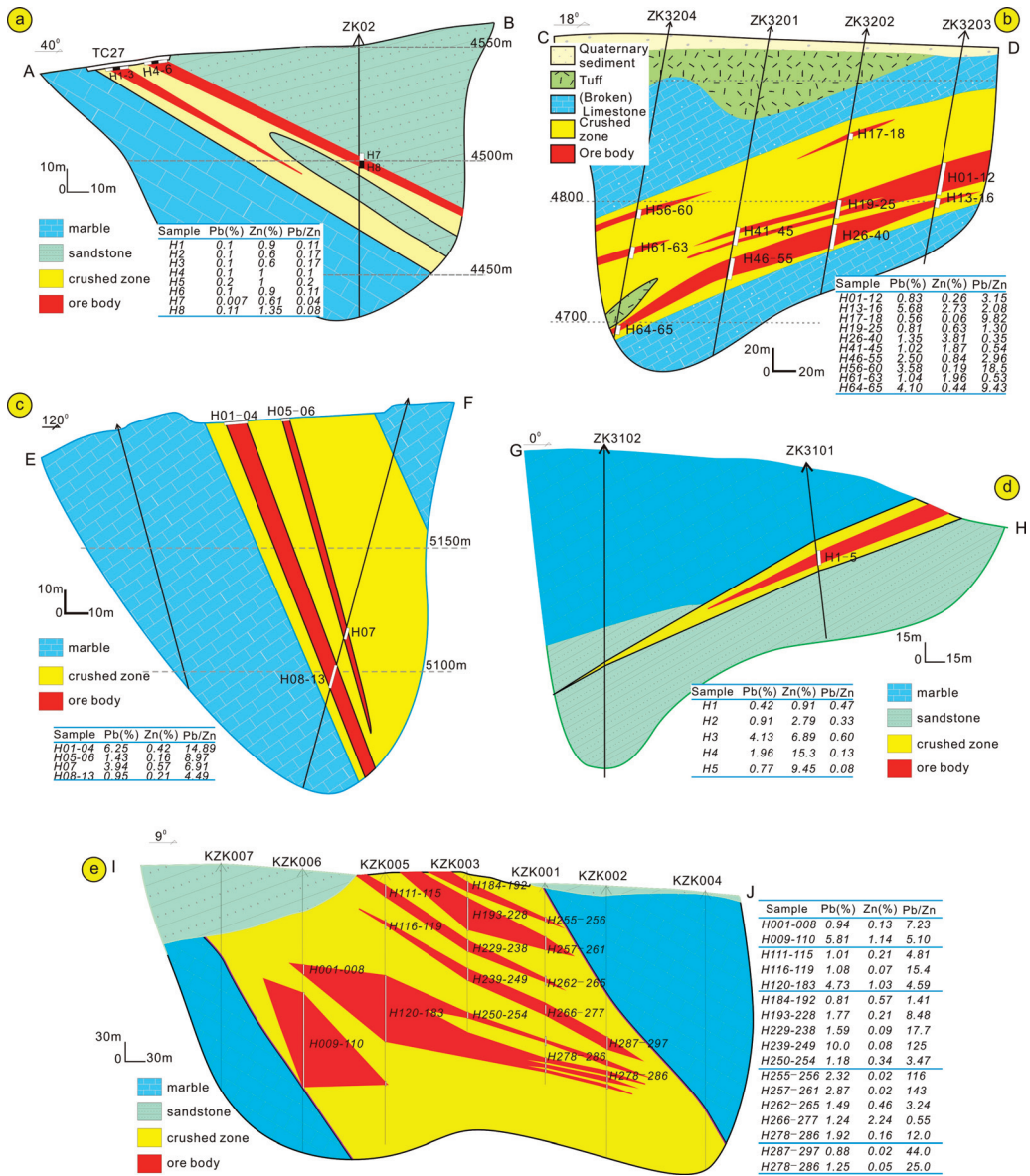


Figure 6. Prospecting line profile maps of (a) Kongjie (KJ), (b) Chuduoqu (CDQ), (c) Quemocuo (QMC), (d) Nabaozhalong (NBZL), and (e) Duocaima (DCM) Pb-Zn deposits in Tuotuohe region.

3.3. Ore Types and Mineral Assemblages

The main ore minerals within both Pb-Zn deposits and prospects within the Tuotuohe region are galena and sphalerite (Table 1; Figure 7g-i), and copper-iron mineralization is also present in the DCM and CDQ deposits (Figure 7d-f), as well as pearceite within the CDQ deposit. The galena-sphalerite-copper assemblage in these deposits represents low-temperature mineralization, and secondary limonite, malachite, azurite, sardinianite, and smithsonite are present in secondary enrichment zones along joints and fractures that formed during weathering. Assaying of drill cores indicates that the lower parts of the

deposits in the study area are Zn-rich, whereas the upper parts are Pb-rich (Figure 3). Mineralization is divided into four ore types: vein-like, brecciated, disseminated, and massive mineralization, with vein-like and massive mineralization being dominant. Ore minerals are hosted by a chalcedony- and calcite-dominated gangue with minor barite. The mineralization in the study area is hydrothermal and formed at low temperatures, as supported by the presence of colloform-textured ore (Figure 7a).

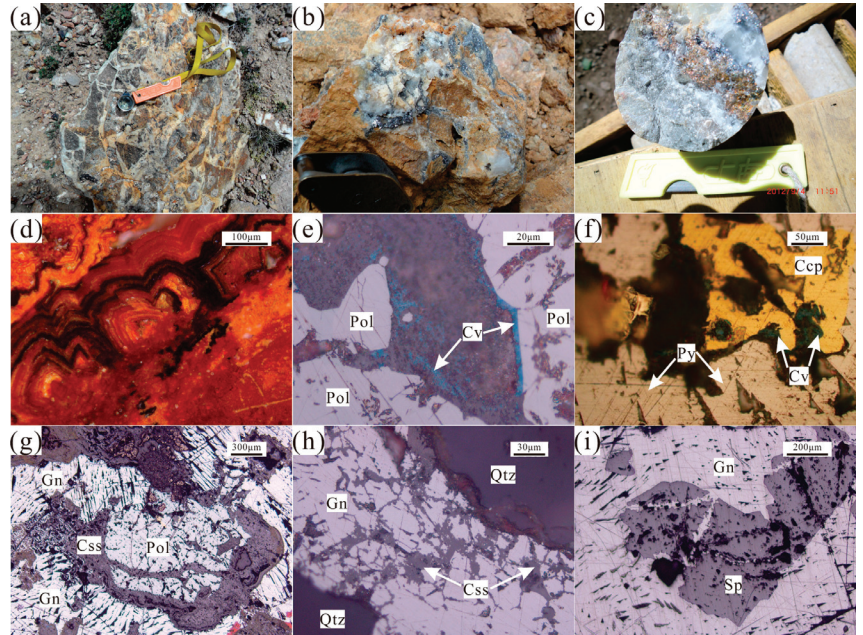


Figure 7. Photographs and photomicrographs of ore from the Pb–Zn deposits in Tuotuohe region. (a) Tectonic breccia cemented by later calcite veins; (b) veined Pb–Zn ore in quartz veins; (c) pyrite mineralization, galena mineralization quartz veins; (d) the internal reflection color of limonite; (e) polybasite with covellite at the margin; (f) pyrite contains chalcopyrite, and covellite is visible along the edge of chalcopyrite; (g) cerussite metasomatizing polybasite and galena; (h) cerussite metasomatizing galena along its crystal edges, and galena is euhedral–subhedral; (i) galena metasomatizing sphalerite along its microfractures. Qtz—quartz; Pol—polybasite; Css—cerussite; Py—pyrite; Ccp—chalcopyrite; Sp—sphalerite; Gn—galena; Cv—covellite.

The brecciated nature of the ore, the various sizes and shapes of breccia zones, the presence of chalcedony and barite with comb structures, and the presence of vein-like mineralization (Figure 7b,c) are all indicative of formation during tensional tectonism and the abundance of mineralization in an area is often controlled by the strength of fissures and the presence of quartz–calcite veins (Figure 7a–c).

3.4. Stages of Mineralization

All mineral assemblages within Pb–Zn deposits in the Tuotuohe region can be divided into hydrothermal and weathering periods of formation (Figure 8). The hydrothermal period of mineralization is divided into quartz–galena, chalcedony–barite–carbonate–galena, and carbonate–gypsum stages of mineralization (stages 1, 2, and 3, respectively).

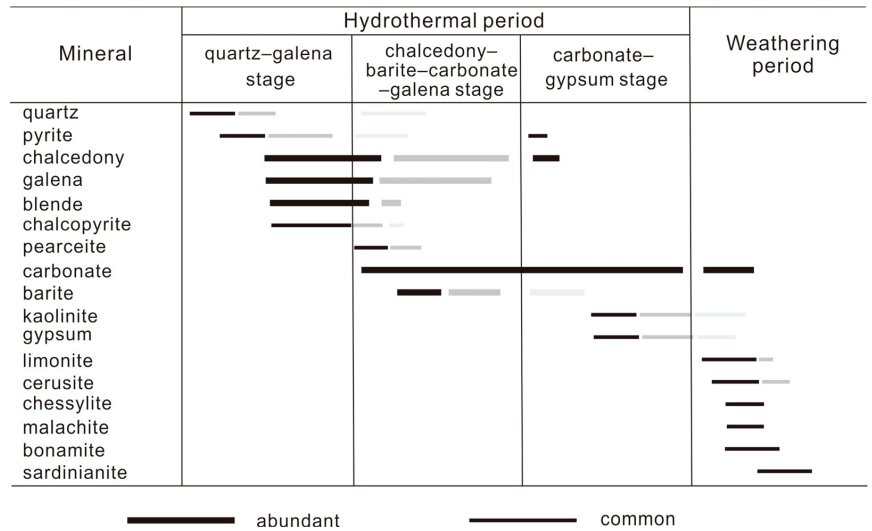


Figure 8. Mineral assemblages in the paragenetic sequence of the Pb–Zn deposits in Tuotuohe region (the shade of colors represents different generations).

3.5. Wallrock Alteration

Mineralization in the study area is associated with significant wallrock alteration that is dominated by silicification and the formation of barite and carbonate alteration, all of which are closely related to Pb–Zn mineralization as corroborated by petrography, mineral assemblages, and cross-cutting vein relationships (Table 1). The primary types of alteration are as follows:

- (1) During stages 1 and 2 of mineralization, silicification takes many forms, forming irregular quartz veins and networks in stage 1 and planar alteration that is closely related to Pb–Zn mineralization in stage 2;
- (2) Barite alteration is characterized by the formation of variegated barite during stage 2 and by less abundant barite associated with gypsum in stage 3;
- (3) Carbonate alteration is associated with stages 2 and 3. The carbonate alteration that formed during stage 2 is more closely related to mineralization and is more voluminous than that which formed during stage 3, with the latter cross-cutting the former.

4. Sampling and Analytical Methods

A total of 45 samples, including quartz and calcite, were obtained for microthermometric analysis. Samples were chosen during comprehensive field investigations of individual ore deposits (Table 2). Fluid inclusion microthermometry and laser Raman spectra analyses were undertaken in the Geofluid Laboratory of Jilin University, China, using samples of 0.25–0.3 mm thickness. Each sample was meticulously examined under a binocular microscope before fluid inclusion microthermometry analysis using a Linkam THMS-600 heating–freezing stage calibrated with purified water and synthetic fluid inclusion standards. This stage has an accuracy of $\pm 0\text{--}2\text{ }^\circ\text{C}$ at temperatures $< 300\text{ }^\circ\text{C}$ and $\pm 2\text{--}5\text{ }^\circ\text{C}$ at temperatures $> 300\text{ }^\circ\text{C}$. Decrepitation was avoided during analysis by first freezing and then heating samples over a range of $-196\text{ to }600\text{ }^\circ\text{C}$ at a heating/freezing rate of $0.1\text{--}1.0\text{ }^\circ\text{C}/\text{min}$ for temperatures $< 10\text{ }^\circ\text{C}$, $5\text{--}10\text{ }^\circ\text{C}/\text{min}$ at temperatures between 10 and $31\text{ }^\circ\text{C}$ and $> 100\text{ }^\circ\text{C}$, and $< 0.5\text{ }^\circ\text{C}/\text{min}$ when approaching phase transformation temperatures. Salinities were determined as wt.% NaCl equivalents and were calculated using the melting temperature of the last crystal of ice within two-phase fluid inclusions using the equation proposed

by [25]. Fluid densities were estimated using fluid inclusion homogenization temperatures and the equation proposed by [26].

Table 2. Summary of fluid inclusions data from the Pb–Zn deposits in Tuotuohe region.

Sample	Host	T _m Ice/°C	Th/°C	Salinity/wt.% NaCl eq.
DCM				
SJ1-7	Quartz	−1.3–−14	115.8–187.8 (14)	2.23–18.19
SJ1-8-1	Quartz	−5–−12	115.9–199.3 (12)	3.05–15.85
SJ1-9	Quartz	−4.6–−13	118.9–211 (7)	7.30–16.72
SJ1-13-1	Quartz	−1.1–−16	105–214.8 (8)	1.90–19.79
SJ1-18	Quartz	−2.3–−12	102.5–203.1 (10)	3.85–15.75
SJ1-16	Quartz	−5.4–−15	122.1–247.6 (12)	8.4–16.34
SJ1-10	Quartz	−7.3–−12	121.3–195.5 (11)	10.87–15.65
CDQ				
SJ1-46	Calcite	−4.4–−11	93.4–240.5 (12)	7.01–14.94
SJ1-47	Calcite	−3.8–−10	98.4–231.9 (13)	6.14–14.31
SJ1-50	Calcite	−6.7–−7.6	90.8–179.1 (9)	10.11–11.23
SJ1-51	Calcite	−3.7–−10	99.4–217.6 (6)	5.99–14.31
SJ1-52	Calcite	−4.8–−11	98.1–243.5 (12)	7.58–14.84
SJ1-53	Quartz	−4.1–−7.4	145.8–21.64 (9)	6.58–10.99
CDQ-B3	Quartz	−4.6–−10.6	167–249 (4)	7.3–14.6
CDQ-B11	Quartz	−5.5–−10.8	176.6–239.7 (12)	8.54–14.8
CDQ-B12	Quartz	−2.6–−9.6	158–228.6 (5)	3.2–13.55
CDQ-B13	Quartz	−5.1–−8	148.4–248.2 (3)	8.4–11.7
CDQ-W4	Quartz	−7.9–−8.9	178–228.7 (2)	11.5–12.07
KJ				
SJ1-22-1	Quartz	−3.9–−13.7	102.3–199.8 (12)	6.29–17.65
SJ1-22-2	Quartz	−6.7–−10.1	98.4–197.7 (13)	10.49–13.44
SJ1-22-3	Quartz	−2–−12.4	132.8–197.2 (9)	4.32–16.44
SJ1-23-1	Quartz	−6.4–−12.5	91.8–220.5 (11)	7.58–16.53
SJ1-24	Quartz	−2.6–−9.4	91.4–236.4 (16)	4.32–13.33
SJ1-25	Quartz	−3–−10.1	85.1–209.6 (7)	4.94–14.10
SJ1-26	Quartz	−3.3–−9.7	86.2–232.7 (8)	5.4–13.66
SJ1-27	Quartz	−5.4–−12.8	174.5–196 (3)	8.4–16.82
QMC				
QH11-58	Quartz	−3.8–−10.7	164.4–259.5 (5)	6.14–14.73
QH11-60	Quartz	−2.6–−8.3	170.5–203.2 (9)	4.32–12.07
SJ1-40	Quartz	−2.7–−13.3	162.6–207.3 (12)	4.48–17.28
SJ1-41	Quartz	−1.4–−12.5	187.5–219.3 (3)	2.4–16.53
SJ1-42	Quartz	−2.2–−10	170.6–218.5 (7)	3.69–13.99
SJ1-43	Calcite	−2.3–−8.9	76–187.9 (8)	3.85–12.77
SJ1-38	Calcite	−2.8–−9.3	105.9–177.6 (9)	4.63–13.22
SJ1-44	Calcite	−3.4–−10.3	75.9–197.3 (7)	5.55–14.31
SJ1-39	Calcite	−2.3–−6.3	89.8–192.2 (10)	3.85–9.60
QH11-56	Calcite	−1.9–−5.6	110.5–131.5 (4)	3.21–8.67
NBZL				
QH11-61	Calcite	−7.1–−8.6	93.4–189.7 (4)	10.62–12.42
QH11-62	Calcite	−3.9–−8.5	97.3–213.4 (6)	6.29–12.31
QH11-63	Calcite	−6.1–−11.8	126.4–168.6 (7)	9.34–15.85
QH11-69	Calcite	−2.5–−8.5	155.9–181.2 (9)	4.17–12.31
NBZLZK005-W10	Calcite	−2.6–−10.6	121.8–232.5 (4)	4.32–14.63
NBZLZK005-W11	Quartz	−5.6–−10.1	123.0–207.6 (12)	8.27–13.88
QH11-67	Quartz	−9–−14.6	117.9–199.9 (12)	12.88–18.45
QH11-68	Quartz	−4.7–−9.5	120.4–184.4 (13)	7.44–13.44
QH11-70	Quartz	−3–−13.9	119.2–204.7 (9)	3.21–17.83

T_m ice = temperature of final ice melting; Th = temperature of homogenization.

The compositions of individual FIs were determined using an RM-2000 laser Raman microprobe (Renishaw, New Mills, UK) with an argon ion laser and a laser source of 514 nm. The scanning range of spectra was set between 100 and 4300 cm^{-1} with an accumulation time of 60 s for each scan. The laser beam width was 1 μm , and the spectral resolution was 0.14 cm^{-1} .

Twenty-five galena samples that formed during leaching and decomposition during mineralization stages 1 and 2 were selected from diverse deposits for S–Pb isotopic analysis using a binocular microscope. These analyses were carried out at the Analytical Laboratory of the Beijing Research Institute of Uranium Geology (ALBRIUG; Table 3), Beijing, China. Sulfide isotope compositions were measured using a Finnigan MAT-251 mass spectrometer and the SO_2 method of [27], with results reported using the conventional $\delta^{34}\text{S}$ notation and ‰ units relative to the Vienna Canon Diablo Troilite (V-CDT) standard as $\delta^{34}\text{S}_{\text{V-CDT}}$. Total uncertainties were estimated to be less than $\pm 0.2\text{‰}$, and GBW 04415 and GBW 04414 Ag_2S were used as external standards, yielding $\delta^{34}\text{S}_{\text{V-CDT}}$ values of $-0.07\text{‰} \pm 0.13\text{‰}$ and $22.15\text{‰} \pm 0.14\text{‰}$, respectively.

Table 3. Sulfur and lead isotope composition of galena from the Pb–Zn deposits in Tuotuohe region.

Sample	$^{208}\text{Pb}/^{204}\text{Pb}$	$^{207}\text{Pb}/^{204}\text{Pb}$	$^{206}\text{Pb}/^{204}\text{Pb}$	$\Delta\beta$	$\Delta\gamma$	$\delta^{34}\text{S}_{\text{V-CDT}}/\text{‰}$
CDQ						
CDQ-B13	38.858	15.664	18.689	15.165	32.634	−3.8
CDQ-B14	38.904	15.682	18.687	16.332	33.856	−2.4
CDQ-B19	38.932	15.689	18.695	16.785	34.600	−1.9
CDQ-W2	38.81	15.651	18.655	14.323	31.358	−1.9
CDQ-B20	38.937	15.692	18.692	16.980	34.733	−1.3
CDQ-B21	38.943	15.694	18.694	17.110	34.892	−1.7
KJ						
KJ-B3	38.895	15.663	18.766	15.100	33.617	−28.7
KJ-B4	38.968	15.674	18.81	15.813	35.557	−29.4
KJ-B1	38.976	15.675	18.809	15.878	35.769	−25.6
KJ-B5	38.923	15.662	18.796	15.036	34.361	−27.5
KJ-B6	38.955	15.665	18.822	15.230	35.211	−29
KJ-B7	38.656	15.647	18.585	14.064	27.265	0.1
KJ-B3	38.895	15.663	18.766	15.100	33.617	−28.7
QMC						
QMC-TC1-B14-2	38.65	15.645	18.579	13.934	27.106	2.4
QMC-3#-TC5-W4	38.715	15.665	18.596	15.230	28.833	3.4
QMC-3#-TC9-B1	38.714	15.664	18.598	15.165	28.807	2.2
QMC-TC1-B11-1	38.764	15.68	18.615	16.202	30.136	2.3
QMC-TC1-B15	38.66	15.649	18.584	14.193	27.372	3.3
QMC-TC1-W4	38.656	15.647	18.585	14.064	27.265	2.9
NBZL						
NBZL-B33	38.644	15.659	18.439	14.841	26.947	6.7
NBZL-B32	38.596	15.643	18.43	13.804	25.671	5.2
NBZL-B34	38.634	15.657	18.433	14.712	26.681	6.1
NBZL-B1	38.575	15.623	18.41	12.508	25.113	9.3
NBZL-B2	38.568	15.634	18.424	13.221	24.927	7.3
NBZL-B3	38.642	15.656	18.458	14.647	26.893	10.1
DCM [28]						
DTC6-1	-	-	-	-	-	−22.45
DTC9-1-3	-	-	-	-	-	−26.72
CQPC [28]						
CWZK01-7	-	-	-	-	-	−15.77
CWZK01-11	-	-	-	-	-	−11.80
CWZK01-13	-	-	-	-	-	−11.13
CWZK01-19	-	-	-	-	-	−7.05

Table 3. Cont.

Sample	$^{208}\text{Pb}/^{204}\text{Pb}$	$^{207}\text{Pb}/^{204}\text{Pb}$	$^{206}\text{Pb}/^{204}\text{Pb}$	$\Delta\beta$	$\Delta\gamma$	$\delta^{34}\text{S}_{\text{V-CDT}}/\text{‰}$
070914-8	-	-	-	-	-	-13.25
KJ [28]	-	-	-	-	-	-28.99
TC32	-	-	-	-	-	-34.53
KJ-1-1	-	-	-	-	-	-26.81
KJ-1-2	-	-	-	-	-	-30.55
KJ-1-3	-	-	-	-	-	-30.55

$$\Delta\beta = [(^{207}\text{Pb}/^{204}\text{Pb})_{\text{CP}} / (^{207}\text{Pb}/^{204}\text{Pb})_{\text{MP}} - 1] \times 1000. \Delta\gamma = [(^{208}\text{Pb}/^{204}\text{Pb})_{\text{CP}} / (^{208}\text{Pb}/^{204}\text{Pb})_{\text{MP}} - 1] \times 1000.$$

Pb isotopic compositions were measured using an Isoprobe-T mass spectrometer and a single filament and are reported with regard to Pb standard reference NBS-981 values [29]: $^{206}\text{Pb}/^{204}\text{Pb} = 16.934 \pm 0.007$, $^{207}\text{Pb}/^{204}\text{Pb} = 15.486 \pm 0.012$, and $^{208}\text{Pb}/^{204}\text{Pb} = 36.673 \pm 0.033$. The accuracy of the mass measurement of 1 μg Pb relative to the NBS 981 values is greater than 0.005% for $^{206}\text{Pb}/^{204}\text{Pb}$ and 0.0005% for $^{208}\text{Pb}/^{206}\text{Pb}$.

The H and O isotope analyses of quartz undertaken during this investigation were carried out using a Finnigan MAT-253 mass spectrometer at ALBRIUG, China, following the procedures outlined by [30]. The results are given in terms of SMOW (Standard Mean Ocean Water), with a precision of $\pm 2\text{‰}$ for δD and $\pm 0.2\text{‰}$ for $\delta^{18}\text{O}$.

The C and O isotope analyses of stage 2 and 3 calcite were performed on an ISOPrime instrument at ALBRIUG, China, and the results are presented as $\delta^{13}\text{C}_{\text{PDB}}$ and $\delta^{18}\text{O}_{\text{PDB}}$ relative to Pee Dee Belemnite (PDB). The analytical precision (2σ) for carbon isotopes is $\pm 0.2\text{‰}$ and for oxygen isotopes is $\pm 2\text{‰}$, and the relationship between $\delta^{18}\text{O}_{\text{SMOW}}$ and $\delta^{18}\text{O}_{\text{PDB}}$ is $\delta^{18}\text{O}_{\text{SMOW}} = 1.03086 \times \delta^{18}\text{O}_{\text{PDB}} + 30.86$ [31].

5. Analytical Results

5.1. Fluid Inclusions

Fluid inclusion phase ratios at room temperature (25 °C) show that two fluid inclusion types are present in quartz and calcite from Pb–Zn deposits in the study area:

Type I: two-phase liquid and vapor (aqueous liquid + vapor) inclusions (Figure 9a–i).

Type II: monophasic liquid (aqueous liquid) inclusions (Figure 9c,f).

Type I fluid inclusions dominate the samples and account for more than 80% of the total fluid inclusion population within the samples. In addition, the vapor-free nature of Type II inclusions means that they are sub-stable; as a result, only Type I inclusions were analyzed during this study. Type I fluid inclusions are liquid-rich, with degrees of fill ranging from 0.6 to 0.9, and have varied morphologies, including round, negative crystal, or irregular, with diameters ranging from 4 to 20 μm (Figure 9). They appear as both isolated inclusions and as clusters along crystal growth orientations, suggesting they are primary inclusions. The absence of liquid CO_2 or clathrate formation during freezing experiments suggests that none of the inclusions contained significant quantities of CO_2 [32].

The microthermometric data are presented in Table 2. Type I fluid inclusions are completely homogenized to liquid at temperatures varying from 80 °C to 260 °C (Th), with the preponderance homogenizing at 120 to 220 °C (Figure 10), covering four stages of mineralization. However, fluid inclusions within quartz that formed during stages 1 and 2 have typically higher homogenization temperatures than those within calcite that formed during stages 2 and 3. These inclusions have densities of 0.833–1.051 g/cm^3 and salinities of 1.90–19.79 wt.% NaCl equivalent, with the majority having salinities of 6–16 wt.% NaCl equivalent (Table 2; Figure 10).

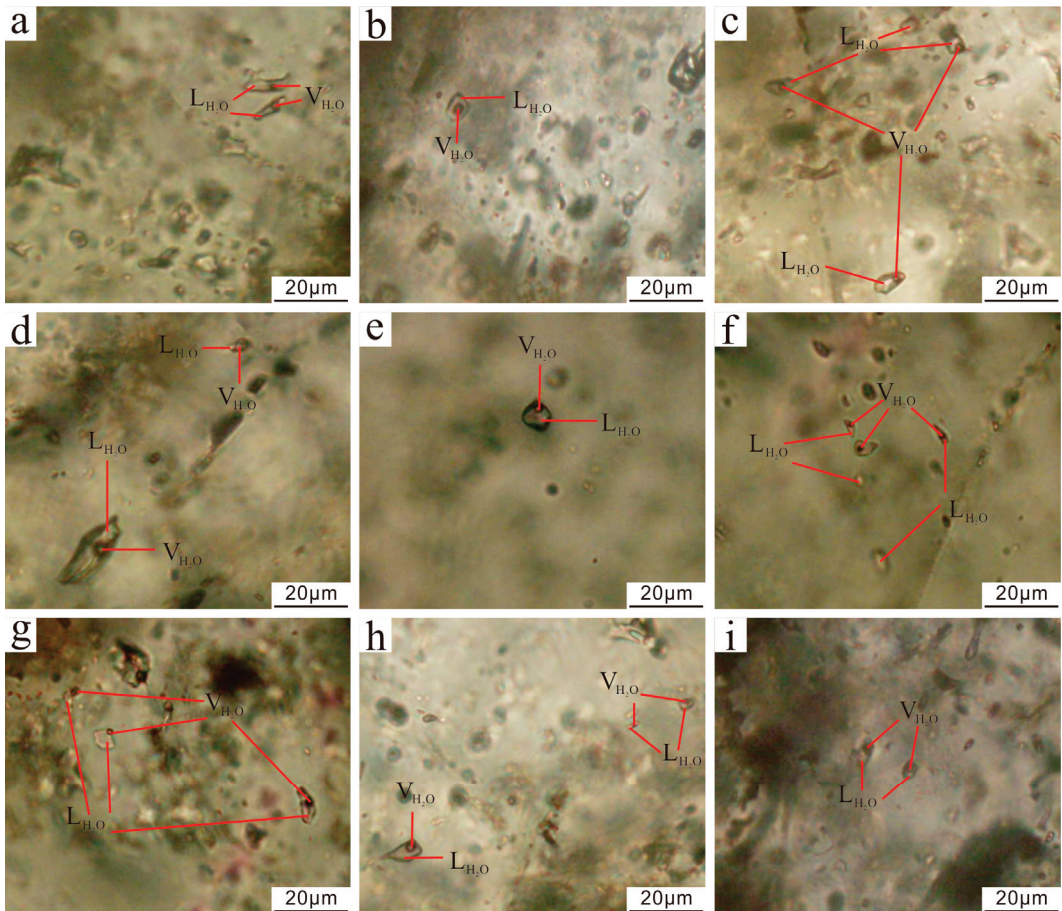


Figure 9. Photomicrographs of fluid inclusions in the Pb–Zn deposits in Tuotuohe region. (a) Type I inclusions in the DCM Pb–Zn deposit; (b) Type I inclusions in the CDQ Pb–Zn deposit; (c) Type I and II inclusions in the CDQ Pb–Zn deposit; (d) Type I inclusions in the KJ Pb–Zn deposit; (e) Type I inclusions in the KJ Pb–Zn deposit; (f) Type I and II inclusions in the KJ Pb–Zn deposit; (g) Type I inclusions in the QMC Pb–Zn deposit; (h) Type I inclusions in the NBZL Pb–Zn deposit; (i) Type I inclusions in the NBZL Pb–Zn deposit.

Representative FIs from the Pb–Zn deposits in the Tuotuohe region were studied using laser Raman spectroscopy to determine their gas compositions. The results suggest that the vapor phases of the Type I FIs are dominated by H_2O and trace amounts of CO_2 are also found in the vapor phases of Type I FIs in the CDQ deposit (Figure 11). In summary, the FIs can be described as the $H_2O - NaCl \pm CO_2$ system.

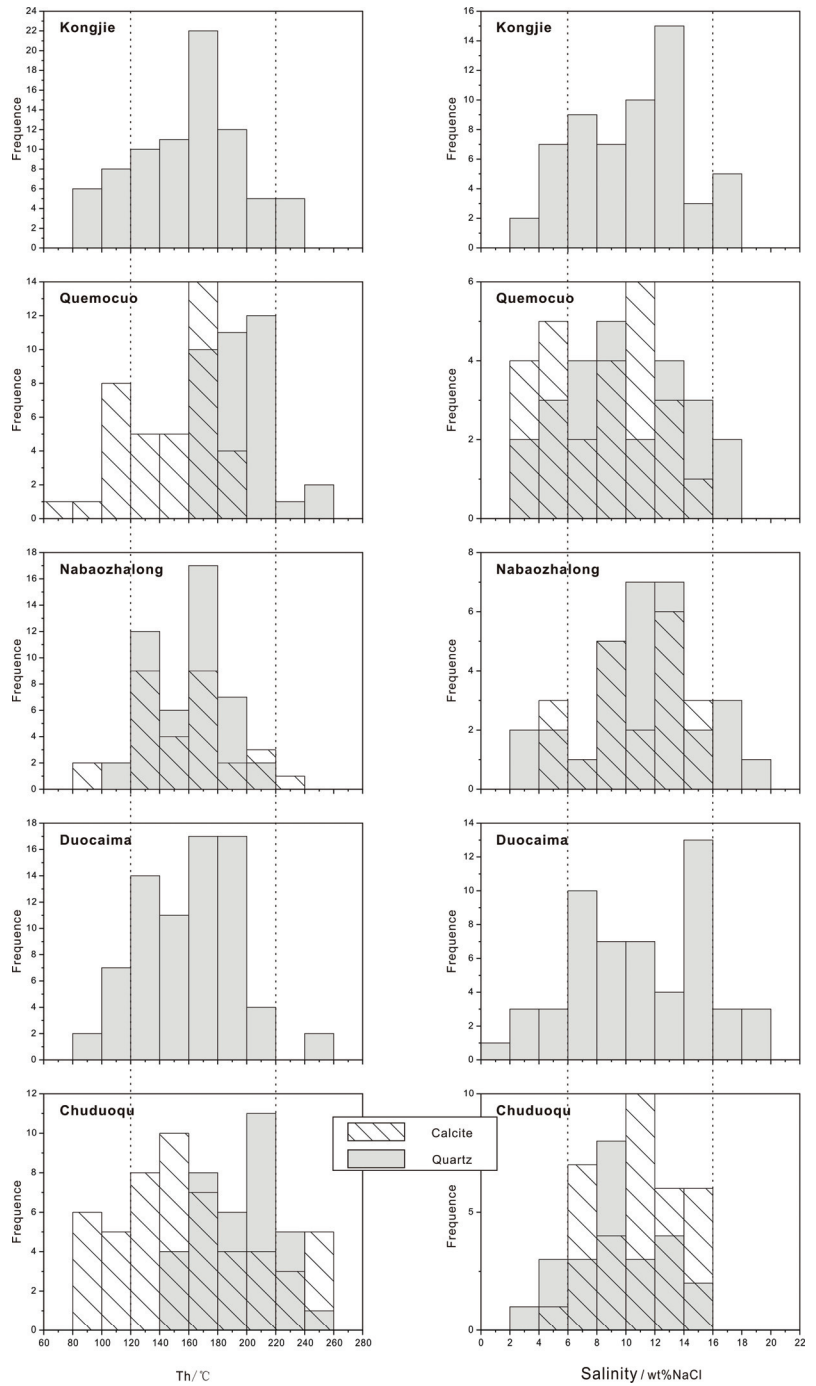


Figure 10. Histograms of salinities and homogenization temperatures of fluid inclusions (the point lines represent the scope of data concentration; the gray slanted part represents the common part of fluid inclusions data within quartz and calcite).

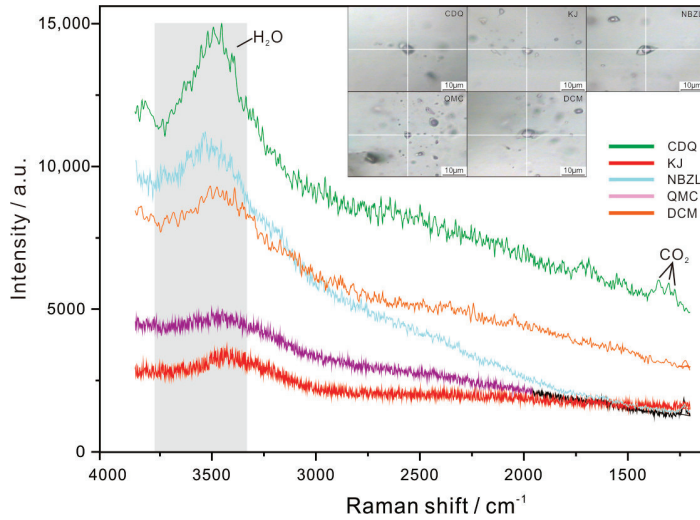


Figure 11. Representative laser Raman spectra for fluid inclusions from the Pb–Zn deposits in Tuotuohe region.

5.2. S Isotope Compositions

The S isotope compositions of galena, together with previously published data [28], are listed in Table 3 and are shown in a histogram in Figure 11. The samples have $\delta^{34}\text{S}_{\text{V-CDT}}$ values of -34.53‰ to $+10.1\text{‰}$ (Table 3; Figure 12), while the DCM and KJ deposits have slightly different $\delta^{34}\text{S}$ values to the other deposits, ranging from -34.53‰ to -7.05‰ , generally between -30‰ and -25‰ . In contrast, the S isotope compositions of the CDQ, QMC, and NBZL deposits are close to zero, ranging from -3.8‰ to $+10.1\text{‰}$ but generally between -5‰ and $+5\text{‰}$ (Table 3; Figure 12). The $\delta^{34}\text{S}_{\text{V-CDT}}$ of the Pb–Zn deposits in the study area have a bimodal distribution (Figure 12), suggesting that the ore-forming metals have a complex source [33].

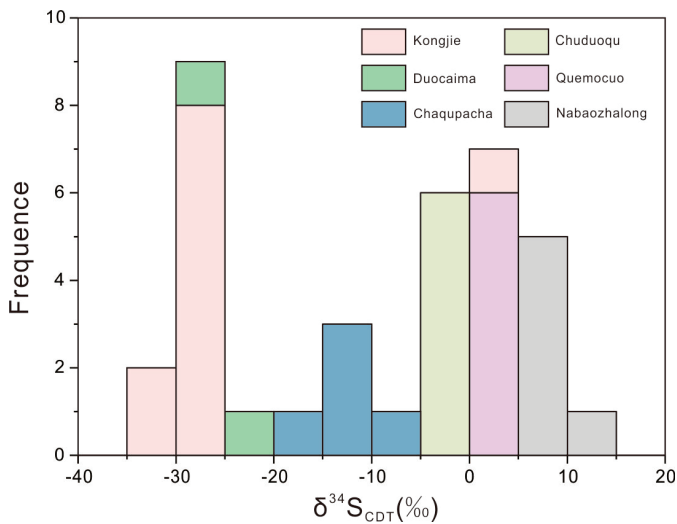


Figure 12. S isotope compositions histogram of the Pb–Zn deposits in Tuotuohe region.

5.3. Pb Isotope Compositions

The data listed in Table 3 indicate that the galena samples obtained from the five deposits within the study area have homogeneous Pb isotopic compositions, with $^{208}\text{Pb}/^{204}\text{Pb}$ values of 38.568–38.976 (mean of 38.779), $^{207}\text{Pb}/^{204}\text{Pb}$ values of 15.623–15.769 (mean of 15.662), and $^{206}\text{Pb}/^{204}\text{Pb}$ values of 18.410–18.810 (mean of 18.624).

5.4. C and O Isotope Compositions

Both new and previously published C and O isotope compositions of individual carbonate minerals from the five deposits analyzed in this study are given in Table 4. Hydrothermal calcite separates have comparatively diverse C and O isotope compositions, with $\delta^{13}\text{C}_{\text{PDB}}$ values of -7.5‰ to -7.9‰ and $\delta^{18}\text{O}_{\text{SMOW}}$ values of $+10.6\text{‰}$ to $+23.4\text{‰}$. The C isotope compositions of samples from these deposits can be broadly separated into two categories: negative values (-7.5‰ to -5.6‰) that are within the range of mantle compositions (-9‰ to -4‰), all of which were from the CDQ deposits, and positive (0.7‰ – 7.9‰) values. The O isotope compositions of samples from these deposits also have an analogous dichotomy, where compositions both correspond and do not correspond with the mantle range of $\delta^{18}\text{O}_{\text{SMOW}}$ compositions (6‰ – 15‰), with samples from the CDQ and KJ deposits having mantle $\delta^{18}\text{O}_{\text{SMOW}}$ values (10.6‰ to 12.1‰ and 11.5‰ to 17‰), whereas samples from the QMC and DCM deposits have higher $\delta^{18}\text{O}_{\text{SMOW}}$ values (15.9‰ to 21.7‰ and 16.4‰ to 23.4‰) that lie outside this range.

Table 4. $\delta^{13}\text{C}$ and $\delta^{18}\text{O}$ values of the Pb–Zn deposits in Tuotuohe region.

Sample	$\delta^{13}\text{C}_{\text{PDB}}/\text{‰}$	$\delta^{18}\text{O}_{\text{PDB}}/\text{‰}$	$\delta^{18}\text{O}_{\text{SMOW}}/\text{‰}$	Data Source
KJ				
KJ-TC27-C1	6.8	−13.5	17	
KJ-TC3-B8	7.9	−16.2	14.2	
KJ-TC3-C6	7.5	−18.3	12	
KJ-TC3-C61	7.1	−18.3	12.1	
KJ-TC3-C7	7.3	−17.5	12.9	
KJ-TC3-C71	7	−18.8	11.5	
CDQ				
CDQ-ZK006-C20	−5.6	−19.2	11.1	
CDQ-ZK006-W13	−6.3	−18.5	11.8	
CDQ-ZK006-W14	−6.2	−18.3	12.1	This paper
CDQ-ZK006-W25	−6.3	−18.7	11.6	
CDQ-ZK006-W26	−7.5	−19.7	10.6	
QMC				
QMC-3#-TC5-W4	4.1	−11.9	18.6	
QMC-TC1-B11-1	0.9	−14.5	15.9	
QMC-TC1-B13	3.8	−9.4	21.3	
QMC-TC1-B15	0.7	−13.8	16.7	
QMC-TC1-C4	2.1	−12.7	17.8	
QMC-TC1-W6	4.8	−8.9	21.7	
DCM				
CWTC5-1	5.8	−13.5	16.9	
CWTC5-2	6.6	−13.4	17.0	
DTC6-1	3.9	−7.2	23.4	
DTC9-1-1	2.6	−12	18.5	
DTC9-1-2	1.7	−9.5	21.1	[28]
CWZK01-1	6.3	−12.6	17.9	
CWZK01-4	4.4	−13.4	17.0	
CWZK01-10	2.4	−14.0	16.4	
CWZK01-16	4.4	−12.8	17.7	
CWZK01-17	2.0	−11.7	18.8	

Table 4. Cont.

Sample	$\delta^{13}\text{C}_{\text{PDB}}/\text{‰}$	$\delta^{18}\text{O}_{\text{PDB}}/\text{‰}$	$\delta^{18}\text{O}_{\text{SMOW}}/\text{‰}$	Data Source
CWZK01-20	2.0	−11.3	19.2	
CQ-001	6.7	−7.6	23.0	
070912-16	6.5	−12.8	17.7	
070912-17	6.2	−13.7	16.7	
070912-18-2	6.0	−13.7	16.7	
070914-21	1.9	−10.9	19.6	
070914-28	1.4	−13.0	17.5	

5.5. H and O Isotope Compositions

Oxygen and hydrogen isotope values were analyzed directly from fluid inclusions within ore-bearing vein quartz from the CDQ deposit, and the results are given in Table 5. Quartz $\delta^{18}\text{O}_{\text{SMOW}}$ values vary from 15.3‰ to 22.2‰ with a mean of 19.0‰, whereas $\delta\text{D}_{\text{SMOW}}$ values obtained from fluid inclusions within these quartz samples range from −96.4‰ to −122.1‰ with a mean of −111.2‰. Calculated $\delta^{18}\text{O}_{\text{H}_2\text{O}}$ values obtained from quartz $\delta^{18}\text{O}_{\text{SMOW}}$ values range from 2.1‰ to 9.5‰ at the mean homogenization temperature of the associated fluid inclusions.

Table 5. δD and $\delta^{18}\text{O}$ values of the CDQ Pb–Zn deposit in Tuotuohe region.

Sample	Type of Qtz Veinlet	$\delta\text{D}_{\text{SMOW}}/\text{‰}$	$\delta^{18}\text{O}_{\text{SMOW}}/\text{‰}$	$\delta^{18}\text{O}_{\text{H}_2\text{O}}/\text{‰}$	Th/°C
CDQ-B3	Qtz–sulfide	−96.4	16.5	6.1	202.4
CDQ-B11	Qtz–sulfide	−122.1	15.3	2.1	202.6
CDQ-B12	Qtz–sulfide	−116.5	19.2	6.6	197.2
CDQ-B13	Qtz–sulfide	−107.3	21.6	9.5	197.2
CDQ-W4	Qtz–sulfide	−113.8	22.2	9.1	201.9

6. Discussion

6.1. Temperature, Density, and Salinity of Ore-Forming Fluids

Type I fluid inclusions homogenize at medium-low temperatures (80 °C to 260 °C, with the majority between 120 °C and 220 °C, covering four stages of mineralization), have medium-low salinity (1.90 to 19.79 wt.% NaCl equivalent, with the majority between 6 and 16 eq. wt.% NaCl equivalent), and have low densities (0.833–1.051 g/cm³), indicative of the conditions of Pb–Zn precipitation within the Pb–Zn deposits of the Tuotuohe region. Homogenization temperatures and salinities positively correlate in a salinity vs. Th diagram (Figure 13), indicating that the abundance of atmospheric water within these systems increases from the early to later phases of mineralization.

Ref. [34] measured the temperature range of CDQ from 144 to 370 °C, of which stages 2 to 4 were more consistent with the results of this study, indicating that the temperature reduction was the result of a slight cooling process and fluid mixture. It is believed that fluid boiling occurs during the third stage of mineralization. According to the temperature measurement results of the fluid package, it can be launched at a pressure of <10 Mpa and a depth of about less than 1 km [32]. This result is also consistent with the P–T conditions of the CDQ deposit that [34] just obtained. From the early stage of mineralization to the late stage, the temperature and salinity continue to decrease, indicating the addition of meteoric water, which coincides with other medium-low temperature hydrothermal vein Pb–Zn deposits [32,34–40]. However, the late-stage fluid evolution in the Aveiro district was found to have high salinity, different from the Braganca district [35], in line with the high salinity characteristics of the fluid measured at the late stage of mineralization reported by [41].

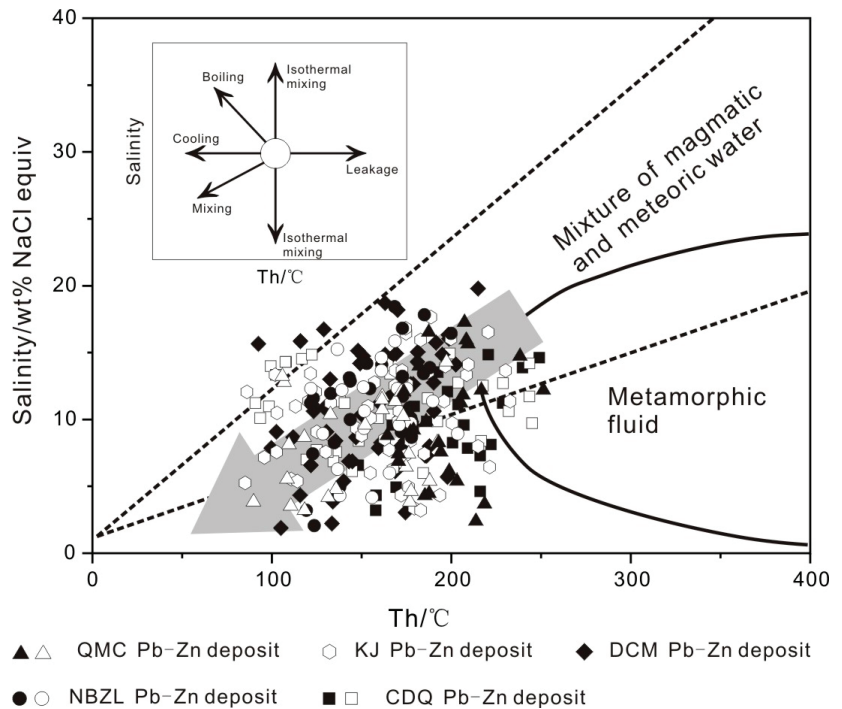


Figure 13. Plot of homogenization temperatures against salinity values of fluid inclusions from the Pb–Zn deposits in Tuotuohe region (dark represents quartz and colorless represents calcite). Inset illustration for different fluid evolution paths is based on [42].

All of the typical deposit fluids listed above show that the mineralization stage evolves from early to late, from high to low temperature, with increasing meteoric water and decreasing salinity. The low-salinity and low-density characteristics are distinctly different from the typical MVT formed in a stable basin where the mineralizing fluid is a high-salinity, high-density thermal brine [43–46].

6.2. Sources of Ore-Forming Metals

Galena samples obtained from Pb–Zn deposits within the Tuotuohe region have a relatively narrow range of $^{208}\text{Pb}/^{204}\text{Pb}$, $^{207}\text{Pb}/^{204}\text{Pb}$, and $^{206}\text{Pb}/^{204}\text{Pb}$ ratios (38.568–38.976, 15.623–15.769, and 18.410–18.810, respectively; Table 3), which is consistent with the medium-low temperature hydrothermal vein Pb–Zn deposits [39,47,48], suggesting that the Pb within these deposits was derived from a single source or from a homogenized mixture of different sources.

The $^{207}\text{Pb}/^{204}\text{Pb}$ vs. $^{206}\text{Pb}/^{204}\text{Pb}$ diagram shown in Figure 14a indicates that the majority of samples lie within the upper crust and orogenic belt fields of [49], whereas the same samples plot within the lower crust and orogenic fields in a $^{208}\text{Pb}/^{204}\text{Pb}$ vs. $^{206}\text{Pb}/^{204}\text{Pb}$ diagram (Figure 14b). These Pb isotope values are indicative of sourcing from the lower and upper crusts and orogenic zones, suggesting that the Pb within the Pb–Zn deposits in the study area was derived from both the mantle and crust [50,51], with the upper crust being the main source of lead for these deposits. These lead isotope discrimination diagrams indicate that the Pb–Zn deposits of the Tuotuohe region formed in an orogenic environment, with the majority of metal originating from the crust.

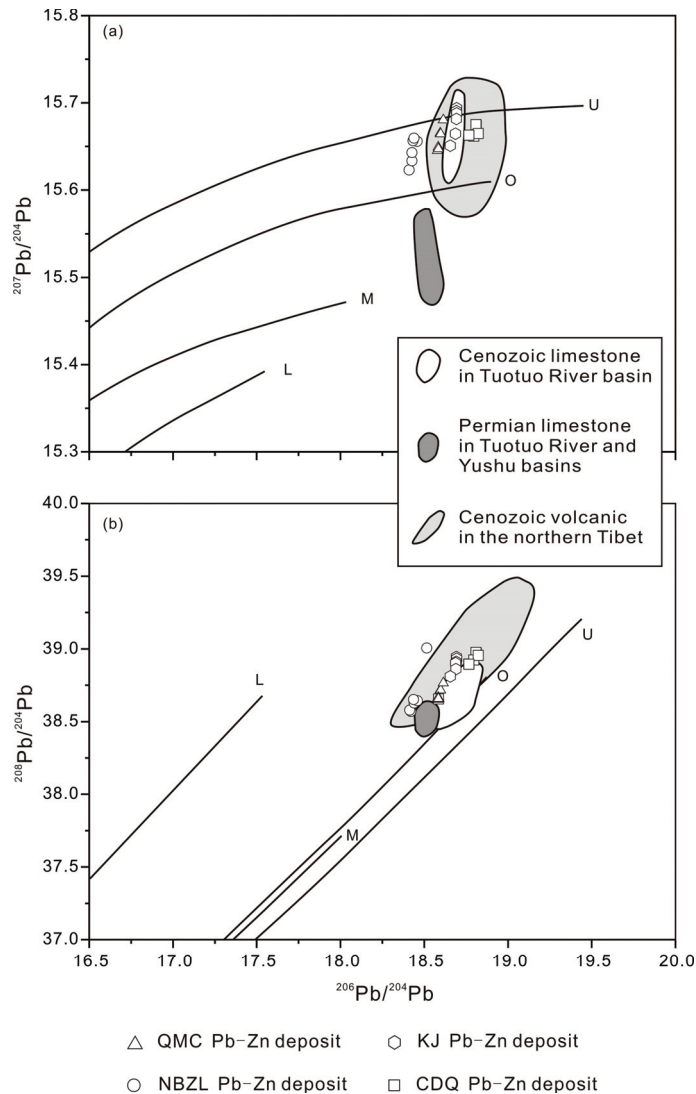


Figure 14. Lead isotope compositions of samples from the Pb–Zn deposits in Tuotuohe region plotted in the model lead evolution diagrams of [49]. (a) $^{207}\text{Pb}/^{204}\text{Pb}$ vs. $^{206}\text{Pb}/^{204}\text{Pb}$; (b) $^{208}\text{Pb}/^{204}\text{Pb}$ vs. $^{206}\text{Pb}/^{204}\text{Pb}$ plot. M: upper mantle-source lead; O: orogenic belt-source lead; U: upper crust-source lead; L: lower crust-source lead.

The Pb isotope compositions of Permian limestones of the Tuotuohe and Yushu basins, Mesozoic and Cenozoic limestones of the Tuotuohe Basin [11], and alkaline Cenozoic volcanics of the northern Tibetan Plateau [52] were also plotted in $^{207}\text{Pb}/^{204}\text{Pb}$ vs. $^{206}\text{Pb}/^{204}\text{Pb}$ and $^{208}\text{Pb}/^{204}\text{Pb}$ vs. $^{206}\text{Pb}/^{204}\text{Pb}$ diagrams, with the Pb isotopes of ore samples being similar to the latter two but significantly different from the former. This suggests that although Permian limestones in the study area host mineralization within the DCM and KJ deposits, these units did not supply any Pb to these deposits. In addition, the Pb isotope compositions of ores in both the $^{207}\text{Pb}/^{204}\text{Pb}$ vs. $^{206}\text{Pb}/^{204}\text{Pb}$ and $^{208}\text{Pb}/^{204}\text{Pb}$ vs. $^{206}\text{Pb}/^{204}\text{Pb}$ diagrams are very similar to those of the Cenozoic volcanics, suggesting that these volcanics may be the source of Pb within the Pb–Zn deposits of the Tuotuohe region.

Ref. [53] proposed a $\Delta\gamma$ - $\Delta\beta$ diagram based on the equations $\Delta\gamma = (\gamma - \gamma_M) \times 1000/\gamma_M$ and $\Delta\beta = (\beta - \beta_M) \times 1000/\beta_M$, where γ = the $^{208}\text{Pb}/^{204}\text{Pb}$ value of a sample, γ_M = the $^{208}\text{Pb}/^{204}\text{Pb}$ value of the mantle (37.47), β = the $^{207}\text{Pb}/^{204}\text{Pb}$ value of a sample, and β_M = the $^{207}\text{Pb}/^{204}\text{Pb}$ value of the mantle (15.33). This approach can help in identifying sources of Pb by determining $\Delta\gamma$ and $\Delta\beta$ values (Figure 15). The vast majority of the samples analyzed during this study plot in the mixed crust and magmatism-related mantle fields in Figure 15 and have similar $\Delta\gamma$ and $\Delta\beta$ values to the Cenozoic volcanics [52] but are different from both Permian and Mesozoic limestones [11] in the study area. This suggests that the metals within the Pb–Zn deposits of the Tuotuohe region were derived from Cenozoic volcanics, indicating, in turn, that this mineralization represents the result of some degree of crust–mantle interaction, as is consistent with the $^{207}\text{Pb}/^{204}\text{Pb}$ vs. $^{206}\text{Pb}/^{204}\text{Pb}$ and $^{208}\text{Pb}/^{204}\text{Pb}$ vs. $^{206}\text{Pb}/^{204}\text{Pb}$ diagrams discussed above. [34] suggests that the primary source of minerals within the CDQ deposit is the regional hydrocarbonate pulp hot fluid system, as well as the Jurassic carbonate that provides a partial contribution.

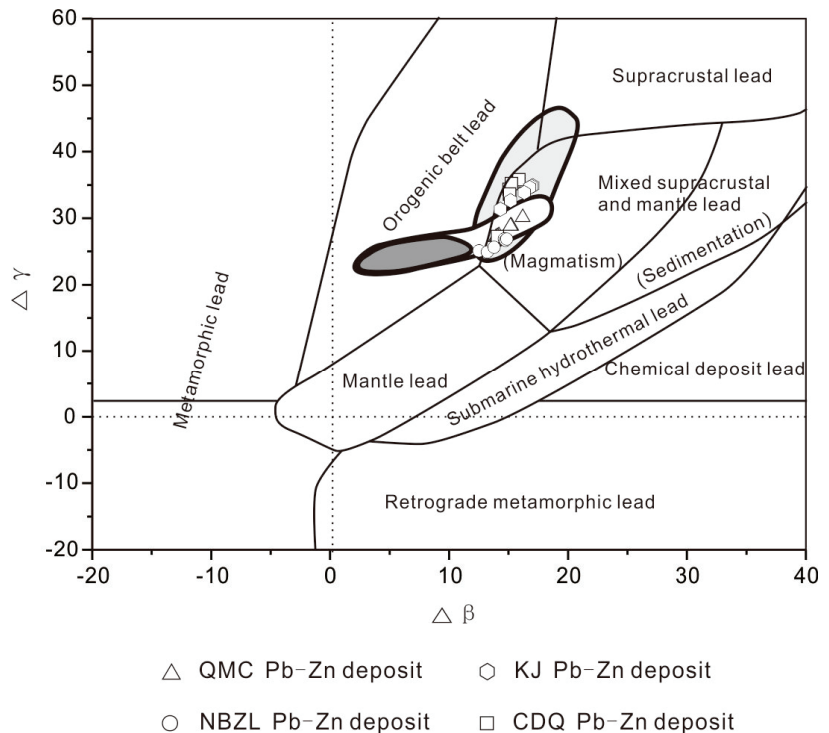


Figure 15. $\Delta\gamma$ - $\Delta\beta$ diagram of ore lead from the Pb–Zn deposits in Tuotuohe region (after [53]).

The results of Pb isotope analysis from different deposits in the study area show that the mineralized material Pb mainly originates from the Cenozoic igneous rocks rather than the ore-bearing strata. The fact that different deposits in the region are distributed in different age strata also proves that there is no special selection of stratigraphy for these deposits, and their mineralization has the same kinetic background and the same metallogenic process. Therefore, the study of this work supports the idea that the mineralized material originates from igneous rocks, and their mineralization is closely related to magma, and these deposits are not MVT-type Pb–Zn deposits that are unrelated to magmatic activity.

Sulfur isotopes are the main mineralizing agents for sulfophile elements precipitated as sulfides, and they also play an important role in the precipitation and enrichment of the metallogenic material [54]. However, there are differences in the $\delta^{34}\text{S}_{\text{V-CDT}}$ values of

the different deposits. The $\delta^{34}\text{S}_{\text{V-CDT}}$ values of samples from the CDQ, QMC, and NBZL deposits are -3.8‰ to -1.3‰ , $+2.2\text{‰}$ to $+3.4\text{‰}$, and $+5.2\text{‰}$ to $+10.1\text{‰}$, respectively, all of which are close to the accepted mantle range [55] and indicate a magmatic control over the mineralizing event in the study area. Ref. [37] obtained Qibaoshan polymetallic ore field S for 0.5–4.3, and ref. [51] obtained 1.4–2.7 in the Aobaotu Pb–Zn deposit, which is relatively consistent with the QMC results in this paper; both of which are considered to be primarily derived from rocks. The $\delta^{34}\text{S}_{\text{V-CDT}}$ values of samples from the CDQ deposit are consistent with the $\delta^{34}\text{S}_{\text{V-CDT}}$ measured in galena and sphalerite by [34] and with the results obtained in Dashishan Sn–Pb–Zn deposits [38]. However, ref. [34] just measured the $\delta^{34}\text{S}_{\text{V-CDT}}$ of the chalcopyrite to be a little higher than the galena and sphalerite, suggesting that the main mineralization stage of CDQ is formed in a stable and uniform hot-liquid environment. Ref. [38] conclude that the mineral logistics body originates from the subdued granite body by contrasting the relationship with the surrounding rocks. Ref. [56] concludes that the results obtained in the Xinling Pb–Zn deposit were consistent with the NBZL deposit and suggest the Pb–Zn mineralization is a magmatic source. This result, combined with the fact that the metals within the deposits were derived from Cenozoic volcanics, suggests that the sulfur within the CDQ, QMC, and NBZL deposits was also derived from a magmatic source.

Samples from the KJ and DCM deposits have mean $\delta^{34}\text{S}_{\text{V-CDT}}$ values of -26.3‰ and -15.5‰ , respectively. These negative $\delta^{34}\text{S}_{\text{V-CDT}}$ values are indicative of sulfide accumulation in an open system with an infinite sulfate reservoir, such as seawater sulfate [35] within sedimentary pore spaces in an anoxic environment [57]. The values are also typical of sedimentary sulfides formed in marine sediments by the bacterial reduction of seawater sulfate via the formation of pyrite, causing the accumulation of diagenetic sulfides with mean $\delta^{34}\text{S}$ values of between -15‰ and -40‰ . Ref. [58] obtained identical $\delta^{34}\text{S}_{\text{V-CDT}}$ values for the DCM deposit but suggest that the DCM deposit belongs to the MVT-type Pb–Zn deposit.

In summary, it is recognized that although the Pb sources of the medium- and low-temperature hydrothermal vein-type Pb–Zn ores in the Tuotuo River area are relatively consistent, with some deposits characterized by the involvement of deep-source magmatic sulfur in mineralization, the sulfur sources of individual Pb–Zn ores, represented by Kongjie, are more complex and may consist of both deep-source magmatic sulfur and sedimentary basin sulfur sources. However, the large positive $\delta^{34}\text{S}_{\text{V-CDT}}$ interval (8.03‰ – 31.36‰ ; [59]) between the $\delta^{34}\text{S}_{\text{V-CDT}}$ of all these deposits and the typical MVT deposits of sulfides represents a large difference in seawater sulfide, implying a non-MVT genetic type.

6.3. Sources of Ore-Forming Fluid

The O and H isotopic compositions of selected minerals at different mineralization stages are widely used in the study of the source and evolution processes of hydrothermal fluids [37,60]. Most samples from the CDQ Pb–Zn deposit plot between magmatic and meteoric water lines in a $\delta\text{D}_{\text{SMOW}}$ vs. $\delta^{18}\text{O}_{\text{H}_2\text{O}}$ diagram (Figure 16), indicating that these samples formed from hydrothermal fluids derived from the mixing of magmatic and meteoric fluids. This drop in the $\delta^{18}\text{O}_{\text{H}_2\text{O}}$ values can be explained by the addition of meteoric waters to the hydrothermal system, resulting in a migration of the $\delta^{18}\text{O}_{\text{H}_2\text{O}}$ [40]. This is consistent with the findings of the study [33,34,36]. Ref. [34] believe that as the mineralization progresses, from the first stage to the third stage, the samples gradually move away from the magmatic water area, indicating that the meteoric water continues to increase, which is also consistent with the results of the study of the fluid temperature and salinity, which also suggests the mixing of different fluids.

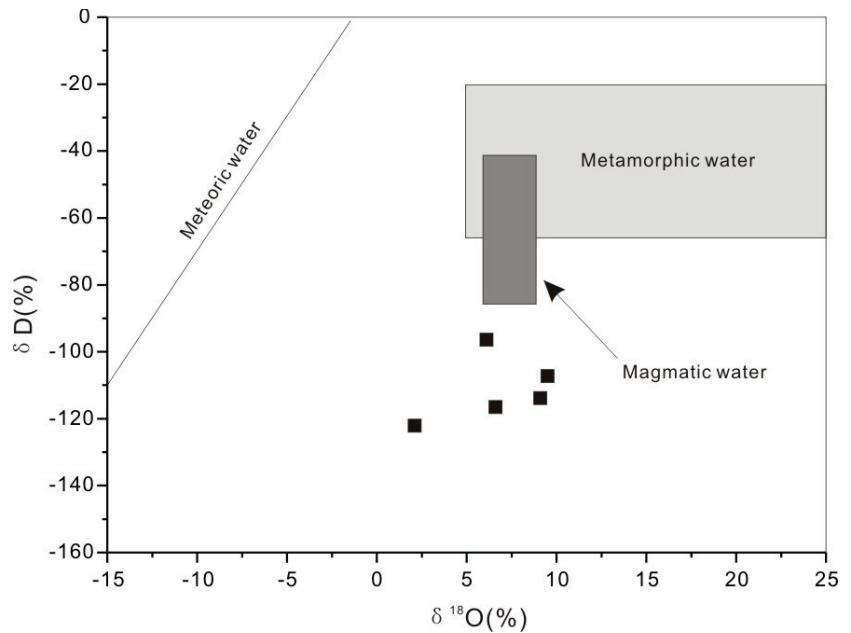


Figure 16. δD - $\delta^{18}\text{O}$ diagram for ore–fluid of the CDQ Pb–Zn deposit in Tuotuohe region. The base diagram is cited from [60].

The differences in the $\delta^{13}\text{C}_{\text{PDB}}$ values of various carbon pools mean that C isotope analysis is an important method for tracing the origin of ore-forming fluids [34]. Five calcite samples from the CDQ deposits have $\delta^{13}\text{C}_{\text{PDB}}$ values of -7.5‰ to -5.6‰ , similar to or slightly higher than the conventional mantle values (-4‰ to -8‰ ; [61]). These samples also have $\delta^{18}\text{O}_{\text{SMOW}}$ values of 10.6‰ to 12.1‰ , which are slightly higher than the mantle (6.0‰ – 10.0‰ ; [61]). All of these samples plot near the mantle field in a $\delta^{13}\text{C}_{\text{PDB}}$ vs. $\delta^{18}\text{O}_{\text{SMOW}}$ diagram (Figure 17). This indicates that the CO_2 within the ore fluids was probably sourced from a magmatic system, perhaps with some input from marine carbonates. This is consistent with the results measured by [34] in the fourth stage of mineralization, as well as the results obtained by [62] that are considered to be from a magmatic source. However, ref. [63] obtained the same results in the Bayji Pb–Zn deposit, which formed in the late phase of orogenic extension and is thought to be primarily derived from the dissolution of pelagic carbonate sequences.

The $\delta^{13}\text{C}_{\text{PDB}}$ and $\delta^{18}\text{O}_{\text{SMOW}}$ compositions of the other 29 calcite samples from the KJ, QMC, and DCM deposits range from 0.7‰ to 7.9‰ , and from 12.9‰ to 23.4‰ , respectively, which is consistent with the C–O results obtained in the Pb–Zn deposit in the Rajasthan region [64]. Ref. [58] conducted a C–O isotopic analysis of calcites and limestones associated with mineralization in the DCM mining area, which is consistent with this paper. These samples plot in-between the mantle and marine carbonate fields in a $\delta^{13}\text{C}_{\text{PDB}}$ vs. $\delta^{18}\text{O}_{\text{SMOW}}$ diagram (Figure 17), but closer to marine carbonate compositions ($\delta^{13}\text{C}_{\text{PDB}} = 0\text{‰} \pm 4\text{‰}$, $\delta^{18}\text{O}_{\text{SMOW}} = 20\text{‰}$ – 24‰ ; [54,65]) and away from the organic carbon compositions ($\delta^{13}\text{C}_{\text{PDB}} = -30\text{‰}$ to -15‰ ; [54]). This suggests that the marine carbonates within the deposits were the main source of carbon, and the carbon from these carbonates was partially re-equilibrated with magmatic fluids during mineralization.

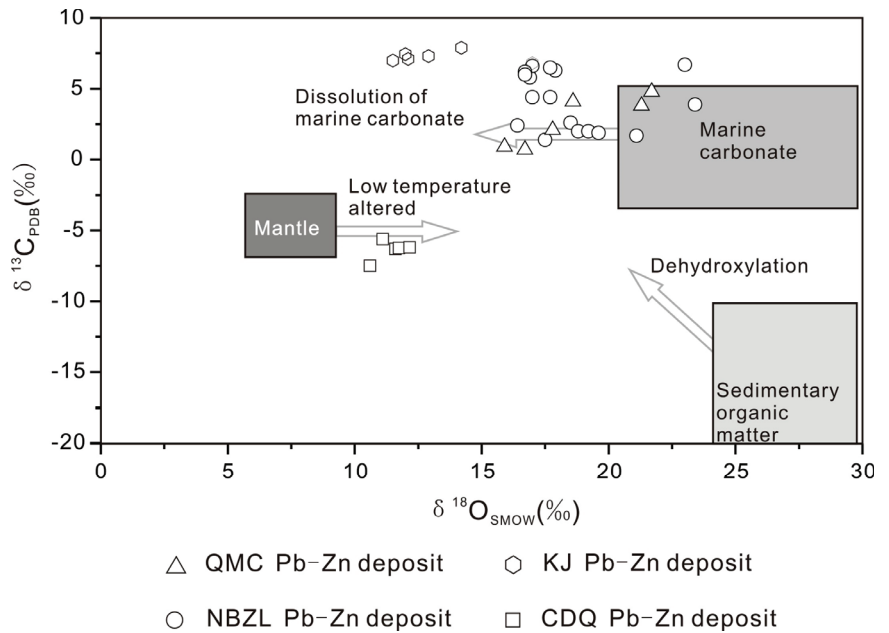


Figure 17. Plots of $\delta^{13}\text{C}_{\text{PDB}}$ vs. $\delta^{18}\text{O}_{\text{SMOW}}$ for the Pb–Zn deposits in Tuotuohe region. C and O isotopic compositions of the DCM Pb–Zn deposit are taken from [28].

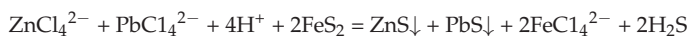
The C–H–O isotope compositions described above suggest that the preponderance of ore-forming fluids was magmatic, as evidenced by fluid inclusion characteristics and sulfur and lead isotope compositions. However, these magmatic fluids evolved by mixing with meteoric water and wallrock interaction prior to mineralization in the study location.

6.4. Pb and Zn Transportation and Deposition Mechanisms

Previous research has indicated that Pb and Zn are transported as aqueous Cl^- and HS^- complexes rather than as bisulfide complexes within hydrothermal solutions, especially under conditions of medium to low temperatures and high salinity [47]. The fluid characteristics and Pb isotope compositions of Pb–Zn deposits in the study area are identical, although the deposits have varying $\delta^{34}\text{S}$ compositions, suggesting that the metals within the ore-forming fluids were not transported as sulfur complexes but were transported mainly by chloride complexes of Pb^{2+} and Zn^{2+} in the ore-forming fluids.

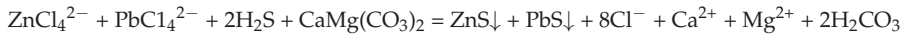
The migration of magmatic fluids to shallower parts of the crust led to the precipitation of Pb and Zn, primarily as the result of three possible processes: cooling [66], fluid mixing/dilution [67], and fluid–rock interaction [68], as follows:

- (1) Cooling: Metal complex solubility is a function of temperature, and cooling reduces both solubility and stability, leading to the precipitation of sphalerite and galena. The study of the CDQ deposit by [34] shows that the temperature continues to decline as mineralization progresses, suggesting that cooling plays an important role;
- (2) Fluid mixing/dilution: Fluid mixing/dilution can lower the salinity of a fluid, reducing the concentrations of H^+ and Cl^- and decreasing the stability of metal complexes, leading to decomposition and precipitation, as follows:



It is also consistent with the results of the C–O and H–O isotopes.

- (3) Fluid–rock reactions: Sphalerite and galena can precipitate as a result of fluid–rock reactions that cause carbonate dissolution and the consequent Ca (+Mg) enrichment of hydrothermal fluids, as follows:



6.5. Mineral Deposit Type

Although the Pb–Zn deposits within the Tuotuohe region are hosted by carbonates, the primary controls on mineralization are extensional fault structures that cross-cut the carbonates rather than the carbonates themselves. Fluid inclusions and C–H–O isotope compositions indicate that the ore-forming fluids were medium-low temperature, medium-low salinity, and low-density fluids that formed by mixing between magmatic and meteoric waters and that were affected by fluid–rock interaction. In addition, S–Pb isotope data suggest that Pb was sourced from Cenozoic volcanics in the study area. These characters are consistent with the Cordilleran-type vein deposits [69–71], which differ from the MVT-type deposits. However, Au was not found in the Pb–Zn deposits in the region, which have some differences from Cordilleran-type vein deposits. Combined, all of these data indicate that the Pb–Zn deposits of the Tuotuohe region are magmatism-related medium-low temperature hydrothermal vein deposits. Ref. [34] suggest that the trapping pressures during ore-forming stage 3 are estimated to range from ~3 to 8 MPa and are mostly concentrated at 5 MPa, which would correspond to depths of 0.3–0.8 km, assuming hydrostatic conditions [72]. Hence, the initial Pb–Zn mineralization in the Chuduoqu Pb–Zn–Cu deposit mainly occurred at depths of less than 0.8 km, which is a shallow mineralization depth. This type of Pb–Zn mineralization depth generally does not exceed 2 km [32,37,39,41,73]. Since the homogenization temperature and isotope characteristics of the five deposits in the region are similar, this paper concludes that the mineralization of the Pb–Zn deposits in the area formed in the shallow area, and the latter degree of erosion varies as a result of the actual deposit of the mineral.

The geological setting and chronology of the formation of Pb–Zn deposits in adjacent regions suggest that the deposits in the study area formed as follows: The Asian–Indian continental collision began in the Paleocene, causing a thickening of the lower crust and associated delamination, fusion, and exhumation. Contemporaneous upwelling of hot asthenospheric material caused partial melting of the eclogitic lower crust, which combined with exhumation-generated adakitic magmas between 40 and 32 Ma [22]. These magmas ascended along structures and steadily exsolved mineralizing fluids. A reduction in temperature and pressure, fluid mixing, and fluid–rock interaction caused the formation of mineralization within the host structures and altered the S–C–O isotope composition of the mineralizing fluid.

7. Conclusions

- (1) The primary structural constraints on the location of Pb–Zn deposits within the Tuotuohe region are faults, although the deposits are primarily carbonate-hosted;
- (2) Fluid inclusion data for these deposits indicate that they formed from medium-low temperature, medium-low salinity, and low-density fluids;
- (3) Pb isotope compositions imply that the Pb within these deposits was derived from Cenozoic volcanics, and C–H–O–S isotope data indicate that the ore-forming fluid was a mixing of magmatic and meteoric water that was affected by wallrock interaction. Pb and Zn were transported in solution as chloride complexes and precipitated as a consequence of cooling, fluid mixing/dilution, and fluid–rock reactions;
- (4) The Pb–Zn deposits within the Tuotuohe region are magmatism-related medium-low temperature hydrothermal vein deposits.

Author Contributions: Conceptualization, Y.Q.; Writing—original draft, Y.Q.; Writing—review & editing, L.Z. and J.S. All authors have read and agreed to the published version of the manuscript.

Funding: This work was funded by the Natural Science Foundation of Jilin Province (20220101161JC), Shandong Provincial Engineering Laboratory of Application and Development of Big Data for Deep Gold Exploration (SDK202203), National Natural Science Foundation of China (41402060), Science and Technology Project of Department of Education, Jilin Province (JJKH20200946KJ), and Self-determined Foundation of Key Laboratory of Mineral Resources Evaluation in Northeast Asia, Ministry of Natural Resources (DBY-ZZ-19-13 and DBY-ZZ-19-15).

Data Availability Statement: Not applicable.

Acknowledgments: We thank Assistant Editor, and two anonymous referees for comments which helped in improving our manuscript and also thank Minxia Ma for funding support and help with analysis and testing.

Conflicts of Interest: The authors declare no conflict of interest.

References

- Hou, Z.Q.; Song, Y.C.; Li, Z.; Wang, Z.L.; Yang, Z.M.; Yang, Z.S.; Liu, Y.C.; Tian, S.H.; He, L.Q.; Chen, K.X.; et al. Thrust-controlled, sediments-hosted Pb-Zn-Ag-Cu deposits in eastern and northern margins of Tibetan orogenic belt: Geological features and tectonic model. *Miner. Depos.* **2008**, *27*, 123–144. (In Chinese with English Abstract)
- Dai, Z.X.; Bai, Y.; Wu, C.G.; Gu, F.; Zhu, M.Y.; Shang, X.Z. *The Gold and Copper Mineralization in Western China and Its Adjacent Regions*; Seismological Press: Beijing, China, 2001; p. 215.
- Deng, J.; Yang, L.Q.; Wang, C.M. Research advances of superimposed orogenesis and metallogenesis in the Sanjiang Tethys. *Acta Petrol. Sin.* **2011**, *27*, 2501–2509. (In Chinese with English Abstract)
- Hu, R.Z.; Turner, G.; Burnard, P.G.; Zhong, H.; Ye, Z.J.; Bi, X.W. Helium and argon isotopic geochemistry of Jinding superlarge Pb-Zn deposit. *Sci. China Ser. D Earth Sci.* **1998**, *41*, 442–448. [CrossRef]
- Huang, Z.L.; Li, W.B.; Chen, J.; Han, R.S.; Liu, C.Q.; Xu, C.; Guan, T. Carbon and oxygen isotope constraints on mantle fluid involvement in the mineralization of the Huize super-large Pb-Zn deposits, Yunnan Province, China. *J. Geochem. Explor.* **2003**, *78*, 637–642. [CrossRef]
- Song, Y.C.; Hou, Z.Q.; Yang, T.N.; Zhang, H.R.; Yang, Z.S.; Tian, S.H.; Liu, Y.C.; Wang, X.H.; Liu, Y.X.; Xue, C.D.; et al. Sediment-hosted Himalayan base metal deposits in Sanjiang region: Characteristics and genetic types. *Acta Petrol. Et Mineral.* **2011**, *30*, 355–380. (In Chinese with English Abstract)
- Wang, G.R.; Song, Y.C.; Zou, G.M.; Hou, Z.Q.; Yang, Z.S.; Yang, T.N.; Zhang, H.R.; Liu, Y.X.; Li, Z.; Wang, Y.K.; et al. History, current status, and next targets of exploration in the Chaqupacha Pb-Zn deposit, southern Qinghai Province. *Acta Petrol. Et Miner.* **2012**, *31*, 79–90.
- Liu, Y.C.; Hou, Z.Q.; Yang, Z.S.; Tian, S.H.; Song, Y.C.; Xue, W.W.; Wang, F.C.; Zhang, Y.B. Fluid inclusion constraints on the origin of Dongmohazhua Pb-Zn ore deposit, Yushu area, Qinghai Province. *Acta Petrol. Sin.* **2010**, *26*, 1805–1819. (In Chinese with English Abstract)
- Liu, Y.C.; Yang, Z.S.; Hou, Z.Q.; Tian, S.H.; Wang, Z.L.; Song, Y.C.; Xue, W.W.; Lu, H.F.; Wang, F.C.; Zhang, Y.B.; et al. Geology and hydrogen, oxygen and carbon isotope geochemistry of Dongmohazhua Pb-Zn ore deposit, Yushu area, Qinghai Province. *Miner. Depos.* **2009**, *28*, 770–784. (In Chinese with English Abstract)
- Tian, S.H.; Yang, Z.S.; Hou, Z.Q.; Gong, Y.L.; Liu, Y.C.; Song, Y.C.; Xue, W.W.; Lu, H.F.; Wang, F.C.; Zhang, Y.B. Rb-Sr and Sm-Nd isochron ages of Dongmohazhua and Mohailaheng Pb-Zn ore deposits in Yushu area, southern Qinghai and their geological implications. *Miner. Depos.* **2009**, *28*, 747–758. (In Chinese with English Abstract) [CrossRef]
- Tian, S.H.; Yang, Z.S.; Hou, Z.Q.; Liu, Y.C.; Song, Y.C.; Wang, F.C.; Lu, H.F. Sulfur, lead, strontium and neodymium isotope compositions of the Dongmohazhua lead-zinc ore deposit in the Yushu area, southern Qinghai: Implications for the sources of ore-forming material in the deposit. *Acta Petrol. Sin.* **2011**, *27*, 2173–2183. (In Chinese with English Abstract)
- Pan, G.T.; Xiao, Q.H.; Lu, S.N.; Deng, J.F.; Feng, Y.M.; Zhang, K.X.; Zhang, Z.Y.; Wang, F.G.; Xing, G.F.; Hao, G.J.; et al. Subdivision of tectonic units in China. *Geol. China* **2009**, *36*, 1–28. (In Chinese with English Abstract)
- Li, Y.L.; Wang, C.S.; Zhao, X.X.; Yin, A.; Ma, C. Cenozoic thrust system, basin evolution, and uplift of the Tanggula Range in the Tuotuohe region, central Tibet. *Gondwana Res.* **2012**, *22*, 482–492. [CrossRef]
- Liu, Y.X.; Hou, Z.Q.; Wang, G.H.; Jiang, X.J.; Li, Z.; Song, Y.C.; Wang, X.H. Basin evolutions of the Tuotuohe River basin and sedimentary response to the uplifting of the Qinghai-Tibet Plateau in the Paleogene-Neogene. *Earth Sci. Front.* **2011**, *18*, 65–76. (In Chinese with English Abstract)
- Mo, X.X.; Pan, G.T. From the Tethys to the formation of the Qinghai-Tibet Plateau: Constrained by tectono-magmatic events. *Earth Sci. Front.* **2006**, *13*, 43–51. (In Chinese with English Abstract)
- Pan, G.T.; Mo, X.X.; Hou, Z.Q.; Zhu, D.C.; Wang, L.Q.; Li, G.M.; Zhao, Z.D.; Geng, Q.R.; Liao, Z.L. Spatial-temporal framework of the Gangdise Orogenic Belt and its evolution. *Acta Petrol. Sin.* **2006**, *22*, 521–533. (In Chinese with English Abstract)
- Tapponnier, P.; Molnar, P. Slip-line field theory and large-scale continental tectonics. *Nature* **1976**, *264*, 319–324. [CrossRef]

18. Molnar, P.; England, P.; Martinod, J. Mantle dynamics, uplift of the Tibetan Plateau, and the Indian monsoon. *Rev. Geophys.* **1993**, *31*, 357–396. [CrossRef]
19. Luo, Z.H.; Mo, X.X.; Hou, Z.Q.; Deng, W.M.; Wang, J.H.; Zhao, Z.D.; Yu, X.H.; Li, J.P. An integrated model for the Cenozoic evolution of the Tibetan plateau: Constraints from igneous rocks. *Earth Sci. Front.* **2006**, *13*, 196–211. (In Chinese with English Abstract)
20. Wu, F.Y.; Huang, B.C.; Ye, K.; Fang, A.M. Collapsed Himalayan-Tibetan orogen and the rising Tibetan Plateau. *Acta Petrol. Sin.* **2008**, *24*, 1–30. (In Chinese with English Abstract)
21. Zhao, R.F.; Zhu, Y.T.; Zhou, Q.H.; Wang, M.C.; Li, J.X.; Sun, N.Y. Discovery of angular unconformity below Triassic strata in the Yushu area, Qinghai. *Geol. Bull. China* **2004**, *23*, 616–619. (In Chinese with English Abstract)
22. Qian, Y.; Tian, S.N.; Li, Y.J.; Sun, F.Y. Zircon U–Pb age and geochemical constraints on the origin and tectonic implication of the Tuotuohe Cenozoic alkaline magmatism in Qinghai–Tibet Plateau. *Acta Geoc.* **2020**, *39*, 67–84. [CrossRef]
23. Qian, Y.; Sun, F.Y.; Li, B.L.; Li, S.J.; Zhao, J.W. Early Permian–Late Triassic magmatism in the Tuotuohe region of the Qinghai–Tibet plateau: Constraints on the tectonic evolution of the western segment of the Jinshajiang Suture. *Acta Geol. Sin. (Engl. Ed.)* **2014**, *88*, 498–516. [CrossRef]
24. Sun, Y.G. Study on Ore-controlling Structure Characteristics and Ore Genesis of Chuduoqu Lead-Zinc Mine in Tuotuohe Region, Qinghai Province. Master’s Thesis, Jilin University, Changchun, China, 2016. (In Chinese)
25. Bodnar, R. Revised equation and table for determining the freezing point depression of H₂O–NaCl solutions. *Geochim. Et Cosmochim. Acta* **1993**, *57*, 683–684. [CrossRef]
26. Liu, B.; Shen, K. *Thermodynamics of Fluid Inclusions*; Geological Publishing House: Beijing, China, 1999; p. 290.
27. Robinson, B.W.; Kusakabe, M. Quantitative preparation of sulfur dioxide, for sulfur-34/sulfur-32 analyses, from sulfides by combustion with cuprous oxide. *Anal. Chem.* **1975**, *47*, 1179–1181. [CrossRef]
28. Li, Z. The Ore Forming Genesis Research of Chaqupacha Lead-Zinc Deposits in Qinghai Province Tuotuohe Area. Master’s Thesis, University of Science and Technology, Beijing, China, 2008; pp. 58–64. (In Chinese with English Abstract)
29. Todt, W.; Cliff, R.; Hanser, A.; Hofmann, A. Re-calibration of NBS lead standards using a ²⁰²Pb + ²⁰⁵Pb double spike. *Terra Abstr.* **1993**, *5*, 396.
30. Clayton, R.N.; Mayeda, T.K. The use of bromine pentafluoride in the extraction of oxygen from oxides and silicates for isotopic analysis. *Geochim. Cosmochim. Acta* **1963**, *27*, 43–52. [CrossRef]
31. Friedman, I.; O’Neil, J.R. Compilation of stable isotope fractionation factors of geochemical interest. In *Data of Geochemistry*; Fleischer, M., Ed.; United States Geological Survey: Reston, VI, USA, 1977; pp. kk1–kk440.
32. Shafaroudi, A.M.; Karimpour, M.H. Mineralogic, fluid inclusion, and sulfur isotope evidence for the genesis of Sechangi lead–zinc (–copper) deposit, Eastern Iran. *J. Afr. Earth Sci.* **2015**, *107*, 1–14. [CrossRef]
33. Qu, G.Y.; Wang, K.Y.; Yang, H.; Sun, Q.F.; Li, J.; Cai, W.Y.; Lai, C.K. Fluid inclusions, H–O–S–Pb isotopes and metallogenic implications of Triassic Hua’naote Ag–Pb–Zn deposit (Inner Mongolia, China) in the eastern Central Asian Orogenic Belt. *J. Geochem. Explor.* **2021**, *225*, 106766. [CrossRef]
34. Sun, Y.G.; Li, B.L.; Sun, F.Y.; Qian, Y.; Yu, R.T.; Zhao, T.F.; Dong, J.L. Ore Genesis of the Chuduoqu Pb–Zn–Cu Deposit in the Tuotuohe Area, Central Tibet: Evidence from Fluid Inclusions and C–H–O–S–Pb Isotopes Systematics. *Minerals* **2019**, *9*, 285. [CrossRef]
35. Marques de Sá, C.; Noronha, F.; Cardellach, E.; Bobos, I. Fluid inclusion and (S, C, O, Pb) isotope study of Pb–Zn–(Cu–Ag) hydrothermal veins from Central and Northern Portugal—Metallogenic implications. *Ore Geol. Rev.* **2019**, *112*, 103043. [CrossRef]
36. Zhang, Y.C.; Gao, S.B.; Zheng, Y.Y.; Jiang, J.S.; Zhang, S.Z.; Jiang, X.J.; Guo, X.R. Mineralogy, fluid inclusions and C–H–O–S–Pb isotopes of the Palaeocene Longgen Pb–Zn deposit in the western Nyainqentanglha belt, Tibet. *Ore Geol. Rev.* **2018**, *102*, 18–43. [CrossRef]
37. Yu, G.Y.; Li, S.D.; Wang, Y.C.; Wang, K.Y. Fluid Evolution and Ore Genesis of the Qibaoshan Polymetallic Ore Field, Shandong Province, China: Constraints from Fluid Inclusions and H–O–S Isotopic Compositions. *Minerals* **2019**, *9*, 394. [CrossRef]
38. Yang, S.S.; Wang, H.; Zhu, X.Y.; Zou, T.; Yang, C.L.; Jiang, H.Y.; Jiang, B.B.; Cheng, X.Y.; Li, Y.J. The Metallogenic Mechanism of Skarn Sn–Polymetallic Deposits in the Southern Great Khingan Range, China: Constraints on the Geological and Geochemical Characteristics of Damogutu Sn–Fe and Dashishan Sn–Pb–Zn Deposits. *Minerals* **2019**, *9*, 418. [CrossRef]
39. Li, S.D.; Chen, C.; Gao, L.L.; Xia, F.; Zhang, X.B.; Wang, K.Y.; Arkin, K. Ore Genesis of the Kuergasheng Pb–Zn Deposit, Xinjiang Province, Northwest China: Constraints from Geology, Fluid Inclusions, and H–O–C–S–Pb Isotopes. *Minerals* **2020**, *10*, 592. [CrossRef]
40. Ke, L.L.; Zhang, H.Y.; Liu, J.J.; Zhai, D.G.; Guo, D.H.; Yang, J.K.; Tan, Q.; Xu, Y.W.; Zhang, M.; Wang, S.G. Fluid Inclusion, H–O, S, Pb and noble gas isotope studies of the Aerhada Pb–Zn–Ag deposit, Inner Mongolia, NE China. *Ore Geol. Rev.* **2017**, *88*, 304–316. [CrossRef]
41. Borojević Šoštarčić, S.; Palinkaš, L.A.; Neubauer, F.; Hurai, V.; Cvetković, V.; Roller-Lutz, Z.; Mandić, M.; Genser, J. Silver-base metal epithermal vein and listwanite hosted deposit Crnac, Rogozna Mts., Kosovo, part II: A link between magmatic rocks and epithermal mineralization. *Ore Geol. Rev.* **2013**, *50*, 98–117. [CrossRef]
42. Shepherd, T.J.; Rankin, A.H.; Alderton, D.H.M. *A Practical Guide to Fluid Inclusion Studies*; Blackie and Son Ltd.: London, UK, 1985.

43. Conliffe, J.; Wilton, D.H.C.; Blamey, N.J.F.; Archibald, S.M. Paleoproterozoic Mississippi Valley Type Pb–Zn mineralization in the Ramah Group, Northern Labrador: Stable isotope, fluid inclusion and quantitative fluid inclusion gas analyses. *Chem. Geol.* **2013**, *362*, 211–223. [CrossRef]
44. Liu, H.G. Research on provenance of MVT Pb–Zn deposits. *IOP Conf. Ser. Mater. Sci. Eng.* **2017**, *207*, 012108. [CrossRef]
45. Wu, T.; Huang, Z.L.; He, Y.F.; Yang, M.; Fan, H.F.; Wei, C.; Ye, L.; Hu, Y.S.; Xiang, Z.H.; Lai, C.K. Metal source and ore-forming process of the Maoping carbonate-hosted Pb–Zn deposit in Yunnan, SW China: Evidence from deposit geology and sphalerite Pb–Zn–Cd isotopes. *Ore Geol. Rev.* **2021**, *135*, 104214. [CrossRef]
46. Liu, Y.C.; Song, Y.C.; Hou, Z.Q.; Xi, D.P.; Li, S.P.; Yue, L.L.; Ma, W.; Tang, B.L. Palynological constraints on the age of the Mississippi Valley-type Changdong Pb–Zn deposit, Sanjiang belt, West China. *Sci. China Earth Sci.* **2021**, *65*, 167–181. [CrossRef]
47. Zhong, R.C.; Brugger, J.; Chen, Y.J.; Li, W.B. Contrasting regimes of Cu, Zn and Pb transport in ore-forming hydrothermal fluids. *Chem. Geol.* **2015**, *395*, 154–164. [CrossRef]
48. Saeidabadi, Z.K.; Karimpour, M.H.; Shafaroudi, A.M.; Rahimi, B.; Corfu, F. Origin of the Kaviro lead deposit in the Neygaran area, Lut Block, Eastern Iran: Constraints from geology, fluid inclusions, and isotope geochemistry. *J. Geochem. Explor.* **2018**, *192*, 85–102. [CrossRef]
49. Zartman, R.; Doe, B. Plumbotectonics—The model. *Tectonophysics* **1981**, *75*, 135–162. [CrossRef]
50. Stacey, J.S.; Kramers, J. Approximation of terrestrial lead isotope evolution by a two-stage model. *Earth Planet. Sci. Lett.* **1975**, *26*, 207–221. [CrossRef]
51. Wang, R.L.; Zeng, Q.D.; Zhang, Z.C.; Guo, Y.P.; Zhang, Z.; Zhou, L.L.; Wang, X.W.; Yu, B. Genesis of the Aobaotu Pb–Zn deposit in the southern Great Xing’an Range, NE China: Constraints from geochronology and C–H–O–S–Pb isotopic and fluid inclusion studies. *Geol. J.* **2022**, *57*, 1391–1412. [CrossRef]
52. Zhao, Z.D.; Mo, X.X.; Dong, G.C.; Zhou, S.; Zhu, D.C.; Liao, Z.L.; Sun, C.G. Pb isotopic Geochemistry of Tibetan Plateau and its implications. *Geoscience* **2007**, *21*, 265–274. (In Chinese with English Abstract)
53. Zhu, B.Q. *The Theory and Application of the Isotopic Systematic in Geoscience Concurrent Discussion of the Continental Crust and Mantle Evolution in China*; Science Publishing House: Beijing, China, 1998; p. 330.
54. Hoefs, J. *Stable Isotope Geochemistry*; Springer: Berlin/Heidelberg, Germany, 2009; p. 285.
55. Harris, A.C.; Golding, S.D.; White, N.C. Bajo de la Alumbrera copper-gold deposit: Stable isotope evidence for a porphyry-related hydrothermal system dominated by magmatic aqueous fluids. *Econ. Geol.* **2005**, *100*, 863–886. [CrossRef]
56. Sun, G.T.; Zeng, Q.D.; Zhou, J.X.; Zhou, L.L.; Chen, P.W. Genesis of the Xinling vein-type Ag–Pb–Zn deposit, Liaodong Peninsula, China: Evidence from texture, composition and in situ S–Pb isotopes. *Ore Geol. Rev.* **2021**, *133*, 104120. [CrossRef]
57. Schwarcz, H.; Burnie, S. Influence of sedimentary environments on sulfur isotope ratios in clastic rocks: A review. *Miner. Depos.* **1973**, *8*, 264–277. [CrossRef]
58. Hao, H.D.; Song, Y.C.; Li, L.S.; Jia, Z.Y.; Wang, Y.K.; Liu, Q. Characteristics of Breccias and C–O–Sr–S Isotope Geochemistry of the Duocaima Pb–Zn Deposit in Tuotuohe, Qinghai Province: Implications for the Ore-forming Process. *Acta Geol. Sin. Engl. Ed.* **2015**, *89*, 1568–1587.
59. Yao, F.L.; Sun, F.Y. (Eds.) *Mineralogy Tutorial*; Geological Publishing House: Beijing, China, 2005. (In Chinese)
60. Taylor, H.P. The Application of Oxygen and Hydrogen Isotope Studies to Problems of Hydrothermal Alteration and Ore Deposition. *Econ. Geol.* **1974**, *69*, 843–883. [CrossRef]
61. Taylor, H.P., Jr.; Frechen, J.; Degens, E.T. Oxygen and carbon isotope studies of carbonatites from the Laacher See district, West Germany and the Alnö district, Sweden. *Geochim. Et Cosmochim. Acta* **1967**, *31*, 407–430. [CrossRef]
62. Li, Y.; Ren, Y.S.; Hao, Y.J.; Yang, Q. Ore-forming fluid characteristics and genesis of vein-type lead-zinc mineralization of Xiaohongshilazi deposit, Jilin Province, China. *Glob. Geol.* **2017**, *20*, 191–199.
63. Liu, Y.F.; Qi, H.W.; Bi, X.W.; Hu, R.Z.; Qi, L.K.; Yin, R.S.; Tang, Y.Y. Two types of sediment-hosted Pb–Zn deposits in the northern margin of Lanping basin, SW China: Evidence from sphalerite trace elements, carbonate C–O isotopes and molybdenite Re–Os age. *Ore Geol. Rev.* **2021**, *131*, 104016. [CrossRef]
64. Fareeduddin; Venkatesh, B.R.; Hanumantha, R.; Golani, P.R.; Sharma, B.B.; Neogi, S. Petrology and Stable Isotope (S, C, O) Studies of Selected Sediment-hosted Basemetal Ore Deposits in the Proterozoic Aravalli-Delhi Fold Belt, Rajasthan. *J. Geol. Soc. India* **2014**, *83*, 119–141. [CrossRef]
65. Veizer, J.; Hoefs, J. The nature of $^{18}\text{O}/^{16}\text{O}$ and $^{13}\text{C}/^{12}\text{C}$ secular trends in sedimentary carbonate rocks. *Geochim. Et Cosmochim. Acta* **1976**, *40*, 1387–1395. [CrossRef]
66. Landtwing, M.; Pettke, T.; Halter, W.; Heinrich, C.; Redmond, P.; Einaudi, M.; Kunze, K. Copper deposition during quartz dissolution by cooling magmatic-hydrothermal fluids: The Bingham porphyry. *Earth Planet. Sci. Lett.* **2005**, *235*, 229–243. [CrossRef]
67. O’Neil, J.R.; Silberman, M.L. Stable isotope relations in epithermal Au–Ag deposits. *Econ. Geol.* **1974**, *69*, 902–909. [CrossRef]
68. Beane, R.; Titley, S. Porphyry copper deposits; Part II: Hydrothermal alteration and mineralization. *Econ. Geol.* **1981**, *75*, 235–269.
69. Sawkins, F.J. Sulfide ore deposits in relation to plate tectonics. *J. Geol.* **1972**, *80*, 377–397. [CrossRef]
70. Benedezú, R.; Fonteboté, L. Cordilleran Epithermal Cu–Zn–Pb–(Au–Ag) Mineralization in the Colquijirca District, Central Peru: Deposit-Scale Mineralogical Patterns. *Econ. Geol.* **2009**, *104*, 905–944. [CrossRef]
71. Kissin, S.A.; Mango, H. Silver vein deposits. In *Treatise on Geochemistry*, 2nd ed.; Elsevier: Oxford, UK, 2014; pp. 425–432.

72. Sibson, R.H.; Robert, F.; Poulsen, K.H. High angle reverse faults, fluid-pressure cycling, and mesothermal gold-quartz deposits. *Geology* **1988**, *16*, 551–555. [CrossRef]
73. Wu, J.; Li, Z.; Zhu, M.J.; Huang, W.T.; Liao, J.; Zhang, J.; Liang, H.Y. Genesis of the Beixiang Sb-Pb-Zn-Sn Deposit and Polymetallic Enrichment of the Danchi Sn-Polymetallic Ore Belt in Guangxi, SW China. *Minerals* **2022**, *12*, 1349. [CrossRef]

Disclaimer/Publisher’s Note: The statements, opinions and data contained in all publications are solely those of the individual author(s) and contributor(s) and not of MDPI and/or the editor(s). MDPI and/or the editor(s) disclaim responsibility for any injury to people or property resulting from any ideas, methods, instructions or products referred to in the content.

Article

Geochemical Characteristics of the Mineral Assemblages from the Niukutou Pb-Zn Skarn Deposit, East Kunlun Mountains, and Their Metallogenic Implications

Xinyu Wang, Shulai Wang, Huiqiong Zhang *, Yuwang Wang, Xinyou Zhu and Xing Yang

Beijing Institute of Geology for Mineral Resources Co., Ltd., Beijing 100012, China

* Correspondence: zhqzhq_2005@163.com; Tel.: +86-010-8492-9180

Abstract: The Niukutou Pb-Zn deposit is typical of skarn deposits in the Qimantagh metallogenic belt (QMB) in the East Kunlun Mountains. In this study, based on detailed petrographical observations, electron microprobe analyses (EMPAs), and laser-ablation-inductively coupled plasma-mass spectrometry (LA-ICP-MS) analyses, we report the major and trace element compositions of the typical skarn mineral assemblages (garnet, pyroxene, ilvaite, epidote, and chlorite) in this deposit. Three hydrothermal mineralization stages with different mineral assemblages of the prograde metamorphic phase were determined, which were distributed from the inside to the outside of the ore-forming rock mass. Grt1+Px1 (Stage 1), Grt2+Px2 (Stage 2), and Px3 (Stage 3) were distinguished in the Niukutou deposit. Furthermore, the ilvaites in the retrograde metamorphic phase can be divided into three stages, namely Ilv1, Ilv2, and Ilv3. The ore-forming fluid in Stage 1 exhibited high Σ REE, U, and Nd concentrations and δ Eu, δ Ce, and LREE/HREE values, which were likely derived from a magmatic-hydrothermal source and formed at high temperatures, high fO_2 values, and mildly acidic pH conditions, and probably experienced diffusive metasomatism in a closed system with low water/rock ratios. In Stages 2 and 3, the ore-forming exhibited lower Σ REE, U, and Nd concentrations and δ Eu, δ Ce, and LREE/HREE values, with high Mn content that had likely experienced infiltrative metasomatism in an open system with high water/rock ratios. From Ilv1 to Ilv3, the δ Eu and U contents decreased, whereas the Mn content increased, indicating that the oxygen fugacity of mineralization was in decline. The ore-forming fluid evolution of the Niukutou deposit can be characterized as follows: from Stage 1 to Stage 3, the hydrothermal fluid migrated from the deep plutons to the shallow skarn and marble; the environment altered from the high fO_2 and temperature conditions to low fO_2 and temperature values, and the pH and Mn contents increased. The fluids contained considerable metal ore-forming materials that were favorable for the enrichment and precipitation of the Fe content. In the retrograde metamorphic phase, with the decrease in oxygen fugacity (from Ilv1 to Ilv3), the temperature and oxygen fugacity of the ore-forming fluid environment decreased, ultimately becoming conducive to the dissolution and precipitation of Pb and Zn elements.

Citation: Wang, X.; Wang, S.; Zhang, H.; Wang, Y.; Zhu, X.; Yang, X. Geochemical Characteristics of the Mineral Assemblages from the Niukutou Pb-Zn Skarn Deposit, East Kunlun Mountains, and Their Metallogenic Implications. *Minerals* **2023**, *13*, 18. <https://doi.org/10.3390/min13010018>

Academic Editor: Maria Boni

Received: 18 November 2022

Revised: 11 December 2022

Accepted: 20 December 2022

Published: 23 December 2022

Keywords: mineralogical characteristics; geochemistry; metallogenic process; Niukutou skarn Pb-Zn deposit; East Kunlun Mountains



Copyright: © 2022 by the authors. Licensee MDPI, Basel, Switzerland. This article is an open access article distributed under the terms and conditions of the Creative Commons Attribution (CC BY) license (<https://creativecommons.org/licenses/by/4.0/>).

1. Introduction

The Qimantagh metallogenic belt (QMB) is a significant Fe-Pb-Zn-Cu (-Ag) mineral belt that extends for 550 km in the East Kunlun Mountains, on the northern Tibetan Plateau (Figure 1a; [1–7]). Skarn deposits in the QMB can be subdivided into several main types based on the dominant metal. Typical Cu (Mo) skarn deposits are found in Kaerqueka, Wulanwuzhuer, and Yazigou (Figure 1b); Fe skarn deposits occur in Yemaquan, Galinge, and Kendekeke, whereas Pb-Zn skarn deposits are found in Weibao, Sijiaoyang, and Niukutou. Furthermore, small deposits and mines are scattered throughout the region, a fact that has attracted the attention of many researchers [7–11]. Published studies

have shown that the skarn mineralization in this area is genetically related to Triassic granitoids [12,13] and that different deposits are generally characterized by a distinct skarn mineral composition. However, the feature(s) of the ore-forming fluids that control the mineralization types in the QMB remain unclear, limiting our understanding of the skarn mineralization mechanisms in the region.

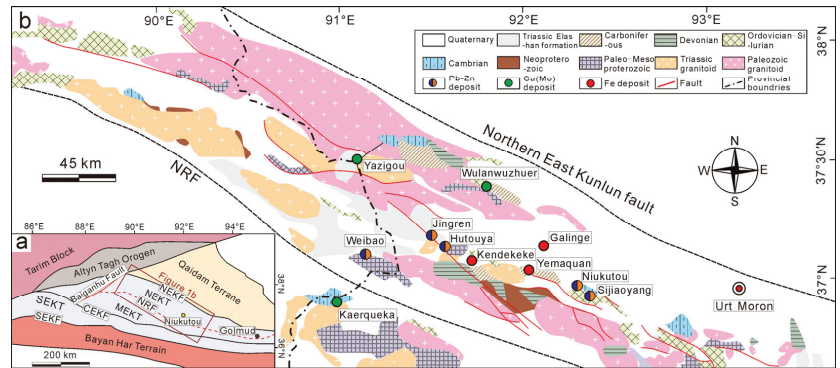


Figure 1. Tectonic framework of the eastern Kunlun area (a) and regional geological and mineral map of the Niukutou deposit (b) (modified from [2,12,13]). Abbreviations: NEKT—Northeast Kunlun terrane; NEKF—Northeast Kunlun fault; NRF—Nalingguole River fault; CEKF—Central-East Kunlun fault; MEKT—Middle-East Kunlun terrane; SEKT—Southeast Kunlun terrane; and SEKF—Southeast Kunlun fault.

The Niukutou Pb-Zn skarn deposit is located in the eastern part of the QMB (Figure 1b). Skarn minerals are strongly developed within the Niukutou deposit, and the deposit's geological structure, zonation pattern, and mineral assemblages have been described [14–17]. However, the detailed mineralogical characteristics and chemistry of the skarn minerals, as well as their implications, have not been examined, hence restricting any discussion of the metallogenic geological conditions and regularity of the Niukutou deposit. Skarn minerals, especially those that preserve complex chemical zonation patterns, can record the composition and evolutionary history of hydrothermal processes. Furthermore, through the application of analytical techniques, including electron microprobe analysis (EMPA) and laser-ablation-inductively coupled plasma-mass spectrometry (LA-ICP-MS), hydrothermally altered minerals have been successfully used as an important probe for researching the environment of the metal accumulation, prospecting, and evolution of ore-forming fluids within ore deposits [18–20].

In this paper, we present the mineralogical characteristics and petrographic features representing the three ore-forming stages, as well as the major and trace element chemical data, for the mineral assemblages in the Niukutou deposit. We discuss the ore-forming conditions and evolution of the ore-forming fluids within the deposit, with the ultimate aim of revealing the processes that underlie the metal ore-forming mechanism and developing a superior understanding of the implications for the Niukutou mineralization.

2. Regional Geology

The Qimantagh area is wedged among the Alтын Tagh Orogen, Qaidam Basin, and Bayan Har terrain and bounded by the Alтын Tagh Fault, the Northern Kunlun Fault, and the Nalingguole River Fault (Figure 1a). Igneous rocks of different ages ranging from the Archean to the Cenozoic occur widely within the Qimantagh area (Figure 1b). The Langyashan Formation, Tanjianshan Group, and Carboniferous strata are the most important host rocks for skarn mineralization within the Qimantagh area [6,7,12,21]. The Mesoproterozoic Langyashan Formation consists of carbonate and clastic rocks locally undergoing greenschist-facies metamorphism [7]. The Ordovician–Silurian Tanjianshan

Group consists of volcano-sedimentary rocks that have also experienced greenschist-facies metamorphism.

Faults in this region generally strike in the NWW and NW directions and are interpreted to have developed before or during skarn alteration, thus usually controlling significant mineralization. The NE- and N-striking fault systems are generally postdated skarns and mineralization [22]. The fold orientations mostly trend from the NWW to the SN. Intrusive rocks formed in the Hercynian and Indosinian periods and were controlled by NW- and NWW-oriented faults. Schistosity and cleavage are common in these rocks.

3. Deposit Geology

The Niukutou Pb-Zn skarn deposit is located in the eastern part of the QMB (Figure 1b) and comprises three ore blocks (or magnetic anomalies) referred to as M1, M4, and M2, from west to east. The Pb-Zn mineralization crops out within the M1 and M4 ore blocks (Figure 2), with the resources being more than 1.14 million tons.

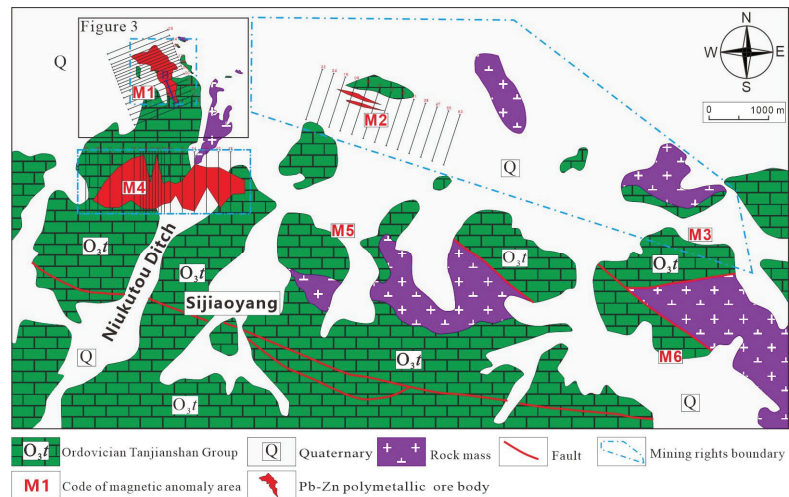


Figure 2. Simplified geological map of the Niukutou Pb-Zn polymetal deposit showing the locations of the M1, M4, and M2 ore blocks.

The Tanjianshan Group and Quaternary deposits are the main sedimentary formations. The Tanjianshan Group is primarily composed of limestone, banded limestone, and marble, representing a set of shallow marine carbonate deposits. Similar to the Hutouya skarn Cu-Pb-Zn deposit, the Tanjianshan Group is the host for the skarn ore bodies in the Niukutou deposit. Where this group contacts with the Triassic granitoids, limestone becomes calc-silicate hornfels with well-developed skarn zonation.

Granodiorite and monzonitic granite are the main intrusive rocks in the M1 and M4 ore blocks (Figure 3). The granodiorite is closely related to Pb-Zn mineralization. The age of the ore-forming-related granites is 375.4 ± 4.6 Ma [5]. The granodiorite occurs both on the surface and at the bottoms of drill holes, and the monzonitic granite occurs only in the M2 ore block.

The ore bodies in the M1 and M4 ore blocks primarily occur in layered skarns (Figure 4a), and most Pb-Zn ore minerals are hosted in johannsenite, ilvaite, and manganhedenbergite skarns (Figure 4b). The main ore textures are heterogeneous granular and columnar. The ore structures are dominated by banded, densely disseminated, and massive patterns. The ore minerals include galena, sphalerite, pyrrhotite, magnetite, pyrite, arsenopyrite, bornite, and chalcopyrite. The main skarn minerals are garnet, johannsenite, ilvaite, manganhedenbergite, actinolite, tremolite, quartz, calcite, and chlorite.

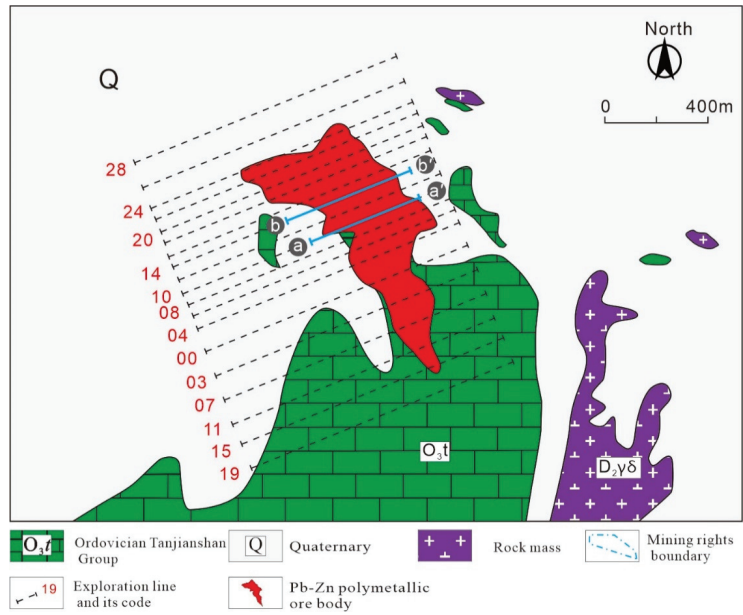


Figure 3. Geological map of the Niukutou M1 ore block.

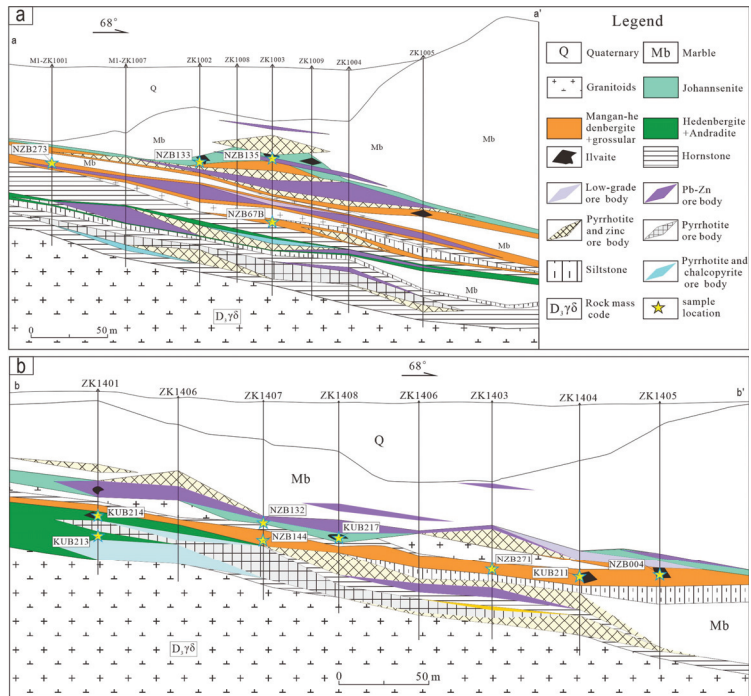


Figure 4. Geological profile of the No. 10 (a) and No. 14 (b) exploration lines in the M1 ore block of the Niukutou deposit.

Based on the mineral assemblages, ore textures, and crosscutting relationships, the skarn formation and mineralization of the Niukutou deposit can be divided into four phases (Figure 5): (1) in the prograde metamorphic phase, the main mineral assemblages consist of anhydrous minerals such as garnet and pyroxene; (2) in the retrograde metamorphic phase, the main mineral assemblage is dominated by hydrous silicate minerals, characteristically ilvaite, actinolite, tremolite, epidote, and chlorite, which often replace prograde garnet/pyroxene; (3) the sulfide phase is the main ore-forming phase, where the mineral assemblage consists of ore minerals such as pyrrhotite, pyrite, sphalerite, galena, and quartz; and (4) in the carbonate phase, the mineral assemblage is characterized by quartz and calcite veins that cut through the skarn and ore minerals.

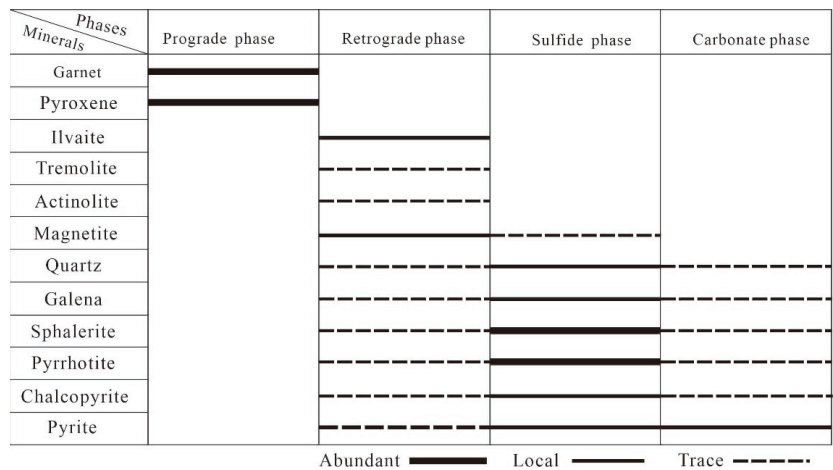


Figure 5. Division of mineralization sequence of the Niukutou skarn deposit.

According to their geological occurrence and mineral texture, the prograde garnets can be divided into two subtypes, Grt1 and Grt2, whereas the prograde pyroxenes can be divided into three subtypes, Px1, Px2, and Px3. The ilvaite in the late phase also has three subtypes, Ilv1, Ilv2, and Ilv3.

Grt1 is usually dark brown (Figure 6a,b), brownish green, or brown in color and is occasionally reddish brown. The crystal diameter is generally greater than 500 μm, with most being greater than 1000 μm. Grt1 often coexists with Px1 (Figure 6a), pyrrhotite (Figure 6b), and magnetite. Grt2 is light brown and brownish green (Figure 6c) with grain sizes of between 500 and 1000 μm; thus, the grain is smaller than in Grt1. Compared with Grt1, the crystal form of Grt2 is incomplete, indicating stronger alteration. Grt2 generally coexists with Px2 or is replaced with Ilv2 (Figure 6d).

Px1 is generally dark green in color and columnar to short columnar and granular in shape. It usually coexists or is replaced with Ilv1 or magnetite (Figure 6e). Px2 is light green (Figure 6f), columnar to short columnar in shape, and found in the M1 ore block and secondarily in the M4 ore block. Generally, it coexists or is replaced with Ilv2. Px2 is associated with pyrrhotite and galena.

Px3 is brown or dark brown in color, with fibrous and long-columnar types (Figure 6i). Px3 often coexists with Ilv3 and develops with sphalerite and galena. It is often cut through by calcite veins in the later stages.

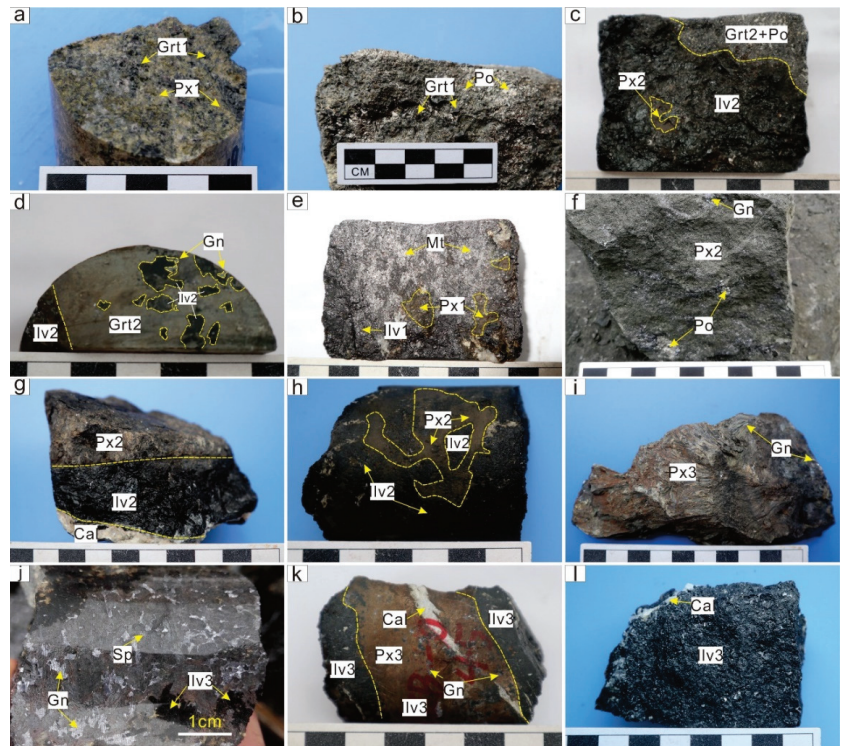


Figure 6. Photographs of representative samples and their relationships to the Niukutou deposit. (a) Granular garnet (Grt1) and hedenbergite (Px1) from the M1 pit; (b) Coarse-grained garnet (Grt1) replaced with pyrrhotite; (c) Granular garnet (Grt2) coexisting with Mn-hedenbergite (Px2), and short-column ilvaite (Ilv2) replaced the garnet (Grt2) and Mn-hedenbergite (Px2), whereas the Mn-hedenbergite (Px2) is residual in the ilvaite (Ilv2); (d) Fine-grained garnet (Grt2) is replaced with short-column Ilvaite (Ilv2); (e) Ilv1 is replaced with disseminated magnetite and the hedenbergite (Px1) is residual in the ilvaite (Ilv2); (f) Disseminated galena and pyrrhotite are developed in the short-column Mn-hedenbergite (Px2); (g) Mn-hedenbergite (Px2) is replaced with ilvaite (Ilv2), the ilvaite skarn is cut through by calcite veins; (h) Short-column ilvaite (Ilv2) replaced the Mn-hedenbergite (Px2); (i) Fibrous or long-column johannsenite (Px3), with minor disseminated galena; (j) Galena and sphalerite are developed between the ilvaite (Ilv3) grains; (k) Ilvaite (Ilv3) replaced johannsenite (Px3), with minor disseminated galena developed in it and cut by calcite veins; (l) The short-column ilvaite (Ilv3) cut by calcite veins. Abbreviations: Grt1, Px1, Ilv1—Garnet, pyroxene, and ilvaite of Stage 1; Grt2, Px2, Ilv2—Garnet, pyroxene, and ilvaite of Stage 2; Px3, Ilv3—Pyroxene and ilvaite of Stage 2; Gn—Galena; Sp—Sphalerite; Po—Pyrrhotite; Mt—Magnetite; Cal—Calcite.

Based on the mineral assemblages and microscopic characteristics, there are three ilvaite-bearing mineral assemblages in the Niukutou deposit (unpublished data): (1) Ilv1 replaced Grt1, Px1, and magnetite (Figure 6e); (2) Ilv2 replaced Grt2, Px2, galena, and magnetite (Figure 6g,h); and (3) Ilv3 replaced Px3 (johannsenite; Figure 6j,k) and is often cut through by calcite and quartz veins (Figure 6l). Grt1 and Px1 are generated in Stage 1 of the prograde metamorphic phase, whereas Grt2/Px2 and Px3 are generated in Stage 2 of the prograde metamorphic phase. Ilv1 to Ilv3 are generated in three different stages of the retrograde metamorphic phase.

4. Mineralogical Characteristics

4.1. Analytical Methods

A total of 36 representative samples from the Niukutou deposit were examined in this study; parts of the sample location are shown in Figure 4. Most samples were collected from the mining pit and drill cores. The paragenetic relationships were studied in thin sections by transmitted polarized light microscopy and in polished thick sections by reflected light microscopy. To further determine the mineralogical characteristics of the Niukutou skarn deposit, we selected skarn and ore minerals in each phase for EMPA analysis. The EMPA analysis and test work were performed at the Institute of Geology, Chinese Academy of Geosciences. The instrument used was a JXA-8100 system (JEOL Company, Tokyo, Japan). The analytical parameters were as follows: accelerating voltage 15 k, beam current 2×10^{-8} A, spectral time 10 s, beam size 5 μm , ZAF correction, and SPI-combined standard sample correction.

The cation numbers and end tuples of the garnet, pyroxene, and amphibole minerals were calculated using Geokit software (GeokitPro20221030) [23], and the cation numbers of epidote and chlorite were calculated using CalcMin software [24].

To obtain the trace elements of the skarn samples, we chose representative skarn minerals (garnet, pyroxene, and ilvaite) and ground them into probe pieces (with thicknesses greater than 100 μm) for LA-ICP-MS analysis.

The laser-ablation system was an yttrium–aluminum garnet laser produced by the New Wave Company, Stockholm, Sweden), with a wavelength of 213 nm. The ICP-MS was performed with a Thermo Element II instrument (Agilent 7700a, NYSE: A, Palo Alto City, United States) (version, manufacturer, city, country). In the process of laser-ablation sampling, helium was used as the carrier gas. Before the helium carried the sample aerosol into the ICP, it was mixed with argon (carrier gas, plasma gas, and compensation gas) through a T-joint. To obtain the best signal strength and stability of standard NIST SRM 612, the experimental conditions were optimized by adjusting the helium and argon gas flows, and the oxide yields were controlled to be less than 0.3%. For unknown samples, the laser-sampling method was single-point erosion: the diameter of the beam spot was 40 μm ; the frequency was 10 Hz; and the energy density was about 9 J/cm², with a 20 s gas blank +40 s sample erosion +20 s washing. The signal detection adopted low-resolution electric field scanning and peak-skipping acquisition, and the detection time for each element was 10 ms. Silicate, quartz, and other minerals were corrected with NIST SRM 610 and GSE-1G as the external standards, and the internal standard element was ²⁹Si; sulfide was corrected with NIST SRM 610 and mass-1 as the external standards.

4.2. Mineralogical Characteristics and Petrographic Features

As previously noted, the prograde garnet–pyroxene and retrograde ilvaite–epidote–chlorite assemblages are the dominant skarn minerals in the Niukutou deposit.

4.2.1. Garnet

Garnet is pervasive in the Niukutou deposit. According to the geological occurrence, microscopic characteristics, and composition, the Niukutou garnet can be divided into two subtypes (Figure 7).

Grt1 is automorphic or semi-automorphic. From the core to the rim, grains show clear growth zonation (Figure 7a–c). Additionally, Grt1 coexists with pyroxene (Px1) in the same stage (Figure 7a,b). It was generally metasomatized by retrograde ilvaite–chlorite–epidote and associated with the magnetite–pyrrhotite–sphalerite ore minerals.

Grt2 is distinguished from Grt1 by its unzoned character (Figure 7c,d). In terms of microscopic mineral texture, Grt2 is generally found around Grt1, suggesting that Grt1 crystallized earlier than Grt2. Some Grt2 exhibits a poor crystal form and develops with cracks (Figure 7e).

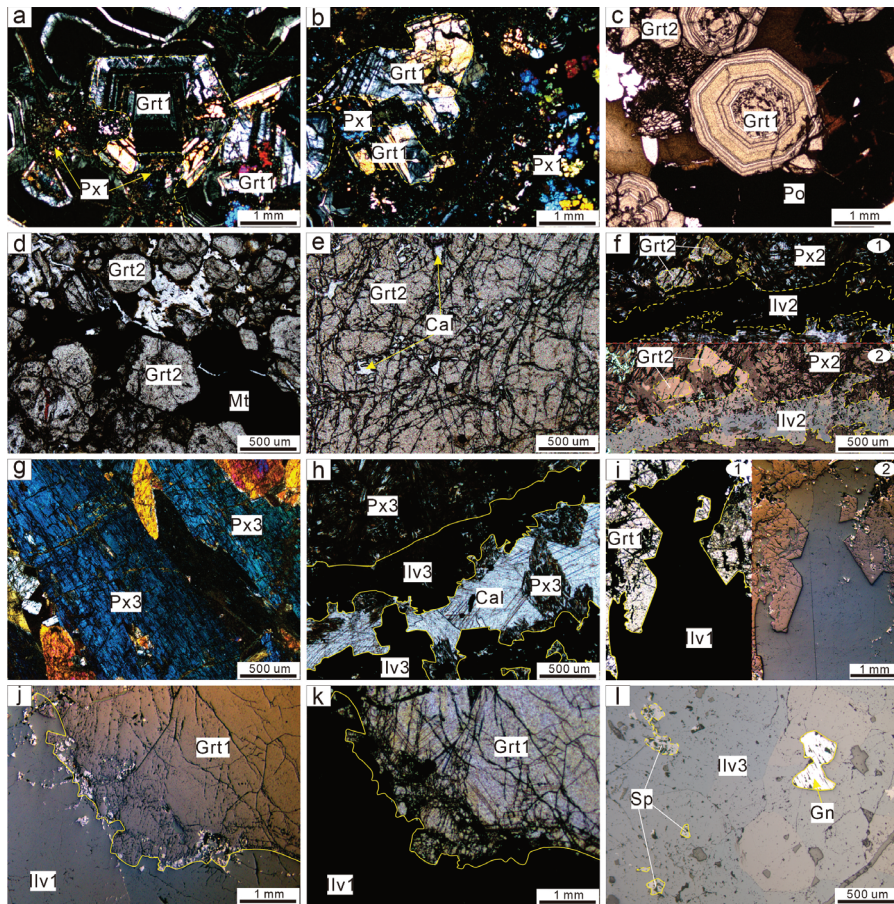


Figure 7. Photomicrographs of representative samples from different stages and their relationships in the Niukutou deposit. (a) Zoned garnet (Grt1) coexisting or replaced with hedenbergite (Px1) in cross-polarized light; (b) Zoned garnet (Grt1) coexisting or replaced with hedenbergite (Px1) in cross-polarized light; (c) Zoned garnet (Grt1) replaced with pyrrhotite, followed by the unzoned garnet (Grt2) in plane-polarized light; (d) Unzoned garnet (Grt2) replaced with magnetite (plane-polarized light); (e) Grt2 developed with cracks; (f) Grt2 and Px2 are replaced with Ilv2 (plane-polarized light in 1 and reflected light in 2); (g) Fibrous or long-column johannsenite (Px3) in cross-polarized light; (h) johannsenite (Px3) is replaced with ilvaite (Ilv3) and cut by a calcite vein (plane-polarized light); (i) Zoned garnet (Grt1) is replaced with the ilvaite (Ilv1, plane-polarized light in 1 and reflected light in 2); (j,k) Zoned garnet (Grt1) is replaced with Ilv1 (reflected light in j and plane-polarized light in k); (l) Disseminated galena and sphalerite developed within Ilv3 (reflected light). Abbreviations: Grt1, Px1, Ilv1—Garnet, pyroxene, and ilvaite of Stage 1; Grt2, Px2, Ilv2—Garnet, pyroxene, and ilvaite of Stage 2; Px3, Ilv3—Pyroxene and ilvaite of Stage 2; Gn—Galena; Sp—Sphalerite; Po—Pyrrhotite; Mt—Magnetite; Cal—Calcite.

4.2.2. Pyroxene

Pyroxene is also one of the main skarn minerals in the Niukutou deposit, and it normally occurs together with garnet; it was formed in the prograde stage.

According to the geological occurrence, microscopic metasomatic relationships, and EMPA composition, the pyroxene in the Niukutou deposit can also be divided into three types.

Under the microscope, Px1 is usually dark green in color and columnar to short columnar and granular in shape; it exhibits a high-grade yellow-green interference color and the typical cross joint of pyroxene (Figure 7a,b). It occurs mostly in the M1 ore block (in the deep part of the drill holes) and often coexists with Grt1 (Figure 7a,b).

In contrast, Px2 is short columnar or fibrous in shape and shows a graded yellow-green interference color (Figure 7f). Px2 coexists with Grt2 and is replaced with Ilv2 (Figure 7f).

Compared to Px2, Px3 is often distributed in the outer zone of the deposit. Px3 has a long-columnar shape and fibrous texture (Figure 7g,h) and shows a dark-green or grass-green color in plane-polarized light. Px3 is often replaced with Ilv3, develops with sphalerite and galena, and is associated with Pb-Zn mineralization.

4.2.3. Ilvaite

The typical ilvaite sample is black and shows a columnar or long-columnar shape. It shows a black or dark-brown color in plane-polarized light and a light-blue color in reflected light (Figure 7f,i,j). There are longitudinal grains on the cylinder measuring 3–10 mm on the long axis. It is soluble in hydrochloric acid and shows a white emulsion shape after dissolution. Quartz, sphalerite, and galena develop between the ilvaite grains and crevices. Calcite veins occasionally cut through the ilvaite. From microscopy, it is difficult to distinguish the three types of ilvaites. However, different mineral assemblages could differentiate the three types of ilvaites.

Ilv1 occasionally replaces Grt1 (Figure 7i–k). Pyrrhotite often develops between Ilv1 and Grt1.

Ilv2 replaces Grt2 and Px2 (Figure 7f). Sphalerite or galena often develops between Ilv1 and Grt1.

Ilv3 generally replaces Px3 (Figure 7h). Sp and Gn often develop within Ilv3 (Figure 7l) or in the contact zone between Ilv3 and Px3. Compared to Ilv2, the galena content of Ilv3 is higher. Additionally, calcite veins cut through or develop within Ilv3.

4.2.4. Epidote

Epidote shows granular to short-columnar structures. Under plane-polarized light, it is light straw yellow and is generally replaced with sphalerite. Under orthogonally polarized light, it has abnormal interference colors. It often replaces prograde garnet and pyroxene, indicating that epidote clearly formed later than the early skarn minerals.

4.2.5. Chlorite

Chlorite is common in the deposit, and we chose only two representative samples for the EMPA. Chlorite is generally replaced with prograde garnet–pyroxene. Under the microscope, chlorite has flake-, scale-, and rose-like shapes.

5. Results

5.1. Major Chemical Elements of Minerals

5.1.1. Garnet

The contents of the major elements and the calculated end-member compositions of the garnets are listed in Table S1. Electron microprobe analyses showed that the garnet crystals from the Nikutou deposit belonged to the andradite–grossular solid solutions and contained less pyralspite (sum of pyrope, spessartine, almandine, and uvarovite; Figure 8).

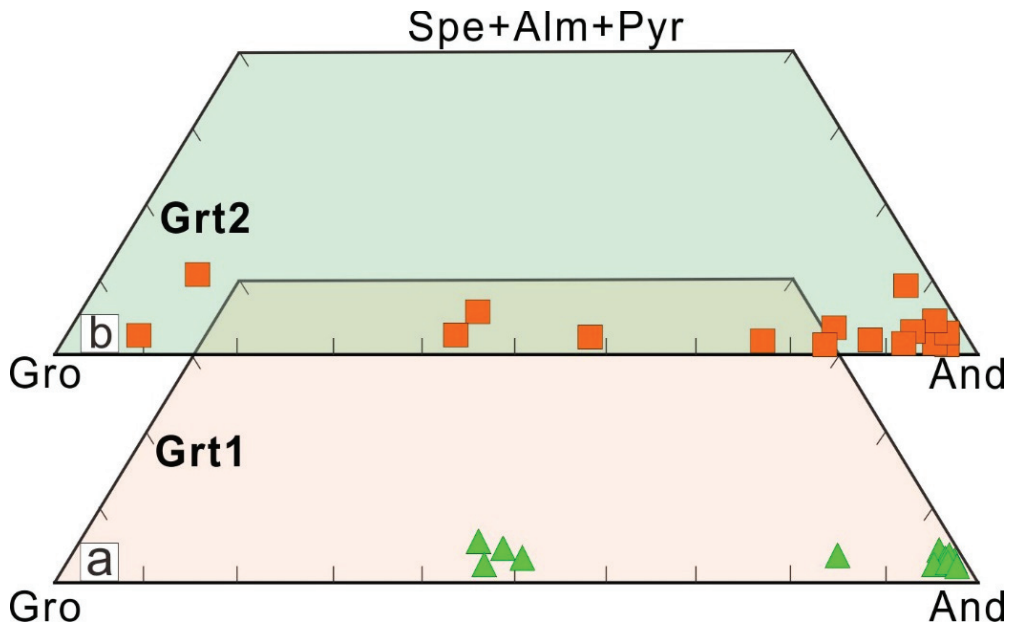


Figure 8. Triangular classification of garnets in the Niukutou deposit (the base diagram is modified from [25]) (a) Grt1–garnets of the first generation with relative enrichment of andradite, represented by green triangles; (b) Grt2–garnets of the second generation with dramatic changes in end-member compositions (andradite and grossular), represented by red squares.

Grt1 had narrow compositional ranges of SiO_2 and CaO but wide compositional ranges of FeO^T and Al_2O_3 . The contents of MnO and MgO were remarkably low (less than 1%). The end-member composition of Grt1 showed wide changes consisting of $\text{And}_{45.08-99.39}\text{Gro}_{0.00-51.55}$ with minor $\text{Pys}_{0.61-3.94}$ (Figure 8a). Well-preserved chemical growth zonation and their analysis results generally showed a decrease in the FeO^T or andradite contents and an increase in the Al_2O_3 or grossular contents from the core to the rim (Figure 9a,b). From the core to the rim, there were slight increases in the MnO content, with negligible changes in TiO_2 and MgO (Figure 9a,b).

Compared to Grt1, Grt2 showed an unzoned character and dramatic changes consisting of $\text{And}_{7.60-97.67}\text{Gro}_{2.12-91.36}$ (Figure 8b), with minor $\text{Pys}_{0.24-10.28}$. Some Grt2 showed slight changes from the core to the rim. Some Grt2 showed “M” and “W” patterns in the variations of the FeO^T (or andradite) and Al_2O_3 (or grossular) contents (Figure 9c,d), respectively, from the core to the rim. These features indicate multi-stage growth. In general, there was a negative correlation between the FeO^T and Al_2O_3 contents in the Niukutou garnets. The MnO content had the same change trend as the Al_2O_3 content, whereas the changes in TiO_2 and MgO were negligible (Figure 9c,d).

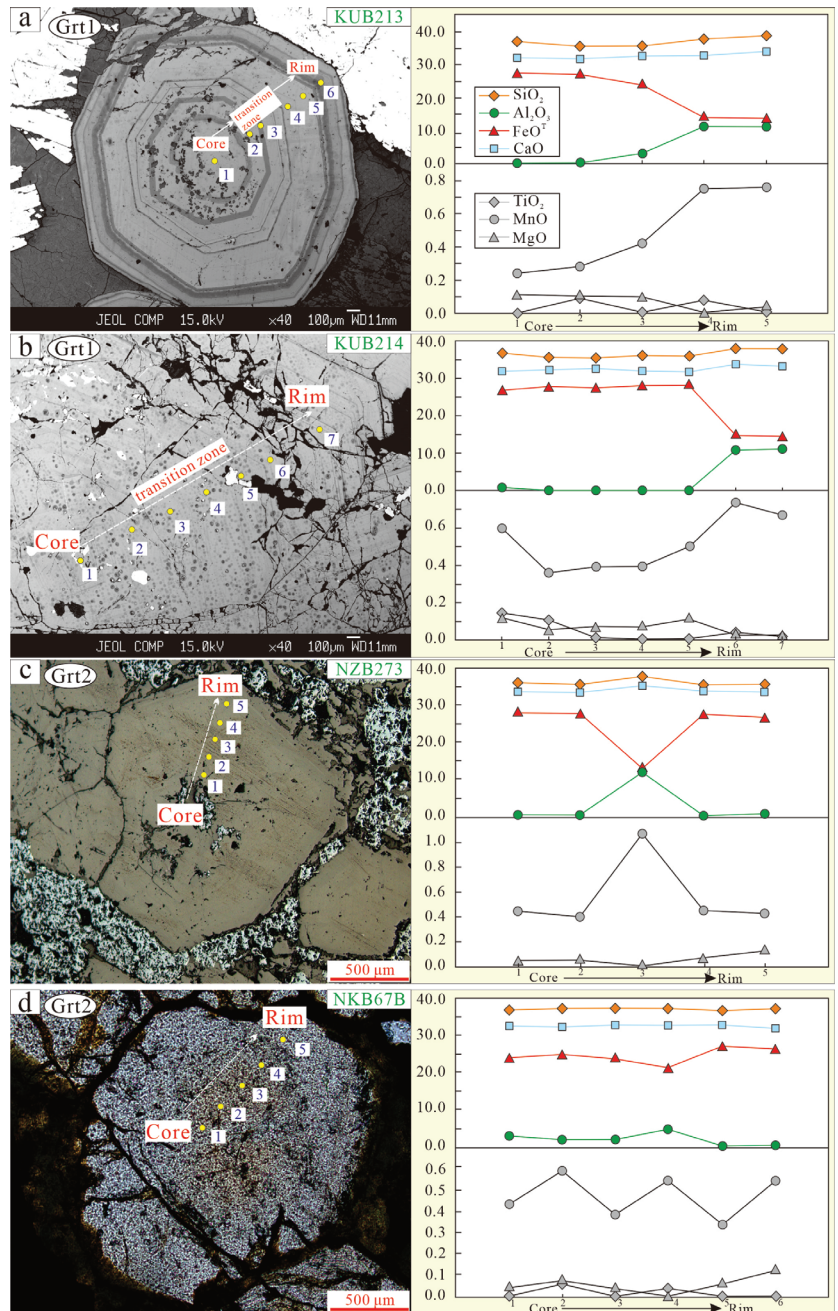


Figure 9. Back-scattered electron and cross-polarized light images for different generations of garnets and their compositional profiles in the Niukutou deposit. (a) Back-scattered electron image and electron probe point position of Grt1; (b) Back-scattered electron image and electron probe point position of Grt1; (c) Reflected light image and electron probe point position of Grt2; (d) cross-polarized light image and electron probe point position of Grt2. Notes: Numbers of 1, 2, 3, 4, 5 is referred to the position of electron probe analysis.

5.1.2. Pyroxene

As shown by the EMPA results (Table S2), Px1 had high contents of SiO₂ and CaO, with SiO₂ = 48.11%–52.75% and CaO = 18.70%–22.44%. It had a variable FeO^T (10.09%–25.50%) content and low MgO (0.62%–11.53%) and MnO (0.99%–4.44%) contents. In terms of the components calculated by the johannsenite–hedenbergite–diopside end members [26], Px1 (Di_{5–65}Hd_{32–80}Jo_{3–15}) was largely composed of hedenbergite, with small amounts of diopside and johannsenite (Figure 10).

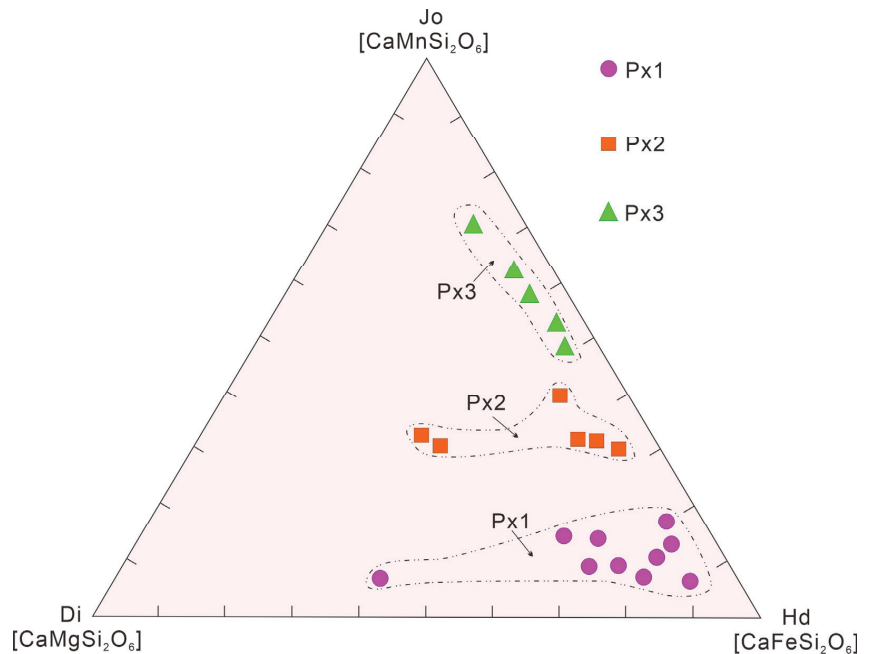


Figure 10. Ternary plots showing the end-member compositions of pyroxenes in the Niukutou deposit.

Compared to Px1, Px2 had relatively invariable contents of SiO₂ (48.64%–50.09%) and CaO (18.70%–23.93%); it also had a variable FeO^T (14.29–21.90) content and low MgO (0.06%–9.24%) and Al₂O₃ (0.01%–0.61%) contents. Regarding the MnO content, Px2 could be distinguished from Px1 by its high MnO content (6.45%–14.33%). Px2 was largely composed of hedenbergite (Di_{6–14}Hd_{67–89}Jo_{4–19}, Figure 10), with smaller amounts of diopside and johannsenite.

Px3 contained SiO₂ (48.32%–49.24%), FeO^T (9.28%–15.75%), CaO (18.29%–21.32%), and MnO (12.60%–19.44%). In terms of the components calculated by the johannsenite–hedenbergite–diopside end members [26], Px3 (Di_{2–4}Hd_{31–53}Jo_{43–65}) was composed of johannsenite and hedenbergite, with a small amount of diopside (Figure 10).

5.1.3. Ilvaite

The EMPA results (Table S3) indicated that ilvaite contained constant SiO₂ (29.45%–30.84%), CaO (12.73%–14.10%), and variable FeO^T (38.58%–48.45%) and Mn (1.78%–13.27%), with small amounts of MgO (0.02%–0.25%) and Al₂O₃ (0.06%–1.28%). From Ilv1 to Ilv3, the MnO content increased and the FeO content decreased (Figure 11). In the Mn–ilvaite and ilvaite end members (Figure 11a), Ilv3 showed the highest composition of Mn–ilvaite (21%–38%), followed by Ilv2 and Ilv1 (Figure 11b,c), with the Mn–ilvaite at 14.99%–17.14% and 5.63%–11.57% (Table S3). All these results indicate the existence of a continuous solid-solution series between ilvaite and manganilvaite (Figure 11).

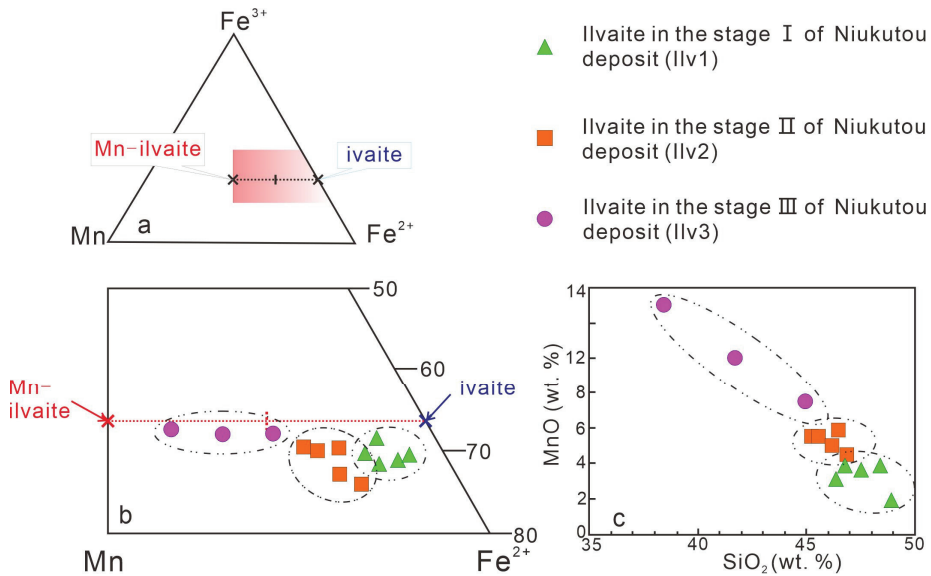


Figure 11. Diagram of $Mn-Fe^{2+}-Fe^{3+}$ components of three generations of ilvaite (a,b), and SiO_2 – MnO contents (c) of Niukutou for three generations of ilvaites (modified from [27]).

5.1.4. Epidote

The EMPA results (Table S4) showed that the main components of epidote were SiO_2 (37.8%–39.06%), Al_2O_3 (22.64%–26.22%), CaO (22.84%–23.76%), and FeO^T (7.83%–11.96%), percentages that fall within the ranges of the epidote group.

5.1.5. Chlorite

The EMPA results (Table S4) showed that the composition varied little; the content of SiO_2 ranged from 25.53 to 26.32%; the content of MgO ranged from 8.33 to 8.97%; the content of FeO^T ranged between 32.00 and 32.50%, and Al_2O_3 varied from 18.65 to 18.78% (Supplementary Table S4). On the chlorite classification diagram (not shown), chlorite from the Niukutou deposit is within the range of iron-magnesium chlorite.

5.2. Trace Elements

The trace element analysis by LA-ICP-MS in the Niukutou deposit was based on the different generations of garnets, pyroxenes, and ilvaites. Each generation was analyzed, and their chemical compositions are presented in Table S5.

Grt1 had medium total rare earth element ($\Sigma REE = 3.22$ – 155.53 ppm) contents and high fractionation between the light and heavy rare earth elements ($LREE/HREE = 0.69$ – 152.48), with variable positive Eu anomalies ($\delta Eu = 1.38$ – 19.58) and nearly positive Ce anomalies (0.95–1.56). The chondrite-normalized REE patterns of Grt1 showed a relatively right-leaning LREE segment and a flat HREE segment (Figure 12a).

Grt2 had low total rare earth element ($\Sigma REE = 10.55$ – 32.63 ppm) contents and high fractionation between the light and heavy rare earth elements ($LREE/HREE = 0.44$ – 5.00), with nearly positive Eu anomalies ($\delta Eu = 0.83$ – 1.67) and variable Ce anomalies (0.54–1.22). Unlike Grt1, the Chondrite-normalized REE patterns of Grt2 showed a relatively right-leaning LREE segment and a flat HREE segment (Figure 12a).

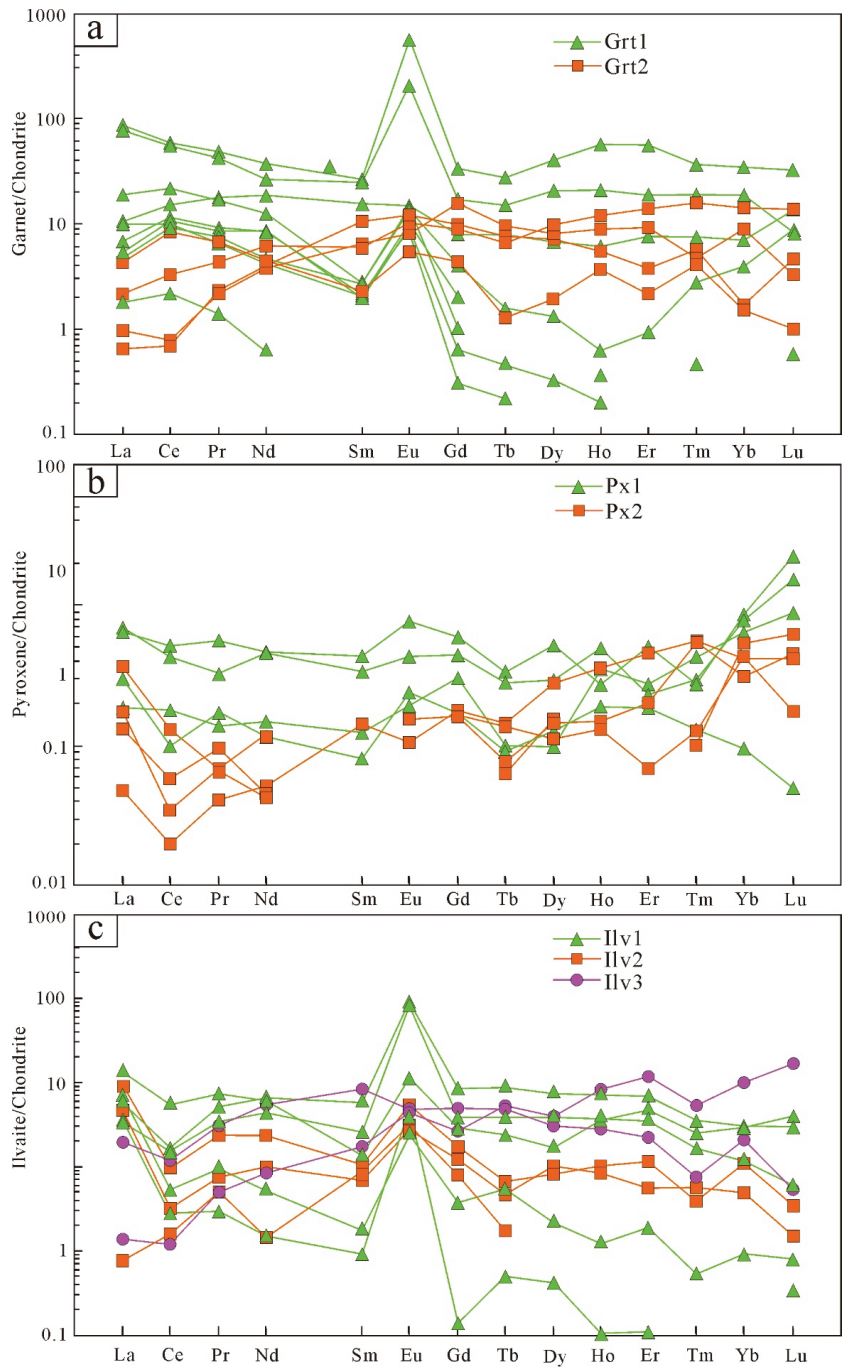


Figure 12. Chondrite-normalized rare earth element (REE) distribution patterns for different generations of garnet (a), pyroxene (b), and ilvaite (c) from the Niukutou deposit. The chondrite-normalized values were calculated in [28].

Px1 had low total rare earth element ($\Sigma\text{REE} = 3.65\text{--}5.45$ ppm) contents and high fractionation between the light and heavy rare earth elements ($\text{LREE}/\text{HREE} = 0.26\text{--}1.76$), with variable positive Eu anomalies ($\delta\text{Eu} = 0.44\text{--}1.74$) and nearly positive Ce anomalies ($0.44\text{--}1.99$). The chondrite-normalized REE patterns of Px1 showed a relatively flat LREE segment and a left-leaning HREE segment (Figure 12b). On the whole, the REE patterns of Px1 were relatively flat.

Px2 had low total rare earth element ($\Sigma\text{REE} = 0.65\text{--}1.65$ ppm) contents and high fractionation between the light and heavy rare earth elements ($\text{LREE}/\text{HREE} = 0.38\text{--}1.18$), with variable positive Eu anomalies ($\delta\text{Eu} = 1.10\text{--}1.48$) and variable Ce anomalies ($0.22\text{--}1.12$). The chondrite-normalized REE patterns of Px2 showed a relatively right-leaning LREE segment and a relatively right-leaning HREE segment (Figure 12b).

Ilv1 had total rare earth element ($\Sigma\text{REE} = 5.22\text{--}44.29$ ppm) contents and low fractionation between the light and heavy rare earth elements ($\text{LREE}/\text{HREE} = 1.57\text{--}32.45$), with clearly positive Eu anomalies ($\delta\text{Eu} = 5.61\text{--}53.19$) and nearly positive Ce ($\delta\text{Ce} = 0.28\text{--}0.54$). The Chondrite-normalized REE patterns of Ilv1 showed a relatively flat LREE segment and HREE segment (Figure 12c).

Ilv2 had total rare earth element ($\Sigma\text{REE} = 0.71\text{--}18.34$ ppm) contents and high fractionation between the light and heavy rare earth elements ($\text{LREE}/\text{HREE} = 2.31\text{--}3.47$), with variable positive Eu anomalies ($\delta\text{Eu} = 2.41\text{--}3.70$) and nearly positive Ce anomalies ($\delta\text{Ce} = 0.25\text{--}0.76$). The Chondrite-normalized REE patterns of Ilv2 showed a steep right-leaning LREE segment and a flat HREE segment (Figure 12c).

Ilv3 had total rare earth element ($\Sigma\text{REE} = 7.44\text{--}8.43$ ppm) contents and high fractionation between the light and heavy rare earth elements ($\text{LREE}/\text{HREE} = 0.16\text{--}1.97$), with variable positive Eu anomalies ($\delta\text{Eu} = 0.73\text{--}1.95$) and nearly positive Ce anomalies ($\delta\text{Ce} = 0.46\text{--}0.50$). The Chondrite-normalized REE patterns of Ilv3 showed a relatively right-leaning LREE segment and a flat HREE segment (Figure 12c).

6. Discussion

6.1. Physicochemical Conditions

6.1.1. Fluid Properties

During the ore-forming processes in the skarn deposits, the mineral composition is sensitive to the changes in the hydrothermal fluid composition. Thus, the skarn minerals provide a continuous chemical record of the hydrothermal processes [29].

Grt1 in the prograde phase showed variations in composition and had andradite-rich cores with oscillatory zoning, reflecting a high prograde temperature [30] depletion in the HREE and variable Eu anomalies. The characteristics of the REEs from Grt1 and Px1 were similar to those resulting from REE partitioning in high-temperature fluids and silicate melts (relative enrichment of LREEs, depletion of HREEs, and variable Eu anomalies), implying that the ore-forming fluid in Stage 1 was derived from a magmatic–hydrothermal source [31,32]. This interpretation was confirmed by the abrupt compositional variations between the core and the rim that were interpreted as changes in the composition-dependent fluid influx [29,33].

In the magmatic–hydrothermal fluids, the Y and REEs and the Y and Ho had similar geochemical properties and showed linear correlations. The Niukutou Grt1 and Px1 samples from Stage 1 exhibited clear linear correlations between the REEs and Y and Ho (Figure 13a,b), likely indicating that there were insignificant changes in the fluid evolution, which could be interpreted as the result of the magmatic–hydrothermal source.

The Niukutou Grt2 and Px2 samples from Stage 2, however, showed insignificant correlations between the REEs and Y (Figure 13a,b), which could reflect either local prograde chemical heterogeneities or changes in the fluid composition during Stage 2 [18,34]. Moreover, the fractionation of the Y and Ho twin pairs from the chondritic ratio (Figure 13b) was an indication that Grt2/Px2 assemblage growth occurred in a complex hydrothermal fluid system [35,36]. Moreover, the unstable composition of the Stage 2 minerals may have

been due to their position in the upper part of the contact metamorphic belt, as they would have been affected by multiple-contact metasomatism.

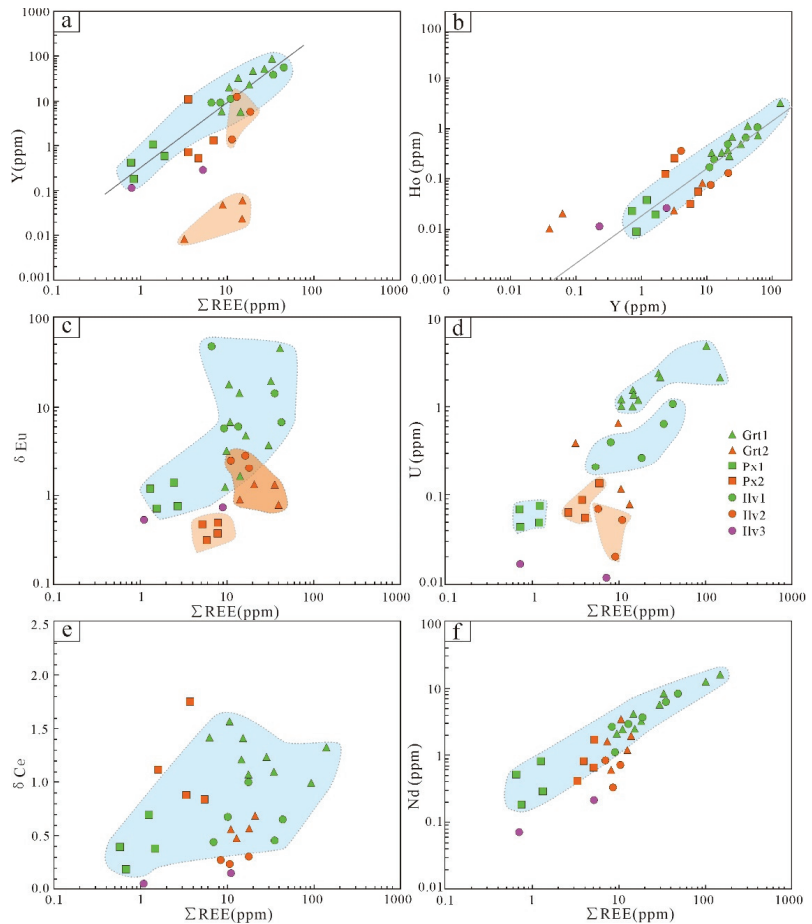


Figure 13. Binary plots of (a) Y versus total rare earth element (Σ REE), (b) Ho versus Y, (c) δ Eu versus Σ REE, (d) U versus Σ REE, (e) δ Ce versus Σ REE, (f) δ Ce versus Σ REE.

The representative quartz + sulfides and quartz + calcite veins that cut the johannsenite (Px3) mineral assemblages (Figures 6l and 7h) signify that the ore-forming fluid in Stage 3 was generated under low-temperature conditions after magnetite and pyrrhotite precipitation. Although Px3 was present in Stage 3, it had low Σ REE, Y, and Y/Ho contents and a high HFSE (high-field strength element) content, and this disparity resulted from the differences in the fluid composition and fluid flow rate [20].

In summary, the Grt1 and Px1 skarn mineral assemblages in Stage 1 resulted from a magmatic–hydrothermal source; the Grt2 and Px2 skarn minerals in Stage 2 may have been caused by a fluid system that was altered by either local protolith chemical heterogeneities or changes in the fluid composition, and the Px3 in Stage 3 may have been generated in a more complex environment with a more variable fluid composition and fluid flow rate.

6.1.2. Oxygen Fugacity
Prograde Metamorphic Phase

Generally, in a hydrothermal system, the $\text{Eu}^{3+}/\text{Eu}^{2+}$ distribution coefficients are essentially independent of the major cation chemistry of the solution, whereas for altrivalent substitutions, they are not. Thus, the δEu anomalies of the minerals can be used to evaluate the redox conditions of the fluid [18,32,37–43]. In addition, based on the similar ion radii and charge balances, reducing the $f\text{O}_2$ can reduce the solubility of U, which facilitates the entrance of U into the mineral crystal. Thus, the different U concentrations of the minerals could indicate the relative $f\text{O}_2$ of the fluid.

From Stage 1 to Stage 3, the δEu and U contents of the garnet and pyroxene gradually decreased (Figure 13c,d), indicating that the oxidizing ability of the environment decreased accordingly. Specifically, an oxidizing environment is favorable for the generation of magnetite. This interpretation is supported by the replacement of Grt1 with magnetite. Subsequently, with the decreasing $f\text{O}_2$, the environment of the ore-forming fluid became more reduced and thus favorable for the dissolution and precipitation of Pb-Zn sulfide minerals.

In addition, according to previous studies [44,45], we constructed a temperature- $\log f\text{O}_2$ phase diagram (Figure 14) of the Ca-Fe-Si-O-H-C system. The hydrothermal fluid system in Stage 1 (Grt1+Px1) had temperatures ranging from 400 to 470 °C, and $\log f\text{O}_2$ values ranging from -23.8 to -19. The simulated temperatures in Stages 2 and 3 were 410–440 and 340–400 °C, respectively, and the corresponding $\log f\text{O}_2$ values ranged from -23–19.5 to -27–23.5, respectively. Generally, these features reflect decreasing $f\text{O}_2$ and temperatures.

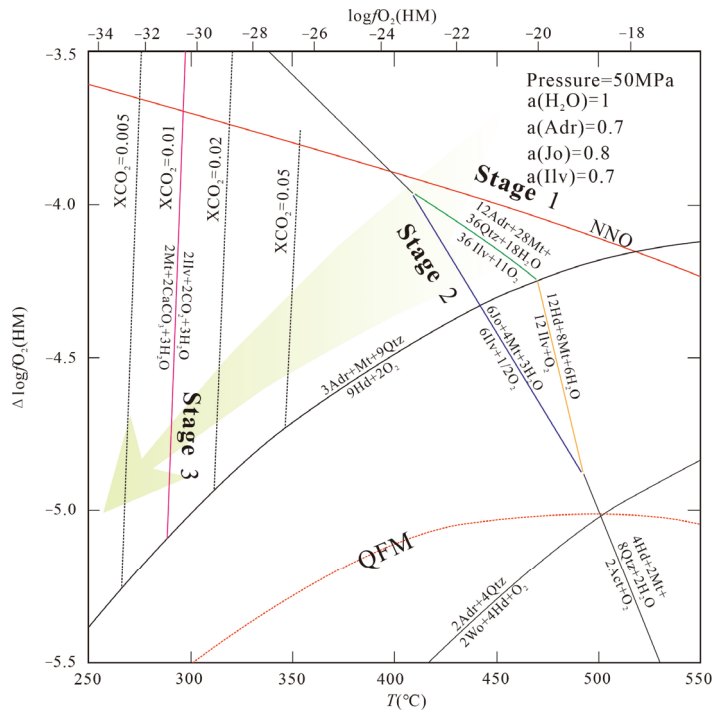


Figure 14. Temperature- $\log f\text{O}_2$ diagram for the Ca-Fe-Si-O-H-C system (modified from [44]). Reactions involving ilvaite are in bold; dotted red lines correspond to the indicated mineral buffer. The arrow indicates the postulated trajectory of $f\text{O}_2$ during skarn development.

Retrograde Metamorphic Phase

The three types of ilvaite in the retrograde metamorphic stage from the inside to the outside were successively distributed in the andradite–hedenbergite skarn belt (inner belt), the grossular–mangan–hedenbergite belt (middle belt), and the johannsenite skarn belt (outer belt). They correspond to three generations of a retrograde metamorphic stage.

From Ilv1 to Ilv3, the δEu and U contents were also decreasing (Figures 12c and 13d,e), indicating that the oxygen fugacity of mineralization was decreasing. With the decrease in oxygen fugacity, the ore-forming fluid environment rapidly decreased, ultimately facilitating the dissolution and precipitation of Pb and Zn elements.

6.1.2.3. pH

Prograde Metamorphic Phase

In addition to the fluid properties of a hydrothermal system, the temperature, cation type, and fluid density also play important roles in the pH of the fluid. Therefore, it is inappropriate to separately describe the pH based on the fluid composition [46]. Fortunately, the REEs and some immobile trace elements in hydrothermal fluids are scarcely affected in magmatic–hydrothermal fluids and pH is largely correlated with their total contents in the fluid [35,47]. It was demonstrated in [38] that LREE-depleted and HREE-enriched patterns with negative or no Eu anomalies form under nearly neutral pH, whereas LREE-enriched and HREE-depleted patterns develop under mildly acidic pH, and the Eu anomalies are positive or significantly controlled by the complexing agents (mainly F, Cl, and B). The Niukutou Grt1 crystals are characterized by an enrichment of LREEs and a depletion of HREEs and have mostly positive Eu anomalies, indicating a mildly acidic pH environment. In comparison, the Grt2 crystals show an enrichment of HREEs and a depletion of LREEs and negative or no Eu anomalies, suggesting nearly neutral pH conditions. The Px3 crystals have relatively more variable LREE/HREE ratios and Eu anomalies, suggesting a more neutral pH in Stage 3.

An investigation [47] of thermal fluids found that pH strongly controls the changes in the REE and Ce anomalies and shows negative correlations with the REEs and Ce. Moreover, theoretical and thermodynamic experiments have suggested that pH significantly affects the fractionation of REEs and Nd and that pH is negatively correlated with the REEs and Nd in hydrothermal fluids [38,48]. An early increasing trend followed by a decreasing trend for the REEs, Ce, and Nd contents from Stage 1 to Stage 3 (Figure 13e,f), indicates an increase in pH during the evolution of the Niukutou hydrothermal fluid.

These changes in pH suggest that the low acidic pH conditions in the early stages (Stage 1) were favorable for the enrichment and mineralization of Fe contents.

Retrograde Metamorphic Phase

From Ilv1 to Ilv3, the trace elements changed from being rich in LREEs, depleted in HREEs, and with a positive Eu anomaly to a variable LREE/HREE ratio and δEu anomaly. With the REEs, the Nd contents and δCe gradually increased, suggesting that the pH value of the fluid environment in the retrograde metamorphic phase gradually decreased.

6.2. Ore-Forming Fluid Evolution

The mineral assemblages of the Niukutou deposit and their geochemical characteristics may reflect the evolution of the hydrothermal fluid. Under a low degree of water–rock reactions in closed conditions, hydrothermal evolution is dominated by diffusion metasomatism, whereas under the conditions of open systems, the evolution is dominated by infiltration metasomatism [32]. The REEs and trace elements of skarn minerals can indicate the nature and evolution of ore-forming fluids [37,49].

The Niukutou Grt1/Px1 in Stage 1 exhibited low LILE and high HFSE and Y-Ho contents. The results suggested that Grt1 was formed under a relatively stable and closed environment with a low degree of water–rock reaction. In addition, the Grt1/Px1/Ilv1 system had a good crystal shape, indicating a slow rate of hydrothermal migration and

crystal growth. In combination with the linear correlation of the Y/REE and Y/Ho ratios, the chemical features suggested that the evolution of the ore-forming fluids produced magmatic–hydrothermal fluids. Based on the above information, we suggest that the generation of the Grt1/Px1 system was mainly via diffusive metasomatism.

Compared to Grt1/Px1, the Y, Ho, and HFSE contents of Grt2/Px2 showed a wide range, suggesting that these minerals were generated under the circumstances of exhumation from very high-grade conditions. Such dynamic and repetitive enrichment and depletion of composition require the fluid flow to have been episodic, possibly caused by periods of metasomatism between the hydrothermal fluid and the wall rocks [29].

Grt2/Px2 had poor crystal form, showed a depletion of LREEs and an enrichment of HREEs, and had variable Eu anomalies, all of which imply the addition of external fluids. The Y/REE and Y/Ho twin pairs from the chondritic ratios are indications that Grt2/Px2 growth occurred in a complex hydrothermal fluid system with a strong degree of water–rock action.

Additionally, evidence from the incomplete crystallization of Grt2/Px2 in Stage 2 showed that the upper skarn zoning developed with pervasive ore-guiding structures. Our results suggested an infiltrative metasomatism with the introduction of a batch of externally derived fluid.

The ilvaite coexisting with the garnet and pyroxene had similar REE patterns. For example, Ilv1 was consistent with the Grt1/Px1 assemblages due to the positive Ce and negative Eu anomalies. This evidence implies that retrograde ilvaite inherited prograde skarns during the hydrothermal process. Based on their coexisting mineral-associated relationships, we conclude that the replacement of prograde garnet/pyroxene probably accounts for the generation of ilvaite in the late phase.

6.3. Implications for Mineralization

As previously noted, the composition of Px1 and Px2 in the Niukutou deposit was johannsenite (Jo, 22%–65%), hedenbergite (31%–74%) and small amounts of diopside (3%–42%), and MnO (6.92%–19.44%), indicating Mn-rich mineral characteristics. In addition, the MnO contents of the Niukutou ilvaite were 1.78%–13.27%, which were higher than those in common ilvaite (Figure 9). Thus, we can infer that the Niukutou skarn is a manganese-type skarn. Many studies have shown that there are two skarn formations in the Qimantagh area, a calcium skarn and a manganese skarn; a calcium skarn generally forms iron polymetallic deposits and copper polymetallic deposits, whereas a manganese skarn forms Pb–Zn (Ag) deposits [45,50–57]. Skarns worldwide have similar characteristics.

In the ternary plot diagrams, it can be seen that the garnet and pyroxene composition plots in specific fields had almost the same range as the typical Pb–Zn skarn deposits in the Qimantagh area such as the Weibao and Sijiaoyang Pb–Zn skarn deposits. However, the Niukutou skarn deposit can be distinguished from these Fe and Cu skarns (Yemaquan and Kaerqueka) by its distinctive mineralogical characteristics and relatively wide range of garnet composition and Mn-rich mineralogical characteristics (Figure 15a,b). All these characteristics indicate that the Niukutou skarn deposit has the potential for Pb–Zn mineralization.

The evidence from the mineral geochemical characteristics showed that Grt1/Px1 in the Stage 1 zonation deposit occurred in the deepest layers with the highest fO_2 and temperatures and a low acidic pH. The skarn minerals were characterized by andradite and hedenbergite, and the mineralization was characterized by magnetite, pyrrhotite, and chalcopyrite.

Grt2/Px2 in the Stage 2 deposit in the middle part indicated moderate fO_2 and temperatures, an acidic to neutral composition, and a relatively higher pH. The skarn minerals were characterized by grossular features and Mn–Hd, whereas the mineralization was characterized by pyrrhotite, sphalerite, and galena.

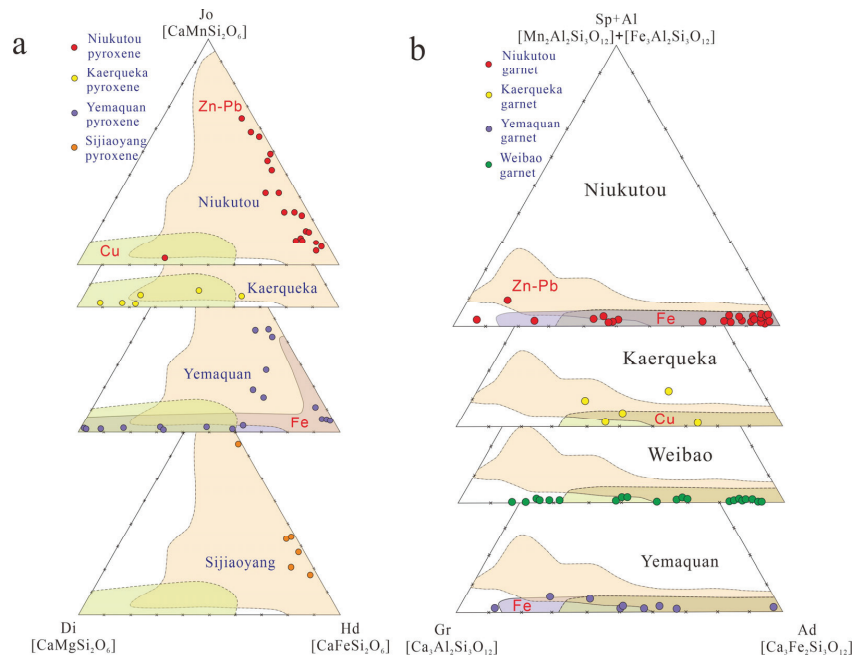


Figure 15. Ternary plots showing the end-member compositions of pyroxenes (a) and garnets (b) from the Niukutou deposit, Qimantagh area (modified after [7]). Data sources: Niukutou, this study; Kaerqueka, Hutouya, and Yemaquan from Feng et al. [21]; Sijiaoyang, [1,50]). Weibao, Kaerqueka, and Hutouya are typical Cu-Pb-Zn skarn deposits in the QMB, whereas Yemaquan and Sijiaoyang are Fe-Cu-Zn and Pb-Zn skarn deposits, respectively. The areas for global Cu, Fe, and Pb-Zn skarn deposits are from Meinert et al. [26]. End members: Jo—johannsenite, Di—diopside, Hd—hedenbergite, Ad—andradite, Gr—grossular, Sp—spessartine, Al—almandine.

The Ilv3 or johannsenite (Px3) deposits in the uppermost part showed low fO_2 and temperatures and had neutral pH compositions. The skarn minerals were characterized by manganilvaite and johannsenite, and the mineralization was characterized by sphalerite and galena.

According to the geochemical characteristics, Grt1/Px1 exhibited low LILE and high HFSE and Y-Ho contents, a strong linear correlation between the Y/REE and Y/Ho ratios, and good crystal shapes, indicating that the metasomatization of the Grt1/Px1 skarn zonation was primarily diffusive metasomatism near the ore-related pluton and that hydrothermal evolution occurred under closed conditions. The Grt2/Px2 deposits showed depletion of LREEs, enrichment of HREEs, and variable Eu anomalies, and the Y/REE and Y/Ho twin pairs deviated from the chondritic linear line and showed a wide range of compositions and incomplete crystallization of the minerals in Stage 2. These observations suggested that Stage 2 was dominated by infiltrative metasomatism. For an open system, this evolutionary interpretation is supported by the pervasive vertical fractures in the middle and upper parts of the skarn zonation.

The three mineral assemblages correspond to three skarn zonation, and these zonation sequences are characterized as follows, moving outward from the intruding granodiorite intrusion: Grt1+Px1+Ilv1 skarn—Grt2+Px2+Ilv2 skarn—Px3+Ilv3 skarn—marble. Fe-S-Cu ore bodies occurred in the Grt1+Px1 skarn, whereas Pb-Zn (or S) ore bodies mainly occurred in the Grt2+Px2+Ilv2 and Px3+Ilv3 skarns.

According to the spatial relationships and geochemical characteristics of the mineral assemblages, the ore-forming fluid evolution of the Niukutou deposit can be described as

follows: from Stage 1 to Stage 3, the hydrothermal fluid migration moved from the deep skarn-related plutons to the shallow skarn and marble, and the environment featured high fO_2 and temperatures to low fO_2 and temperatures and an increasing pH and Mn content (Figure 16). The three generations of ilvaites (Ilv1 to Ilv3) in the retrograde stage had the same characteristics of zonation and fluid evolution.

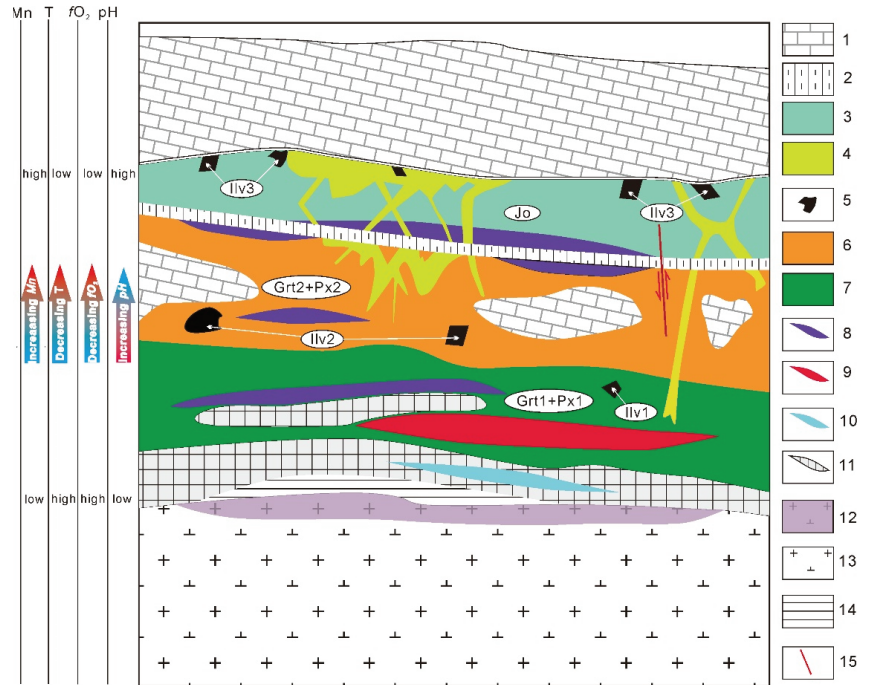


Figure 16. Profile showing the skarn zonation and evolution process of the ore-forming fluid in the Niukutou Pb-Zn skarn deposit: 1—Marble, 2—Siltstone, 3—Ilv3 + Px3 (johannsenite) skarn zonation, 4—epidote + chlorite skarn, 5—Ilvaite, 6—Grt2+Px2 skarn zonation, 7—Grt1+Px1 skarn zonation, 8—Pb-Zn ore body, 9—Fe ore body, 10—Cu ore body, 11—Pyrrhotite (S) ore body, 12—altered granodiorite pluton, 13—Granodiorite pluton, 14—Hornstone belt, and 15—Fault.

During the migration of the ore-forming fluid, magnetite, chalcopyrite, arsenopyrite, and pyrrhotite, all of which are high-temperature ore minerals, precipitated in Stage 1. The environment was favorable for the enrichment and mineralization of the Fe content [58,59]. Thus, permeability may eventually have been reduced, thereby obstructing the fluid channels [60–62]. Then, a strong pressure increase could have caused hydraulic fracturing when the hydrostatic pressure exceeded the lithostatic pressure. However, the permeability increased as fractures opened and the pressure decreased, and this, in turn, promoted mineral formation and likely created an open system for metasomatism in Stages 2 and 3.

In Stage 2, the environment changed from oxidizing conditions with a mildly acidic pH to relatively reducing conditions with a relatively neutral pH; subsequently, the Fe^{2+} and Mn^{2+} would precipitate to generate the mangan-hedenbergite. Additionally, due to the increasing pH, Al^{3+} precipitated to generate the grossular minerals. Furthermore, the environment was favorable for the precipitation of pyrrhotite and sphalerite. With the evolution of the hydrothermal fluid, the fluid became more reducing and neutral, the temperature became lower, and further enrichment in Mn occurred, leading to the highest MnO content in Stage 3 among the skarn minerals.

Similarly, from Ilv1 to Ilv3, the ore-forming environment rapidly declined. The reducing nature of the ore-forming fluid was beneficial to the deposition of the Pb-Zn complex and the precipitation and enrichment of the Mn-rich skarns; this may explain why the Pb-Zn ore bodies were closely associated with the Mn-rich skarns.

7. Conclusions

Based on the field geology, petrographic observations, and mineral geochemistry studies, the following conclusions were drawn:

(1) Three mineral assemblages in a prograde metamorphic phase and their corresponding mineralization stages were distinguished in the Niukutou deposit. From Stages 1 to 3, the temperature and fO_2 decreased, whereas the pH increased. The ilvaite (Ilv1 to Ilv3) in the retrograde metamorphic phase also indicate lower temperatures, decreased fO_2 , and lower pH.

(2) The metallogenic process in Stage 1 was primarily diffusive metasomatism under a low degree of water–rock reactions in the closed condition. The ore-forming fluid in Stages 2 and 3 may have experienced infiltrative metasomatism with the introduction of a batch of externally derived fluid.

(3) The Niukutou deposit belongs to a manganese skarn pattern, and the skarn zonation and mineral geochemical characteristics show that the hydrothermal fluid migrated from the deep plutons to the shallow marble. The environments evolved from high fO_2 and temperatures to low fO_2 and temperatures and showed increasing pH and Mn contents, ultimately resulting in the close association between the Pb-Zn ore bodies and Mn-rich skarns.

Supplementary Materials: The following supporting information can be downloaded at: <https://www.mdpi.com/article/10.3390/min13010018/s1>; Table S1: Electron microprobe analysis (%) of garnet from the Niukutou deposit; Table S2: Electron microprobe analysis (%) of pyroxene from the Niukutou deposit; Table S3: Electron microprobe analysis (%) of ilvaite from the Niukutou deposit; Table S4: Electron microprobe analysis (%) of epidote and chlorite from the Niukutou deposit; Table S5: The LA-ICP-MS in-situ microanalysis results of garnet, pyroxene and ilvaite in the Niukutou deposit.

Author Contributions: S.W., H.Z., Y.W. and X.Z. offered advice to this work; X.W., Y.W., X.Y. and X.Z. finished the field work; X.W. performed the experiments and organized this paper. All authors have read and agreed to the published version of the manuscript.

Funding: The research was funded by the National Key Research and Development Program of China (no. 2017YFC0601204, no. 2017YFC0601305, and no. 2017YFC0602403), and the Key Science and Technology Projects of China Copper Industry Co. (no. QHHXLCZYB007, QHHX-KZ-JF2020-001).

Data Availability Statement: The authors confirm that the data supporting the findings of this study are available with in the article (or its supplementary materials).

Acknowledgments: We thank Cai Yawei, Li Yan, and Yang Baoxia for providing access to the drill core, underground workings, and laboratories for sampling and experimental analyses. Additionally, many reviewers have provided numerous comments, which helped significantly improve the clarity and quality of this manuscript.

Conflicts of Interest: The authors declare no conflict of interest.

References

1. Feng, C.Y.; Wang, X.P.; Shu, X.F.; Zhang, A.K.; Xiao, Y.; Liu, J.N.; Ma, S.C.; Li, G.C.; Li, D.X. Isotopic Chronology of the Hutouya Skarn Lead-Zinc Polymetallic Ore District in Qimantage Area of Qinghai Province and Its Geological Significance. *J. Jilin Univ.* **2011**, *41*, 1806–1817. (In Chinese with English abstract)
2. Feng, C.Y.; Wang, S.; Li, G.C.; Ma, S.C.; Li, D.S. Middle to late Triassic granitoids in the Qimantage area, Qinghai Province, China: Chronology, geochemistry and metallogenic significances. *Acta Petrol. Sin.* **2012**, *28*, 665–678. (In Chinese with English abstract)
3. Mao, J.W.; Zhou, Z.H.; Feng, C.Y.; Wang, Y.T.; Zhang, C.Q.; Peng, H.J.; Yu, M. A preliminary study of the Triassic large-scale mineralization in China and its geodynamic setting. *Geol. China* **2012**, *39*, 1437–1471. (In Chinese with English abstract)

4. Wang, X.Y.; Zhu, X.Y.; Li, J.D.; Wang, Y.W.; Long, L.L.; Li, S.T.; Wu, J.R.; Cheng, X.Y.; Jiang, B.B. Genesis and geological significance of manganilvaite in the Niukutou deposit, Qinghai Province. *Acta Geol. Sin.* **2020**, *94*, 2279–2290. (In Chinese with English abstract)
5. Wang, X.Y.; Zhu, X.Y.; Li, J.D.; Wang, Y.W.; Jiang, B.B.; Wu, J.R.; Huang, X.K.; Zhao, Z.Y. Two stage magmatisms and their skarn-type mineralization in the Niukutou ore district, Qinghai Province. *Acta Petrol. Sin.* **2021**, *37*, 1567–1586.
6. Zhong, S.H.; Feng, C.; Seltmann, R.; Li, D. Middle Devonian volcanic rocks in the Weibao Cu–Pb–Zn deposit, East Kunlun Mountains, NW China: Zircon chronology and tectonic implications. *Ore Geol. Rev.* **2017**, *84*, 309–327. [CrossRef]
7. Zhong, S.H.; Feng, C.; Seltmann, R.; Dolgoplova, A.; Andersen, J.C.Ø.; Li, D.; Yu, M. Sources of fluids and metals and evolution models of skarn deposits in the Qimantagh metallogenic belt: A case study from the Weibao deposit, East Kunlun Mountains, northern Tibetan Plateau. *Ore Geol. Rev.* **2018**, *93*, 19–37. [CrossRef]
8. Gao, Y.B.; Li, W.Y.; Qian, B.; Li, K.; Li, D.S.; He, S.Y.; Zhang, Z.W.; Zhang, J.W. Geochronology, geochemistry and Hf isotopic compositions of the granitic rocks related with iron mineralization in Yemaquan deposit, East Kunlun, NW China. *Acta. Petrol. Sin.* **2014**, *30*, 1647–1665. (In Chinese with English abstract)
9. Yu, M.; Feng, C.Y.; Bao, G.Y.; Liu, H.C.; Zhao, Y.M.; Li, D.X.; Xiao, Y.; Liu, J.N. Characteristics and zonation of skarn minerals in Galinge iron deposit, Qinghai Province. *Miner. Depos.* **2013**, *32*, 55–76. (In Chinese with English abstract)
10. Yu, M.; Feng, C.Y.; Mao, J.W.; Santosh, M.; Zhu, Y.F.; Zhao, Y.M.; Li, D.X. The Qiman Tagh Orogen as a window to the crustal evolution in northern Tibetan Plateau. *Earth Sci. Rev.* **2017**, *167*, 103–123. [CrossRef]
11. Zhao, Y.M.; Tan, H.J.; Xu, Z.N.; Yuan, C.G.; Bi, C.S.; Zheng, R.L.; Li, D.X.; Sun, J.H. The calcic-skarn iron ore deposits of Makeng type in southwestern Fujian. *Bull. Inst. Miner. Depos. Chin. Acad. Geol. Sci. (Album)* **1983**, *1*, 1–141. (In Chinese with English abstract)
12. Zhong, S.H.; Feng, C.; Seltmann, R.; Li, D.; Dai, Z. Geochemical contrasts between Late Triassic ore-bearing and barren intrusions in the Weibao Cu–Pb–Zn deposit, East Kunlun Mountains, NW China: Constraints from accessory minerals (zircon and apatite). *Miner. Depos.* **2018**, *53*, 855–870. [CrossRef]
13. Zhong, S.H.; Feng, C.; Seltmann, R.; Li, D.; Qu, H. Can magmatic zircon be distinguished from hydrothermal zircon by trace element composition? The effect of mineral inclusions on zircon trace element composition. *Lithos* **2018**, *314–315*, 646–657. [CrossRef]
14. Jian, R.T.; Zhao, X.K.; Yang, F.; Li, J.D.; Wu, J.R. New progress in prospecting for Niukutou iron polymetallic deposit, Qinghai. *Acta Mineral. Sin.* **2017**, *34*, 821–823. (In Chinese with English abstract)
15. Li, J.D.; Wang, X.Y.; Zhu, X.Y.; Wu, J.R.; Cai, Y.W.; Li, Y.; Guo, T.J.; Jiang, B.B. Finding and significance of ilvaite in the Qimantag area—with the example of Niukutou lead and zinc deposit. *Min. Explor.* **2019**, *10*, 1550–1558. (In Chinese with English abstract)
16. Li, J.D.; Wang, X.Y.; Zhu, X.Y.; Wu, J.R.; Cai, Y.W.; Li, Y.; Guo, T.J.; Jiang, B.B. The preliminary discussion of the Hercynian metallogenic period in Qimantag area—with the example of Niukutou lead and zinc deposit. *Min. Explor.* **2019**, *10*, 1775–1783. (In Chinese with English abstract)
17. Zhao, X.K.; Jian, R.T.; Yu, C.; Yang, F.; Li, J.D. Geological Characteristics and Prospecting Indicators of Niukutou Fe–Pb–Zn Polymetallic Deposit in Qinghai Province. *Mor. Min.* **2018**, *585*, 10–16. (In Chinese with English abstract)
18. Gaspar, M.; Meinert, L.D.; Moretti, R. REE in skarn systems: A LA-ICP-MS study of garnets from the Crown Jewel gold deposit. *Geochim. Cosmochim. Acta* **2008**, *72*, 185–205. [CrossRef]
19. Zhai, D.G.; Liu, J.J.; Zhang, H.Y.; Wang, J.P.; Su, L.; Yang, X.A.; Wu, S.H. Origin of oscillatory zoned garnets from the Xieertala Fe–Zn skarn deposit, northern China: In situ LA-ICP-MS evidence. *Lithos* **2014**, *190*, 279–291. [CrossRef]
20. Baghban, S.; Hosseinzadeh, M.; Moayyed, M.; Mokhtari, A.A.; Gregory, D.D. Geology, mineral chemistry and formation conditions of calc-silicate minerals of Astamal Fe–LREE distal skarn deposit, Eastern Azarbaijan province, NW Iran. *Ore Geol. Rev.* **2015**, *68*, 79–96. [CrossRef]
21. Feng, C.Y.; Yu, M.; Li, D.X.; Li, G.C.; Zhou, A.S.; Li, X. Fluid inclusion geochemistry of Bashierxi tungsten-tin deposit in Qimantag area, Xinjiang. *Miner. Depos.* **2013**, *32*, 20–36. (In Chinese with English abstract)
22. Gao, Y.B. The Intermediate-Acid Intrusive Magmatism and Mineralization in Qimantag, East Kunlun Mountains. Ph.D. Thesis, Chang’an University, Xi’an, China, 2013.
23. Lu, Y.F. Geokit: Geochemical software package built by VBA. *Geochemistry* **2004**, *33*, 459–464. (In Chinese with English abstract)
24. Brandelik, A. CALCMIN—an EXCEL™ Visual Basic application for calculating mineral structural formulae from electron microprobe analyses. *Comput. Geosci.* **2009**, *35*, 1540–1551. [CrossRef]
25. Meinert, L.D. Skarns and skarn deposits. *Geosci. Can.* **1992**, *19*, 145–162.
26. Meinert, L.D.; Dipple, G.M.; Nicolescu, S. World skarn deposits. *Econ. Geol. 100th Anniv. Vol.* **2005**, 299–336. [CrossRef]
27. Bonev, I.K.; Vassileva, R.D.; Zotov, N.; Kouzmanov, K. Manganilvaite, $\text{CaFe}^{2+}\text{Fe}^{3+}(\text{Mn}, \text{Fe}^{2+})(\text{Si}_2\text{O}_7)\text{O}(\text{OH})$, a new mineral of the ilvaite group from Pb–Zn skarn deposits in the Rhodope Mountains, Bulgaria. *Can. Mineral.* **2005**, *43*, 1027–1042. [CrossRef]
28. Sun, S.S.; McDonough, W.F. Chemical and isotopic systematic of oceanic basalts: Implications for mantle composition and processes. *Geol. Soc. Lond. Spec. Publ.* **1989**, *42*, 313–345. [CrossRef]
29. Jamtveit, B.; Wogelius, R.A.; Fraser, D.G. Zonation patterns of skarn garnets: Records of hydrothermal system evolution. *Geology* **1993**, *21*, 113–116. [CrossRef]
30. Dietvorst, E.J.L. Retrograde garnet zoning at low pressure in metapelitic rocks from kemio, SW Finland. *Contrib. Mineral. Petrol.* **1982**, *79*, 37–45. [CrossRef]

31. Flynn, R.T.; Burnham, C.W. An experimental determination of rare earth partition coefficients between a chloride containing vapor phase and silicate melts. *Geochim. Cosmochim. Acta*. **1978**, *42*, 685–701. [CrossRef]
32. Park, C.P.; Song, Y.G.; Kang, I.M.; Shim, J.; Chung, D.H.; Park, C.S. Metasomatic changes during periodic fluid flux recorded in grandite garnet from the Weondong W-skarn deposit, South Korea. *Chem. Geol.* **2017**, *451*, 135–153. [CrossRef]
33. Jamtveit, B.; Hervig, R.L. Constraints on transport and kinetics in hydrothermal systems from zoned garnet crystals. *Science* **1994**, *263*, 505–508. [CrossRef] [PubMed]
34. Wood, S.A. The geochemistry of rare earth elements and yttrium in geothermal waters. *Spec. Publ. Soc. Econ. Geol.* **2003**, *10*, 133–158.
35. Bau, M. Controls on the fractionation of isovalent trace elements in magmatic and aqueous systems: Evidence from Y/Ho, Zr/Hf, and lanthanide tetrad effect. *Contrib. Mineral. Petrol.* **1996**, *123*, 323–333. [CrossRef]
36. Anders, M.; Grevesse, N. 1989. Abundances of the elements: Meteoritic and solar. *Geochim. Cosmochim. Acta* **1989**, *53*, 197–214. [CrossRef]
37. Xiao, X.; Zhou, T.F.; White, N.C.; Zhang, L.J.; Fan, Y.; Wang, F.Y.; Chen, X.F. The formation and trace elements of garnet in the skarn zone from the Xinqiao Cu-S-Fe-Au deposit, Tongling ore district, Anhui province, Eastern China. *Lithos* **2018**, *302*, 467–479. [CrossRef]
38. Bau, M. Rare-earth element mobility during hydrothermal and metamorphic fluid–rock interaction and the significance of the oxidation state of europium. *Chem. Geol.* **1991**, *93*, 219–230. [CrossRef]
39. Sverjensky, D.M. Europium redox equilibria in aqueous solution. *Earth Planet. Sci. Lett.* **1984**, *67*, 70–78. [CrossRef]
40. Van Westernen, W.; Allan, N.L.; Blundy, J.D.; Purton, J.A.; Wood, B.J. Atomistic simulation of trace element incorporation into garnets—comparison with experimental garnet–melt partition data. *Geochim. Cosmochim. Acta* **2000**, *64*, 1629–1639. [CrossRef]
41. Smith, M.P.; Henderson, P.; Jeffries, T.E.R.; Long, J.; Williams, C.T. The rare earth elements and uranium in garnets from the Beinn an Dubhaich Aureole, Skye, Scotland, UK: Constraints on processes in a dynamic hydrothermal system. *J. Petrol.* **2004**, *45*, 457–484. [CrossRef]
42. Zhong, S.H.; Seltmann, R.; Shen, P. Two different types of granitoids in the Suyunhe large porphyry Mo deposit, NW China and their genetic relationships with molybdenum mineralization. *Ore Geol. Rev.* **2017**, *88*, 116–139. [CrossRef]
43. Zhong, S.H.; Seltmann, R.; Qu, H.; Song, Y. Characterization of the zircon Ce anomaly for estimation of oxidation state of magmas: A revised Ce/Ce* method. *Mineral. Charact. Petrol.* **2019**, *113*, 755–763. [CrossRef]
44. Delgado, J.; Soler, A. Ilvaite stability in skarns from the northern contact of the Maladeta batholith, Central Pyrenees (Spain). *Eur. J. Mineral.* **2010**, *22*, 363–380.
45. Yu, M. Metallogenic Mechanism of the Galinge Polymetallic Iron Skarn Deposit, Qimantagh Mountains, Qinghai Province. Ph.D. Thesis, Peking University, Beijing, China, 2017.
46. Dziggel, A.; Wul, K.; Kolb, J.; Meyer, F.M.; Lahaye, Y. Significance of oscillatory and bell-shaped growth zoning in hydrothermal garnet: Evidence from the Navachab gold deposit, Namibia. *Chem. Geol.* **2009**, *262*, 262–276. [CrossRef]
47. Inguaggiato, C.; Censi, P.; Zuddas, P.; Londoño, J.M.; Chacón, Z.; Alzate, D.; Brusca, L.; D’Alessandro, W. Geochemistry of REE, Zr and Hf in a wide range of pH and water composition: The Nevado del Ruiz volcano-hydrothermal system (Colombia). *Chem. Geol.* **2015**, *417*, 125–133. [CrossRef]
48. Michard, A. Rare earth element systematics in hydrothermal fluids. *Geochim. Cosmochim. Acta.* **1989**, *53*, 745–750. [CrossRef]
49. Peng, H.J.; Zhang, C.Q.; Mao, J.W.; Santosh, M.; Zhou, Y.M.; Houe, L. Garnets in porphyry–skarn systems: A LA-ICP-MS, fluid inclusion, and stable isotope study of garnets from the Hongni–Hongshan copper deposit, Zhongdian area, NW Yunnan Province, China. *J. Asian Earth Sci.* **2015**, *103*, 229–251. [CrossRef]
50. Feng, C.Y.; Zhao, Y.M.; Li, D.X.; Liu, J.N.; Xiao, Y.; Li, G.C.; Ma, S.C. Skarn types and mineralogical characteristics of the Fe-Cu-polymetallic Skarn deposits in the Qimantage area, western Qinghai Province. *Acta. Geol. Sin.* **2011**, *85*, 1108–1115. (In Chinese with English abstract)
51. Zhao, Y.M.; Lin, W.W.; Bi, C.S.; Li, D.X.; Jiang, C.J. *Skarn Deposits in China*; Beijing: Geological Publishing House: Beijing, China, 1990; pp. 1–354. (In Chinese with English abstract)
52. Zhao, Y.M.; Feng, C.Y.; Li, D.X.; Liu, J.N.; Xiao, Y.; Yu, M.; Ma, S.C. Metallogenic setting and mineralization-alteration characteristics of major skarn Fe-polymetallic deposits in Qimantag area, western Qinghai Province. *Miner. Depos.* **2013**, *32*, 1–19. (In Chinese with English abstract)
53. Li, D.X.; Feng, C.Y.; Zhao, Y.M.; Li, Z.F.; Liu, J.N.; Xiao, Y. Mineralization and alteration types and skarn mineralogy of Kaerqueka copper polymetallic deposit in Qinghai Province. *J. Jilin Univ.* **2011**, *41*, 1818–1830. (In Chinese with English abstract)
54. Liu, J.N.; Feng, C.Y.; Zhao, Y.M.; Li, D.X.; Xiao, Y.; Zhou, J.H.; Ma, Y.S. Characteristics of intrusive rock, metasomatites, mineralization and alteration in Yemaquan skarn Fe-Zn-polymetallic deposit, Qinghai Province. *Miner. Depos.* **2013**, *32*, 77–93. (In Chinese with English abstract)
55. Ma, S.C.; Feng, C.Y.; Zhang, D.J.; Shu, X.F.; Liu, J.N.; Du, S.J. Alteration and mineralization zoning of Hutouya polymetallic deposit in Qimantage area, Qinghai Province. *Miner. Depos.* **2013**, *32*, 109–121. (In Chinese with English abstract)
56. Xiao, Y.; Feng, C.Y.; Liu, J.N.; Yu, M.; Zhou, J.H.; Li, D.X.; Zhao, Y.M. LA-MC-ICPMS zircon U-Pb dating and sulfur isotope characteristics of Kendekeke Fe-polymetallic deposit, Qinghai Province. *Miner. Depos.* **2013**, *32*, 177–186. (In Chinese with English abstract)

57. Wang, S.; Feng, C.Y.; Li, S.J.; Jiang, J.H.; Li, D.S.; Su, B.S. Zircon SHRIMP U-Pb dating of granodiorite in the Kaerqueka polymetallic ore deposit, Qimantage Mountain, Qinghai Province, and its geological implications. *Geol. China* **2009**, *36*, 74–84. (In Chinese with English abstract)
58. Hu, H.; Li, J.W.; Lentz, D.; Ren, Z.; Zhao, X.F.; Deng, X.D.; Hall, D. Dissolution -reprecipitation process of magnetite from the Chengchao iron deposit: Insights into ore genesis and implication for in-situ chemical analysis of magnetite. *Ore Geol. Rev.* **2014**, *57*, 393–405. [CrossRef]
59. Sun, Z.Y.; Wang, J.B.; Wang, Y.W.; Long, L.L. Geochemical Characteristics of Mineral Assemblages from the Yamansu Iron Deposit, NW China, and Their Metallogenic Implications. *Minerals* **2020**, *39*, 39. [CrossRef]
60. Zhang, Y.; Shao, Y.J.; Zhang, R.Q.; Li, D.F.; Liu, Z.F.; Chen, H.Y. Dating Ore Deposit Using Garnet U–Pb Geochronology: Example from the Xinqiao Cu–S–Fe–Au Deposit, Eastern China. *Minerals* **2018**, *8*, 31. [CrossRef]
61. Kolb, J. The role of fluids in partitioning brittle deformation and ductile creep in auriferous shear zones between 500 and 700 °C. *Tectonophysics* **2008**, *446*, 1–15. [CrossRef]
62. Sun, Z.Y.; Wang, J.B.; Wang, Y.W.; Long, L.L.; Hu, Q.T.; Wang, M.L.; Li, D.D.; Xie, H.J. Two generations of garnets and their relevance for the hydrothermal fluid evolution of the Hongyuntan deposit, NW China. *Ore Geol. Rev.* **2022**, *122*, 103513. [CrossRef]

Disclaimer/Publisher’s Note: The statements, opinions and data contained in all publications are solely those of the individual author(s) and contributor(s) and not of MDPI and/or the editor(s). MDPI and/or the editor(s) disclaim responsibility for any injury to people or property resulting from any ideas, methods, instructions or products referred to in the content.

Article

Origin of Zn-Pb Mineralization of the Vein Bt23C, Bytíz Deposit, Příbram Uranium and Base-Metal Ore District, Czech Republic: Constraints from Occurrence of Immiscible Aqueous–Carbonic Fluids

Jana Ulmanová¹, Zdeněk Dolníček¹, Pavel Škácha^{1,2} and Jiří Sejkora^{1,*}

¹ Department of Mineralogy and Petrology, National Museum, Cirkusová 1740, 193 00 Prague 9, Czech Republic; jana.ulmanova@nm.cz (J.U.); zdenek.dolnicek@nm.cz (Z.D.); skachap@seznam.cz (P.Š.)

² Mining Museum Příbram, Hynka Kličky Place 293, 261 01 Příbram VI, Czech Republic

* Correspondence: jiri.sejkora@nm.cz

Abstract: The mineralogical, fluid inclusion, and stable isotope (C, O) study was conducted on a Late Variscan Zn-Pb vein Bt23C, Příbram uranium and base-metal district, Bohemian Massif, Czech Republic. The vein is hosted by folded Proterozoic clastic sediments in exo-contact of a Devonian-to-Lower-Carboniferous granitic pluton. Siderite, dolomite-ankerite, calcite, quartz, baryte, galena, sphalerite, V-rich mica (roscoelite to an unnamed V-analogue of illite), and chlorite (chamosite) form the studied vein samples. The banded texture of the vein was modified by the episodic dissolution of earlier carbonates and/or sphalerite. Petrographic, microthermometric, and Raman studies of fluid inclusions proved a complicated fluid evolution, related to the activity of aqueous fluids and to an episode involving an aqueous–carbonic fluid mixture. Homogenization temperatures of aqueous inclusions decreased from ~210 to ~50 °C during the evolution of the vein, and salinity varied significantly from pure water up to 27 wt.% NaCl eq. The aqueous–carbonic fluid inclusions hosted by late quartz show highly variable phase compositions caused by the entrapment of accidental mixtures of a carbonic and an aqueous phase. Carbonic fluid is dominated by CO₂ with minor CH₄ and N₂, and the associated aqueous solution has a medium salinity (6–14 wt.% NaCl eq.). The low calculated fluid δ¹⁸O values (−4.7 to +3.6‰ V-SMOW) suggest a predominance of surface waters during the crystallization of dolomite-ankerite and calcite, combined with a well-mixed source of carbon with δ¹³C values ranging between −8.2 and −10.5‰ V-PDB. The participation of three fluid endmembers is probable: (i) early high-temperature high-salinity Na>Ca-Cl fluids from an unspecified “deep” source; (ii) late low-salinity low-temperature waters, likely infiltrating from overlying Permian freshwater partly evaporated piedmont basins; (iii) late high-salinity chloridic solutions with both high and low Ca/Na ratios, which can represent externally derived marine brines, and/or local shield brines. The source of volatiles can be (i) in deep crust, (ii) from interactions of fluids with sedimentary wall rocks and/or (iii) in overlying Permian piedmont basins containing, in places, coal seams. The event dealing with heterogeneous CO₂-bearing fluids yielded constraints on pressure conditions of ore formation (100–270 bar) as well as on the clarification of some additional genetic aspects of the Příbram’s ores, including the reasons for the widespread dissolution of older vein fill, the possible re-cycling of some ore-forming components, pH changes, and occasionally observed carbon isotope shift due to CO₂ degassing.

Citation: Ulmanová, J.; Dolníček, Z.; Škácha, P.; Sejkora, J. Origin of Zn-Pb Mineralization of the Vein Bt23C, Bytíz Deposit, Příbram Uranium and Base-Metal Ore District, Czech Republic: Constraints from Occurrence of Immiscible Aqueous–Carbonic Fluids. *Minerals* **2024**, *14*, 87. <https://doi.org/10.3390/min14010087>

Academic Editors: Changqing Zhang and Yitian Wang

Received: 23 November 2023

Revised: 6 January 2024

Accepted: 9 January 2024

Published: 11 January 2024



Copyright: © 2024 by the authors. Licensee MDPI, Basel, Switzerland. This article is an open access article distributed under the terms and conditions of the Creative Commons Attribution (CC BY) license (<https://creativecommons.org/licenses/by/4.0/>).

Keywords: Příbram uranium and base-metal district; Zn-Pb vein mineralization; fluid inclusions; stable isotopes; Ca–Na–Cl brines; carbonic inclusions; immiscible fluids; basinal fluids

1. Introduction

The Příbram ore area consists of two principal districts comprising the Late Variscan uranium and base-metal vein mineralizations: the westward lying Březové Hory ore

district, where base-metal mineralization prevails over uranium ores, and the eastward Příbram uranium and base-metal district, where uranium ores predominate (Figure 1). The Příbram uranium and base-metal district is the most important hydrothermal vein-type uranium deposit in the Czech Republic and one of the largest vein-type uranium deposits worldwide. About 50,000 tons of U were mined out there during 40+ years of post-WWII exploitation (1948–1991), and the parallel extraction of base metals and silver yielded more than 6000 t Pb, 2400 t Zn and 28 t Ag [1]. The Příbram uranium and base-metal district consists of 9 individual ore deposits containing 20 vein clusters with more than 2500 hydrothermal veins within an area of 40×20 km.

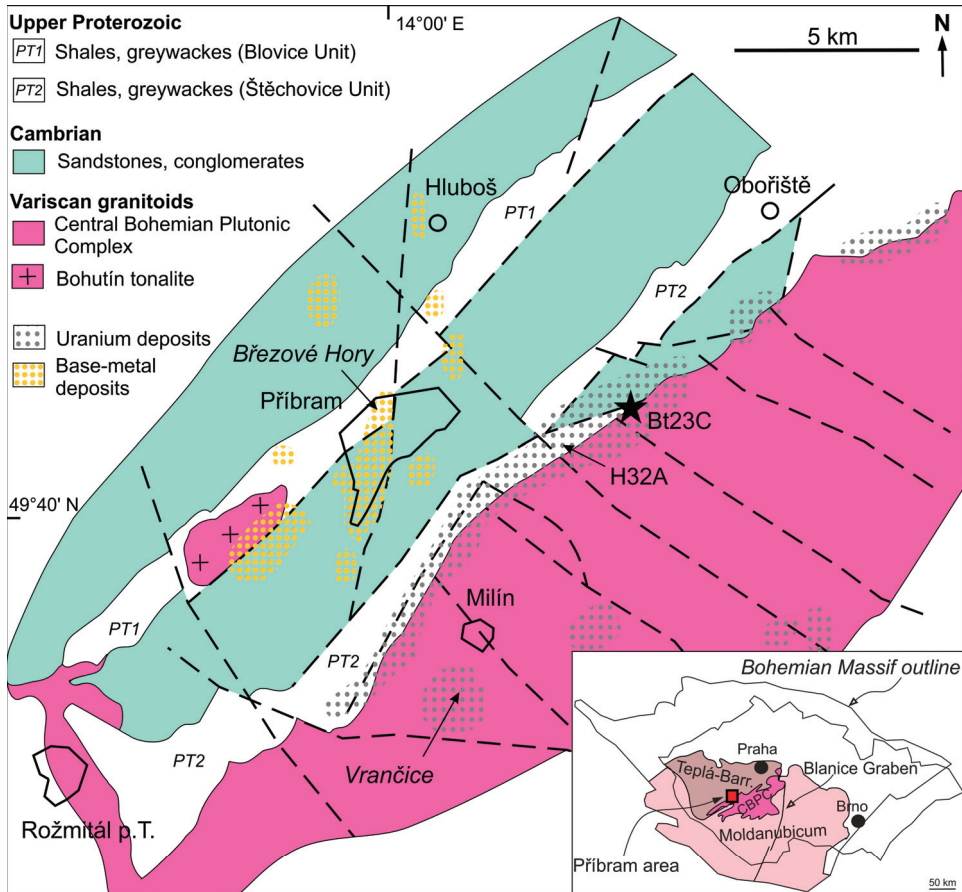


Figure 1. Geological position of the Příbram ore area, studied vein Bt23C, and sites mentioned in the text (modified from [2]).

Despite its economic significance, only a very limited amount of modern genetic data is available for this ore district, including the fluid inclusion studies. To date, only three works deal with investigation of fluid inclusions in the Příbram ore area. The most comprehensive study by [2] was based on the investigation of 30 specimens, originated mostly from the base-metal deposits. Only six samples (formed exclusively by calcite) of their dataset were sourced from uranium deposits. Two additional samples from base-metal deposits were studied in the bachelor thesis by [3]. Both works reported exclusively aqueous fluid inclusions without any volatile gases in concentrations detectable by microthermometric

measurements; Raman analysis of gas bubbles of L + V fluid inclusions was not applied. The most recent paper by [4] was focused on the base-metal vein H32A, Háje deposit, Příbram uranium and base-metal district. That study confirmed the predominance of gases-absent aqueous inclusions, but traces of CO₂, CH₄, and N₂ were identified by Raman analysis of vapour bubbles in a small part of aqueous inclusions. These gases occurred in various mutual proportions across the whole paragenesis of the vein H32A except of late calcite. The total amount of gases was always very low, as in none of the studied inclusions was the formation of clathrate or the liquid-vapour phase equilibria in gas bubbles observed during microthermometry.

In this contribution, we present new evidence on the occurrence of gases in the fluids giving rise to Příbram's base-metal mineralization. In the studied Zn-Pb mineralization of the vein Bt23C, we found aqueous fluid inclusions containing volatile gases in high concentrations allowing for the formation of clathrate or the heterogenization of a non-aqueous phase during cooling as well as fluid inclusions exclusively formed by a non-aqueous phase (i.e., carbonic inclusions). Such fluid inclusions were not previously reported from any other vein in the whole Příbram ore area. The detailed study of this fluid event allowed us to precisely characterize P-T conditions of vein formation, which were poorly constrained up to date. The source of some fluid components was checked by the carbon and oxygen isotope study of carbonates and quartz. Moreover, we have discussed some additional genetic consequences resulting from the recognition of activity of such gas-enriched fluids in the Příbram ore district.

2. Background

2.1. Geological Setting

The Příbram area is located in the core part of the Bohemian Massif (Figure 1), which belongs to the Central European Variscides consolidated during the Variscan Orogeny at the end of Palaeozoic. The ore deposits are situated in metasedimentary rocks of the Teplá-Barrandian Unit in exo-contact of the Central Bohemian Plutonic Complex (CBPC). The Teplá-Barrandian Unit comprises several mutually tectonically separated crustal blocks formed by Neo-Proterozoic rocks with different pre-Variscan tectono-metamorphic evolution, magmatic history and provenance. The folded Proterozoic rocks are covered by volcano-sedimentary sequences of the Barrandian Palaeozoic, which originated during the Cambrian to Devonian [5–10]. The crust-scale [11] tectonic contact between the Teplá-Barrandian and the Moldanubian units was intruded by the CBPC in the Uppermost Devonian-to-Lower Carboniferous (~354–336 Ma; [12–15]). The CBPC is dominated by various types of granitic rocks with subordinate bodies of quartz diorites, durbachites, and gabbros. The end of Variscan orogenic processes was followed by a collapse of the orogen associated with fault segmentation of the basement, its uplift, and rapid erosion [11]. The early post-orogenic evolution also comprised the moulding of piedmont basins, which were filled up by predominantly clastic freshwater molasse of the Uppermost Carboniferous-to-Lower Permian age [16–18]. However, most of these Upper Palaeozoic sediments were eroded during the Mesozoic and Tertiary, with negligible preserved relics being preserved only today (Blanice Graben in inset of Figure 1).

The studied area is situated in contactly metamorphosed Upper-Proterozoic marine siliciclastic sediments of the Dobříš series forming a large anticline structure. There are five sequences of sedimentary rocks within the Dobříš series differing in the content of siltstones, mudstones, conglomerates, and sandstones [19]. The so-called conglomerate-sandstone P2 succession hosts the base-metal ore bodies of the vein Bt23C. The facially very variable character of the rocks with prevailing sandstone and siltstone layers, elongated lenses of conglomerates and thin tuffite interbeds are typical for this series. The overlying volcano-sedimentary sequence of the Barrandian Palaeozoic is represented by Cambrian marine clastic sediments (mainly graywackes and siltstones) in the Příbram ore area (Figure 1). The whole sedimentary sequence is intruded by two populations of dykes of magmatic rocks. The first group is represented by “diabase” (=strongly hydrothermally altered palaeobasalt)

dykes, which are older than Variscan granites of the CBPC. The second group comprises porphyres, porphyrites, lamprophyres, aplites, and pegmatites, which are younger than granites and occur commonly either in granitic rocks, or in the close exo-contact of the CBPC [19].

2.2. Ore Mineralization of the Příbram Area

The earliest ore mineralization recognized in the Příbram ore area comprises rare Au-bearing coulisse-arranged quartz veins. Quartz gangue with minor carbonates, chlorite, and illite-muscovite hosts high-fineness gold associated with arsenopyrite and Bi-tellurides [20]. The Au contents reach up to 100 g/t. Origin of this early mineralization was bound to progressive cooling (300–400 °C at the beginning, ca. 180 °C at the end) of low-salinity (1.2 to 7.0 wt.% NaCl eq.) aqueous solutions, which were likely generated during thermal alteration of host Proterozoic sediments caused by intrusion of the CBPC [20]. A significant mineralogical reworking of early gold mineralization can occur in places where younger base-metal veins crosscut the Au-bearing veins, mainly due to input of base metals, Ag, and Sb [20].

The superimposed steep N–S to NW–SE striking ore veins are mainly hosted by the Upper Proterozoic or Cambrian sediments and partly follow the dykes of hydrothermally strongly altered “diabases”. The paragenetic situation is largely similar in both uranium and base-metal districts of the Příbram ore area, although significant differences can occur locally. Previous studies have invariably emphasized the complicated multi-stage evolution of vein ore deposits in the Příbram area, typically with 7 to 15 respective hypogene mineralization (sub)stages [4,21–23]. These features are associated with the position of the ore area near the crust-scale tectonic structure [11]. Four major mineralization stages were recognized in the Příbram area: the earliest siderite-sulphidic, calcite, calcite-uraninite and the latest calcite-sulphidic. In the longitudinal direction from SW to NE, the extent of the younger mineralization stages grows at the expense of the older ones [19]. The mineralization is very rich, with more than 300 mineral species described from the Příbram area [24]. The Fe-poor sphalerite, galena, pyrite, minerals of the tetrahedrite group, and locally also Ag–Pb–Sb, Pb–Sb, and/or Ag–Cu–Sb sulphosalts are the typical ore minerals of the base-metal mineralization. The ore minerals are usually hosted by carbonate (siderite, dolomite-ankerite, and most commonly calcite), less frequently quartz, and/or baryte gangue. The uranium mineralization consists especially of uraninite, less frequently coffinite and/or U-bearing anthraxolite, which are hosted by a multi-phase calcite vein.

The poly-phase nature of the Příbram uranium and base-metal mineralizations is also confirmed by available geochronological data, which suggest long-lasting hydrothermal activity from the Lower Carboniferous to the Triassic [25–27]. The biotite Ar–Ar cooling ages of CBPC magmatites and associated dyke rocks constrained the uppermost possible age of the early base-metal mineralization at 336–338 Ma [25]. The Rb–Sr dating of siderite and sphalerite from the earliest siderite-sulphidic stage gave age of 330 ± 4 Ma [26]. The U–Pb dating of uraninite from the superimposed calcite-uraninite stage yielded Permian dates 275 ± 4 and 278 ± 4 Ma [27], which well agree with results obtained by K–Ar dating of associated micas (274 ± 7 and 268 ± 7 Ma) [26]. Finally, the Rb–Sr dating of sphalerite and associated calcite and dolomite from the late post-uranium sulphidic mineralization gave ages 276 ± 3 Ma and 224 ± 3 Ma, respectively [26].

The previous fluid inclusion and stable isotope studies showed that the early Pb–Zn mineralization of the siderite-sulphidic stage from the Březové Hory district has formed from exclusively aqueous fluids featured by high temperatures (250–300 °C), high salinities (14–23 wt.% NaCl eq.), and highly positive $\delta^{18}\text{O}$ values (6‰–10‰ V-SMOW). The source of these fluids is interpreted in a deep circulation in the hot crustal rocks [2]. The origin of reduced sulphur with calculated $\delta^{34}\text{S}$ values –5 to –8‰ V-CDT is sought in the host rocks. A decrease in fluid temperature (to ~60 °C), fluid $\delta^{18}\text{O}$ values (2‰–6‰ V-SMOW), and fluid salinities (3–10 wt.% NaCl eq.) characterize late stages of early Pb–Zn mineralization with dolomite, calcite, and baryte gangue. The superimposed uranium mineralization formed

from low-salinity (<5 wt.% NaCl eq.), low-temperature (<150 °C), near-zero $\delta^{18}\text{O}$ (−3 to 3‰ V-SMOW) aqueous fluids, which were dominated by surface waters experiencing only shallowly seated circulation [2]. During the late stages of hydrothermal activity, the participation of low-temperature high-salinity Ca–Na–Cl solutions was also found, representing either brines of external marine provenance or locally generated “shield brines” [4].

2.3. Vein Bt23C

The vein Bt23C belongs to the Bytíz deposit, which was the most important uranium deposit in the Příbram area. The Bytíz deposit, situated in the central part of the Příbram uranium and base-metal district, yielded more than 50% of the Příbram’s uranium ores, which were extracted from a total of 782 veins.

The vein Bt23C is located in the vein cluster Bt17B–Bt22 in the arch part of the Příbram anticline. This vein cluster was explored from the surface to the depth of 1300 m. The steep (dip 65–90°) hydrothermal veins and their branches strike NW–SE and N–S, exceptionally NE–SW. Some parts of this vein cluster can be characterized as stockworks. The main NW–SE striking veins and part of their veinlets represent the prolongation of the NW part of the Zduchovice tectonic zone continuing from the CBPC into Proterozoic sediments. The base-metal ores occurred in all depth levels in many NW–SE striking veins containing the siderite-sulphidic mineralization [19]. There is a predominance of sphalerite over galena in the vein cluster Bt17B–Bt22 and sphalerite content increases with increasing depth [28].

The vein Bt23C is one of the important veins of the NW–SE direction (310–330°) with the dip 65–80° to the SW. The width of the vein Bt23C is 20 cm on average, and 75 cm in maximum. The vein was exposed on the 15th, 17th, 20th, 21st, 22nd, and 23rd levels of the shaft No. 19.

The shape of the ore bodies is elongated in most cases. They occur in the proximity of the junctions with faults and other veins, especially in sites where (i) strike of the vein changes to NNW–SSE and the dip is around 70°, (ii) a wider thickness of the vein occurs or (iii) additional fracturing manifested by the presence of veinlets is observed. The vertical extent of the ore-mineralized part of the vein is limited by a fault dipping ca. 45° to the SE above the 20th level. In depth, the Bt23C vein is terminated by a fault structure on the 23rd level [28,29].

The mineralization of the vein Bt23C consists of simple Zn>Pb base-metal association with banded or drusy texture, in development typical for the Příbram ore area. Sphalerite and galena are reported as the main ore minerals of the vein Bt23C, which are accompanied by calcite, siderite, quartz, and minor baryte, whereas pyrite, pyrrhotite, bournonite, and cubanite are accessories [19].

3. Samples and Analytical Methods

The well-documented archive samples used for this study were collected at the 20th level (in depth of 900–950 m) at place, where the vein Bt23C crosscuts an Au-bearing quartz-sulphide vein, which was studied in detail by [20].

The standard doubly polished plates (~100- μm -thick) were prepared from selected representative samples that are deposited in the Mineralogical collection of the National Museum in Prague. Mineral composition and textures of samples were studied by a polarizing microscope Nikon Eclipse ME600 (Nikon Co., Tokyo, Japan) and an electron microprobe Cameca SX-100 (AMETEK, Inc., Berwyn, PA, USA). The chemical composition of selected minerals was measured by the latter apparatus in the wave-dispersive mode using acceleration voltage of 15 kV, beam current of 10 nA (micas, chlorites) or 5 nA (carbonates) and beam diameter of 2 μm (micas, chlorites) or 4 μm (carbonates). The following elements were determined in micas and chlorites: Al, Ba, Ca, Co, Cs, Cu, F, Fe, K, Mg, Mn, N, Na, Ni, P, Pb, Rb, Sb, Si, Sr, and Zn. The following elements were determined in carbonates: Al, Ba, Ca, Co, Cu, Fe, Mg, Mn, Na, Ni, P, Pb, Si, Sr, and Zn. The following analytical lines and standards were used for determination of individual elements: K α

lines: albite (Na), fluorapatite (P), BN (N), celestine (S), Cr₂O₃ (Cr), diopside (Mg), halite (Cl), hematite (Fe), chalcocopyrite (Cu), LiF (F), Ni (Ni), rhodonite (Mn), sanidine (K, Al), TiO₂ (Ti), V (V), wollastonite (Ca, Si); *L* α lines: baryte (Ba), Cs-glass (Cs), Rb-Ge glass (Rb); *L* β line: celestine (Sr); *M* α line: vanadinite (Pb). The acquisition time on the peak was typically between 10 and 30 s (150 s for N), whereas acquisition time on each background was half of the peak time. Content of oxygen was calculated from stoichiometry. The raw counts were converted to wt.% using the standard PAP procedure [30]. The contents of elements, which are not included in tables of mineral compositions, were always below the detection limits. The detection limits varied between 0.05 and 0.1 wt.% for most elements except for F and N, which were around 0.2 wt.%. The data were corrected for overlaps Ti vs. V, Mn vs. Cr, and Ca vs. P.

After removing the carbon coating by re-polishing, the fluid inclusion petrography was carried out following the descriptive and genetic criteria given by [31] and fluid inclusion assemblages (FIAs) concept [32]. Microthermometric measurements were obtained from 561 fluid inclusions using a Linkam THMSG 600 heating-freezing stage (Linkam Scientific Instruments, Surrey, UK) operating in a temperature range of -196 to 600 °C and attached to an Olympus BX-51 polarizing microscope (Olympus Co., Tokyo, Japan) with $20\times$ and $50\times$ long-working-distance objectives. The stage was calibrated using natural fluid inclusions with known temperatures of phase transitions between -56.6 and 374.1 °C. The precision of measurements is ± 0.1 °C in the temperature span between 0 and 50 °C and ± 0.5 °C at 374.1 °C. In aqueous inclusions, the following parameters were measured: freezing temperature (T_f), temperature of initial melting (T_i), homogenization temperature (T_h), melting temperature of last crystal of hydrohalite ($T_{m_{hh}}$), ice ($T_{m_{ice}}$) and clathrate ($T_{m_{cla}}$). In aqueous-carbonic and carbonic inclusions, melting temperature of solid CO₂ ($T_{m_{CO_2}}$) and temperature of partial homogenization of carbonic phase ($T_{h_{car}}$) were also obtained. In inclusions, where $T_{h_{car}} < T_{m_{cla}}$, the $T_{h_{car}}$ was measured before freezing of the inclusion. The degree of fill (F) was estimated as the $L/(V + L)$ ratio at room temperature. Salinities of aqueous inclusions were calculated as wt.% NaCl eq. using the equation by [33]. For aqueous-carbonic inclusions, salinities were calculated using equations by [34] and [35] for three- and four-phase clathrate-melting associations, respectively. Microthermometric data on carbonic inclusions were further processed (calculation of bulk fluid composition, densities, and isochores) using the FLUIDS software packages [36] with calibrations by [37–39].

The chemical composition of carbonic phase of fluid inclusions was determined by a DXR dispersive Raman Spectrometer (Thermo Fisher Scientific, Inc., Waltham, MA, USA) attached to a confocal Olympus microscope. The Raman signal was obtained using an unpolarised 532 nm solid-state, diode-pumped laser and detected by a CCD detector. The parameters of measurements were as follows: $100\times$ objective, 5 s exposure time, 200 exposures (in order to increase the signal/noise ratio), 10 mW laser power, 50 μ m pinhole spectrograph aperture, and spectral range 1000 – 4200 cm⁻¹. The quantification of gaseous components was based on quantitative measurement of peak areas [40] and calibration using natural fluid inclusions with known proportions of CH₄, N₂, and CO₂.

For stable isotope analyses, ca. 0.1 g of pure mineral phase was handpicked under binocular microscope and ground in an agate mortar. The carbonates were converted to CO₂ by reaction with 100% orthophosphoric acid [41] in vacuum at 25 °C. The measurement of isotopic compositions of carbon and oxygen of the resultant CO₂ gas was realized using Delta V Advantage isotope-ratio mass spectrometer (Thermo Fisher Scientific, Inc., Waltham, MA, USA) operating using dual inlet methodology in the Laboratories of the Czech Geological Survey in Prague. Powdered samples of quartz were washed with hydrochloric acid at 25 °C to remove possible impurities (especially carbonates). Oxygen was extracted by fluorine, cleaned on 5 Å molecular sieve, and its $\delta^{18}O$ value was determined on a Finnigan MAT 253 mass spectrometer (Finnigan MAT GmbH, Bremen, Germany) at the University of Lausanne (T. Vennemann analyst). The results of C and O isotope analyses are conventionally expressed in delta (δ) notation as per mil (‰) deviation from

commonly used standards V-PDB and V-SMOW, respectively. Uncertainty is better than ± 0.05 , ± 0.1 , and $\pm 0.2\%$ for carbonate $\delta^{13}\text{C}$, carbonate $\delta^{18}\text{O}$, and quartz $\delta^{18}\text{O}$, respectively. The dolomite $\delta^{18}\text{O}$ value was corrected for fractionation during chemical preparation of the sample by a value of -0.84 [42]. The isotopic composition of the parent fluid was calculated using the fractionation factors published by [43–45].

4. Results

4.1. Vein Mineralogy

Mineralogical investigations of studied samples revealed three mineralizing events (Figure 2). Banded, veinlet, and drusy textures of the vein fill are common and often complicated by the replacement of older mineral phases by younger minerals. The presence of siderite, dolomite-ankerite, quartz, calcite, baryte, sphalerite, galena, chlorite, and mica was confirmed in the vein fill.

Stage	1	2	3
Siderite	■		
Sphalerite	■		
Galena	■		
Baryte		■	■ ?
Dolomite-ankerite		■	
Mica			■
Chlorite			■
Quartz			■
Calcite			■

Figure 2. Paragenetic sequence of the vein Bt23C based on the studied samples. Note that the position of baryte is unclear, because its relationships to quartz, mica, and chlorite are not known.

4.1.1. Stage 1

Stage 1 comprises siderite, sphalerite, and galena (Figure 2). The coarse-grained Mn-rich siderite ($\text{Sid}_{56-71}\text{Rdc}_{14-28}\text{Mag}_{11-18}\text{Cal}_{1-7}$) is the oldest mineral of the vein (Figure 3a,b), which occurs in relatively small amounts. An indistinct oscillatory zoning is sometimes observed in a BSE image. Siderite is always strongly corroded and replaced by younger phases, especially calcite, quartz, sphalerite, and galena.

The coarse-grained brown sphalerite grows on siderite in bands up to 3 cm thick. In polished sections, no anisotropy, or inclusions of other ore phases (i.e., “chalcopyrite disease”) are observed. In thin sections, a very detailed oscillatory zoning of sphalerite is observed with yellow, orange, red, brownish, and dark-brown zones (Figure 3c). Sphalerite is strongly cracked with fissures filled mainly by calcite and less by dolomite-ankerite.

Galena is a subordinate ore mineral, forming a 5 mm thick outer “growth zone” on sphalerite, lined by own crystal faces in apical part. In reflected light, no marks of deformation are observed on galena grains.

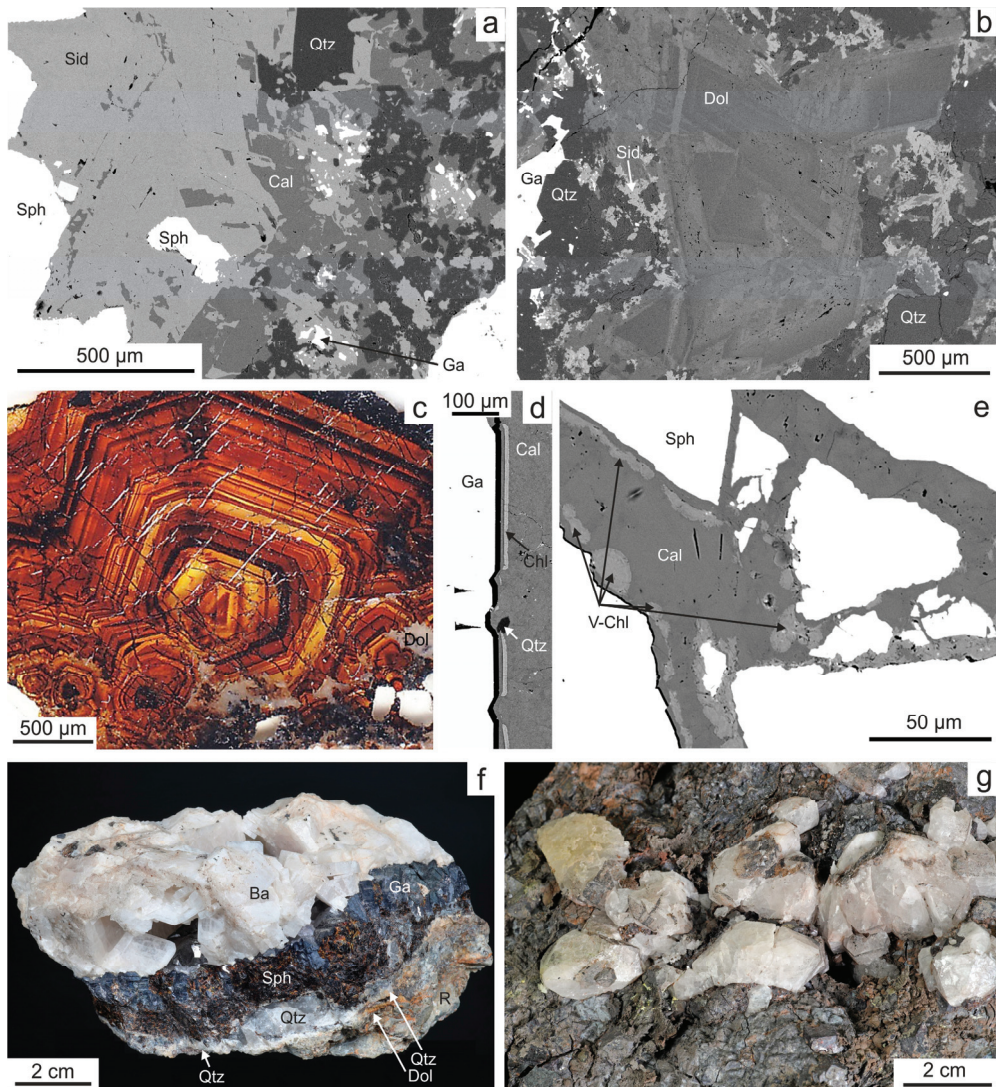


Figure 3. Mineral composition and textures of the studied samples. (a) Replacement of siderite (Sid) by sphalerite (Sph), quartz (Qtz), and calcite (Cal). BSE image, sample Pb-668. (b) Siderite (Sid) strongly replaced by quartz (Qtz) and zoned dolomite-ankerite (Dol). Ga—galena. BSE image, sample Pb-668. (c) Detailed oscillatory zoning of sphalerite in transmitted light. Note minor replacements of sphalerite by dolomite-ankerite (Dol) in the lower part of the picture. Sample Pb-668. (d) Thin zone of chlorite (Chl) lining the crystal face of galena (Ga) overgrown by calcite (Cal). BSE image, sample Pb-670. (e) Cavities in fractured sphalerite (Sph) filled by calcite (Cal) and V-rich chlorite (V-Chl). BSE image, sample Pb-666. (f) Ore band composed of sphalerite (Sph) and galena (Ga) overgrown by coarsely tabular baryte (Ba). The contact of host rock (R) and sulphide band was subsequently twice fractured, giving rise to early dolomite-ankerite (Dol) veinlets and late quartz (Qtz) veinlet. Note that calcite originally filling the remaining drusy cavities in baryte was removed by acid etching. Sample Pb-668. (g) Euhedral crystals of quartz growing on sphalerite-galena ore. Note that the youngest calcite was artificially removed by etching. Sample Pb-666.

4.1.2. Stage 2

Stage 2 involved crystallization of carbonate of the dolomite-ankerite series (Figure 2), which are the least frequent carbonates in the vein Bt23C. They form fillings of some cracks in ore bands (Figure 3c) as well as replacements at the expense of siderite, but they predate calcite and baryte. They display strong oscillatory compositional zoning (Figure 3b) with compositions evolving from dolomite to Mg-rich ankerite ($\text{Dol}_{31-65}\text{Ank}_{34-50}\text{Ktn}_{1-19}$).

4.1.3. Stage 3

Stage 3 is characterized by crystallization of mica, chlorite, quartz, and calcite (Figure 2), which followed the most intense fracturing of the early vein (Figure 3e,f). Rare small nests of fine-grained mica are enclosed in quartz-calcite aggregates. Mica has an uncommon composition, as vanadium (1.06–1.37 apfu V, based on 11 atoms of oxygen) prevails over $^{\text{vi}}\text{Al}$ (0.21–0.33 apfu) in all analyses, and the contents of P (≤ 0.15 apfu), Fe (≤ 0.26 apfu), Mg (≤ 0.27 apfu), Ca (≤ 0.13 apfu), Zn (≤ 0.05 apfu), and Pb (≤ 0.03 apfu) are elevated (Table 1). The sum of interlayer cations varies at 0.80–0.91, suggesting compositions between roscoelite and an unnamed $^{\text{vi}}\text{V}$ -dominated analogue of illite.

Table 1. Representative compositions of mica from the vein Bt23C. Oxides are in wt.%, the apfu values are calculated on the basis of 11 atoms of oxygen.

An. No	1	2	3	4	5	6
Sample	Pb-666	Pb-666	Pb-666	Pb-666	Pb-666	Pb-666
P ₂ O ₅	1.58	1.26	1.58	2.45	2.26	2.32
SiO ₂	44.02	44.62	43.66	43.84	44.44	42.71
Al ₂ O ₃	12.91	12.23	12.52	13.35	12.73	12.43
V ₂ O ₃	21.96	23.86	22.16	18.41	21.36	21.18
Sb ₂ O ₃	b.d.	b.d.	b.d.	0.26	0.18	0.21
MgO	1.95	1.75	1.94	2.55	1.98	1.93
MnO	0.09	0.07	0.08	0.14	0.12	0.11
FeO	2.90	2.70	3.00	4.37	3.14	3.09
ZnO	0.62	0.70	0.78	0.77	1.04	0.29
CaO	1.20	0.98	1.29	1.64	1.61	1.64
PbO	0.89	0.87	1.09	1.40	1.48	1.74
Na ₂ O	b.d.	0.09	b.d.	b.d.	b.d.	b.d.
K ₂ O	6.23	6.74	6.31	5.85	6.12	6.24
F	0.11	0.26	0.28	0.33	0.11	0.32
Total	94.46	96.13	94.69	95.36	96.57	94.21
P ⁵⁺	0.097	0.077	0.097	0.149	0.136	0.144
Si ⁴⁺	3.186	3.201	3.176	3.156	3.165	3.134
^{iv} Al ³⁺	0.717	0.723	0.726	0.694	0.699	0.721
T sum	4.000	4.000	4.000	4.000	4.000	4.000
^{vi} Al ³⁺	0.384	0.311	0.347	0.439	0.370	0.354
V ³⁺	1.274	1.372	1.293	1.063	1.220	1.246
Sb ³⁺	b.d.	b.d.	b.d.	0.008	0.005	0.006
Mg ²⁺	0.210	0.187	0.210	0.274	0.210	0.211
Mn ²⁺	0.006	0.004	0.005	0.009	0.007	0.007
Fe ²⁺	0.176	0.162	0.183	0.263	0.187	0.190
Zn ²⁺	0.033	0.037	0.042	0.041	0.055	0.016
O sum	2.083	2.074	2.080	2.096	2.054	2.030
Ca ²⁺	0.093	0.075	0.101	0.127	0.123	0.129
Pb ²⁺	0.017	0.017	0.021	0.027	0.028	0.034
Na ⁺	b.d.	0.013	b.d.	b.d.	b.d.	b.d.
K ⁺	0.575	0.617	0.586	0.537	0.556	0.584

Table 1. Cont.

An. No	1	2	3	4	5	6
Sample	Pb-666	Pb-666	Pb-666	Pb-666	Pb-666	Pb-666
I sum	0.796	0.814	0.829	0.845	0.859	0.911
Catsum	6.769	6.796	6.787	6.787	6.762	6.777
F ⁻	0.025	0.059	0.064	0.075	0.025	0.074

b.d.—below detection limit; I sum = K + Na + 2Ca + 2Pb.

Trioctahedral chlorite is commonly associated with calcite, quartz, and mica and usually forms thin layers on crystals of sulphides or on the walls of cracks in them (Figure 3d,e). It belongs to chamosite in classification scheme by [46] with Si = 2.81–2.97 apfu (based on 14 atoms of oxygen), $Fe^{2+}/(Fe^{2+} + Mg) = 0.58–0.73$, low Mn (≤ 0.04 apfu), low Ca (≤ 0.09 apfu), often elevated V (≤ 0.51 apfu), and sometimes elevated Zn (≤ 0.14 apfu; Table 2).

Table 2. Representative compositions of chlorite from the vein Bt23C. Oxides are in wt.%, the apfu values are calculated on the basis of 14 atoms of oxygen. Where possible, total Fe was recalculated to Fe^{2+} and Fe^{3+} according to [47].

An. No.	1	2	3	4	5	6	7	8	9	10	11	12	13
Sample	Pb-670	Pb-670	Pb-670	Pb-670	Pb-670	Pb-667	Pb-667	Pb-667	Pb-666	Pb-666	Pb-666	Pb-666	Pb-666
P ₂ O ₅	b.d.	b.d.	b.d.	b.d.	b.d.	0.13	0.14	b.d.	b.d.	b.d.	b.d.	b.d.	0.53
SiO ₂	25.83	25.53	26.00	26.15	25.08	27.47	27.83	26.70	27.33	27.33	26.53	26.82	25.62
Al ₂ O ₃	18.06	17.72	18.56	17.58	19.04	18.15	19.37	19.12	18.48	18.04	16.95	17.30	15.41
V ₂ O ₃	b.d.	b.d.	b.d.	b.d.	b.d.	0.46	0.49	0.57	1.11	2.78	3.73	4.24	5.56
Fe ₂ O ₃	1.96	1.93	2.11	1.98	2.38	2.14	1.90	2.25	3.45	3.50	n.a.	n.a.	n.a.
MgO	7.11	7.21	6.98	7.39	7.12	10.88	10.39	9.07	10.93	8.92	9.81	9.53	7.90
CaO	0.56	0.56	0.67	0.73	0.68	0.22	0.12	0.10	b.d.	0.13	0.34	b.d.	0.41
MnO	0.22	0.21	0.21	0.24	0.28	0.19	0.17	0.32	0.14	0.24	0.23	0.14	0.17
FeO	33.77	32.94	33.31	33.00	32.92	28.14	27.68	29.97	26.90	27.42	30.33	29.29	27.75
ZnO	b.d.	b.d.	b.d.	b.d.	b.d.	0.17	0.25	b.d.	1.75	0.81	1.33	b.d.	0.23
PbO	0.20	0.23	b.d.	b.d.	b.d.	b.d.	b.d.	b.d.	b.d.	b.d.	0.17	0.65	0.51
Na ₂ O	b.d.	b.d.	b.d.	b.d.	0.15	b.d.	b.d.	b.d.	b.d.	0.22	0.21	b.d.	b.d.
K ₂ O	b.d.	b.d.	b.d.	b.d.	b.d.	b.d.	0.18	b.d.	b.d.	b.d.	b.d.	b.d.	0.28
Total	87.71	86.33	87.84	87.07	87.65	87.95	88.52	88.10	90.09	89.39	89.75	87.97	84.37
P ⁵⁺	b.d.	b.d.	b.d.	b.d.	b.d.	0.012	0.013	b.d.	b.d.	b.d.	b.d.	b.d.	0.051
Si ⁴⁺	2.882	2.889	2.881	2.924	2.792	2.946	2.948	2.889	2.882	2.916	2.873	2.926	2.932
Al ³⁺	2.375	2.364	2.424	2.317	2.498	2.294	2.419	2.438	2.297	2.268	2.163	2.225	2.078
V ³⁺	b.d.	b.d.	b.d.	b.d.	b.d.	0.040	0.042	0.049	0.094	0.238	0.324	0.371	0.510
Fe ³⁺	0.165	0.164	0.176	0.167	0.199	0.173	0.151	0.183	0.274	0.281	n.a.	n.a.	n.a.
Mg ²⁺	1.183	1.216	1.153	1.232	1.182	1.739	1.641	1.463	1.718	1.419	1.583	1.550	1.348
Ca ²⁺	0.067	0.068	0.080	0.087	0.081	0.025	0.014	0.012	b.d.	0.015	0.039	b.d.	0.050
Mn ²⁺	0.021	0.020	0.020	0.023	0.026	0.017	0.015	0.029	0.013	0.022	0.021	0.013	0.016
Fe ²⁺	3.151	3.118	3.087	3.086	3.065	2.524	2.453	2.712	2.372	2.446	2.747	2.673	2.656
Zn ²⁺	b.d.	b.d.	b.d.	b.d.	b.d.	0.013	0.020	b.d.	0.136	0.064	0.106	b.d.	0.019
Pb ²⁺	0.006	0.007	b.d.	b.d.	b.d.	b.d.	b.d.	b.d.	b.d.	b.d.	0.005	0.019	0.016
Na ⁺	b.d.	b.d.	b.d.	b.d.	0.032	b.d.	b.d.	b.d.	b.d.	0.045	0.044	b.d.	b.d.
K ⁺	b.d.	b.d.	b.d.	b.d.	b.d.	b.d.	0.024	b.d.	b.d.	b.d.	b.d.	b.d.	0.041
Catsum	9.848	9.847	9.819	9.835	9.876	9.783	9.739	9.775	9.786	9.714	9.906	9.776	9.718
F/FM	0.73	0.72	0.73	0.71	0.72	0.59	0.60	0.65	0.58	0.63	0.63	0.63	0.66
T	138	135	122	118	153	98	75	108	88	51	n.a.	n.a.	n.a.
log f _{O₂}	−59.4	−59.7	−61.3	−62.2	−56.4	−63.6	−68.4	−62.4	−63.1	−71.1	n.a.	n.a.	n.a.

b.d.—below detection limit; F/FM = $Fe^{2+}/(Fe^{2+} + Mg^{2+})$; T—temperature (°C) calculated using chlorite compositional thermometry by [47]; log f_{O₂}—oxygen fugacity calculated according to [47]; n.a.—not applicable.

Quartz occurs in two forms. Frequent are idiomorphic crystals (up to 2 cm in size) with milky white or light gray color, which either overgrow (and partly also along cracks replace) sulphidic aggregates (Figure 3f,g and Figure 4a,b) or accompany chlorite (Figure 3d). Less prominent are microscopic xenomorphic quartz grains, which replace, often together with chlorite and calcite, the older siderite (less frequently dolomite-ankerite) gangue, especially along their boundaries with other minerals (Figure 3a,b). In thin section, a distinct growth

zoning of quartz megacrysts is visible, where clear parts alternate with bleary zones rich in fluid inclusions (Figure 4a,b).

White calcite grows on or replaces older phases or fills younger cavities or cracks (Figure 3a,d,e). Its chemical composition is characterized by a variable amount of rhodochrosite component ($\text{Ca}_{88-98}\text{Rdc}_{2-12}\text{Sid}_{0-2}$).

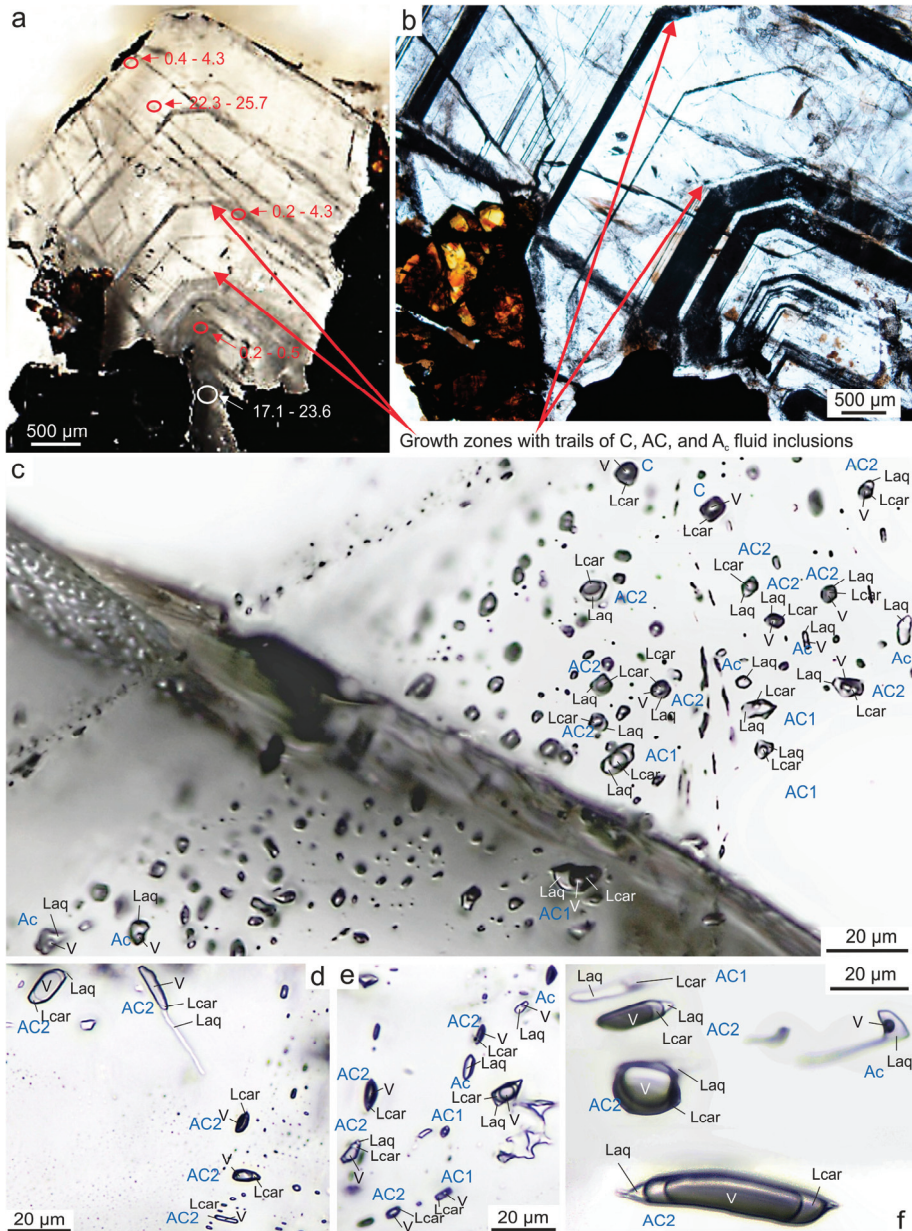


Figure 4. Zonation and fluid inclusions in quartz crystals. (a) Zoned crystal of quartz in transmitted light with marked areas containing C, AC and AC inclusions. Numeric values refer to ranges of

salinity of A_{L+V} inclusions. Sample Pb-666. (b) Detail of lower part of Figure 4a; yellow-brown inclusions are grains of sphalerite. (c–f) Microphotographs of some quartz-hosted trails containing C, AC, and A_c fluid inclusions from samples Pb-666b (c–e) and Pb-666 (f). Laq—aqueous solution, Lcar—liquid carbonic phase, V—vapour.

4.1.4. Baryte

Baryte was only found in one hand specimen, where it postdates sulphides and predates calcite (Figure 3f); however, its relationship to quartz, dolomite-ankerite, and phyllosilicates remains unclear due to the absence of crosscut evidence. Baryte forms milky white coarse-tabular crystals up to several cm in size in the central band of the vein with common ancient drusy cavities fulfilled by calcite (Figure 3f).

4.2. Fluid Inclusions

4.2.1. Petrography and Typology of Fluid Inclusions

The fluid inclusions were studied in six doubly polished plates prepared from three hand specimens covering the whole paragenetic evolution of the vein Bt23C. Fluid inclusions suitable for conventional microthermometric analysis were found in quartz, sphalerite, dolomite, calcite, and baryte. Three main types of fluid inclusions were distinguished based on their phase composition at room temperature: aqueous–carbonic (AC), carbonic (C), and aqueous (A).

The AC inclusions were found exclusively in the quartz host, where they usually occur within variably long trails (suggesting their pseudosecondary and secondary origin). In these trails AC inclusions almost always coexist with aqueous inclusions, whereas AC inclusions predominate, and A inclusions are relatively rare (Figure 4c–f). Sporadically, the AC inclusions were found also as solitary inclusions. In one section (Pb-666), which was cut parallel with crystallographic axis z of a quartz crystal, AC inclusions (as well as C inclusions) were found only in the central part of the quartz crystal in a limited area between two well-defined growth zones (Figure 4a,b). The AC inclusions have irregular, oval or negative-crystal shape with sizes from 6 to 55 μm (Figure 4c–f). At room temperature, they are either three-phase (aqueous solution + liquid carbonic phase + vapour carbonic phase) or two-phase (aqueous solution + liquid carbonic phase). Based on their filling ratio, they can be divided into two subtypes, which coexist on the same trails. In subtype AC_1 , the aqueous phase occupies 50–90 vol.%, whereas in subtype AC_2 , the aqueous phase takes less than 50 vol.%. Wide variations in mutual proportions of aqueous and carbonic phase are typical for inclusions present in individual trails (Figure 4c–f) as well as for solitary inclusions.

The C inclusions coexist with AC and A inclusions on trails in quartz host (Figure 4c). In addition, one pseudosecondary or secondary inclusion belonging to this type was also found in sphalerite. At room temperature, C inclusions appear to be monophasic (liquid carbonic phase) or two-phase (liquid carbonic phase + vapour carbonic phase). Their shape is usually rounded or slightly irregular, with sizes between 6 and 32 μm . Interestingly, within some trails the C and AC inclusions richest in the carbonic phase clearly tend to concentrate in a narrow zone, which follows the places where change of the curvature of the ancient microfracture appeared (Figure 5).

The A inclusions are widespread in all studied minerals. Primary (P), pseudosecondary (PS) and secondary (S) inclusions were identified. In some inclusions in quartz and sphalerite, solids were also rarely present, which were identified by Raman spectroscopy as siderite and in one case as chlorite. Due to their nature and rare occurrence, it is evident that these solids are accidentally trapped phases, which have no influence on the behaviour of fluid inclusions during microthermometry, and thus their presence is neglected in the following text. According to their phase composition and association, the aqueous inclusions can be divided into three subtypes. The first subtype (A_c) represents inclusions in quartz coexisting on trails (PS or S character) with AC and C inclusions. These aqueous inclusions are mostly two-phase with up to 20 vol.% of vapour phase or liquid monophasic. Their shapes are irregular, rounded or elongated with sizes up to 30 μm (Figure 4c–f).

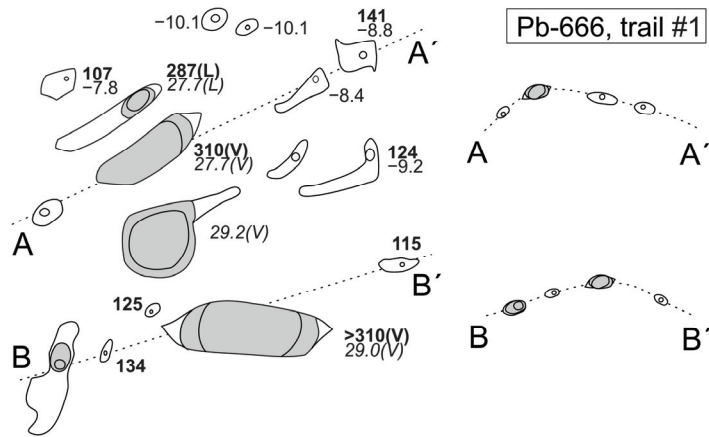


Figure 5. A sketch showing spatial distribution of various types of fluid inclusions within part of trail #1 hosted by quartz, with indication of some collected microthermometric parameters (T_h —in bold, $T_{h_{car}}$ —in italics, $T_{m_{ice}}$ —in normal). Carbonic phase is gray and aqueous solution is shown in white. Right part of the picture illustrates vertical distribution of inclusions across sections A-A' and B-B'.

The second subtype (A_{L+V}) represents two-phase aqueous inclusions, in which the vapour phase occupies 5–20 vol.% (mostly around 10 vol.%). They are abundant in quartz, where they occur on distinct growth zones (Figure 6a) or on trails. They are the most frequent type in sphalerite, where they occur mostly on trails (Figure 6c), rarely as solitary inclusions or sometimes on growth zones (Figure 6b), where they have a very small size (up to 6 μm) and have a very dark (sometimes even black) appearance making them very difficult objects for microthermometry. In calcite and dolomite, they occur in three-dimensional clusters or on trails. Their shape varies from irregular, rounded to negative-crystal shape (mostly carbonates, sometimes sphalerite) with sizes from 1 to 100 μm (mostly around 15 μm).

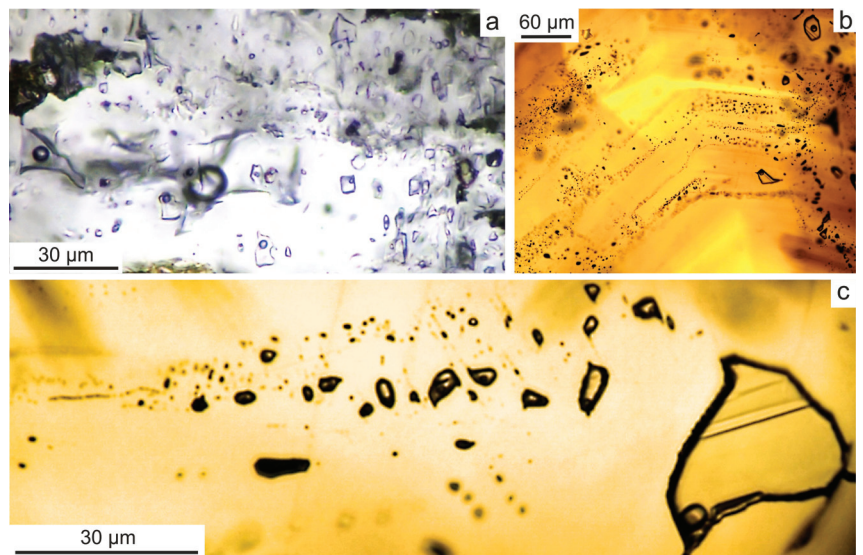


Figure 6. Cont.

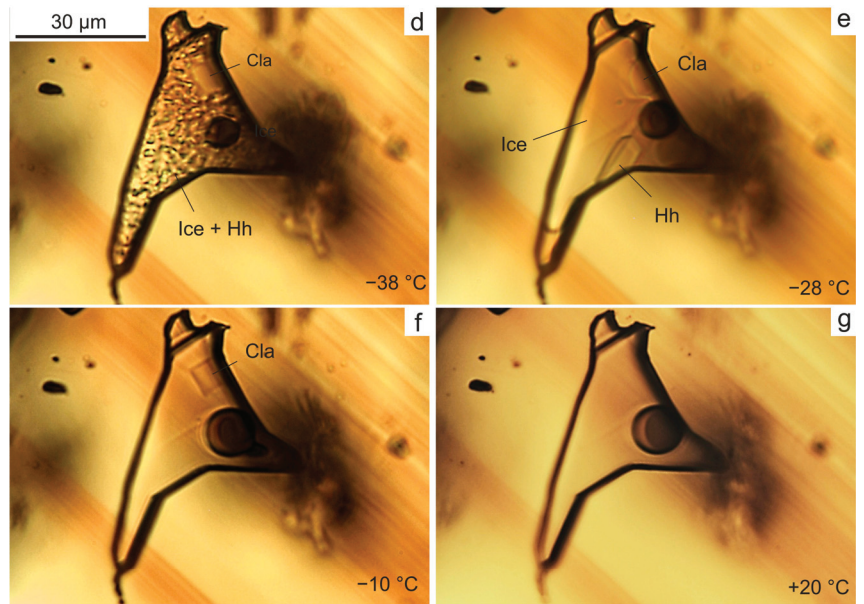


Figure 6. Microphotographs of aqueous fluid inclusions. (a) Primary A_{L+V} inclusions on outer growth zone in quartz, sample Pb-666b. (b) Primary inclusions on growth zones in sphalerite, sample Pb-668. (c) Trail of pseudosecondary A_{L+V} inclusions in sphalerite, sample Pb-666b. (d–g) Phase transitions in a pseudosecondary A_{L+V} inclusion in sphalerite from the sample Pb-668 during cryometry. Hh—hydrohalite, Cla—clathrate.

The third subtype (A_L) represents monophasic liquid inclusions, that are the only type of inclusions in baryte, where they occur only on trails. They are the prevailing type in calcite, where they appear in three-dimensional clusters as well as on trails, often together with A_{L+V} inclusions. They are also abundant as secondary inclusions in sphalerite, dolomite, and quartz, where they also occur as primary inclusions on the outer growth zones coexisting with A_{L+V} inclusions. These inclusions have irregular or oval shapes and vary from 1 to 55 μm in size.

4.2.2. Microthermometry

Only four bulk homogenization temperatures were measured for AC inclusions ranging between 274 and 310 $^{\circ}\text{C}$ to both liquid (AC_1) and vapour (AC_2 ; Table 3). Other inclusions would homogenize at even higher temperatures, but they decrepitated prior reaching the homogeneous state. The carbonic phase of AC and C inclusions froze around -100°C . Melting of solid CO_2 was observed in a close range of temperatures between -57.9 and -57.2°C , which suggest minor amounts of other low-condensable gases in addition to CO_2 . Clathrate melting temperatures in AC_1 and AC_2 inclusions range between 3.5 – 11.7°C and 3.5 – 9.4°C , respectively; in C inclusions, either clathrate formation or melting was not observed. It is interesting that inclusions, where the carbonic phase homogenizes to vapour, yielded a lower and wider interval of $T_{m,cla}$ (3.5 – 8.9°C) than inclusions displaying $T_{h,car}$ to liquid (7.8 – 11.7°C), no matter whether they were rich in the carbonic phase or aqueous solution. Partial homogenization of the carbonic phase occurs either to liquid (L) in wide temperature intervals ranging from -11.5 to 30.5°C , -2.2 to 29.5°C and -0.6 to 30.9°C or to vapour (V) at temperatures 25.1 – 29.2°C , 28.0 – 30.7°C and 27.7 – 30.9°C for AC_1 , AC_2 and C inclusions, respectively. Within single trails (containing AC_1 , AC_2 and C inclusions together), $T_{h,car}$ occurred in three modes: (i) only to liquid in a relatively narrow range (within 7.6°C at maximum; four trails); (ii) only to vapour always in narrow

temperature intervals (within up to 3 °C; six trails); (iii) in both homogenization modes in a wide interval (five trails, for example trail #1: 14.1–27.7 °C (L) and 27.7–29.2 °C (V); Table 3).

Table 3. Microthermometric data from A_c, AC, and C inclusions. Temperature parameters in °C, salinity in wt.% NaCl eq. n—number of measurements, F—degree of fill.

Sample	Mineral	Trail	Gen.	Type	n	F	Th _{tot}	Th _{car}	Tm _{CO2}	Tm _{ice}	Tm _{cla}	Salinity
Pb-666	Quartz	1	PS	AC1	2	0.80–0.85	287–295 (L)	14.1–27.7 (L)	–57.5		5.8–7.8	4.3–7.8
Pb-666	Quartz	1	PS	AC2	3	0.15–0.35	310 (V)	28.0–29.2 (V)	–57.5		3.5–8.2	3.6–11.3
Pb-666	Quartz	1	PS	C	2			27.7–29.0 (V)	–57.5			
Pb-666	Quartz	1	PS	Ac	11	0.90–0.95	107–141 (L)			–10.1/–7.8		11.5–14.1
Pb-666	Quartz	2	PS	AC1	3	0.10–0.40		25.1–28.1 (V)	–57.5		3.6–4.0	10.6–11.2
Pb-666	Quartz	2	PS	C	2			26.2–28.1 (V)	–57.5			
Pb-666	Quartz	2	PS	Ac	8	0.90–0.95	109–170 (L)			–8.5/–7.9		11.6–12.3
Pb-666	Quartz	3	PS	AC1	1	0.65		29 (V)	–57.5		3.5	11.3
Pb-666	Quartz	3	PS	C	2			28.5–29.1 (V)	–57.5			
Pb-666	Quartz	3	PS	Ac	6	0.95	105–236 (L)			–8.7/–8.4		12.2–12.6
Pb-668	Quartz	4	PS	AC2	1	0.30		29.8 (V)	–57.2		8.9	2.2
Pb-668	Quartz	4	PS	Ac	1	0.80	268 (L)			–4.1		6.6
Pb-668	Quartz	5	PS	C	1	0.00		29.9 (L)	–57.4			
Pb-668	Quartz	5	PS	Ac	1	0.80	210 (L)			–4.3		6.7
Pb-668	Quartz	6	PS	AC1	1	0.65		15 (L)	–57.5		9.1	1.8
Pb-668	Quartz	7	PS	AC1	1	0.55		29.9 (L)	–57.3		8.9	2.2
Pb-668	Quartz	8	PS	C	1			28.9 (V)				
Pb-669	Quartz	9	PS	AC2	1	0.20		28.9 (V)				
Pb-666b	Quartz	10	PS/S	AC1	3	0.7–0.8		–5.5/–2.1 (L)	–57.8		8.8–8.9	4.0–4.5
Pb-666b	Quartz	10	PS/S	C	1			30.0 (V)	–57.7			
Pb-666b	Quartz	11	PS/S	AC1	1	0.75		–1.9 (L)	–57.8		8.8	4.1
Pb-666b	Quartz	12	PS/S	AC1	6	0.50–0.85		–9.3/–1.8 (L)	–57.9/–57.8		9.0–11.7	3.0–4.8
Pb-666b	Quartz	12	PS/S	AC2	5	0.10–0.45		–2.2/–1.7 (L)	–57.9/–57.8		9.0–9.4	3.0–3.8
Pb-666b	Quartz	12	PS/S	C	3			–2.3/–1.8 (L)	–57.9/–57.9			
Pb-666b	Quartz	13	PS/S	AC1	3	0.50–0.60		–4.3/0.6 (L)	–57.3		8.9–9.4	3.3–4.3
Pb-666b	Quartz	13	PS/S	Ac	1	0.90	187 (L)					
Pb-666b	Quartz	14	PS	C	2			28.6–30.2 (V)	–57.7			
Pb-666b	Quartz	14	PS	Ac	1	0.95	140 (L)			–7.9		11.6
Pb-666b	Quartz	15	PS/S	C	3			27.7–30.3 (V)	–57.7			
Pb-666b	Quartz	15	PS/S	Ac	2	0.95	93–117 (L)			–10.1/–7.9		11.2–14.1
Pb-666b	Quartz	16	PS/S	AC1	5	0.50–0.80		–11.5/–7.6 (L)	–57.8		8.8–10.8	4.1–5.1
Pb-666b	Quartz	17	PS/S	AC2	2	0.20–0.30		30.3–30.7 (V)	–57.4		7.5–7.8	4.3–4.9
Pb-666b	Quartz	17	PS/S	C	5			27.8–30.6 (V), 30.9 (L)	–57.4/–57.5			
Pb-666b	Quartz	17	PS/S	Ac	1	0.95	193 (L)					
Pb-666b	Quartz	18	PS/S	AC1	7	0.5–0.9		1.3–30.5 (L)	–57.5/–57.2		7.9–9.5	1.9–4.1
Pb-666b	Quartz	18	PS/S	AC2	11	0.1–0.4		14.0–29.5 (L), 29.9–30.8 (V)	–57.3/–57.2		5.5–8.4	3.2–8.3
Pb-666b	Quartz	18	PS/S	C	2			–0.6 (L), 29.8 (V)	–57.9/–57.3			
Pb-666b	Quartz	18	PS/S	Ac	7	0.8–0.95	69–90 (L)			–7.2/–5.2		8.1–10.7
Pb-666b	Quartz	19	PS/S	AC2	1	0.10		30.1 (V)	–57.4		4.6	9.7
Pb-666b	Quartz	19	PS/S	C	2			29.5–29.8 (V)	–57.4			
Pb-666b	Quartz	20	PS/S	AC1	1	0.50		26.3 (L)	–57.4		7.8	9.4
Pb-666b	Quartz	20	PS/S	C	2			29.6–30.8 (V)	–57.4			
Pb-666b	Quartz	20	PS/S	Ac	3	0.85–0.95	55–185 (V)			–7.8/–7.2		10.7–11.5
Pb-666c	Quartz	21	P?	AC1	1	0.70		0.5 (L)			10.9	
Pb-666b	Sphalerite	22	PS/S	C	1			28.8 (V)	–57.6			

The A_c inclusions homogenized always to liquid in a wide interval of temperatures (55–193 °C). They froze out between –57 and –41 °C and remained colorless. Only one temperature of initial melting was observed at –37.0 °C. The last phase to melt was always ice, which disappeared at temperatures between –10.1 and –4.0 °C (with maximum variability in a single trail within 2.3 °C; Table 3).

All A_{L+V} inclusions homogenized to liquid. Primary and pseudosecondary inclusions homogenized at temperatures 60–220 °C, 162–205 °C, 175–195 °C, and 64–136 °C in quartz, sphalerite, dolomite, and calcite, respectively (Table 4). The pseudosecondary or secondary (PS/S) inclusions homogenized between 93 and 219 °C. The A_{L+V} inclusions froze at temperatures from –88 to –30 °C and often became darker or brownish. Temperatures of initial melting for all genetic types of fluid inclusions ranged from –49 to –37 °C and –55 to –49 °C in quartz and sphalerite, respectively. Melting of hydrohalite was recorded for primary and pseudosecondary inclusions at –31.1 °C and from –26.3 to –23.8 °C, for pseudosecondary or secondary inclusions from –24.5 to –22.6 °C and from –33.2 to –24.0 °C in quartz and sphalerite, respectively (Table 4). In most inclusions, ice

was the last phase to melt, which occurred at temperatures from -27.2 to -0.1 °C, from -19.6 to -11.0 °C, from -12.1 to -2.5 °C, and from -21.9 to -0.1 °C for primary and pseudosecondary inclusions in quartz, sphalerite, dolomite, and calcite, respectively. In pseudosecondary or secondary inclusions, ice melts from -25.9 to -7.6 °C. In ca. one third of A_{L+V} inclusions hosted by quartz, sphalerite and dolomite, clathrate was the last melting phase (Figure 6d–g); however, in some small, dark and/or low-salinity inclusions (especially those hosted by carbonates or sphalerite) the clathrate observation was very difficult, and it is possible that it was overlooked in some inclusions. Last crystal of clathrate melts at temperatures from -17.2 to -3.2 °C and from -7.8 to -1.8 °C for P and PS inclusions in quartz and sphalerite, respectively, and from -9.1 to 3.4 °C for pseudosecondary or secondary inclusions.

Table 4. Microthermometric data from aqueous A_{L+V} and A_L inclusions. Temperature parameters in °C, salinity in wt.% NaCl eq. n—number of measurements.

Sample	Mineral	Gen.	Type	n	T_{htot} (L)	T_i	T_{mhh}	T_{mice}	T_{mcla}	Salinity
Pb-666	Quartz	P	A_{L+V}, A_L	42	60–205	−49		−24.9/−0.1	−5.1/−4.8	0.4–25.7
Pb-666	Sphalerite	PS/S	A_{L+V}	42	116–198	−50/−47	−34.0/−24.0	−25.9/−9.2	−9.6/−0.9	13.1–26.4
Pb-666	Calcite	P	A_{L+V}, A_L	16	120–136			−21.9/−0.2		0.4–24.8
Pb-667	Calcite	P	A_{L+V}, A_L	24	64			−10.2/−0.2		0.4–14.2
Pb-668	Quartz	P	A_{L+V}	13	84–213			−10.4/−3.1		5.1–14.4
Pb-668	Quartz	PS	A_{L+V}	11	137–220			−9.2/−0.9		1.6–13.1
Pb-668	Quartz	PS/S	A_{L+V}	5	131–204			−11.2/−3.9		6.3–15.2
Pb-668	Sphalerite	P	A_{L+V}	7	173–203	−50/−49	−24.7/−24.3	−14.0/−12.6	−7.8/−6.5	16.6–17.8
Pb-668	Sphalerite	PS	A_{L+V}	41	173–196	−55/−49	−26.0/−24.0	−15.6/−11.0	−5.5/−1.7	15.0–19.2
Pb-668	Dolomite	P	A_{L+V}	22	175–195			−12.1/−3.1		5.1–16.1
Pb-668	Dolomite	PS	A_{L+V}	4	177–180			−11.4/−2.5		4.2–15.4
Pb-668	Dolomite	PS/S	A_{L+V}	24	108–187			−8.6/−7.6	−4.8/1.3	11.2–12.4
Pb-669	Baryte	PS/S	A_L	51			−26.1/−24.7	−19.6/−0.2		0.4–22.2
Pb-670	Calcite	P	A_{L+V}, A_L	15	82–109			−3.3/−0.1		0.2–5.4
Pb-666b	Quartz	P	A_{L+V}	35	65–198	−49	−31.1	−27.2/−2.5	−17.2/−3.2	3.9–27.2
Pb-666b	Quartz	PS/S	A_{L+V}, A_L	31	93–219	−49	−24.5/−22.6	−14.5/−1.8	−9.1/+3.4	3.1–18.3
Pb-666b	Sphalerite	P	A_{L+V}	1	205		−23.8	−12.5		16.5
Pb-666b	Sphalerite	PS	A_{L+V}	3	190–197	−50	−26.2	−19.6/−19.1	−7.7/−7.4	21.9–22.0
Pb-666b	Sphalerite	PS/S	A_{L+V}	11	105–188	−50	−24.7	−12.9/−12.7	−1.1/−1.0	16.6–16.8
Pb-666b	Sphalerite	S	A_{L+V}, A_L	7	105			−0.9/−0.2		0.4–1.6
Pb-666c	Quartz	P	A_{L+V}	19	120–188			−14.3/−12.8	−4.0	16.7–18.1
Pb-666c	Sphalerite	PS	A_{L+V}	7	162–188		−26.3/−25.8	−14.6	−4.2/−2.0	18.3

The A_L inclusions were artificially stretched by overheating to allow for the measurement of cryometric data in the presence of vapour phase. The freezing out of A_L inclusions occurred between -73 and -33 °C. Initial melting was observed only in pseudosecondary or secondary inclusions in baryte at -54.0 and -53.0 °C. Ice as the last solid phase melted at temperatures from -2.6 to -0.2 °C, from -12.8 to -0.2 °C, and from -11.8 to -0.8 °C for P and PS inclusions in quartz, calcite, and baryte, respectively. In pseudosecondary or secondary inclusions in baryte and in late secondary inclusions hosted by sphalerite, ice melted from -19.6 to -0.2 °C and from -0.9 to -0.2 °C, respectively (Table 4).

4.2.3. Raman Spectroscopy

The Raman analysis was used to determine the composition of the non-aqueous phase in C, AC, A_c , and A_{L+V} inclusions. The CO_2 is the predominating volatile in the carbonic phase of quartz-hosted AC and C inclusions (Figure 7). In most of them, the contents of CO_2 are 95–100 mol.%; only two inclusions of analyzed 43 contained a lower amount of CO_2 (87 and 88 mol.%). The other identified gases were N_2 (0–5 mol.%) and CH_4 (0–9 mol.%). Gaseous phase of A_c inclusions hosted by quartz has a similar composition ($CO_2 = 86–98$, $N_2 = 0–3$, $CH_4 = 1–11$ mol.%). The vapour bubbles in A_{L+V} inclusions in trails yielded a similar composition ($CO_2 = 96–98$, $N_2 = 1–2$, $CH_4 = 1–2$ mol.%), as well as that in a primary A_{L+V} inclusion in dolomite ($CO_2 = 99$, $N_2 = 0$, $CH_4 = 1$ mol.%). In contrast, A_{L+V} inclusions from the quartz-hosted growth zones seem to have very different compositions: while

one inclusion from the central part of the crystal has predominant N₂ (68 mol.%) with 21 mol.% of CH₄ and 11 mol.% of CO₂, an inclusion from the edge of the same crystal was dominated by CH₄ (58 mol.%) with 31 mol.% of CO₂ and 11 mol.% of N₂. Gaseous phase of A_{L+V} inclusions in sphalerite has variable compositions, but CO₂ is always the prevailing component (CO₂ = 59–99, N₂ = 0–20, CH₄ = 1–36 mol.%). In many cases the acquisition of Raman spectra from water-dominated inclusions was hampered by the movement of usually small gaseous bubbles.

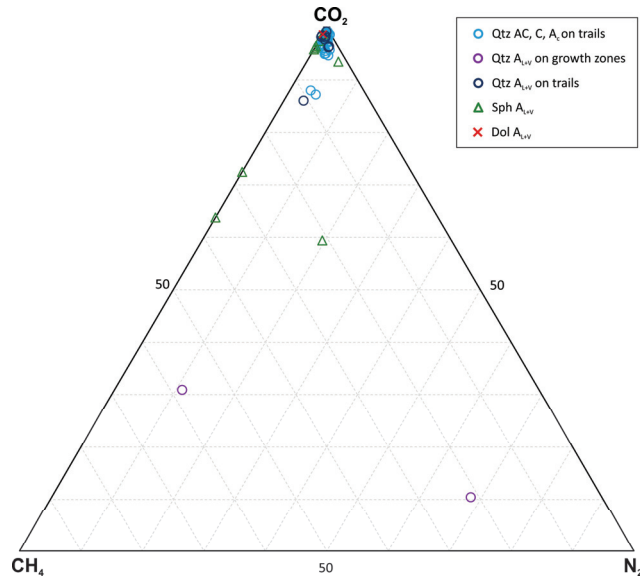


Figure 7. Raman-based chemical composition of non-aqueous phase of fluid inclusions in the CH₄-CO₂-N₂ plot. Data in mol.%.

4.3. Stable Isotopes

The isotopic composition of C and/or O was determined in three carbonate samples and two quartz separates from the same samples that were used for the fluid inclusion study. The carbonate (calcite and dolomite-ankerite) samples gave very limited ranges of both δ¹³C (between −7.1 and −7.8‰ V-PDB) and δ¹⁸O (between 16.2 and 18.5‰ V-SMOW) values (Table 5). Quartz also yielded mutually very similar δ¹⁸O values: a turbid central part and a colorless margin of a crystal gave 19.0 and 19.4‰ V-SMOW, respectively (Table 5).

Table 5. The determined δ¹³C and δ¹⁸O values for carbonates and quartz from the vein Bt23C and fluid δ¹³C and δ¹⁸O values calculated for the ranges of homogenization temperatures of primary A_{L+V} fluid inclusions. Note that one Th outlier was neglected for quartz-r Pb-666.

Sample	Mineral	Paragenetic Stage	δ ¹³ C _{mineral} (‰ V-PDB)	δ ¹⁸ O _{mineral} (‰ V-SMOW)	Temperature (°C)	δ ¹³ C _{fluid} (‰ V-PDB)	δ ¹⁸ O _{fluid} (‰ V-SMOW)
Pb-668	Dolomite	2	−7.8	16.2	175–195	−8.2/−8.9	+2.3/+3.6
Pb-667	Calcite	3	−7.1	18.5	50–64	−9.9/−10.5	−4.7/−2.6
Pb-670	Calcite	3	−7.8	16.3	82–109	−9.8/−10.1	−2.4/+0.6
Pb-666	Quartz-c	3	-	19.0	60–136	-	−8.8/+2.2
Pb-666	Quartz-r	3	-	19.4	68–156	-	−6.8/+4.5

c—core; r—rim of the crystal.

5. Interpretation and Discussion

5.1. Composition, Trapping Mode, and P–T Conditions of Fluid Inclusions

5.1.1. AC, C, and A_c Inclusions

The chemical composition of the non-aqueous phase in AC, C and A_c inclusions is, except for three methane-rich outliers, CO₂-dominated and not very variable (0–3 mol.% CH₄ and 0–3 mol.% N₂). Moreover, salinities of A_c inclusions lie in quite close interval (6.6–14.1 wt.% NaCl eq., mostly around 11 wt.% NaCl eq.) compared to A_{L+V} and A_L inclusions from quartz (see below) and they produce a horizontal trend in a Th–Tm_{ice} plot (Figure 8b). The AC inclusions yield salinities 1.8 to 11.3 wt.% NaCl eq., which are mostly in a comparably wide interval as A_c inclusions. One measured temperature of initial melting (T_i = –37.5 °C) indicates the presence of Mg- and/or Fe-chlorides beside Na-chloride [48].

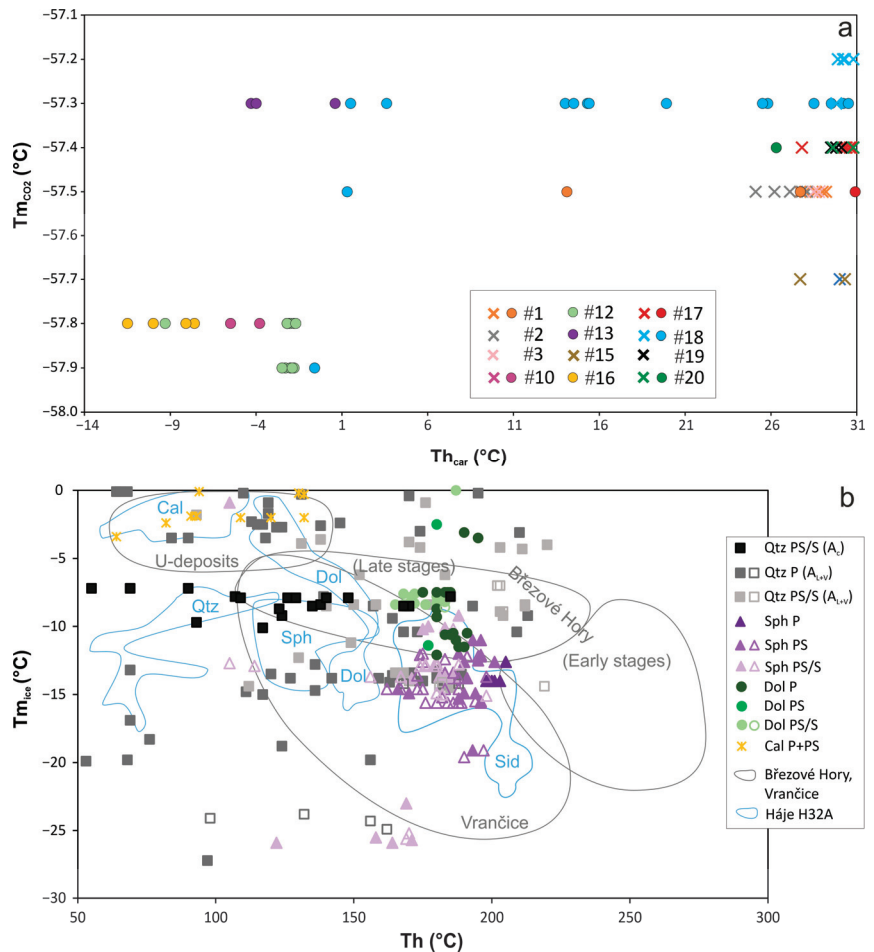


Figure 8. (a) Th_{car}–Tm_{CO2} plot for AC and C fluid inclusions in individual trails (numbered as in Table 3). Cross and dot symbols denote inclusions with Th_{car} mode to vapour and liquid, respectively. (b) Th–Tm_{ice} plot for aqueous inclusions. Blank and full symbols are for inclusions, where clathrate and ice were the last melting phases, respectively. Comparative data from the uranium deposits and Březové Hory and Vrančice base-metal deposits are from [2], data from H32A vein are from [4].

The huge variability in phase composition of trail-hosted co-existing fluid inclusions belonging to types C, AC and A_c in quartz host suggests that these inclusions might have been trapped from a heterogeneous fluid mixture. The occurrence of such fluids is welcome for geologic interpretation because it allows one to determine the trapping P-T conditions from microthermometric data only. However, wide variations of phase composition of a population of fluid inclusions can also be the result of some superimposed processes. Therefore, it is highly important to have solid evidence for heterogeneous trapping. According to [49], the following four main criteria should be complied: 1. simultaneous trapping of all the inclusions of the population of interest; 2. very scattered degree of filling, homogenization temperatures, and compositions; 3. The frequency distribution diagrams non-symmetrical and flattened, particularly towards high temperatures, but more or less similar for the liquid and the vapour; 4. serious evidence indicating that no leakage and/or necking-down can be suspected.

The inclusions with contrasting phase compositions occur on the same trails and thus seem to be formed contemporaneously (e.g., [32]). Moreover, the specific arrangement of fluid inclusions further supports an idea of heterogeneous trapping. This applies for some trails containing “linear” groups of inclusions richest in the carbonic phase, which concentrate in places where a change of curvature of ancient microfracture appeared (Figure 5). Such behaviour is consistent with the coeval trapping of a heterogeneous fluid mixture in an open fracture (future vein), where “bubbles” of carbonic fluid experienced some gravitational separation from aqueous solution due to their lower density. Consequently, bubbles of carbonic fluid can be trapped only in upward blinded “gravity traps” occurring within suitably shaped microfractures (case A in Figure 9). The criterion 3 is difficult to assess because not many bulk homogenization temperatures were measured due to the common limitations. There are usually only a few water-rich inclusions within each trail, and sometimes they are completely missing; homogenization data of water-rich inclusions are thus rare. Similarly, only a very limited amount of bulk homogenization data was obtained for aqueous–carbonic inclusions, most of which decrepitated prior to reaching the homogeneous state. Although very limited, the obtained homogenization data seem to follow the basic condition of wide variability. The involvement of post-entrapment alteration due to refilling, stretching, leakage or necking-down can be difficult to identify. The petrographic evidence for necking-down is missing in our case, as inclusions with very complex morphology or pairs of fluid inclusions still connected through a thin bridge were not observed. However, such petrographic evidence is not definitely unequivocal. Nevertheless, the occurrence of solitary inclusions with a comparably variable phase composition, such as show trail-hosted fluid inclusions, strongly supports the opinion that necking-down is not the key reason explaining the wide phase variability of the studied fluid inclusions. The absence of necking-down is also evidenced from differences in the salinity of aqueous solutions in neighbouring fluid inclusions, which was observed in a few trails (i.e., #1, #18; Figure 5). Partial leakage and stretching, if any, did not affect the studied inclusions significantly. Both these processes would alter the density of enclosed fluid, which is sensitively mirrored by the Th_{car} values. Fluid inclusions in two thirds of investigated trails show the minimum variability of this parameter (Table 3, Figure 8a), which is in line with a complete absence of secondary halos of micro-inclusions containing ejected fluid (e.g., [50,51]). In contrast, fluid inclusions in trails #1 and #18 show bimodal or wide variability in multiple parameters: in salinities of A_c inclusions, Th_{car} of AC and C inclusions, and/or Tm_{CO_2} of AC and C inclusions (Table 3, Figures 5 and 8a). This is likely consistent with a longer healing period for these microfractures rather than with a multi-stage refilling of part of the present inclusions (no crosscuts by another trails of inclusions were observed in these cases). Although these trails do not follow the definition of FIAs, they are also useful because they illustrate highly dynamic changes of chemical composition and/or density of fluids in the studied hydrothermal system over a period somewhat longer than those represented by FIAs. In summary, we suggest that most of the fluid inclusions showing highly variable

phase composition were not significantly disturbed due to post-entrapment alterations and thus represent a geologically meaningful record.

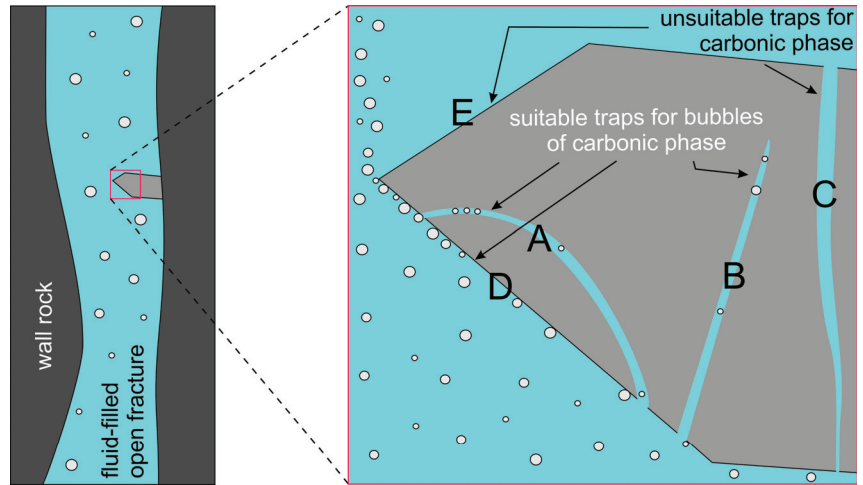


Figure 9. A sketch illustrating the process of trapping of fluid inclusions with different phase composition due to the existence of local gravity traps combined with local partial separation of both immiscible phases. Note the upward movement of bubbles of carbonic fluid due to their lower density. (A–C)—microfractures in mineral host; (D,E)—growth zones in mineral host.

In a population of fluid inclusions that enclosed a heterogeneous fluid mixture, the minimum homogenization temperature of inclusions, which trapped an uncontaminated fluid end member (pure aqueous solution or carbonic phase), represents the true trapping temperature, and the fluid pressure can be located for this temperature at the isochore of non-aqueous fluid [52–54]. For P–T modeling, the lowest $T_{h\text{tot}}$ of A_c inclusions (55–140 °C) of each trail were considered as true trapping temperatures; these values correspond very well with temperatures calculated from the semi-empirical chlorite thermometry, according to [47], applied to associated chlorite (51–153 °C; Table 2). Trapping pressures were obtained from isochores constructed for carbonic inclusions, which likely represent the non-aqueous fluid endmember. In such carbonic-rich inclusions, thanks to low trapping temperatures and very low solubility of water in the carbonic phase in low-P, low-T conditions (e.g., [55]), only a thin film of the aqueous phase can be expected, which is invisible under a polarizing microscope due to optical reasons [56], and therefore no bulk homogenization temperatures (T_h) can be measured. Hence, the amount of water in this invisible (but essential for hermetization of the inclusions) aqueous rim was quantified according to experimental data about the solubility of water in CO_2 presented by [55] and included in the calculation of bulk compositions (Table 6), bulk densities (Table 6), and isochores of carbonic fluids (Figure 10). The obtained P–T conditions of the trapping of these fluid inclusions are visualized in Figure 10. The lowest pressure conditions were located at 100 bar and 55 °C (trail #20). Most of the trails had a pressure condition located between 122 and 170 bar with a narrow range for each trail (max. 18 bars), except for trail #18, where the pressure ranges from 115 to 268 bar and the temperature lies around 69 °C. Even higher-pressure conditions could be suggested for trail #12; however, no A_c inclusions were present in this trail, so only isochore of carbonic phase limits the uppermost possible pressure conditions (Figure 10).

Table 6. Bulk chemical composition, bulk density and some microthermometric parameters for carbonic inclusions used for estimation of P-T conditions. Composition of non-aqueous phase is based on Raman analysis. Temperature parameters are in °C. Water contents in carbonic fluid were corrected according to experimental data by [55].

FI No.	Trail	Th _{car}	Tm _{CO2}	vol.% H ₂ O	X (H ₂ O)	X (CO ₂)	X (CH ₄)	X (N ₂)	D (g/cc)
2146	1	29.0 (V)	−57.5	0.2	0.0180	0.9325	0.0281	0.0214	0.249
2148	1	27.7 (V)	−57.5	0.2	0.0183	0.9513	0.0216	0.0088	0.247
2154	2	26.2 (V)	−57.5	0.2	0.0194	0.9466	0.0226	0.0113	0.231
2155	2	28.1 (V)	−57.5	0.2	0.0186	0.9295	0.0234	0.0286	0.240
2149	3	28.8 (V)	−57.5	0.2	0.0176	0.9465	0.0269	0.0089	0.255
2150	3	28.5 (V)	−57.5	0.2	0.0177	0.9510	0.0243	0.0070	0.255
3363	12	−2.3 (L)	−57.9	0.7	0.0198	0.9574	0.0117	0.0112	0.801
3380	14	30.2 (V)	−57.7	0.6	0.0457	0.9417	0.0065	0.0060	0.291
3381	14	28.6 (V)	−57.7	0.6	0.0495	0.9375	0.0053	0.0077	0.268
3383	15	30.3 (V)	−57.7	0.2	0.0154	0.9757	0.0040	0.0048	0.296
3384	15	27.7 (V)	−57.7	0.2	0.0163	0.9749	0.0040	0.0048	0.280
3409	18	−0.6 (L)	−57.9	0.4	0.0114	0.9697	0.0132	0.0055	0.791
3413	18	29.8 (V)	−57.3	0.1	0.0092	0.9878	0.0031	0.0000	0.302
3432	20	30.8 (V)	−57.4	0.1	0.0079	0.9784	0.0025	0.0112	0.292
3433	20	29.6 (V)	−57.4	0.1	0.0084	0.9779	0.0025	0.0112	0.276

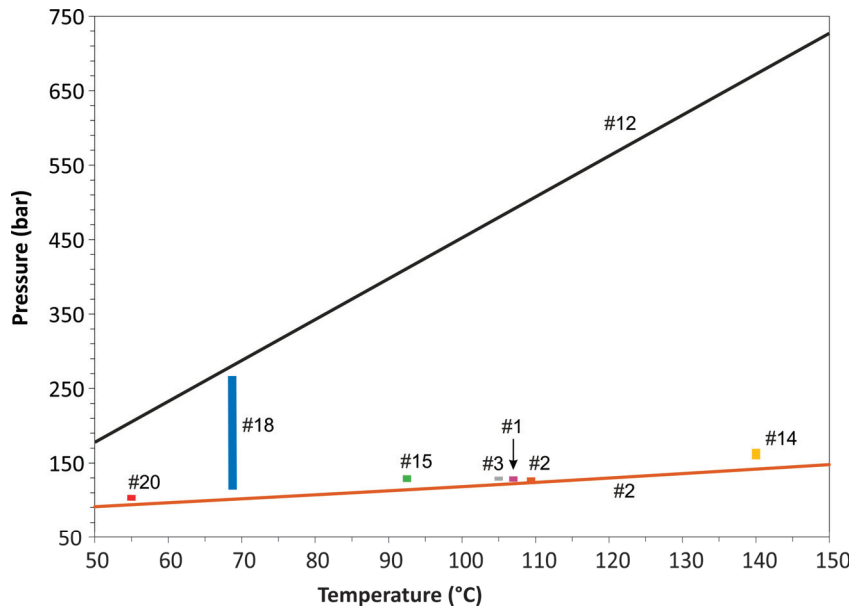


Figure 10. Estimated P-T conditions for immiscible aqueous–carbonic fluids hosted by trails in quartz from the vein Bt23C. Two marginal isochores for minimum and maximum densities of carbonic phase are visualized together with pressure ranges for individual trails, calculated for minimum recorded Th value of associated A_c inclusions.

The present-day position of the studied samples, which were taken in the mine from depths of around 900–950 m, requires minimum pressures of 90–95 bars under hydrostatic conditions. The higher pressures than these minimum possible values reflect the missing overburden formed by the rocks of the Teplá-Barrandian unit and its sedimentary cover, which were eroded since the time of mineralization (i.e., over time span from ~Permian to Quaternary). Whereas the thickness of eroded basement rocks is difficult to quantify, the original thickness of the Permian sedimentary cover in the adjacent Blаницe

Graben (Figure 1) is estimated at ca. 700 [18] or 2500 m [57]. Therefore, the calculated pressure variations can reflect either the changing thickness of this sedimentary cover due to sedimentation or subsequent erosion (in case if the duration of the mineralizing process took place over tens of million years), or fluctuations between lithostatic and hydrostatic fluid regime (in case if the duration of the mineralizing process was shorter than the velocity of sedimentation/erosion). In any case, the participation of the latter process can be potentially suggested from the highly variable densities of the carbonic phase of fluid inclusions recorded in trails #1, #17, and #18. Considering the unchanged fluid temperature, the pressures calculated for the minimum and maximum densities of carbonic fluid hosted by fluid inclusions of trail #18 yielded a maximum value (268 bar) ca. 2.5 times higher than the minimum one (115 bar), which is typical for fluctuations between hydrostatic and lithostatic load and participation of the crack-seal mechanism of vein development (e.g., [53,58,59]).

5.1.2. A_{L+V} and A_L Inclusions

Contrary to A_C and A_C inclusions, the aqueous (A_{L+V} and A_L) inclusions are mostly considered to contain a homogeneously trapped fluid phase due to limited ranges of homogenization temperatures. The only exception represents the primary A_{L+V} inclusions in quartz, which yielded most variable data scattered in both T_h and salinities ($T_h = 60\text{--}220\text{ }^\circ\text{C}$, 0.4–27.2 wt.% NaCl eq.; Figure 8b). Wide differences in fluid salinity are usually attributed to different growth zones (Figure 4a), pointing to oscillatory changes in fluid source(s); a rare episode of mutual mixing of both low-salinity and high-salinity end-members is also illustrated in a growth zone containing inclusions with variable salinities within 13.5 wt.% NaCl eq. However, the broad variability is often observed in homogenization temperatures of aqueous fluid inclusions hosted within single well-defined growth zone (with T_h ranges up to 145 $^\circ\text{C}$), even in zones displaying essentially constant salinity. Because some of these inclusions contain Raman-detectable gases and/or display formation of clathrate during cryometry, we suggest that they likely trapped water-dominated members of a heterogeneous fluid mixture, similar to the above discussed A_C and AC inclusions. The difference is in a complete absence of inclusions rich in the carbonic phase. This feature, however, can be again potentially explained due to the gravity separation of both fluid endmembers differing in density and thus the formation of local microenvironments around growing crystal essentially devoid of larger “bubbles” of the carbonic phase (e.g., growth zone E in Figure 9), whose presence is a necessary pre-requisite for the formation of carbonic inclusions. Finally, it must be emphasized that fluid events giving rise to a majority of aqueous inclusions in quartz growth zones were not identical to those in which trail-hosted coexisting A_C , AC and C inclusions formed, as clearly indicated by differences in both the salinity of aqueous solutions and the composition of non-aqueous phase.

The temperatures of the initial melting of primary inclusions in quartz (from -49 to $-37\text{ }^\circ\text{C}$) and sphalerite (from -55 to $-49\text{ }^\circ\text{C}$) and for PS/S inclusions from baryte (from -54.0 to $-53.0\text{ }^\circ\text{C}$) mostly suggest the presence of CaCl_2 [48], which is also likely present in dolomite and in some inclusions in calcite because of their low freezing temperatures. Projecting the $T_{m_{hh}}$ and $T_{m_{ice}}$ data into the phase diagram of the system $\text{NaCl}\text{--}\text{CaCl}_2\text{--}\text{H}_2\text{O}$ (Figure 11), we can recognize at least three types of fluids. The first one is a high-salinity CaCl_2 -rich fluid with bulk salinity between 22 and 24 wt.% NaCl eq. and with a $\text{NaCl}/(\text{NaCl} + \text{CaCl}_2)$ ratio between 0.25 and 0.43, showing a faint subhorizontal trend in Figure 11 that corresponds to one primary inclusion in quartz and in one trail of PS/S inclusions in sphalerite. The second fluid is a high-salinity (16–21 wt.% NaCl eq.) NaCl-rich fluid with a $\text{NaCl}/(\text{NaCl} + \text{CaCl}_2)$ ratio between 0.63 and 0.88 occurring in PS, PS/S inclusions in sphalerite and PS/S inclusions in quartz and baryte. The third one is a medium-salinity (10–11 wt.% NaCl eq.) NaCl-rich fluid occurring only in late secondary inclusions in quartz and baryte with $\text{NaCl}/(\text{NaCl} + \text{CaCl}_2)$ ratio between 0.63 and 0.82.

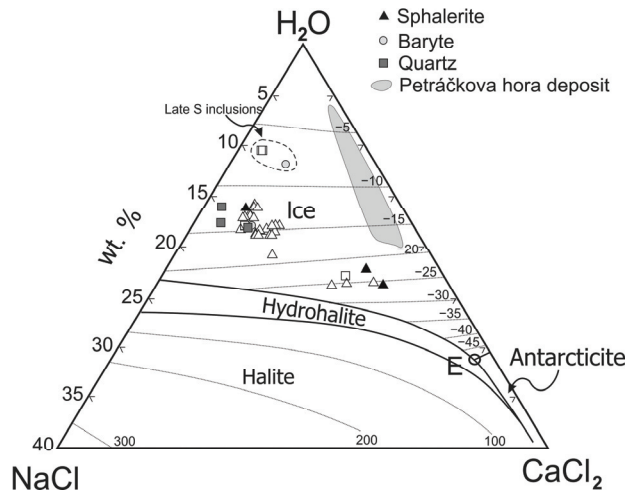
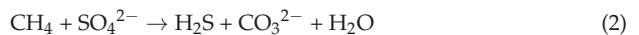


Figure 11. Composition of high-salinity aqueous inclusions from the vein Bt23C expressed in terms of the system NaCl–CaCl₂–H₂O (isotherms in field of ice are from [60,61]). Open and full symbols refer to inclusions, in which clathrate and ice melted as the last phase, respectively. Published data from the Petrůčkova hora Au deposit, interpreted as late-magmatic fluids derived from rocks of Central Bohemian Plutonic Complex [62], are shown for comparison.

The vapour bubbles of primary aqueous inclusions in quartz show completely different proportions of gases (i.e., N₂- or CH₄-dominated; Figure 7) than those of trail-hosted AC, C and A_c inclusions (CO₂-dominated). Such differences could suggest different sources of volatiles at different stages of mineralization, significant fractionation of gases during fluid migration and evolution, such as the consumption of some gas compound(s) during fluid evolution due to their reactions with wall rocks, earlier vein fill or other compounds present in the fluid. The latter case applies especially to CO₂, which can be reacted in the presence of aqueous solutions with limestones or other carbonates, forming bicarbonates well soluble in aqueous fluids [63]:



Similarly, methane is often mentioned as a reductant in hydrothermal systems [64–66], for example, for sulphate dissolved in fluids, giving rise to hydrogen sulphide necessary for precipitation of sulphides:



To further complicate the overall picture, the trail-bound aqueous inclusions hosted by quartz have a very similar chemical composition of non-aqueous phase, when compared with the AC, C and A_c inclusions, but a markedly wider range of salinity. This observation implies that occurrence of gases was not strictly coeval with only a single portion of aqueous fluid. The chemical composition of the non-aqueous phase of PS/S inclusions in sphalerite is quite variable and, in some inclusions, it is similar to inclusions in quartz and, in another ones, it is different, which can also manifest the re-filling phenomena, in addition to above-mentioned possibilities.

5.2. Isotopic Composition of the Fluids

In Table 5, there are listed the fluid δ¹⁸O and δ¹³C values calculated for the ranges of homogenization temperatures of primary fluid inclusions in the appropriate samples. Both calcites yield low fluid δ¹⁸O values between –4.7 and +0.6‰ V-SMOW, which suggests the

predominance of surface waters (e.g., meteoric waters with negative $\delta^{18}\text{O}$ values, seawater with near-zero $\delta^{18}\text{O}$ values) that did not undergo significant isotope exchange with rocks at elevated temperatures [67]. Similar results, but with much greater ranges, also yielded both quartz samples (-8.8 to $+4.5\text{‰}$ V-SMOW). The early dolomite fluids have slightly positive $\delta^{18}\text{O}$ values between $+2.3$ and $+3.6\text{‰}$ V-SMOW, which may be compatible either with a more significant isotope exchange of the above-mentioned surface fluids with rocks, or with some mixing of surface fluids with waters rich in ^{18}O (e.g., magmatic waters or metamorphic waters; [67]). The fluid salinities decrease with the fluid $\delta^{18}\text{O}$ values in carbonate samples (Figure 12a), which favors the mixing hypothesis involving two fluids with contrasting salinities and $\delta^{18}\text{O}$ values. The quartz data yielded an opposite trend (Figure 12a); however, broad overlaps of fluid $\delta^{18}\text{O}$ values of both quartz samples are obvious, which leads to serious uncertainty. Nevertheless, quartz median values also fall to near-zero $\delta^{18}\text{O}$ area, but, in contrast to carbonates, there is a lack of correlation with fluid salinity. On the other hand, the fluid temperature shows good positive correlation when plotted against fluid $\delta^{18}\text{O}$ for all studied samples (Figure 12c).

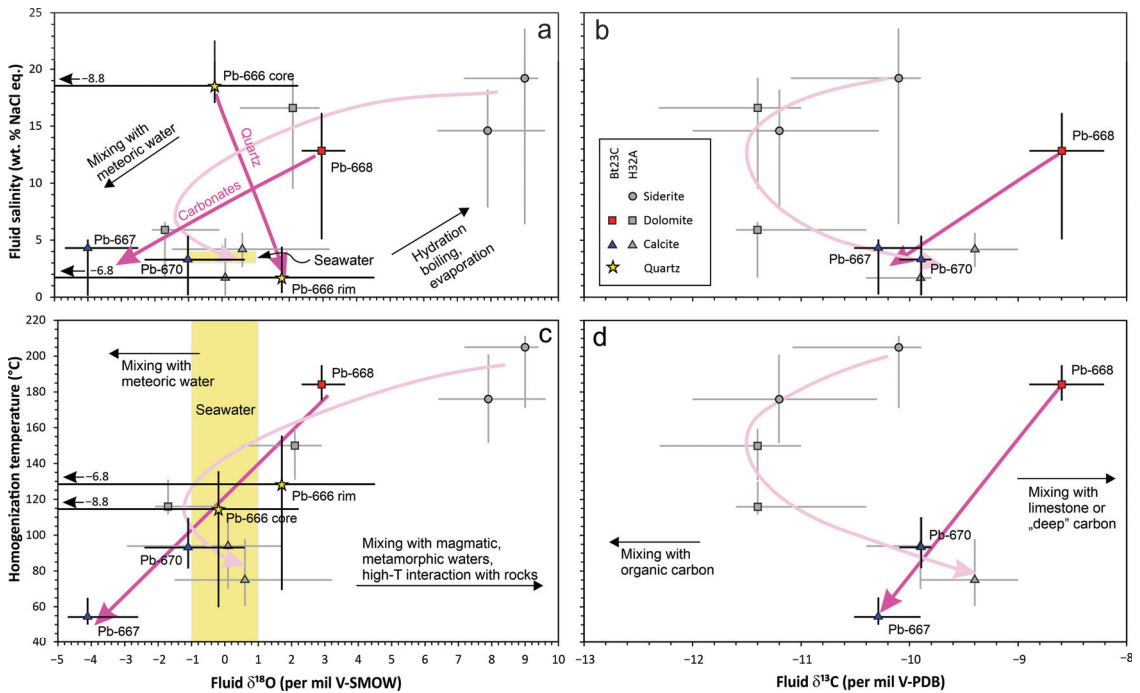


Figure 12. Ranges of calculated fluid $\delta^{13}\text{C}$ and $\delta^{18}\text{O}$ values for Stage 2 dolomite, Stage 3 calcite, and Stage 3 quartz samples from the vein Bt23C and their correlation with fluid salinity and homogenization temperatures of A_{L+V} fluid inclusions. (a) Fluid $\delta^{18}\text{O}$ vs. salinity plot. (b) Fluid $\delta^{13}\text{C}$ vs. salinity plot. (c) Fluid $\delta^{18}\text{O}$ vs. homogenization temperature plot. (d) Fluid $\delta^{13}\text{C}$ vs. homogenization temperature plot. Data points refer to median values of the whole data sets, bars refer to whole variability in the given sample. Arrows characterize the evolutionary trend. Note that few salinity and Th outliers were neglected for quartz Pb-666 and calcite Pb-667. The comparative data (gray color) from the Ag-Pb-Zn-Sb vein H32A, Hájé deposit, Příbram uranium and base metal district, are from [4].

The fluid $\delta^{13}\text{C}$ values calculated for all carbonates are much more consistent and range between -8.2 and -10.5‰ V-PDB (Table 5). Such values suggest a well-mixed source of carbon, originating potentially from limestones/marbles ($\delta^{13}\text{C}$ close to 0‰ V-PDB),

igneous or lower crust carbon ($\delta^{13}\text{C}$ values between -5 and -8‰ V-PDB), and carbon derived from oxidation of organic matter ($\delta^{13}\text{C}$ values between -20 and -35‰ V-PDB or even lower; [68]). Alternatively, it can be assumed that a significant intra-vein re-cycling of carbon took place during processes of dissolution of early vein carbonates, which were followed by precipitation of later carbonates from the same fluid. When plotting fluid $\delta^{13}\text{C}$ values against fluid salinity or temperature, similar negatively correlated trends are observed in both cases (Figure 12b,d), which can only be explained by the mixing of fluids with contrasting characteristics.

5.3. Possible Sources of the Fluids

Most important fluid events recorded in the Bt23C vein were also reported from other parts of the Příbram ore area, implying for the same fluid source and evolution. Previous studies [2,4] have demonstrated that three basic types of aqueous fluids participated during the formation of ore deposits in the Příbram area.

The earliest reported fluid is a high-temperature ($170\text{--}300\text{ °C}$), high-salinity ($15\text{--}24\text{ wt.}\%$ NaCl eq.), high- $\delta^{18}\text{O}$ ($7\text{‰}\text{--}10\text{‰}$ V-SMOW) Na>>Ca–Cl brine, which participated during the crystallization of the early portion of the siderite-sulphidic stage [2,4]. The ultimate origin of these fluids is not known, because although these fluids operated relatively soon after the ending of the Variscan metamorphic and magmatic activity, their composition is very different from those of metamorphic and/or magmatic fluids in the given area [29,62,69,70] (cf. composition of late-magmatic fluids from a porphyry-style Au deposit Petrůvka hora; Figure 11). The authors of [2,4] interpreted these fluids as deeply circulated waters, whose original signature was strongly modified due to a pronounced interaction with hot crustal rocks. In the Bt23C vein, these fluids were likely associated with the crystallization of early sphalerite, whose primary and pseudosecondary inclusions occupy an essentially identical field in the Th–Tm plot (Figure 8b). The end of this early stage could be associated with a decrease in salinity, homogenization temperature and/or fluid $\delta^{18}\text{O}$ value [2,4], as is also manifested by Bt23C dolomite data (Figures 8b and 12a,c).

The late portions of the vein paragenesis in the Příbram ore area crystallized from fluids, which were essentially sourced from surface waters. The most frequent are low-temperature ($\text{Th} < 150\text{ °C}$), low-salinity ($<7\text{ wt.}\%$ NaCl eq.), near-zero $\delta^{18}\text{O}$ (-3 to 3‰ V-SMOW) fluids, whose origin is mainly associated with partly evaporated Lower Permian freshwater piedmont basins, developed in the area at the time of mineralization [2,4]. At the vein Bt23C, the content of numerous low-salinity, low-temperature fluid inclusions hosted by quartz and calcite, characterized by near-zero fluid $\delta^{18}\text{O}$ values, can be related to this fluid source. The feasibility of the hypothesis dealing with the source of fluids in Permian basins is also supported by the V-rich compositions of phyllosilicates associated with quartz (Tables 1 and 2), since vanadium is a characteristic element of Permian basins and their mineralizations in the wider area [71–74].

The third type of fluids reported by [4] is hosted by some secondary fluid inclusions in calcite. Fluid inclusions are characterized by low homogenization temperatures ($<50\text{--}62\text{ °C}$), high salinity (ca. $30\text{ wt.}\%$ NaCl eq.) and Ca>Na–Cl composition. The authors of [4] interpreted these fluids as external basinal brines of marine provenance (e.g., [75]) or local upward migrating shield brines originating from the long-lasting interaction of meteoric waters and relatively cold crustal rocks [76]. This fluid endmember can be present in part of high-salinity inclusions hosted by quartz and calcite, namely, those with predominance of CaCl_2 over NaCl (Figure 11).

In addition, at least two other types of fluids participated during the formation of the vein Bt23C, up to date unknown from other sites in the Příbram ore area. The first one represents the low-temperature NaCl-dominated Na–Ca–Cl brines hosted by part of primary fluid inclusions in paragenetically late quartz and possibly also calcite (the Na/Ca ratios were not determined in calcite fluids). Although these fluids seem to have essentially identical chemical compositions to those of early NaCl-dominated Na–Ca–Cl brines hosted by sphalerite (Figure 11), we suggest that they must be predominantly sourced from a

surface source because of their much lower $\delta^{18}\text{O}$ values. These late fluids can be derived from marine sources, as was already above suggested for CaCl_2 -rich Na–Ca–Cl brines. The Late Variscan to post-Variscan low-temperature high-salinity chloridic fluids with highly variable Ca/Na ratios and near-zero $\delta^{18}\text{O}$ values are frequently reported from various types of vein mineralizations of the Bohemian Massif including the uranium deposits (e.g., [77–79]).

Another specific fluid is the quartz-hosted heterogeneous mixture of a carbonic phase and a medium-salinity aqueous solution. Such fluid was recognized for the first time in the Příbram ore area. The aqueous solution can represent a mixture of both the above-mentioned types of surface waters (i.e., chloride-rich brines and low-salinity basinal waters). The origin of associated volatiles can be explained in several ways. Firstly, gaseous components could be sourced from the deeper lithosphere and migrated upward along deep fault structures. This may be valid especially for CO_2 , because a significant portion of carbon bound in carbonates has a “deep” isotopic signature [2,4] and this work and CO_2 is usually a dominating compound among volatiles derived from lower parts of the Earth’s crust [31]. Secondly, some gases (including CO_2 , CH_4 , and N_2) could have been produced during the hydrothermal alteration of organic matter contained in sedimentary wall rocks and by radiolysis of hydrocarbons that were migrated together with aqueous fluids and gave rise to anthraxolite-bearing uranium mineralization, whose source is supposed in organic-matter rich horizons of the host Proterozoic sequences [80,81]. Thirdly, considering the participation of fluids from overlying Permian piedmont basins, we can assume that the source of volatiles (including CO_2 , CH_4 , and N_2) was due to the maturation of organic matter from coal seams, which occur at the base of sedimentary sequences of the neighbouring Blanice Graben [16,57]; sedimentary basins are in general the fertile sources of fluids with various gaseous compounds [53,82,83]. To date, we do not have enough information to allow for the unequivocal interpretation of the origin of volatiles, which is why further research is necessary to distinguish among the mentioned possibilities.

5.4. Constraints on Ore Genesis in the Příbram Area

The recognition of a fluid event characterized by activity of a CO_2 -rich carbonic phase together with an aqueous solution during formation of a typical Zn–Pb ore vein has some implications on interpretations of the genesis of the base-metal mineralization in the Příbram ore area.

A widespread feature of ore veins in the Příbram uranium and base-metal district is the partial corrosion of older vein filling followed by the cementation of free space by younger hydrothermal minerals. The dissolution experienced especially by carbonates (siderite, dolomite-ankerite) and sulphides (galena, sphalerite, Pb–Sb sulphosalts) was evidently a process, which occurred several times during the paragenetic evolution of the vein (e.g., [4,20,84–86]). Across the district, the most prominent signs of dissolution were recorded around the drusy cavities, fractures, grain boundaries, growth zones and cleavage planes of a mineral (Figure 13). The textural evidence indicates that an intense dissolution was experienced also by siderite, dolomite-ankerite and sphalerite in the vein Bt23C (Figure 3a,b). The best developed corrosion cavities were filled up by mineral phases coeval with or postdating the activity of CO_2 -dominated carbonic fluid. This suggests that the dissolution was caused by CO_2 -induced increased acidity of aqueous fluids. In this case, the mechanism of dissolution of carbonates can be characterized by reactions such as those illustrated by Equation (1).

The corrosion of earlier mineral phases was often also associated with the fracturing of the vein. Hence, the invasion of corroding fluids would be connected with tectonic movements, which likely re-opened the migration paths from the source of carbonic fluids to the hydrothermal system of the originating vein. As such, the flow of carbonic fluid would be a relatively short episode, which is consistent with a relatively rare occurrence of fluid inclusions containing this fluid system.

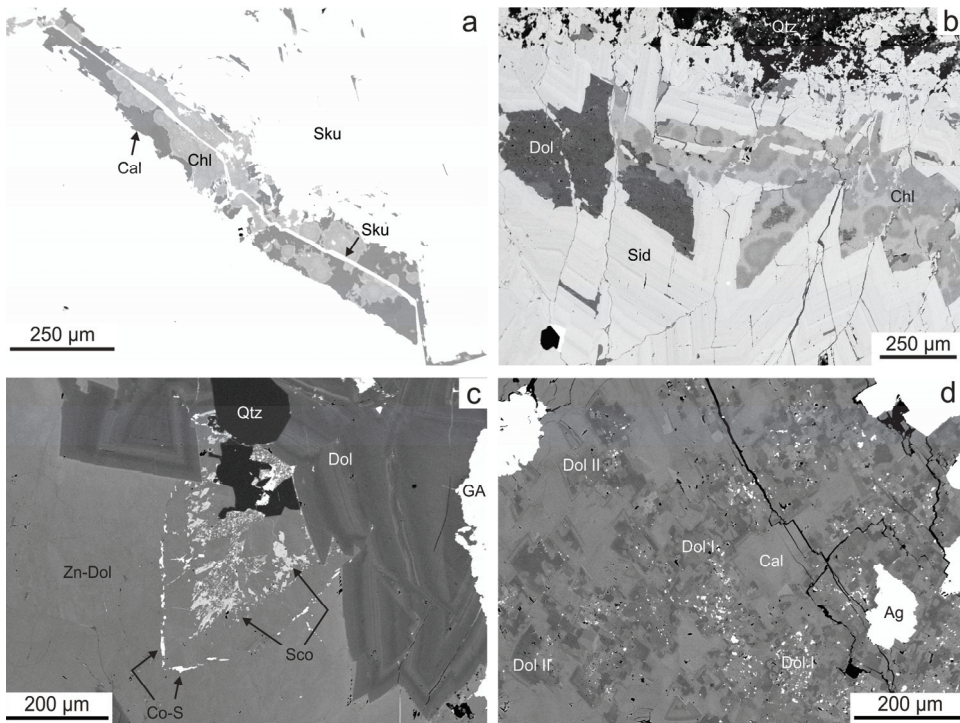


Figure 13. Examples of extensive corrosion and dissolution of older vein filling from other deposits in the Příbram uranium and base-metal district on BSE images. (a) Selective corrosion of certain growth zones in skutterudite (Sku), with free space filled up by zoned Ni-rich chlorite (Chl) and calcite (Cal). Sample Pb-847, dump sample, probably vein B128 (?), Brod deposit. (b) Selective dissolution of a growth zone in siderite (Sid), with open space being filled up by dolomite-ankerite (Dol) and zoned chlorite (Chl). Qtz—quartz. Sample Pb-859, vein H32A, Háje deposit. (c) Intense replacement of Mn,Zn-rich sphaerocobaltite (Sco) by Zn-rich dolomite (Zn-Dol). Original margin of crystal of sphaerocobaltite is lined by small crystals of a Co-sulphide (Co-S). Dol—dolomite, Qtz—quartz, GA—galena + native silver. Sample Pb-766, dump of the shaft No. 9, Jerusalem deposit. (d) Strongly corroded dolomite I (Dol I) with minute inclusions of native silver (white, Ag), followed by zoned dolomite II (Dol II) without any signs of dissolution. Remaining space is filled up by calcite (Cal). Sample Pb-756, vein B117, Brod deposit, 6th mine level.

The interaction of CO₂-rich carbonic fluid with earlier vein fill rich in sulphides and carbonates would lead to a progressive decrease in the acidity of the original fluid due to the consumption of CO₂ (Equation (1)) down to levels at which new portions of carbonates and/or sulphides begin to crystallize. In such a scenario, the substantial re-cycling of mineral-forming components is likely, which can be suggested from the existing chemical and isotopic data, although some alternative explanations could also be possible. The close $\delta^{13}\text{C}$ values of carbonates (siderite, dolomite-ankerite, and calcite) from various mineralization stages were confirmed by this study and [4]. Furthermore, elevated contents of Mn are reported in all these carbonates, although they evidently crystallized from distinctly sourced fluids ([2,4], as well as this work). Similarly, all generations of sphalerite in the vein H32A are anomalously enriched in In and Sn [4] pointing to possible re-cycling of these elements by later fluids. The uniform Pb isotopic composition of galena from various paragenetic stages was interpreted in terms of the re-cycling of ore lead deposited in the earliest stage [2]. The very local re-cycling of vein components is also nicely mirrored

in the chemical composition of chlorite: if chlorite crystallized in the vein portion containing Pb-Sb sulphosalts, it becomes enriched in Sb (H32A vein—[4]), whereas if it grew in another part of the same vein without Sb-minerals, it is Sb-absent (Bt23C vein—this work; H32A vein—[4]).

The slight increase in $\delta^{13}\text{C}$ values of parent fluids, from which the paragenetically late calcite crystallized in the vein H32A (Figure 12b,d) but was unrecognized in the vein Bt23C (Figure 12b,d), can be related to isotope fractionation caused by the local CO_2 degassing of the fluids, as hypothesized by [4]. The pH changes of hydrothermal fluids caused by fluid-rock/gangue reactions involving CO_2 can be the reason for sulphur isotopic disequilibrium between co-existing galena and sphalerite, as suggested by [4] in case of the H32A vein.

The widely scattered Th and salinity data similar to those of the studied quartz also characterize aqueous inclusions hosted by quartz II from the base-metal vein H32A occurring in essentially identical paragenetic position (i.e., postdating dolomite-ankerite, contemporaneous with chlorite, and preceding calcite [4]). The H32A sample, however, contained only a very small amount of CO_2 in the fluid inclusions, detectable in vapour bubbles by Raman analysis, but not by corresponding phase transitions during cooling. Nevertheless, it seems plausible that the quartz-hosted CO_2 -bearing fluid inclusions may represent a district-scale fluid episode. The traceability of this mineralizing event across the wider area is also highlighted by very low oxygen fugacities of parent fluids ($\log f_{\text{O}_2}$ ranging between -71 and -56 bar) calculated from the chemical composition of associated chlorite (Table 2, Figure 14), which are essentially identical for the veins Bt23C and H32A (Figure 14).

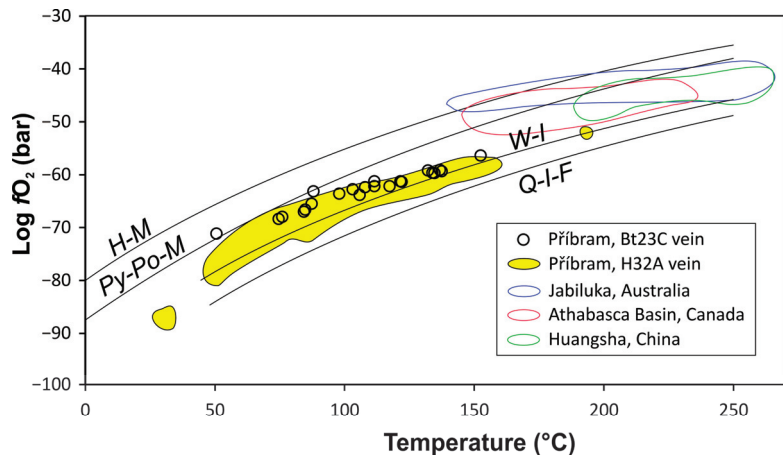


Figure 14. Temperature- f_{O_2} plot for chlorites from the vein Bt23C. Reference curves of common buffers were calculated from data presented by [87]. Comparative data from the H32A vein are from [4], and data for some other uranium deposits are from [88–91]. Abbreviations: F—fayalite, H—hematite, I—iron, M—magnetite, Po—pyrrhotite, Py—pyrite, Q—quartz, W—wüstite.

6. Conclusions

The Bt23C vein, hosted by folded Proterozoic clastic sediments in exo-contact of a large Variscan granite pluton, represents a typical development of Late-Variscan base-metal Zn>Pb mineralization of the Přebřam ore area. Sphalerite and galena ores are hosted by gangue formed especially by Mn-enriched carbonates including early siderite, younger dolomite-ankerite, and late calcite. Quartz, baryte, chlorite, and V-rich mica (roscoelite to an unnamed V-analogue of illite) are subordinate components of the gangue. Banded and drusy textures of the vein were significantly modified by intra-vein dissolution and replacement by later hydrothermal mineral phases.

The fluid inclusion study conducted on sphalerite, dolomite-ankerite, calcite, baryte, and quartz revealed the overall decrease in fluid temperature (from ~210 to ~50 °C) throughout the paragenetic sequence, whereas salinity varied significantly from pure water up to 27 wt.% NaCl eq. A short episode characterized by the activity of a mixture of a medium-salinity aqueous solution and a CO₂-dominated carbonic phase was identified during the crystallization of quartz.

The C and O stable isotope study conducted on carbonates and quartz yielded low calculated fluid δ¹⁸O values (−4.7 to +3.6‰ V-SMOW), suggesting the predominance of surface waters, while fluid δ¹³C values (−8.2 to −10.5‰ V-PDB) are likely linked to well-mixed “deep” and organic sources of carbon.

Three sources of aqueous fluids are suggested based on available data: (i) early high-temperature high-salinity Na>Ca-Cl fluids from an unspecified “deep” source; (ii) late low-salinity low-temperature waters, likely infiltrating from overlying Permian partly evaporated freshwater piedmont basins; (iii) late high-salinity chloridic solutions with both high and low Ca/Na ratios, which can represent either externally derived marine brines, or local shield brines. The source of CO₂-rich volatiles can be seen in (i) deep crust, (ii) sedimentary wall rocks, and (iii) overlying Permian piedmont basins containing, in places, coal seams.

The newly recognized fluid episode dealing with an immiscible aqueous–carbonic fluid mixture allowed for the precise calculation of pressure conditions of ore formation (100–270 bar), which were poorly constrained up to now. Moreover, the occurrence of a CO₂-rich fluid episode gave possible reasons for some previously reported genetic aspects of the Příbram ores, including the widespread corrosion of the early vein fill, re-cycling of some vein components, S isotope disequilibrium among co-existing sulphides, and δ¹³C shifts due to CO₂ degassing.

Author Contributions: Conceptualization, J.U. and Z.D.; investigation, J.U. and Z.D.; resources, P.Š.; writing—original draft preparation, J.U., Z.D., P.Š. and J.S.; writing—review and editing, J.U., Z.D., P.Š. and J.S. All authors have read and agreed to the published version of the manuscript.

Funding: This research was funded by the Czech Science Foundation, grant number 19-16218S and by the Ministry of Culture of the Czech Republic (long-term project DKRVO 2024–2028/1.I.a; National Museum, 00023272).

Data Availability Statement: All data are contained in this work.

Acknowledgments: F. Buzek, B. Čejková (Czech Geological Survey, Prague), and T. Vennemann (University of Lausanne) are thanked for stable isotope analyses of carbonates and quartz, respectively. L. Vrtiška (National Museum, Prague) is acknowledged for photography of the sample Pb-668 (Figure 3f). Constructive comments by two journal reviewers are highly appreciated.

Conflicts of Interest: The authors declare no conflict of interest. The funders had no role in the design of the study; in the collection, analyses, or interpretation of data; in the writing of the manuscript; or in the decision to publish the results.

References

1. Litochleb, J.; Černý, P.; Litochlebová, E.; Sejkora, J.; Šreinová, B. The deposits and occurrences of mineral raw materials in the Střední Brdy Mts. and the Brdy piedmont area (Central Bohemia). *Bull. Miner.-Petr. Odd. Nár. Muz.* **2003**, *12*, 57–86. (In Czech)
2. Žák, K.; Dobeš, P. Stable isotopes and fluid inclusions in hydrothermal deposits: The Příbram ore region. *Rozpr. Čs. Akad. Věd* **1991**, 1–109.
3. Hamet, P. Nature of Fluid Inclusions in Some Hydrothermal Minerals from the Příbram Ore District. Bachelor Thesis, Masaryk University Brno, Brno, Czech Republic, 2013. (In Czech)
4. Dolníček, Z.; Ulmanová, J.; Sejkora, J.; Knižek, F.; Škácha, P. Mineralogy and genesis of the Pb-Zn-Sb-Ag vein H32A in the Příbram uranium and base-metal district, Bohemian Massif, Czech Republic. *Ore Geol. Rev.* **2023**, *162*, 105695. [CrossRef]
5. Dallmeyer, R.D.; Urban, M. Variscan versus Cadomian tectonothermal activity in northwestern sectors of the Teplá–Barrandian zone, Czech Republic: Constraints from ⁴⁰Ar/³⁹Ar ages. *Geol. Rundsch.* **1998**, *87*, 94–106. [CrossRef]

6. Zulauf, G.; Schritter, F.; Riegler, G.; Finger, F.; Fiala, J.; Vejnar, Z. Age constraints on the Cadomian evolution of the Teplá–Barrandian unit (Bohemian Massif) through electron microprobe dating of metamorphic monazite. *Zt. Deutsch. Geol. Ges.* **1999**, *180*, 627–639. [CrossRef]
7. Franke, W. The mid-European segment of the Variscides: Tectonostratigraphic units, terrane boundaries and plate tectonic evolution. In *Orogenic Processes: Quantification and Modelling in the Variscan Belt*; Franke, W., Haack, V., Oncken, O., Tanner, D., Eds.; Special Publications, Geological Society: London, UK, 2000; Volume 179, pp. 35–56.
8. Dörr, W.; Zulauf, G.; Fiala, J.; Franke, W.; Vejnar, Z. Neoproterozoic to Early Cambrian history of an active plate margin in the Teplá–Barrandian unit—A correlation of U–Pb isotopic dilution-TIMS ages (Bohemia, Czech Republic). *Tectonophysics* **2002**, *352*, 65–85. [CrossRef]
9. Sláma, J.; Dunkley, D.J.; Kachlík, V.; Kusiak, M.A. Transition from island-arc to passive setting on the continental margin of Gondwana: U–Pb zircon dating of Neoproterozoic metaconglomerates from the SE margin of the Teplá–Barrandian Unit, Bohemian Massif. *Tectonophysics* **2008**, *461*, 44–59. [CrossRef]
10. Hajná, J.; Žák, J.; Kachlík, V.; Chadima, M. Deciphering the Variscan tectonothermal overprint and deformation partitioning in the Cadomian basement of the Teplá–Barrandian unit, Bohemian Massif. *Int. J. Earth Sci. (Geol. Rundsch.)* **2012**, *101*, 1855–1873. [CrossRef]
11. Dörr, W.; Zulauf, G. Elevator tectonics and orogenic collapse of a Tibetan-style plateau in the European Variscides: The role of the Bohemian shear zone. *Int. J. Earth Sci. (Geol. Rundsch.)* **2010**, *99*, 299–325. [CrossRef]
12. Holub, F.V.; Cocherie, A.; Rossi, P. Radiometric dating of granitic rocks from the Central Bohemian Plutonic Complex (Czech Republic): Constraints on the chronology of the thermal and tectonic events along the Moldanubian–Barrandian boundary. *Compt. Rend. Acad. Sci. Paris Earth Planet. Sci.* **1997**, *325*, 19–26. [CrossRef]
13. Janoušek, V.; Gerdes, A. Timing the magmatic activity within the Central Bohemian Pluton, Czech Republic: Conventional U–Pb ages for the Sázava and Tábor intrusions and their geotectonic significance. *J. Czech Geol. Soc.* **2003**, *48*, 70–71.
14. Žák, J.; Holub, F.V.; Verner, K. Tectonic evolution of a continental magmatic arc from transpression in the upper crust to exhumation of mid-crustal orogenic root recorded by episodically emplaced plutons: The Central Bohemian Plutonic Complex (Bohemian Massif). *Int. J. Earth Sci. (Geol. Rundsch.)* **2005**, *94*, 385–400. [CrossRef]
15. Janoušek, V.; Wiegand, B.; Žák, J. Dating the onset of Variscan crustal exhumation in the core of the Bohemian Massif: New U–Pb single zircon ages from the high-K calc-alkaline granodiorites of the Blatná suite, Central Bohemian Plutonic Complex. *J. Geol. Soc.* **2010**, *167*, 347–360. [CrossRef]
16. Pešek, J.; Holub, V.; Jaroš, J.; Malý, L.; Martínek, K.; Prouza, V.; Spudil, J.; Tásler, R. *Geology and Deposits of the Upper Paleozoic Limnic Basins of the Czech Republic*; Czech Geological Survey: Prague, Czech Republic, 2001; 243p. (In Czech)
17. Martínek, K.; Blecha, M.; Daněk, V.; Franců, J.; Hladíková, J.; Johnová, R.; Uličný, D. Record of palaeoenvironmental changes in a Lower Permian organic-rich lacustrine succession: Integrated sedimentological and geochemical study of the Rudník member, Krkonoše Piedmont Basin, Czech Republic. *Palaeogeogr. Palaeoclimat. Palaeoecol.* **2006**, *230*, 85–128. [CrossRef]
18. McCann, T. *The Geology of Central Europe: Precambrian and Palaeozoic*; Geological Society: London, UK, 2008.
19. Komínek, J. *Geology of the Wide Surroundings and of the Deposit, Part I and II. Final Report on the Uranium District Příbram*; Unpublished Report; DIAMO: Příbram, Czech Republic, 1995; 418p. (In Czech)
20. Sejkora, J.; Dolníček, Z.; Zachariáš, J.; Ulmanová, J.; Šrein, V.; Škácha, P. Mineralogical and fluid inclusion evidence for reworking of Au mineralization by Ag-Sb-base metal-rich fluids from the Bytíz deposit, Příbram uranium and base-metal ore district, Czech Republic. *Minerals* **2022**, *12*, 1539. [CrossRef]
21. Piša, M. Mineralogenesis of the Pb-Zn deposit in Bohutín near Příbram. *Sbor. Geol. Věd, Lož. Geol.* **1966**, *7*, 1–164. (In Czech)
22. Komínek, J. *Paragenetic Sequence of Hydrothermal Minerals at the Příbram Uranium Deposits*; Unpublished report; Československý uranový průmysl: Příbram, Czech Republic, 1972. (In Czech)
23. Blüml, A.; Slačik, J.; Tacl, A. *Mineralogical Investigation of the Pošepečný Vein at the Vrančice Deposit South of Milín*; Unpublished report; Rudné doly: Příbram, Czech Republic, 1975. (In Czech)
24. Příbram District. Available online: <https://www.mindat.org/loc-779.html> (accessed on 20 December 2022).
25. Žák, K.; Vlačšímský, P.; Snee, L.W. ⁴⁰Ar/³⁹Ar cooling ages of selected rocks of the Příbram ore region and the question of timing of sulfidic hydrothermal mineralization. *Geosci. Res.* **1997**, *172*–173.
26. Kříbek, B. K-Ar mica/illite and Rb-Sr sphalerite dating and geotectonic setting of Late Variscan and Post-Variscan sulphide and uranium mineralizations of the Bohemian Massif (Czech Republic). In Proceedings of the 11th SGA Biennial Meeting, Antofagasta, Chile, 26–29 September 2011; pp. 108–110.
27. Anderson, E.B. *Isotopic-Geochronological Investigation of the Uranium Mineralization of Czechoslovakia*; Unpublished Report 1962-87; Czechoslovak Uranium Industry: Příbram, Czech Republic, 1987.
28. Prokeš, S.; Knížek, F. Polymetallic ore mineralization at the Příbram uranium deposit. *Sbor Symp. Horn. Příbram Vědě Techn. Lož. Geol.* **1986**, *87*–99. (In Czech)
29. Author Collective. *General Calculation of Reserves of the Příbram Uranium Deposit to 1.1.1984*; Unpublished report; DIAMO SUL: Příbram, Czech Republic, 1984. (In Czech)
30. Pouchou, J.L.; Pichoir, F. “PAP” (φρZ) procedure for improved quantitative microanalysis. In *Microbeam Analysis*; Armstrong, J.T., Ed.; San Francisco Press: San Francisco, CA, USA, 1985; pp. 104–106.

31. Roedder, E. Fluid inclusions. *Rev. Mineral.* **1984**, *12*, 1–644.
32. Goldstein, R.H.; Reynolds, T.J. Systematics of fluid inclusions in diagenetic minerals: SEPM Short Course 31. *Soc. Sediment. Geol.* **1994**, *199*. [CrossRef]
33. Bodnar, R.J. Revised equation and table for determining the freezing point depression of H₂O–NaCl solutions. *Geochim. Cosmochim. Acta* **1993**, *57*, 683–684. [CrossRef]
34. Diamond, L.W. Stability of CO₂ clathrate hydrate + CO₂ liquid + CO₂ vapour + aqueous KCl–NaCl solutions: Experimental determination and application to salinity estimates of fluid inclusions. *Geochim. Cosmochim. Acta* **1992**, *56*, 273–280. [CrossRef]
35. Bozzo, A.T.; Chen, J.R.; Barduhn, A.J. The properties of hydrates of chlorine and carbon dioxide. In Proceedings of the 4th International Symposium on Fresh Water from the Sea 3, Heidelberg, Germany, 4–9 September 1973; Delyannis, A., Delyannis, E., Eds.; pp. 437–451.
36. Bakker, R.J. Package FLUIDS 1. Computer programs for analysis of fluid inclusion data and for modelling bulk fluid properties. *Chem. Geol.* **2003**, *194*, 3–23. [CrossRef]
37. Soave, G. Equilibrium constants from a modified Redlich–Kwong equation of state. *Chem. Engineer. Sci.* **1972**, *27*, 1197–1203. [CrossRef]
38. Duan, Z.; Møller, N.; Weare, J.H. An equation of state for the CH₄–CO₂–H₂O system: II. Mixtures from 50 to 1000 °C and 0 to 1000 bar. *Geochim. Cosmochim. Acta* **1992**, *56*, 2619–2631. [CrossRef]
39. Duan, Z.; Møller, N.; Weare, J.H. A general equation of state for supercritical fluid mixtures and molecular dynamics simulation of mixture PVTX properties. *Geochim. Cosmochim. Acta* **1996**, *60*, 1209–1216. [CrossRef]
40. Burke, E.A.J. Raman microspectrometry of fluid inclusions. *Lithos* **2001**, *55*, 139–158. [CrossRef]
41. McCrea, J.M. On the isotopic chemistry of carbonates and a palaeotemperature scale. *J. Chem. Phys.* **1950**, *18*, 849–857. [CrossRef]
42. Friedman, I.; O’Neil, J.R. *Compilation of Stable Isotope Fractionation Factors of Geochemical Interest*; United States Geological Survey: Reston, Virginia, 1977; pp. 1–12.
43. O’Neil, J.R.; Clayton, R.N.; Mayeda, T.K. Oxygen isotope fractionation in divalent metal carbonates. *J. Chem. Phys.* **1969**, *51*, 5547–5558. [CrossRef]
44. Zheng, Y.F. Calculation of oxygen isotope fractionation in anhydrous silicate minerals. *Geochim. Cosmochim. Acta* **1993**, *57*, 1079–1091. [CrossRef]
45. Ohmoto, H.; Goldhaber, M.B. Sulfur and carbon isotopes. In *Geochemistry of Hydrothermal Ore Deposits*, 3rd ed.; Barnes, H.L., Ed.; J. Wiley & Sons: New York, NY, USA, 1997; pp. 517–611.
46. Bayliss, P. Nomenclature of the trioctahedral chlorites. *Can. Mineral.* **1975**, *13*, 178–180.
47. Inoue, A.; Inoué, S.; Utada, M. Application of chlorite thermometry to estimation of formation temperature and redox conditions. *Clay Miner.* **2018**, *53*, 143–158. [CrossRef]
48. Borisenko, A.S. Izučenie solevovo sostava rastvorov gazovo-židkikh vključenij v mineralach metodom kriometrii. *Akad. Nauk SSSR Sibir. Odd.* **1977**, *8*, 16–27. (In Russian)
49. Ramboz, C.; Pichavant, M.; Weisbrod, A. Fluid immiscibility in natural processes: Use and misuse of fluid inclusion data: I. Phase equilibria analysis—A theoretical and geometrical approach. *Chem. Geol.* **1982**, *37*, 1–27. [CrossRef]
50. Vityk, M.O.; Bodnar, R.J. Textural evolution of synthetic fluid inclusions in quartz during reequilibration, with applications to tectonic reconstruction. *Contrib. Mineral. Petrol.* **1995**, *121*, 309–323. [CrossRef]
51. Vityk, M.O.; Bodnar, R.J.; Dudok, I.V. Fluid inclusions in “Marmarosh Diamonds”: Evidence for tectonic history of the Folded Carpathian Mountains, Ukraine. *Tectonophysics* **1996**, *255*, 163–174. [CrossRef]
52. Roedder, E.; Bodnar, R.J. Geologic pressure determinations from fluid inclusion studies. *Ann. Rev. Earth Planet. Sci.* **1980**, *8*, 263–301. [CrossRef]
53. Hurai, V.; Kihle, J.; Kotulová, J.; Marko, F.; Świerczewska, A. Origin of methane in quartz crystals from the Tertiary accretionary wedge and fore-arc basin of the Western Carpathians. *Appl. Geochem.* **2002**, *17*, 1259–1271. [CrossRef]
54. Dolníček, Z.; Kropáč, K.; Janičková, K.; Urubek, T. Diagenetic source of fluids causing the hydrothermal alteration of teschenites in the Silesian Unit, Outer Western Carpathians, Czech Republic: Petroleum-bearing vein mineralization from the Stříbrník site. *Mar. Petrol. Geol.* **2012**, *37*, 27–40. [CrossRef]
55. Spycher, N.; Pruess, K.; Ennis-King, J. CO₂–H₂O mixtures in the geological sequestration of CO₂. I. Assessment and calculation of mutual solubilities from 12 to 100 °C and up to 600 bar. *Geochim. Cosmochim. Acta* **2003**, *67*, 3015–3031. [CrossRef]
56. Diamond, L.W. Introduction to phase relations of CO₂–H₂O fluid inclusions. In *Fluid Inclusions in Minerals: Methods and Applications*; De Vivo, B., Frezzotti, M.L., Eds.; Pontignano: Siena, Italy, 1994; pp. 131–158.
57. Suchý, V.; Zachariáš, J.; Sýkorová, I.; Kořínková, D.; Pešek, J.; Pachnerová Brabcová, K.; Luo, Q.; Filip, J.; Světlík, I. Palaeo-thermal history of the Blanice Graben (the Bohemian Massif, Czech Republic): The origin of anthracite in a late-Variscan strike-slip basin. *Int. J. Coal Geol.* **2022**, *263*, 104129. [CrossRef]
58. Ramsay, J.G. The crack-seal mechanism of rock deformation. *Nature* **1980**, *284*, 135–139. [CrossRef]
59. Urubek, T.; Dolníček, Z.; Kropáč, K. Genesis of syntectonic hydrothermal veins in the igneous rock of teschenite association (Outer Western Carpathians, Czech Republic): Growth mechanism and origin of fluids. *Geol. Carpath.* **2014**, *65*, 419–431. [CrossRef]
60. Oakes, C.S.; Bodnar, R.J.; Simonson, J.M. The system NaCl–CaCl₂–H₂O. I.: The ice liquidus at 1 atm total pressure. *Geochim. Cosmochim. Acta* **1990**, *54*, 603–610. [CrossRef]

61. Shepherd, T.J.; Rankin, A.H.; Alderton, D.H.M. *A Practical Guide to Fluid Inclusion Studies*; Blackie: Glasgow, Scotland; London, UK, 1985.
62. Zachariáš, J.; Pertold, Z.; Pudilová, M.; Žák, K.; Pertoldová, J.; Stein, H.; Markey, R. Geology and genesis of Variscan porphyry style gold mineralization, Petrářkova hora deposit, Bohemian Massif, Czech Republic. *Miner. Deposita* **2001**, *36*, 517–541. [CrossRef]
63. Dublyansky, Y.V. Speleogenetic history of the Hungarian hydrothermal karst. *Environm. Geol.* **1995**, *25*, 24–35. [CrossRef]
64. Markl, G.; Burisch, M.; Neumann, U. Natural fracking and the genesis of five-element veins. *Miner. Deposita* **2016**, *51*, 703–712. [CrossRef]
65. Burisch, M.; Gerdes, A.; Walter, B.F.; Neumann, U.; Fettel, M.; Markl, G. Methane and the origin of five-element veins: Mineralogy, age, fluid inclusion chemistry and ore forming processes in the Odenwald, SW Germany. *Ore Geol. Rev.* **2017**, *81*, 42–61. [CrossRef]
66. Zhu, D.; Liu, Q.; Zhang, J.; Ding, Q.; He, Z.; Zhang, X. Types of fluid alteration and developing mechanism of deep marine carbonate reservoirs. *Geofluids* **2019**, *3630915*, 1–18. [CrossRef]
67. Sheppard, S.M.F. Characterization and isotopic variations in natural waters. *Rev. Mineral.* **1986**, *16*, 165–183.
68. Hoefs, J. *Stable Isotope Geochemistry*, 4th ed.; Springer: Berlin/Heidelberg, Germany; New York, NY, USA, 1997.
69. Zachariáš, J.; Pudilová, M.; Žák, K.; Morávek, P.; Litochleb, J.; Váňa, T.; Pertold, Z. P-T-X conditions of gold-bearing mineralization within the Central Bohemian Metallogenic Zone. *Acta Univ. Carol. Geol.* **1997**, *41*, 167–178.
70. Zachariáš, J.; Žák, K.; Pudilová, M.; Snee, L.W. Multiple fluid sources/pathways and severe thermal gradients during formation of the Jílové orogenic gold deposit, Bohemian Massif, Czech Republic. *Ore Geol. Rev.* **2013**, *54*, 81–109. [CrossRef]
71. Johan, Z.; Povondra, P. Vanadium- and copper-bearing dolomite nodules from Permian sediments near Horní Kalná, Czechoslovakia. *N. Jahrb. Mineral. Abh.* **1987**, *157*, 245–266.
72. Vavříň, I.; Frýda, J. Cu-Ag-V-Hg mineralization in melaphyre from Studenec near Jilemnice (Podkrkonoší area). *J. Czech geol. Soc.* **1996**, *41*, 33–41. (In Czech)
73. Vytopilová, H. Mineralogy of Hydrothermal Occurrences with Cu-Mineralization in Palaeovolcanites of the Podkrkonoší Area. Master's Thesis, Palacký University, Olomouc, Czech Republic, 2011. (In Czech)
74. Havelcová, M.; Sýkorová, I.; René, M.; Mizera, J.; Coubal, M.; Machovič, V.; Strunga, V.; Goliáš, V. Geology and petrography of uraniumiferous bitumens in Permo-Carboniferous sediments (Vrchlabí, Czech Republic). *Minerals* **2022**, *12*, 544. [CrossRef]
75. Bottomley, D.J.; Gregoire, C.D.; Ravens, K.G. Saline groundwaters and brines in the Canadian Shield: Geochemical and isotopic evidence for a residual evaporite brine component. *Geochim. Cosmochim. Acta* **1994**, *58*, 1483–1498. [CrossRef]
76. Frapé, S.K.; Fritz, P. Geochemical trends from groundwaters from the Canadian Shield. In *Saline Waters and Gases in Crystalline Rocks*; Fritz, P., Frapé, S.K., Eds.; Geological Association of Canada: St. John's, NL, Canada, 1987; Volume 33, pp. 19–38.
77. Kříbek, B.; Žák, K.; Dobeš, P.; Leichmann, J.; Pudilová, M.; René, M.; Scharm, B.; Scharmová, M.; Hájek, A.; Holeczy, D.; et al. The Rožná uranium deposit (Bohemian Massif, Czech Republic): Shear zone-hosted, late Variscan and post-Variscan hydrothermal mineralization. *Miner. Deposita* **2009**, *44*, 99–128. [CrossRef]
78. Dolníček, Z.; Fojt, B.; Prochaska, W.; Kučera, J.; Sulovský, P. Origin of the Zálesí U–Ni–Co–As–Ag/Bi deposit, Bohemian Massif, Czech Republic: Fluid inclusion and stable isotope constraints. *Miner. Deposita* **2009**, *44*, 81–97. [CrossRef]
79. Dolníček, Z.; René, M.; Hermannová, S.; Prochaska, W. Origin of the Okrouhlá Radouň episyenite-hosted uranium deposit, Bohemian Massif, Czech Republic: Fluid inclusion and stable isotope constraints. *Miner. Deposita* **2014**, *49*, 409–425. [CrossRef]
80. Kříbek, B.; Žák, K.; Spangenberg, J.E.; Jehlička, J.; Prokeš, S.; Komínek, J. Bitumens in the late Variscan hydrothermal vein-type uranium deposit of Příbram, Czech Republic: Sources, radiation-induced alteration, and relation to mineralization. *Econ. Geol.* **1999**, *94*, 1093–1114. [CrossRef]
81. Straka, P. Anthraxolite-uranium mineral: Composition, structural features and genesis. *Asp. Min. Miner. Sci.* **2020**, *5*, 623. [CrossRef]
82. Littke, R.; Krooss, B.M.; Idiz, E.F.; Frielingsdorf, J. Molecular nitrogen in natural gas accumulations: Generation from sedimentary organic matter at high temperatures. *Am. Assoc. Petrol. Geol. Bull.* **1995**, *79*, 410–430.
83. Lüders, V.; Reutel, C.; Hoth, P.; Banks, D.A.; Mingram, B.; Pettke, T. Fluid and gas migration in the North German Basin: Fluid inclusion and stable isotope constraints. *Int. J. Earth Sci.* **2005**, *94*, 990–1009. [CrossRef]
84. Kutina, J. Genetische Diskussion der Makrostrukturen bei der geochemischen Untersuchung des Adalbert-Hauptganges in Příbram. *Chem. Erde* **1955**, *17*, 241–323.
85. Škácha, P.; Sejkora, J.; Plášil, J.; Dolníček, Z.; Ulmanová, J. Grimmitite, NiCO₂S₄, a new thiospinel from Příbram, Czech Republic. *Eur. J. Mineral.* **2021**, *33*, 175–187. [CrossRef]
86. Sejkora, J.; Dolníček, Z.; Škácha, P.; Ulmanová, J.; Vrtiška, L. Unusual mineralization with willemite from the area of the central part of the Příbram uranium and base-metal district (Czech Republic). *Bull. Mineral. Petrolog.* **2022**, *30*, 224–242. (In Czech) [CrossRef]
87. Frost, B.R. Introduction to oxygen fugacity and its petrologic importance. *Rev. Mineral. Geochem.* **1991**, *25*, 1–9.
88. Nutt, C.J. Chloritization and associated alteration at the Jabiluka unconformity-type uranium deposit, Northern Territory, Australia. *Can. Mineral.* **1989**, *27*, 41–58.
89. Alexandre, P.; Kyser, K.; Polito, P. Alteration mineralogy and stable isotope geochemistry of Paleoproterozoic basement hosted unconformity-type uranium deposits in the Athabasca Basin, Canada. *Econ. Geol.* **2005**, *100*, 1547–1563. [CrossRef]

90. Alexandre, P.; Kyser, K.; Jiricka, D.; Witt, G. Formation and evolution of the Centennial unconformity-related uranium deposit in the south-central Athabasca Basin, Canada. *Econ. Geol.* **2012**, *107*, 385–400. [CrossRef]
91. Wu, D.; Pan, J.; Xia, F.; Huang, G.; Lai, J. The mineral chemistry of chlorites and its relationship with uranium mineralization from Huangsha uranium mining area in the Middle Nanling Range, SE China. *Minerals* **2019**, *9*, 199. [CrossRef]

Disclaimer/Publisher’s Note: The statements, opinions and data contained in all publications are solely those of the individual author(s) and contributor(s) and not of MDPI and/or the editor(s). MDPI and/or the editor(s) disclaim responsibility for any injury to people or property resulting from any ideas, methods, instructions or products referred to in the content.

MDPI AG
Grosspeteranlage 5
4052 Basel
Switzerland
Tel.: +41 61 683 77 34

Minerals Editorial Office
E-mail: minerals@mdpi.com
www.mdpi.com/journal/minerals



Disclaimer/Publisher's Note: The statements, opinions and data contained in all publications are solely those of the individual author(s) and contributor(s) and not of MDPI and/or the editor(s). MDPI and/or the editor(s) disclaim responsibility for any injury to people or property resulting from any ideas, methods, instructions or products referred to in the content.



Academic Open
Access Publishing

mdpi.com

ISBN 978-3-7258-2272-0